



Grant Agreement No.: 226479

# SafeLand

Living with landslide risk in Europe: Assessment,  
effects of global change, and risk management strategies

7<sup>th</sup> Framework Programme  
Cooperation Theme 6 Environment (including climate change)  
Sub-Activity 6.1.3 Natural Hazards

## Deliverable 4.1

Review of Techniques for Landslide Detection, Fast Characterization, Rapid  
Mapping and Long-Term Monitoring

Work Package 4.2 – Remote Sensing Technologies for Landslide Detection,  
Monitoring and Rapid Mapping

Deliverable Leader: Unil

Revision: 2 – Approved

February 2012

Rev.	Deliverable Responsible	Controlled by	Date
0	UNIL	Specialized research institutes	Summer 2010
1	UNIL	ICG-NGI	October 2010
2	UNIL (updated version)		February 2012



## SUMMARY

One of the main aims of the European project SafeLand in the 7<sup>th</sup> Framework Program is to develop innovative mapping and monitoring methods in order to improve the methods for regional landslide risk assessment and design of early warning systems. More specifically, Area 4 of SafeLand addresses the technical and practical issues related to monitoring and early warning for landslides. During the last decade, different monitoring and remote sensing techniques have undergone rapid development. In order to summarize these scientific and technical advances, the University of Lausanne, in close collaboration with 18 European institutions, has produced the project Deliverable 4.1: *Review of Techniques for Landslide Detection, Fast Characterization, Rapid Mapping and Long-Term Monitoring*<sup>1</sup>.

The core of this deliverable consists of two main chapters:

- (a) Chapter two summarizes, from a theoretical point of view, the different ground-based and remote sensing techniques currently used to investigate, map and monitor landslides. Each technique described in the deliverable has benefited from the expertise of specialized research groups.
- (b) Chapter three shows the main applications of the remote sensing techniques to landslides through the synthesis of seventeen case studies.

This review aims to represent a common reference for the different deliverables of SafeLand Area 4. In addition to being a state-of-the art overview, this deliverable provides helpful and extensive support for non-specialists and students interested in the application of new techniques to different mass movements such as landslides, rockfall, etc.

---

<sup>1</sup> To quote this document:

SafeLand deliverable 4.1, 2010. *Review of Techniques for Landslide Detection, Fast Characterization, Rapid Mapping and Long-Term Monitoring*. Edited for the SafeLand European project by Michoud C., Abellán A., Derron M.-H. and Jaboyedoff M. Available at <http://www.safeland-fp7.eu>

## Note about contributors

The following organisations contributed to the work described in this deliverable:

### Lead partner responsible for the deliverable:

Institut de Géomatique et d'Analyse du Risque, Université de Lausanne (UNIL)

*Deliverable prepared by:*

Clément Michoud, Antonio Abellán, Marc-Henri Derron, Michel Jaboyedoff

### Partner responsible for quality control:

*Revision 0 – Chapter 2 Reviewers:*

All sections of the chapter 2, which summarizes the different techniques and methods, were written and reviewed by at least two specialized experts of independent institutes. The reviews guarantee the quality of this chapter.

*Revision 1 - Deliverable General Reviewer:*

Farrokh Nadim (ICG-NGI)

### Main contributors:

Åknes/Tafjord Early Warning Centre (IKS): *L.H. Blikra, L. Kristensen*

AMRA Scarl: *G. Fornaro*

Bureau de Recherches Géologiques et Minières (BRGM): *G. Grandjean, M. de Michele, D. Raucoules*

Centre National de la Recherche Scientifique, Institut de Physique du Globe de Strasbourg (CNRS- IPGS): *J.-P. Malet, A. Tonnellier*

Centre National de la Recherche Scientifique, Laboratoire de Géodynamique Interne et de Tectonophysique de Grenoble (CNRS-LGIT): *D. Jongmans*

Centro Servizi di Geoingegneria S.r.l. (CSG): *E. Abbiate, M. Lovisolo*

Geological Survey of Austria (GSA): *I. Baron, R. Supper*

Geological Survey of Slovenia (GeoZS): *M. Carman, M. Jemec, S. Kumelj*

International Center for Geohazards, Geological Survey of Norway (ICG-NGU): *R. Hermanns, J.-S. L'Heureux, T. Oppikofer*

International Center for Geohazards, NORSAR (ICG-NORSAR): *I. Lecomte, M. Roth*

International Center for Geohazards, Norwegian Geotechnical Institute (ICG-NGI): *S. Bazin, A. A. Pfaffhuber*

International Center for Geohazards, University of Oslo (ICG-UiO): *T. Eiken*

International Institute for Geo-information Sciences and Earth Observation (ITC): *N. Kerle, A. Schtumpf*

Joint Research Center (JRC): *M. van d. Eeckhaut, J. Hervás*

Università degli studi di Firenze (UNIFI): *N. Casagli, F. Catani, F. Cigna, V. Tofani*

Università di Salerno (UNISA): *L. Cascini, D. Peduto*

Universitat Politècnica de Catalunya (UPC): *J. Gili*

Université de Lausanne (UNIL): *A. Abellán, M.-H. Derron, F. Humair, M. Jaboyedoff, C. Michoud*



## Acknowledgements

On behalf of the SafeLand European project, the editors of the deliverable 4.1 would like to thank all authors and reviewers for their excellent and motivated contributions in the conception and the redaction of this deliverable. The editors show their deep grateful to:

E. Abbiatte, S.E. Amran, I. Baron, J.I. Barredo S. Bazin, L.H. Blikra, J. Calvet, M. Carman, N. Casagli, L. Cascini, F. Catani, F. Cigna, M. van den Eeckhaut, T. Eiken, G. Fornaro, J. Gili, G. Grandjean, R. Hermanns, J. Hervás, P. Horton, F. Humair, M. Jemec, D. Jongmans, N. Kerle, L. Kristensen, S. Kumelj, I. Lecomte, M. Lovisolo, J.-S. L'Heureux, A. Loye, G. Luzi, J.-P. Malet, R. Metzger, M. de Michele, F. Nadim, T. Oppikofer, A. Pedrazzini, D. Peduto, A.A. Pfaffhuber, J. Poesen, D. Raucoules, J.S. Rømming, P.I. Rosin, M. Roth, A. Schtumpf, R. Supper, V. Tofani, A. Tonnellier, L. Vandekerckhove, J.M. Vilaplana.



---

## List of acronyms

<b>2SM</b>	Two strata model
<b>A-DInSAR</b>	Advanced Differential Interferometric Synthetic Aperture Radar
<b>AEM</b>	Airborne electromagnetics
<b>ALOS</b>	Advanced Land Observing Satellite
<b>ALS</b>	Aerial Laser Scanner
<b>ANN</b>	Artificial Neural Networks
<b>ASAR</b>	Advanced Synthetic Aperture Radar
<b>ASTER</b>	Advanced Spaceborne Thermal Emission and Reflection Radiometer
<b>ATM</b>	Airborne Thematic Mapper
<b>Bn</b>	Normal Baseline
<b>Bt</b>	Temporal Baseline
<b>CCD</b>	Charged Coupled Device
<b>CMOS</b>	Complementary Metal Oxide Semiconductor
<b>CMP</b>	Common Mid-Point
<b>CNES</b>	Centre National d'Études Spatiales
<b>CPT</b>	Cone Penetration Test
<b>CVA</b>	Change Vector Analysis
<b>DB</b>	Dark-Bright Set
<b>DDV</b>	Dense Dark Vegetation
<b>DEM</b>	Digital Elevation Model
<b>DGPS</b>	Differential Global Positioning System
<b>DIC</b>	Digital Image Correlation
<b>DInSAR</b>	Differential Interferometric Synthetic Aperture Radar
<b>DMC</b>	Disaster Monitoring Constellation
<b>DN</b>	Digital Number
<b>DOS</b>	Dark Object Subtraction
<b>DSM</b>	Digital Surface Model
<b>DTM</b>	Digital Terrain Model
<b>EM</b>	Electromagnetics
<b>EO</b>	Exterior Orientation
<b>ERS</b>	European Remote Sensing
<b>ERT</b>	Electrical Resistivity Tomography
<b>ESA</b>	European Space Agency
<b>GB-InSAR</b>	Ground Based Interferometric Synthetic Aperture Radar
<b>GCP</b>	Ground Control Point

---

<b>GEOBIA</b>	Geographic Object-Based Image Analysis
<b>GEOSS</b>	Global Earth Observation System of Systems
<b>GIS</b>	Geographic Information System
<b>GLCM</b>	Grey Level Co-Occurrence Matrices
<b>GLOF</b>	Glacial-Lake Outburst Flow
<b>GMES</b>	Global Monitoring for Environment and Security
<b>GNSS</b>	Global Navigation Satellite System
<b>GPR</b>	Ground Penetrating Radar
<b>GPS</b>	Global Positioning System
<b>GSD</b>	Ground Sampling Distance
<b>HEM</b>	Helicopter-borne electromagnetics
<b>HHS</b>	Homogenous Half-Space model
<b>HIS</b>	Hue-Saturation-Intensity
<b>HM</b>	Histogram Matching
<b>HRDEM</b>	High Resoluton Digital Elevation Model
<b>I</b>	Intensity (of the laser signal)
<b>IGRF</b>	International Geomagnetic Reference Field
<b>HIS</b>	Intensity-Hue-Saturation
<b>InSAR</b>	Interferometry Synthetic Aperture Radar
<b>INSPIRE</b>	Infrastructure for Spatial Information in Europe
<b>IO</b>	Interior Orientation
<b>IP</b>	Induced Polarization
<b>IWLSR</b>	Iteratively Weighted Least Squares Regression
<b>JAXA</b>	Japan Aerospace Exploration Agency
<b>LIDAR</b>	Light Detection and Ranging
<b>LOS</b>	Line of Sight
<b>MAD</b>	Multivariate Alteration Detection
<b>MASW</b>	Multichannel Analysis of Surface Waves
<b>MDDV</b>	Modified Dense Dark Vegetation
<b>MLC</b>	Maximum Likelihood Classification
<b>MM</b>	Modified Minnaert
<b>MNCR</b>	Manual No Change Regression
<b>MPGC</b>	Multi-Photo Geometrically Constrained
<b>MS</b>	Multispectral
<b>MTF</b>	Modulation Transfer Function
<b>NASA</b>	National Aeronautics and Space Administration
<b>NDVI</b>	Normalized Difference Vegetation Index
<b>NIR</b>	Near Infrared
<b>OBIA</b>	Object-Based Image Analysis

---

---

<b>OOA</b>	Object-Oriented Analysis
<b>PAN</b>	Panchromatic
<b>PCA</b>	Principal Component Analysis
<b>PIF</b>	Pseudoinvariant Feature
<b>PIFR</b>	Pseudoinvariant Feature Regression
<b>PIV</b>	Particle Image Velocimetry
<b>PSI</b>	Persistent Scatterer Interferometry
<b>PS-InSAR</b>	Permanent Scatterer InSAR
<b>RADAR</b>	Radio Detection And Ranging
<b>RFM</b>	Rational Function Model
<b>RMSE</b>	Root Mean Square Error
<b>RPC</b>	Rational Polynomial Coefficients
<b>RT</b>	Roto-Translation
<b>SAM</b>	Spectral Angle Mapper
<b>SAR</b>	Synthetic Aperture Radar
<b>SAT-PP</b>	Satellite Image Precision Processing
<b>SBAS</b>	Small Baseline Subset
<b>SLR</b>	Single Lens Reflex
<b>SP</b>	Self Potential
<b>SPOT</b>	Satellite Pour l'Observation de la Terre
<b>SR</b>	Simple Regression
<b>SRTM</b>	Shuttle Radar Topographic Mapping
<b>SVM</b>	Support Vector Machines
<b>TDI</b>	transfer delay integration
<b>TEM</b>	Transient Electromagnetics
<b>TIN</b>	Triangle irregular Network
<b>TLS</b>	Terrestrial Laser Scanner
<b>UAV</b>	Unmanned Aerial Vehicle
<b>UPN</b>	Unchanged Pixel Normalization
<b>UTM</b>	Universal Transverse Mercator
<b>VES</b>	Vertical Electric Sounding
<b>VHR</b>	Very High Resolution
<b>WGS</b>	World Geodetic System
<b>XYZ</b>	3D coordinates



# CONTENTS

<b>1. INTRODUCTION .....</b>	<b>17</b>
<b>2. DATA AND TECHNIQUES .....</b>	<b>23</b>
<b>PART A - PASSIVE OPTICAL SENSORS .....</b>	<b>25</b>
1. GENERAL PRE-PROCESSING STEPS .....	26
1.1. Digitizing .....	26
1.2. Geometric correction .....	26
1.3. Radiometric correction .....	28
1.4. Filtering and Texture .....	32
1.5. Orthorectification .....	33
1.6. Data fusion .....	34
2. GROUND-BASED IMAGING .....	35
2.1. Sensor and platform development .....	35
2.2. Visual interpretation .....	36
2.3. Ground-Based Digital Photogrammetry .....	36
2.4. Digital Image Analysis of Ground-Based Photographs .....	37
2.5. Analysis of videos .....	37
3. AERIAL IMAGING .....	39
3.1. Analogue vs. digital camera systems .....	39
3.2. Panchromatic vs. Natural Color and Near Infrared .....	40
3.3. New sensor platforms .....	41
3.4. Visual interpretation .....	42
3.5. Automated techniques of image interpretation .....	43
4. SATELLITE IMAGING .....	44
4.1. Sensors and platform development .....	44
4.2. Visual Interpretation .....	48
4.3. Stereoprocessing .....	48
4.4. Supervised classification techniques .....	52
4.5. Unsupervised classification and clustering techniques .....	53
4.6. Change detection .....	54
4.7. Digital Image Correlation (DIC) .....	56
4.8. Object-oriented concepts .....	56
5. APPENDIX .....	63
<b>PART B - ACTIVE OPTICAL SENSORS .....</b>	<b>65</b>
1. BASIC PRINCIPLES OF LASER RANGING .....	66
1.1. Distance calculation .....	66
2. ELECTRONIC DISTANCE METERS .....	68
2.1. General overview of the sensor .....	68
2.2. Method .....	71
2.3. Main commercial systems .....	72
2.4. Output .....	73
2.5. Main applications .....	74
3. TERRESTRIAL LASER SCANNER .....	76
3.1. General overview of the sensor .....	76
3.2. Method .....	79
3.3. Main commercial systems .....	83

3.4.	Output.....	86
3.5.	Main applications .....	87
4.	AERIAL LASER SCANNER .....	91
4.1.	General overview of the sensor .....	92
4.2.	Method .....	94
4.3.	Output.....	97
4.4.	Main applications .....	98
<b>PART C - ACTIVE MICROWAVE SENSORS .....</b>		<b>103</b>
1.	RADAR WAVE PRINCIPLES.....	105
1.1.	Introduction .....	105
1.2.	Range and Phase Shift.....	106
2.	INTERFEROMETRIC RADAR DISTANCE-METER .....	107
3.	DIFFERENTIAL SAR INTERFEROMETRY .....	108
3.1.	Synthetic Aperture Radar .....	109
3.2.	SAR Interferometry (InSAR) .....	115
3.3.	Differential SAR Interferometry (DInSAR).....	125
4.	MULTI-TEMPORAL REPEAT-PASS InSAR (ADVANCED DInSAR) .....	131
4.1.	Introduction .....	131
4.2.	PS-based A-DInSAR techniques or PSI (full resolution / dominant scatterering) .....	134
4.3.	Interferogram stacking techniques (low resolution / distributed scatterering) .....	146
4.4.	Final remarks.....	150
5.	GROUND-BASED InSAR.....	151
5.1.	Introduction .....	151
5.2.	The GBInSAR instrumentation .....	152
5.3.	Characteristics of application .....	154
6.	POLARIMETRY FOR SOIL MOISTURE ESTIMATION .....	158
6.1.	Introduction .....	158
6.2.	Soil moisture estimation.....	159
<b>PART D - GEOPHYSICAL INVESTIGATIONS .....</b>		<b>165</b>
1.	GROUND-BASED GEOPHYSICAL INVESTIGATIONS.....	167
1.1.	Introduction .....	167
1.2.	Methods.....	171
1.3.	Discussion .....	193
1.4.	Conclusions .....	195
2.	ACOUSTIC AND MICRO-SEISMIC MONITORING.....	195
2.1.	Introduction .....	195
2.2.	The pioneering period – identification of AE signals and limitations of the technique .....	200
2.3.	The recent period – micro-seismic monitoring and characterization of AE signals.....	203
2.4.	Conclusions.....	212
3.	INTRODUCTION TO OFFSHORE METHODS .....	213
3.1.	Multi-beam systems .....	213
3.2.	2D and 3D high resolution seismic .....	216
3.3.	Summary and conclusions.....	218
4.	STAKES OF THE AERIAL GEOPHYSIC .....	218
<b>PART E - GEOTECHNICAL GROUND-BASED MONITORING SYSTEMS.....</b>		<b>221</b>
1.	INTRODUCTION .....	222
2.	EXTENSOMETERS .....	222
2.1.	Probe extensometers.....	222
2.2.	Fixed borehole extensometers .....	222
2.3.	Wire extensometers .....	223
3.	INCLINOMETERS .....	224
3.1.	Probe inclinometers.....	224
3.2.	Automatic probe inclinometer system.....	227
3.3.	In-place inclinometers .....	228



4.	PIEZOMETERS .....	229
4.1.	Observation wells .....	229
4.2.	Open standpipe piezometers .....	230
4.3.	Twin-tube hydraulic piezometers .....	232
4.4.	Pneumatic, vibrating wire and electrical resistance piezometers .....	233
5.	CONTACT EARTH PRESSURE CELLS .....	235
6.	MULTIPARAMETRIC IN PLACE SYSTEMS .....	236
6.1.	DMS system .....	236
<b>PART F - OTHERS TECHNIQUES .....</b>		<b>239</b>
1.	GLOBAL NAVIGATION SATELLITES SYSTEMS (GNSS, GPS...) .....	240
1.1.	Introduction .....	240
1.2.	Basic principle .....	240
1.3.	Field procedures .....	242
1.4.	Some considerations on the use of GNSS in landslide monitoring and its precision .....	244
1.5.	Examples .....	246
1.6.	Trends .....	246
2.	INTRODUCTION TO CORE LOGGING .....	247
<b>3. APPLICATION TO LANDSLIDES: CASE STUDIES .....</b>		<b>253</b>
1.	Monitoring Tessina landslide, Italy, from optical remotely sensed imagery .....	255
2.	Landslide mapping by textural analysis of ATM data: a case study from the LOS Vélez district, south eastern Spain .....	261
3.	Using TLS for rockslide monitoring. Case study of the Eiger collapse, Swiss Alps .....	267
4.	Structural analysis using color coded information derived from 3D point clouds .....	275
5.	Using TLS for rockfall detection and prediction .....	277
6.	Susceptibility assessment at regional scale based on areal LIDAR datasets. Application to the canton of Vaud, western Switzerland .....	281
7.	The application of LIDAR-derived images for landslide inventory and susceptibility mapping in the Flemish Ardennes, Belgium .....	287
8.	Characterization and analyses of surface deformation, mass movements and alpine region lifting with PSInSAR techniques/methods .....	293
9.	Landslide detection and mapping at the basin scale by means of radar-interpretation .....	297
10.	Integration of PSInSAR data and ground-based instrument measurements for landslide characterization and monitoring at the local scale .....	303
11.	A new approach to the use of DInSAR data in landslide studies at different scales: the case study of National Basin Authority of Liri-Garigliano and Volturno rivers .....	307
12.	Microseismic monitoring at the unstable rock slope at Åknes, Norway .....	313
13.	Landslide of Rindberg / Sibratsgfäll investigated with airborne geophysical survey .....	319
14.	Site-specific geotechnical investigations for landslide characterization and detection. Application at the Åknes rockslide, western Norway .....	323
15.	From early warning to site-specific kinematic analysis: the case of Bagnaschino landslide .....	329
16.	Detecting and mapping landslides in Salazie area, La Réunion, using remote sensing techniques .....	335
17.	Vallcebre landslide, Spain, monitoring, from wire extensometers to GB-InSAR .....	339
<b>4. DISCUSSION .....</b>		<b>347</b>
4.1.	Advantages and limitations of each method .....	347
4.2.	Appropriate techniques according to landslide situation .....	352
4.3.	Innovative techniques and further developments .....	353
<b>5. CONCLUSIONS .....</b>		<b>359</b>
<b>6. REFERENCES .....</b>		<b>363</b>
6.1.	General references within the deliverable .....	363
6.2.	Specific references for the chapter 2A .....	363

---

6.3.	Specific references for the chapter 2B.....	374
6.4.	Specific references for the chapter 2C.....	377
6.5.	Specific references for the chapter 2D .....	383
6.6.	Specific references for the chapter 2E.....	392
6.7.	Specific references for the chapter 2F .....	392
<b>7.</b>	<b>GLOSSARY .....</b>	<b>397</b>

# INTRODUCTION



# 1. INTRODUCTION

European countries are exposed to numerous geohazards, such as landslides, debris flows and rockfalls, which endangered inhabitants and infrastructures. One of the main aims of the European project SafeLand in the 7<sup>th</sup> Framework Programme is to develop innovative mapping and monitoring methods in order to improve the methods for regional landslide risk assessment and design of early warning systems. More specifically, Area 4 of SafeLand addresses the technical and practical issues related to monitoring and early warning for landslides. During the last decade, different monitoring and remote sensing techniques have undergone rapid development. In order to summarize these scientific and technical advances, the University of Lausanne, in close collaboration with 18 European institutions, has produced the project Deliverable 4.1: “*Review of Techniques for Landslide Detection, Fast Characterization, Rapid Mapping and Long-Term Monitoring*”.

Initially, only remote sensing methods were going to be taken into account; but afterward, the co-authors decided to also include ground-based techniques, which were not described in the other deliverables of SafeLand project. The core of this deliverable consists of two main chapters (2 and 3), which aim to develop the basic technical knowledge for (a) landslide detection (new landslides recognition from space or airborne imagery), (b) fast characterization (retrieving information on failure mechanism and volume involved), (c) rapid mapping (fast semi-automatic image processing for changes detection and/or target detection; hotspot mapping), and (d) long-term monitoring (processing data for retrieving deformation patterns and time-series).

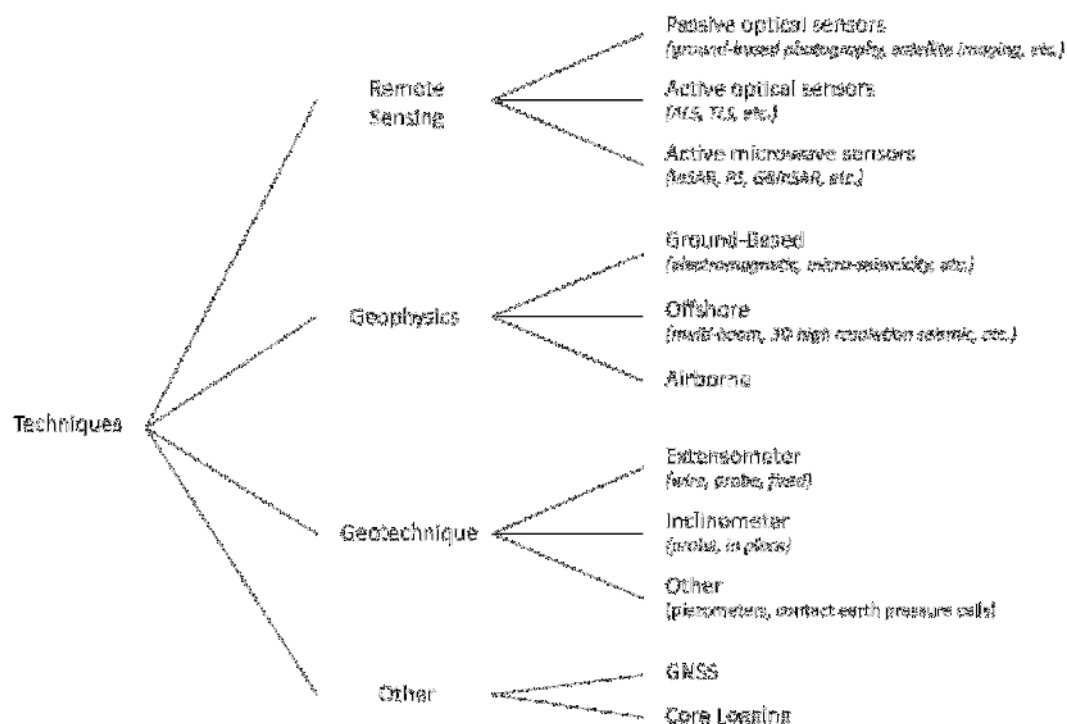
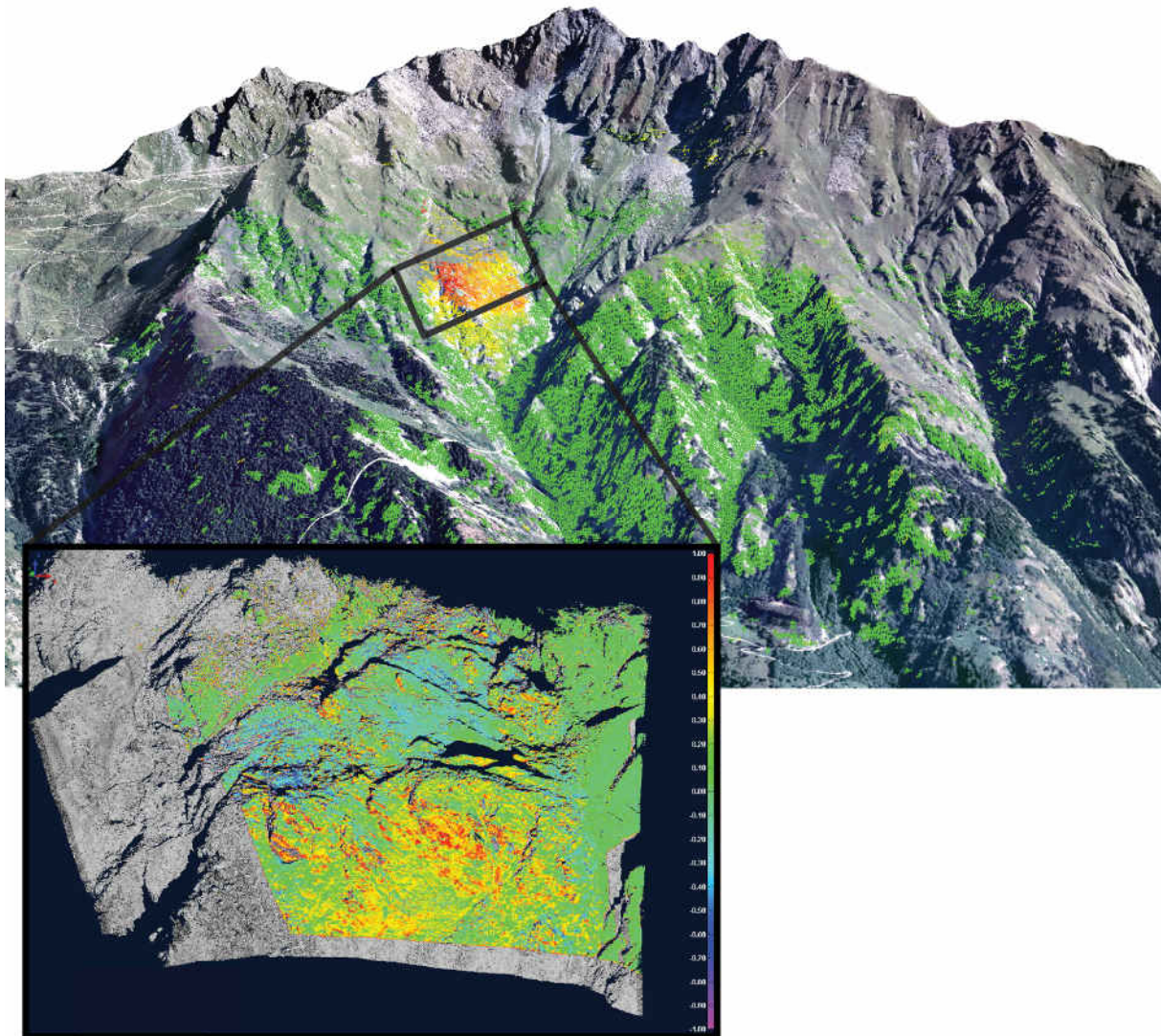


Figure 1 : structure of the major chapter of the deliverable exploring the state of the art and the theory of remote sensing and ground based techniques applied to landslides detection, fast characterization, rapid mapping and long-term monitoring.

Chapter 2 summarizes the different techniques and methods from a theoretical point of view. These include: (1) optical images from ground based and space borne sensors, (2) airborne and terrestrial laser scanning, (3) ground-based and space borne radar interferometry, (4) ground based, airborne and offshore geophysical investigations, (5) geotechnical ground-based monitoring systems, and (6) global navigation satellite systems. Each technique described in the deliverable has benefited of the expertise of specialized research groups. The structure of this chapter is illustrated in Figure 1.

Chapter 3 shows the main applications of these techniques to landslides, through the synthesis of seventeen case studies. To this end, each partner provided different examples which summarize the state-of-the-art of a given technique for different hazards in several situations. As an example, Figure 2 shows a combination of Ground-Based Radar Interferometry and Terrestrial Laser Scanning for huge rockslide characterization and monitoring.



*Figure 2 : example of a combination of remote sensing method applied to huge rockslide characterization and monitoring, integrating 2011 GB-InSAR data of the entire instable area (up: green: stable > red: 8 mm displacements in two weeks) with a comparison of 2006 and 2011 TLS point clouds (down) of the frontal part of the rockslide (Aerial photo ©Swisstopo; GBInSAR and TLS data ©IGAR-UNIL).*

The state of the art overview demonstrates the fast evolution of techniques having a strong impact on landslide mapping and monitoring. For example, thanks to high resolution satellite imagery or aerial laser scanning, the way we are currently characterizing and monitoring landslides has drastically changed. In addition, A-DInSAR gives now reliable information to monitor slope movements at a regional scale.

In addition to being a state-of-the art overview, this deliverable provides helpful and extensive support for non-specialists and students interested in the application of new monitoring techniques to different types of mass movement. It also aims to be a common reference for the different deliverables of SafeLand Area 4, specifically for the Deliverable 4.3, “*Creation and updating of landslide inventory maps, landslide deformation maps and hazards maps as input for quantitative risk assessment using remote sensing technologies*”, the Deliverable 4.4, “*Guidelines for the selection of appropriate remote sensing technologies for monitoring different types of landslides*”, and the Deliverable 4.8, “*Guidelines for monitoring and early-warning systems in Europe – Design and required technology*”.





# **DATA AND TECHNIQUES**



---

## 2. DATA AND TECHNIQUES

---

- <b>PART A:</b> Passive Optical Sensors	p. 25
- <b>PART B:</b> Active Optical Sensors	p. 65
- <b>PART C:</b> Active Microwave Sensors	p. 103
- <b>PART D:</b> Geophysical Investigations	p. 165
- <b>PART E:</b> Geotechnical Ground-Based Monitoring Systems	p. 221
- <b>PART F:</b> Other Techniques	p. 239

---

*Table 1 (below) : Summary of the main characteristics of the techniques discussed in this deliverable. To go further, please read the appropriate section.*

CLASS	TECHNIQUE	MEASURED PARAMETER	POSITION OF THE SENSOR	THEORETICAL RESOLUTION		
				ACCURACY	Spatial ( <i>grains / line layer</i> <i>m2</i> )	Temporal ( <i>time lapse</i> <i>between acq.</i> )
PASSIVE OPTICAL SENSORS	□ Ground-Based Imaging	Surface radiance (Displacement/ Surface Features/ Surface Elevation)	G	cm	1-100 (mid range)	second - year (1)
	□ Aerial Imagery	Surface radiance (Displacement/ Surface Features/ Surface Elevation)	A	m	1-100	month - years
ACTIVE OPTICAL SENSORS	□ Satellite Imaging	Surface radiance (Displacement/ Surface Features/ Surface Elevation)	S	m	0.1-1 (VHR)	days
	□ Distance-Meters	Distance	G	mm	0.01-1	second - year (1)
ACTIVE MICROWAVE SENSORS	□ Terrestrial Laser (TLS)	3D coordinates	G	cm	10-100	hour - years (1)
	□ Airborne Laser (ALS)	3D coordinates	A	dm	0.1-1	hour - years (1)
ACTIVE MICROWAVE SENSORS	□ Interferometric Radar (Distance-Meter)	Distance	G	mm	0.01-1	minute - years (1)
	□ Differential InSAR	Distance	S	mm	0.001-1	month
ACTIVE MICROWAVE SENSORS	□ Advanced InSAR	Distance	S	mm	0.0001-0.001-1	month
	□ Ground-Based InSAR	Distance	G	mm	0.05-2	minute - years (1)
ACTIVE MICROWAVE SENSORS	□ Polar And Pollinear	Soil Moisture	S	mm	0.001	month
GROUND BASED GEOPHYSIC SENSORS	□ Seismics	Elastic parameters related to bulk modulus and shear modulus	G	dm-nl	0.1-1	weeks-years
	□ Electricity	Resistivity-conductivity, self potential, chargeability	G	dm-nl	0.1-1	weeks-years
GROUND BASED GEOPHYSIC SENSORS	□ Electromagnetic (low frequency)	Resistivity/conductivity	G	> m	0.01-0.1	weeks-years
	□ Ground Penetrating Radar	Electrical permittivity	G	cm-nl	0.1-10	weeks-years
GROUND BASED GEOPHYSIC SENSORS	□ Gravimetry	Density	G	m	0.01-1	weeks-years
	□ Borehole geophysics	All geophysical parameters depending the logging tool, + hydrology, etc.	G	cm-dm	1	days-years
OFFSHORE SENSORS	□ 2D and 3D seismic	Reflected acoustic energy	M	dm-nl	0.1-1	days - years (1)
	□ Seismic	3D coordinates, backscatter,	M	cm-nl	0.1-1	days - years (1)
OFFSHORE SENSORS	□ Multi-fas-seam	3D coordinates, backscatter,	M	cm-nl	0.1-1	days - years (1)
	□ Extensometers	Distance	G	mm	max ~1	second - year (1)
GEOTECHNICAL SENSORS	□ Inclinoimeters	Tilt	G	mm	max ~1	second - year (1)
	□ Piezometers	Water pressure	G	-	max ~1	second - year (1)
GEOTECHNICAL SENSORS	□ Contact Earth Pressure Cells	Distribution, intensity and direction of total stress	G	-	max ~1	second - year (1)
	□ Multiparametric In Place Systems		G	-	max ~1	second - year (1)
OTHER SENSORS	□ Global Navigation Satellite System (GNSS)	3D coordinates	G	mm	10 <sup>-2</sup> to 10 <sup>-2</sup>	second - year (1)
	□ Core Logging	Mechanical parameters and Rock quality	G	cm	max ~1	day - year (1)

Position of the sensor: G – Ground Based; A – Aerial; S – Satellite; M – Marine

Temporal resolution: (1) – On demand

# PART A

## PASSIVE OPTICAL SENSORS

---

- <b>SECTION 1:</b> General Pre-Processing Step	p. 26
- <b>SECTION 2:</b> Ground-Based Imaging	p. 35
- <b>SECTION 3:</b> Aerial Imaging	p. 39
- <b>SECTION 4:</b> Satellites Imaging	p. 44

---

### Sections 1, 2, 3 and 4

- **Authors:** A. Stumpf<sup>1,2</sup>, N. Kerle<sup>1</sup>, J.-P. Malet<sup>2</sup>

- **Reviewers:** J. Hervás<sup>3</sup>, M. Van d. Eeckhaut<sup>3</sup>

<sup>1</sup>. School for Disaster Geo-information Management, International Institute of Geo-Information Sciences and Earth Observation (ITC), United Nation University, Enschede, The Netherlands. [stumpf24883@itc.nl](mailto:stumpf24883@itc.nl)

<sup>2</sup>. Centre National de la Recherche Scientifique (CNRS), Institut de Physique du Globe de Strasbourg (IPGS), France.

<sup>3</sup>. Joint Research Center, Ispra, Italia.

Stumpf A., Kerle N., Malet J.-P., 2010. *Passive Optical Sensors*. In the Deliverable 4.1 of the European project SAFELAND: *Review of Techniques for Landslide Detection, Fast Characterization, Rapid Mapping and Long-Term Monitoring*. Edited in 2010 by Michoud C., Abellán A., Derron M.-H. and Jaboyedoff M. Available at <http://www.safeland-fp7.eu>

## 1. GENERAL PRE-PROCESSING STEPS

### 1.1. DIGITIZING

Analogue recording systems are getting gradually replaced by digital systems, whereas large archives of analogue photographs, especially aerial photographs, represent a valuable source of historical information. Furthermore, the geometric resolution of analogue photography is still slightly higher than geometric resolution opto-electronic devices. Thus, analogue photography is expected to still play an important role for the most accurate photogrammetric tasks in the future [Kraus, 2007]. Scanning is the first necessary step to integrate them into modern Geographic Information Systems (GIS) and digital image analysis. Some low cost, flatbed scanners offer a satisfactory spatial and radiometric resolution for digitizing large scale aerial photographs, but introduce geometric distortions into the scanned image. High-end scanners, designed for digital photogrammetry, (Zeiss/Intergraph PS, Leica/Helava DSW, ISM's, Vexcel, and Wehrli) are characterized by a high geometric accuracy (2-4  $\mu\text{m}$ ), a high geometric resolution (4-12.5  $\mu\text{m}$ ) and a high radiometric accuracy (1-2 grey values). In general newer more mature instruments (DSW 500, SCAI, RM-2, and UltraScan 5000) lead to better results, while quality is also highly dependent on proper calibration, maintenance, environmental conditions and high performance software tools. As eventual errors introduced during the scanning process will substantially influence the results of consequent image analysis the user should be aware of those aspects [Baltsavias, 1999].

### 1.2. GEOMETRIC CORRECTION

An appropriate geometric correction of images involves the modeling of systematic (scan skew, mirror-scan velocity variance, panoramic distortion, platform velocity, earth rotation, perspective) and non-systematic (altitude, variance in altitude and angles) errors to derive a relationship between the image and a global coordinate system [Jensen, 2005].

Due to the introduction of off-nadir views with very high resolutions an accurate modeling of geometric distortions gains even more importance today. If this step is not performed properly their digital interpretation or fusion with other datasets will fail or lead to bad or misleading results. Systematic distortions, especially those related to the instrumentation are generally well known by the operators of satellite and airborne photogrammetry and corrected at ground receiving stations or by image vendors [Toutin, 2004].

In ground-based and low-altitude airborne photography non-metric “off-the shelf” digital cameras are recently more frequently in use. The use of such systems for photogrammetric applications renewed the interest in proper calibration methods of the camera what usually is done on 2D/3D test fields or during the image acquisition itself, latter often referred as on-the-job or self-calibration [Luhmann et al., 2006]. Analytical self-calibration of analogue and digital cameras already reached maturity. Very commonly bundle-block adjustment is used to determine the exterior orientation of multiple camera views. Thereby, interior and exterior orientation of the acquired images can be obtained at the same time. However, where the network geometry in the image is weak, previous calibration on a test field might be favorable to first determine interior orientation parameters and account for lens distortion. Nowadays, this can be a fully automatic procedure to employ consumer grade cameras on low and medium accuracy levels [Ergun et al., 2010].

Distortions in images taken by metric cameras can originate from variations in the platform altitude, platform velocity, and platform orientation, uncertainties in calibration parameters, panoramic views, earth rotation, curvature and relief. Finally deformation will also occur when the large corrected images are projected on the tangent plane of the reference ellipsoid that is approximation of the geoid.

All those possible distortions require geometric corrections using models and mathematical functions such as, either 2D/3D polynomial models, 3D rational functions, rigorous 2D/3D physical models and deterministic models. A simple affine polynomial model requires at least 3 well-distributed ground control points (GCPs). More complex models will need at least 5 GCPs. Similarly, in close range photogrammetric applications algorithms that perform a relative orientation of multiple images will need five [Stewénus et al., 2006] or at least three [Kalantari et al., 2009] matching points. Regardless of the approach, more than the minimum number of GCPs should be employed in order to obtain an optimum solution. The stepwise removal of distortions with 2D/3D physical models is generally applied at ground receiving station and resulting products are sold at different processing steps (e.g. raw, georeferenced, geocoded). Whatever mathematical models are used, four basic processing steps can be distinguished (Figure 3):

- acquisition of image(s) and pre-processing of metadata
- acquisition of the ground points (control/check/pass)
- computation of correction model parameters
- image(s) rectification

Slight differences occur using empirical models where metadata is useless and 2D empirical models where the Z-elevation coordinates for GCPs and Digital Elevation Models (DEMs) are needless [Toutin, 2004]. Further issues concerning orthorectification such as adequate resampling methods and topographic information are treated below.

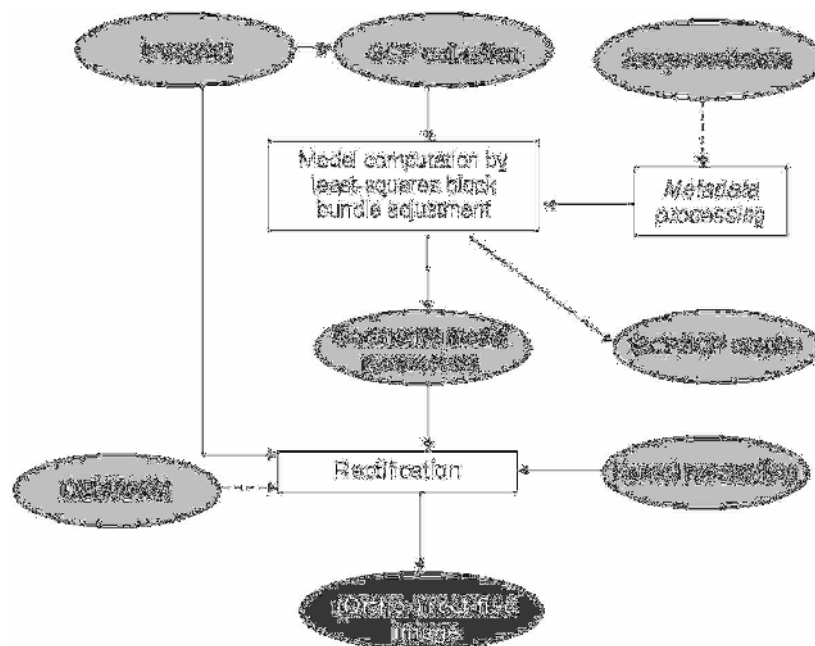


Figure 3 : Typical workflow for geometric correction [Toutin, 2004]

A good overview of geometric correction models mainly for satellite and airborne imagery is given by Toutin [2004]. An evaluation of typically achieved accuracies was more recently published by Sertel et al. [2007]. Due to ongoing frequent launches of high-resolution satellites Rational Function Models (RFM) currently receive greater attention. RFMs are usually derived from satellite onboard instruments including GPS and improvised star sensors [Sadasiva Rao et al., 2006]. They are used to determine Rational Polynomial Coefficients (RPCs) for the generation of DEMs. Their accuracy can be increased considering additional GCPs [Hu and Tao, 2002], whereas there is no complete agreement if in some cases less than six GCPs are enough [Martha et al., 2010a]. RFMs proved to lead to highly accurate results independently from the sensor and are an important alternative where satellite agencies may not like to release the complex camera model and metadata [Nagasubramanian et al., 2008].

### 1.3. RADIOMETRIC CORRECTION

Digital sensors record the intensity of electromagnetic radiation from Earth's Surface as a digital number (DN). Its value range is dependent on the bit-depth of the acquired product (typically 8 or 16 bit) and does not necessarily represent the bit-depth that was originally recorded by the sensor (typically from 8 to 11 bit). The intensity received at the sensor is not only dependent on the spectral characteristics of the earth surface but on a number of further parameters such as atmospheric conditions, viewing geometry, sun angle, and so on. Where the actual reflectance of a ground target is of interest and/or a comparison of spectral characteristics between different images is intended previous radiometric correction is essential [cf. Song et al., 2001]. Absolute and relative radiometric corrections are two basically different approaches to perform those tasks, respectively.

A product level including corrections of sensor inherent radiometric errors (e.g. destriping of Landsat TM images) with sensor specific parameters may be ordered readily preprocessed from corresponding data providers or space agencies. However, those products in general represent the incoming radiance at the sensor and usually do not include a radiometric



correction of scene specific atmospheric effects. Numerous approaches have been developed for the correction of atmospheric effects to gain surface reflectance and might be grouped into the following main categories [Clark et al., 2002; Gao et al., 2009]:

Ground calibration methods [e.g. Ferrier, 1995; Xu and Huang, 2008]

- Empirical atmospheric correction with scene derived parameters
  - Dark Object Subtraction (DOS) [Chavez, 1988; 1996; Song et al., 2001]
  - Dense Dark Vegetation (DDV) [Kaufman et al., 1997]
  - Modified Dense Dark Vegetation (MDDV) [Song et al., 2001]
  - Path Radiance [Wen et al., 1999]
- Radiative transfer models (A good overview was given recently by Gao et al. [2009] and some further examples are listed here)
  - EXACT [Popp, 1995]
  - SMAC [Rahman and Dedieu, 1994]
  - 6S [Vermote et al., 1997]
  - Durchblick [Holzer-Popp et al., 2001]
- Hybrid approaches [e.g. Clark et al., 2002]

Based on radiative transfer models absolute radiometric correction methods convert the DNs within a satellite or airborne image into the corresponding reflectance of the surface. The inputs for the models are typically atmospheric and sensor parameters for the acquisition date [Richter, 1990] topographic information [Richter, 1998] or DNs of dark image objects in one or multiple sensor channels [e.g. Chavez, 1988; Kaufman, 1989; Kaufman et al., 1997]. While the necessary sensor parameters are mostly included in the header files of satellite images and global DEMs are now commonly available, the provision of accurate atmospheric parameters for the acquisition data is often difficult. Profound assessment of absolute radiometric correction methods with respect to the quality of classification and change detection [Schroeder et al., 2006; Song et al., 2001] reveals that the more complex methods do not necessarily lead to more accurate results.

As another category we might consider Topographic Normalization methods. Especially in mountainous areas there is a strong influence of the topography on the signal recorded by spaceborne optical sensors. The signal from equal surfaces may vary considerably according to their position on slopes oriented away or towards the sun. The effects influence increases towards low sun angles and causes problems for many subsequent steps of image analysis. A comprehensive evaluation of different techniques was recently provide by Richter et al. [2009]. They concluded that visually best results are achieved with the modified Minnaert (MM) method, although sometimes the C approach yields better results for the visible bands

in the blue to red spectral region. However, further research should evaluate on a global basis which method performs best in which situation.

During relative radiometric correction (Normalization) the radiometric properties of a subject image are adjusted to match the radiometric properties of a reference image. Therefore a mathematical relationship based on image statistics (i.e. standard deviation, minimum-maximum) the histograms or most commonly on a linear regression function, is established between the two images.

The normalized image then should appear to have been acquired under the same solar and atmospheric conditions as the reference image. Typically the image with the most favorable radiometric properties (e.g. low atmospheric water content) is chosen as a reference. Resulting values of the subject image are unitless and only comparable relatively within a set of similar corrected images if the reference did not undergo absolute radiometric correction before. A great variety of relative correction techniques has already been developed and tested for the first generation of medium to high resolution satellites, especially from the Landsat program [c.f. Janzen et al., 2006; Over et al., 2003; Yang and Lo, 2000]:

- Simple Regression (SR), [Jensen, 1983]
- Histogram Matching (HM)
- Pseudoinvariant Feature (PIF), [Schott et al., 1988]
- Pseudoinvariant Feature Regression (PIFR), [Du et al., 2002; Du et al., 2001; Paolini et al., 2006]
- Dark-Bright Set (DB), [Hall et al., 1991]
- No Change Set (NC), [Elvidge et al., 1995]
- Other Statistical methods [Yuan and Elvidge, 1996]
- Manual No Change Regression (MNCR), [Over et al., 2003]
- Unchanged Pixel Normalization (UPN), [Ya'allah and Saradjian, 2005]
- Ridge methods [Chen et al., 2005; Song et al., 2001]
- Artificial Neural Network [Velloso et al., 2002]
- Iteratively weighted least squares regression (IWLSR), [Zhang et al., 2008b]
- Ordinal conversion [Nelson et al., 2005]
- Multivariate alteration detection (MAD), [Canty et al., 2004]

Most commonly used linear regression methods in general require the manual or automated selection of unchanged targets in the images to be normalized. Eckhardt [1990] gave a list of criteria such as similar altitude or minimal amount of vegetation for choosing the targets.

Hong [2007] presented a comprehensive review of common radiometric normalization methods for Landsat and stated a number of particular advantages and drawbacks.

Simple Regression (SR) works well if changes between the scenes are not too big and geometric coregistration is sufficiently accurate. Histogram matching (HM) is useful for scenes with slightly different sun angles or atmospheric effects. It is not dependent on an accurate spatial coregistration of the images. When the matching is performed band to band the internal coherence of the image bands is distorted. HM shows weaknesses if surface changes and/or cloud cover are too strong. It produces favorable results for an optical comparison but due to its non-linear transformation it affects the relative distribution of spectral change. Yang and Lo [2000] noted that in general visually and statistically robust methods (such as the HM, and NC methods) tend to reduce the magnitude of spectral change. On the other hand, the DB and PIFR methods cut down only a moderate degree of spectral change and favor better results for change detection. Both methods are not dependent on geometric coregistration of the scenes but require intervention for the selection of unchanged targets (PIFR) or appropriate threshold values (DB) to define dark and bright pixel sets. Finding a suitable number of unchanged objects may represent problem if the time step between the two scenes is too large or the sensor parameters strongly differ. The number of common unchanged targets further decreases when more than two images should be considered [Paolini et al., 2006].

If land and water is present in the images and changes in solar illumination geometries, phenological conditions and landcover are not too large No Change Set (NC) is a valuable method. The method is computationally efficient and does not comprise the need of identifying dark and bright pixels. It reduces cloud, shadow, and snow effects, uses a large percentage of the total number of image pixels and distributes normalization error among different land-cover types [Yuan and Elvidge, 1996].

A number of problems occur when applying most of those image processing methods on high to very high resolution images. The higher resolution complicates the selection of unchanged features, only one band is recorded in the near-infrared and thermal spectra are typically not recorded with VHR sensors [Hong, 2007; Hong and Zhang, 2008].

In general there is no best universal solution for radiometric correction. Especially for relative normalization the most suitable method is rather dependent on the satellite data, the specific scene and the purpose of its application. However, a few general statements might be possible. For a simple visual comparison, histogram matching (HM) which is implemented in several image-processing software tools might be an efficient choice. For change detection Multivariate Alteration Detection (MAD), and Pseudoinvariant Feature Regression (PIFR) offer efficient automated approaches without any need for additional atmospheric data or manual selection of image samples.

Newer approaches such as Iteratively weighted least squares regression (IWLSR), [Zhang et al., 2008b] and Ordinal Conversion [Nelson et al., 2005] demonstrate promising results and

wait for evaluation on data from different sensors and with respect to different applications. Considering the wide variety of approaches analysts must be aware of the particular strength and weaknesses of existing procedures to choose the most efficient approach.

While for classification and post-classification change detection radiometric correction might be even dispensable [Song et al., 2001], there is a general agreement that any correction method enhances the results of direct change detection and other applications.

Comparison of the spectral signatures of forest patterns on Landsat TM images after absolute and relative radiometric correction techniques [Janzen et al., 2006] demonstrated a better performance of relative correction methods. Thus, especially when relative differences in the spectral properties are rather important than absolute values, relative radiometric normalization is an attractive alternative. It avoids the difficulties in obtaining accurate atmospheric and sensor parameters, is usually less computationally intensive and easier to apply than absolute radiometric correction.

#### **1.4. FILTERING AND TEXTURE**

Image enhancement techniques most commonly rely on operations within a template of a certain extent, moving over the image and redefining pixel values based on neighborhood relations. This can be done directly on the image domain or on a Fourier transformed representation of the image, whereas the latter approach is especially favorable if a large template should be used and/or the noise in the image has a periodical pattern.

Low-pass filters such as median, mode or mean filters are commonly used to remove artifacts from an image but lead to a loss of local detail. Depending on the size of the smoothing window the resulting image has a typically blurred appearance but high-frequency noise has been removed.

High-pass filters are useful to emphasize local variations of texture such as abrupt transitions in brightness. The result is an image representation with enhanced edges and suppressed low frequency detail within homogenous areas. High-pass filtering can be achieved by subtracting a low pass filtered image from the original. Other methods such as Sobel, Prewitt, Roberts or Laplacian filters involve the use of a kernel. The distribution of grey values within the spatial domain of the kernel is used to quantify the local contrast of each pixel relative to its neighbors. Pixels with a high contrast in the local neighborhood obtain higher values and thereby edges in the image are enhanced. Such operators are also known edge detection filters and have been demonstrated as useful to detect to highlight hummocky main bodies, accumulation zones, crowns and back scarps of landslides [Eyers et al., 1998; Mason et al., 1998]. The noise level in an image is typically higher in the high spatial frequencies, what will be emphasized and should be considered for the application of a high-pass filter.

Low- and high-pass filters are also commonly involved in the pre-processing of image matching [e.g. Honda and Nagai, 2002] and image correlation procedures for displacement measurement [e.g. Leprince et al., 2007b]. For a comprehensive overview of filtering techniques for image registration or image enhancement the interested reader is referred to Zitová and Flusser [2003] or Schowengerdt [2007], respectively.

Hervás and Rosin [1996] were among the first who combined a number of more complex Grey-Level-Co-Occurrence-Matrices (GLCM after Haralick et al., 1973) to quantify differences between landslides and spectrally and textural similar features. Hervás et al. [1996] noted that the down slope movements also affect the directional components of texture. Whitworth et al. [2005] demonstrated the utility of GLCM texture measures to quantify the hummocky surfaces roughness caused by landslides in Jurassic clays.

Geometrically selective filters like a rectangularity filter [Hervás et al., 2003] have been reported as useful to remove undesired remnant “scene noise” like buildings and agricultural crop patterns after performing change detection and thresholding on VHR imagery for landslide mapping purposes.

### 1.5. ORTHORECTIFICATION

Especially VHR imagery from off-nadir viewing sensors needs to be orthorectified to account for terrain-related distortions. Ground control points, an appropriate sensor model and a DEM with sufficiently high resolution and accuracy are incorporated in this process. Stereo-pairs and triplet satellite images are now more commonly available at better prices and can be used for the derivation of DEMs. Alternatives are provided through costless and globally available datasets from the SRTM [Jarvis et al., 2008] or ASTER [ASTER-GDEM-VALIDATION-TEAM, 2009] however, with a rather low resolution and accuracy. DEMs with very high resolution and high accuracy can also be obtained with SAR or LIDAR but are still rather cost intensive and may represent an alternative in special cases.

Orthorectification is implemented in a user friendly way in most commercial and many Open Source software applications and can be considered as mature techniques. However, image coregistration and orthorectification methods still undergo further development for automated registration with increased accuracy. Recently proposed methods include the more accurate automatic extraction of GCPs from reference images [Gianinetto and Scaioni, 2008] or their stepwise refinement through image correlation and statistical correlation with DEMs [Leprince et al., 2007a]. Once the image is registered with respect to a DEM, Nearest Neighbor, Bilinear Interpolation and Cubic Convolution are the most commonly used resampling methods to point image pixels from 2D coordinates to 3D coordinates on the surface. The Nearest Neighbor algorithm is the fastest choice and simply assigns the value of the nearest pixel in the image to the new coordinate system. It has the advantage that the original pixel value will remain for the orthorectified image. Bilinear Interpolation and Cubic Convolution techniques combine a greater number of nearby cells to compute the value of the transformed cell. The Cubic Convolution method avoids the sometimes jagged appearance that arises from the use of the Nearest Neighbor method and gives a somewhat sharper image than the Bilinear Interpolation method. In exchange the original pixel values are changed and the method is rather computational intensive. Especially for further use of correlation techniques aliasing that is often introduced by the mentioned kernel methods should be avoided. Sinc functions and Modulation Transfer Function (MTF) resampling are further more sophisticated resampling methods. Both also make use of a kernel window, whereas, MTF includes the empirical modeling of the optical and electronic properties of the specific sensor. Leprince et al. [2007a] further introduced resampling with Inverse Transformation Matrices to minimize aliasing effects in consequent image correlation.

## 1.6. DATA FUSION

Hundreds of different data fusion methods are mentioned in scientific literature and/or are available in image processing software packages. According to their position in image processing workflows they can be categorized as signal level, pixel level, feature level, and decision level fusion methods [Dong et al., 2009] (Figure 4).

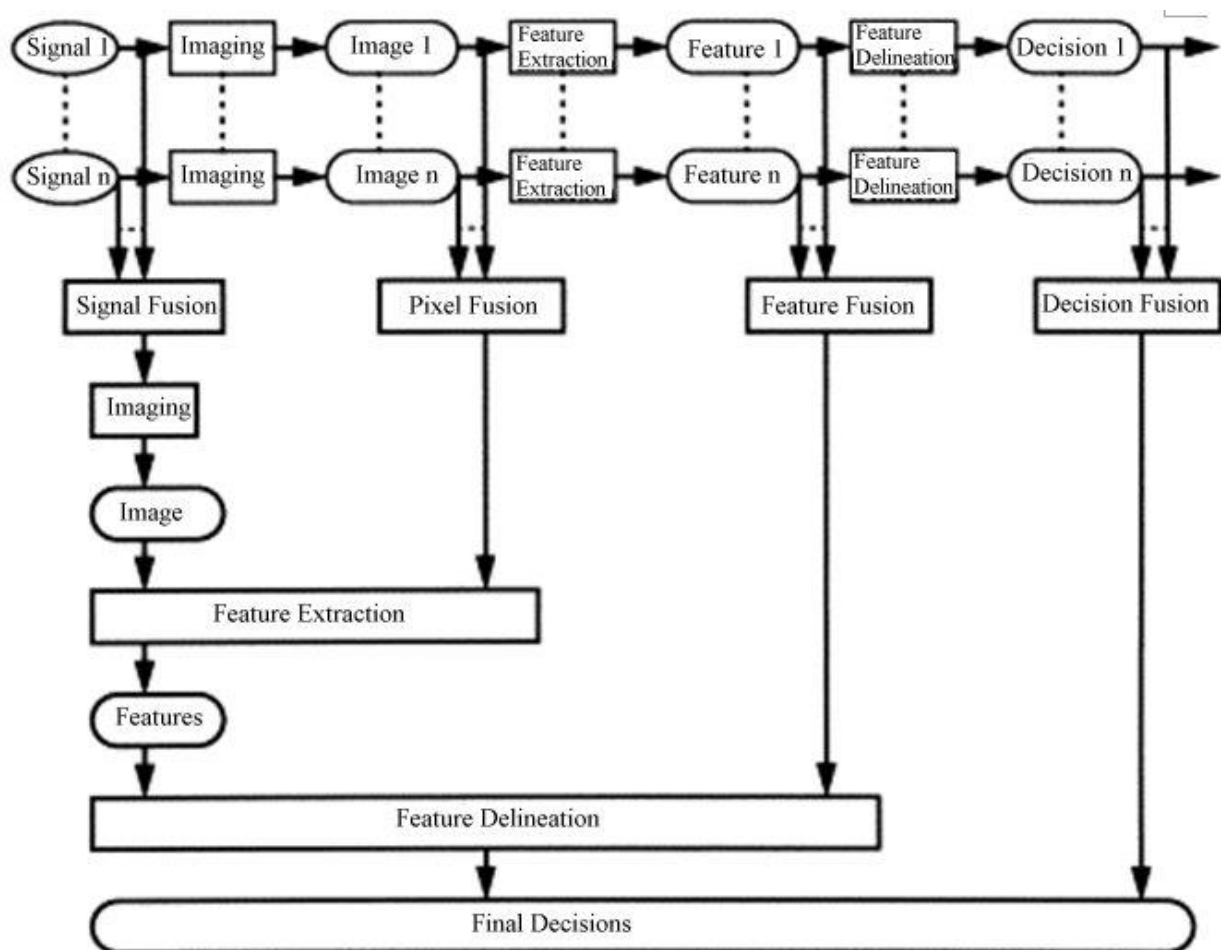


Figure 4 : Conceptual overview of data fusion at different processing levels [Dong et al., 2009]

Standard fusion algorithms such as Principal Component Analysis (PCA), Intensity-Hue-Saturation (IHS) or the Brovey-Transformation are very common methods for fusion of multispectral channels with a panchromatic image of higher resolution (pansharpening). They are implemented in image processing software to obtain more details for visual interpretation or to reduce the number and degree of correlation in hyperspectral or multitemporal datasets. IHS can be used for pansharpening of multispectral imagery, whereas the resulting Intensity-channel is simply replaced by the corresponding panchromatic image. The main limitation of this method is that the number of input bands is restricted to three. More bands can be transformed with PCA to separate color from intensity information in the multispectral image. The success of these pixel-based approaches largely depends on a very exact image coregistration and they tend to distort the original spectral signatures. Newer approaches include Wavelet Fusion and fusion methods that weigh the influence of the panchromatic

image based on dependency of local texture. It has been demonstrated that the latter method can produce results with smaller deviation in the grey values [Hirschmugl et al., 2005].

In recent years especially the use of wavelets - now already implemented in standard image processing software - and artificial neural networks gained greater popularity. The latter is part of a large number of fusion methods functioning on feature or decision level incorporating multiple datasets in a probabilistic [Bendjebbour et al., 2001] or rather deterministic [Martha et al., 2009a] framework.

The final aim of data fusion is to integrate complementary and redundant information to increase the information content in a particular scene and thereby increase the success of identification and classification of image objects such as landslides [Chang et al., 2007], the accuracy of landcover classifications [e.g. Sarkar et al., 2005], the reliability of change detection analysis or the success of military operations [Dong et al., 2009]. A variety of the mentioned techniques useful for pansharpening has been evaluated with respect to their effect on change detection with VHR satellite imagery by Bovolo et al. [2010]. They concluded that the Minimum Mean Square Error [Garzelli et al., 2008] is the most reliable method for this purpose.

## 2. GROUND-BASED IMAGING

### 2.1. SENSOR AND PLATFORM DEVELOPMENT

For most practical applications of ground-based imaging digital cameras replaced analogue systems and cost-efficient, non-metric, single lens reflex (SLR) cameras are nowadays a commonly used, cost-efficient alternative to rather expensive metric systems. Due to the exploitation of mass consumer market the sensor resolution is increasing rapidly, whereas of 6 to 12 Mega-pixel cameras (e.g. Figure 5, most left) being readily affordable (100-300 EUR) for both the layperson and the scientist. Costs for commercial SLR cameras commonly used for photogrammetric measurements are in the range of 1,000-2,000 EUR, whereas the top-end high resolution cameras with up to 160 Mega-pixel resolutions (> 20,000 EUR) still wait for scientific applications. Thereby, it is worth noting that especially scientific measurements can benefit from higher resolutions but that radiometric and geometric quality of the acquired imagery are at least of equal importance. Although, in some cases vendor-provided camera parameter might be sufficient for the photogrammetric interpretation of single views, the correction of geometric distortions is crucial for tasks such as the generation of highly accurate Digital Surface Models (DSM) [Chandler et al., 2005].



Figure 5 : Typical sensors for terrestrial photogrammetric surveys in historical order (left to right): Phototheodolite Zeiss Photo, Linhof Metrika, Rolleiflex 6006, and Nikon D300

As many geomorphological processes (e.g. debris flows) exceed the maximum frame rate of solid state digital cameras video cameras (20-30 Hz) and high-speed cameras ( $> 100$  Hz) became valuable components for the in-situ and laboratory observations [e.g. Arattano and Marchi, 2000; Imaizumi et al., 2005; Zakeri et al., 2008]. Recent advances in direct georeferencing, imaging sensor technology and easy access to inexpensive telecommunication enhanced the implementation of mobile mapping systems. Although most systems do not target top-level accuracy they offer quick and flexible disaster response for natural hazards and systems for real-time monitoring of debris flows are under development [Yin et al., 2007].

The mentioned sensors systems operate in general in the visible spectrum of light. Most CCD based cameras are partly sensible in the NIR and special systems for night vision (especially for military operations) and laboratory measurements are available. While NIR measurements are useful for studies of rock fractures in the laboratory [Brady and Rowell, 1986] no example for ground-based NIR imaging of landslides was found in the literature.

## **2.2. VISUAL INTERPRETATION**

Analogue photographs are valuable testimonies for historical evolution of landslides and other landscape features. Digital photography is often the first source of information during and short after a given event and helpful to reconstruct the failure process. Photos remain as a valuable source of information especially where traces of landslide processes are removed quickly due to natural processes or human efforts. Repeated terrestrial photography can be used to assess displacement directly through observations of surfaces [Schmidt and Nüsser, 2009] or indirectly through associated changes of landscape elements [e.g. Coe et al., 2009]. Multiple images can be used to assess displacements by identifying the same objects in multiple images [Arattano and Marchi, 2000]. Information about the granulometric composition of deposits can be derived from manually assessment or with computer-aided visual interpretation [Genevois et al., 2001]. Similarly, structural characteristics of rock masses such as volumetric fracture intensity can be derived from terrestrial photos and reveal information on rock slope stability [Crosta, 1997].

## **2.3. GROUND-BASED DIGITAL PHOTOGRAMMETRY**

Photogrammetric methods have been extended with great success to the generation of high resolution DSMs. Created at one single time step, such models reveal detailed information on the structure of a particular slope. DSMs generated from terrestrial photographs of rock cuts have been analyzed in detail to determine rock mass discontinuities [Roncella et al., 2005; Sturzenegger and Stead, 2009] and DSMs of river channels have been created noting their usefulness to assess changes of the river bed and model flows in the channel [Chandler et al., 2002].

In principle any ground deformation process of sufficient magnitude can be revealed analyzing multiple photogrammetric DEMs of the same location. This approach has been followed for studies of rock-glaciers [Ladstädter and Kaufmann, 2005], coastal cliff erosion [Lim et al., 2010], lava flows [Robson and James, 2007] and the monitoring of landslides [Cardenal et al., 2008]. DSMs from present consumer-grade SLR cameras can achieve sufficient accuracy when proper methods are used (convergent networks with self-



calibration), even in cases of pre-calibrated cameras or when there is a lack of externally surveyed control points. Therefore they are an interesting alternative to more accurate but also more expensive LIDAR scanning campaigns.

## **2.4. DIGITAL IMAGE ANALYSIS OF GROUND-BASED PHOTOGRAPHS**

Concepts for a real-time warning system incorporating terrestrial photography have been proposed to monitor volcanic activity [Honda and Nagai, 2002] and landslides [Kandawasvika, 2009]. Their potential use for early warning systems remains restricted to processes where daytime observations offer sufficient information, while at the same time valuable information for process understanding can be gained from continuous observations. Recently a system for the automated retrieval of displacement fields via digital image correlation of daily to hourly ground-based image acquisitions has been proposed and results have been demonstrated to be in good agreement with point-wise GPS measurements [Travelletti et al., 2009].

The applied technique can be considered as a special application of correlation techniques also applied on video footages (3.2.5) and satellite imagery (3.4.7), whereas the main differences are frame frequencies (lower than video but typically higher than airborne imagery), scale (higher resolution and lower spatial coverage than airborne and satellite imagery) and an oblique camera view (compared to airborne and satellite imagery).

## **2.5. ANALYSIS OF VIDEOS**

As direct observations of fast moving landslides are rather rare digital and analogue video recordings are very useful documents to distribute observations within the scientific community but also to raise public awareness. Early collections of video material [e.g. Costa and Williams, 1984] led to a better understanding of the dynamics of debris flows and settled the base for many studies of their dynamic behavior. The widespread of small digital cameras with favorable prices increased the amount of amateur footages that are often available via the Internet. For most people without the specific scientific background those records may constitute the only opportunity to actually see a landslide and gain understanding of related hazards and risks.

Interpretation of videos became a common tool for the qualitative monitoring of landslide behavior in experimental designs [e.g. Enet and Grilli, 2007; Ilstad et al., 2004; Ochiai et al., 2004]. Field studies often integrate [e.g. Jibson, 2006] or even fully rely [e.g. Fujisawa and Ohara, 2008] on video captures to assess failure mechanisms, down slope processes and estimate velocities of real natural events. Video cameras may also be integrated into monitoring systems to observe critical slope units [e.g. Mantovani et al., 2000] or channels [e.g. Marchi et al., 2002]. However, because of restricted reliability (night, fog during rainfall events, etc.) video captures should only be an additional element within early warning systems. On the other hand they still reveal a lot of information for comparison with other monitoring instruments and validation data for numerical models.

Considerable research has been carried out towards an automated evaluation of surface velocities of debris flows [e.g. Arattano and Marchi, 2000; Genevois et al., 2001] from video footages.

The determination of surface velocities is general referred as image velocimetry. Five different approaches, applicable on textured surfaces, can be distinguished [Itakura et al., 2005].

Spatial filtering is based on a grating lines filter placed between a moving object and a photo detector. The periodical variation of the light intensity passing through the filter is directly related to the velocity of the object perpendicular to the filter grate. A setup of two photo detectors with filter lines perpendicular to one another can be used to obtain x and y velocity components of the surface on a moving object [Aizu and Asakura, 1987].

The Spatio-Temporal Derivative Space Method [Ando, 1986] is based on luminance vectors of a pixel and its neighborhood with time. Assuming that luminance of pixel within a defined neighborhood region would not change without any movement, x and y components of the movement are calculated in order to reduce difference in vector space. A crucial step of this method is the definition of the size of the neighborhood area. If the movement of the surface is nearly uniform the errors but also the resolution of measurements decrease with a larger chosen neighborhood areas. However, many surfaces (e.g. debris flows) do not demonstrate a uniform movement and an optimal size (e.g. order of the moving particles) exists. An iterative increasing measurement area can be used to stepwise reduce an intrinsic error term and define the optimal scale of the observation [Inaba et al., 2000].

The encoding of digital videos attempts to exploit redundancies between consecutive or temporally close video images. Most commonly this is done for compression purposes. Instead of saving both consecutive images in full size only parts of the images where changes occur are stored in the second image, while the rest of the information is obtained from unchanged areas of the first image. Motion is estimated by block matching algorithms and encoded as motion vectors. The latter reproduce the changes and are a crude approximation to optical flow, although heavily corrupted by noise [Coimbra and Davies, 2005]. Several methods, e.g. motion segmentation [Avrithis et al., 1999] or the use of vector fields with associated confidence maps have been developed for the analyses of MPEG motion vectors and were successfully applied to surveillance camera captures or images of debris flows [Koyama et al., 2000].

Cross-correlation techniques such as correlation-based optical flow and classical particle image velocimetry (PIV) [e.g. White et al., 2003] are most frequently applied to measure velocity fields on multiple images of fluids and surfaces. Thereby the content of search windows in at least two consecutive images is cross-correlated to determine the average spatial shift maximizing the cross-correlation function. Commonly a two-dimensional discrete Fourier transform is used to facilitate the evaluation of the cross-correlation function [Quénot et al., 1998]. A wide range of different techniques is readily available, while most of them rely on three different stages of image processing [Barron et al., 1994].

Despite their differences, many of these techniques can perform:

1. Filtering to extract signal structure of interest and enhance the signal-to-noise ratio
2. Extraction of local correlation surfaces

### 3. Integration of measurements to produce a 2-D flow field, often including smoothening of derived motion vectors

If the observed surface is a plane parallel to the image plane the derivation of the motion vectors is a straightforward task [e.g. Take et al., 2004]. However, many natural surfaces expose irregular surfaces and there is often no unrestricted choice of view angles in a real-world situation. Thus, many practical applications will include a fourth step if metric vectors in the object domain are desired. If the object-domain resembles a plane oblique to the image plane it is possible to approximate the position of points in 3D space (and consequently vectors) by introducing an interface plane between object and image space [Arattano and Grattoni, 2000].

In general natural surfaces expose more complex geometries than that of a plane and the derivation of 3D motion vectors will require at least stereoviews of the object. In such cases a single view images can reveal 2D motion vectors in the object space if additional information about the surface geometry is available. Related techniques are more commonly in use for the processing of multitemporal photographs and are treated in sections 3.2.4 and 3.4.7.

Considerable progress has also been made in recent years in the analysis of video surveillance for security applications. Main tasks are the real-time recognition and tracking of moving objects but also the recognition of unusual events [e.g. Choudhary et al., 2008], what might be of particular interest for additional components of early warning systems (to see further, please read the deliverable 4.7 of the SafeLand project).

## 3. AERIAL IMAGING

### 3.1. ANALOGUE VS. DIGITAL CAMERA SYSTEMS

Digital systems are cost saving (no film, no photo lab and better automation possibility), the product derivation is time saving (no film development, no scanning and possible automation of the digital workflow), and resulting images have a higher quality in terms of radiometric dynamics, signal to noise ratio and reproducible color and in-flight image control [Reulke, 2003]. Analogue film cameras have a standard square format of 23cm, whereas the market for digital cameras is subdivided in large, medium and small format cameras. Among those digital systems the development of large-format area arrays cameras stagnates and is replaced by systems that integrate multiple medium and small format cameras (with individual lenses and CCD arrays). Many already combine more than 86 megapixels of array area and can be considered as the most advanced digital systems for the aerial image acquisition over large areas. The Intergraph Digital Mapping Camera DMC, for example, achieves a Ground Sampling Distance (GSD) of 20 cm if a flight height of 2000 m is assumed. The German Society of Photogrammetry, Remote Sensing and Geoinformation is currently running a large initiative for the evaluation of new systems [Cramer et al., 2009]. While the geometric resolution of digital cameras still lags slightly behind the resolution of similar analogue systems the location accuracy is quite similar and they achieve a higher radiometric image quality. For the generation of DSMs this leads to superior results from the digital systems [Cramer, 2009]. In many cases analogue cameras purchased before the raise of CCD/CMOS will continue to be used operationally, so that at present and in the near future we can still find products from both instrument types on the market. At the same time the development of

analogue films is still advancing and leads to grainless images at ten microns, while the sensitivity increases by a factor of five, thereby reducing necessary illumination time significantly [Brandes, 2003]. A recent review [Honkavaara et al., 2009] revealed that high-quality digital systems, despite their already common operational use, still need further enhancement in terms of overlapping spectral channels, incomplete camera parameters or on-flight atmospheric correction. Some of these issues have already been recognized or partly solved by the manufactures.

### **3.2. PANCHROMATIC VS. NATURAL COLOR AND NEAR INFRARED**

The traditionally most used film for aerial photography is panchromatic (sensitive in the range from 400 nm-780 nm) black and white film. The film is available in a wide range of resolutions, gradations and sensitivities. Its geometric resolution is usually higher than that of color films and with an appropriate set of filters it can also be used during hazy or misty weather. Color and color-infrared are at present more and more commonly used film types in aerial surveys. Corresponding films comprise three photo sensitive layers to generate a color composite which is built out of the colors blue, yellow-green and red of the visible spectrum. In case of color infrared usually the blue layer is substituted by a layer sensible in the near infrared spectrum. Black and white infrared film is alternatively used for vegetation surveys where an increased contrast of different vegetation types or water bodies is required. A further advantage of infrared aerial photography is that in this part of the spectrum atmospheric interferences are lower.

Instead of representing light by the intensity of a chemical reaction on the film material digital systems convert light into an electric signal. Two sensor types, charge-coupled device (CCD) and complimentary metal-oxide semiconductor (CMOS) are currently in use in commercial systems. The mass production of CCD arrays has so far reached a higher maturity. CMOS arrays are in general cheaper to produce and more susceptible to noise but have the advantage that each cell can be read individually with a lower consumption of power. Multispectral images can be derived by charging parts of the array differently, by filtering of the incoming light or by splitting the incoming light into desired spectral components. The necessary trade-off between spectral and spatial resolution remains similar as for analogue images.

For the derivation of DEMs panchromatic pictures with higher spatial resolution are favorable, while for landcover classification and the detection of landcover changes multispectral information is mostly indispensable.

Current spaceborne sensor development suggests that commercial systems with 25 cm GSD will be implemented by 2012. Due to US regulations it is still under discussion if the full resolution imagery or only a downsampled version (50 cm) will be available for general sale (<http://spatialnews.geocomm.com/dailynews/2009/jan/05/news2.html>). This will probably focus the application of airborne mapping systems on to the local scale, where they still can achieve higher resolutions and on the use of multiple camera views for a very detailed photogrammetric reconstruction of surfaces. Spaceborne imagery can be acquired within less than 24 h for any area of the world and the data product can be delivered in less than 25 h. The operational revisit time of spaceborne sensors is higher and in certain cases the delivery time (minimized to 7 h after order) might be even less than the time required only to get the tower clearance for an aircraft to start mapping (not including mapping and delivery time)

[Eckardt et al., 2009]. For this reason the methodological review of analysis techniques will concentrate on very high resolution and mainly local scale applications.

### 3.3. NEW SENSOR PLATFORMS

Recently a number of Unmanned Aerial Vehicles (UAV, Figure 6), often equipped with low-cost non-metric camera systems, have been used for applications such as vegetation mapping, monitoring of crops or landslides and photogrammetric derivation of DSMs. They can be deployed with great flexibility and were demonstrated to be especially useful for the acquisition of sub-decimeter resolution imagery (Figure 7) on local scale.



Figure 6 : UAVs for cost-efficient acquisition of VHR imagery. Upper: [Laliberte and Rango [2009], Lower: Niethammer et al. [forthcoming]

There they can supply imagery with such a resolution very cost effectively and with a temporal resolution defined in accordance with the specific task. UAVs can be equipped with GPS receiver to obtain a first rough approximation of the sensors exterior orientation (EO), also referred as direct georeferencing. Consequently, via integrated geo-referencing, remaining systematic errors of the direct georeferencing solution can be corrected with the aid of additional image observations [Cramer, 2001]. A calibration of the camera previous to image acquisition can define the interior orientation (IO) of the camera. EO, IO and a topographic model of the underlying surface are combined to iteratively enhance the parameters for the EO, which is used for orthorectification when a certain degree of accuracy is reached. An RMSE (XY) of less than 0.5 m can be achieved with this approach [Laliberte et al., 2008]. Similar accuracies can be achieved if instead of camera calibration or onboard GPS receiver a dense grid of GCPs is distributed on the observed object and measured with DGPS [Niethammer et al., 2009].

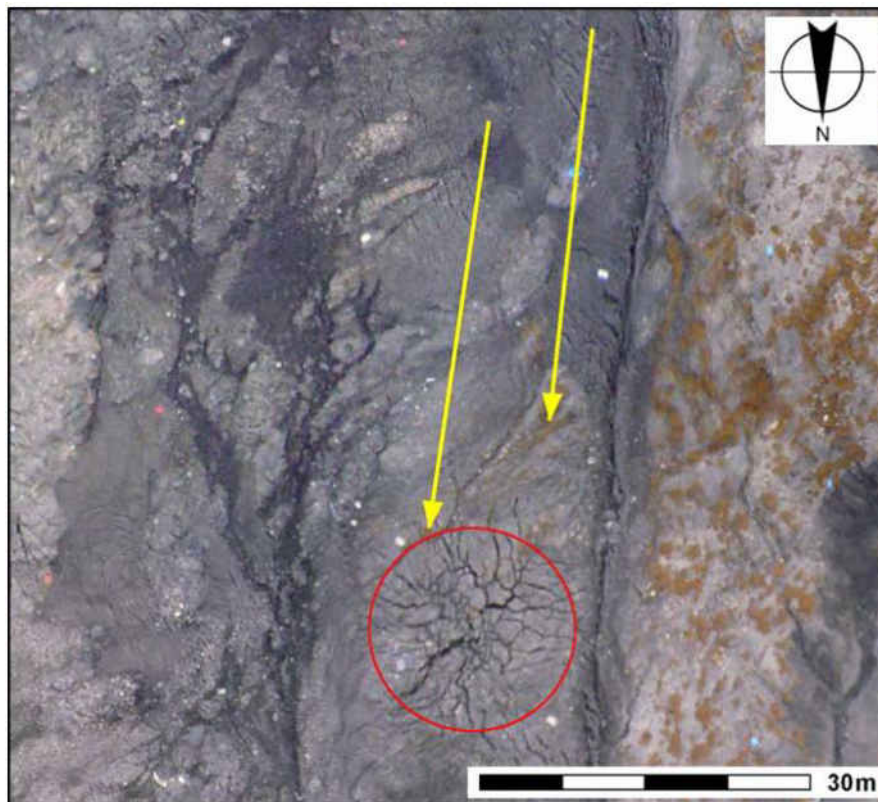


*Figure 7 : Displacement, surface fractures and soil moisture patterns as revealed from a UAV acquired image. Super Sauze mudslide, France [Niethammer et al., 2009].*

### 3.4. VISUAL INTERPRETATION

The visual interpretation of aerial photography has a long history comprising applications such as military operations, agriculture, forestry and geology or the creation of topographic maps. Landslide inventories are traditionally prepared by a combination of visual interpretation of aerial photographs and field work. Despite their time-consuming and labor intensive nature, those are still the most common methods in many scientific studies [Hovius et al., 1997; Korup et al., 2004] and the inventorization carried out by administrative bodies [Hervás and Bobrowsky, 2009].

The human interpreter thereby relies on his personal experience and can take into account color, tone, shape, size, pattern, texture, shadows and contextual information from single or multiple images. Stereoscopy helps to simulate the third dimension, whereas the interpretation benefits greatly in many applications. As the birds-eye view is a very unfamiliar perspective for most people the success of interpretation depends largely on the experience of the interpreter. Even still if experts are assigned with the image interpretation resulting landslide inventories comprise a large degree of subjectivity [Galli et al., 2008; Wills and McCrink, 2002]. False color representations may help to enhance the contrast between background and the area of interest. However, the human eye is in general less sensitive to spectral differences than modern sensors and not all information contained in the image can be used at once by the interpreter. Considering furthermore the time necessary for the visual inspection of large areas, current and future development goes strictly toward automated and semi-automated methods for image interpretation.

### 3.5. AUTOMATED TECHNIQUES OF IMAGE INTERPRETATION

Despite certain differences in acquisition and pre-processing of aerial photographs most analysis techniques apply similar for them as for satellite imagery. Thus, a generic overview of image analysis methods will be given below under 3.4. However, the generation and of multitemporal DTMs is a field where aerial photographs are still the dominant source of stereo data and it is worth adding another paragraph overviewing studies that involved aerophotogrammetry for the study of landslides.

Comparison of multitemporal DTMs (Figure 8) is typically carried out by a simple subtraction, whereas the subtraction between two epochs cannot provide the overall volume of the displaced mass but, this difference allows an estimation of the volume of the uplifted and subsided parts of the terrain between the two epochs [Weber and Herrmann, 2000]. However, average displacement velocities can be derived if the thickness of the landslide body is known from geophysical measurements [Brückl et al., 2006].

Photogrammetric elaborated DTMs can be compared in this way also with DTMs from other sources such as airborne LIDAR scans. An important prerequisite is in any case an accurate alignment of the DTMs through the identification of homologous points on non moving terrain parts [Bitelli et al., 2004]. Furthermore, effects of vegetation and changes of vegetation have to be considered. Several filtering methods are available to remove vegetation from LIDAR point clouds, whereas aerotriangulation is typically restricted to ground points. DTM subtraction implies that individual DTM errors can be combined as independent random variables. With the assumption of normal distribution, this combined error can be used as standard deviation [Dewitte et al., 2008]. Repeated photogrammetric surveys were conducted to monitor the eruption of Stromboli Volcano and the analysis of the multi-temporal DTMs allowed the quantification of erosion/accumulation phenomena to determine a mass balance, useful for the implementation of a stability analysis [Baldi et al., 2005]. A set of six historical aerial photographs was used to create DTMs and evaluate the deformation of the La Clapière landslide (France). It was noted that due to the frequency of aerial surveys this method is mostly only suitable for slow moving landslides but also the potential of these data for slip surface characterization was pointed out [Casson et al., 2005]. The activity of the Tessina landslide (Italy) similarly has been documented with a set of multiple DTMs constructed from historical aerial photographs [van Westen and Getahun, 2003]. Thereby, it was possible to reconstruct activity and involved volumes through several decades.



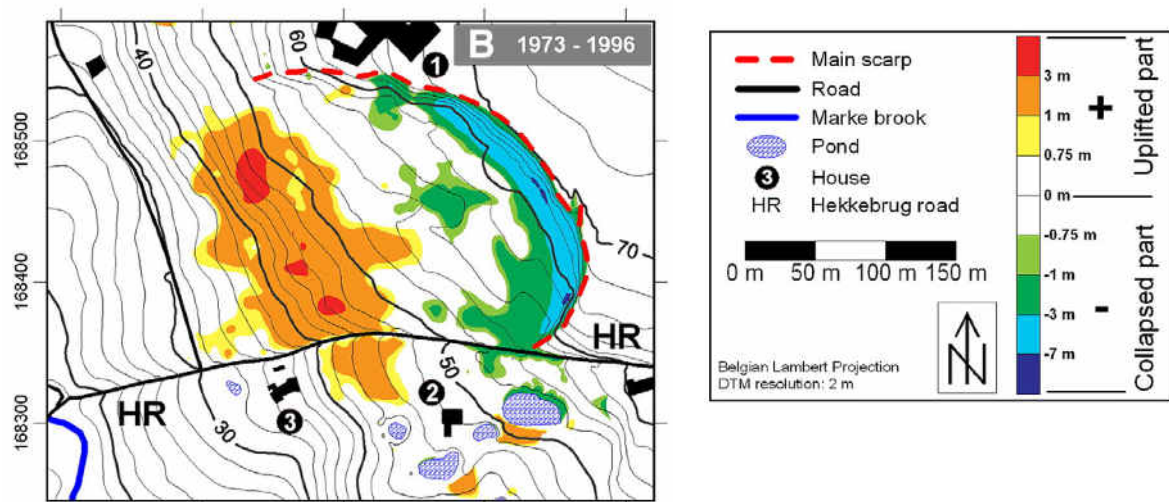


Figure 8 : Map of vertical ground displacements within a landslide in western Belgium inferred from the comparison between DTMs from 1973 and 1996. DTMs were generated from photogrammetrically ground spot heights. [Dewitte et al., 2008]

## 4. SATELLITE IMAGING

### 4.1. SENSORS AND PLATFORM DEVELOPMENT

More than 150 earth observation satellites are currently in orbit, whereas the majority carry passive sensors, measuring electromagnetic radiation from the Earth's surface or atmosphere [Tatem et al., 2008]. Over 250 launches of private and public satellites are expected between 2009- 2018 [Euroconsult, 2009].

In recent years four main innovations contributing to enhance the value of datasets provided by passive optical satellite sensors can be summarized.

1. As mentioned frequently throughout this document the achieved Ground Sampling Distance (GSD) of passive optical sensors reduced considerably during recent years. This is achieved through transfer delay and integration sensors (TDI, e.g. IKONOS, Quickbird), whereas the view of the sensor changes according to the speed of the satellite and the same surface is scanned several times, or staggered CCD lines shifted half a pixel against each other (e.g. Orbview-3, Spot-5) [Jacobsen, 2006].
2. Previously used across-track acquisition mode for stereo imagery has been largely replaced through satellites with along-track stereo imaging capabilities (ALOS Prism, Cartosat-1, ASTER, and SPOT-5). This technique allows the acquisition of stereo imagery with minimal time delay and decorrelation between the stereopairs.
3. The development of innovative three mirror anastigmatic (TMA) telescopes enabled the construction of a series of mini-satellites (e.g. RapidEye) mainly manufactured by the British company SSTL. Those systems can provide high-resolution imagery at relatively low costs and satellite constellations like the Disaster Monitoring Constellation (DMC) or RapidEye enable daily revisit times.



4. Short revisit times, international agreements (International Charter Space & Major Disasters, GMES SAFER), effort of private companies (e.g. Google) and web-based communities (e.g. OpenStreetMap) enable access to VHR satellite imagery up to one day after major disasters (compare Figure 9, Figure 10) and consequent fast assessment of damages and critical points on the ground.

The highest resolutions commercially available are currently provided by the companies Geoeye and Digital Globe. After OrbView-3 failed in March 2007 Geoeye is at the moment operating with the Ikonos (1 m PAN , 4 m MS ) and Geoeye-1 satellites (0.41 m PAN, 1.65m MS). The launch of Geoeye-2 with a GSD of 0.25 m is planned for the years 2011-2012, whereas, due to current U.S. regulations, only a resampled version (0.5 m) of the data will be available for public market.



*Figure 9 : Satellite imagery of an area affected by landslides during the Haiti earthquake of 12/01/2010. The first images were acquired 17.5h after the event and published 12h later, Source: Google Earth.*

Since 2001 Digital Globe operates the Quickbird (0.61 m PAN, 2.44 m MS) satellite and recently extended its fleet with the WorldView-1 (since 2007, 0.5m PAN) and WorldView-2 (since 2009, 0.5 m PAN, 2 m 8-band MS). Similar high resolutions are achieved by EROS-B (0.7 m PAN), Cartosat-2 (0.82 m PAN), Kompsat-2 (1 m PAN, 4 m MS) the Russian Resurs DK-1 [Petrie, 2008]. SSTL recently announced plans for the construction of a mini-satellite named SSTL ART (0.6 m PAN, 2.4 m MS) to provide submeter resolution at less than 0.2 EUR per km<sup>2</sup>. The launch of the French satellites Pleiades-1 and 2 (0.7 m PAN, 2 m MS) is scheduled for 2010 and 2011, respectively. EROS-C (0.7 m PAN, 2.8 m MS) is expected to be launched already this year and KOMPSAT-3's (0.7 m PAN 2.8 m MS) launch is planned for 2011.



Figure 10 : Multitemporal imagery from RapidEye capturing surfaces changes during the Chilean earthquake 2010. Left: Forested region with steep slope in proximity to Constitución (2010-01-22), Middle: Same scene after the Chilean earthquake 2010-02-27 (hours after the event) showing exposures of bare soil due to landsliding, Right: Results change detection. Source: [http://www.rapideye.de/upload/documents/Press\\_Releases/ChangeDetection\\_Chile-Earth-Quake\\_2010-03-04.pdf](http://www.rapideye.de/upload/documents/Press_Releases/ChangeDetection_Chile-Earth-Quake_2010-03-04.pdf)

Whereas the area of resolutions between 2.5 and 10 m has been formerly rather sparsely occupied by SPOT-5 and EROS-A in recent years a number of larger Asian satellites and SSTL based mini-satellites filled that segment. Avoiding an extensive listing of satellites only a few systems will be explained here. The Indian Cartosat-1 (2.5 m PAN) offers geometric and radiometric characteristics making it an interesting option especially for DSM generation. It is complemented by the series of Indian satellites equipped with multispectral sensors (LISS III 5.8 m, LISS IV 23.5, AWiFIS 56 m). The Taiwanese Formosat-2 (2 m PAN, 8 m MS) imagery is available with worldwide coverage and offers similar imaging characteristics as SPOT-5. Meanwhile Thailand's THEOS satellite (2 m PAN, 15 m MS) is still waiting for launch. A comprehensive satellite system including panchromatic (PRISM 2.5 m) multispectral (AVNIR 10 m) and L-band radar (PALSAR) was launched in 2006 by the Japanese JAXA. A number of mini-satellites including for example the RapidEye (Figure 10) constellation and the UK-DMC 2 are largely based on the SSTLs platform 150 (2.5 m PAN, 5 m MS) and 100 (22 m MS), respectively. As part of the SPOT Continuity Program, SPOT 6 and SPOT 7 are currently under development planned to be launched in 2012 and 2014, respectively. The panchromatic channel of those systems is planned to provide ground resolution of 2m. Similarly NASA is planning to continue the LANDSAT program with a Data Continuity Mission (LANDSAT DCM) by December 2012.

A comprehensive overview of potentially interesting, active and planned satellite missions is provided in Table 1. A more complete overview of active and planned sensors including a large number of further SSTL-based microsatellites and platforms with dual use for military and commercial applications is provided in the Appendix of this document.

Table 2 : Current and planned satellite missions for passive remote sensing of the earth surface with a minimal resolution of 30 m. Note that the table was compiled from a great variety of online sources and future launch dates might be a subject of frequent change.

Satellite	Channels	Resolution [m]	Launch	Mission duration
Landsat 7	panchromatic	15	15-Apr-99	end around 2012
	7-bands multispectral	30		

Landsat DCM	panchromatic 8-bands multispectral	15 30	2012	???
CBERS-2	panchromatic 9-bands multispectral	2.7 20 - 260	21-Oct-03	planned for 2 years
CBERS-2B	panchromatic 9-bands multispectral	2.7 20 - 260	19-Oct-07	planned for 2 years
CBERS-3	panchromatic 12-band multispectral	5 (10) 20 - 80	postponed to	planned for 2 years
CBERS-4	panchromatic 12-band multispectral	5 (10) 20 - 80	2011	planned for 2 years
Terra Aster	14-bands multispectral along-track stereoview	15 - 90 15	18-Dec-99	planned for 6 years
RESOURCESAT-	3 - band visible + NIR 8-band multispectral	5.8 23.5 - 56	17-Oct-03	planned for 5 years
RESOURCESAT-	3 - band visible + NIR 8-band multispectral	5.8 23.5 - 56	late 2010	planned for 5 years
RESOURCESAT-	panchromatic 3 - 4 bands visible + 10-band multispectral hyperspectral(200	2.5 5.8 23.5 - 80 25???	mid 2011	planned for 5 years
ALOS	panchromatic 4 - band visible + NIR along-track triplet view	2.5 10 2.5	23-Oct-06	planned for 5 years
Cartosat 1	along-track stereo	2.5	5-May-05	planned for 5 years
SPOT 5	panchromatic 4 - band visible + NIR along-track stereoview	2.5(5) 10 5	4-May-02	planned for 5 years
SPOT 4	panchromatic 4 - band visible + NIR	10 20	24-Mar-98	planned for 5 years
SPOT 6	panchromatic	2 m	2012	10 years?
SPOT 7	multispectral	8 m	2012	10 years?
Formosat 2	panchromatic 4 - band visible + NIR	2 8	21-May-04	planned for 5 years
Kompsat 2	panchromatic 4 - band visible + NIR	1 4	28-Jul-06	planned for 4 years
Kompsat 3	panchromatic 4 - band visible + NIR	submeter < 4	2010	planned for 4 years
Ikonos	panchromatic 4 - band visible + NIR	1 4	24-Sep-99	planned for 8 years
Cartosat 2	panchromatic	1	10-Jan-07	planned for 5 years
Cartosat 2A	panchromatic	1	28-Apr-08	planned for 5 years
EROS A	panchromatic	1.9	5-Dec-00	planned for 10 years
EROS B	panchromatic	0.82	25-Apr-06	planned for 10 years
EROS C	panchromatic 4 - band multispectral	0.7 2.8	Sep-2010	planned for 10 years
Quickbird	panchromatic	0.61	18-Oct-01	planned for 5 years

	4 - band visible + NIR	2.44		
World View 1	panchromatic	0.5	18-Sep-07	planned for 7.25 year
World View 2	panchromatic	0.46	8-Oct-09	planned for 7.25 year
	8 - band multispectral	1.84		
Pleiades 1	panchromatic	0.50	Oct-2010	planned for 10 years
	4 - band visible + NIR	2.00		
Pleiades 2	panchromatic	0.5	2011	planned for 10 years
	4 - band visible + NIR	2		
Geoeye 1	panchromatic	0.5	6-Sep-08	7-10 years
	4 - band color	2		
GeoEye-2	panchromatic	0.25 (0.5)	late 2012	7-10 years
	4 - band color	2		

## 4.2. VISUAL INTERPRETATION

VHR spaceborne remote sensing products can be expected to gradually replace aerial photographs for the purpose of landslide mapping and monitoring. Earlier attempts to take advantage of satellite imagery for landslide mapping still suffered from the rather coarse resolution of Landsat imagery [Petley et al., 2002]. It has been demonstrated that the integrated use of optical and radar data can partly compensate coarse resolution and is helpful to characterize in high and low relief areas [Singhroy et al., 1998]. New sensors with higher resolutions can already provide sufficient ground resolution for comprehensive inventorying of large landslides and to some extent also mud- and debris flows [Haeberlin et al., 2005].

Several studies have taken advantage of VHR satellite imagery for visually interpreting the imagery. It has been suggested that visual interpretation of spaceborne imagery is suitable for the creation of inventories [e.g. Proske et al., 2008], the planning of ground campaigns [Owen et al., 2008] and in certain cases also for the detection and assessment of fissures and tension cracks [Youssef et al., 2009]. There are already VHR satellite missions operating with ground resolutions up to 0.41 m (Geoeye-1) and up to eight spectral bands WorldView-2. Further satellites with a ground resolution of up to 0.25 m (Geoeye-2) are under construction. Keeping this in mind while revising Table 1 it can be concluded that spaceborne imagery can already reach similar, if not superior quality compared to aerial photography. However, problems of visual interpretation remain the same as stated in 3.3.4.

## 4.3. STEREOPROCESSING

One possible way to observe morphology or morphological changes of the earth's surface is the generation of Digital Surface Models (DSMs) from stereopairs images at one or subsequent epochs, respectively. In digital photogrammetry automatic matching procedures are employed for the 3D point measurement over wide areas. This implies that the same object (pixel) is visible and can be identified in two images from different perspectives. Several problems such as decorrelation within the two images, low resolution and low performance of matching algorithm have been solved in recent years. Difficulties with variable atmospheric conditions at different times of across-track image acquisition motivated the implementation of a number of along-track mapping platforms, whereas the first of their kind were the Aster sensor on board of the Terra satellite (1999) and Spot 5 (2002). Aster DSMs have already been used in several geomorphological [e.g. Bubenzer and Bolten, 2008;

Kääb, 2005] and risk assessment studies [Fourniadis et al., 2007]. A global DSM derived from the multiple stereopairs is available for free, however, with a rather high mean RMSE of 9.35 m and a rather low resolution of 30 m [ASTER-GDEM-VALIDATION-TEAM, 2009].

Costs of high resolution satellite images with stereo capabilities are decreasing and accurate DSMs are becoming more attractive for a wider range of applications. An increased number of sensors with along-track stereo-acquisition capabilities give a strong advantage in comparison with former multi-date across-track stereo-data acquisition because the radiometric image variations are less and the correlation success rate in any image matching process increases.

In modern VHR satellites two different approaches are implemented to realize stereo-imaging capabilities. Several satellites have one pointable lens and change the viewing angle to capture stereo images of the same area along the same track (e.g. Ikonos, WorldView, and Quickbird). As stereo imaging is reducing the imaging capacity, their price is considerably higher than for one single scene (e.g. Quickbird 2.3 times higher price). During the time needed for the turn-around of the lens to another view direction no other image can be acquired. Thus, the required time restricts the imaging capacity (for Quickbird by a factor of 9). Newer pointable sensors such as the one on board of WorldView-2 are therefore designed to change the viewing direction much faster [Büyüksalih and Jacobsen, 2007]. Another class of satellites is equipped with multiple fixed cameras (two or three), which record images of the same from different viewing angles due to the forward movement of the platform along the track (e.g. Cartosat-1 with forward and backward, ALOS/PRISM with forward, nadir and backward) [Wolff and Gruen, 2008]. To fully exploit both new imagery types Rational Function Models (RFPs) [e.g. Zhang, 2005] and physical models [e.g. Toutin, 2006] became main lines of research in recent years with considerable advances in terms of more stable and accurate algorithms.

Table 3 : Minimum size of objects to be recognized in various types of RS imagery (after Mantovani et al. [1996] and Wang [2004], modified by Zhang et al. [2005])

Data Source		Spatial resolution (m)	Landslide size (m)
LandsAT-5	MSS	30	300
	TM	30	300
LandsAT-7	ETM	30	300
	PAN	15	150
SPOT-1,2,4	XS	20	200
	PAN	10	100
SPOT-5	XS	10	100
	PAN1	5	50
	PAN2	2.5	25
IKONOS	XS	4	40
	PAN	1	10
QUICKBIRD	XS	2.44	25
	PAN	0.61	6
Aerial photos 1:50,000		0.5	5
Aerial photos 1:25,000		0.25	2.5
Aerial photos 1:10,000		0.1	1

As a rule of thumb the resolution of the photogrammetrically derived DSM should have a resolution at two times lower (more for better accuracy) than the input data. It has been demonstrated that under favorable atmospheric conditions, DSMs with a pixel-spacing of 2m and 3m can be derived from Quickbird and Ikonos stereopairs, respectively [Büyüksalih and Jacobsen, 2007]. An accuracy of vertical RMSE of 5 m and 1.5 m has been reported for DSMs (5 m resolution) generated from stereopairs from WorldView-1 using no and one accurate GCP, respectively [Cheng and Chaapel, 2008]. More recently Martha et al. [2010b] demonstrated that in some cases GCPs are dispensable to obtain accurate landslide volume estimations from multitemporal DSMs (Figure 11).

In general the DSM quality is largely dependent upon image resolution, landcover type and the adopted image matching algorithm. A comparative study of different software packages with Quickbird and Ikonos stereo imagery at different test sites revealed that a Multi-Photo Geometrically Constrained (MPGC) as implemented in SAT-PP leads to superior results with a heighting accuracy of close-to two pixels [Poon, 2007]. Expressed in pixels the DSMs generated from ALOS PRISM [Maruya and Ohyama, 2008; Wolff and Gruen, 2008] achieve very similar accuracies. Due to a unique design dedicated in particular to stereo imaging, DSMs generated from the Indian Cartosat-1 (GSD 2.5 m) stand out by high accuracy. It has been demonstrated that subpixel accuracy can be reached for a 10m spaced DSM [Martha et al., 2010a]. Sacrificing some accuracy also DSMs with finer resolution (up to 2.5 m) can be derived from the stereo pairs [Gianinetto, 2008].



Considerable differences in accuracy also occur in dependence of the sun angle elevation and the local valley orientation [Martha et al., 2010a]. The greater variety of available input data and processing algorithms, a common standard for assessing the final products and communicate it to the end user becomes desirable [Poon, 2007].

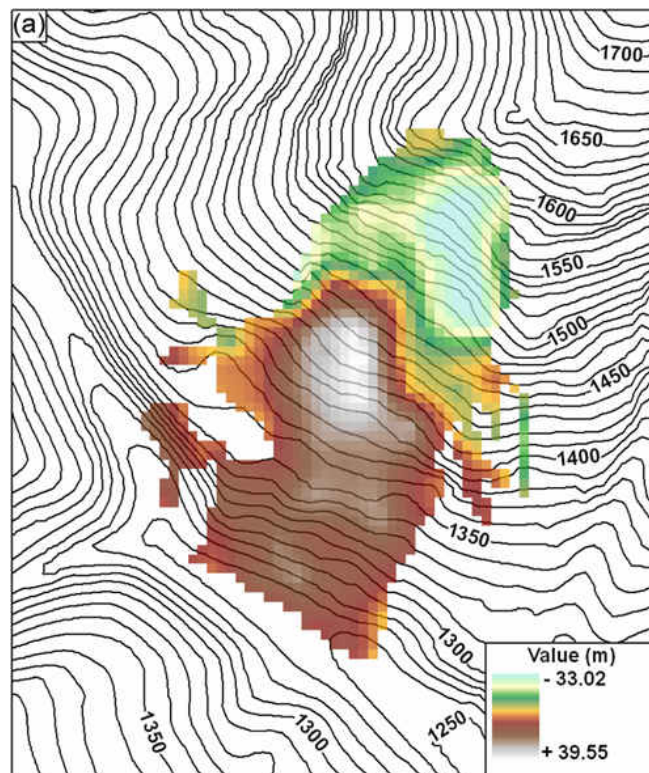


Figure 11 : Volumetric analysis of the Salna landslide, Indian Himalayas. Elevation difference due to landsliding with lowering and rising parts of the surface [Martha et al., 2010b]

DSMs are an important input for orthorectification of any kind of imagery of the earth surface. Higher resolution and accuracy of the DSM helps to reduce distortion and other topographic effects and thereby reduces possible errors during later processing steps such as change detection or image correlation.

Applications of monotemporal DEMs are, for instance, landform classifications [Schneevoigt et al., 2008], structural geology [Murphy and Burgess, 2006] and ecosystem studies [Tenenbaum et al., 2006]. In most hazard assessment procedures, such as for floods and landslides, topography is an important factor and photogrammetric DEMs constitute a cost-effective alternative where suitable ground-based information is not available [e.g. Nichol et al., 2006; Roessner et al., 2000]. More recently Martha et al. [2009a] showed that incorporation of post-failure DSMs derived from satellite stereo views are suitable to identify the type of failure. Radar interferometric techniques show particular strength quantifying small or subtle surface deformation and laser scans are a highly accurate source to quantify surface deformation and displaced volumes. For sudden large scale events they are often not suitable and photogrammetric techniques become more attractive. Several studies demonstrated the usefulness of multitemporal DSMs from satellite captured stereopairs to detect and quantify ground deformation processes [Martha et al., 2009b; Tsutsui et al., 2007]. While most photogrammetric investigations of landslide volumes and ground deformation

still rely on the aerial photographs that provide higher resolution [Dewitte et al., 2008; Walstra et al., 2007] it can be expected that the new VHR sensors with submeter GSD will gradually replace aerial photography in the future.

#### **4.4. SUPERVISED CLASSIFICATION TECHNIQUES**

Despite a great variety of possible methods supervised classification typically involves the six following processing steps.

1. Deciding the number and nature of targeted classes
2. Choose a representative set of training pixels for all desired classes
3. Training of a chosen classifier algorithm with the training data
4. Apply the parameters estimated by the classifier to the whole image
5. Produce tabular summaries of the obtained classification results
6. Accuracy assessment using test data

A practical minimum for the number of training pixels is ten times the number of features (typically the number of bands) employed for the classification. For satellite images with a low number of spectral bands this number of samples can mostly be provided relatively easy while the task gets more difficult using hyper spectral data.

The most common supervised approach for image classification is the Maximum Likelihood Classification (MLC). Based on a set of samples, probability functions are derived in multivariate feature space and used to calculate the probability of each pixel in the image to belong to one of the given classes. Finally, the class with the highest probability is assigned to the pixel. Additionally prior probabilities for the occurrence of a class can be integrated in the classification and the definition of accuracy thresholds is helpful to avoid misclassifications of pixels with low preferences toward a certain class membership. Borghuis et al. [2007] used a supervised MLC for the detection of typhoon triggered landslides in Taiwan.

If the amount of training data and/or computational capacity is limited the Minimum Distance Classification is an appropriate alternative. Thereby, class memberships are defined by the shortest (mostly Euclidean) distance to the centre of a given class. A more sophisticated extension of the approach is the Mahalanobis Classifier that accounts for the scaling of the coordinate axes, correlations between the different features and can provide curved as well as linear decision boundaries. However, the computational expense grows quadratic with the number of features. The k-nearest neighbor algorithm defines the class membership of a pixel based on the class membership of the k nearest neighbors within the feature space. K defines the number of considered neighbors and is usually chosen to be an odd number between 1 and 5 or larger to reduce the effect of noise within training data. Parallelepiped Classification can be considered as a very simple classification method. A bounding box is constructed around a set of samples in multivariate space. Classes are consequently assigned according to the position of the unclassified pixel within those bounding boxes. However, this approach comprises



several drawbacks in the classification of pixels that lay outside or in the overlap of the bounding boxes.

It has been recognized that pixel-based approaches lack to consider contextual information and Markov Random Fields have been successfully introduced to a large number of image classifications tasks [Serpico and Moser, 2007]. The underlying assumption is that the class value of a pixel is to some degree conditional independent to its neighborhood. The probability density function among a local neighborhood is determined and used to remove outliers.

Experimental results on Formosat-2 imagery indicate that this technique can increase the accuracy of landslide detection [Chang, 2006; Hsieh, 2006].

Another large group of supervised classifiers are non parametric models such as Linear Discriminators, Support Vector Machines (SVM), Artificial Neural Networks (ANN) and Random Forests. Many of them have been applied for landcover classification [e.g. Gislason et al., 2006; Kavzoglu and Colkesen, 2009]. Danneels et al. [2007] compared MLC and ANN to detect landslides on ASTER images, whereas ANN provided the better results. The obtained map, stating the probability of each pixel to belong to a landslide, was refined by applying threshold segmentation on the probability map. Consequently, a larger number of false positives were eliminated through expert-knowledge based on decision rules including for example thresholds of slope. Marcelino et al. [2003] evaluated several simple supervised classifiers (MAXVER, Bhattacharyya, ISOSEG) combined with a variety of image fusion techniques for landslide mapping with Landsat TM imagery in southern Brazil. From visual assessment of the results they concluded that Wavelet Transform and the MAXVER classifier led to the best results. The study was later continued demonstrating positive results for general landcover classification but, due to regeneration of vegetation there was strong confusion between landslide and pasture areas [Marcelino et al., 2009].

Image texture can alternatively be used to pixel-based information in supervised classification. For instance, Hervás and Rosin [1996] used a supervised semi-automated texture discrimination technique based on the image texture spectrum, which quantifies texture in terms of frequency distribution of local pixel intensity variation, to discriminate landslides with hummocky surface or multiple scarps on high-resolution Deadalus ATM imagery of a semi-arid area in Spain. This supervised technique proved superior to unsupervised texture measures derived from grey-level co-occurrence matrix statistics. Incorporated into a classification scheme the additional information from texture helped to distinguish the vegetated surfaces of the landslides from surrounding pasture and enhanced the accuracy. Several other studies tested a number of different GLCM texture measures to distinguish between landslide-affected areas and stable parts [Carr and Rathje, 2008; Fernández et al., 2008; Whitworth et al., 2002; 2005; Whitworth et al., 2006]. They generally agreed that texture is able to enhance class separability as well as the accuracy of the classification and highlight GLCM entropy as an especially useful measure.

#### **4.5. UNSUPERVISED CLASSIFICATION AND CLUSTERING TECHNIQUES**

Unsupervised classification and clustering techniques can be used to obtain a first overview of the inherent structure of a given dataset. On the one hand this technique does not comprise the

need of sample, but on the other hand, obtained classes must usually be interpreted and labeled by the user. Typically the user defines the number of targeted classes and a clustering algorithm assigns pixels to the different classes according to their position in a multivariate space. Many different algorithms using different similarity measures have been proposed. Those used commonly are based on simple distance measures in multivariate space [Richards and Jia, 2006]. Borghuis et al. [2007] employed unsupervised classification using SPOT-5 imagery combined with a slope mask what produced a 63% area concordance with the manually mapped landslides. The performance was better than with other supervised classification methods. Unsupervised classification was also used by Dymond et al. [2006], taking into account bright areas on slopes only steeper than 5°. However only landslides greater than 10,000 m<sup>2</sup> were checked and no independent data set was used for verification. Testing eight different methods for landslide mapping with SPOT-5 imagery Joyce et al. [2008] concluded that the spectral angle mapper (SAM), supervised classification and NDVI thresholding were the most accurate semi-automated techniques compared with the results achieved with parallelepiped, minimum distance to means, principal components, and multitemporal image differencing.

#### **4.6. CHANGE DETECTION**

Joyce et al. [2009] noted that if multi-temporal imagery of a given area can be provided change detection is certainly the most promising approach for landslide mapping and monitoring. Change detection has a long known history and most methods have been developed for the evaluation of changes in land-use and land-cover. A great number of techniques is available and can be grouped into algebra, transformation, classification, advanced models, GIS approaches, visual analysis and other approaches [Lu et al., 2004]. Despite the great variety of proposed approaches, change-detection methods usually comprise a modeling phase and a subtraction phase. Thereby the modeling phase is the application of algorithms to infer meaning from spectral data. Subtraction compares data from different dates via image algebra or other methods [Kennedy et al., 2009]. While there is no general agreement on the best available method Differencing, PCA, Change Vector Analysis (CVA) and Post-Classification Comparison are at present most frequently used [Lu et al., 2004].

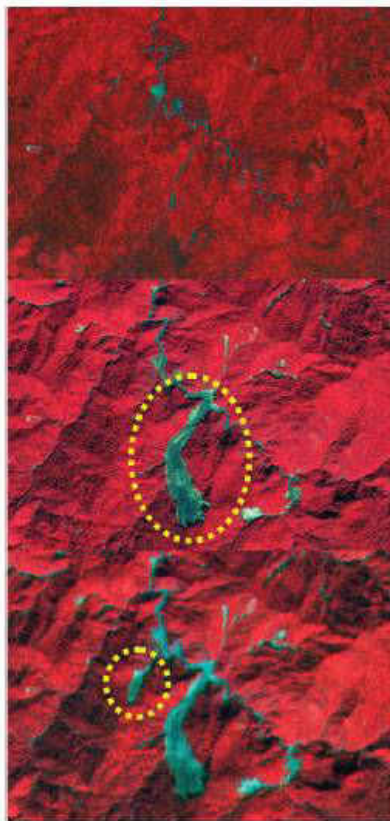


*Figure 12 : SPOT imagery showing the evolution of landslide from before (a) and after two typhoons (b,c), [Rau et al., 2007]*

For landslide mapping Cheng et al. [2004] carried out change detection by differencing the band ratios of IR and red channel of SPOT images. A change-threshold was manually defined from the histogram of the difference image and a slope mask of  $22^\circ$  was applied to filter out changes not related to landslides. Nichol and Wong [2005] tested several change detection methods to detect landslides, including subtraction of single bands and band ratios and post-classification comparisons using the Neural Network classifier and the Maximum Likelihood classifier (MLC). Best results were obtained using MLC and led to detection rates of 67% in grassland areas and 71% in woodland areas. Rau et al. [2007] examined a series of optical satellite imagery with a temporal resolution of about 19 days for a period of 2.5 years (Figure 12). They combined CVA and NDVI for change detection with empirical thresholding and were able to monitor seasonal dynamics and landslide triggered by three major typhoons. Hervás et al. [2003] combined image differencing with an automated thresholding technique to differentiate between change and no change areas. The technique was applied on simulated IKONOS imagery of the Tessina landslide (Italy). Discrimination of landslide active and stable areas was further accomplished by applying a rectangular blob filtering technique on the thresholded difference image. The method was also demonstrated useful for long-term landslide monitoring, especially when datasets with even better spatial and temporal resolution are getting available.

#### 4.7. DIGITAL IMAGE CORRELATION (DIC)

Measuring the offset of pixels in at least two consequent images of an area can help to coregister the images and to gain information on the direction and magnitude of horizontal ground displacements. Different implementations of this concept have been proposed in the past [Crippen, 1992; Puymbroeck et al., 2000; Strang and Nguyen, 1996; Yamaguchi et al., 2003] to measure for example ground displacement along ruptured faults or due to slow moving landslides. The increased availability of high resolution earth observation products and a number of sophisticated algorithms readily implemented in software tools (Correli [Hild et al., 2002], MIC-MAC [Pierrot-Deseilligny and Paparoditis, 2006] or MEDICIS [CNES], PICMATCH [JPL]) contribute to a recently more frequent use of this concept for observation of terrestrial and also extraterrestrial surfaces [e.g. Tokumaru and Dimotakis, 1995]. Delacourt et al. [2007] summarized the prerequisites for the application of DIC as follows:

*“The correlated images have to share a common (ground or image) geometry, which is obtained either by orthorectifying both images (the correlation is performed in the ground geometry) or by resampling a secondary image in the geometry of a reference image (correlation performed in the image geometry). A DEM is necessary in both cases and its required accuracy is inversely related to the difference in viewing angles of the correlated images. Ideally, two different DEMs, contemporary to each correlated image, should be used.”*

Kääb [2002; 2004], Berthier et al. [2005] and Scherler et al. [2008] applied DIC on aerial photographs and imagery from ASTER and SPOT and obtained surface velocity fields with accuracies in the range of 1 to 1/20 of the respective pixel sizes.

Yamaguchi et al. [2003] were among the first to use DIC techniques for landslide monitoring and successfully detected displacement within correlating SPOT imagery. However, they did not provide information on the accuracy of the obtained displacement vectors. Delacourt et al. [2004] used a combination of aerial photographs and Quickbird imagery to determine the displacement field of the La Clapière landslide. They conclude that practically, measurement of displacement reaching from 0.1 to hundreds of pixels can be performed. With VHR imagery ( $GSD \leq 1$  m) motion as low as 0.1 m can be detected, whereas the accuracy strongly decreases if imagery from different sensors is compared. The study has later been extended using a series of aerial photographs for DIC and the generation of corresponding DEMs at each time step. Obtained displacements were found to be in excellent accordance with ground measurements from electronic distance-meters [Casson et al., 2005]. More recently a user friendly software tool has been developed and its applicability for operational use demonstrated [Leprince, 2008]. Optical correlation can be applied with sub pixel accuracy over few years where vegetation causes a loss of coherence for DInSAR techniques (cf. section 2.C.3). The increase in spatial resolution of the new satellites will allow a better accuracy in the computation of lateral displacements using correlation techniques once a comprehensive archive will be acquired [Delacourt et al., 2009].

#### 4.8. OBJECT-ORIENTED CONCEPTS

Due to the increasing availability of VHR remote sensing datasets and the raise of professional software tools Object-Based Image Analysis (OBIA) has been introduced in a

wide range of scientific disciplines, especially during the last decade. OBIA, also referred as GEOBIA (Geographic Object-Based Image Analysis) or OOA (Object-Oriented Analysis), builds on long known methods for segmentation, edge-detection, feature extraction and image classification. In a first step a segmentation algorithm divides the image into meaningful homogenous areas (Figure 15, Figure 16). Consequent classification labels the derived objects based on rules from expert knowledge and/or training-data. It is frequently pronounced that the Object-Based approach can overcome several restrictions of traditional pixel-based image analysis methods [Blaschke, 2010].

- Due to greater detail in VHR resolution images statistical separability between classes gets reduced, what leads to a salt-and-pepper appearance of the classification results
- Objects have additional spectral information compared to single pixels (means, medians, minimum, maximum, variance, mean ratios in different bands, etc.)
- Segments reveal additional spatial information (shape, size, distances, neighborhood, topologies etc.)
- The analysis of geographic objects is in better agreement with the human perception and the composition of the earth surface
- OBIA is more suitable for multi-scale analysis approaches
- Facilitated mining, -querying and -modeling of remote sensing data with richer semantics, and greater integration with vector-based GIS.
- The integration of additional datasets as object features is relative straight-forward.

With respect to the implemented algorithms, image segmentation can be divided into four categories, which are point-based, edge-based, region-based and combined approaches. Deeper insights into the technical implementation of these segmentation concepts can be gained from works such as Haralick and Shapiro [1985] and Pal and Pal [1993]. A crucial step of OBIA states the choice of the segmentation method and the corresponding parameters. Considering the Shannon sampling theorem, an object-size should be of the order of ten pixels to ensure that it will be completely independent of its random position and its orientation relative to the sampling scheme. Region-growing algorithms have become a widely used segmentation method and similar to other segmentation methods, require a number of parameters to determine the maximum degree of heterogeneity. Criteria for heterogeneity can be defined through color (grey values in different channels), shape, texture, class memberships and others. In any case, a suitable set of parameters constraining the degree of heterogeneity within single objects and/or among all objects has to be determined. Allowing a larger degree of heterogeneity in general results in larger objects. Consequently, the choice of the parameters is directly related to the resolution of the image and the desired scale of the analysis. The choice of the maximum heterogeneity and scale of the analysis can be adjusted to the heterogeneity and size of a group of target objects. At the same time, we can observe that in many cases significant objects emerge at different analysis within the same image [Blaschke, 2010], what complicates the task of finding an appropriate scale. This is especially the case if the process of interest manifests on different scales or if little prior

information about the scale of a respective process is at hand. In many works the evaluation of the best segmentation method and parameters is still done by simple trial and error and visual inspection of the obtained results (subjective evaluation), whereas several studies already investigated methods for an objective evaluation and optimization of the segmentation [Zhang et al., 2008a].

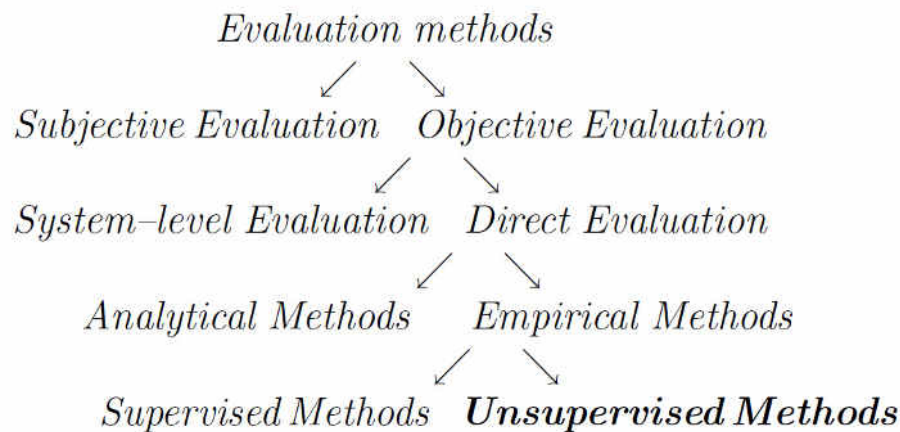


Figure 13 : Conceptual overview of methods for segmentation optimization [Zhang et al., 2008a]

System-level evaluation (Figure 13) can provide a statement on the most suitable segmentation methods for a specific set of consequent processing steps. Analytical methods evaluate the performance of an adopted algorithm in terms of computational efficiency but are not appropriate to judge the obtained results. Supervised methods comprise the need of defined objects of interest as delineated on the ground or by a human interpreter. Discrepancies between geometry and/or feature values of manual and automated delineated objects are then used to determine the segmentation with the best fit. However, providing the necessary samples is time consuming and especially if the characteristics of the objects of interest vary strongly in shape, size, color and texture there might be no unique solution. Furthermore, it can be argued whether subjective delineated objects are really a good reference [Zhang et al., 2008a]. Within unsupervised evaluation methods a great number of criteria evaluating intra-region uniformity, inter-region disparity and semantic cues exist. The resulting best segmentation varies considerably on the chosen criteria and the performance of each criteria differs largely from image to image [Zhang et al., 2008a].

We can conclude that for relative homogenous objects like houses or crops it is possible to estimate one best segmentation method and one best set of related parameters using supervised and unsupervised empirical methods. However, dealing with objects such as landslides or vegetation patches, which differ considerably in shape, size, texture and color, finding the optimal segmentation becomes an ill-posed problem and proposed approaches appear not suitable.

A trial and error evaluation by a human interpreter is one possible choice but might not be satisfactory due to the large amount of subjectivity and, as it is time consuming, it reduces the benefits of the automated image processing. An evaluation on the system-level is possible if sufficient samples for all objects of interest can be provided [e.g. Laliberte and Rango, 2009].

A strictly different solution for the problem of finding the optimal segmentation method and parameters was recently conceptualized by Baatz et al. [2008] as illustrated in Figure 14.

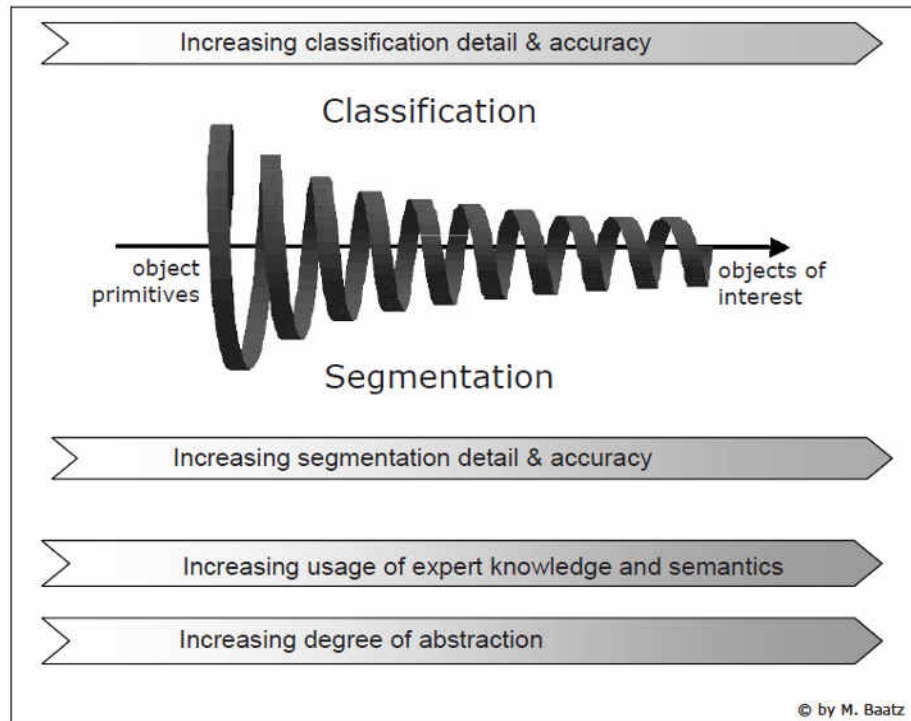


Figure 14 : The conceptual workflow of object-oriented image analysis [Baatz et al., 2008]

Instead of basing the classification process on one static image segmentation the process starts with object primitives that are altered during iterative steps. This includes for example the definition of subsets after an initial segmentation and the local refinement of their borders. It also includes the possibility to look at objects on different hierarchical levels, whereas statistic measures can be employed to evaluate relationships between different levels (e.g. number or standard deviations of sub-objects) or to the local neighborhood within each level (e.g. difference to neighborhood objects). In each iterative step further object characteristics, knowledge and semantics can be integrated approaching the form of an object of interest. During each step statistic measures are stored in variables. Absolute and relative values as well as their evolution during processing steps (e.g. persistency of borders) are assumed to be an important tool for auto-adaptive strategies to provide robust results relatively independent from the initial segmentation parameters and over any expected variability of object characteristics [Baatz et al., 2008].

A further important advantage of the OBIA approach is the possibility to incorporate additional datasets as object features. According to the classification of Dong et al. [2009] this falls into the category of feature level data fusion. Thereby the original datasets undergo no physical change but are present as object features to enhance boundaries and classification efficiency. This includes for example the integration of multitemporal data [Park and Chi, 2008], DEM derivatives [Barlow et al., 2006] or thematic data such as river network [Martha et al., 2009a]. As most classification techniques build on the assumption that given object classes can be recognized as homogenous clusters in feature space it is recommendable to



differentiate a higher number of classes (e.g. active vs. inactive landslides, debris flows vs. deep seated rock slides) as the number of integrated additional features (from the same or different datasets) increases. If this is not considered clusters may include many outliers and get very dispersed among feature space [e.g. Moine et al., 2009].

Beyond the potential benefits for landslide mapping and monitoring (further outlined in D 4.3) valuable data for hazard and risk assessment comes from neighboring disciplines with OBIA approaches. It has been demonstrated that the concept is suitable for the detection of geological lineaments [Mavrantza and Argialas, 2008] or fault lines [Marpu et al., 2008], geomorphological mapping [van Asselen and Seijmonsbergen, 2006], the quantification of landcover changes [e.g. Riedel et al., 2008] or the indirect evaluation of social vulnerability [Ebert et al., 2009]. A comprehensive review of case studies and current developments in the application of OBIA concepts was recently provided by Blaschke [2010]. From there it can be concluded that the concept is so far most frequently used in landcover and land use classifications with especially good results in urban environments.

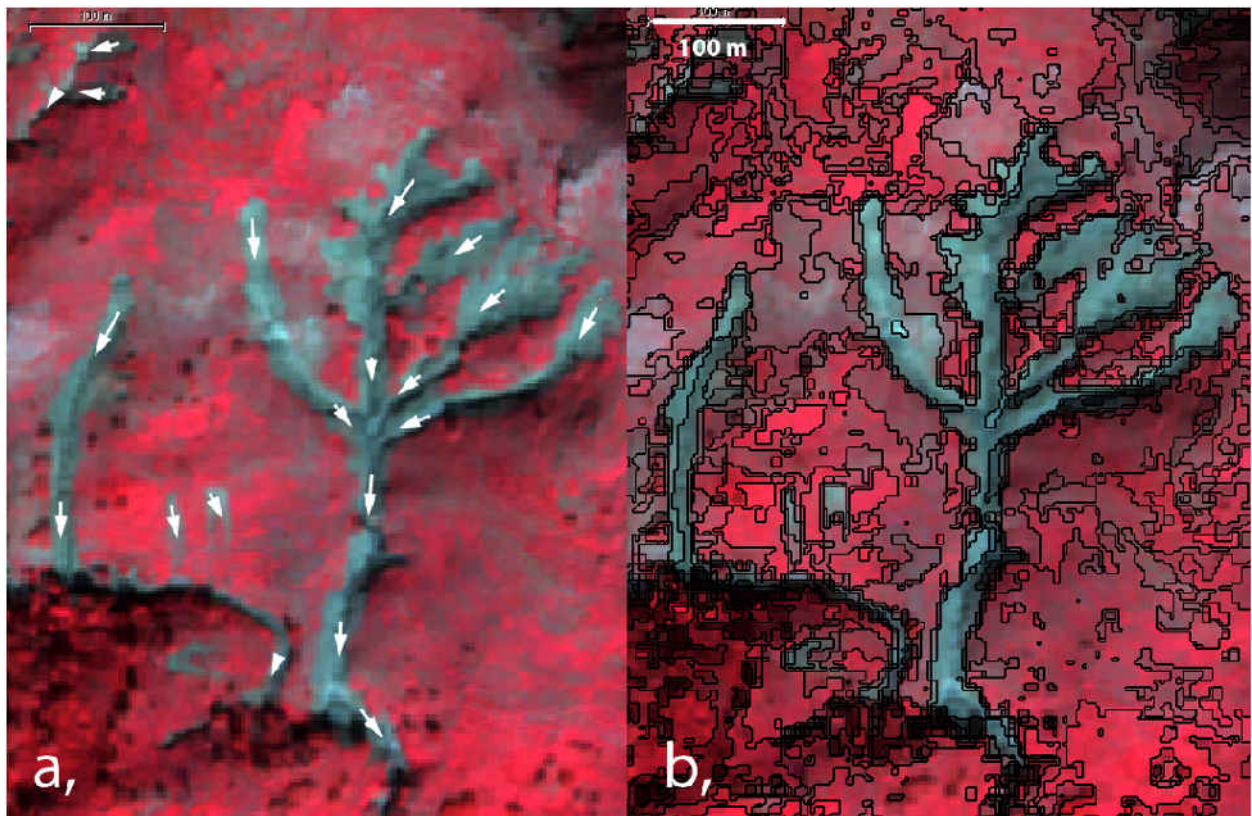
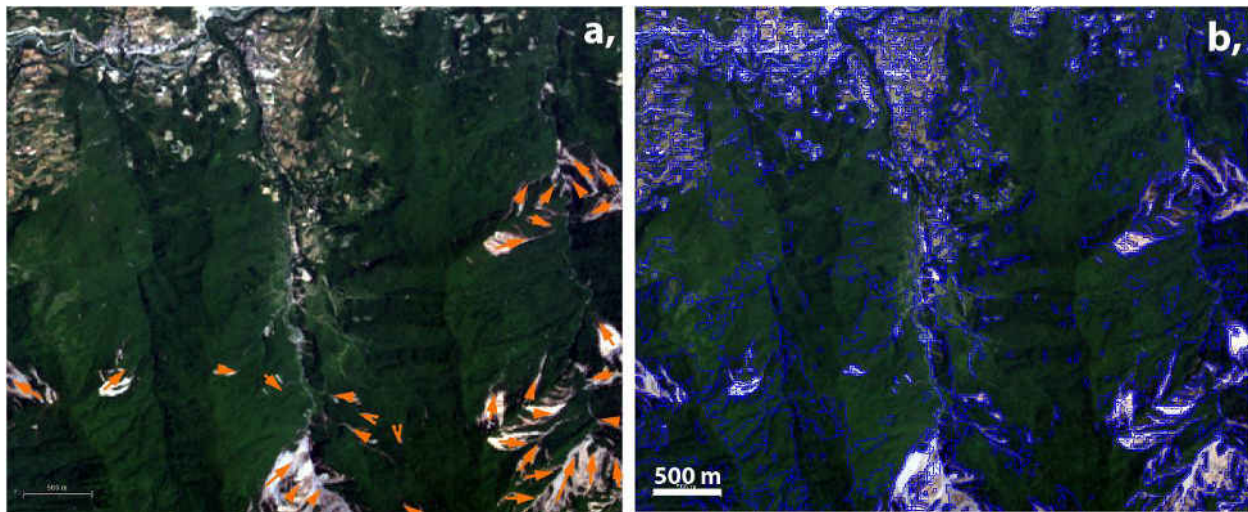


Figure 15 : Result of image segmentation on post-landslide image at Messina, Italy 2009 (Quickbird, 0.41 m pansharpened). a, The white arrows in the input image indicate the flow path of several debris flows, b, Results after image segmentation – The resulting image objects have additional features such as shape, size and texture, which can be used to enhance the classification.





*Figure 16 : Result of image segmentation on post-landslide image at Wenchuan, China 2008 (ALOS, 10 m multispectral). a, The orange arrows in the input image indicate the position and direction path of several rock slides, b, Results after image segmentation – The resulting image objects have additional features such as shape, size and texture, which can be used to enhance the classification.*

OBIA is still a very young and emerging discipline what comprises a number of general and landslide specific challenges. As mentioned above a meaningful integration of additional data (e.g. established landslide inventories, DEMs, multi-temporal images), parameters (e.g. hierarchies between scars, deposits, toes, reactivation of deposits) and methods (e.g. change detection) is needed. New methods and tools for accuracy assessment (e.g. thematic and geometric comparison with expert inventories) dealing with object specific characteristics such as fuzzy thematic information and complex geometries [Schöpfer et al., 2008] should be tested. In the pan-European context of SAFELAND further landslide specific case studies can investigate the adaptability of OBIA workflows to different environments. First steps should include a comprehensive statistical evaluation of assumable landslide specific object-features on a broad set of images of different processes from different regions. Any kind of semi-automated or fully automated system will need a comprehensive amount of training and test data, what should be considered in the implementation of a European landslide inventory.

A database of well documented samples or samples interactively provided by an expert are useful to train stochastic models for image information mining such as described by Datcu et al. [2003], (Figure 17). Similar to the hierarchical order of objects and sub-objects in OBIA the system uses a multi-resolution image pyramid and furthermore, an initially unsupervised clustering of the image content based in multidimensional feature space (grey values and texture). A set of class primitives is provided to a user that labels the object and thereby provides the training data to the system. A Bayesian network is fed by that training data and labels the unsupervised part of the image based on similarities, or more specific on their proximity in feature space.

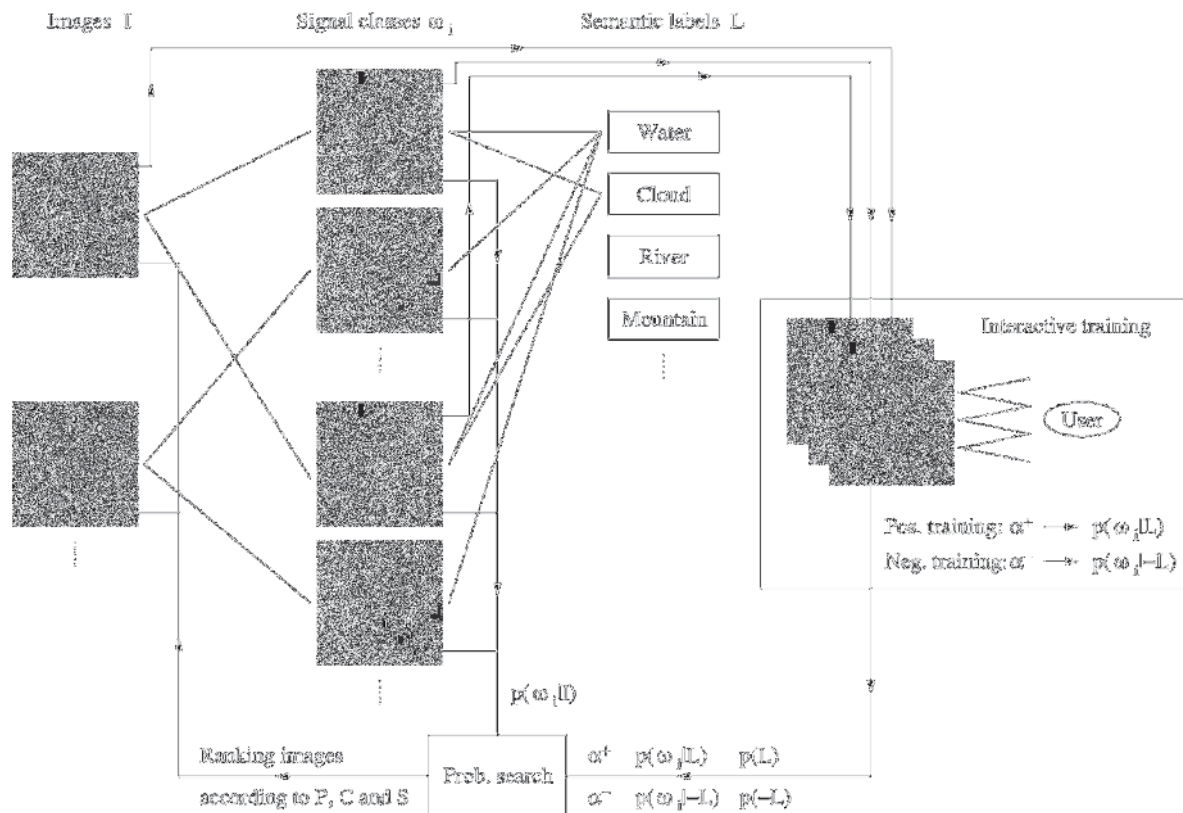
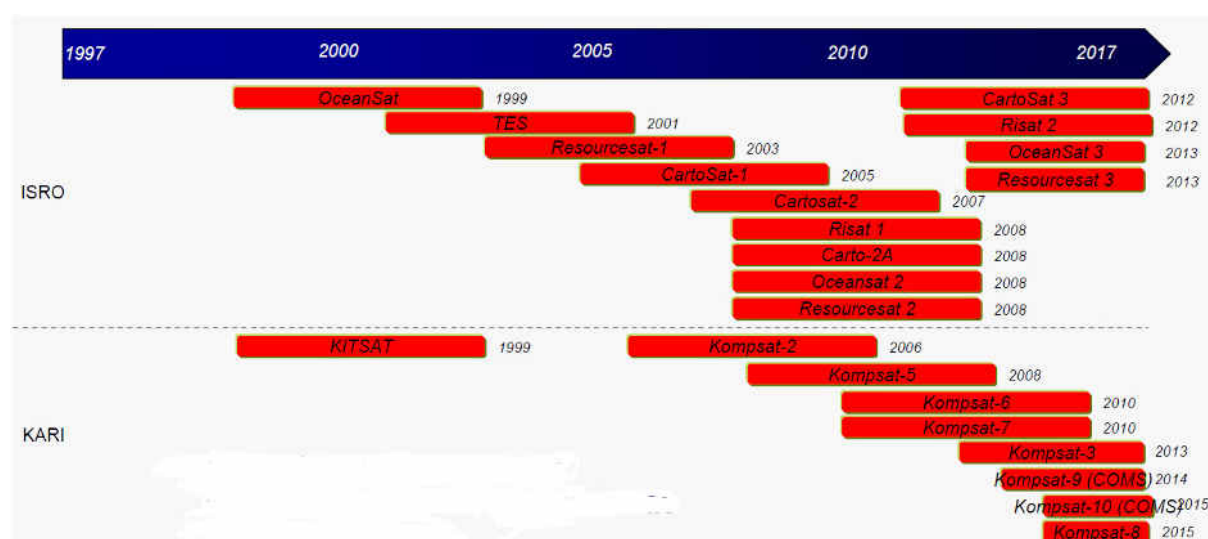
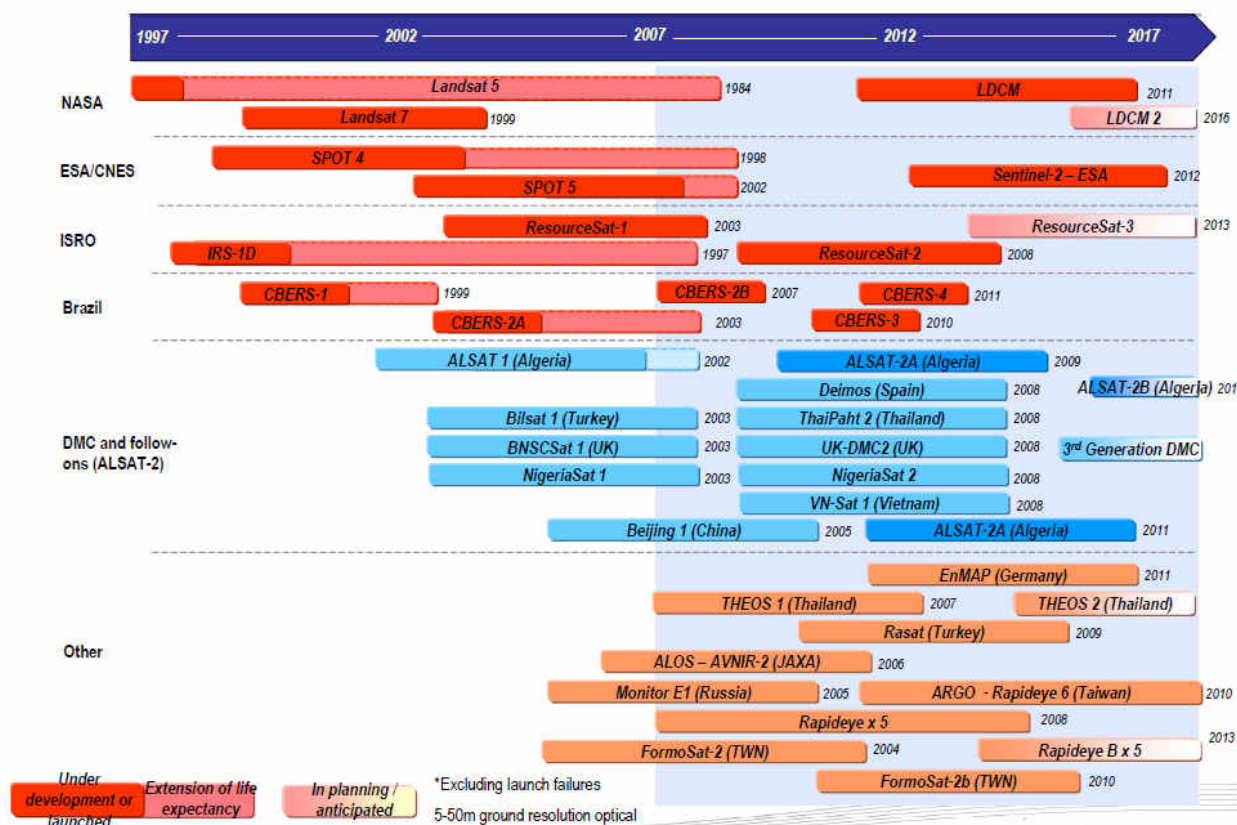
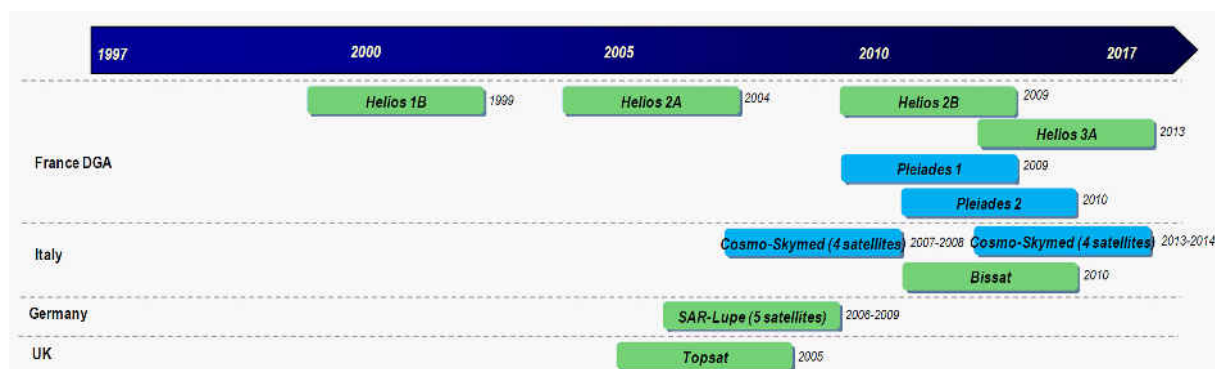


Figure 17 : Conceptual representation of Bayesian model for image mining [Datcu et al., 2003]

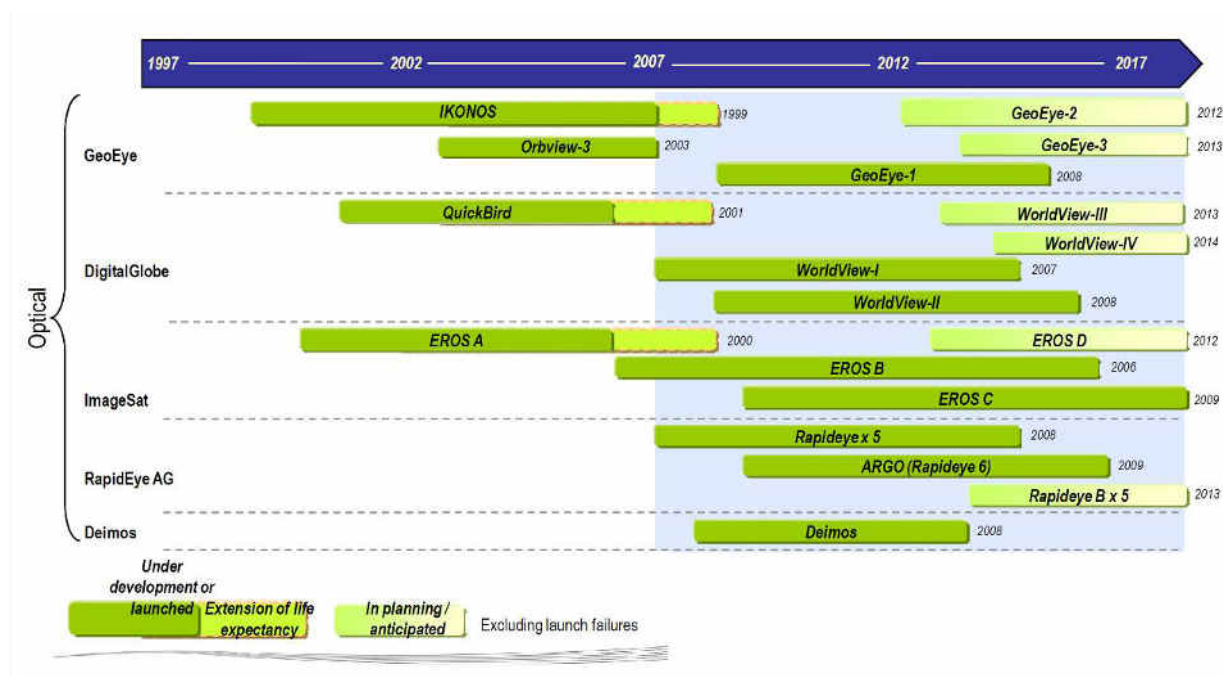
The formalization and implementation of such models in combination with objective methods for the determination of segmentation and classification parameters is a promising approach to take full advantage of the increasing availability of remote-sensing data from supranational initiatives (GEOSS, GMES) on an operational basis. Considering environmental changes (e.g. climate change, urbanization) the latter is essential for a frequent updating in hot spot areas and quick response after major events. In a way OBIA also converges with current efforts of object-oriented modeling of a European spatial data infrastructure (INSPIRE; <http://inspire.jrc.ec.europa.eu>). This may simplify the interoperability with ground-based monitoring systems, the construction of comprehensive knowledge bases and the communication of results in the future.

## 5. APPENDIX





Appendix 3: Roadmap for European defense Earth observation satellites [Euroconsult, 2008].



Appendix 4: Commercially operated optical satellites launched to 2007, Planned/Anticipated: 2007-2016,[Euroconsult, 2008].

---

# PART B

## ACTIVE OPTICAL SENSORS

---

---

- <b>SECTION 1:</b> Basic Principles of Laser Ranging	p. 66
- <b>SECTION 2:</b> Electronic Distance Meter (EDM)	p. 68
- <b>SECTION 3:</b> Terrestrial Laser Scanner (TLS)	p. 76
- <b>SECTION 4:</b> Aerial Laser Scanner (ALS)	p. 91

---

### Sections 1, 2, 3 and 4

- **Authors:** A. Abellán<sup>1</sup>, M. Jaboyedoff<sup>1</sup>, C. Michoud<sup>1</sup>, M.-H. Derron<sup>1</sup>
- **Reviewer:** T. Oppikofer<sup>2,3</sup>

<sup>1</sup>. Institute of Geomatics and Risk Analysis (IGAR). Université de Lausanne, Switzerland. [antonio.abellanfernandez@unil.ch](mailto:antonio.abellanfernandez@unil.ch)

<sup>2</sup>. International Center for Geohazards (ICG), Oslo, Norway.

<sup>3</sup>. Geological Survey of Norway (NGU), Trondheim, Norway.

Abellán A., Jaboyedoff M., Michoud C., Derron M.H., Oppikofer, T., 2010. *Active Optical Sensors (LASERS)*. In the Deliverable 4.1 of the European project SAFELAND: *Review of Techniques for Landslide Detection, Fast Characterization, Rapid Mapping and Long-Term Monitoring*. Edited in 2010 by Michoud C., Abellán A., Derron M.-H. and Jaboyedoff M. Available at <http://www.safeland-fp7.eu>



This part of Deliverable 4.1 (*Review of methodologies for landslide detection, fast characterization, rapid mapping and long-term monitoring*) is focused in the description of Active Optical Sensors, also referred to as LASERs (Light Amplification by Stimulated Emission of Radiation). A laser is a device that produces and emits a beam (or a pulse series) of highly collimated, coherent, monochromatic, directional and in phase electromagnetic radiation.

This part is divided into four sections. Section 1 describes the basic principles of laser ranging and scanning. Sections 2, 3 and 4 describe the different techniques, Electronic Distance Meter (EDM), Terrestrial Laser Scanner (TL) and Aerial Laser Scanner (ALS), respectively. These three techniques are complementary: whereas EDM allow for a high accuracy (mm scale) acquisition of single points, scanning systems (TLS and ALS) allow for the acquisition of million points with centimetre-level accuracy.

Basic principles of the laser technique and methods for ranging, scanning, filtering and/or aligning of the laser datasets will be described in the following sections. Furthermore, a description of the main applications (distance calculation, monitoring, landslide displacement computation, structural analysis, etc.) for landslides will also be discussed in this report. Finally, some practical case studies on the use of this technique are provided in the Chapter 4 of this Deliverable.

Direct visibility is required between the electronic device and the surveyed point. Distance calculation was initially carried out at specific points using reflectors (referred to as prisms or targets), which return the laser beam into the direction of its source. Currently, distance measurements can be carried out directly over the terrain surface (i.e., without artificial reflectors), which is highly recommended in hazardous areas.

Two interesting books have been recently published: “*Topographic laser ranging and scanning*”, by Shan and Toth (2008) and “*Laser Scanning for the Environmental Sciences*”, by Heritage and Large (2009). The former reflects the state-of-the-art of all the physical aspects of the sensor (components, calibration, waveform analysis, quality control of LIDAR data, filtering and feature extraction techniques, etc). The latter provides a number of applications of the LIDAR technique to the environmental and geosciences, being of great value for those researches in the field of geomorphology, geostatistics, remote sensing and GIS.

## **1. BASIC PRINCIPLES OF LASER RANGING**

### **1.1. DISTANCE CALCULATION**

Two different methods for distance (also called range) calculation are possible (Wehr and Lohr, 1999): phase and pulse method. The former allows more accurate range determination but suffers from a limited range (Petrie and Toth, 2008). Alternatively, the latter allows a greater range, being this circumstance the main reason for which most of the ALS and TLS used for Earth surface observations usually employ pulse laser method (Wehr and Lohr, 1999; Baltsavias, 1999).

### 1.1.1. Pulse method

Distance measurement (range:  $\rho$ , fig. 1) is based on the Time-Of-Flight (TOF) of the laser pulse, as already stated in equation 1:

$$\rho = c \cdot (\text{TOF}/2) \quad [\text{equation 1, Petrie and Toth, 2008}]$$

Where  $c$  = speed of light

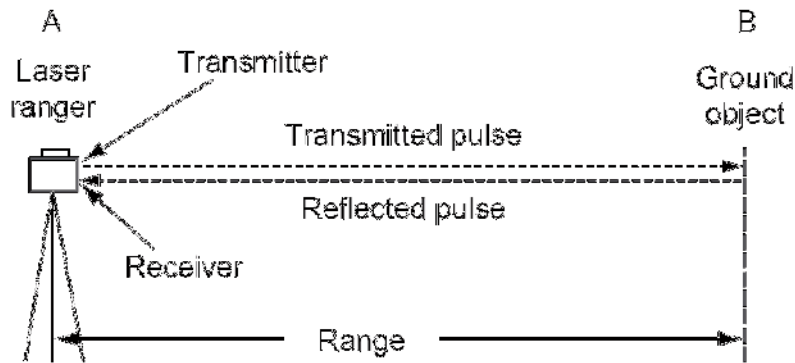


Figure 18: Basic operation of a laser rangefinder (from Petrie and Toth, 2008).

The range measurement is performed on an area equal to the spot dimension (SD; also called beamwidth). Although the laser signal is highly collimated, the spot dimension increases with distance due to the laser beam divergence (equation 2):

$$\text{SD} = \rho \cdot \tan \alpha + a \quad [\text{equation 2, Petrie and Toth, 2008}]$$

Where  $\alpha$  = angle of divergence;  $a$  = initial beam size;

Equation in any consistent units of SD and  $\rho$ .

Figure 19 shows the shape of the waveform of the returned pulse. The recording of the last pulse can be performed in order to obtain the return signal from the ground surface (in place of vegetation).

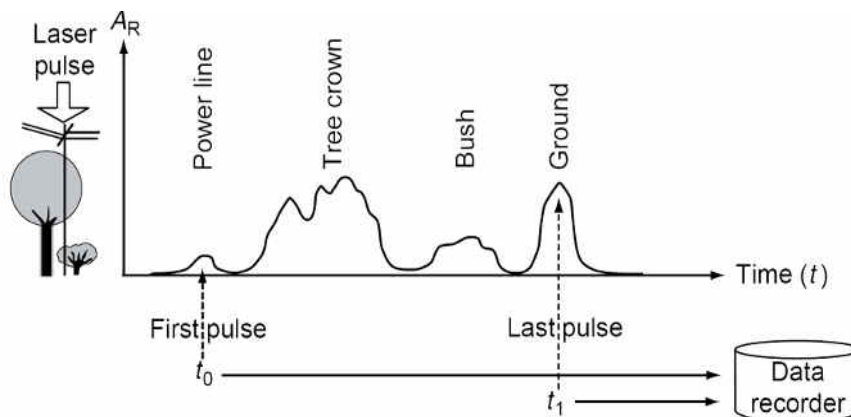


Figure 19: View of the complete waveform of the returned pulse. The first and last pulse can be seen in this picture (from Petrie and Toth, 2008; original figure by Brenner, 2006).

### 1.1.2. Phase comparison method

Range calculation can also be performed using laser radiation emitted through a continuous beam, instead of a series of pulses. Range is calculated in a two steps process (Figure 20):

- Firstly, a rough distance value is calculated by measuring the *total number of wavelengths*. In order to solve the “ambiguity problem”, a multi-frequency phase measuring system is normally employed: the wavelength of the laser signal is rapidly changed  $n$  times, allowing for the univocal calculation of the number of waves.
- Secondly, a more precise calculation is obtained by comparing the differences in phase between the transmitted and received signals of the laser beam.

Although its high accuracy (submillimetre level), this method for distance calculation suffers for a limited maximum range, typically below 100 m. Hence, its practical applications in landslide detection, characterization and monitoring are limited.

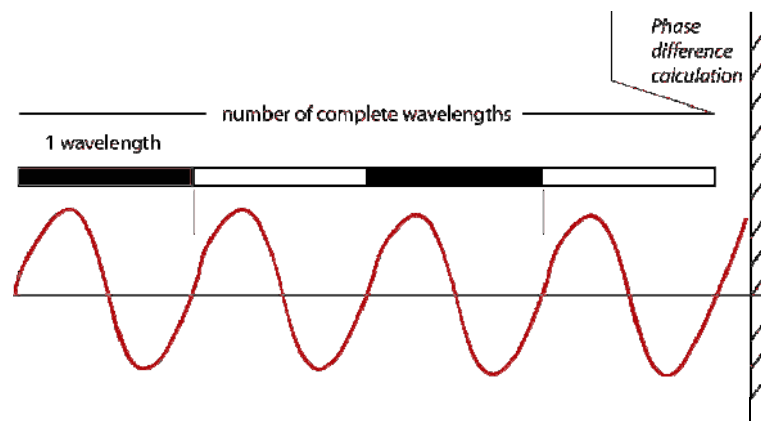


Figure 20: Fundamentals of range measurement through phase comparison method.

## 2. ELECTRONIC DISTANCE METERS

### 2.1. GENERAL OVERVIEW OF THE SENSOR

An **Electronic Distance Meter (EDM)** is an instrument that sends and receives a laser beam, allowing for distance calculation depending on the properties of the returned signal (time of flight or phase difference, as explained above). EDM were developed during the late 1950's and early 1960's and started to be used by surveyors for distance measurements (Dallaire, 1974) and deformation monitoring.

Main components of a laser device are the laser source material, an energy source and a mirror. Lasers are usually classified according to its source material: gas lasers, solid-state lasers and semiconductor lasers. The study of the different source materials, physics of the laser beam, energy source, etc. are beyond the scope of this report, which focuses on the practical use of laser sensor for landslide studies. Nevertheless, the book by Petrie and Toth (2008) provides a detailed overview of the main principles of laser components.

EDM are specifically designed for distance calculation. When using EDM in combination with other devices able for angle calculation (e.g. theodolites), 3D coordinates (x, y, z) of single points can be obtained. These two types of measurements (distance and angle) are



usually conducted using a **Total Station**. First total stations were developed in the 1980's. A modern device is shown in Figure 21.



*Figure 21: The TOPCON GPT-8200 Series Reflectorless - Robotic Total Station (picture from topcon.com)*

The main advantages of this sensor are the precision of the measurements (millimetre level), the low cost and the high potential of automation.

Following devices are commonly used in combination with EDMs and/or total stations:

- Tripod: this object is normally used to stabilize and positioning the surveying instrument. Alternatively, EDM may be placed over a permanent base, e.g. concrete pillars.
- Reflector (Figure 22): devices designed for the reflection of the laser signal back to its source (i.e., the EDM or total station) with a minimum loss of energy.

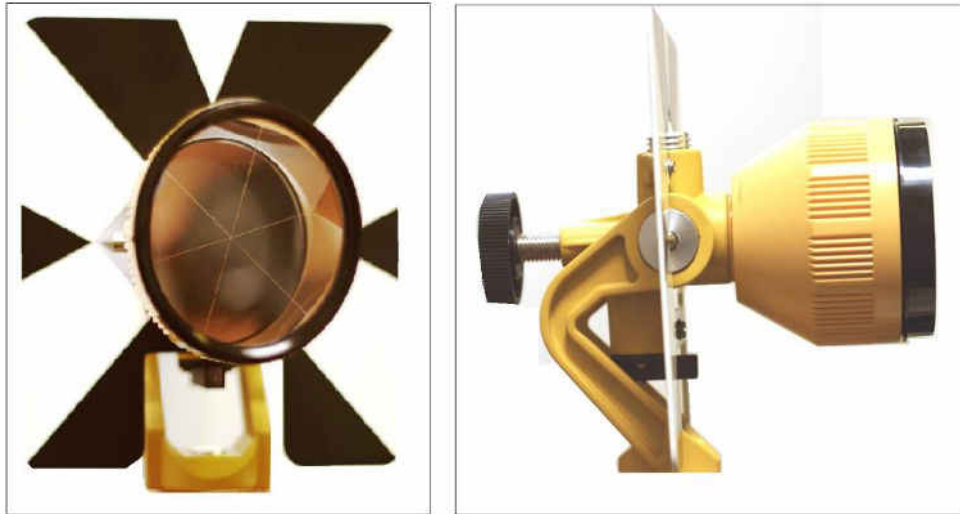


Figure 22: : frontal and lateral view of a prism reflector.

### 2.1.1. Accuracy

Lasers allow for very accurate measurements in one dimension (range or distance). The typical accuracy of the EDM is  $\pm 1.5\text{mm}$  within maximum distances of about 800-1000m (Manetti et al., 2007). Electro-optical distance meters based on infra-red light allow for the acquisition of single points with an accuracy ( $1\sigma$ ) of up to  $\pm [1\text{mm} + 10^{-6} * \text{distance}]$  (Settles et al., 2008).

It has to be mentioned that the instrumental accuracy is affected by unfavourable conditions, as follows:

- high reflecting surfaces;
- very rough surfaces;
- weather conditions;
- very bright ambient conditions;
- excessive range.

EDM accuracies also depend on the operating mode. When using reflectors, range measurements are more accurate than those measurements directly reflected on the ground surface, due to the higher intensity of the returned signal

Laser precisions required for long term deformation (e.g. monthly or yearly changes) are lesser than that required for short-term measurements (e.g. surveying and/or daily changes). Changes in the geometry of the slope are usually plotted using a 3D vector or alternatively computing the horizontal and vertical angles.

### 2.1.2. Resolution

Spatial resolution (also referred to as point density) of this sensor is on demand, i.e. from few points per m<sup>2</sup> up to few points by km<sup>2</sup>. These sensors allow for a high accurate acquisition of single points of the terrain surface but are not designed for a wide coverage of the whole slope.

Typical point density for mapping purposes is around 50-100 points per km<sup>2</sup> (the higher the topographical variability of the area, the higher the point density should be).

Typical point density for monitoring purposes is from 20 to 30 control points per analyzed slope (the higher the number of points and the accuracy of the sensor, the more reliable the results are).

### 2.1.3. Maximum range

Maximum range depends on the type of instrument and reflectivity of the surveyed point. Very high distances (up 5.000 meters) can be acquired when using artificial reflectors (e.g. prisms). In opposition, maximum range decreases its value up to 5 times when directly reflecting the laser over the terrain surface (max. range up to 1000 m).

## 2.2. METHOD

### 2.2.1. Data acquisition

**Best practices** for distance calculation (laser ranging) are as follows (USACE, 2002):

- A tripod and theodolite must be accurately plumbed and levelled over a fix base (e.g. a tripod or a concrete foundation). Concrete pillars with centring plates guarantee an increased accuracy (Malet et al., 2002) by preventing eccentricity errors and by facilitating positioning and trimming of the apparatus.
- A "warm up" period prior to the use of the total station is recommended.
- In case of using reflectors, they must be must be placed perpendicularly to the total station.
- In order to assure the repeatability of the measurement, the measurement should be conducted at least 3 times (five readings are recommended).
- Measurements should be corrected taken into account the meteorological influence. Barometric pressure and temperature should be measured in each station in a shadow emplacement, and not exposed to direct wind. Formulas for atmospheric correction are explained in chapter 5 of USACE (2002) manual.
- In order to maintain certain coherence in the measurements, the same total station and reflector shall be used during the whole monitoring period.
- When using a total station mounted over a tripod, the horizontality of the system should be checked few times during the day (the instrument suffer a certain drift out of the level as the day progresses).

- Line Of Sight (LOS) is the imaginary line from the sensor to the surveyed point. Direct visibility is mandatory to perform distance measurements.
- Finally and needless to say, the stable control points (fixed stations) must be outside of the expected moving area of the landslide. Otherwise, displacement measurement will be underestimated due to a "global drifting". A movement of a control point can however be detected, when always the same instrument position is used.

### 2.2.2. 3D coordinate calculation

3D coordinates of the terrain are usually obtained through *triangulation* or *trilateration* methods:

- A *triangulation* system consists of a series of overlapping triangles in which a given side and two angles are measured. Using basic trigonometric formulas (Figure 23), it is easy to calculate the length of the remaining sides and the angles of the remaining vertex.
- *Trilateration systems* consist of a series of overlapping triangles in which the length of all the sides and only few angles are measured to obtain azimuth.

Triangulation and trilateration techniques are used for accurate detection of terrain deformation. A more detailed description of both methods is given in different surveying books (e.g. Chandra, 2005).

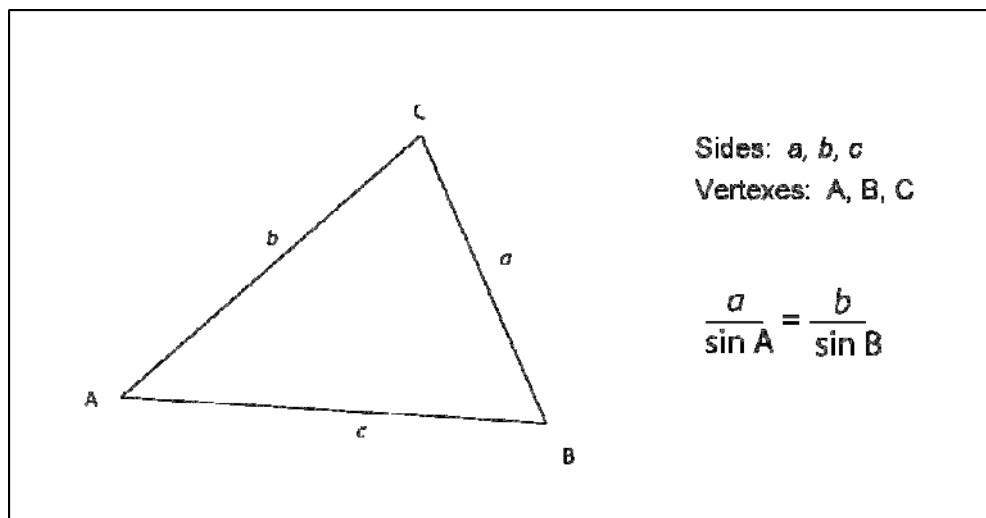


Figure 23: Basic trigonometric formula for triangulation method.

## 2.3. MAIN COMMERCIAL SYSTEMS

### 2.3.1. Electronic Distance Meters

There are two types of EDM operating modes:

- **Reflector-EDM**, which requires a reflector device (e.g. prism) and hence, physical contact with the surveyed point by a second operator. This operating mode allow for the acquisition of points at very long distances (typically up to 5000 m).

- **Reflectorless-EDM**, which does not require any reflector device, i.e., the instrumental will acquire the coordinates of the natural features (rocks, soil, vegetation, etc). Maximum distances are more reduced than using a reflector-EDM. Nevertheless, its operability is higher: only one person is needed for the fieldwork campaign. This operating mode allow for the acquisition of points at medium distances (typically up to 1000 m).

### 2.3.2. Total stations

Total stations allow for the acquisition of:

- Horizontal angle,  $\theta$
- Vertical angle,  $\varphi$
- Distance,  $\rho$

As a combination of both measurements, the XYZ coordinates of a point is obtained. These coordinates are relative to the internal coordinate system of the total station. Total stations allow for the electrical (instead of optical) acquisition of angles and distances. Digital measurements eliminate the errors due to optical measurements. Total stations also incorporate a collector device, which allow the downloading and processed of the recorded datasets using an external PC.

There are three types of total station operating modes (USACE, 2007):

- **Reflector-total station**, which requires a reflector device (e.g. prism) and hence, physical contact with a second operator with the surveyed point. This operating mode allow for the acquisition of points at very long distances (typically up to 5000 m).
- **Reflectorless-total station**, which does not require any reflector device, i.e., the instrumental will acquire the coordinates of the natural features (rocks, soil, vegetation, etc). Maximum ranges are lower than using reflector-total stations. Nevertheless, its operability is higher: only one person is needed for the fieldwork campaign. This operating mode allow for the acquisition of points at medium distances (typically up to 1000 m).
- **Robotic-total station**, which allow the automatic tracking of specific control points previously defined. No operator is needed for the automatic acquisition of the control points coordinates. The maximum range depends on the type of instrumental and on the operating mode: reflector or reflectorless total station (up to 5000 and 1000 meters, respectively).

## 2.4. OUTPUT

The measurements obtained with an EDM or Total Stations are distances and 3D coordinates.

### 2.4.1. Distances

Distances from a well known positioning point (e.g. concrete pillar) are usually acquired with EDMs. As practical applications for landslides, distance calculation allow for the detection of

the terrain displacements along time (see 1.5.2). Similarly, an automatic measurement of distances along time allow for the monitoring of the displacements over single points of the slope (see 1.5.3).

### **2.4.2. 3D coordinates**

3D coordinates of the terrain surface (X, Y, Z) are the main output of surveying campaigns. A set of 3D points is commonly used in conventional topography to generate maps (see 1.5.1).

## **2.5. MAIN APPLICATIONS**

### **2.5.1. Digital Elevation Models and topographic maps**

Digital Elevation Models (DEMs) and topographic maps are 2D representations of the 3D geometry of the terrain. These representations are usually performed as follows:

- a) Acquisition of 3D coordinates of the terrain surface. The higher the slope variability, the higher the density of points. Similarly, the larger the scale of the map (e.g. 1:25.000, 1:10.000, 1:500, etc.), the higher the density of points.
- b) Interpolation: creation of a Triangular Irregular Network (TIN) or a square grid in the XY plane with the altitude Z as attribute for each TIN node resp. grid value.
- c) Creation of contour lines or altitude-scaled colouring for the Z representation.

DEMs and topographic maps are the basis for further studies on landslide detection, fast characterization and monitoring.

### **2.5.2. Landslide displacements**

The landslide field of displacements can be measured either using point based (e.g. total stations, DGPS, etc.) or area based techniques (photogrammetry, radar techniques, laser scanning, etc.). An example of the former is depicted in Figure 24. Four essential aspects must be borne in mind when studying landslide displacements (Malet et al., 2002): the degree of accuracy required, the geomorphodynamic characteristics of the moving mass, the various site constraints and, lastly, the resources available for the operation. For example, the measurement of single points using EDM can be conducted using two different techniques:

- Using artificial reflectors: this technique is recommended when very accurate measurements are required, e.g. for real time monitoring of millimetre or centimetre level of accuracy.
- Using natural features: reflectorless measurements are recommended for very active rockfall areas, in following cases: (a) when operator's safety can not be assured and (b) when reflector can be destroyed due to rock impacts. An example of this technique is described in Mikoš et al. (2005).

The repetition of EDM measurements over fixed points allow for real-time monitoring and the implementation of early warning systems (see next section).

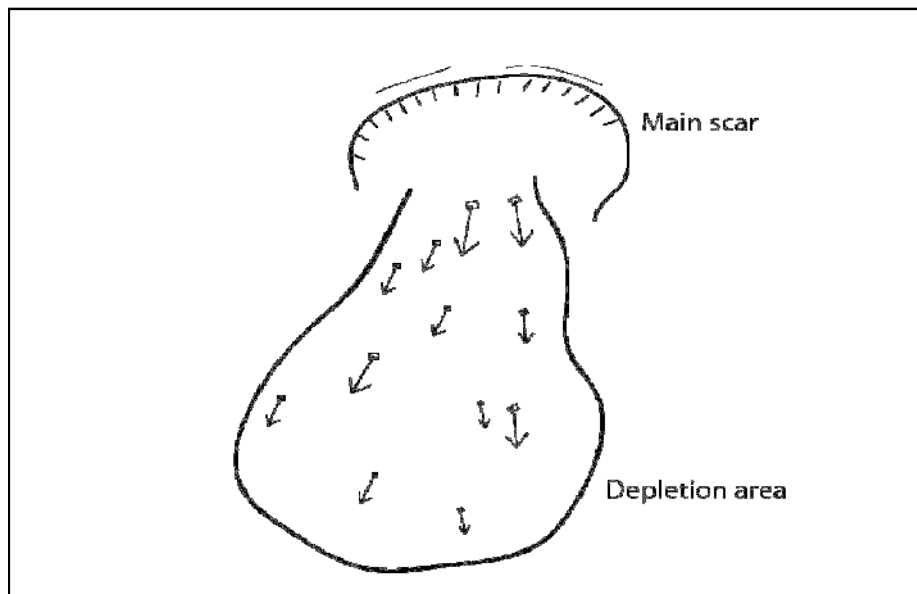
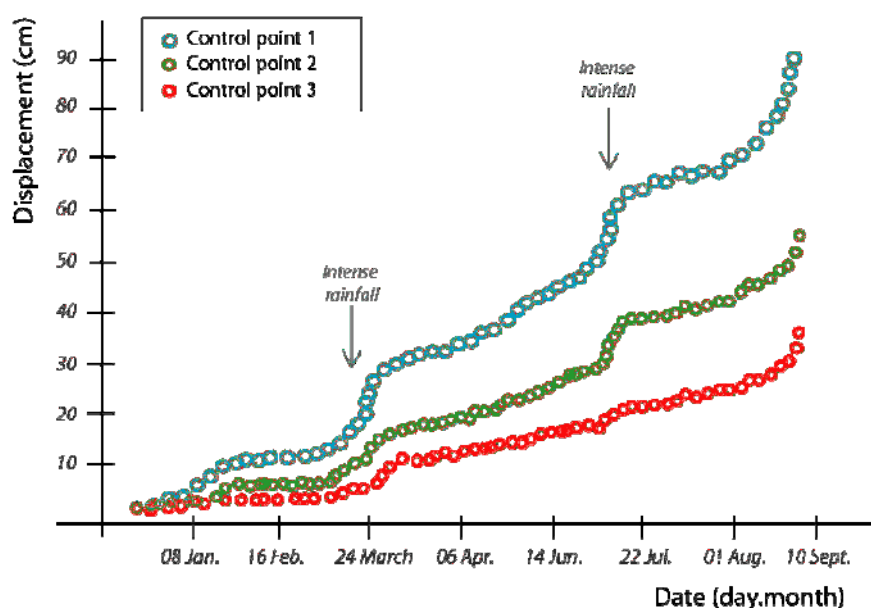


Figure 24: Sketch of the displacements measured at certain point of the landslide.

### 2.5.3. Real-time monitoring

Real-time monitoring of single points of the slope (natural features and/reflectors) can be conducted using a robotic total station. Millimetric accuracies can be obtained using these techniques. As an output of the system, displacements vs. time curve series are obtained (Figure 25). The prediction of the date of failure can be inferred plotting inverse velocity against time (Saito, 1969; Fukuzono, 1985). Some examples of rockfall prediction are discussed in Crosta and Agliardi (2003).

Finally, it is important to mention that a high degree of autonomy and automation can be obtained using EDMs: measurements can be transmitted via satellite to a control station, which may be handily accessed via a standard internet connection.



*Figure 25: Displacements vs. time for three different control points measured with a robotic total station. The influence of the water content (intense rainfall) in the acceleration of the landslide can be observed in the graphic.*

### 3. TERRESTRIAL LASER SCANNER

The acronym LIDAR stands for Light Detection and Ranging. When mounted over a ground-based platform, this instrument is also known as a Terrestrial Laser Scanner (TLS) or ground-based LIDAR. This new technology acquires dense 3D information of the terrain with high accuracy, high resolution (mm to cm order) and very high data acquisition speeds. TLSs appeared at the end of the 1990's and are currently used in a widespread variety of Earth sciences applications, such as landslide characterization and monitoring. The number of publications on this instrumental in landslide characterization and monitoring has increased considerably in the last 5 years (e.g. Slob and Hack, 2004; Bauer et al., 2005; Rosser et al., 2005; Lim et al., 2006; Jaboyedoff et al., 2007; Oppikofer et al., 2008; Sturzenegger and Stead, 2009). Technical information on standards, specifications and quality control of different TLS is provided in Hiremagalur et al. (2007). Finally, useful information in the use of TLS for rock slope characterization is discussed in Kemeny and Turner (2008).

#### 3.1. GENERAL OVERVIEW OF THE SENSOR

This instrument (Figure 26) consists of:

- a transmitter/receiver of infrared laser pulses for distance calculation (see section 1)
- a scanning device, formed by an internal system of rotating mirrors and/or a rotating instrument.

In opposition with the EDM described in the previous chapter, the combination of laser ranging and scanning devices allow for a very fast acquisition speed, typically thousands of points per second. As a result, millions of points can be obtained in each data acquisition. Range measurement can be undertaken using either the first or last pulse of the return signal.

An overview of laser ranging, profiling and scanning are already discussed by different authors (e.g. Lichti and Jamtsho, 2006; Teza et al., 2007; Petrie and Toth, 2008). Therefore, this section of the Deliverable will focus in basic principles of the TLS technique and method. As regards practical applications for landslides, laser systems can be used for the acquisition of large volumes of 3D coordinates of the terrain, with a high accuracy and at an extremely fast recording rate.



*Figure 26: TLS ILRIS-3D (Optech) at different locations.*



### 3.1.1. Accuracy

Technical characteristics supplied by the different manufacturers show point accuracy ranging from mm to cm values, mainly depending on the range and the TLS model (i.e.  $\sigma \sim 0.7$  cm at 100 m for the ILRIS 3D model). A review of the different commercial systems is discussed in section 2.3. The accuracy of the measurement is a main function of the range, the reflectivity of the material, the complexity of the scanned surface and the angle of incidence, as follows:

- Range: the higher the range, the lower the accuracy is (see technical specifications for each instrument)
- Reflectivity of the material: the lower the reflectivity, the lower the accuracy is (Voegtli et al., 2008)
- Surface complexity: the higher the complexity of the material, the lower the accuracy is (Abellán et al., 2009).
- Incident angle: the higher the obliquity of the incidence angle, the lower the accuracy is (Lichti, 2007, Ingensand et al., 2006).

For practical applications, the accuracy of a given TLS dataset can be estimated through the comparison of two different point clouds acquired consecutively. As practical guidance, the quality of the measurement can be improved by:

- Perform data acquisition as closest and perpendicular to the slope as possible.
- Filtering the low reflective points and the areas similarly oriented to the LOS and by the deletion of erroneous points, i.e. vegetation, wires, birds, unexpected points, etc.
- For monitoring purposes, a good practice (although not mandatory) is to be consistent with the location of each station during the different periods of time.

Finally, it has to be mentioned that error in comparison of the TLS datasets is not only influenced by the instrumental error, but also by alignment and modelling errors (Teza et al., 2007). The alignment error mainly depends on the alignment method and point density. The modelling error is also influenced by the density of points, as was tested by Abellán et al. (2009) through the comparison of two point clouds acquired consecutively. Figure 27 shows the percentiles of the error as a function of the density of points in a basaltic cliff (Abellán et al., 2009). As expected, the smaller the density of points, the lower the accuracy of the comparison. Nevertheless, the values of the 75<sup>th</sup>, 90<sup>th</sup> and 95<sup>th</sup> percentiles show similar values of the error for point spacing below 4.7 cm (e.g. 2.3cm, see Figure 27), meaning that no significant improvements are obtained by decreasing the point spacing. As a result, a more efficient density of point from a computational point of view can be obtained.

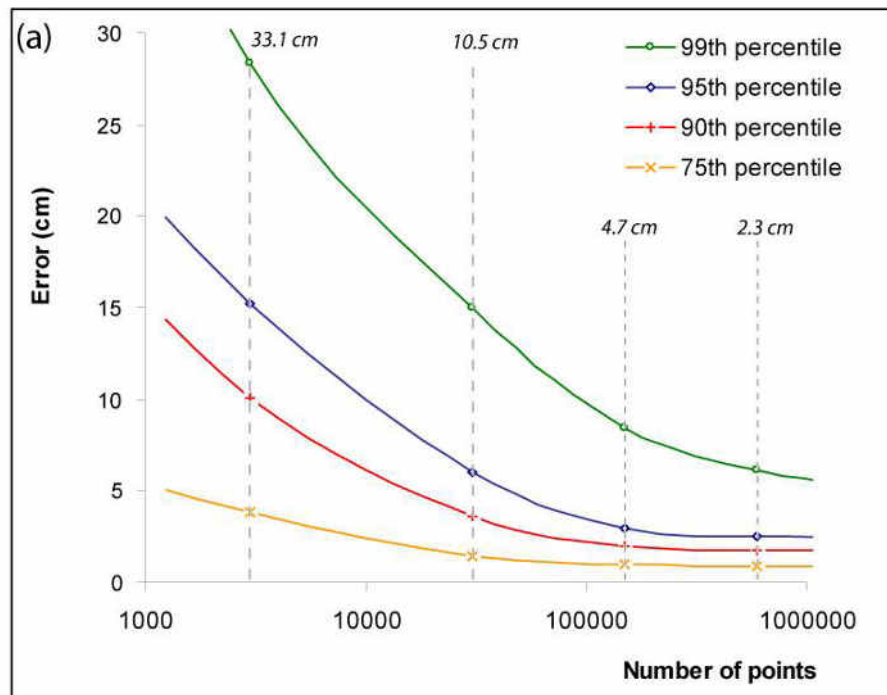


Figure 27: Assessment of the quality of the rock face modelling: variance of the error for different densities of points (extracted from Abellán, 2009).

### 3.1.2. Resolution

Laser scanner's resolution is a parameter that determines the level of detail that can be observed from a scanned point cloud. This parameter can be divided into range and angular (or spatial) resolution:

- Range resolution is the ability of a rangefinder to resolve two objects on the same line of sight and is governed by pulse length for a pulsed system (Kamerman, 1993).
- Angular resolution is the ability to resolve two objects on adjacent sight lines. This parameter is governed by two parameters: sampling interval (also called point spacing, which is user defined) and laser spot dimension (which is a fixed, but range depending value, see section 1).

The density of points is user defined as an angular spacing between adjacent sight lines. In practice, the technical operator should borne in mind that sampling interval is range dependent: the areas located farther away from the TLS suffer for a low sampling interval compared to the closer ones.

The estimation of the TLS resolution is usually misunderstood and commonly interpreted as equal to the point spacing, obviating the influence of the laser beam width. This influence is of great value when sampling interval is in the same order of magnitude or even lower than the laser beamwidth. In these cases, fine details are effectively blurred, as discussed by Lichti and Jamtsho (2006). In order to find a proper value for the estimation of the resolution value, these authors proposed the used of the *Effective Instantaneous Field of View* (EIFOV). The

optimal sampling interval proposed by Lichti and Jamtsho (2006) is 86% of the laser beamwidth.

Table 4 provides a rough guide for the definition of the sampling interval (or point spacing) during a fieldwork campaign using a commercial TLS (ILRIS 3D model). The parameters of the laser beamwidth for this instrumental are as follows:  $\alpha = 0.00974^\circ$ ;  $a = 12$  mm (Optech, 2009).

*Table 4: Optimal point spacing for the TLS ILRIS 3D model. This parameter was calculated as 86% of the spot dimension (Lichti and Jamtsho, 2006).*

Range (m)	50	100	150	200	250	300	350	400	450	500	550	600
Optimal sampling interval (cm)	1.8	2.5	3.2	4.0	4.7	5.4	6.1	6.9	7.6	8.3	9.1	9.8

### 3.1.3. Maximum range

Maximum range of the different TLS equipments depends on the type of instrumental (see section 2.3). As guidance, the maximum range provided by the manufacturer for highly reflective materials is almost double to the maximum range achievable in real slopes, which are characterized by a 20% reflectivity. As an example, tests with a TLS ILRIS 3D at different geological sites and obtained a maximum range of around 600-900 meters for dry surfaces.

### 3.1.4. Intensity

The intensity is defined as the amount of reflected signal with respect to the emitted one. Its value is usually normalized on a scale ranging from 0 to 255. This parameter is usually recorded in addition to the 3D coordinates.

Although this parameter may give an idea of the object material, automatic classifications suffer from certain ambiguity: same value of the intensity may be recorded for different materials at a different range. This is due to the fact that the intensity parameter mainly depends on the range, angle of incidence, soil moisture, and object material.

### 3.1.5. Colour

In addition to the intensity of the returned signal, some TLS devices are able to obtain the colour of the object. The colour (R, G, B) for each scanned point are captured with independent detector. Alternatively, colour information can be recorded through an internal or external digital camera (CMOS Sensor), with the result that each pixel of the photograph may be attributed to each point of the scanned surface.

An example of spectral classification of different material based on colour attributes is discussed in Lichti (2005).

## 3.2. METHOD

### 3.2.1. Data acquisition

The laser beam is directly reflected on the land surface, obviating the need for intermediate reflectors. The origin of the Cartesian Coordinate System ( $P_0 = 0,0,0$ ) is usually set at the centre of the TLS instrument. Coordinates of each point are acquired in a polar system ( $\rho$ :

range;  $\theta$ : horizontal angle;  $\varphi$ : vertical angle). The binary file acquired by the TLS can be transformed (parsed) into a Cartesian system (x, y, z) or other file formats used in commercial software. As a result, a point cloud consisting of millions of x,y,z points can be obtained.

A thorough planning of the scanning campaign prior to fieldwork is highly recommended by taking into consideration following characteristics:

- Point density: the number of points by a given area is user defined. Therefore, angular resolution should be considered in advance, taking into account the necessary number of points for a correct representation of the scanned slope.
- Location of the stations in order to minimize the shadow areas: when the laser beam is parallel to the orientation of the geological surface, data acquisition may suffer from occlusion problems (e.g. Lichti, 2007; Sturzenegger et al., 2007; Lato et al., 2009).
- Number of scans: the minimum number of scans necessary for a complete coverage of the slope should be studied in advance, considering the Field of View (FoV) of the different instruments (e.g. FoV of the ILRIS 3D model = 40x40°)
- Overlapping areas: a minimum of 20 or 30% overlapping area is recommended for the further coregistration of the point clouds acquired from the same station.

Data acquisition performed from the same point of view minimizes the geometry variations during two epochs, making further comparison of TLS datasets more accurate. When acquiring TLS datasets for monitoring purposes, it is recommended (but not strictly necessary) to perform fieldwork campaign using constant station(s).

### 3.2.2. 3D coordinate calculation

Terrestrial Laser Scanners acquire the Coordinates of each point in a polar system ( $\rho$ : range;  $\theta$ : horizontal angle;  $\varphi$ : vertical angle). These coordinates are relative to the internal coordinate system of the total station or the laser scanner. The acquisition of the 3D coordinates in a Cartesian system can be easily conducted using following equation (equation 3):

$$[x \ y \ z]^t = \rho [\cos \theta \cos \varphi, \cos \theta \sin \varphi, \sin \varphi]^t$$

### 3.2.3. Filtering

The scattering of the TLS measurements around its “true” value should be taken into account when dealing with TLS datasets. A previous manual cleaning of the TLS datasets is necessary in most of the cases in order to improve the overall quality of the point cloud. The acquired datasets that do not belong to the surface terrain (e.g. vegetation, wires, mobile objects, etc) must be deleted before the processing of the point cloud.

Secondly, some automatic algorithms to filter the “erroneous” points may be applied, mainly detecting which points belong to vegetation. This filtering is usually carried out either looking to differences in geometry or to differences in Intensity. Although automatic filtering of trees is a relatively simple task, the filtering of small plants and bushes is usually a manual, time consuming task.

In some cases, noise reduction tasks can be also carried out. For instance, filtering or interpolation averaging can reduce the instrumental error (e.g. Bornaz and Rinaudo, 2004; Lindenbergh and Pfeifer, 2005). In order to reduce the error in data comparison for small scale deformation detection, a Nearest Neighbour (NN) averaging technique can be applied (e.g. Abellán et al., 2009).

### 3.2.4. Registration of the point cloud

“Registration” is the process towards a set of point clouds (e.g. all the scans that describe an object) is aligned into another system of coordinates. More specifically, following terms are commonly employed:

- The term “merging”, “alignment” or “unification” is usually applied when the scans of a single fieldwork campaign are referenced into a common file using an internal coordinate system.
- The term “georeferencing” is usually employed when the scans are registered into a well known, external coordinate system, e.g. UTM or national grids. Georeferencing is usually performed using an external, already referenced point cloud (such as an already georeferenced ALS point cloud) or using ground control points previously acquired using a total station or a DGPS.

Registration of the point cloud is usually a affine transformation that consists in the combination of a translation and a rotation. In 3D this affine transformation can be described by a 4x4 matrix with 3x3 terms for the rotation,  $r_{11}$  to  $r_{33}$ , 3 terms for the translation,  $t_{14}$  to  $t_{34}$ , and a scaling factor in the fourth line (equal to 1 for affine transformations without scaling) (Stephens, 2000; Lichti et al., 2002; Oppikofer et al., 2009).

$$\mathbf{M}_{\text{trans}} = \begin{pmatrix} r_{11} & r_{12} & r_{13} & t_{14} \\ r_{21} & r_{22} & r_{23} & t_{24} \\ r_{31} & r_{32} & r_{33} & t_{34} \\ 0 & 0 & 0 & 1 \end{pmatrix}$$

Registration of the point cloud usually consists in a two steps process:

- Step 1: A preliminary, rough registration by a visual identification of homologous points (also referred to as N point pairs, e.g. edges of blocks, intersection of discontinuities, reflecting targets, etc.) in the overlapping area of the different scans. The higher the number (and accuracy) of the selected points, the better the alignment is. Reasonably good results can be obtained using 3 to 5 homologous points equally distributed over the 3D scene. In opposition, the use of collinear points may not give a univocal solution and should be avoided.
- Step 2: an optimization of the alignment can be carried out using an Iterative Closest Points (ICP) procedure (Besl and McKay, 1992; Chen and Medioni, 1992) once reference systems of both scans resemble each other (see step 1). Through this

algorithm, the differences between points are iteratively reduced by a minimization of a mean square cost function. This iterative process can be improved by progressively reducing the “search distance” parameter from few metres up to a few centimetres.

### 3.2.5. Comparison of sequential TLS datasets

3D temporal variations of the terrain can be detected by comparing sequential datasets in accordance with the methodology described in Rosser et al. (2005) and Lim et al. (2006). A brief description is as follows:

- a) Acquisition of the reference point cloud ( $R_0$ , see previous section)
- b) Construction of the Surface of reference ( $S_0$ )
- c) Acquisition of data point clouds  $D_1, D_2, \dots, D_n$
- d) Alignment of these datasets with  $S_0$  (explained below)
- e) Comparison between  $S_0$  and successive  $D_i$
- f) Calculation of the differences for each period of comparison.

As stated above, the registration is usually carried out in two stages: (a) a preliminary registration by a visual identification of homologous points and (b) optimization of the alignment using ICP procedure. Nevertheless, a lack of convergence may be possible when the geometries between two epochs are very different. In order to improve the alignment procedure, the section of the point cloud that changed between the two epochs should be automatically selected and ignored for the alignment. The single point distances between the  $S_0$  and the successive  $D_i$  can be computed using commercial software (e.g. data vs. reference comparison in the IMInspect module of PolyWorks). The direction of comparison can be defined as the “shortest distance” between different datasets or following an user-defined direction. Differences ( $D_i f_i$ ) between two epochs can be calculated for each point as shown in equation 3:

$$D_i f_i = \text{Distance}[S_i P_0] - \text{Distance}[S_0 P_0] \quad [\text{equation 3}]$$

Where  $P_0$  is the centre of origin of coordinates (0,0,0). Part of the value of  $D_i f_i$  is due to systematic (instrumental and methodological) errors. The other part is due to “real changes” in certain parts of the slope. As regards the sign criteria, we use positive values when the time of flight of the laser signal for  $D_i$  is higher than that of  $S_0$ . As a result, positive values correspond to a lack of material at a given point, i.e. detachment of the material. Likewise, negative values correspond to an increase in material, i.e. scree deposits, or a displacement towards the origin of coordinates. This negative displacement may also reflect the pre-failure deformation in a part of the slope (i.e. Abellán et al., 2010). The calculation of the volume of the main rockfalls can be performed using commercial software (e.g. the “surface to plane” command of IMInspect module, PolyWorks).

### 3.3. MAIN COMMERCIAL SYSTEMS

Terrestrial Laser Scanners can be classified according to its measuring principle (phase vs. pulse measurement) or to its maximum range (short, medium or long range). For practical applications in landslides, a classification of the different commercial systems based in its maximum range is commonly used. Practical applications of the short range TLS are limited by its maximum range (below 100m). In opposition, medium (max. range from 100 to 350 m) and long range (max. range up to 1200m) TLS's are commonly preferred in landslides applications.

A description of the TLS devices usually employed in landslide investigations is provided in subsequent sections. The main characteristics of each device are summarized in Table 5.

*Table 5: Main characteristics of the TLS most commonly used for landslide applications (summarized and updated from Kemeny and Turner, 2008). The values of these parameters are provided from the manufactures and independent validation should be performed.*

Manufacturer	Optech	Riegl	Trimble	I-Site	Mdl
Model	ILRIS-3D	LMS-Z620	GX 3D	4400 LR	Quarryman pro
Maximum range in natural slopes (20% reflectivity)	700 m	750 m	350 m	300 m	400 m
Accuracy	7mm at 100m	10 mm at 100 m	7 mm at 100 m	20 mm at 50 m	50 mm at 50 m
Scanning rate	2000 points / second	11000 points / second	5000 points / second	4400 points / second	250 points / second
Beam divergence angle	0.00974°	0.15 mrad	3mm at 50m	140 mm at 50 m	173 mm at 50 m

#### 3.3.1. Optech

**Model:** ILRIS-3D (*intelligent Laser Range Imaging System*)

**Maximum range:**

- on artificial targets (90% reflectivity): 1500m
- on natural slopes (20% reflectivity): 700m

**Accuracy:** 7mm at 100m

**Scanning rate:** 2500 points / second

**Beam divergence angle:** 0.00974°

**Wavelength:** 1550nm

**Digital Camera (internal):** 6.6 Megapixels

**Field of View** (vertical x horizontal angle): 40° x 40°

**Optional components:**

- ILRIS-36D: motorized pan and tilt base (increases Field of View: for 360°x360°)
- ILRIS-3D\_ER: Enhanced range (increases the maximum range up to 40%)
- ILRIS-3D\_MC: Motion compensation (allows its use in a moving platform, used in combination with a GPS and Inertial System; lower accuracy)
- ILRIS-3D\_HD: High density scanning (increases the laser repetition rate, allowing for a faster data acquisition: 8000 points/second)
- External GPS.
- External Digital Camera

**Software:**

- Polyworks (Innovmetric): viewing, aligning, meshing and processing of the point clouds. Feature extraction, 2D and 3D measurements, etc.
- Parser (Optech Inc): generation of the point cloud from the binary file produced by the TLS



*Figure 28: TLS ILRIS 3D (Picture extracted from: [www.Optech.ca](http://www.Optech.ca))*

### **3.3.2. Riegl**

Although 5 different models of TLS manufactured by Riegl are currently available, only the medium and long range TLS will be summarized in this report. Given to the fact that landslide applications of short range TLS (maximum range below 200 m) are limited, the short range models were excluded from this review.

**Models:** LMS-Z420i; LMS-Z620 and LPM-321



**Maximum range:**

- in artificial targets (80% reflectivity): 1000m <sup>(1)</sup>, 2000m <sup>(2)</sup> and 6000m <sup>(3)</sup>
- in natural slopes (20% reflectivity): 350m <sup>(1)</sup>, 750m <sup>(2)</sup> and 1500m <sup>(3)</sup>

**Accuracy at 100m:** 10mm <sup>(1)</sup> 10mm <sup>(2)</sup> and 25mm <sup>(3)</sup>

**Scanning rate (points / second):** 11000 <sup>(1), (2)</sup> and 1000 <sup>(3)</sup>

**Beam divergence angle:** 0.15mRad

**Wavelength:** near infrared

**Digital Camera (internal):** 10 Megapixels <sup>(1), (2), (3)</sup>

**Field of View** (vertical x horizontal angle): 80° x 360° <sup>(1), (2)</sup>, 150° x 360° <sup>(3)</sup>,

**Optional components:**

- External GPS
- External Digital Camera
- Internal synchronizer for GPS/INS

**Software:**

- Riscan Pro: viewing, aligning, meshing and processing of the point cloud. Feature extraction, 2D and 3D measurements, etc.

**Notes:**

<sup>(1)</sup> LMS-Z420i; <sup>(2)</sup> LMS-Z620; <sup>(3)</sup> LPM-321



Figure 29: TLS LMS-Z620 (extracted from [www.Rieglusa.com](http://www.Rieglusa.com))

### 3.3.3. Trimble

**Models:** Trimble GX 3D

**Maximum range:**

- in artificial targets: unknown
- 20% reflectivity: 350m

**Accuracy:** 7mm at 100m

**Scanning rate:** 5000 points / second

**Beam divergence angle:** 3 mm at 50 m

**Wavelength:** 532 nm

**Digital Camera (internal):** Yes

**Field of View** (vertical x horizontal angle): 60x360 degrees



Figure 30: Trimble GX 3D (extracted from [www.trimble.com](http://www.trimble.com))

## 3.4. OUTPUT

### 3.4.1. 3D point cloud

Laser ranging and scanning systems generate a huge quantity of information: the 3D coordinates of million points of the terrain surface are obtained as a result of each data acquisition. These TLS datasets are also referred to as *point cloud* or *scans*.

The simple visualization of the unprocessed point cloud may be a valuable tool for the understanding of the 3D geometry of the scanned terrain.

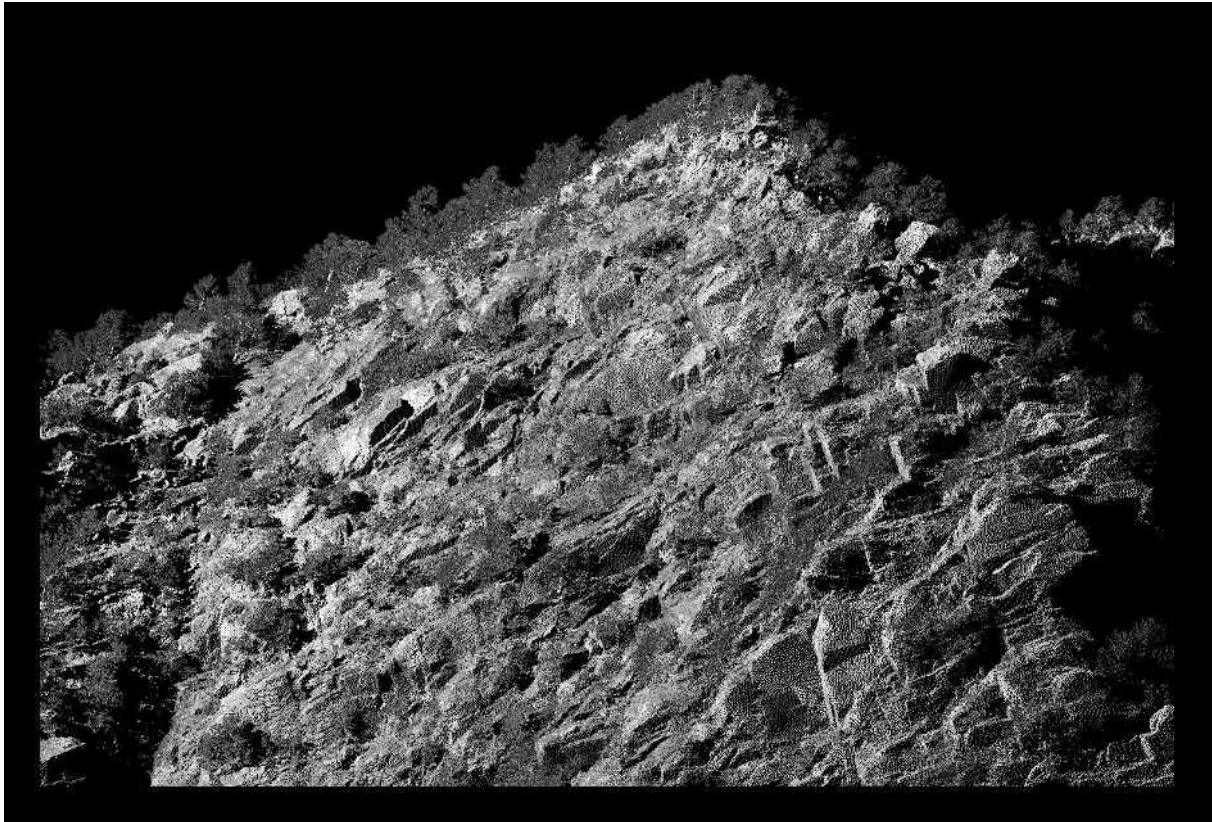


*Figure 31: 3D point cloud of a rock slope. Discontinuity planes and vegetation are visible in this figure. The gray shades represent the intensity of the returning signal with low intensity (dark gray) on vegetated areas and high intensity (white) on rock surfaces perpendicular to the line-of-sight.*

### **3.4.2. High resolution DEM**

High Resolution Digital Elevation Models (HRDEMs) are accurate representations of the 3D geometry of the terrain performed with a great quantity of 3D information, e.g. obtained through a TLS. HRDEMs are usually performed as follows: (a) acquisition of 3D coordinates of the terrain surface; (b) Interpolation: creation of a Triangular Irregular Network (TIN) and (c) generation of a square mesh.

HRDEMs are the basis for further studies such as landslide mapping, detection, modelling, fast characterization and monitoring.

## **3.5. MAIN APPLICATIONS**

During last five years, the use of TLS on different natural and artificial slopes is considerably improving our understanding of landslide phenomena. Different applications are undergoing rapid development, mainly in the following aspects: use of high-resolution, high-accuracy DEM for 3D mapping and/or modelling; characterization of discontinuities; landslide displacement detection; rockfall detection and prediction.

### **3.5.1. Mapping**

Landslide mapping (delimitation of the moving areas, geometry of the slide, mapping of landslide features such as scars, etc) can be directly carried out using the point cloud or in a

LIDAR derived HRDEM. Given the high accuracy and resolution of the datasets, landslide mapping can be carried out at an unprecedented detail.

### 3.5.2. Modelling

HRDEM are the basis for further treatments such as:

- Kinematic modelling: rockfall trajectories, the modelling of debris-flow paths, etc.
- Static modelling: safety factor, limit equilibrium, etc.

An example of rockfall and debris flow runoff calculation using a LIDAR derived HRDEM is provided in the Chapter 4 of this deliverable (case studies). As discussed in Abellán et al. (2006), a more accurate information on the detachment location, joint orientation, volume of detached blocks and characterization of rockfall trajectories and energies are obtained using TLS derived HRDEM.

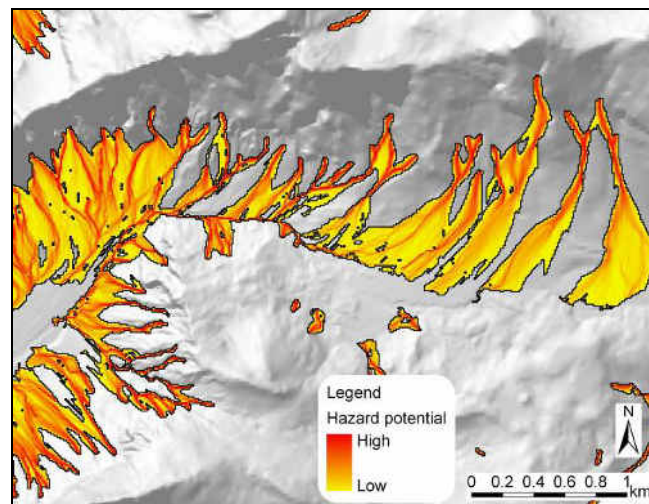


Figure 32: Debris flow modelling (Horton et al., 2008).

### 3.5.3. Structural analysis

Structural analysis of the main families of discontinuities can be derived either from a DEM or directly from the TLS point cloud. Different techniques for feature extraction can be applied, either manually (best fitting plane of a selected section of the point cloud) or automatically (e.g. calculation of the orientation of the TINs, calculation of the orientation of square meshes, use of the covariance matrix, etc.).

Two commercial softwares are currently focused in the calculation of the discontinuities orientation based on TLS datasets: Coltop 3D (Jaboyedoff et al., 2007) and Split Fx (Kemeny et al., 2006). As an example of the former, the slope aspect and the slope angle can be visualized in a unique colour in fig 16. Using this colour-coded information, the orientation of the discontinuities can then be obtained in a univocal way and plotted in stereographic projection.

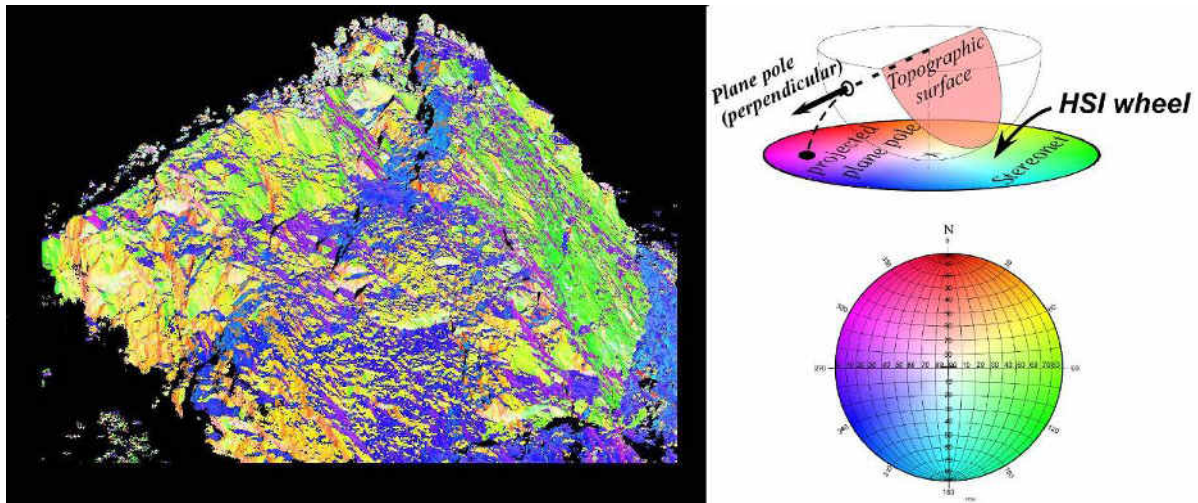


Figure 33: Colour-coded representation of the slope aspect and slope angle. Application to a real rockslope (modified from Coltop 3D.com and Jaboyedoff et al., 2007).

### 3.5.4. Landslide displacements

Multi-temporal comparison of TLS datasets allow for accurate computation of landslide displacements. This deformation can be computed using different methods:

- Calculating displacement vectors at different parts of the slope by identifying identical points on the data and the reference point clouds.
- Point cloud comparisons: computation of the distance between two adjacent points in the data and the reference point clouds (e.g. “shortest distance” or following a comparison vector) using a point-to-point or point-to-surface ICP algorithm.
- Rigid body transformation: computing the roto-translation matrices between the data and the reference point clouds associated to the displacement of certain parts of the slope (Montserrat and Crosetto, 2008; Oppikofer et al., 2009).



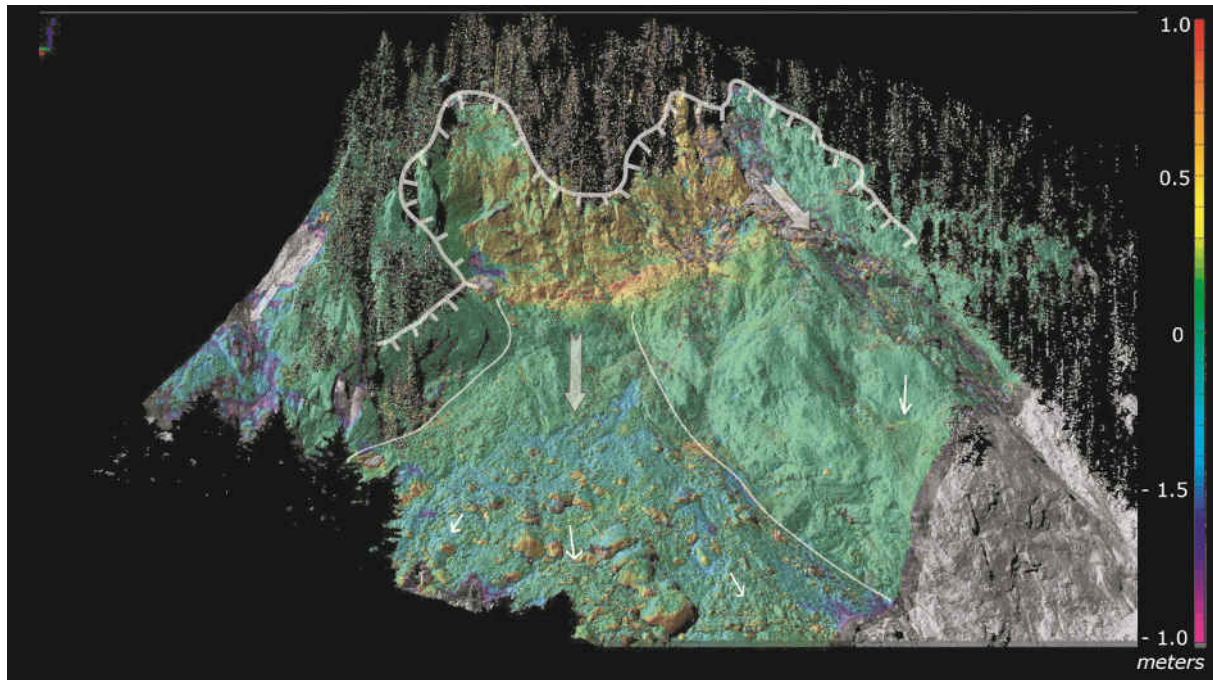


Figure 34: landslide precursory displacements at Val Canaria, Ticino, Swiss Alps. Figure extracted from Pedrazzini et al., 2010.

### 3.5.5. Rockfall detection and prediction

TLS sequential datasets can be compared to detect 3D temporal variations of the terrain. Using this method, it is possible to detect sudden changes in the morphology of the slope, allowing the characterization of the morphology, magnitude, frequency and location of the detachment area of the rockfalls occurred during the monitoring period (e.g. Rosser et al., 2005; Lim et al., 2006; Abellán et al., 2009). Similarly, this technique is able for the detection of rockfall precursory indicators such as minor rockfall events leading to grater failures (Rosser et al., 2007) and small-scale deformations (Abellán et al., 2009; Abellán et al., 2010).

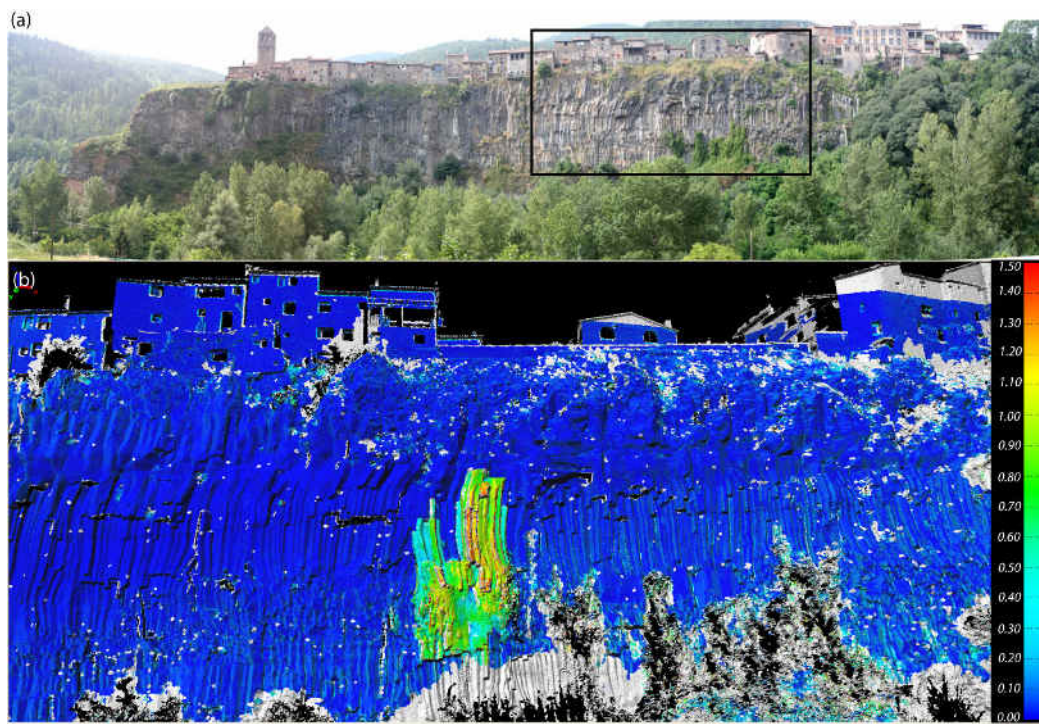


Figure 35: (a) Basaltic cliff at Castellfolit de la Roca. The frame corresponds to Fig. 18b (b) Comparison of TLS models showing a 50 m<sup>3</sup> rockfall event. Colour scale from 0 (blue) to 1.5 m (red). Figure extracted from Abellán et al., 2009.

An example on the application of TLS for rockfall detection and prediction is provided in the chapter 4 of this deliverable (see “case studies” section).

## 4. AERIAL LASER SCANNER

Laser scanner instruments mounted on an airborne-based platform are known as Aerial-LIDAR or Aerial Laser Scanner (ALS). This instrument allows for the acquisition of the 3D coordinates of millions of points belonging to the terrain surface with decimetre-level accuracy. This instrumental is widely used for topographical purposes, such as the generation of High Resolution Digital Elevation Models (HRDEM).

The use of HRDEM for landslide hazard mapping at regional scale started to be used in the beginning of this century. The widely extended use of the Geographic Information Systems (GIS) during the 1990ies allowed for the fast incorporation of such a detailed maps into real landslide applications.

High resolution datasets obtained from ALS has allowed the extension of local scale techniques for landslide detection, mapping, monitoring and characterization over wider areas, e.g. regional scale. Nowadays, ALS derived HRDEM are widely used in the scientific community, providing a better understanding of landslide detection, mapping, characterization and monitoring.

#### 4.1. GENERAL OVERVIEW OF THE SENSOR

ALS is a technological evolution of the Aerial Laser Profiles, which consists basically in a laser rangefinder mounted on an airborne platform. Early airborne laser profiles instrumentals appeared in the middle of the 60's decade.

ALS basically consists of three components (Figure 36):

- a) A laser scanner (see section 3)
- b) A positioning system (differential GPS)
- c) An Inertial Measurement Unit (IMU).

In addition, an imaging device (e.g. video camera) usually forms part of the ALS system.

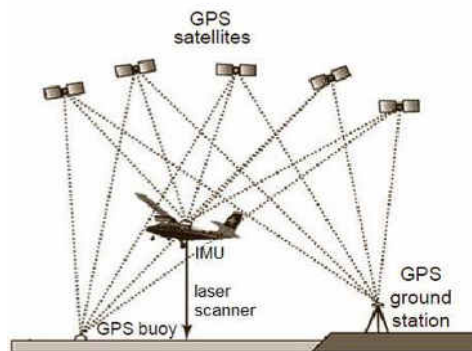


Figure 36: main components of an ALS (extracted from Petrie and Toth, 2009)

##### 4.1.1. Accuracy

Although there is a lack of commonly accepted standards on ALS accuracy determination and calibration procedures (Habib and Van Rens, 2008), accuracy of ALS systems usually range from 10 to 30 cm. This variation of the values is due to the great number of parameters that influence in the final accuracy (Baltsavias, 1999). Indeed, this parameter is a combination of the accuracy of the (a) laser rangefinder, (b) scanning device, (c) Inertial System (IMU), (d) GPS and (e) time offsets. Furthermore, the accuracy depends on external parameters, such as (a) range (i.e. flying height), (b) position of the laser beam, (c) direction of the laser beam, (d) slope angle (the error of the ALS datasets is higher in steep slopes than in flat surfaces) and (e) existence of vegetation.

It is important to mention that the accuracy specifications stated by manufacturers and service providers should be checked by the final user. This verification can be carried out through: (a) the comparison of the statistical error in overlapping areas of the point cloud (overlapping strips) or (b) the comparison of the point cloud and ground control points. Guidelines for the estimation of the vertical accuracy (ASPRS LIDAR Committee, 2004) states that the 95th percentile method of the error shall be employed to determine accuracy instead of the commonly used Root Mean Square Error (RMSE) or standard deviation (1 sigma). Accuracy requirements for ALS datasets depends on the final purpose, i.e. monitoring requires better accuracy than regional mapping.

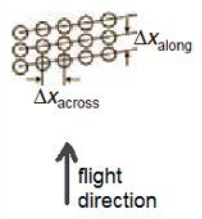


#### 4.1.2. Resolution

The resolution of a point cloud is usually referred to as the size of the smallest feature that can be measured. It is usually expressed as the number of points per area (e.g. points/m<sup>2</sup>), although laser beamwidth is also affecting this parameter (see section 3.1.2 of Active Optical Sensors for a complete explanation).

ALS systems allow for the acquisition of a high density of information (2-4 points per m<sup>2</sup>) over wide areas. Nevertheless, this parameter is controlled by the flying height and the ratio between flying velocity and scanning speed. Basic formulas for the calculation of this parameter are described in Shan and Toth, 2009 (Table 6). ALS resolution may reach values of 1 point per 5 or 10 m<sup>2</sup>).

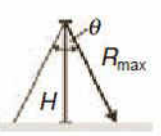
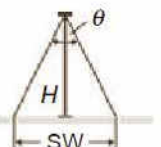
Table 6: Basic formulas for the calculation of the resolution (extracted from Shan and Toth, 2009).

	Point spacing	Across $\Delta x_{\text{across}}$	$\Delta x_{\text{across}} = \frac{\theta}{N} \cdot \frac{H}{\cos^2\left(\frac{\theta}{2}\right)}$	$H$ altitude $\theta$ angular FOV $N$ number of points in one scanning line
		Along $\Delta x_{\text{along}}$	$\Delta x_{\text{along}} = \frac{v}{f_{\text{sc}}}$	$V$ forward speed $f_{\text{sc}}$ scanning rate or scan frequency

#### 4.1.3. Maximum range

The maximum range of an ALS system is mainly limited to the maximum range of the laser range finder. Normal flying heights range from 1 to 3 km, although higher flying heights are possible (up to 6 km). Relationships between maximum range ( $R_{\text{max}}$ ), Swath width (SW) and flying height ( $H$ ) is provided in Table 7 (Shan and Toth, 2009).

Table 7: Basic formulas that correlate maximum range ( $R_{\text{max}}$ ), Swath width (SW) and flying height ( $H$ ). (extracted from Shan and Toth, 2009).

	Altitude above ground $H$	$H = R_{\text{max}} \cdot \cos\left(\frac{\theta}{2}\right)$	$R_{\text{max}}$ max. slant range $\theta$ angular FOV
	SW	$SW = 2 \cdot H \cdot \tan\left(\frac{\theta}{2}\right)$	SW swath width $H$ altitude $\theta$ angular FOV

#### 4.1.4. Intensity

The intensity is defined as the amount of reflected signal with respect to the emitted one. Its value is usually normalized on a scale ranging from 0 to 255. This parameter is usually recorded in addition to the 3D coordinates.

## **4.2. METHOD**

Figure 37 provides an overview of the processing steps, from campaign planning to the delivery of a final product, typically a HRDEM. The customer usually defines the following parameters: extension of the surveying area, density of points and survey accuracy.

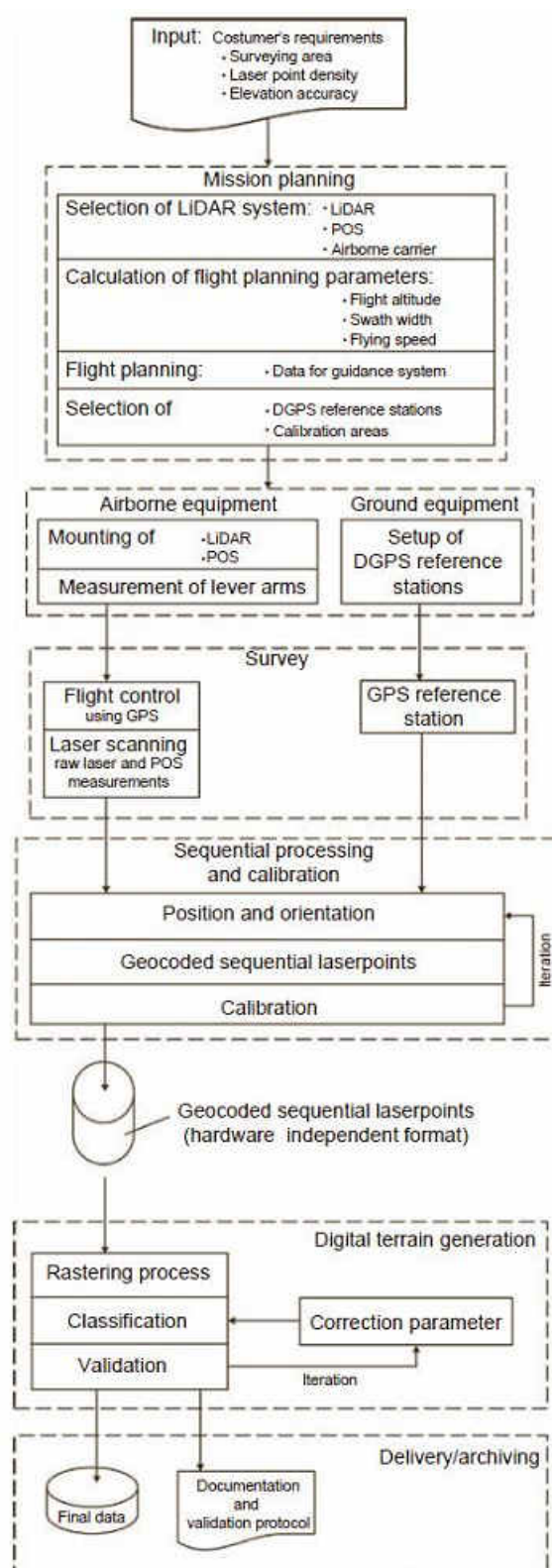


Figure 37: Overview of the processing steps, from campaign planning to the delivery of a HRDEM (extracted from Shan and Toth, 2009)

#### 4.2.1. Data acquisition

The laser beam is directly reflected on a portion of the land surface equal to the laser beamwidth at a given height. Coordinates of each point are usually acquired in a polar system ( $\rho$ : range;  $\theta$ : horizontal angle;  $\varphi$ : vertical angle) and has to be synchronized with the Inertial system and the variable position obtained through the GPS. As a result, a point cloud consisting of millions of  $x,y,z$  points is obtained.

Given that groups dealing with ALS datasets for landslide studies are usually final users, only a few comments on “data acquisition procedures” will be given. A more detailed explanation is discussed in different papers and books (e.g. Baltsavias, 1999; Heritage and Large, 2008; Shan and Toth, 2009; Vosselman and Maas, 2010). The scanning campaign should be defined by taking into consideration the required point density, accuracy and scanned area. These parameters are a main function of the height of flight.

#### 4.2.2. Filtering of erroneous points

Before the generation of the DEM, the acquired points that do not belong to the point cloud (e.g. vegetation, buildings, wires, etc.) should be deleted (Figure 38).

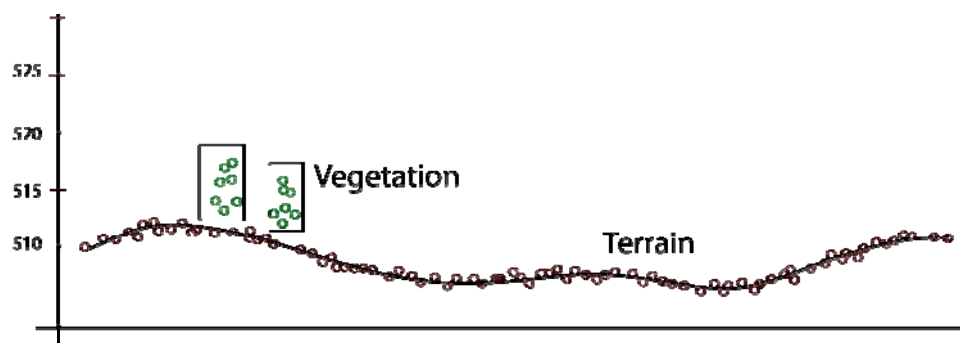


Figure 38: Classification of the point cloud into points belonging to the terrain surface and points belonging to vegetation.

Different semi-automatic procedures for the detection of these points can be used, based on geometrical aspects (terrain points are more continuous than the points belonging to vegetation), in the intensity of the returned signal (the intensity of the laser signal after reflecting in the vegetation is lower than after reflecting in the terrain surface) or in the detection of multiple returns (first pulses are usually related with vegetation cover, last pulse usually corresponds to the terrain surface, see Figure 39). Although these semi-automatic filters may help in the deletion of non terrain points, a visual inspection and a final manual filtering is necessary. Dense vegetation cover can significantly decrease the density of ground points.

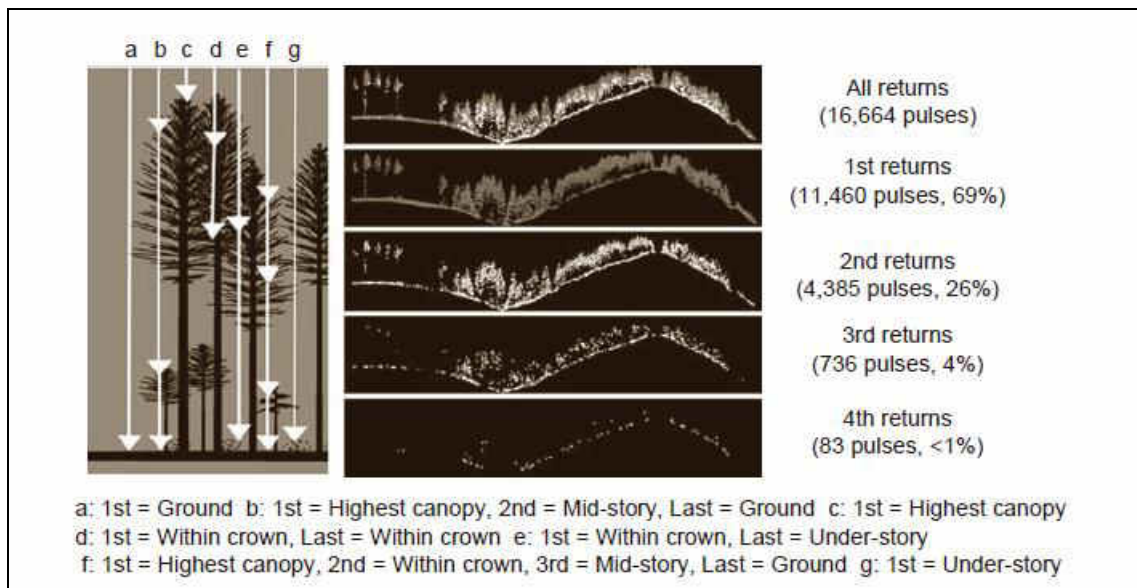


Figure 39: Detection of multiple returns from ALS: (a) Schematic illustration showing seven laser pulses over a vegetated area; (b) profile (transect) obtained from the point cloud data using different returns of the laser pulse. Extracted from Harding (2009). Graphics courtesy of Bob McGaughey, USDA Forest Service PNW Research Station.)

#### 4.2.3. GPS/IMU integration and registration

GPS provides position and velocity of the aircraft, while the IMU system provides attitude and inclination of the system with respect to the horizon. The integration of these two components is a key step in the processing of the datasets: the final accuracy is quite sensitive to this processing step.

“Registration” of a set of point clouds (e.g. all the scans that describe the terrain surface) is the transformation from a local reference system into a real world coordinate system, e.g. UTM. Georeferencing is usually performed using the DGPS and calibrated using ground control points.

### 4.3. OUTPUT

#### 4.3.1. ALS point cloud

The 3D coordinates of million points of the terrain surface are obtained after each flight. The simple visualization of the unprocessed point cloud may be a valuable tool for the understanding of the 3D geometry of the scanned terrain, e.g. landslide features (scarps, topographic roughness and waviness, etc). The inspection of the ALS point cloud has the advantage over HRDEMs that it allows to retrieve ground information where the actual data points are. Furthermore, visual inspection avoids interpolation artefacts from the DEM creation.

#### 4.3.2. High resolution DEM (HRDEM)

After data acquisition and filtering of erroneous points (e.g. wires, vegetation, birds, etc), a high resolution DEM is usually obtained. This product is obtained by rasterizing and interpolation the ALS point cloud. Cell size is user defined, but at least a few points per cell

are recommended. Assuming homogeneous point coverage over the study area, the minimum recommended HRDEM cell size,  $d$ , is given by Equation 4:

$$d = \sqrt{\frac{A}{n}} \quad [\text{Equation 4}]$$

where  $A$  is the surface covered by the ALS point cloud and  $n$  is the total number of ground points in the dataset.

HRDEM are high accuracy representations of the topographical surface obtained with a great density of information. The visualization of the HRDEMs can be highly improved by using:

- High resolution orthophotos: colour images obtained from an aerial sensor can be wrapped to the HRDM, allowing for a realistic visualization of the slope
- Hillshade maps: View-shaded representation of the topography taking into account the slope orientation (slope aspect and slope angle). Hillshade maps are generated using the 3D information provided by the HRDEM and a user-defined light source (in general: sun elevation angle of  $45^\circ$ ; sun azimuth of  $315^\circ$ ). An example of hillshade map is shown in Figure 40.



Figure 40: HRDEM and picture of the west face of the Grand Muveran Mountain (Switzerland). Picture from Jaboyedoff et al. (2007). Source of the ALS dataset: MNT MO/MNS.

#### 4.4. MAIN APPLICATIONS

Main applications of ALS derived HRDEM are focused on detection, mapping, characterization, monitoring and modelling of mass movements such as landslides, debris flows, rockfalls and deep-seated gravitational slope deformations (DSGSD).

Table 8: Main applications of ALS for landslide studies.

	Mapping	Characterization	Monitoring	Modelling
<b>Deep seated Landslide</b>	✓	✓	✓	✓
<b>Shallow landslide</b>	✓	✓	-	✓
<b>Rockfall</b>	✓	✓	-	✓
<b>Debris flow</b>	✓	✓	-	✓
<b>DSGSD</b>	✓	✓	✓	✓

Symbols: ✓: feasible application using ALS -: non feasible application using ALS

#### 4.4.1. Mapping

Slope movements have distinct morphologic features (i.e. the head scarp, the main sliding body and the deposits) that can be recognized not only in the field, but also on remote sensing data, such as ALS derived DEMs (Chigira et al., 2004; McKean & Roering, 2004; Derron et al., 2005; Carter et al., 2007; Schulz, 2007; Dewitte et al., 2008). Landslide mapping can be directly carried out on the hillshade of the HRDEM using classical mapping techniques based on expert criteria. Alternatively, semi-automatic techniques may give an insight into the delimitation of the moving area (see McKean and Roering, 2004). A compilation (from Oppikofer, 2009) is shown as follows (table 6):

Table 9 :Different applications of ALS derived HRDEM for landslide mapping (modified from Oppikofer, 2009).

Chigira et al. (2004)	Shallow landslides detection in vegetated areas. These movements were not detected by using aerial photographs or field survey.
McKean and Roering (2004)	ALS derived HREM to automatically delimit a landslide in New Zealand using the surface roughness of the topography
Derron et al. (2005a; 2005b)	Large rockslides investigation in western Norway (Åknes and Oppstadhornet rockslides, respectively) by means of ALS derived DEM: delimitation of the main rockslide features (scarps, lateral faults, fracture orientations, scree slopes, etc).
Van Den Eeckhaut et al. (2005)	Use of LIDAR derived hillshade maps and expert knowledge in mapping deep-seated landslides. This work compares landslide inventories using HRDEM compared to conventional mapping (fieldwork campaigns).
Schulz (2007)	ALS derived HRDEM to map 173 shallow and deep-seated landslides in the coastal cliffs near Seattle (Washington, USA).

#### 4.4.2. Characterization

Landslide characterization (i.e. landslide magnitudes, conditioning factors such as slope angle, discontinuity orientations, etc.) can be carried out either on the raw ALS point cloud or on a HRDEM. To this end, the use of GIS tools is widely used. Some examples are discussed as follows:

- The steepness of the slope is one of the most important conditioning factors for slope stability and can be easily derived from a HRDEM (e.g. Rouiller et al., 1998;



Baillifard et al., 2003; Guzzetti et al., 2003; Jaboyedoff & Labiouse, 2003; Baillifard et al., 2004; Frattini et al., 2008; Loya et al., 2009). As a result, landslide prone areas can be detected and used to produce regional susceptibility maps.

- As discussed by many authors (e.g. Hoek and Bray, 1981; Bieniawski, 1993; Romana, 1993; Hoek, 2000), discontinuity orientation and its relationship with the geometry of the slope is a key factor in the stability of a slope. The characterization of the discontinuity orientation using an ALS point cloud in combination with simple kinematic feasibility tests allows for the accurate detection of rockfall prone areas. Some examples are discussed by: Gokceoglu et al., (2000); Meentemeyer & Moody (2000); Günther (2003), Jaboyedoff et al. (2004), Jaboyedoff et al., (2007), Lan et al., 2010.

#### **4.4.3. Landslide monitoring**

ALS time series datasets allow for the comparison of the topographic relief at different epochs. Due to its wide coverage and high accuracy, ALS is a valuable tool for the monitoring of unstable areas, either for the detection and volume calculation of already fallen areas as for the detection of movements of decimetre level.

Three methods are discussed in Travelletti et al. (2008) for the monitoring of LIDAR derived DEMs: (a) the benchmark method, consisting in the computation of local displacements and rotations at selected fixed placements (e.g. blocks, tree trunks, etc.); (b) the point cloud comparison (data to reference, see section 3.2.5), either using a “shortest distance” method or computing the differences through a given vector and (c) the correlation of shaded relief images, based on automatic identification of common features between successive images (see Delacourt et al., 2004).

As an example, Dewitte et al. (2008) shows a DEM comparison (extracted from photogrammetry and ALS) to monitor over a 50 years time period a deep-seated rotational landslide located in the Ardennes (Belgium). Finally, Figure 41 computes the vertical differences between the pre and post- failure surfaces in a landslide in Val Canaria, Switzerland (extracted from Pedrazzini et al., 2010).



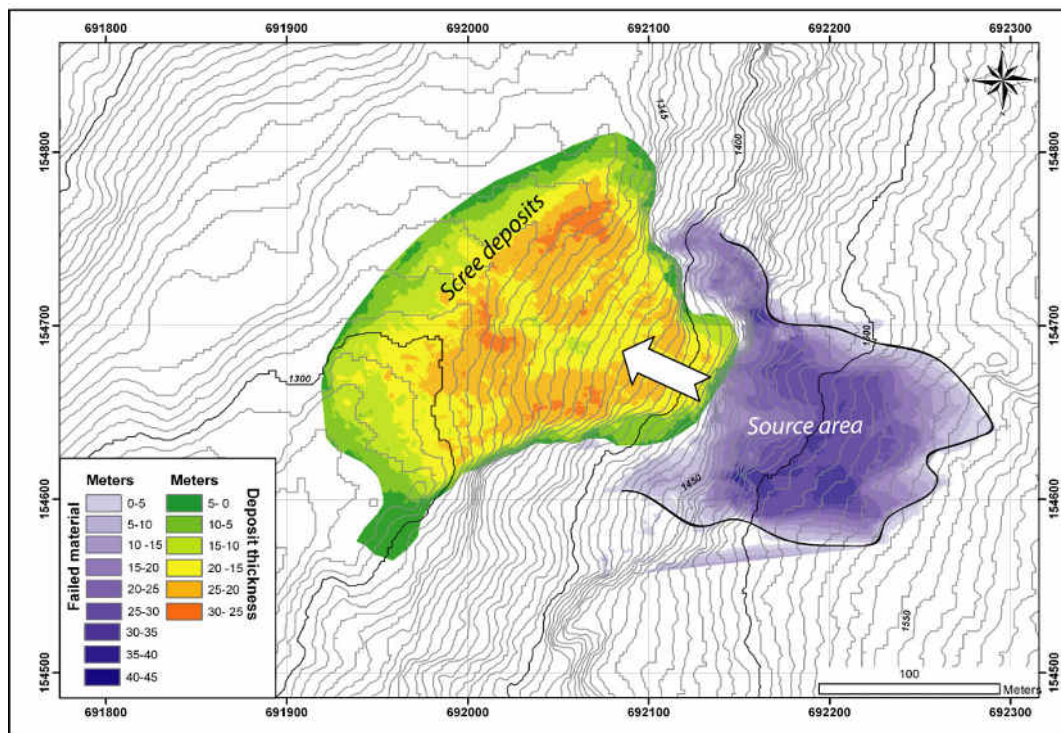
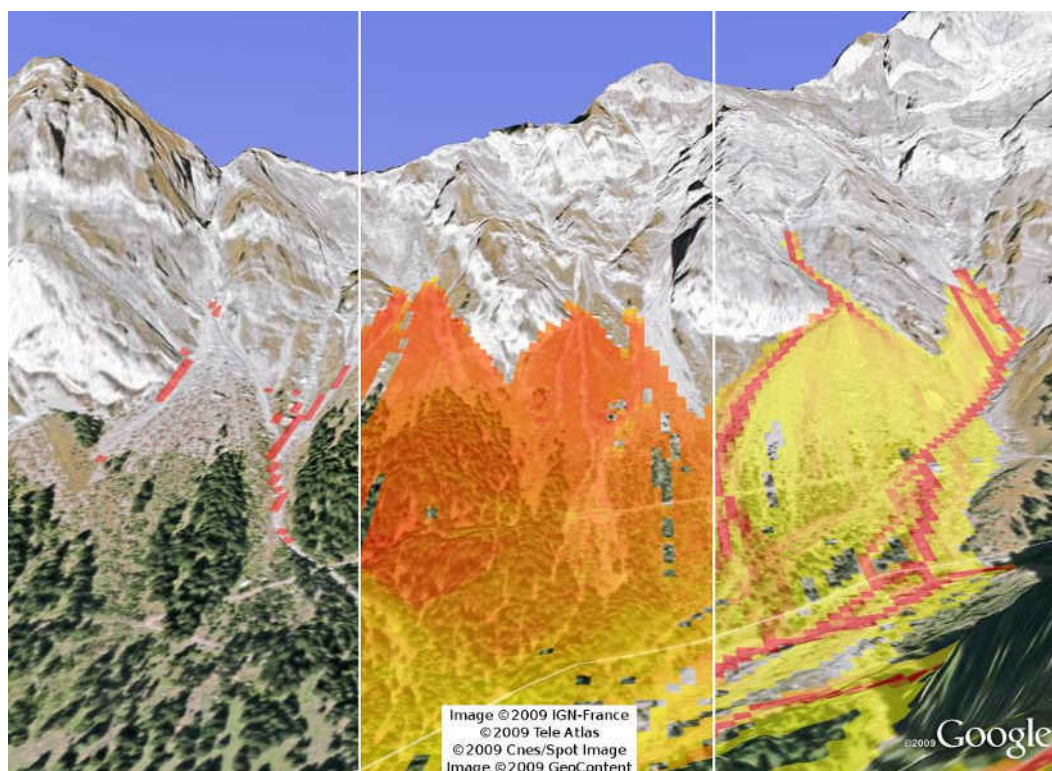


Figure 41: Comparison of pre and post – failure surfaces using aerial and terrestrial laser scanning datasets. Source area and scree deposits are clearly visible in the figure. Image from Pedrazzini et al., 2010 (with permission from the author).

#### 4.4.4. Modelling

The modelling of a landslide (i.e. run-out distances of a debris flow, energy and trajectories calculation, etc.) can be greatly improved using an accurate 3D representation of the terrain. Needless to say, each mass movement process requires different modelling approaches, as follows:

- a) Several authors (e.g. Hoek, 2000; Agliardi and Crosta 2003; Gianin, 2004) have pointed out how the slope is one of most important parameters in rockfall simulation. Currently, different commercial and non commercial software allow for the numerical calculation of rockfall trajectories, energies, maximum run-out, etc. (e.g. RocFall, RockFall analyst, CRISP, Conefall, Rotomap, Rockyfor3D, etc.). A complete example of high resolution 3D modelling of rockfalls is discussed in Agliardi and Crosta (2003). Complementarily, rockfall run-out area can be modelled using the generalization of the shadow angle theory in a GIS environment (Dorren and Seijmonsbergen, 2003; Jaboyedoff et al., 2008).
- b) Debris flow modelling is usually based on two types of algorithms (Horton et al., 2008): flow direction and run-out distance calculation. The reliability of the results generally increases with the accuracy and the resolution of the HRDEM. An example of debris flow modelling is shown in Figure 42.



*Figure 42: Illustration of the model Flow-R, with sources detection, runout energy and probability. Figure from Jaboyedoff et al. (2010).*

# PART C

## ACTIVE MICROWAVE SENSORS

---

- <b>SECTION 1:</b> Radar Wave Principles	p. 105
- <b>SECTION 2:</b> Interferometric Radar Distance-Meter	p. 107
- <b>SECTION 3:</b> Differential SAR Interferometry	p. 125
- <b>SECTION 4:</b> Multi-Temporal Repeat-Pass InSAR	p. 131
- <b>SECTION 5:</b> Ground-Based InSAR	p. 151
- <b>SECTION 6:</b> Polarimetry for Soil Moisture Estimation	p. 158

---

### Sections 1, 2 and 3

- **Authors:** C. Michoud<sup>1</sup>, M.-H. Derron<sup>1</sup>, A. Abellán<sup>1</sup>, M. Jaboyedoff<sup>1</sup>
- **Reviewer:** G. Fornaro<sup>2</sup>

<sup>1</sup>. *Institute of Geomatics and Risk Analysis (IGAR). Université de Lausanne, Switzerland. clement.michoud@unil.ch*

<sup>2</sup>. *AMRA Scarl, Naples, Italia.*

Michoud C., Derron M.-H. Abellán A., Jaboyedoff M., Fornaro G., 2010. *Radar Wave Principles, Interferometric Radar Distance-Meter and Differential SAR Interferometry*. In the Deliverable 4.1 of the European project SAFELAND: *Review of Techniques for Landslide Detection, Fast Characterization, Rapid Mapping and Long-Term Monitoring*. Edited in 2010 by Michoud C., Abellán A., Derron M.-H. and Jaboyedoff M. Available at <http://www.safeland-fp7.eu>

### Section 4

- **Authors:** V. Tofani<sup>1</sup>, G. Fornaro<sup>2</sup>, F. Cigna<sup>1</sup>, F. Catani<sup>1</sup>
- **Reviewer:** C. Michoud<sup>3</sup>, M.-H. Derron<sup>3</sup>

<sup>1</sup>. *Earth Sciences Department, Università degli Studi di Firenze, Italia. veronica.tofani@unifi.it*

<sup>2</sup>. *AMRA Scarl, Naples, Italia.*

<sup>3</sup>. *Institute of Geomatics and Risk Analysis (IGAR). Université de Lausanne, Switzerland.*

Tofani V., Fornaro G., Cigna F., Catani F., 2010. *Multi-Temporal Repeat-Pass InSAR*. In the Deliverable 4.1 of the European project SAFELAND: *Review of Techniques for Landslide Detection, Fast Characterization, Rapid Mapping and Long-Term Monitoring*. Edited in 2010 by Michoud C., Abellán A., Derron M.-H. and Jaboyedoff M. Available at <http://www.safeland-fp7.eu>

## Section 5

- **Authors:** V. Tofani<sup>1</sup>, J. Gili<sup>2</sup>, G. Luzi<sup>1\*</sup>, F. Catani<sup>1</sup>

- **Reviewer:** M.-H. Derron<sup>3</sup>

<sup>1</sup> Earth Sciences Department, Università degli Studi di Firenze, Italia. [veronica.tofani@unifi.it](mailto:veronica.tofani@unifi.it)

<sup>1\*</sup> Moved after his contribution.

<sup>2</sup> Department of Geotechnical Engineering and Geosciences, Universitat Politècnica de Catalunya, Barcelona, Spain.

<sup>3</sup> Institute of Geomatics and Risk Analysis (IGAR). Université de Lausanne, Switzerland.

Tofani V., Gili J., Luzi G., Catani F., 2010. *Ground-Based InSAR*. In the Deliverable 4.1 of the European project SAFELAND: *Review of Techniques for Landslide Detection, Fast Characterization, Rapid Mapping and Long-Term Monitoring*. Edited in 2010 by Michoud C., Abellán A., Derron M.-H. and Jaboyedoff M. Available at <http://www.safeland-fp7.eu>

## Section 6

- **Author:** G. Fornaro<sup>1</sup>

- **Reviewer:** C. Michoud<sup>2</sup>

<sup>1</sup> AMRA Scarl, Naples, Italia. [fornaro.g@irea.cnr.it](mailto:fornaro.g@irea.cnr.it)

<sup>2</sup> Institute of Geomatics and Risk Analysis (IGAR). Université de Lausanne, Switzerland.

Fornaro G., 2010. *Polarimetry for Soil Moisture Estimation*. In the Deliverable 4.1 of the European project SAFELAND: *Review of Techniques for Landslide Detection, Fast Characterization, Rapid Mapping and Long-Term Monitoring*. Edited in 2010 by Michoud C., Abellán A., Derron M.-H. and Jaboyedoff M. Available at <http://www.safeland-fp7.eu>

# 1. RADAR WAVE PRINCIPLES

## 1.1. INTRODUCTION

Radar technologies have been developed since the beginning of the 20<sup>th</sup> century, first to remotely detect objects. The acronym Radar states for Radio Detection And Ranging. Radio-waves, or microwaves, are electromagnetic waves of wavelength from 1 mm to 1 m. Then radar methods have been used for accurate detection of movements and Earth surface imaging. The principles Radar technologies and applications are described in many publications, books and encyclopedias. About the radar imaging part used in environmental and Earth sciences, Massonnet and Feigl (1998), Hanssen (2001) and Woodhouse (2006) provide worthy introductions and overviews.

There are two kinds of Radar systems (Hanssen, 2001): bistatic radars use two different antennas, one for the emission and one for the reception of the electromagnetic wave; On the other hand, monostatic radars use only one antenna for both tasks. This last configuration is the most frequently applied technology for environmental purposes. A Radar transmitting antenna emits a wave by pulses with a predefined wavelength (Table 10) amplitude and phase. The Radar receiving antenna estimates the range (with the two-way travel time) and measures the amplitude and the phase of the backscattered pulses. The way the radar waves travel and are reflected to the antenna depend on several factors such as: pressure, temperature and partial water pressure of the environment, atmospheric layering, roughness and dielectric properties of the target (strongly influenced by the moisture and salt content) (Hanssen, 2001; Norland, 2006). In remote sensing, environmentalists usually describe a radar wave by its wavelength, because it gives some information about how the waves interact with the surface (roughness, interferences). Signal processing specialists prefer to work with frequencies as most of the computations are done in the frequency domain (convolution, filtering).

*Table 10 : Main bands traditionally used by the Standard Radar Nomenclature (Woodhouse, 2006).*

Band	Wavelength	Frequency
<b>P</b>	Decimetric ( 30 cm to ~ 1m )	0.3 – 1 GHz
<b>L</b>	Decimetric (~ 15 to 30 cm)	1 – 2 GHz
<b>S</b>	Decimetric (7.5 cm to ~ 15 )	2 – 4 GHz
<b>C</b>	Centimetric (~ 3.75 to 7.5 cm)	4 – 8 GHz
<b>X</b>	Centimetric (~ 2.5 to 3.75 cm)	8 – 12 GHz

Compared to the optical and near infrared sensors, the radio waves are much less influenced and attenuated by the atmospheric conditions. As shown in the Figure 43, the attenuation of waves used by Radar systems is less than 0.1 decibel per kilometer (after Preissner, 1978). So data can be acquired even during heavy rainfalls (even though some significant interactions are reported for X-Band systems) or strong fog; however these are not the optimal conditions.

Moreover, as a radar is an active sensor (sending the initial signal), data can be acquired as well during the night than during the day.

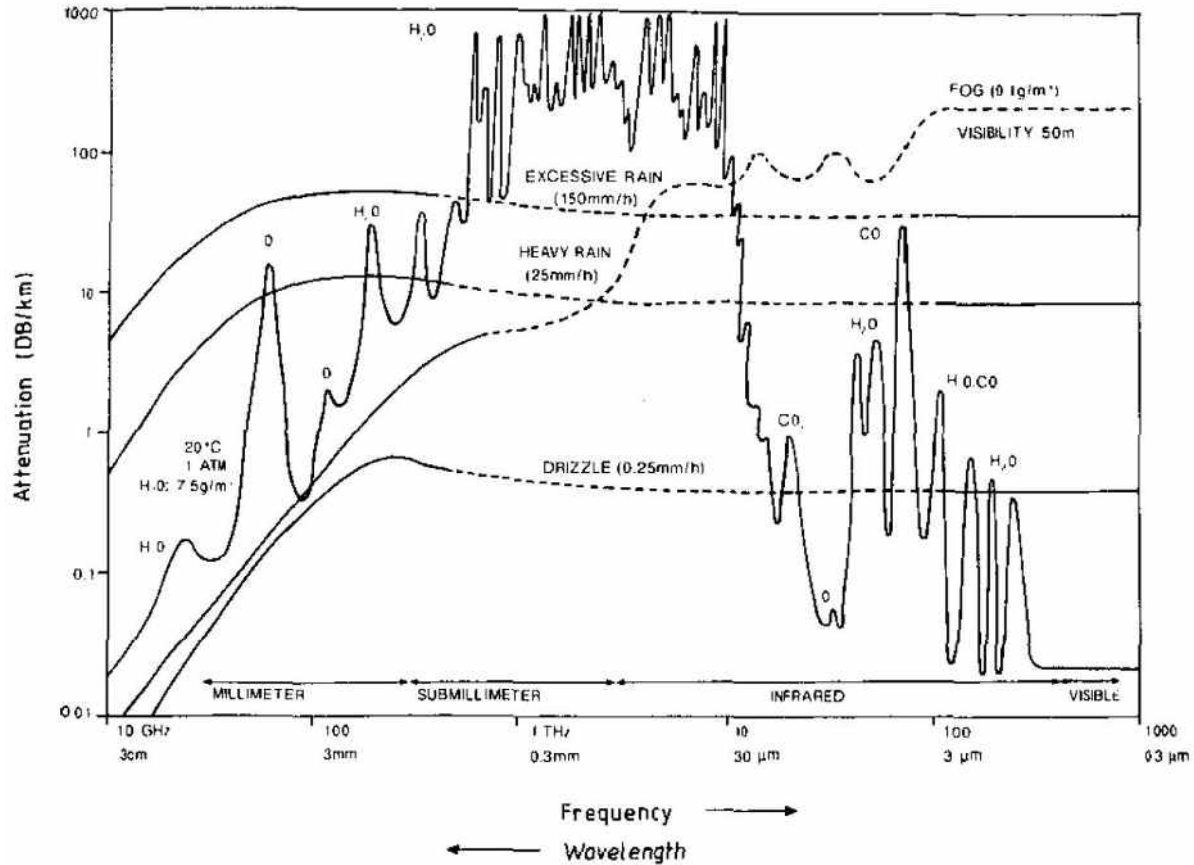


Figure 43 : attenuation of an electromagnetic wave by the atmosphere, depending of the wavelength for a clear weather, with shown for fog, heavy rain and drizzle. Contrary to the optical and near infrared, radio waves are only few attenuated by the atmospheric conditions (After Preissner 1978, cited in Peckham 1991 and Woodhouse 2006).

The choice of the frequencies used by the Radar sensors is regulated by the International Telecommunications Union. Usually, the space-borne sensors are transmitting radio waves in the bands X, C and L (Table 10). The longer the wavelength is, the worse the accuracy is both in terms of spatial resolution and measurement precision, but the better is the penetration capacity and the stability of the returned signal with respect to environmental changes..

## 1.2. RANGE AND PHASE SHIFT

Mathematically, the phase shift corresponds to:

$$\Phi = \frac{2\pi}{\lambda} \times \Delta R \quad \text{where} \quad \Delta R = 2R$$

$$\Leftrightarrow \Phi = \frac{4\pi}{\lambda} \times R$$

In this formula,  $\Phi$  is the phase shift in radians,  $\lambda$  the wavelength in meter and  $R$  the distance in meter from the sensor to the ground target.

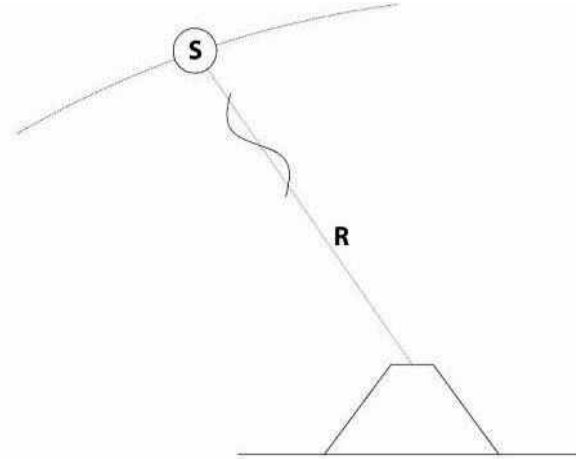


Figure 44 : representation of the Radar wave along the line of sight. The wave with a wavelength of  $\lambda$  is doing the 2-way of  $2R$  from the sensor  $S$  to the ground target. As the sensor emitted the wave knowing the original phase, it can record the phase shift when the wave comes back.

So we can deduce in theory the distance  $R$  knowing the phase shift:

$$\Leftrightarrow R = \frac{\lambda}{4\pi} \times \Phi$$

## 2. INTERFEROMETRIC RADAR DISTANCE-METER

One direct application of the phase shift principle is the continuous monitoring of instabilities assessing the movements of punctual ground targets by Radar distance-meters. All the information including in this chapter comes from the case study of the Tafjorden instability in Norway (Norland, 2006).

As described before, the phase shift is function of the wavelength and the range:

$$\Leftrightarrow \Phi = \frac{4\pi}{\lambda} \times R$$

But practically,  $R$  is defined as

$$R = \frac{1}{n} \times \frac{C_0 \times t_{2way}}{2} \quad \text{where} \quad \begin{cases} C_0 = \text{velocity of light in vacuum} \\ t_{2way} = \text{travel time sensor} > \text{target} + \text{return} \\ n = \text{spatial and temporal index of refraction} \end{cases}$$

Indeed, even if the Radar amplitudes are only few influenced by atmospheric conditions (the attenuation of the signal is negligible in almost all used bandwidths), the phases are very sensitive (Figure 45 and chapter 3.3.3.2). In fact, the spatial and temporal index of refraction depends of the pressure, the temperature and of the partial water vapor pressure which can be estimated using the relative humidity of the atmosphere (Norland, 2006).

$$n = 77.6 \times \frac{p}{T} + 3.734 \cdot 10^5 \times \frac{e}{T^2} \quad \text{where} \quad \begin{cases} p = \text{pressure in mbar} \\ T = \text{temperature in } ^\circ\text{K} \\ e = \text{partial water vapor pressure in mbar} \end{cases}$$

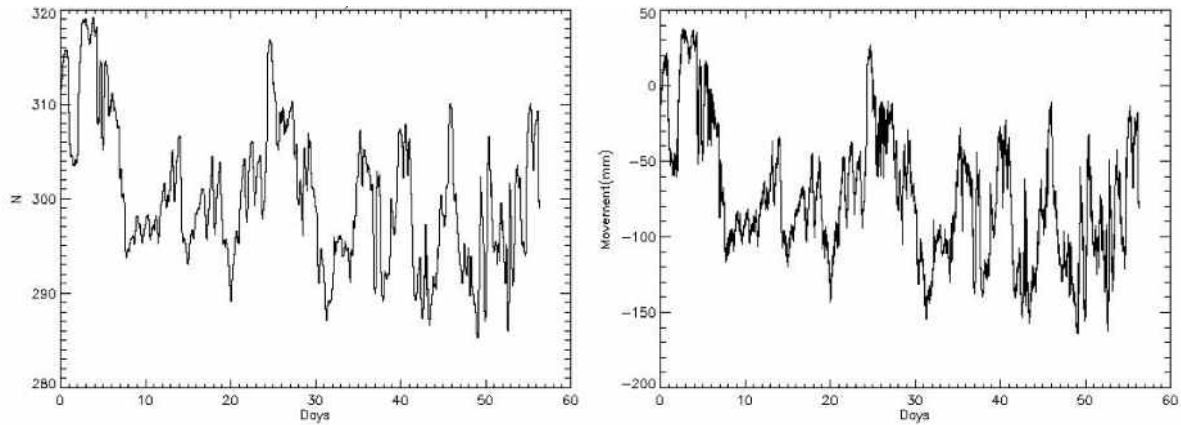


Figure 45 : strong correlations between the spatial and temporal index of refraction  $n$  (left) and the variation of range measured (right) (Norland, 2006; modified).

As shown in the figures above, there is a strong correlation between atmospherically conditions and displacement results. To separate the signal influenced by the atmosphere and the signal influenced by ground displacements, it is useful to introduce a second target on a stable part (Figure 46).

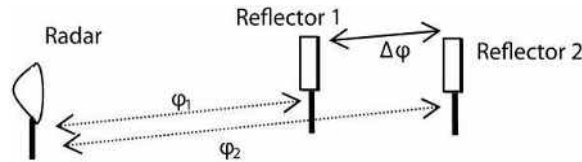


Figure 46 : theoretical arrangement for interferometric distance-meter (Norland, 2006).

So, assuming one reflector as fix, all variations of phase coming from the spatial and temporal index of refraction and not from the displacement can be filtered. Then, comparing phase results between the two reflectors by interferometry (phases differences), it is possible to assess the displacements of the second target (Norland, 2006).

$$\Delta\phi = \Phi_2 - \Phi_1 = \frac{4\pi}{\lambda} \times (R_2 - R_1)$$

$$\Rightarrow \Delta R = \frac{\lambda}{4\pi} \times \Delta\phi$$

So, in the case study of the Taffjorden instability, the reflectors are monitored with accuracy better than 0.1 mm at 2.9 km (Norland, 2006).

### 3. DIFFERENTIAL SAR INTERFEROMETRY

The main use of Differential Synthetic Aperture Radar Interferometry (DInSAR) is the detection of small deformations or movements at the surface, analyzing the phase differences



between two scenes acquired at different times. The Differential Synthetic Aperture Radar Interferometry is a combination of three main processing steps: first the Synthetic Aperture Radar (SAR), then the Interferometry (InSAR), and finally the Differential InSAR (DInSAR). These steps are described hereafter.

### 3.1. SYNTHETIC APERTURE RADAR

#### 3.1.1. Radar imagery

In Radar imagery, a coherent and polarized wave is emitted by an antenna and the amplitude and the phase shift of each backscattered pulse are recorded in a complex number (Woodhouse, 2006):

$$z = A \cdot e^{i \cdot \Phi} \quad \text{where} \quad \begin{cases} z = \text{value for each cells} \\ A = \text{amplitude} \\ \Phi = \text{phase shift} \end{cases}$$

The amplitude of the backscattered signal is a function of the wave initial state, the environment crossed by the wave and the capacity of the target (reflectance, moisture) to reflect the wave (Figure 47). During the post-processing, it is easy to distinguish the emitted signal from the backscattered one. Moreover, airborne and satellite sensors are not looking vertically downwards but they are side-looking, avoiding the problem of knowing from which side of the nadir the pulse is backscattered.

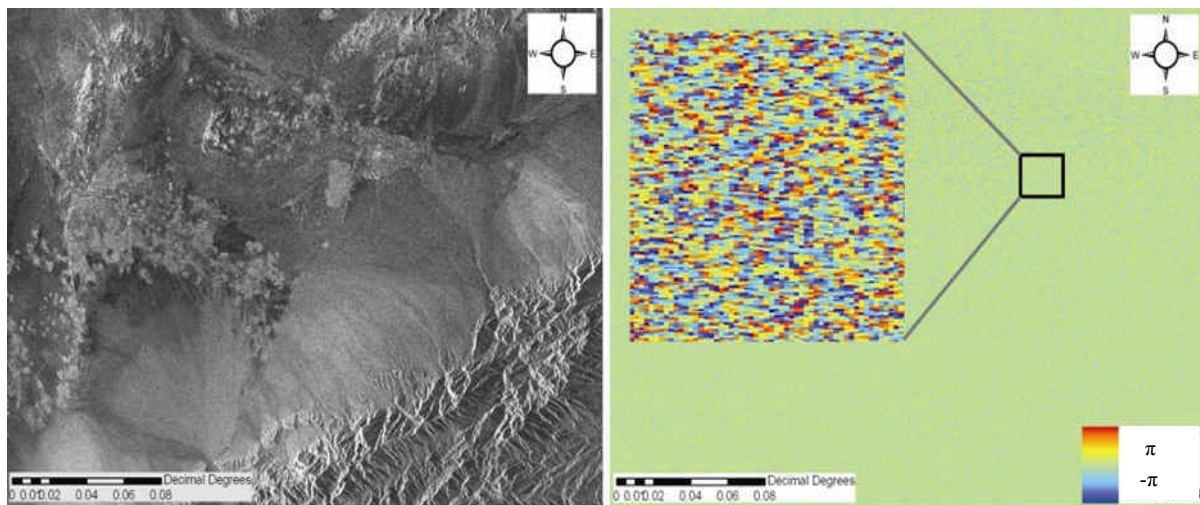


Figure 47 : Complex SAR image with the return amplitudes (left) and phases (right) of Bam area in Iran, December 2003 (Michoud et al., 2009).

In most cases, space borne Radar sensors are monostatic. So, the power of the return wave can be determined by the following formula detailed in the ESA Radar course III (website address in references):

$$P_r = P_t \times \frac{G^2 \lambda^2 \sigma}{(4\pi)^3 R^4} \quad \text{where} \quad \begin{cases} P_r = \text{Power received (W)} \\ P_t = \text{Power emitted (W)} \\ G = \text{Gain of the antenna} \\ \lambda = \text{Radar wavelength (m)} \\ \sigma = \text{radar scattering cross section (m}^2\text{)} \\ R = \text{distance antenna – target (m)} \end{cases}$$

But the effective area of the antenna is related to the gain by:

$$S = \frac{\lambda^2 G}{4\pi} \Rightarrow P_r = P_t \times \frac{S^2 \sigma}{4\pi \lambda^2 R^4}$$

The formula above gives the mean power per pixel in function of the size of the antenna. The bigger the antenna is, the higher the mean received power will be. And the higher the mean received power is, the better is the resolution. So one practical limit of the system is the maximal possible size of the antenna in space. It was demonstrated that to get a metric resolution from space borne sensor, a kilometer long antenna is needed (Prati, 2008).

To overcome this technical impossibility and obtain a reasonable ground resolution, a new acquisition method has been developed since the 50s (Wiley, 1954): the Synthetic Aperture Radar (SAR).

### 3.1.2. Synthetic Aperture Radar

Imagined in 1951 by Carl Wiley (Wiley, 1954; Hanssen, 2001), the Synthetic Aperture Radar principle wants to sum several echoes of the same target during the post-processing to improve the azimuthal resolution. Indeed, when the sensor transmits pulses along its track, the same ground target can reflect several times different echoes (Figure 48). Using the Doppler beam sharpening with the frequency information contained in the phase (Woodhouse, 2006), it is possible to differentiate two scatterers within the beam. So, the effective antenna aperture moving along the flight line is larger than in reality. In this way, the azimuthal resolution is improved (Figure 49). This process of synthesis can be compared to the multi-tracks processes in seismic geophysics.

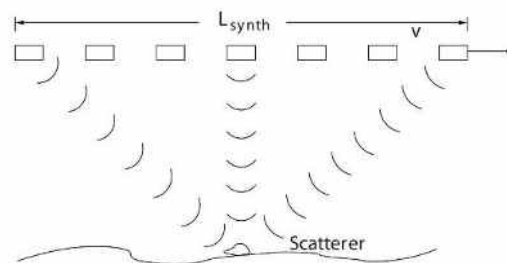


Figure 48 : Synthetic Aperture Radar principles. The same ground scatterer is shot from different points of view synthesizing an aperture much larger than the physical size of the real antenna, increasing the azimuth resolution (Lauknes, 2004).

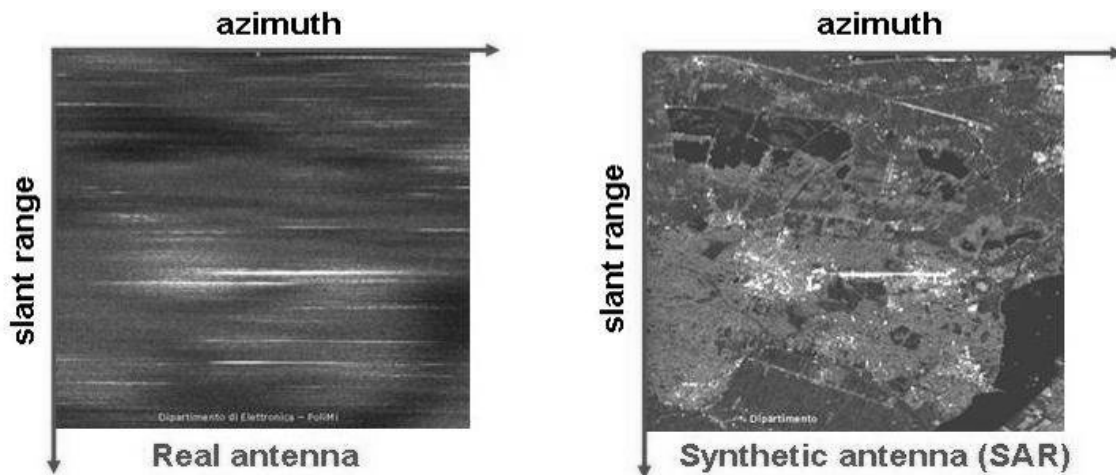


Figure 49 : Real Aperture Radar (left) and Synthetic Aperture Radar (right). The azimuth resolution is much better with SAR technology (Prati, 2008).

Once the azimuthal resolution has been improved by the SAR acquisition, it is also important to increase the range resolution. As explained in Woodhouse (2006), the shorter the pulse is, the better the range resolution is; but generating short pulses requires high peak power, actually not available on a satellite. In practice, a linear frequency modulated or chirped pulse (Figure 50) is used (Hanssen, 2001; Lauknes, 2004; Woodhouse, 2006). Thanks to a frequency post processing using the Fourier Transform, the echoes can be separated and re-attributed to their original ground target. Indeed, this technology allows to emit a chirped pulse of 40  $\mu$ s with a range resolution similar with a pulse of 60 ns (Woodhouse, 2006). However, to perform this technique, it has to be assumed that the fly is stable (reasonable in a satellite) and that the frequency variation law (modulation) is well known.

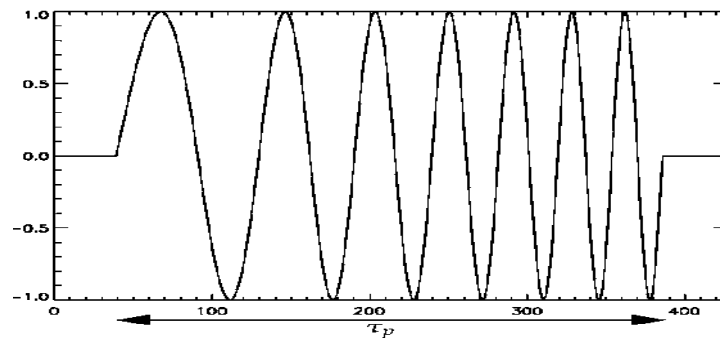


Figure 50 : linear chirp waveform – amplitude function of time (arbitrary units). Typical pulse durations for ERS and Envisat ASAR are between 30 and 40 micro seconds. (Lauknes, 2004).

### 3.1.3. Terminology and Space Resolution

The spaceborne acquisition of SAR images often uses specific terms which have to be defined or remembered in this section (to go further, see the website of the Canadian Center for Remote-Sensing).

- Ascending / Descending orbit: South-North / North-South trajectory of the platform.

- Azimuth: distance along the spaceborne flight direction. The azimuthal resolution can be performed by Synthetic Aperture Radar techniques.
- Complex signal: each pixel is registered by a complex number, keeping the information on the amplitude and the phase of the return signal. This is the raw data for an InSAR study.
- Ephemerides: satellite position and velocity vectors at any time  $t$ .
- Fringe: line of an interferogram corresponding of one color cycle.
- Ground range: distance along the perpendicular of the flight direction on the ground's surface. The range resolution can be performed emitting chirped pulses.
- Line of Sight: trajectory of the chirp between the radar antenna and the ground scatterers.
- Look angle  $\theta$ : angle between the vertical and the LOS.
- Master / Slave images: reference / comparative images in interferometry.
- Nadir: projection on the Earth's surface of the platform's trajectory.
- Near / Far range: part of the image closest to / furthest from the Nadir.
- Resolution: size of the smallest object detectable by the sensor.
- Slant range: distance along the perpendicular of the azimuth on the SAR image. The slant range can be different of the ground range due to geometrical distortion, as explained in the following chapter.
- Track / Frame: Est-West / North-South limit of a SAR image.

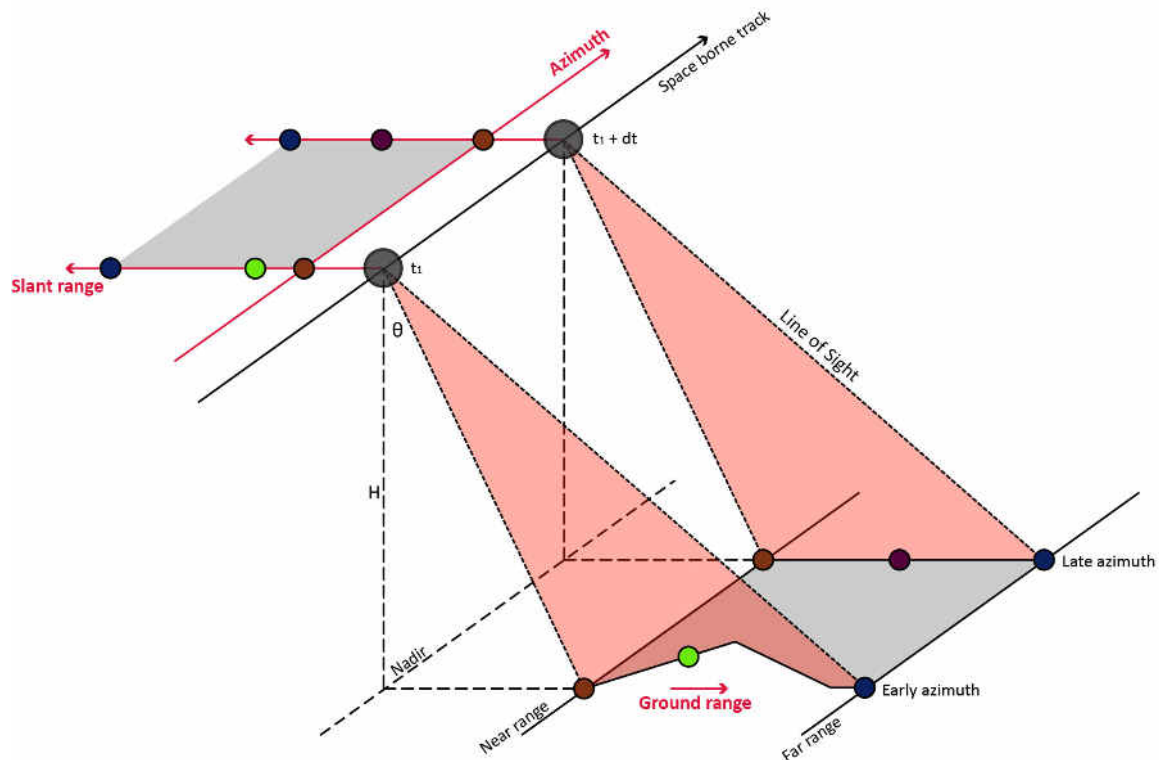


Figure 51 : geometry of SAR acquisition (Prati, 2008, modified)

### 3.1.4. Geometric and radiometric distortions

The satellite does not emit pulses vertically; there is always a look angle generally higher of  $10^\circ$  (depending of the sensor). Two types of geometric distortion (Hanssen, 2001; Squarzoni, 2003; Lauknes, 2004; Woodhouse, 2006) can be produced in rough relief areas: the foreshortening and the layover. A third possible effect, the shadowing, is a radiometric distortion (Figure 52).

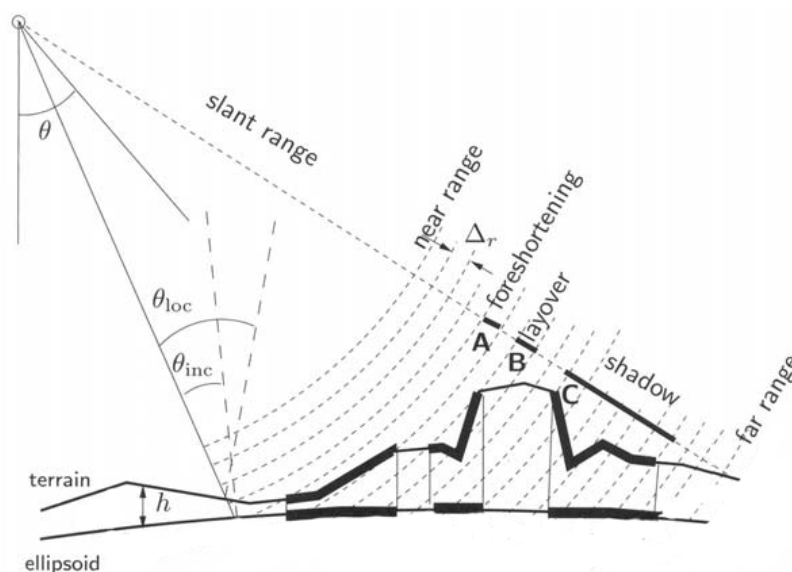


Figure 52 : from ground range to slant range. (Hanssen, 2001, modified)

Foreshortening may happen when a slope, with its normal vector looking towards the sensor, is less steep than the look angle. In this case, the surface will be smaller in the slant geometry than in reality (e.g. Figure 53). The layover may happen when the slope is steeper than the look angle. In this case, the backscattered pulse from the top of the slope will be collected by the sensor before the pulse reflected from the bottom of the slope (Figure 9). Then the top of the slope will be considered as closer in the slant range than the bottom, and the slope will look as reversed. The closer the slope is from the Nadir, the stronger the geometric distortions will be (Woodhouse, 2006). Indeed, the look angle is smaller close to the near range than to the far range and so more distortions are typically observed in the near range.

To correct both geometric distortions, foreshortening and layover, information on the real topography are used. By geocoding SAR images using a DEM, it is possible to rectify these distortions, as schematized in the Figure 54.

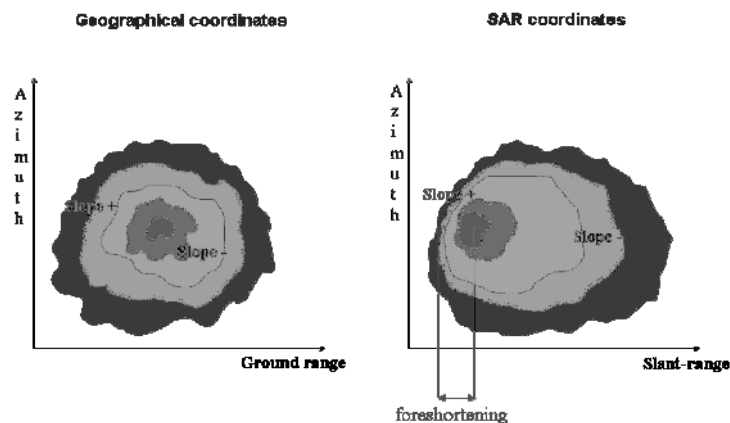


Figure 53 : schematic differences between ground range (left) and slant range (right), with a foreshortening slope (Prati, 2008).

The last distortion, shadowing, is a radiometric distortion that corresponds to an absence of signal (Figure 52). This distortion is the most restricting because the lost information is not recoverable. The only way to obtain additional data is to shoot from different positions, e.g. once in ascending orbit and the second time in descending orbit.

The last and facultative step of all processing is the geocoding, to transform and uniform the pixel sizes in a ground-coordinate system (Lauknes, 2004). For this process, Ground Control Points, DEM and precise orbit data are needed (ESA, Figure 54).

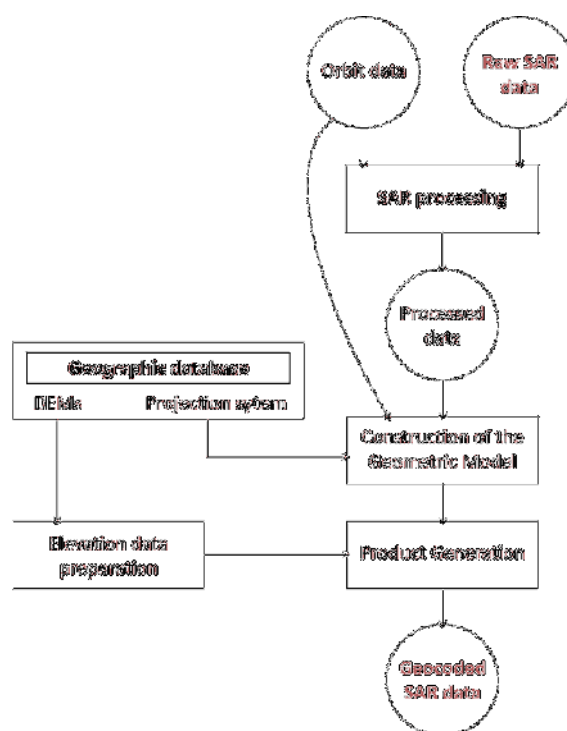


Figure 54 : Geocoding of SAR image (ESA document, 2008, modified)

### 3.2. SAR INTERFEROMETRY (INSAR)

Interferometric Synthetic Aperture Radar (InSAR) is a method to produce images of the interferometric phases of an area using images acquired from two different points of view. With SAR images as in optical stereoscopy, two images of an object from two distinct points of view allow seeing in relief and building Digital Elevation Models.

The interferograms shown as examples in the following chapters are processed using free ESA Envisat ASAR dataset of the Bam region (southeast Iran), where a strong earthquake occurred the 26th of December 2003.

Table 11 : raw input of Bam interferograms (free raw Envisat ASAR dataset provided by ESA).

Image	Sensor	Date	Normal Baseline
Sar1 (Slave)	ASAR Envisat	11 <sup>th</sup> of June 2003	475 m
Sar2 (Master)	''	3 <sup>rd</sup> of December 2003	0 m
Sar3 (Slave)	''	7 <sup>th</sup> of January 2004	520 m

#### 3.2.1. Preparation of the dataset

##### 3.2.1.1.Focusing

SAR is radar: similarly to surveillance radars, it therefore allows discriminating, i.e., resolving the targets in distance by measuring the delays of the transmitted pulses: the

narrower the pulse the higher the system range resolution. As already pointed out in a previous section, in order to limit the peak power and therefore to simplify the transmitter, usually chirp signal are used in transmission. These classes of pulses are characterized by large bandwidth duration products: to achieve short pulses the echoes that form the radar image must be correlated with the transmitted replica of the chirp signal. The received signal, i.e. the raw data, is therefore subject to a processing (range focusing) to achieve the maximum range resolution. Furthermore, SAR exploits the movement of the sensor to synthesize an antenna which is much larger, typically between 100 and 1000 times, the size of the real antenna mounted on-board the satellite (about 10m for the ERS and Envisat cases). Accordingly, the raw data must be further processed (azimuth focusing) along the azimuth direction to synthesize the large antenna and hence to achieve the highest azimuth resolution. Depending on the frequency and resolution, the azimuth focusing is generally more complex than the range focusing: it is intrinsically two-dimensional and space variant. However, thank to the research carried out in the last years, efficient focusing algorithms that make use of Fast Fourier Transform codes have been developed. In Bamler (1992) different focusing algorithms are compared.

It should be pointed out that to trade off between the coverage (swath width) and the resolution, SAR sensors may operate in different modes, see Fig 13. In the classical mode, referred to as stripmap mode, the antenna pointing is fixed: The movement of the sensor allows collecting the information from a ground strip. In the spotlight mode, the beam is steered backward in such a way to illuminate only a fixed portion (the ground spot): the size of the synthesized antenna and therefore the resolution is increased at the expense of the coverage. On the other hand by steering or better scanning the beam over different range swaths, SAR system may increase the range coverage at the expense of the azimuth resolution. Depending on the operational mode, the focusing operation must take into account the characteristics of the acquisition in order to properly process the signal and hence to achieve a full focusing. Most of the commercial packages allow focusing data for any acquisition mode. However, in case of beam steering the acquisition characteristics can impact also the subsequent interferometric processing steps: for instance spotlight and scansar interferometric acquisitions must be synchronized along the azimuth in such a way to limit the variability of the response of the scene as a function of the azimuth angle (aspect angle).

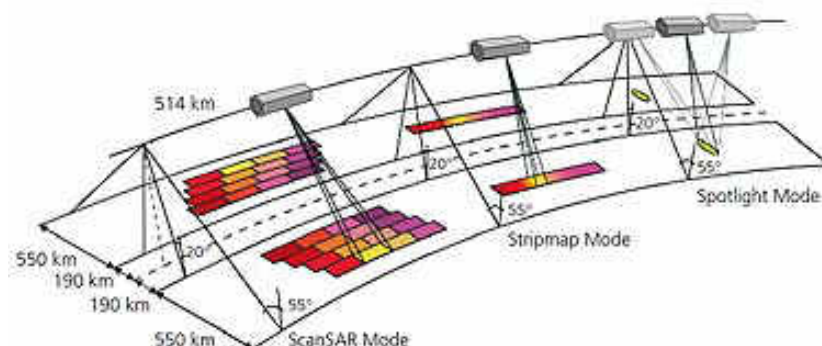


Figure 55 : different operational modes of SAR systems



### **3.2.1.2.Co-registration**

Image registration is a process that aims to obtain a precise overlap between two or more images relative to the same object. Such images may be acquired from separated positions, by different sensors and/or at different times. For SAR interferometry, images need to be precisely aligned, with sub-pixel accuracy, to extract the phase interference relative to the same ground target, which is imaged at different positions in the two images due to distortion effects related to the different imaging geometry associated a) with a non zero orbit spatial separation, b) with the presence of orbit crossing. Incorrect alignments of the focused images, usually known as Single Look Complex (SLC) images, cause coherence losses in the interference operation, which, in turn, translate into inaccuracies in the final product.

Co-registration procedures for SAR images are based on the estimation of the so called azimuth and range warp-functions, i.e., the functions describing the transformation that maps the slave image onto the reference master image and that are subsequently used for resampling the slave image onto the reference master image grid. Warp functions are generally modeled in such a way to account for a few distortion effects: bilinear expansions are frequently used to account for rotation and scaling effects due to acquisition track crossing. Accordingly, warping functions are described in terms of few parameters that are estimated starting from control points. In the case of radar images, for the accuracy required in coherent data processing, such control points cannot be generally identified starting from features (road crossing, edges, etc.), because of the speckle noise. Ground corner reflectors could be exploited; however in practice matching measures of small image patches are employed to evaluate a sufficient number of tie points for the parameters estimate.

Standard image co-registration procedures based on polynomial expansion of the warp functions have been extensively used in the past to implement interferometry at small spatial baseline separation. However, accurate image registration of SAR data takes on a sub-pixel basis, where the passes span an orthogonal baseline interval of the order of few kilometers and the temporal intervals of several years (as it happen in interferometric stacking and persistent scatterers Interferometry for ground deformation monitoring) becomes a rather challenging step due to effects of topography and the presence of large temporal decorrelation which impair the accurate measurements of local distortions. Even more challenging is the registration of images for the latest high resolution SAR systems (i.e. TerraSAR-X and COSMO/SKYMED). To overcome the limitations of standard techniques, modern co-registration techniques make use of a geometrical computation of the warp functions starting from the orbital information and from an external (rough) DEM, (Sansosti 2006). This procedure allows easily achieving very accurate registration almost in all cases of interest for interferometrical application,

### **3.2.1.3.Filtering**

In differential SAR Interferometry, angular imaging diversity is an unavoidable effect due to the impossibility to repeat exactly the same orbit: it also plays a positive role for the localization of the ground scatterers: In any case it is the source of noise that adds to the interferograms Besides the generation of image geometric distortions, which are usually compensated via a registration step, the interferometric phase associated with the topography plays a modulation role that causes, for a distributed scattering, the presence of incoherent components between the two images. For a planar surface this effect is known as spectral shift effect and it is shown schematically in the left part of Figure 14. The result is the introduction

of decorrelation noise on the interferometric fringes which is usually referred to as geometrical, spatial, or baseline decorrelation. Spatial decorrelation can be counteracted by proper filtered of the co-registered SLC images aimed at zeroing the unwanted components: the filtering is known as Common Band filtering and is schematically shown in the right part of Figure 14. Angular decorrelation is also present in the azimuth direction due to possible differences in the antenna beam pointing in the two acquisitions (Doppler centroid decorrelation). Common band filtering can be therefore beneficial also along the azimuth direction in the presence of large excursion of the Doppler Centroid. While in the azimuth direction the common band filtering is space invariant, the range filtering should be dependent on the local topography. In Fornaro and Monti Guarnieri 2002 it is discussed an efficient procedure for range space variant filtering. It should be pointed out that common band filtering should be performed only when the scattering is assumed to be distributed: this assumption is not verified in the case of strong scatterers and hence it is generally not implemented in permanent scatterers monitoring: Conversely it is usually performed in approaches like the low resolution monitoring via the Small BAseLine Subset approach.

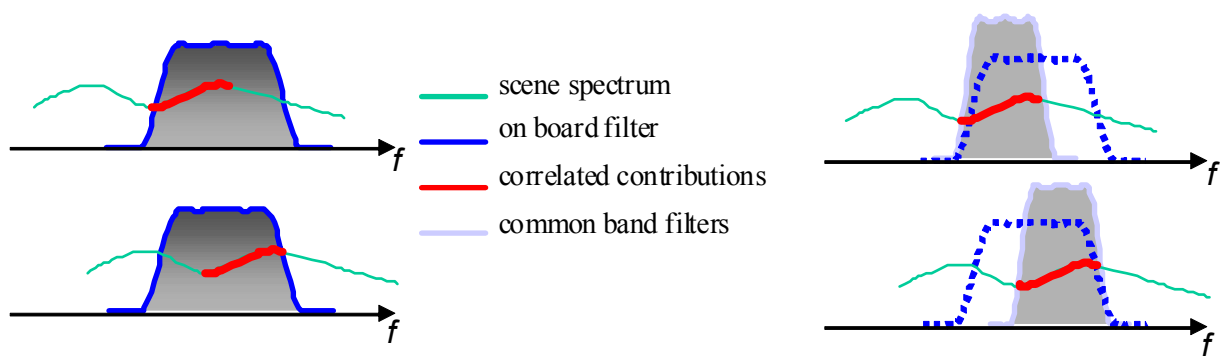


Figure 56 : the spectral shift effect (left) and the common band filtering (right)

### 3.2.2. Interferometric phase

Mathematically, the radar interferometry is defined by the difference of 2 phase shifts acquired by the sensor in two distinct times. So the formula 1 is the base of this method. More mathematical developments, which use the variables introduced in the Figure 57, are available on the following publications: Bamler & Hartl (1998), Massonnet and Feigl (1998), Hanssen (2001), Lauknes (2004), Catani et al. (2005), Colesanti & Wasowski (2006), Woodhouse (2006), Ferretti et al. (2007).

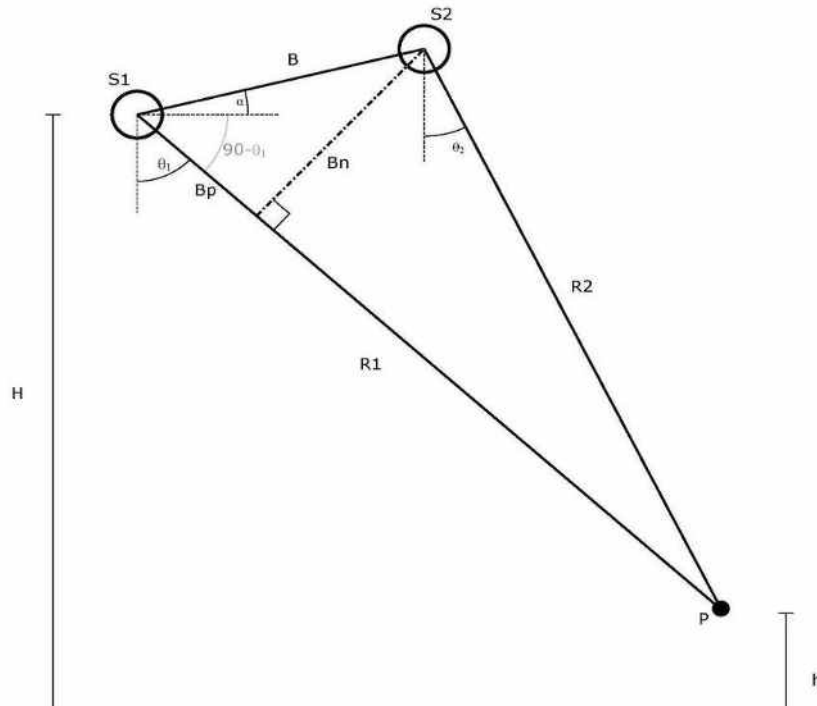


Figure 57 : InSAR acquisition parameters.  $S1$  and  $S2$  are the two antennas acquiring the image SAR 1 and SAR 2.  $S1$  flight at the altitude  $H$ .  $P$  is a ground scatterer at the altitude  $h$ .  $R1$  and  $R2$  are the distances between  $P$  and  $S1$  or  $S2$ .  $B$  is the distance between the two sensors (baseline),  $B_p$  and  $B_n$  being resp. the parallel and normal of  $B$  to  $R1$ . The angle between the vertical and  $R1$  (resp.  $R2$ ) is  $\theta_1$  (resp.  $\theta_2$ ). (Catani et al., 2005, modified)

Mathematical approach for one reflector acquired twice:

$$\varphi = \Phi_1 - \Phi_2$$

$$\Leftrightarrow \varphi = \frac{4\pi}{\lambda} \times R_1 - \frac{4\pi}{\lambda} \times R_2 = \frac{4\pi}{\lambda} \times (R_1 - R_2)$$

Due to the big distance considered, the approximation  $B_p \approx R_1 - R_2$  can be admitted.

$$\Rightarrow \varphi \approx \frac{4\pi}{\lambda} \times B_p$$

$$\Rightarrow \varphi \approx \frac{4\pi}{\lambda} \times B_n \times \tan(\theta_1 - \alpha) \approx \frac{4\pi}{\lambda} \times B \times \sin(\theta_1 - \alpha)$$

Published with these two different forms, the formula 2 expresses the theoretical geometric relations of a raw interferogram (Figure 58).

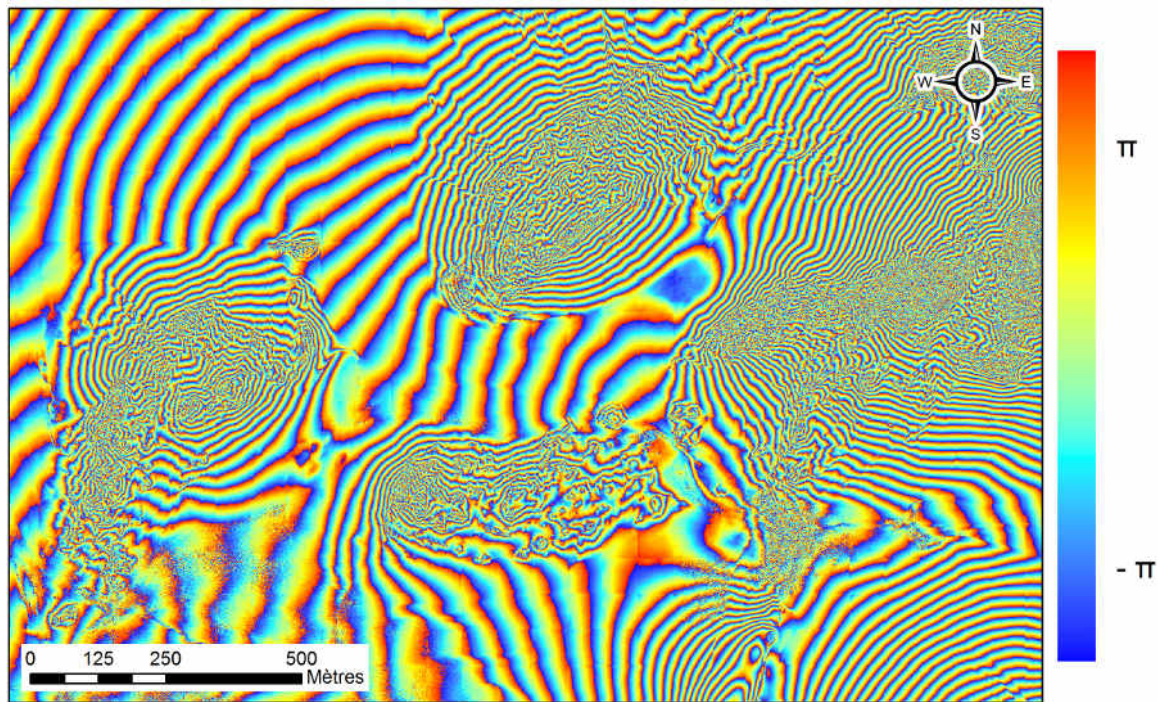


Figure 58 : interferogram using the images Sar2 and Sar3. One fringe is represented by one color cycle (from blue to yellow). (Michoud et al., 2009; processed with Erdas Imagine 9.2™)

### 3.2.3. Interferogram flattening

The topography is not the only contribution in an interferogram; there is also the flattening phase, which can be defined as “the phase variation proportional to the slant range displacement of the point target” (Ferretti et al., 2007). Removing this orbital contribution by an operation called interferogram flattening, it results fringes only influenced by the topography (and possibly the ground displacement) and proportional to it (Ferretti et al., 2007).

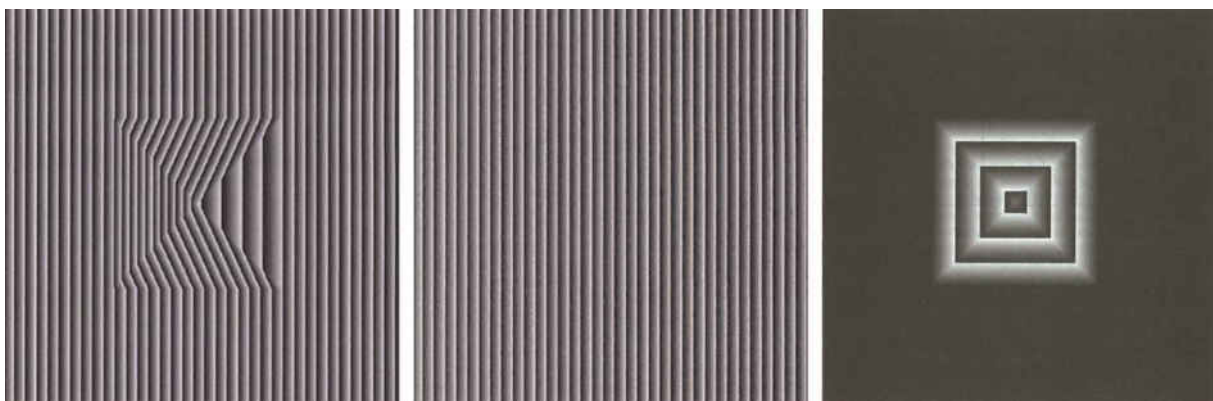


Figure 59 : theoretical interferogram simulating a pyramid. Left: raw interferogram – Center: flattening phase – Right: fringes proportional to the topography. (Woodhouse, 2006)

### 3.2.4. Altitude of ambiguity

The variation of the topography which creates an interferometric cycle of  $2\pi$  is called altitude of ambiguity  $h_a$  (Massonnet and Feigl, 1998). In an interferogram, it corresponds to the altitude constituted by one complete fringe (from blue to red in the Figure 58).

$$\Delta\phi = n \times 2\pi, \quad \forall n \in \mathbb{N}$$

$$h_a = \frac{\lambda}{4\pi} \times \frac{H \cdot \tan \theta_1}{B_n} \times 2\pi = \frac{\lambda}{2} \times \frac{H \cdot \tan \theta_1}{B_n} \quad \text{and for ERS} \quad h_a \approx \frac{9400}{B_n}$$

Considering the case of a normal baseline of 200 m, the altitude of ambiguity for ERS is 47 m. As shown later, the shorter the normal baseline is, the bigger the altitude of ambiguity is and the less accurate the altitude measurement is (Figure 64). But regarding to the geometrical loss of coherency, the normal baselines cannot be indefinitely long (cf.). To generate DEMs from ERS-satellite images, there is an optimum of the normal baseline at about 300-400 m (Ferretti et al., 1997).

### 3.2.5. Phase unwrapping

The fact that the interferometric phase is measured modulo  $2\pi$  creates an ambiguity that must be removed by a course of phase unwrapping. This step converts each ambiguous  $2\pi$  cycle to the absolute value of the interferometric phase (Figure 60 and Figure 61).

As suggested in the Figure 60, a certain continuity of phase values recorded is required to unwrap correctly the interferogram. Actually, several answers are acceptable for one initial wrapped interferogram (Ferretti et al., 2007). Actually, if the variation of the topography between two following scatterers is equal to the altitude of ambiguity (unwrapped phase 2 in the Figure 60), this gap is not considered in this processing step and the result will be without gap (unwrapped phase 1 in the Figure 60). Ferretti et al. (2007) emphasizes on the necessity to use “a-priori information to get the right solution”.

The other key point to assure a continuity of the values is to use only pixels which have a good coherence (cf. chapter 3.3.3), reducing the incoherent noise. Bernardino et al. (2003) advise to take only the pixels whose coherence is greater than 0.3.

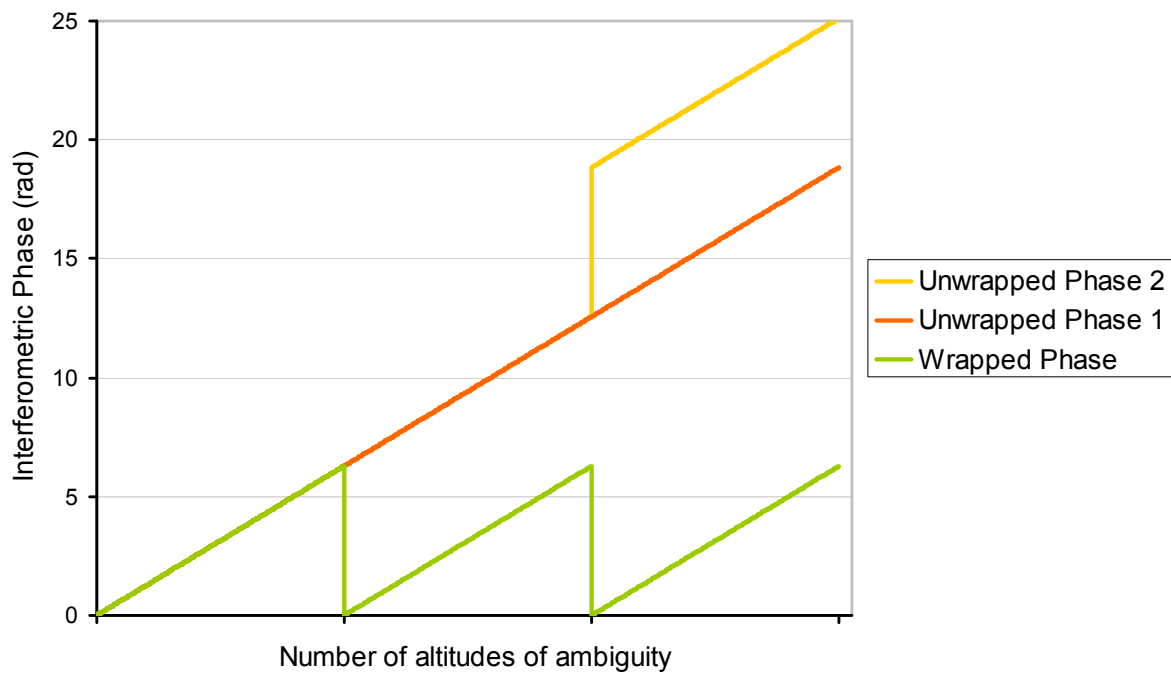


Figure 60 : difficulties of phase unwrapping. In fact, it exists several ways to unwrap correctly an interferogram. (Massonnet and Feigl, 1998, modified)

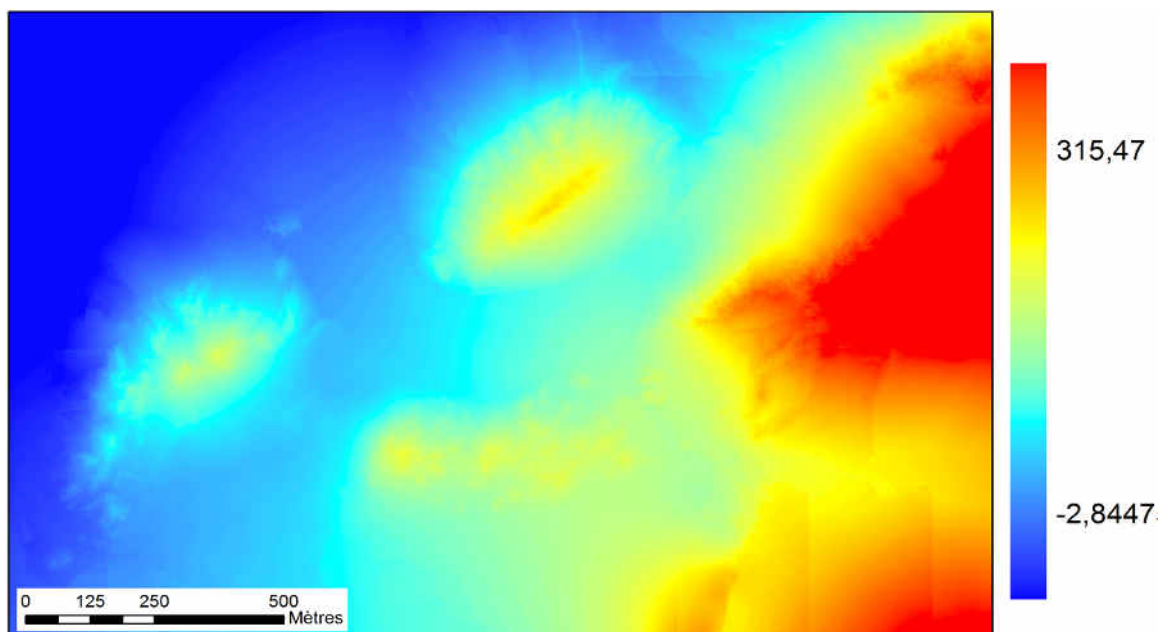


Figure 61 : unwrapped interferogram [Sar2|Sar3] of Bam area. (Michoud et al., 2009; processed with Erdas Imagine 9.2™)

### 3.2.6. DEM construction

The last step of the processing aims to construct numerically the DEM. The Figure 62 shows the helpful parameters needed to perform the model. The platform flying always at the same altitude,  $\alpha$  is nil (cf. Figure 57). Moreover, the approximation  $[S_1L] = [S_1P] = R_1$  is admitted.

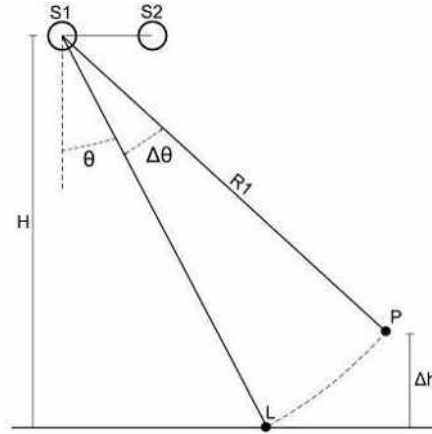


Figure 62 : parameters needed to calculate the altitude variations. (Michoud et al., 2009)

$$\begin{cases} \cos(\theta) = \frac{H}{R_1} \\ \cos(\theta + \Delta\theta) = \frac{(H - \Delta h)}{R_1} \end{cases} \Leftrightarrow \begin{cases} R_1 = \frac{H}{\cos(\theta)} \\ \Delta h = H - R_1 \times \cos(\theta + \Delta\theta) \end{cases}$$

Now,  $\cos(\theta + \Delta\theta) = \cos\theta \times \cos\Delta\theta - \sin\theta \times \sin\Delta\theta$  and for  $\Delta\theta$  small,  $\begin{cases} \cos\Delta\theta \approx 1 \\ \sin\Delta\theta \approx \Delta\theta \end{cases}$

$$\Rightarrow \Delta h \approx H - R_1(\cos\theta - \Delta\theta \times \sin\theta)$$

$$\Rightarrow \Delta h \approx H - \frac{H}{\cos\theta}(\cos\theta - \Delta\theta \times \sin\theta)$$

$$\Rightarrow \Delta h \approx H \left( 1 - \frac{\cos\theta}{\cos\theta} + \Delta\theta \times \frac{\sin\theta}{\cos\theta} \right)$$

$$\Rightarrow \Delta h \approx H \times \Delta\theta \times \tan\theta$$

Now, deriving  $\varphi$  in the formula 6 according to  $\theta$ , we obtain  $\frac{d\varphi}{d\theta} = \frac{4\pi}{\lambda} \times B \times \cos\theta$

As L and P are close, therefore we admit  $\Delta\theta$  small and  $\frac{d\varphi}{d\theta} = \frac{\Delta\varphi}{\Delta\theta}$

$$\Rightarrow \Delta\theta = \frac{1}{B} \times \frac{\lambda}{4\pi} \times \frac{\Delta\varphi}{\cos\theta}$$

$$\Rightarrow \Delta h \approx H \times \frac{1}{B} \times \frac{\lambda}{4\pi} \times \frac{\Delta\varphi}{\cos\theta} \times \tan\theta$$



$$\Rightarrow \Delta h \approx \frac{\lambda}{4\pi} \times \frac{H \cdot \tan \theta}{B_n} \times \Delta \varphi$$

Therefore, it is possible to obtain from the interferometric phase of two close scatterers the variation of altitude. Performing this method for all the pixels in the SAR images, it is possible to get a relative DEM of the area (Figure 63). Due to the initial ambiguity of  $2\pi$ , the model cannot characterize the absolute altitudes, but only the variations of the topography. If the exact altitude of one pixel is known, it is then possible to shift the entire area to achieve a good DEM. To get a good DEM accuracy and to limit noise artifacts, it is advisable to process several SAR pairs and to average the results in order to decrease the signal to noise ratio (Ferretti et al., 2007).

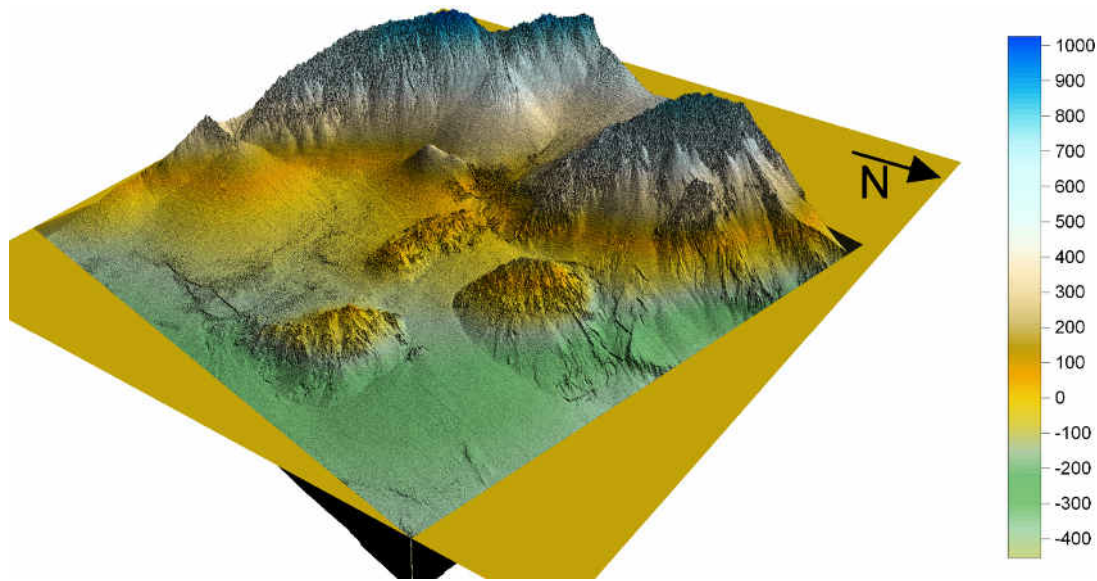


Figure 63 : Topography of BAM area, provided by the processing of the interferogram [Sar2|Sar3]. The model has a 20 m grid and a vertical accuracy of 1.5 m. (Michoud et al., 2009; processed with Surfer 8™)

The Shuttle Radar Topography Mission (SRTM), achieved in February 2000 by the NASA, scanned the Earth surface with two Radar antennas (C-band and X-band). Thanks to SRTM, it exists now a worldwide DEM at 90 m resolution (from 60°N to 56°S) and an American DEM at 30 m resolution (SRTM technical factsheet, JPL 2005).

For the data from the satellites ERS, the threshold of detection of a coherent signal regarding to the noise is  $\pi/6$  (Catani et al., 2005). The following formulas show the importance of the normal baseline in the vertical accuracy ( $\Delta h$ ) of a DEM (Figure 64). The longer the normal baseline is, the more accurate the DEM is.

$$As \quad \Delta h \approx \frac{\lambda}{4\pi} \times \frac{H \cdot \tan \theta}{B_n} \times \Delta \varphi \quad \text{and} \quad \Delta \varphi = \frac{\pi}{6}$$

$$\Rightarrow \Delta h = \frac{\lambda}{24} \times \frac{H \cdot \tan(\theta_1)}{B_n} \quad \text{and for ERS,} \quad \Delta h \approx \frac{800}{B_n}$$



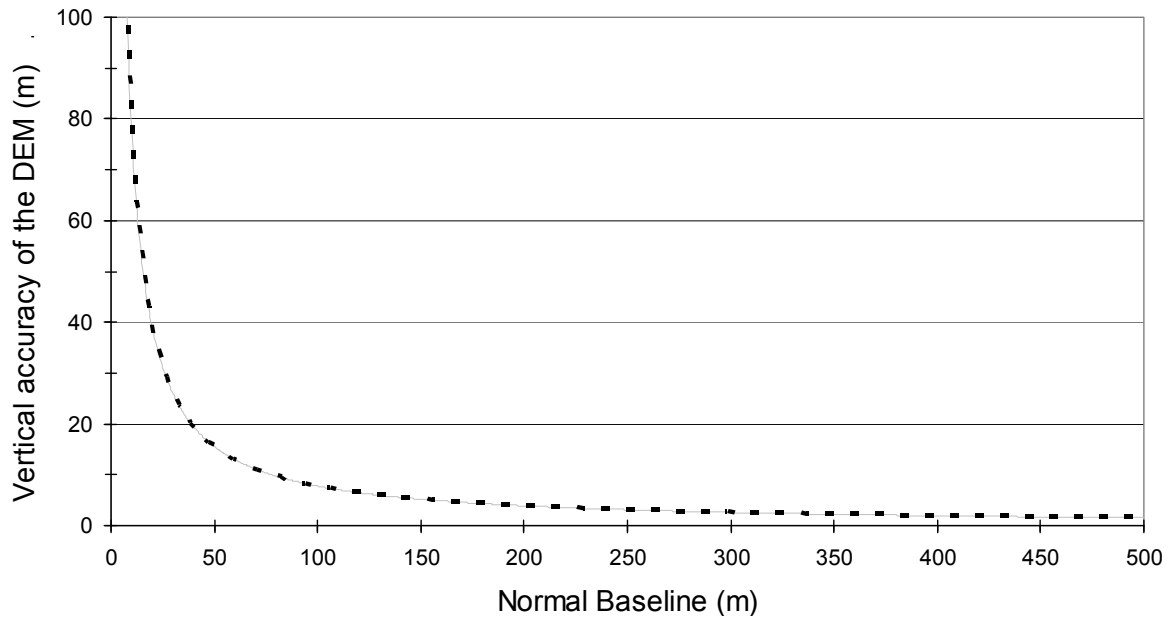


Figure 64 : vertical accuracy of a DEM regarding to the normal baseline of the interferometric pair. The function is calculated with the ERS parameters:  $\lambda = 5.6$  cm,  $H = 785$  km and  $\theta_i = 23^\circ$ . The longer the normal baseline is, the more accurate the DEM is.

### 3.3. DIFFERENTIAL SAR INTERFEROMETRY (DINSAR)

The main goal of differential InSAR (DInSAR) technique is to identify and quantify small ground deformations. Indeed, the phase difference is produced, provided by two contributions: the topography and the deformations (Figure 65). More information is available on Massonnet and Feigl (1998), Lauknes (2004), Catani et al. (2005), Colesanti and Wasowski (2006), Woodhouse (2006), Ferretti et al. (2007).

$$\Phi_{\text{way}} = \Phi_{\text{topography}} + \Phi_{\text{deformation}}$$

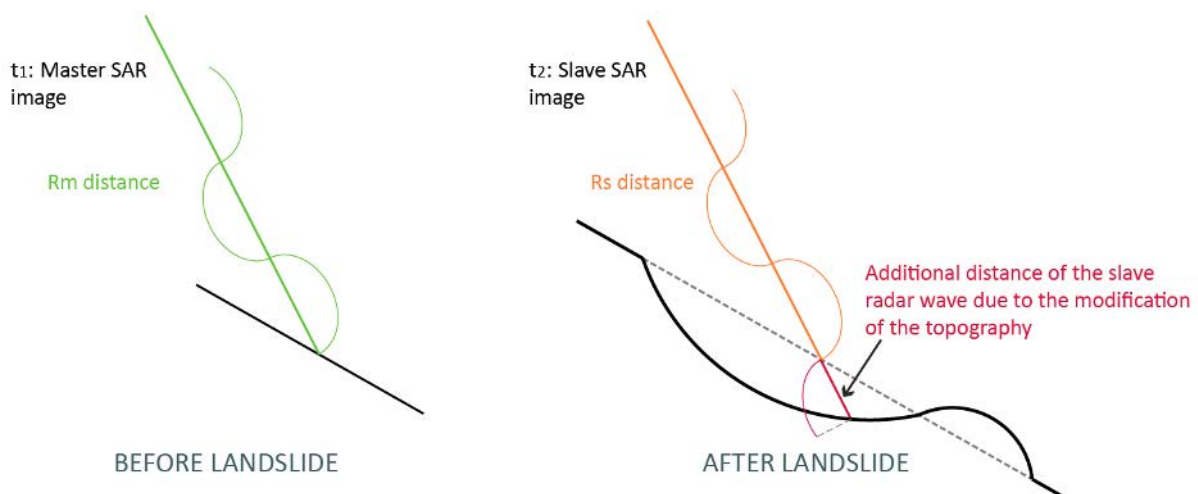


Figure 65 : Influences of a slope deformation on the phase decay. The way of the slave SAR image is longer than the way of the master SAR image, due to the rotational landslide (Michoud et al., 2009, modified).

### 3.3.1. Topographic phase

In DInSAR, the topographic phase is considered as an artifact. Indeed, the relief contribution scrambles the signal created by the ground deformations. The base of DInSAR techniques consists in using an ante-deformation DEM to perform a theoretical interferogram synthesizing the phase contribution of the topography. In this way, it is then possible to remove from the 2-way travel phase this topographical contribution to extract the deformation phase (Figure 66).

$$\Phi_{\text{deformation}} = \Phi_{\text{way}} - \Phi_{\text{topography}}$$

There are two methods to estimate the topographic contributions (Figure 66):

- Using an interferometric pair with the shortest temporal baseline as possible (e.g. from ERS Tandem). It is assumed that there is no ground deformation between the two acquisitions. Then the 2-way travel phase is equal to the topographic phase. But, this solution is not the best way to process due to recommendations made in the chapter 3.2.6 and for the unavoidable effects related to the propagation of the radiation through the atmosphere which typically varies between the two passes.
- Using an external DEM produced by another method (ALS, topographic maps, etc.). This way to process is the most powerful, because it uses one product independent of the SAR images. It allows to prevent errors due to bad SAR raw dataset.

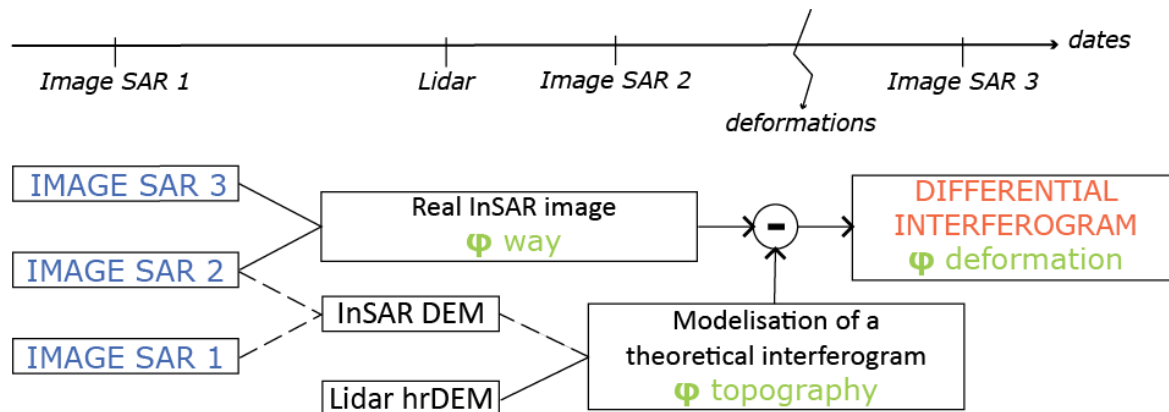


Figure 66: creation of a Differential SAR Interferogram. The DEM injected provides a theoretical interferogram only influenced by the relief. The topographical phase is removed of the 2-way travel phase to isolate the deformation phase. (ESA, 2008, modified)

### 3.3.2. Deformation phase

Let consider the processing to be perfect and that all the contributions, the deformation phase excepted, are removed. The movements detected (Figure 68) by the formula shown below is in reality a projection of the deformations along the LOS (Figure 67) and not the 3D vector of displacement. The first publications on landslide monitoring with DInSAR techniques were published by Fruneau et al. (1996) and Carnec et al. (1996).

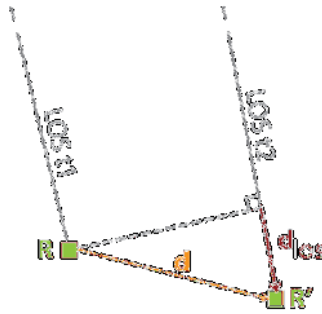


Figure 67 : projection of the displacements on the LOS. The red vector  $d_{los}$  is the projection of the real displacement (orange vector  $d$ ) on the LOS. (Prati, 2008, modified)

Therefore, displacements perpendicular to the LOS are not detectable. In the following development,  $d$  represents the deformation and  $d_{los}$  is the projection on the real displacement on the LOS.

$$R_s = R_m + d$$

$$\Leftrightarrow \varphi_{def} = \frac{4\pi}{\lambda} \times d_{los}$$

$$\Leftrightarrow d_{los} = \frac{\lambda}{4\pi} \times \varphi_{def}$$

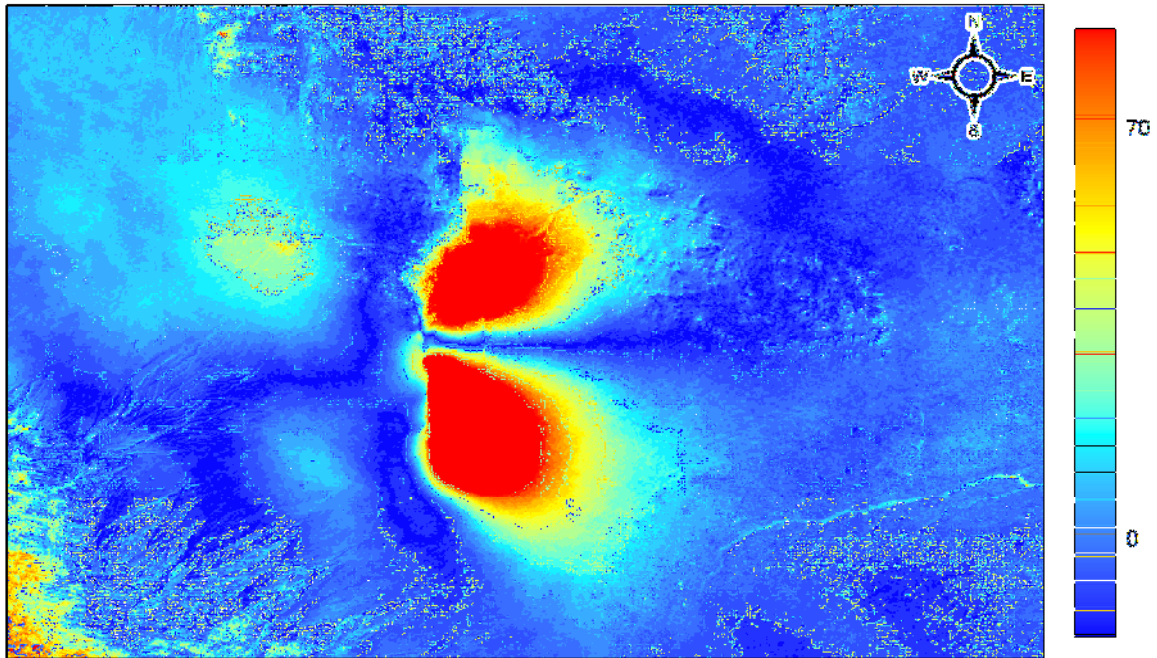


Figure 68 : unwrapped DInSAR [Sar2|Sar3] of Bam. (Michoud et al., 2009; processed with GSAR)

Finally, the accuracy of the detection depends on the Radar wavelength used and the threshold of detection of  $\pi/6$  (chapter 3.2.6).

$$\text{As } \Delta\varphi_d = \frac{\pi}{6}, \quad \Delta d_{\text{los}} = \frac{\lambda}{4\pi} \times \Delta\varphi_d = \frac{\lambda}{4\pi} \times \frac{\pi}{6} = \frac{\lambda}{24}$$

Admitting a perfect processing, the accuracy expected can be subcentimetric; ERS and Envisat, which use C-band (5.6 cm), can reach an accuracy of 2.33 mm.

Unfortunately, all expressions and formulas shown above are available only for ideal conditions, and it is never the case on the Earth. Indeed, the SAR signal can be noised by atmospheric disturbances, orbital inaccuracy, etc. So it is very important to know all the contributions which can influence the radar signal, to process the data and interpret properly the results.

### 3.3.3. Limitations of conventional DInSAR

Several noise sources can influence the phase of the SAR signal. It is important to know all of them to be able to isolate only the interesting phases (Massonnet and Feigl, 1998; Lauknes, 2004; Hanssen, 2005; Colesanti and Wasowski, 2006; Ferretti et al., 2007).

$$\varphi_{\text{total}} = \varphi_{\text{decorrelation}} + \varphi_{\text{atmospheric}} + \varphi_{\text{orbital}} + \varphi_{\text{way}}$$

This section aims to explain those contributions.

#### 3.3.3.1. Geometric and temporal decorrelation

Both temporal and spatial decorrelations contribute to a loss of coherence (2.3.4) between different SAR acquisitions.

The temporal decorrelation is due to changes of geometrical and electrical properties of the scatterer surface. Indeed, the evolutions of vegetation, morphology (erosion, rockfall, etc.), land use (farmed crops, fallow field, etc.) and soil moisture influence a lot the reflected signal. Now, those factors can change in time according to seasons and human activities. Therefore Massonnet and Feigl (1998) advise to use SAR images acquired always at the same period of the year to limit the temporal decorrelation. Usually, the best seasons are beginning of spring and end of fall, when trees have only few leaves and without snow covering the ground.

A too big difference of point of view (too long spatial baseline) between two SAR acquisitions creates the geometrical decorrelation. Bamler and Hartl (1998) indicate the existence of a critical baseline above which the interferometric signal is only composed by noise; this critical baseline is estimated at almost 1000 m for ERS dataset. It can be calculated thanks to the following formula (sarmap, 2008):

$$B_{n_{\text{critical}}} = \frac{\lambda \times R \times \tan\theta}{2 \times R_s}$$

where  $\lambda$  is the wavelength,  $R$  the range,  $\theta$  the look-angle and  $R_s$  the pixel spacing (respectively 5.6 cm, 870 km, 23° and ~12.5 m for ERS).

#### 3.3.3.2. Atmospheric artifacts

Even if the Radar wave amplitudes are not much attenuated by the atmosphere (Figure 1), the phase is sufficiently influenced by atmospheric conditions to perturb results. Atmospheric

conditions will change the velocity of propagation. Actually the variation in time and space of the partial water pressure in the troposphere is the main controlling factor (Zebker et al., 1997; Norland, 2006). Moreover, the variations of pressure and temperature can influence slightly the signal (Norland, 2006). Massonnet and Feigl (1998) advise to use SAR images acquired during night to limit the atmospheric artifact. As the atmosphere is colder and dryer than during the day, the Radar signal is less perturbed.

### 3.3.3.3. Orbital artifacts

It is very important to know the relative position of the platforms during the acquisitions. Indeed, as exposed in the formulas shown above, the values of the normal baselines are required by the interferometric equations. To limit the orbital artifacts due to bad positioning, precise orbits datafiles, called ephemerides (e.g. Delft or Doris precise orbits) are imported during the processing (Lauknes, 2004; Ferretti et al., 2007).

### 3.3.4. Coherence

To have an objective idea of the accuracy and the final reliability of an interferogram, the coherence index was created. Massonnet and Feigl (1998) define the coherence as “the degree of agreement between neighboring pixels in an interferogram”. The bigger the coherence is, the lower the artifacts are and the better the processing will be.

The coherence  $\gamma$  of an interferogram (Figure 69) processed with the complex SAR images  $S_1$  and  $S_2$  is calculated in this way:

$$\gamma = \frac{E[S_1 \cdot \overline{S_2}]}{\sqrt{E[|S_1|^2] \cdot E[|S_2|^2]}}$$

where  $E$  represents the statistical expectation and  $\overline{S_2}$  the conjugated complex of  $S_2$ . A coherence of 0 means that results are only composed by random phase noise and a coherence of 1 by very good signal with no noise (Prati, 2008). Colesanti and Wasowski (2006) explain that in practice, the coherence is computed “assuming ergodicity for the interferometric signal and, therefore, estimating  $E[\#]$  using all pixels within a (e.g. rectangular) window centred in the image element”.

Hanssen (2005) advises to consider a-priori coherence expected in an area before ordering dataset to assess the feasibility and reliability of processed interferograms. Indeed, according to practical observations (Massonnet and Feigl, 1998; Berardino et al., 2003; Colesanti et al., 2004; Lauknes, 2004; Michoud et al., 2009), the coherence is better in arid or urban areas than in wooded counties where temporal decorrelations are stronger.

The following figure aims to compile all notes written before to optimize the coherence and the reliability of differential interferometric results.



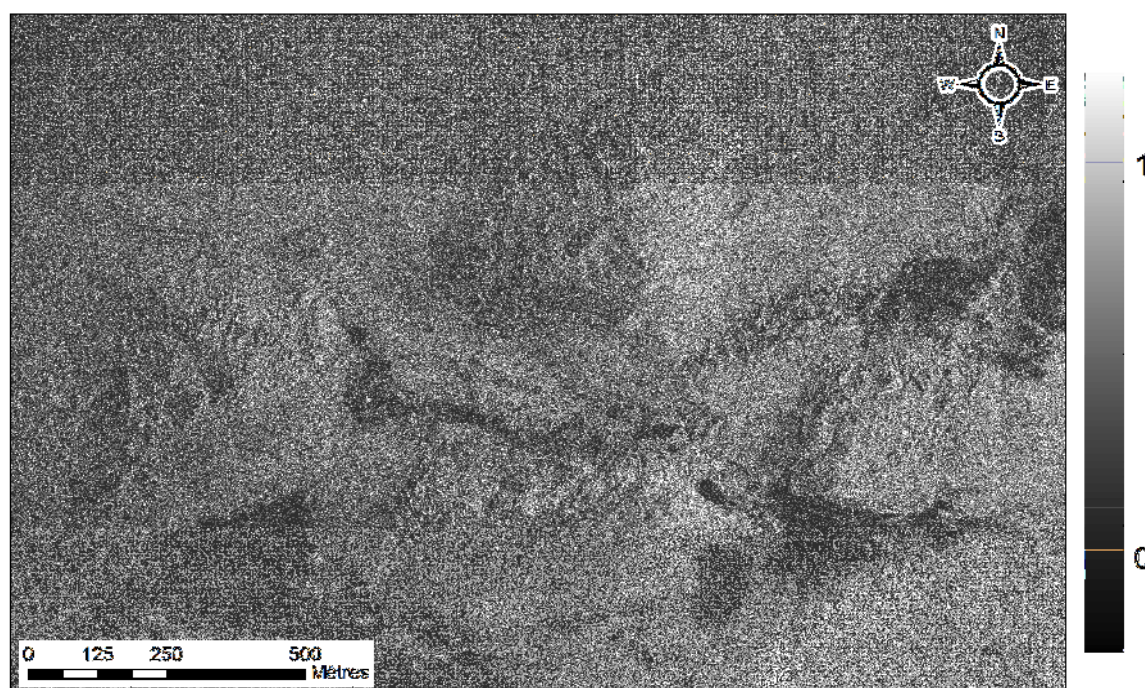


Figure 69 : coherences of the interferogram [Sar2|Sar3] of Bam. (Michoud et al., 2009; processed with Erdas Imagine 9.2™)

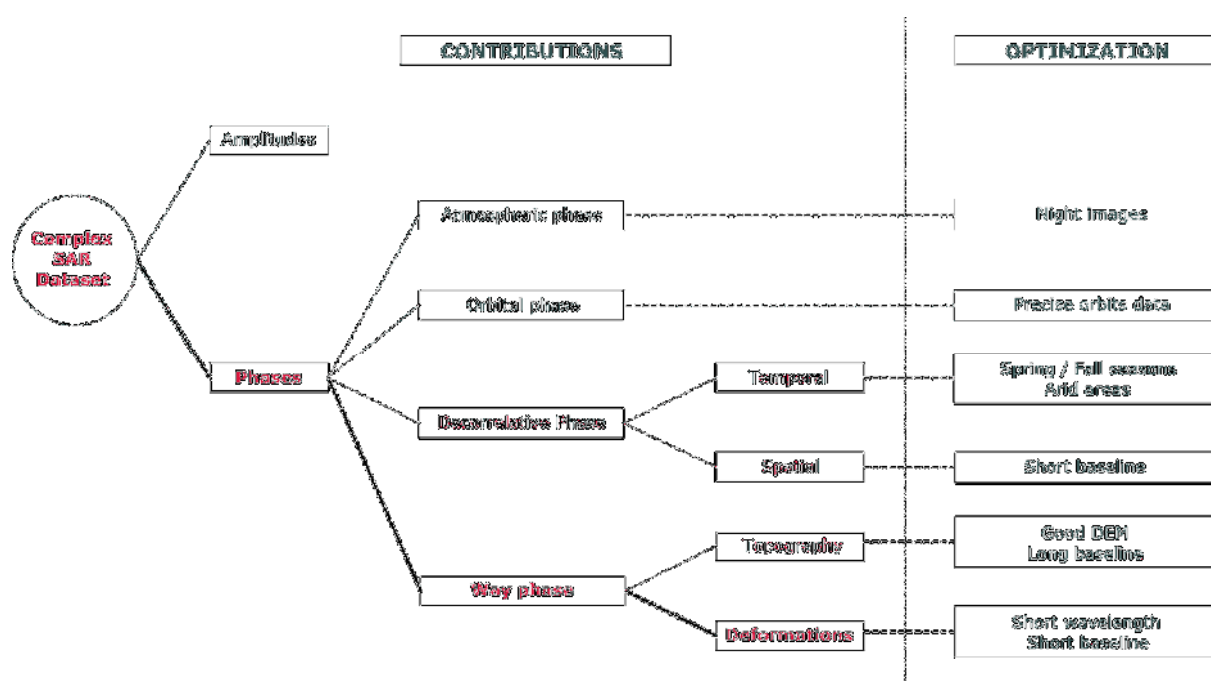


Figure 70 : optimization of the DInSAR processing. The best way to process dataset with good coherences and reliability is to choose night scenes from the beginning of spring or end of fall (snow and leaves free) with the shortest baselines as possible. (Michoud et al., 2009, modified)

## 4. MULTI-TEMPORAL REPEAT-PASS INSAR (ADVANCED DINSAR)

### 4.1. INTRODUCTION

A remarkable improvement in the quality of DInSAR results for ground deformation mapping and monitoring is given by the Advanced DInSAR techniques (A-DInSAR). These techniques make use of large multi-temporal stacks of space-borne SAR images acquired over the same area, in order to identify radar targets on which is possible to detect and measure displacements along the LOS (Line Of Sight) direction, over time.

The basis of the A-DInSAR techniques, as well as the standard DInSAR, is the separation of different components from the interferometric phase,  $\varphi_{\text{INTERF}}$ : the topographic component,  $\varphi_{\text{TOPO}}$ , the movement component,  $\varphi_{\text{MOV}}$ , the atmospheric contribution,  $\varphi_{\text{APS}}$  and the noise component,  $\varphi_{\text{NOISE}}$ :

$$\varphi_{\text{INTERF}} = \varphi_{\text{TOPO}} + \varphi_{\text{MOV}} + \varphi_{\text{APS}} + \varphi_{\text{NOISE}}$$

A-DInSAR techniques overcome most of the limitations of the standard single-interferogram approach (DInSAR), such as temporal and geometric decorrelation and the atmospheric phase delay and, unlike conventional Interferometry, they allow increasing the measurement accuracy from centimetre up to millimetre. These techniques also overcome the standard approach both in terms of deformation modeling capabilities and quality of measures (Crosetto et al., 2005b) :

- **Temporal deformation modelling:** A-DInSAR are able to provide a whole description of the temporal behaviour of a deformation field, whereas standard DInSAR techniques temporally sample a given deformation phenomenon with only two acquisitions (Figure 71).
- **Quality of measures:** A-DInSAR techniques allow the estimation of different error sources that may affect the interferometric observations and the separation of movement signals from the other phase components (e.g. topographic errors, atmospheric component), achieving a good precision and reliability of deformation measures. This component analysis can't be performed using the standard DInSAR approach.

The output of an A-DInSAR analysis consists in a set of radar targets, for which the following information can generally be extracted (Figure 72):

- geographic coordinates (E, N) and heights
- mean deformation rates (precision can be up to 0.1 mm/year; it depends mainly on the distance from the reference point)
- time series of displacements (precision can be up to 1 mm on a single measurement)
- quality index (e.g. coherence)



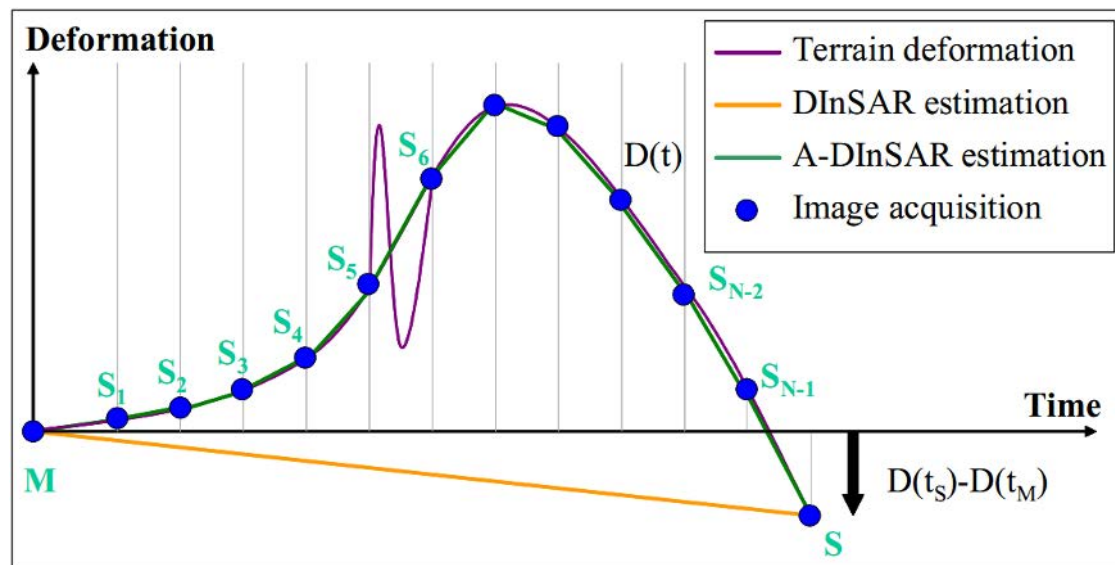


Figure 71 : Temporal sampling of a deformation phenomenon performed with the DInSAR and A-DInSAR techniques (Crosetto et al., 2005b).

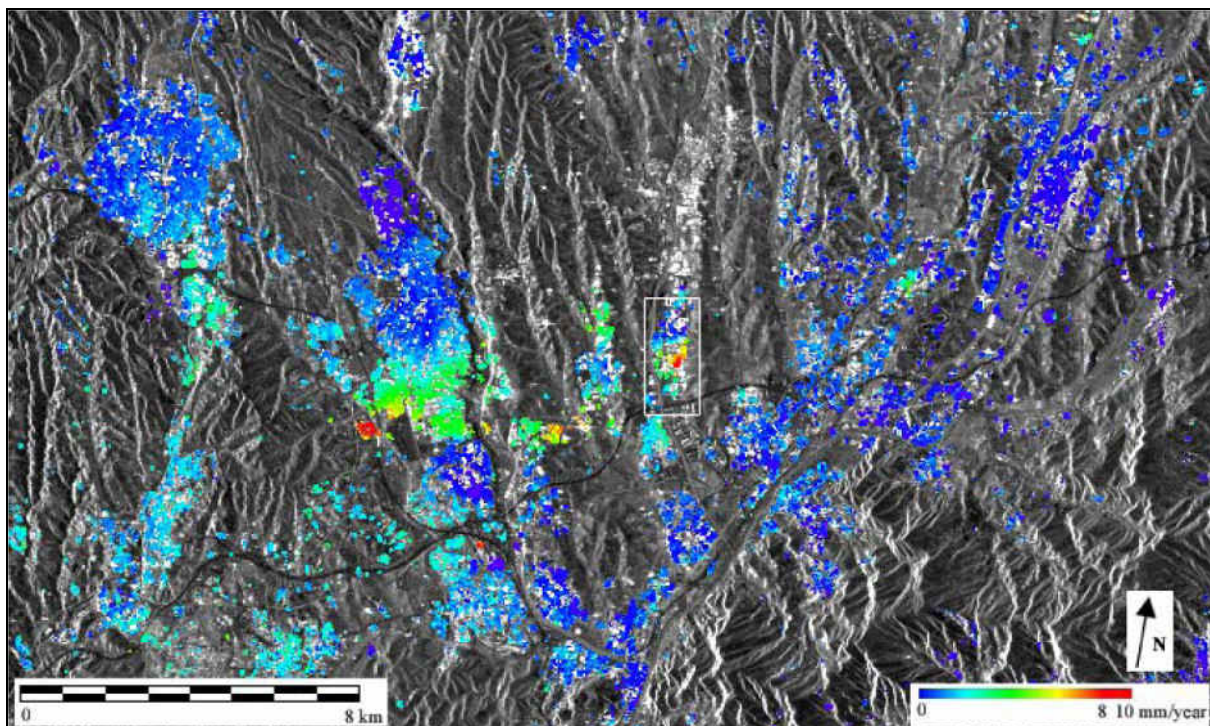


Figure 72 : Example of results from an Advanced DInSAR analysis: mean deformation rates measured by means of multi-interferometric analysis of ERS 1995-2000 data (Crosetto et al., 2005b).

In general, at least 15-20 radar images acquired along the same nominal orbit (i.e. same acquisition geometry), are necessary to perform a multi-interferometric analysis. Nevertheless, the actual number depends on the characteristic of the area of interest and the type of SAR sensor to be used.



As mentioned above, only the pixels characterized by a low level of phase noise, are exploited to derive the deformation estimations, even if SAR sensors perform a regular 2D sampling of the terrain. Consequently, the ability of A-DInSAR to fully describe a deformation phenomenon depends temporally on number of available images, and spatially on the availability of “good pixels”, i.e. pixels which are characterized by a low level of phase noise. According to the type of analysis and the number of radar data available, A-DInSAR allows getting a radar target density even exceeding 1,000 points/km<sup>2</sup>.

In order to guarantee the measurement of ground deformations in areas with low coherence, it is also possible to install artificial corner reflectors or active transponders (Allievi et al., 2004) and monitor building, infrastructures and non coherent areas affected by different types of deformation phenomena (e.g. landslides, building collapse) (Crosetto et al., 2005b).

In the last years, several A-DInSAR techniques have been developed and experimented on multi-temporal interferometric data, such as the Permanent Scatterers (PS-InSAR) technique, the Interferometric Point Target Analysis (IPTA), the Persistent Scatterers Pairs - Differential SAR Interferometry (PSP-DIFSAR), the Stable Point Network (SPN), the Small BASeline Subset (SBAS), the Coherent Pixel Technique (CPT) and the Stanford Method for Persistent Scatterers (StaMPS). These techniques are different from each other in the interferometric processing chain, the pixel selection criterion (amplitude- or coherence-based), the processing approaches used to separate the different phase components (e.g. atmospheric phase) and the deformational model of the targets (linear, non-linear). Their modelling and processing strategies are strictly dependent on the type of application at hand (Berardino et al., 2002; Costantini et al., 2000; Duro et al., 2003; Ferretti et al., 2000; Hooper et al., 2004; Mora et al., 2003; Werner et al., 2003).

The temporal evolution of the deformation is generally modelled with linear functions in most of the A-DInSAR approaches (Ferretti et al., 2000; Ferretti et al., 2001) and, in few other cases, a more complex description of the temporal behaviour of the deformation can be used (Berardino et al., 2002; Mora et al., 2003; Colesanti et al., 2003; Lanari et al. 2004; Hooper et al., 2004).

Thanks to the availability of historical SAR data, it is possible to reconstruct more than 17 years of temporal evolution of past and current ground deformation, starting from 1992 (thanks to ERS1/2 archives) and up to present days (ENVISAT, RADARSAT-1/2, ALOS, COSMO-SkyMed, TerraSAR-X).

Many applications have demonstrated the capabilities of these techniques for the detection of slow land surface deformations (up to a few cm/year) and for the understanding of the spatial distribution and temporal evolution of displacements, in built-up areas affected by slow or very slow landslides (Berardino et al., 2003; Bovenga et al., 2006; Catani et al., 2005b; Colesanti and Wasowski, 2004, 2006; Colesanti et al., 2003; Farina et al., 2003, 2006, 2008; Hilley et al., 2004; Metternicht et al., 2005; Righini et al., 2008), tectonic motions (Bürgmann et al., 2006; Colesanti et al., 2003; Musson et al., 2004; Vilardo et al., 2009), subsidence (Canuti et al., 2005; Colesanti et al., 2005; Colombo et al., 2003; Dixon et al., 2006; Ferretti et al., 2000; Herrera et al. 2009; Stramondo et al., 2008), volcanic activity (Lanari et al., 2004; Salvi et al., 2004; Tizzani et al., 2007).

On the basis of InSAR processing approach, two different groups of A-DInSAR techniques can be distinguished (Wasowski et al. 2007) (Table 12) :

- **PS-based A-DInSAR techniques or PSI (Persistent Scatterers Interferometry):** these A-DInSAR techniques study the amplitude and phase information over single isolated objects characterized by high temporal signal stability. This approach is usually implemented by computing differential interferograms of all the acquisitions with respect to the same reference master image, then performing advanced phase analyses on the pixels exhibiting stable SAR response throughout the stack. The points selected with such a criterion are usually called Persistent Scatterers (PS) and the technique itself is called PSI (Persistent Scatterers Interferometry).
- **Interferogram stacking techniques:** these A-DInSAR approaches exploit more spatially distributed information in differential interferograms obtained from interferometric pairs with small perpendicular baseline and then infer, with a complex averaging operation (complex multi-looking), the connected time series of phase values due to ground deformation. These techniques mitigate the decorrelation phenomena, maximizing the number of pixels exploited and improving the SNR (Signal-to-Noise Ratio).

*Table 12 : List of ADInSAR techniques*

<b>Persistent Scatterers Interferometry</b>	<b>Interferogram Stacking Techniques</b>
PS-InSAR (Permanent Scatterers InSAR) IPTA (Interferometric Point Target Analysis) PSP (Persistent Scatterers Pair) SPN (Stable Point Network) StaMPS (Stanford Method for Persistent Scatterers)	SBAS (Small Baseline Subset) CPT (Coherent Pixel Techniques)

Most of the A-DInSAR techniques belonging to these two different classes are separately described in the following sections.

#### **4.2. PS-BASED A-DINSAR TECHNIQUES OR PSI (FULL RESOLUTION / DOMINANT SCATTERERING)**

As discussed in the previous section, PS-based A-DInSAR techniques are based on the analysis of amplitude and phase information over single isolated objects (called Persistent Scatterers, PS) characterized by a high temporal signal stability and dominating a resolution cell on the ground.

In the PSI processing, interferograms formed with a single master scene are analyzed at single look resolution (analyses are carried out on a pixel-by-pixel basis, with no filtering of the interferograms) in order to maximize the Signal-to-Noise Ratio (SNR) of the resolution elements containing a single dominant scatterer.

The first PS-based approach was developed for InSAR applications by Ferretti et al. (2000, 2001), with further enhancements by Colesanti et al. (2003), and it was called and patented by Politecnico di Milano (POLIMI, Italy) as the Permanent Scatterers Technique (PS-InSAR).

Several A-DInSAR techniques have then been developed in the last ten years after PS-InSAR (e.g., Adam et al., 2003; Crosetto et al., 2003; Lyons and Sandwell, 2003; Werner et al., 2003) and they are usually referred to the term Persistent Scatterers Interferometry (PSI). It is noting that the term “Permanent Scatterers” is instead directly associated to the patented PS-InSAR technique whereas, “Persistent Scatterers Interferometry” is usually employed to indicate all the PS-based techniques (Crosetto and Pasquali, 2008).

#### 4.2.1. PS-InSAR (Permanent Scatterers InSAR)

The Permanent Scatterers InSAR (PS-InSAR) is a PSI technique, developed and patented in the late '90 by Politecnico di Milano (Italy), and now exclusively licensed to its spin-off company TeleRilevamento Europa - TRE (Ferretti et al., 2000, 2001).

PS-InSAR allows the identification of Permanent Scatterers (PS) through the analysis of pixel amplitude dispersion with time, over data-stack of at least 20-30 SAR acquisition.

PS are objects on the ground that return stable signals to the satellite sensor (remain coherent over long time intervals) and are smaller than the resolution pixel cell (point-like scattering mechanism). They typically correspond to objects on man-made structures, such as buildings, bridges, dams, water-pipelines, antennas, as well as to stable natural reflectors (e.g. exposed rocks) (Figure 73) (Colesanti et al., 2003; Ferretti et al., 2000, 2001).



Figure 73 : Examples of man-made structures and stable natural scatterers that return stable signals back to the satellite (<http://www.treuropa.com>).

PS-InSAR allows detecting and estimating, for each PS, mean annual deformation rate (accuracy between 0.1 and 1 mm/year) along the sensor-target direction and historical deformation series (precision up to 1-2 mm for each single measure).

The methodology allows obtaining good phase coherence from nearly all radar scenes regardless of geometrical baseline (perpendicular baseline for ERS up to 1.6 km), exploiting all available radar scenes in the historical archive, estimating and removing atmospheric phase contributions from the deformation phase signal.

The technique can be used with different approaches, for both large scale studies (e.g. landslide inventory mapping) and high-resolution applications on limited areas (e.g. landslide rapid mapping and monitoring, stability assessment of individual buildings or structures) (Figure 74 and Figure 75).

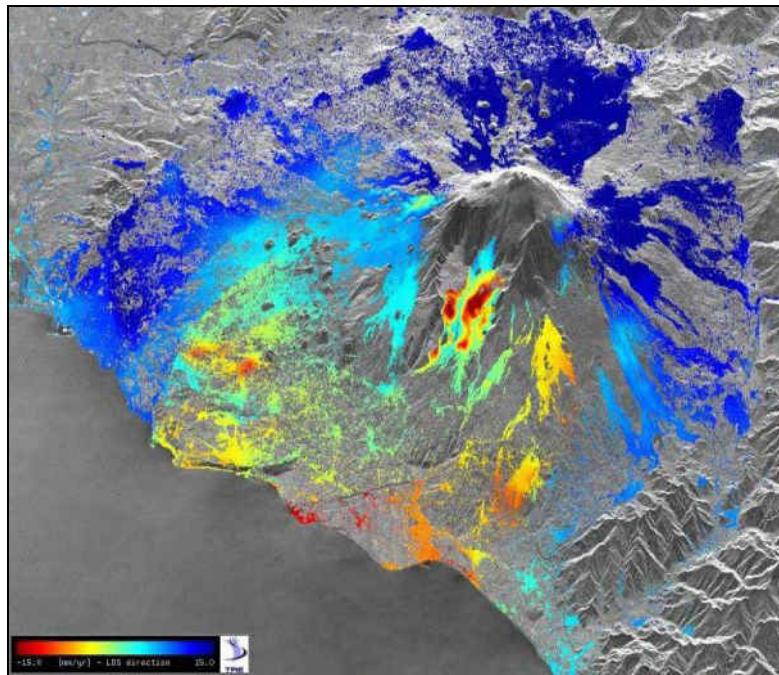


Figure 74 : Example of PS-InSAR analysis at large scale: ground deformation due to active faults in the S flank of Mount Etna (Italy) (<http://www.treuropa.com>).

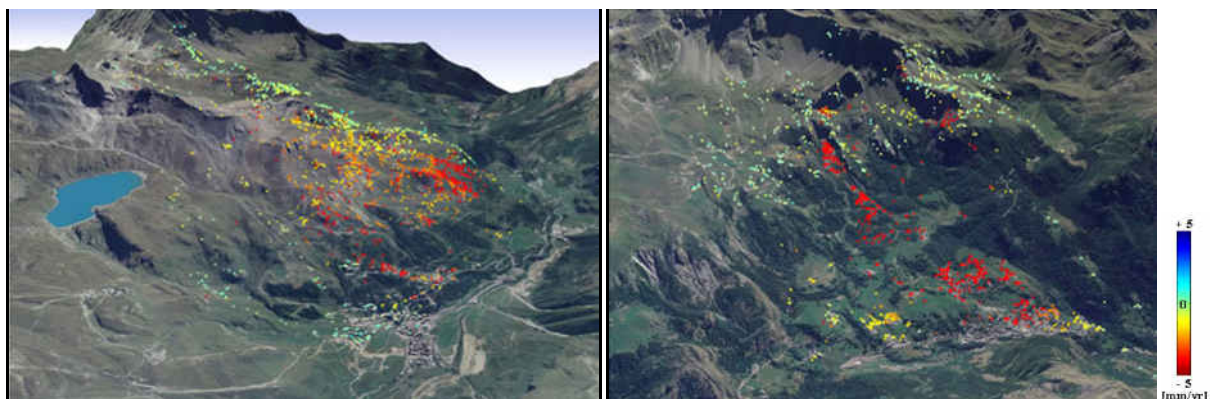


Figure 75 : Example of PS-InSAR analysis at local scale. Left: deep-seated gravitational slope deformation on Motta Pleté, Alpine region (Italy). Right: gravitational slope deformation threatening the village of Valtournanche, Alpine region (Italy). The local analysis allowed the definition of the landslide boundaries and state of activity, integrating information by geo-morphological studies on both the areas (<http://www.treuropa.com>).

TRE has recently developed a new algorithm, SqueeSAR, which exploits phase signals also for Distributed Scatterers (DS) and uses them, together with Permanent Scatterers, for monitoring ground displacements with the same accuracy as a conventional PS-InSAR analysis. These targets, the DS, consist of an extensive area where the back-scattered energy is less strong than PS, but statistically homogeneous within the area (e.g. non-cultivated lands, desert areas) (<http://www.treuropa.com>).

#### 4.2.2. IPTA (Interferometric Point Target Analysis)

The Interferometric Point Target Analysis (IPTA) is a PSI technique, developed by Gamma Remote Sensing and Consulting AG (Switzerland). As well as the other PSI approaches,

IPTA exploits the temporal and spatial characteristics of interferometric signatures collected from point targets to accurately map surface deformation histories, terrain heights and relative atmospheric path delays. It allows using both the coherence-based and the amplitude-based pixel selection criterion (Werner et al., 2003a; 2003b; Wegmuller et al., 2004; Strozzi et al., 2006). Figure 76 gives an overview of its processing chain.

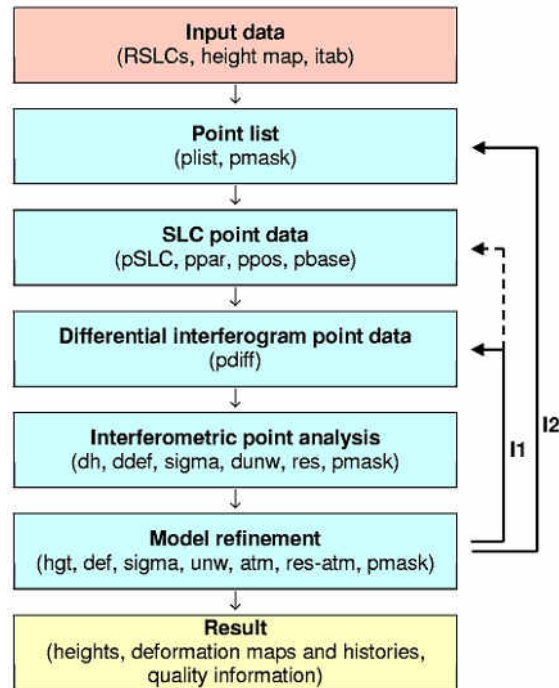


Figure 76 : Interferometric Point Target Analysis (IPTA) processing approach (Werner et al., 2003a; 2003b)

The phase model implemented in IPTA is the same as used in conventional Interferometry (Figure 77): the unwrapped interferometric phase is expressed as the sum of a topographic phase, a deformational phase, a differential path delay phase (also called atmospheric phase), and phase noise (or decorrelation) terms.

An important aspect of IPTA is that for point targets no spatial decorrelation occurs, permitting interpretation of the interferometric phase of pairs with long baselines, even above the critical baseline (Werner et al., 2003a). Obviously, a reflector must also remain stable over the time period of interest to permit analysis of the phase history. Based on these ideas one important objective of IPTA is to achieve a more complete use of the available data. Through the use of point targets, interferometric pairs with long baselines can be used. Consequently, more observations are available with respect to conventional SAR Interferometry, permitting reduction of errors resulting from the atmospheric path delay and leading to better temporal coverage (Figure 78).



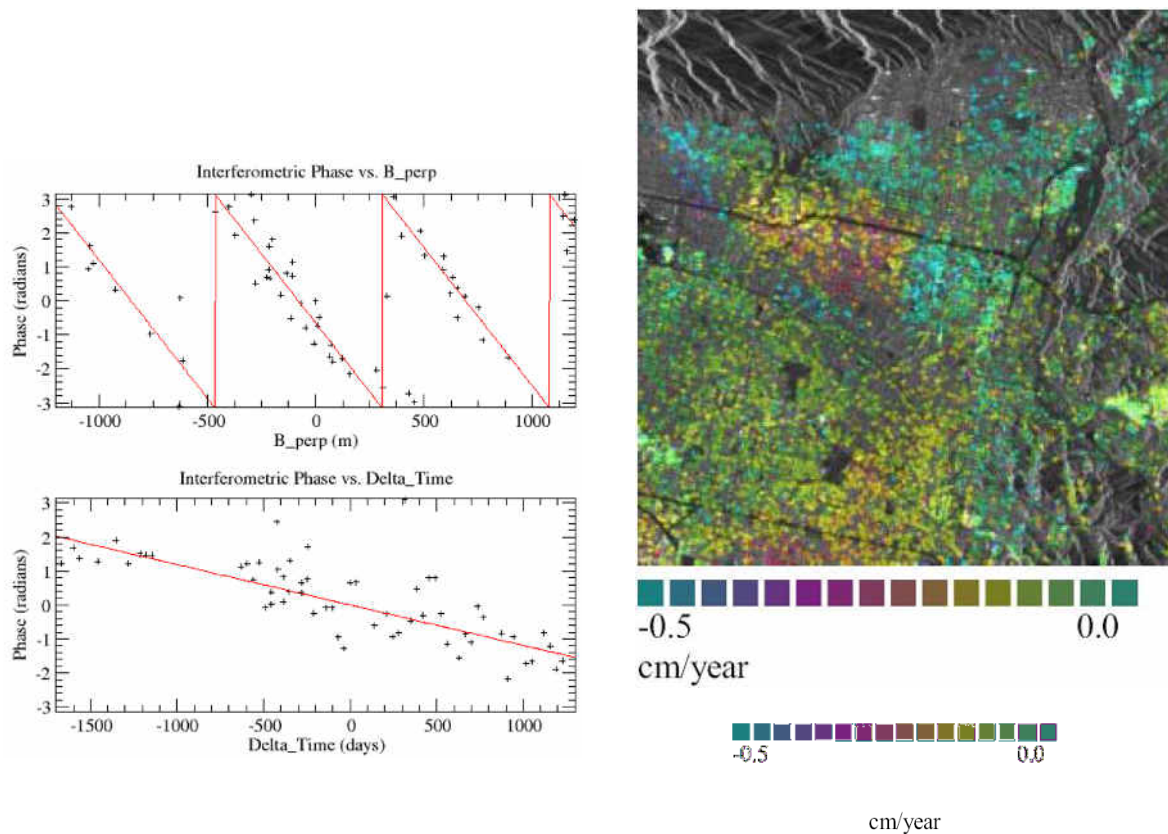


Figure 77 : Two-dimensional regression analysis of differential interferometric phase difference of two close points in a stack of 59 ERS interferograms (left). Linear deformation rate due to subsidence associated with the Raymond Fault zone in south Pasadena – USA (right) (Werner et al., 2003a).

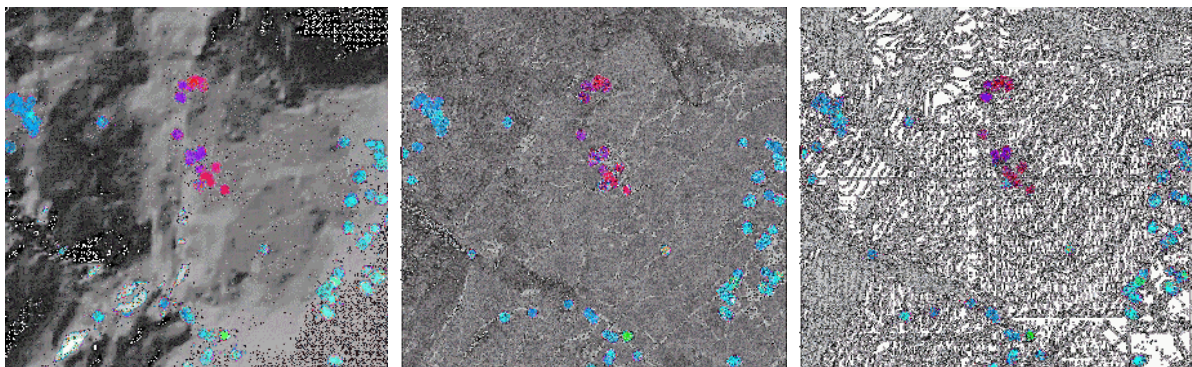


Figure 78 : IPTA analysis of the Montagnon (Switzerland) landslide: PT over shaded relief, ortho-photo and topographic map (www.gamma-rs.ch).

Most of IPTA analyses have been performed to monitor slow and temporally uniform deformation, for which temporal and spatial sampling of the signal is very good. In the case of high deformation rates the capability of IPTA to use pairs with large baselines have the advantages that high phase gradients can be reduced if shorter observation intervals become available (Figure 79). In addition, large scale corrections such as baseline errors and the large scale component of the atmospheric distortions can be estimated independently of the areas with high deformation gradients and interpolated or extrapolated to get relatively accurate corrections for the entire area.

Gamma Remote Sensing has recently developed an approach for the integration of ERS and ENVISAT ASAR data into the Interferometric Point Target Analysis (IPTA). This integration is very relevant for current time monitoring. Furthermore, the accuracy of current time monitoring based on a smaller number of ASAR acquisitions can be improved through the integration of additional ERS acquisitions, e.g. through a better identification of adequate points and through a more accurate estimation of the related point heights (Wegmuller et al., 2006).

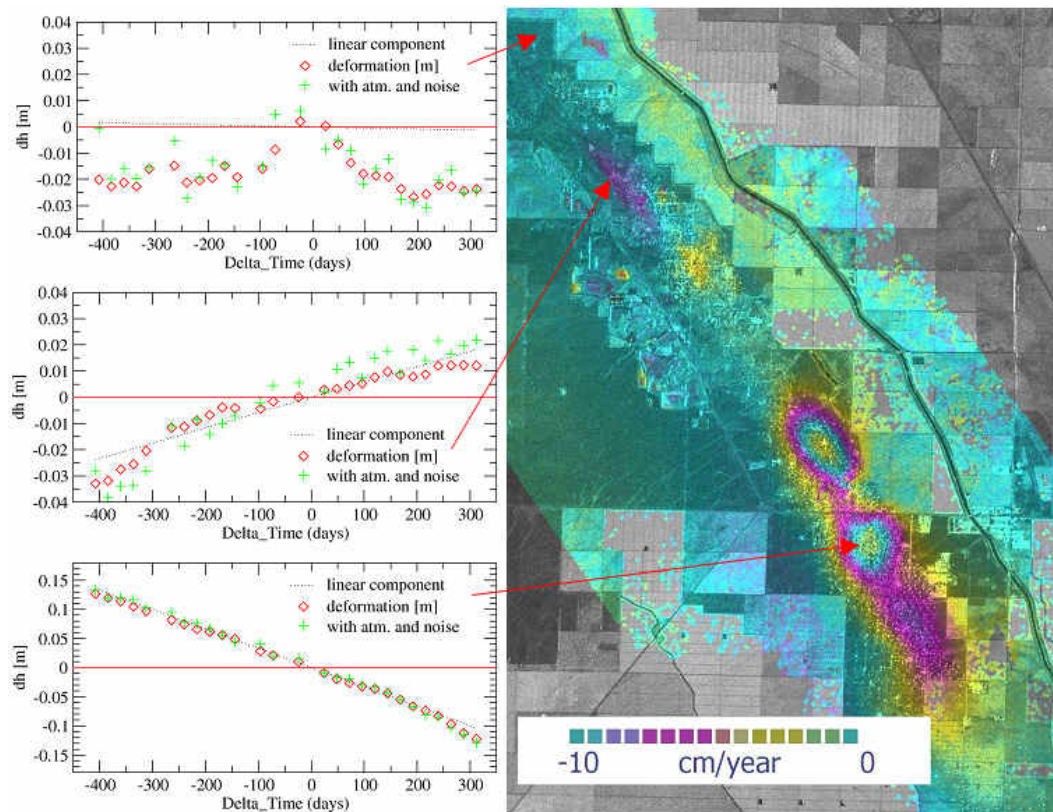


Figure 79 : Map of linear deformation rate and selected deformation histories of rapid subsidence at the Lost Hills oil field, California, monitored between February 2002 and February 2004, by means of IPTA technique on RADARSAT data (Wegmuller et al., 2006).

#### 4.2.3. PSP (Persistent Scatterer Pairs)

Persistent Scatterers Pairs - Differential SAR Interferometry (PSP-DIFSAR) is a PSI technique, developed recently by Telespazio/e-GEOS (a Finmeccanica/Thales company) (<http://www.telespazio.it>, <http://www.e-geos.it>).

PSP technique efficiently allows identifying Persistent Scatterers in series of full resolution SAR images and retrieving the corresponding terrain height, displacement velocity and time series. This approach differs from standard PSI methods because during the processing it detects and removes atmosphere phase artefacts by exploiting their spatial correlation, without using model-based interpolations starting from a preliminary set of measurements obtained by radiometric or low resolution analyses. PSP does not require data calibration or pre-selection of radiometrically stable points, thus is not affected by errors in the pre-selection or by the density of pre-selected points. Moreover, the method is characterized by the exploitation of



redundant information, which makes for a very good robustness to noise (Costantini et al., 2009).

PSP-DIFSAR technique jointly exploits spatial and temporal properties of SAR data, in order to improve the density and the accuracy of the measurements. Its results with large stacks of SAR data have successfully shown its capabilities both for the density and the accuracy of deformation measurements.

The PSP approach can also provide valid tools for the identification and analysis of distributed scatterers, i.e. scatterers that do not behave as point-like objects, but nevertheless keep a good degree of coherence over time. In fact, the distributed scatterers can be recognized by analyzing, together with the temporal properties, the spatial correlation properties of the images acquired at different times (Costantini et al., 2009).

First applications of PSP technique have been carried out to monitor subsidence in Bologna and Napoli (Italy) (Costantini et al., 2000a e 2000b), ground instability in Maratea (Italy) (Berardino et al., 2003) (Figure 80), rock-slides and deep-seated gravitational slope deformations in Valfurva and Valdisotto areas (Italy) (Figure 81) and, most recently, the approach has been tested with X-band COSMO-SkyMed data (Costantini et al., 2009).

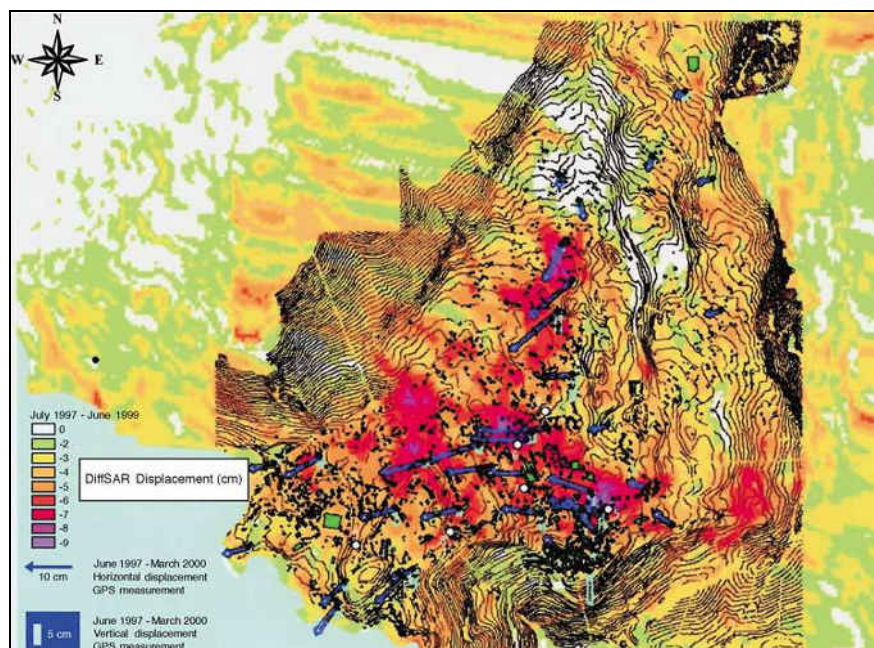


Figure 80 : Ground displacement map of Maratea landslide (Italy), monitored between August 1997 and January 2000 by means of PSP technique on ERS data and results from the GPS survey (June 1997–March 2000) (Berardino et al., 2003).



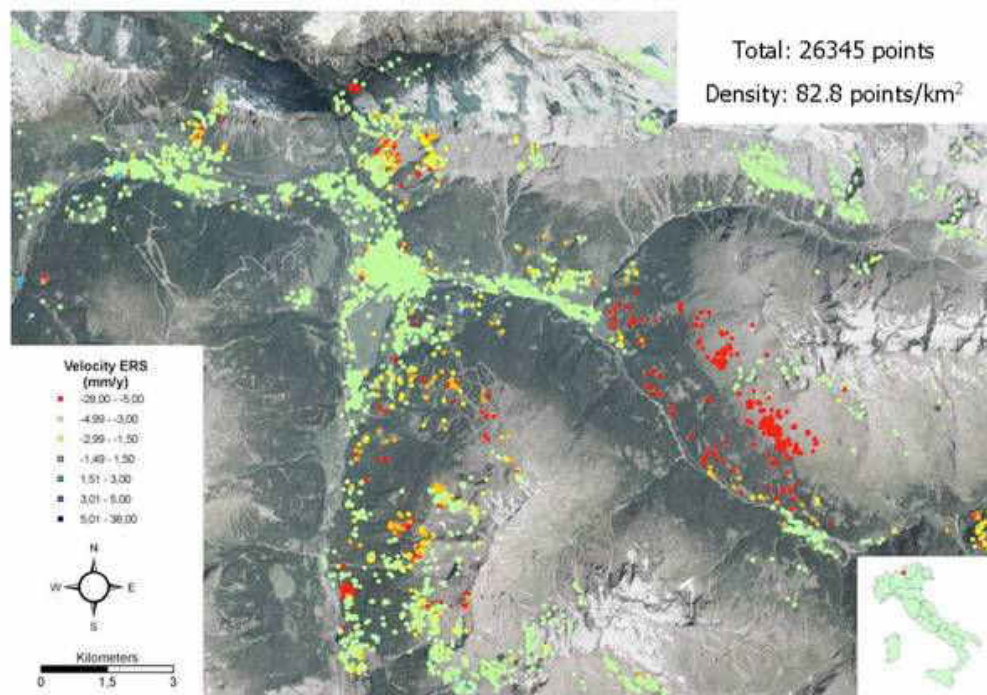


Figure 81 : Deformation map in the area of Valfurva and Valdisotto (Italy), monitored by means of PSP-DIFSAR technique on ERS1/2 data in the framework of PREVIEW project (Righini et al., 2008).

#### 4.2.4. SPN (Stable Point Network)

The Stable Point Network (SPN) is a PSI technique, developed by Altamira Information SL as the result of research collaborations with CNES (Centre National d'Etudes Spatiales, French Space Agency), ESA (European Space Agency). Its processing chain was the first advanced interferometric approach capable of merging the new ASAR data with the historical ERS-1/2 data (Arnaud et al., 2003; Duro et al., 2005).

SPN software uses the DIAPASON (Differential Interferometric Automated process Applied to Survey Of Nature) interferometric chain for all SAR data handling, e.g. co-registration work and interferogram generation.

Figure 82 gives an overview of the SPN processing steps: starting from a set of multi-temporal SAR images, the mean displacement rates, height errors and time series can be extracted. The quality of the results is related with the number of acquisitions (an increase of SAR images improves the quality of measurements) and an error of 1 mm/year for deformation rates and 2 m for height errors can be achieved (Herrera et al., 2009b).

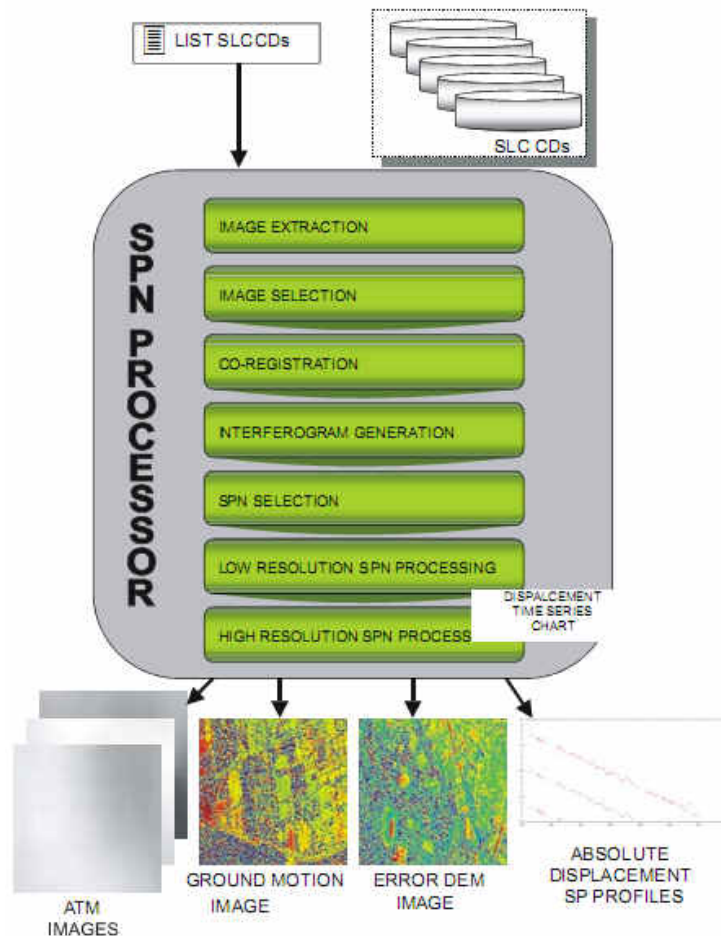


Figure 82 : Stable Point Network processing chain flow chart (Herrera et al., 2009b).

SPN is very flexible and the software can work at any resolution, any frequency and with cropped images. In particular, the algorithm can either work at full resolution (for ERS and ENVISAT is 4 m by 20 m) selecting the measurement points by analyzing the amplitude of the set of SLC SAR images, or at reduced resolution (e.g. 40 by 40 m) selecting ground surface natural reflectors or Stable Point (SP) by interferometric multi-look coherence (Herrera et al. 2009a).

The amplitude selection mode is based on analyzing the temporal stability of the electromagnetic response to the radar signal (backscattering) for each pixel of the study area. If the geometry of the ground surface that corresponds to a certain pixel does not vary significantly along time, the backscatter is similar for every acquired SAR image, and the pixel is selected as a SP. The coherence based approach, rather performs an average of the backscattering of neighbour pixels, increasing the measurement point density, and it is particularly useful for non-urban and vegetated areas where ground surface scatterers (buildings, structures, metallic objects) are scarce (Herrera et al., 2009b).

In Figure 83 is reported an example of subsidence mapping using PSI data elaborated with the SPN amplitude-based approach, whereas in Figure 84 is reported an example of mapping and monitoring of geomorphologic processes in mountainous area by means of the SPN coherence-based approach.

A detailed description of the SPN algorithm can be found in Crosetto et al. (2008) where some examples of urban subsidence monitoring are shown. To date the performance of the SPN method has been mainly validated in subsidence analysis (Herrera et al., 2009a, 2009b).

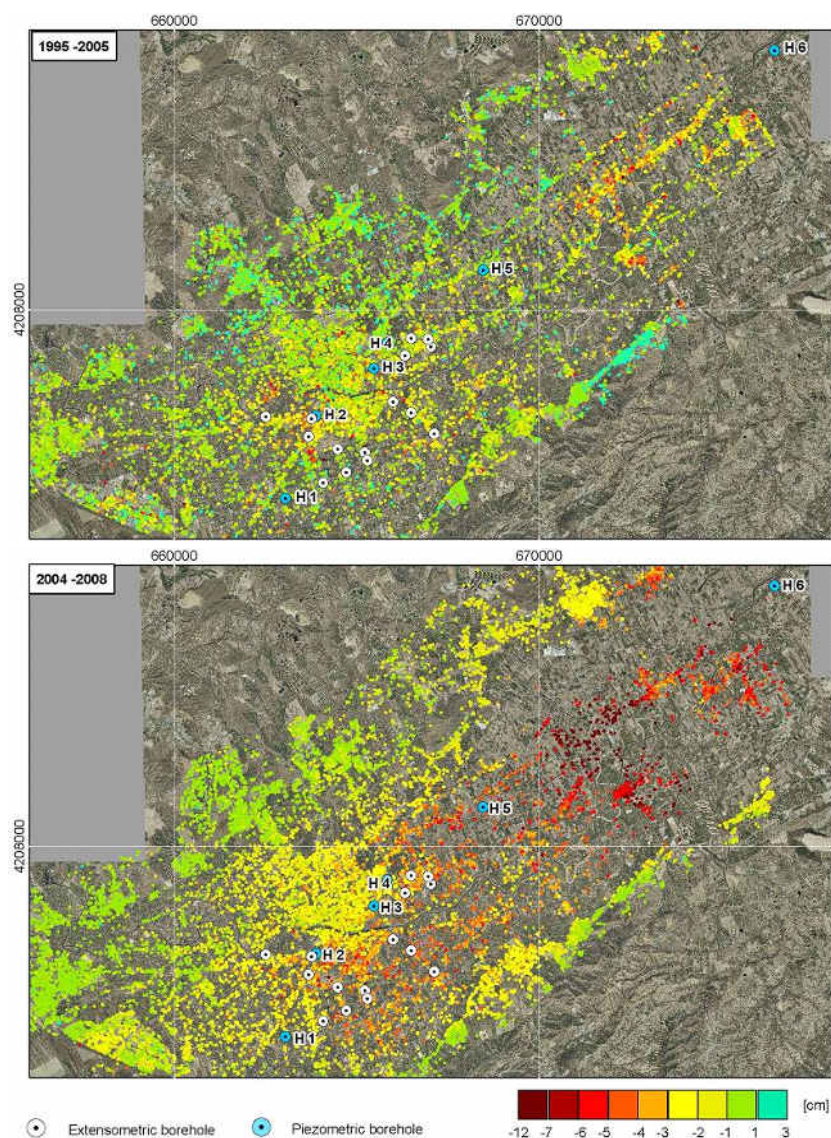


Figure 83 : Total deformation estimated with amplitude-based SPN technique (full resolution) between July 1995 and December 2005 (top) and between January 2004 and December 2008 (bottom) in the area of Murcia (SE Spain) (Herrera et al., 2009a).



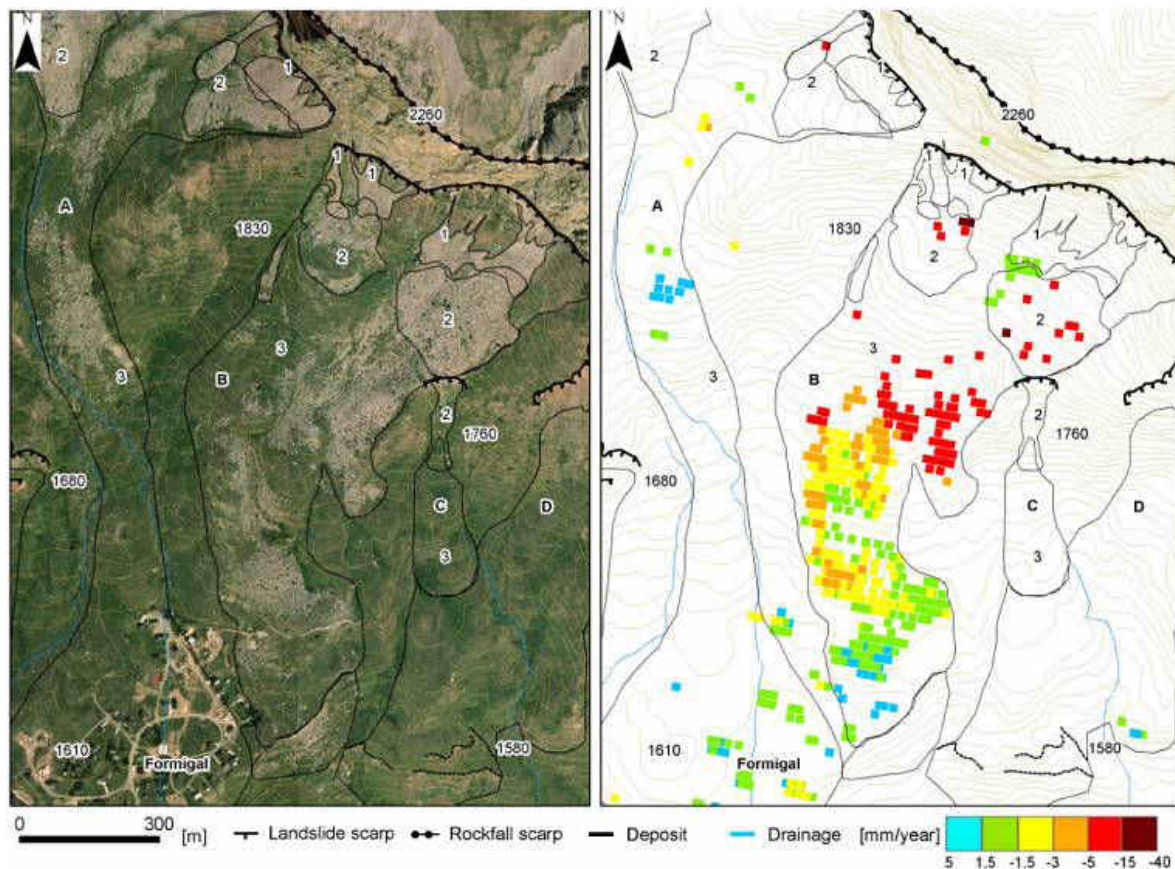


Figure 84 : Map of Formigal landslide (Central Pyrenees, Spain) showing the displacement velocity estimated with the coherence-based SPN techniques (low resolution) in the analyzed ERS1/2 and ENVISAT descending orbits between 1995 and 2007 (Herrera et al., 2009b).

#### 4.2.5. StaMPS (Stanford Method for Persistent Scatterers)

The Stanford Method for Persistent Scatterers (StaMPS) is a PSI technique developed by the Stanford University, for analyzing episodic crustal deformation in non-urban environments, with application to volcanic settings (Hooper et al., 2004 and 2007).

Most of PSI algorithms identify an initial set of PS pixels by the analysis of their amplitude distribution over time in a series of interferograms. These methods work best in urban areas where man-made structures increase the likelihood of finding a non-fluctuating scatterer in any given pixel but, the density of PS pixels in natural terrains, however, is generally too low to obtain any reliable results (Hooper et al., 2004).

StaMPS is based primarily on interferometric phase characteristics and finds low-amplitude pixels (Persistent Scatterers, PS) with phase stability that are not identified by the other amplitude-based algorithms. Scatterers with stable phase characteristics independent of amplitudes associated with man-made objects can be found, and thus the technique is also applicable to areas where conventional InSAR fails due to complete decorrelation of the majority of scatterers, yet a few stable scatterers are present (Hooper et al., 2004).

StaMPS algorithm involves removing the residual topographic component of flattened interferogram phase for each PS, then unwrapping the PS phases both spatially and temporally. The approach also uses the spatial correlation of the phases rather than a well-

defined (e.g. linear) phase history and a prior assumptions about temporal nature of deformations, so that temporally-variable processes (e.g. volcanic deformation) can be observed (Figure 85 and Figure 86).

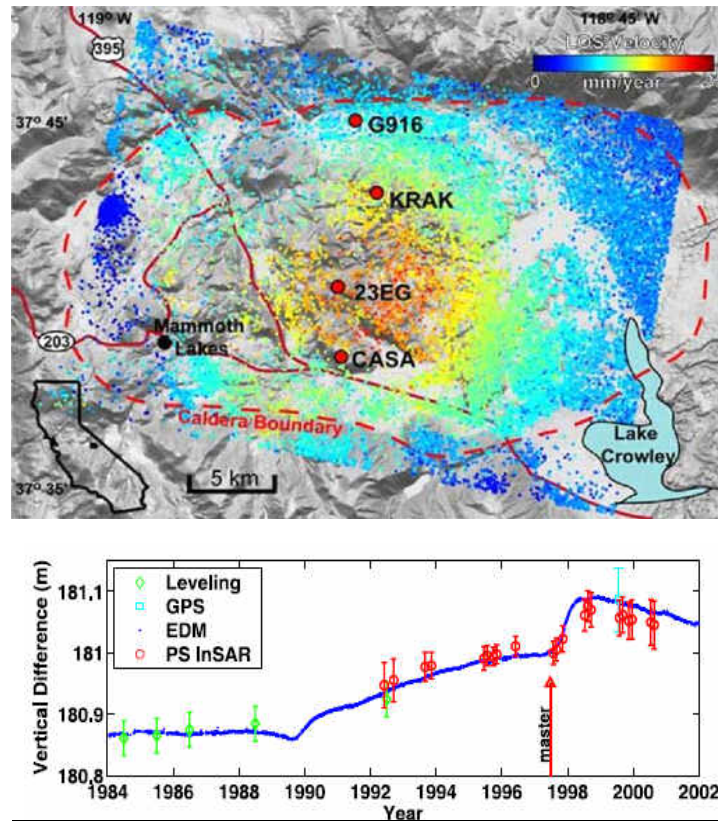


Figure 85 : Mean deformation rates and example of time series achieved by means of StaMPS technique in the area of Long Valley Caldera area, California (Hooper et al., 2004).

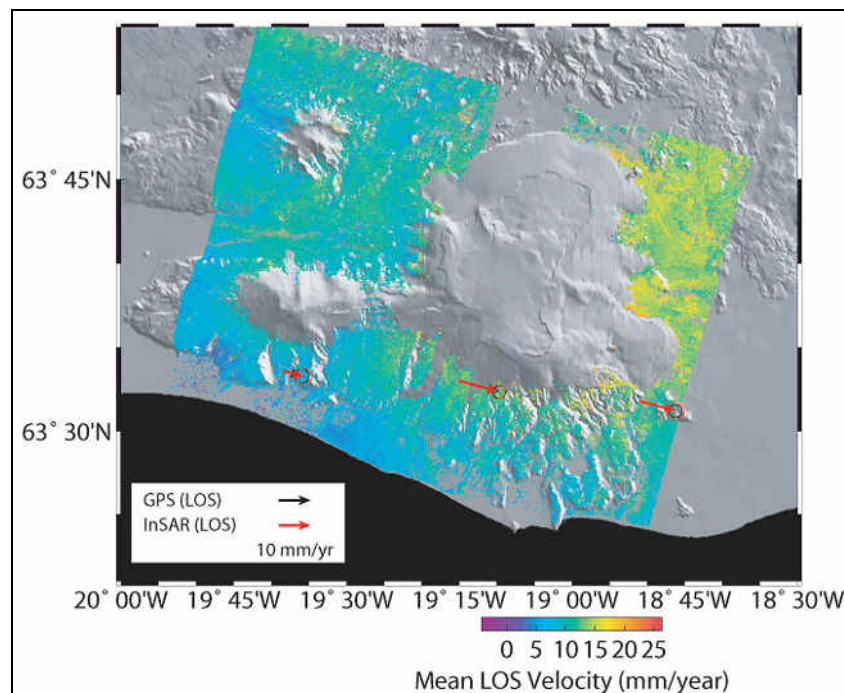


Figure 86 : Mean deformation velocities for stable InSAR pixels in the area of Katla Volcano, Iceland, measured on a data-stack of ERS images acquired between 1995 and 1998 and processed with the StaMPS technique. GPS velocities relative to Reykjavik on the North American plate are also plotted and projected into the satellite line-of-sight (Hooper and Pedersen, 2007).

### 4.3. INTERFEROGRAM STACKING TECHNIQUES (LOW RESOLUTION / DISTRIBUTED SCATTERING)

Interferogram stacking techniques are the direct extension of the classical DInSAR technique to the multipass case. Since the first description of the technique (Gabriel et al., 1989), the DInSAR technique, which was originally derived with respect to two acquisitions (a single interferogram), was applied to detect the presence of ground displacements in mainly in volcanic areas and after earthquakes. The standard two pass DInSAR was however limited by the presence of at least two error sources: the atmospheric propagation delay (APD) and the inaccuracies of the external DEM used in the elimination of the topography component from the signal interferences. Above limitations were overcome for the first time by the PS techniques exploiting long acquisition sequences, i.e., by generating a multitemporal/multibaseline (MT/MB) interferogram stack. Differently from the PS technique, which is tailored to the monitoring of dominant scatterer, interferogram stacking techniques assume the scattering to be distributed. The first interferometric stacking technique proposed in the literature has been the Small Baseline Subset (SBAS) technique (Berardino et al., 2002) developed by the Institute for Electromagnetic Sensing of the Environment (IREA) of the Italian National Research Council ([www.irea.cnr.it](http://www.irea.cnr.it)).

#### 4.3.1. SBAS (Small Baseline Subset)

Following the lines of the classical (single-pair) DInSAR analysis, SBAS carries out an analysis of multilook interferograms: the multilook operation, i.e. a spatial averaging which is carried out by exploiting the hypothesis that the scattering is distributed, allows increasing the phase signal quality. The angular decorrelation is a phenomenon which is associated with

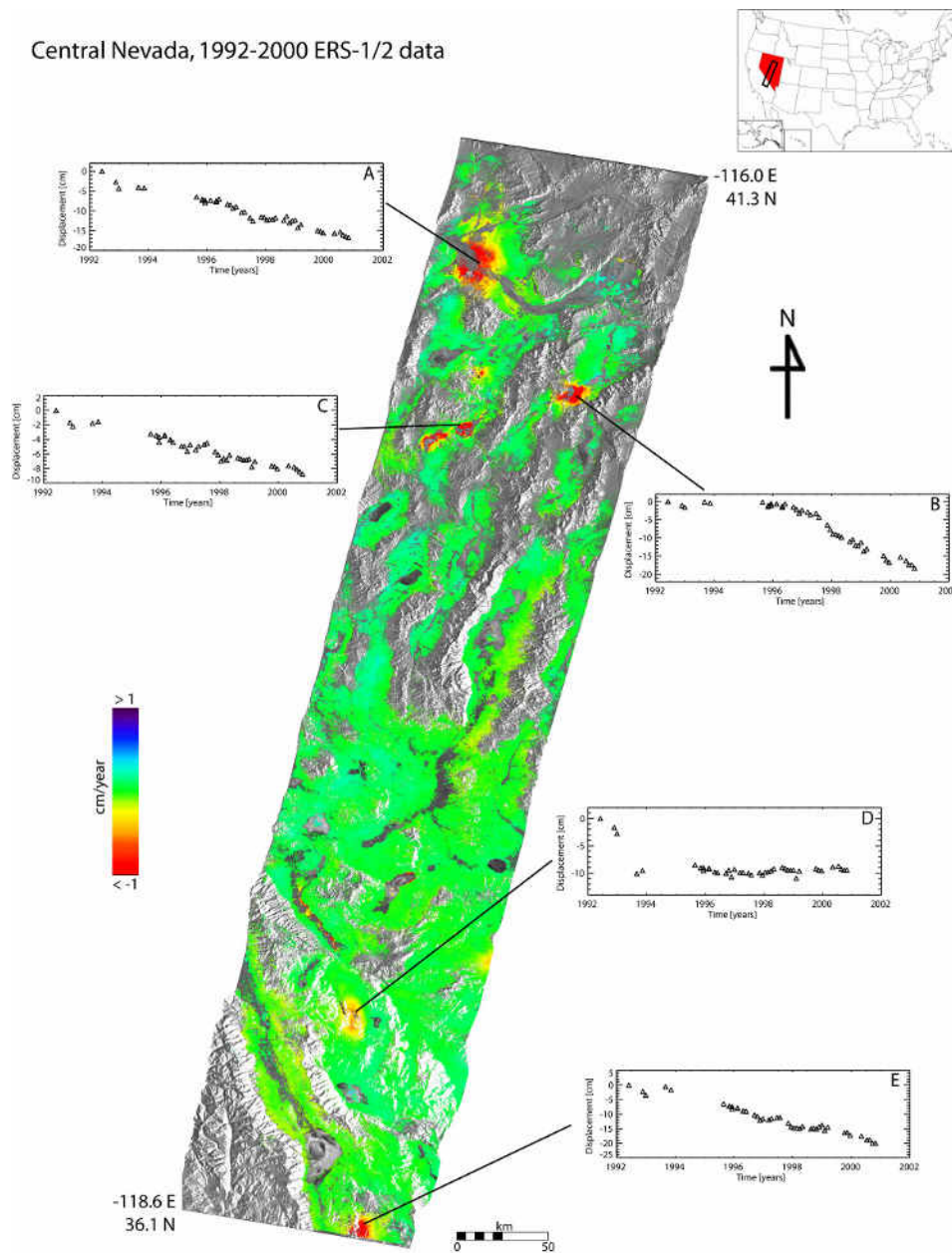
scattering changes of the phase caused even by small variations of the radar line of sight direction in elevation (induced by orbital separation) and/or aspect (induced by doppler centroid); temporal decorrelation is due to changes over the time of the scattering. The SBAS technique uses only interferograms generated by choosing thresholds on the spatial and temporal baselines, that is the spatial orbital and temporal separations, respectively, and on the Doppler centroid difference thus limiting the effects of angular and temporal decorrelation. After the unwrapping, which can be performed with algorithms commonly used in SAR Interferometry (for instance the Minimum Cost Flow algorithm) the interferograms, which embed the information of the phase variation between two acquisitions, are inverted to retrieve the phase signal over the stack of acquisitions. The SBAS approach, by using the Singular Value Decomposition (SVD) technique allows also handling the case in which, due to the limitations on the baselines, the acquisitions are grouped in different independent subsets. This latter feature allows also easily integrating data of different sensors (f.i. ERS and ENVISAT).

After the inversion the deformation time series are separated from atmospheric contribution and possible DEM errors (residual topographic) via the use of proper filtering based on the deterministic and statistical characterization of the single components.

The phase unwrapping represents, as for all other techniques, the most critical step of the SBAS approach. Advanced PhU algorithm such as that proposed in (Pepe and Lanari 2006) or in the Enhanced Spatial Difference (ESD) approach (Fornaro et al 2009a) allows improving the performances of this class of radar monitoring techniques.

The SBAS approach has been widely applied for the investigation of deformations associated with several phenomena, such as those occurring in volcanic areas, fault deformation (Lanari et al 2007, Atzori et al. 2008), mining and in general underground excavation, and landslides. In (Casu et al. 2006) a detailed analysis of the accuracy achieved by DinSAR stacking (particularly SBAS), is presented. Figure 87 shows an example of the SBAS (low resolution) product relevant to a very large area (Casu et al 200)





IREA-CNR Napoli / University of Miami

Figure 87 : Mean deformation velocities of an area of about 600Kmx100Km obtained with the SBAS technique in Nevada USA (Copyright IEEE).

Several techniques have been also proposed for the extension/integration of the low resolution SBAS processing chain for the analysis of deformation at the highest resolution. Among them it is worth to highlight the straightforward extension of SBAS approach (Lanari et al. 2004) to the high resolution data in which, always by limiting the spatial baseline, the data set to the highest resolution is compensated for small scale deformation and atmospheric phase propagation delay resulting from the low resolution analysis. The limitation on the baselines may be however, on high resolution data, inappropriate because at this scale generally the scattering occur with respect to dominant scatterers which in most of the cases do not exhibit angular and temporal decorrelation. Another technique, known as 4D (space-velocity)

imaging or tomography, is based on both the amplitude and the phase information of the signal (Fornaro et al 2009b, Fornaro et al 2010). This technique does not limit the baselines: beside the possibility to locate persistent scatterers even interfering within the image pixels, it also outperforms the classical persistent scatterers technique in terms of detection of targets at the highest resolution that can be monitored by the radar technique (Fornaro et al 2009c). Figure 88 shows the results of the application of the tomographic technique to the area of Rome, see (Fornaro et al 2010).

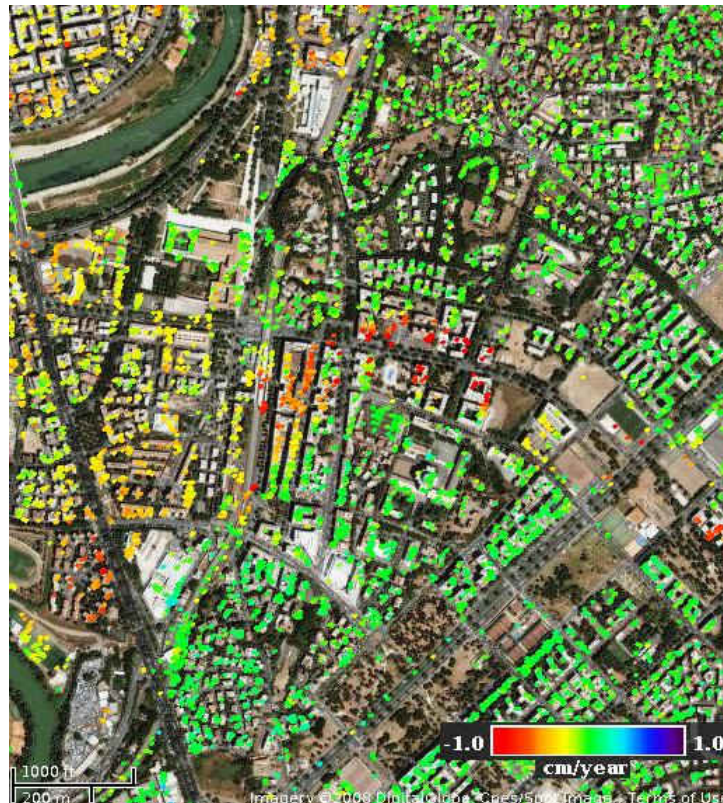


Figure 88 : Mean deformation velocities in the city of Rome obtained via the full resolution tomographic analysis (Copyright IEEE).

#### 4.3.2. CPT (Coherent Pixel Techniques)

The Coherent Pixel Technique (CPT) is a DInSAR stacking technique developed by Remote Sensing Laboratory of the Universitat Politècnica de Catalunya (Blanco et al. 2008) which is very similar to the SBAS algorithm. In particular, as for the SBAS approach, it applies to interferograms which have been spatially averaged (multilooked) and hence well fits with distributed scattering such as that occurring over bare soils. Differently from the SBAS approach, the CPT technique uses a Minimum Spanning Tree (MST) strategy to connect the acquisition stack, and therefore to generate the interferograms. On one hand this strategy can reduce the computational effort, on the other hand it limits the degree of redundancy of the interferogram network and therefore it may be more critical in terms of robustness with respect to phase unwrapping errors. Another special feature of the CPT approach is related to the implementation of a step which allows, via modelling, to retrieve the linear deformation component and DEM error contribution prior to extraction of the non linear component. In



this sense the technique is very similar to the ESD approach proposed in (Fornaro et al 2009a).

Figure 89 presents the results obtained by using the CPT technique for monitoring the urban subsidence in Murcia with 39 TerraSAR-X images from 18/07/2008 to 25/11/2009 within the framework of a project involving the Universitat Politècnica de Catalunya and the Universitat de Alicante. The TerraSAR-X images were provided by DLR in the framework of the scientific project GEO0389.

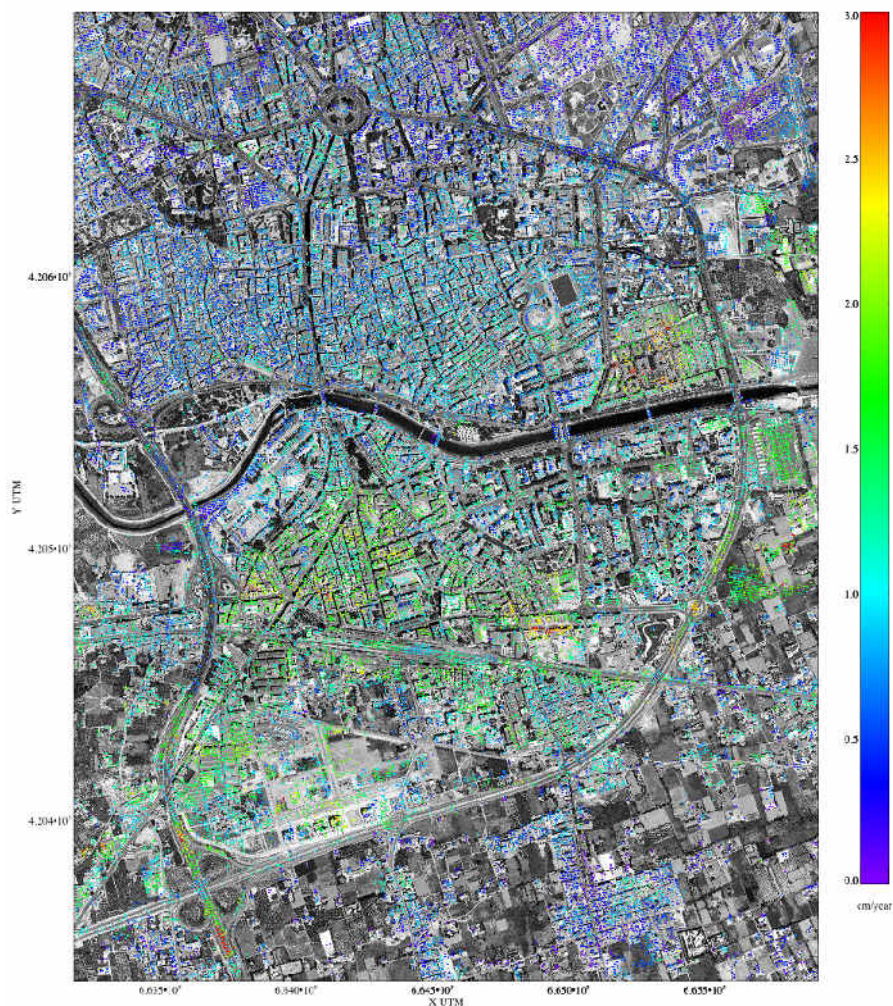


Figure 89 : Mean deformation velocities in the city of Murcia obtained via the (low resolution) CPT technique applied to TerraSAR-X data (Courtesy of the RSLab of the Universitat Politècnica de Catalunya).

#### 4.4. FINAL REMARKS

Spaceborne DInSAR technology is rather mature and many applications examples on medium resolution data are available in the current literature. Among all the applications, spanning from the monitoring of volcanic and seismogenetic areas to the underground extraction and resource management, etc., the monitoring of landslides is the most challenging one mainly

due to the presence of vegetation and the of slope variation. The latter causes in most of cases the loss of visibility on one of orbit typology (ascending or descending).

The new generation high and very high resolution satellite SAR systems, such as COSMO-SKYMED, TerraSAR-X and the upcoming Tandem-X represent certainly a significant improvement for the technology in terms of data availability and coverage. Nonetheless, the temporal sampling (related to the so-called revisiting time) and the scene viewing geometry cannot be freely set in the case of satellites: both factors represent a rather stringent limitation especially for the monitoring of landslides where the dynamic of the phenomenon, and both the exposition and slope are highly variable. One of the future challenges in terms of development of the DInSAR technology is certainly associated with the possibility to migrate to airborne sensors. In this case operational flexibility would be strongly improved in terms repetition and orientation of the passes. However, compensation of the effects associated with the track instability represents a major technological gap.

## **5. GROUND-BASED INSAR**

### **5.1. INTRODUCTION**

Differential Interferometry based on SAR images (DInSAR) was first developed for data from spaceborne platforms, but most of these methods can be applied to data from ground-based microwave interferometer. Ground-based differential interferometry (GBInSAR) became more and more popular in the last ten years, in particular for monitoring landslides and instable slopes. A recent overview about this technique can be found in (Luzi, 2010).

It is possible to acquire SAR images through a portable SAR set up on a stable area. The synthetization of the radar antenna is usually obtained by the linear and regular motion of a microwave transceiver on a rail. Ground-based radar installations are usually at their best when monitoring small objects like buildings, small urban areas or single hillsides, while imaging from satellite radar is able to monitor very large areas. As for satellites data, GBInSAR images acquired at different dates can be used for interferometry when the decorrelation among the different images is kept low. Satellite observations are sometimes not fully satisfactory because of a lengthy revisit time or of changes on observational geometry. In ground-based interferometry, the high number of measurements, available with less than hourly cadence, makes decorrelation of minor concern. Moreover satellite interferometry can only imagine sites with a proper visibility and from where the component of the displacement along the line of sight of the satellite can be observed.

Satellite and ground-based radar interferometry are derived from the same physical principles but they are often characterized by specific problems mainly due to the difference of geometry of the observation. In the last decade several papers have been issued about the feasibility of monitoring buildings or structures (Tarchi et al., 1997), glaciers (Luzi et al., 2007), volcanoes (Casagli et al., 2003, Antonello et al., 2006) and landslides (Tarchi et al., 2003b, Leva et al. 2003), this last one appearing to be the most consolidated application. A number of experimental results demonstrate the effectiveness of GBInSAR for remote monitoring of terrain slopes and as an early warning system to assess the hazard of rapid landslides.

## 5.2. THE GBINSAR INSTRUMENTATION

Despite the use of the same physical principle, the satellite and ground-based approaches differ in some aspects. In particular radar sensors of different kinds are usually employed mainly because of technical and operational reasons. While satellite SAR systems due to the need of a fast acquisition are based on standard pulse radar, continuous wave step frequency (CWSF) radars are usually preferred in ground-based observations. The Joint Research Center (JRC) has been a pioneer of this technology and in this centre the first prototype was born. The first paper about a GBInSAR interferometry experiment dates back to 1999 (Tarchi et al., 1999), reporting a demonstration test on dam. The used equipment was composed of a radar sensor based on Vectorial Network Analyser (VNA), a coherent transmitting and receiving set-up, a mechanical guide, a PC based data acquisition and a control unit.

After some years a specific system, known as GBInSAR LiSA, reached an operative state and became available to the market by Ellegi-LiSALab company which on June 2003 obtained an exclusive licence to commercially exploit this technology from JRC. The basic and simplest schematic of the radiofrequency set-up used for radar measurements is shown in Figure 90 along with a simple scheme of the GBInSAR acquisition. Advanced versions of this set-up have been realized in the following years to improve stability and frequency capabilities (Rudolf et al., 1999 and Noferini et al., 2005). This apparatus is able to generate microwave signals of increasing frequencies sweeping a radiofrequency band. This approach, which apparently differs from the standard pulse radar, has actually the same physical meaning, because a temporal pulse can be obtained after Fourier anti-transforming of the frequency data (the so called synthetic pulse approach).

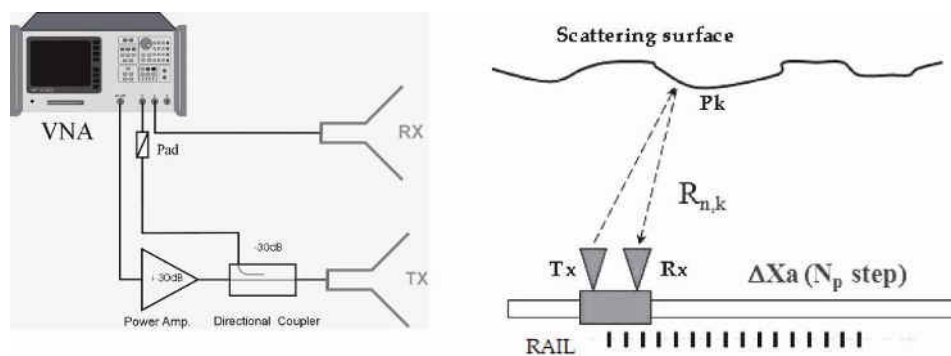


Figure 90 : A) Basic scheme of the RF section of a C band transceiver based on the Vectorial Network Analyser VNA. B) GB SAR acquisition through a linear motion.

The rapid growth of microwave technology that occurred in the last years encouraged the development and realization of different instruments (Pipia et al., 2007 Bernardini et al., 2007). In the last few years an Italian company, IDS Ingegneria dei Sistemi (<http://www.idscopy.com/it/>) has started commercializing the first off-the-shelf GBInSAR system, the IBIS-L, which is based on a Ku-band SAR sensor, see Figure 91. Recently a ground-based interferometer with a non-SAR approach has been designed with similar monitoring purposes (Werner et al., 2008). Data are processed in real time. An algorithm combines the received amplitude and phase values stored for each position and frequency values, to return complex amplitudes (Fortuny J. and A.J. Sieber, 1994). The optimization of focusing algorithms has been recently updated by Reale et al, 2008 and Fortuny, 2009. To

reduce the effect of side lobes in range and azimuth synthesis (Mensa D.L., 1991), data are corrected by means of a window functions (Kaiser, Hamming etc.), for range and azimuth synthesis. The attainable spatial resolutions and ambiguities are related to radar parameters through the relationships shown in Table 13. The accuracy of the measured phase is usually a fraction of the operated wavelength: by using centimetre wavelengths, a millimetre accuracy can be attained. The phase from complex images can suffer from the ambiguity due to the impossibility of distinguishing between phases that differ by  $2\pi$ . Single radar images are affected by noise and related interferometric maps must be obtained through adequate phase stability between the pair of images: only pairs whose coherence loss can not affect the accuracy of the interferometric maps are usable. This task is of major difficulty when the considered time period is of the order of months.

A detailed analysis to the possible causes of decorrelation in the specific case of GBInSAR gathering many images per day for continuous measurements has been discussed by some researchers (Luzi et al., 2004 and Pipia et al., 2007). For campaigns carried out on landslides moving only few centimeters per year, when the sensor is periodically installed at repeated intervals several months apart over the observation period, a novel method has been proposed (Noferini et al., 2005).

*Table 13 : Calculated resolution available from a CWSF radar observation;  $B$  radiofrequency bandwidth,  $\lambda$  in vacuum wavelength,  $\Delta f$  frequency step,  $L_x$  rail length,  $R$  range,  $c$  light velocity.*

Range resolution	$\Delta R_r = \frac{c}{2B} \perp$
Azimuth resolution	$\Delta R_{az} = \frac{\lambda_c}{2L_x} \cdot R$
Non ambiguous range (m )	$R_{na} = \frac{c}{2\Delta f}$

As mentioned, the monitoring of instable slopes through GBInSAR interferometry is a well consolidated application largely reported in literature (Leva et al. 2003, Pieraccini et al., 2003, Tarchi et al., 2003a). The investigation and interpretation of the patterns of movement associated with landslides have been undertaken by using a wide range of techniques, including the use of survey markers: extensometers, inclinometers, analogue and digital photogrammetry, both terrestrial and aerial. In general, they suffer from serious shortcomings in terms of spatial resolution. GBInSAR, thanks to its spatial and temporal sampling can overcome the restrictions of the conventional point-wise measurement.





*Figure 91 : IBIS-L, the first GBInSAR system commercially available.*

### **5.3. CHARACTERISTICS OF APPLICATION**

Here are presented the main characteristics of some devices that were directly experienced by the University of Firenze, namely LiSA-Mobile by Ellegi-Lisalab and IBIS-L by IDS. The two systems share most of the basic features, the main difference being that IBIS-L generates the microwave signal by using an industrialized method derived from a prototype developed in collaboration with the Department of Electronics of the University of Firenze, while LiSA-Mobile is based on a Network Analyzer (NA). This theoretically allows LiSA-Mobile to spread on a wider waveband, although for most geological applications the optimal parameters generally vary within a relatively restricted range. A new version of LiSA-Mobile, faster and lighter, has been produced to fulfill the need of an application in emergency conditions, though it uses no more a Network Analyzer to generate the microwave signal.

Therefore, the main differences in the choice of a GBInSAR lie especially in the policies and in the software adopted by the two companies. IDS favours a more commercial use of its system and makes the customer able to carry out on his own any campaign. On the other side Ellegi-Lisalab preferably sells a service and hence grants a major flexibility both in the radar parameters and in the mechanical part.



### **IBIS-L:**

- Target distance: 10 - 4000 m.
- Central frequency: 17.2 GHz (Ku band) or 9.7 GHz (X band).
- Bandwidth: 300 MHz.
- Polarization: VV.
- Synthetic aperture: 2 m.
- Range resolution: 0.5 m.
- Azimuth resolution (at 500 m): 2.2 m.
- Scansion time: <5 minutes.
- Opening angles: 70° (azimuth), 60° (elevation).
- Minimum and maximum displacement measured: from mm/y to 1 - 2 m/day.
- Notes: the system can also be installed in a static configuration (IBIS-S); in this case it can be mounted on a single tripod, it has a scansion time of 1 msec and it can be used to measure the vibrations of the target, though it is not able to produce 2D displacement maps. A GBInSAR operating in X band is also produced. Aresys, a spin-off of the Politecnico di Milano, developed another software able to elaborate the data collected by the radar by using a technique similar to the Permanent Scatterers approach (Ferretti et al., 2000) to reduce limitations due to vegetation and atmospheric effects.

The Figure 92 shows a displacement map of the Torgiovannetto landslide (Perugia, central Italy) elaborated through IBIS-L system.

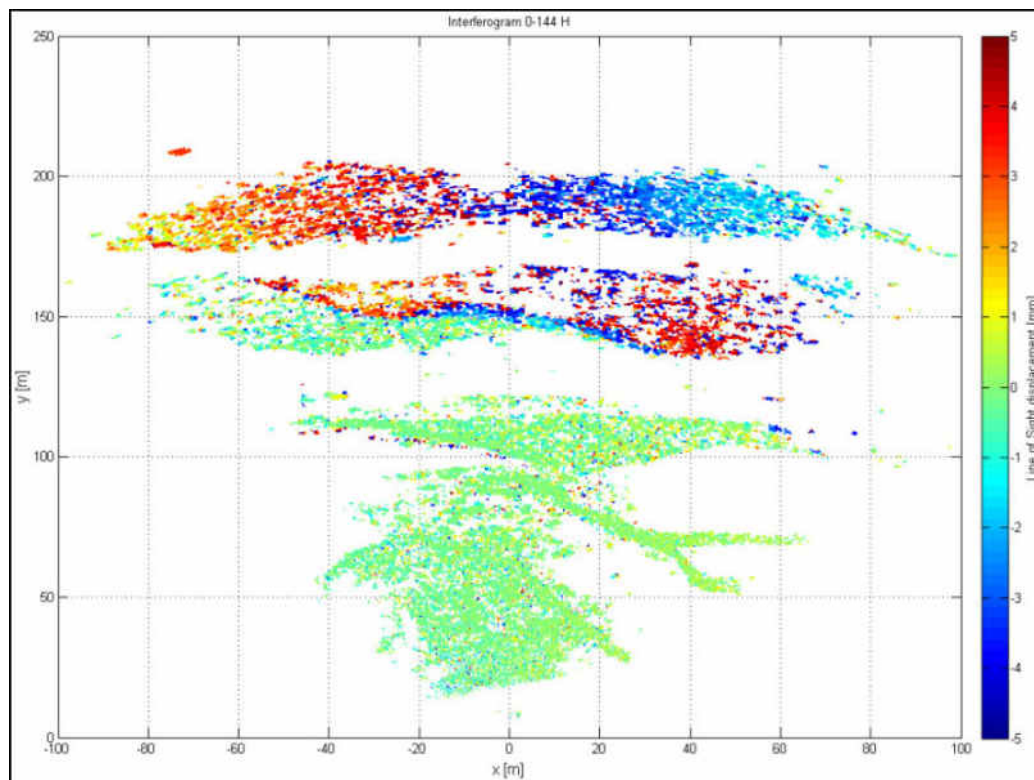


Figure 92 : Displacement map of the Torgiovannetto landslide (Perugia, central Italy). A software able to elaborate data using a technique similar to the Permanent Scatterers approach (Ferretti et al., 2000) is also available.

### LiSA-Mobile:

- Target distance: 10 - 4000 m.
- Central frequency: 17.2 GHz (Ku band, the new version); from 10 MHz to 20 GHz (the version with NA).
- Bandwidth: up to 400 MHz (the new version); no theoretical limit (the version with NA).
- Polarization: VV.
- Synthetic aperture: 2-3 m (no theoretical limit).
- Range resolution: 0.38 – 0.75 m (the new version); depending on the bandwidth (the version with NA).
- Azimuth resolution (at 500 m): varies depending on the synthetic aperture and on the central frequency adopted. Using a 3 m long rail and a central frequency of 17.2 GHz the azimuth resolution at 500 m is 1.5 m.

- Scansion time: varies depending on the rail length. The new system performs 3 m of synthetic aperture in 3 minutes.
- Opening angle: 50° (can vary up to 120° depending on the antennas installed).
- Minimum and maximum displacement measured: from mm/y to 3 - 4 m/day (the new version).
- Notes: the new version of LiSA-Mobile, especially designed for being used in emergency condition, has an electric consumption of less than 100 W, while the NA version consumes about 1000 W. Both systems can be installed on a tripod to work in static configuration. Also the rail can be mounted on two tripods to improve its prompt installation.

Below a displacement map of the Torgiovanetto landslide monitored by using the system of Ellegi-Lisalab is shown (Figure 93).

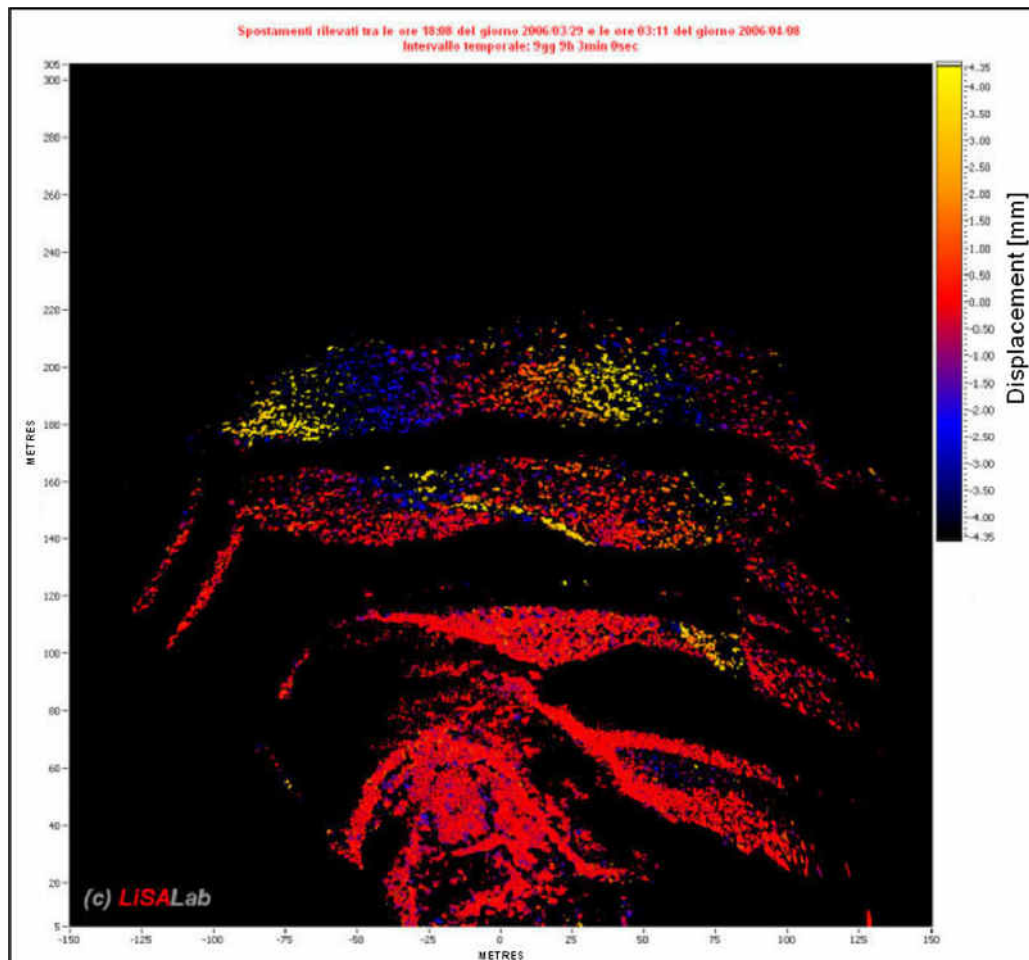


Figure 93 : Displacement map of the Torgiovanetto landslide (central Italy) elaborated by using the GBInSAR system of Ellegi-Lisalab.

It should be underlined that some features, such as the maximum displacement rates that can be successfully measured, the minimum and maximum range distance, the limitations due to the vegetation and so on, are only partly tied to the characteristics of the radar system as they also depend dramatically on the conditions of the monitored target and on other parameters that influence each other.

## **6. POLARIMETRY FOR SOIL MOISTURE ESTIMATION**

### **6.1. INTRODUCTION**

Polarimetry deals with the vector nature of the electromagnetic fields: radar polarimetry concerns with the utilization of polarimetry in radar applications.

A polarimetric Synthetic Aperture Radar (SAR) system measures the electric field, backscattered by the scene, including its polarisation state and hence the scattering matrix. The interaction of the transmitted wave with a scattering object transforms its polarisation. Therefore, the polarisation of the backscattered wave depends on the polarisation of the transmitted wave as well as on the scattering properties of the imaged objects.

One special characteristic of SAR polarimetry is that it allows a discrimination of different types of scattering mechanisms. This becomes possible because the observed polarimetric signatures depend strongly on the actual scattering process.

In comparison to conventional single-channel SAR, the inclusion of SAR polarimetry consequently can lead to a significant improvement in the quality of classification and segmentation results. Certain polarimetric scattering models even provide a direct physical interpretation of the scattering process, allowing an estimation of physical ground parameters like soil moisture and surface roughness, as well as unsupervised classification methods with automatic identification of different scatterer characteristics and target types.

SAR polarimetry additionally offers some limited capability for separating multiple scattering mechanisms occurring inside the same resolution cell and can be deemed as a first step in resolving the ambiguous scattering problem in SAR, as mentioned above. With polarimetric decomposition techniques a received signal can be split into a sum of three scattering contributions with orthogonal polarimetric signatures. This can be used for extracting the corresponding target types in the image, even in the case that they are occurring superimposed. Also, if a signal is disturbed by undesired orthogonal contributions, in this way the relevant components can be extracted.

Radar polarimetry has a wide spectrum of applications in

- Agriculture: to discriminate different agricultural fields (Lemoine et al., 1994);
- Forestry: biomass estimation and discrimination of different species (Le Toan et al., 1992; Rignot et al., 1995);
- Hydrology: surface roughness and soil moisture (Lin et al., 1994; Dubois et al., 1995);
- Snow moisture measurements (Shi and Donzier, 2000);

- Geology: characterization of geological structures (Oh et al., 1992);
- Geohazard: detection of surface changes produced by landslides (Czuchlewski et al., 2003).

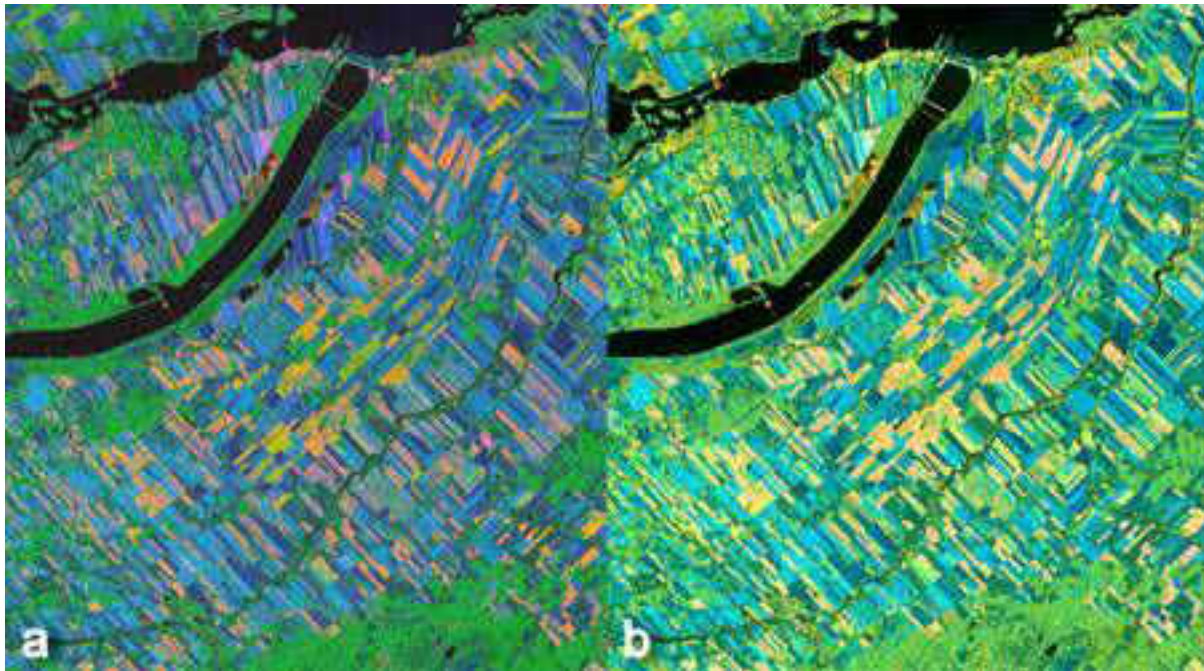


Figure 94 : Example of scattering mechanism decomposition images from fully polarimetric RADARSAT-2 data (a) and comparison with simulated results (source: Canada Centre for Remote Sensing, <http://www.ccrs.nrcan.gc.ca>)

## 6.2. SOIL MOISTURE ESTIMATION

The backscatter coefficient of sparsely vegetated land is related to the frequency, angle of incidence and polarization of the incident wave, as well as to the roughness of the soil and its complex dielectric constant in Ulaby et al. (1982), Tsang et al. (1985) and Beckmann and Spizzichino (1987). This in turn depends on the composition and density of the soil and, above all, on its water content. Therefore, it is theoretically possible to estimate the soil moisture data using Synthetic Aperture Radar (SAR).

More precisely, considering that at microwave frequencies the thickness of penetration into the soil is of the order of centimeters, what is possible is to estimate the water content in the topsoil to a depth of about 5 cm (Ulaby et al., 1982) (the exact thickness value depends on the frequency and in turn on the water content and the intensity of the incident radiation). However, in practice the estimation of soil moisture is complicated by the fact that the dependence of the backscattering coefficient of dielectric constant is masked by the strong dependence on the roughness of the soil. Therefore, methods for estimating the water content must necessarily be based on empirical, semi-empirical or theoretical direct models, providing the backscatter coefficient as a function of the complex dielectric constant and the parameters describing the roughness of the soil (including, obviously, the nature of the incident wave). Moreover, to distinguish the effect of moisture from the surface roughness at the inversion stage, the roughness of the land must be known or otherwise provided (e.g. if you want to

monitor developments over time in the water content of a specific small area, the roughness can be measured in situ once and for all, and humidity can be estimated from time to time by SAR data), or it needs to have more measurements at different frequency and/or polarization and/or incidence angle (that is not possible with ERS data, but e.g. with ENVISAT, although with a time of revisiting excessive, or COSMO-SkyMed).

Use of models is therefore mandatory for retrieving soil parameters. Typically used models are divided in empirical, theoretical and semi-empirical.

- Empirical models establish a simplified relation between the surface parameter and the diffuse field. The simplicity is however paid with a limitation of the validity outside the site of calibration.
- Theoretical models are based on the evaluation of the scattered field starting from the knowledge of the tangential electric and magnetic components on the interface between the air and the terrain. Approximations in the evaluation of the field components at the interface pose a limitation to the range of acceptable values of the dielectric constant and of the roughness.
- Semi-empirical models are obtained by a simplification of the theoretical models in terms of parameter empirically estimated. This class of models has characteristics which are intermediate with respect to the above classes.

Earlier studies using single frequency and single polarization SIR-B (Shuttle Imaging Radar-B) imagery could only describe the dependence of backscattering coefficient on the surface parameters (mainly, roughness and dielectric constant) separately. The inversion of soil moisture information from radar backscatter became more rigorous after the availability of polarimetric radar data. For example, Oh et al. (1992) developed a model for estimating the rms height of the soil surface and its moisture content from simultaneous ratio measurements of the ratios between the HV and VV polarization and HH and VV polarization where “H” and “V” stand for horizontal and vertical polarizations, respectively, in either transmit or receive mode of radar operation.

In Dubois et al. (1995) an empirical model that only requires measurements of HH and VV channels at a frequency between 1.5 and 11 GHz to retrieve both rms roughness height and soil moisture from bare soils was developed.

An algorithm based on the regression analysis of the simulated surface backscattering coefficients by the theoretical model was developed in Shi et al. (1997) to provide an estimation of soil moisture and surface roughness parameter from L-band SAR co-polarized measurements over bare and short vegetated fields. This algorithm was applied to a series of AIRSAR and SIR-C measurements obtained over the Little Washita River watershed near Chickasha, Oklahoma. The values of the retrieved soil moisture and surface roughness parameter for a number of bare and short-vegetated fields were compared with those sampled on the ground in near concurrence with the AIRSAR and SIR-C measurements. A reasonable agreement was found between the retrieved and measured values. The rms errors of the comparison were estimated to be 3.4% and 1.9 dB for soil moisture and surface roughness parameter, respectively.



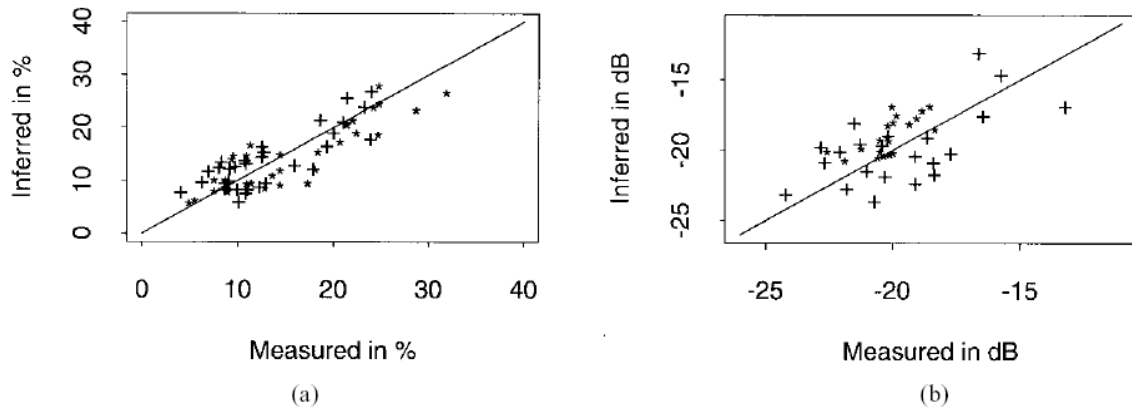


Figure 95 : Comparison in Shi et al. (1997) between the inferred and ground measured soil moisture and surface roughness parameter from all available SIR-C (+) and AIRSAR (\*) L-band images. IEEE copyright.

Based on observations indicating the potential of using correlation information among polarimetric data for the separation of moisture and roughness, and the demonstration in laboratory about the relationship between surface roughness and the eigenvalues of the polarimetric coherency matrix (which themselves have a physical significance in terms of scattering amplitude) a different approach for decoupling soil moisture and roughness over bare soils was proposed in Hajnsek et al. (2003). The model is an extension of the small perturbation method. The application of the technique to experimental data acquired by the E-SAR airborne system collected over two test sites in Germany (Weiherbach and Elbe-Auen) showed good agreement between the inverted values and ground measurements. The low rms errors for the normalized roughness (i.e. the surface rms height normalized to the wavelength/ $2\pi$ ) from 0.14 to 0.11 and for soil moisture content from 5 to 10 [vol.%] over both test sites indicated that the structure of the data is in accordance with the predictions of the model over a large range of surface conditions. The inversion accuracy was high enough to point out the seasonal variation effects. It was also pointed out that the moisture content estimation is much very sensitive to incidence angle variations. Sensitivity analysis with respect to terrain variations have shown that 1 degree in terrain slope variation leads to an rms error variation in the order of 0.25 [vol.%].

To visually appreciate the coverage of the estimation, a sample result from this paper reporting the estimated soil moisture over the two test sites is shown in Figure 96.

A strong limitation for surface parameter estimation from polarimetric SAR data is the presence of vegetation. In the case of bare surfaces, satisfactory estimation results for soil moisture estimation can be achieved using theoretical as well as empirical or semiempirical approaches. However, bare fields are only a special case: agricultural fields are covered by different crop types over large periods of their yearly cycle. The presence of vegetation increases the complexity of the scattering scenario: the waves propagate through and interact with the vegetation layer and then interact with the underlying surface. Therefore, vegetation and surface effects are superimposed in the measured scattering signature and the separation of the individual contributions becomes more complex.

This, combined with the fact that most natural surfaces are temporarily or permanently covered by vegetation, restricts significantly the importance of radar remote sensing for a wide spectrum of geophysical and environmental applications.

One approach for solving the problem of surface parameter inversion under vegetation cover is to use longer wavelengths (lower frequencies). P-band is, for example, such a potential frequency candidate with sufficient high penetration into and through vegetation layers. However, first experimental results at P-band indicate that this approach solves only one part of the problem.

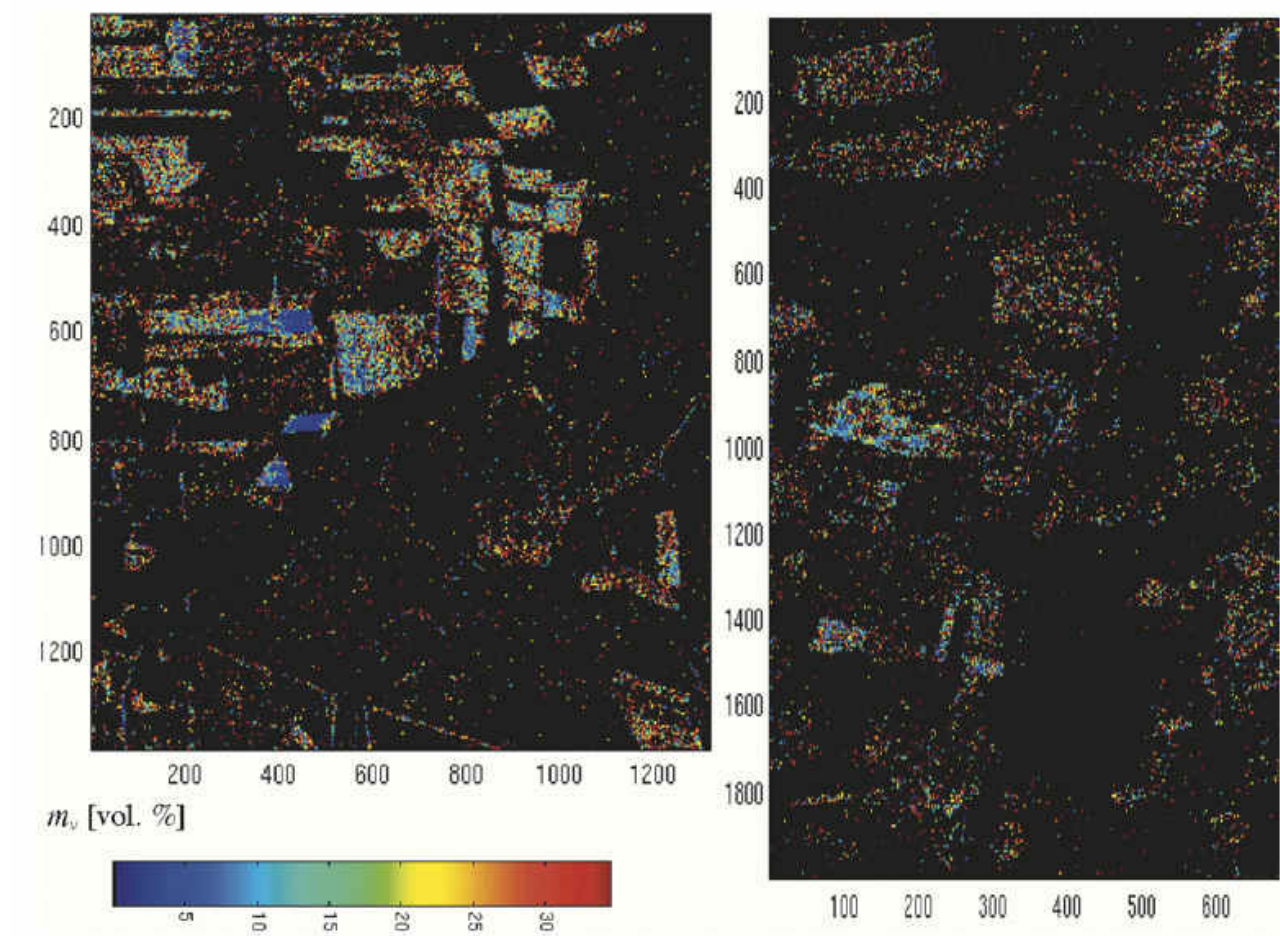


Figure 96 : Estimated surface roughness  $k_s$ , ranging from 0 to 1; not valid areas are indicated with black Hajnsek et al. (2003). (left) Elbe-Auen test site and (right) Weiherbach test site in Germany. IEEE copyright.

Furthermore, the fact that the effective roughness is scaled by the wavelength makes moderate rough bare surfaces to appear very smooth at P-band, implying low backscattering coefficients often close to the system noise floor. In this case, additive noise becomes a significant limitation. Thus, single frequency and conventional polarimetry alone seem to be unable to resolve satisfactorily the problem.

In Hajnsek et al. (2009), the authors discuss the potential of using quad-polarimetric data for the separation of vegetation and ground scattering components and the estimation of moisture of the underlying soil. Polarimetric-decomposition techniques were used to decompose the

scattering signature into individual (canonical) scattering components; the inversion of moisture of the underlying soil by using the ground-related scattering component has been investigated. The performance of the decomposition approaches has been validated at L-band using fully polarimetric airborne SAR data acquired in the frame of the AgriSAR campaign by the E-SAR system of DLR over a time span of four months in summer 2006.

Key step of the procedure is the separation of volume from dihedral and surface contributions: after this step, soil moisture is retrieved by inverting from the dihedral and surface components as both depend on the dielectric properties of the ground. The performance of the soil-moisture estimation has been compared against ground measurements over a whole vegetation-growing period. The comparison of the estimated soil moisture over the whole vegetation period demonstrated a large variance of the estimation performance of the dihedral as well as of the surface derived soil-moisture component. During the vegetation growth for all the three crop types, the dihedral component has the highest appearance and the best performance when compared with the ground measurements. However, this changes when the crop vegetation gets into the mature state. Here, the presence of the surface component increases, leading to a good soil moisture performance. In summary, it can be stated that, during the vegetation-growing cycle, the dominance of the scattering mechanisms are changing, and depending on it, either the dihedral or the surface component is able to provide reasonable soil-moisture estimates. The approach has been extended in Jagdhuber et al. (2009) to a multiangular observation which can be obtained only by using airborne systems to increase the success estimation rate, see Figure 97.

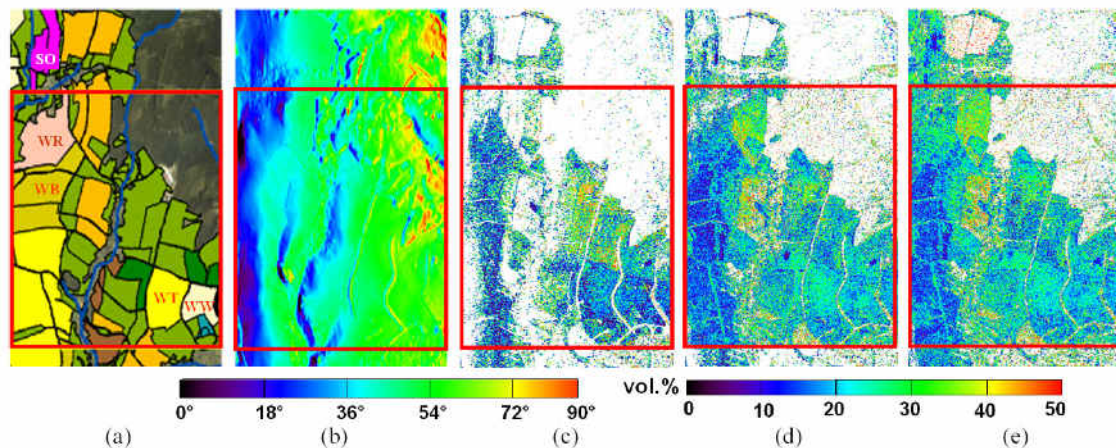


Figure 97 : Exemplarily results from Jagdhuber et al. (2009), (a) the land use, (b) the local incidence angle in degrees as well as (c-e) the estimated soil moisture in vol.% is displayed for three different incidence angle constellations (3c: master [one acquisition], 3d: master-perpendicular [two acquisitions], 3e: master-opposite-perpendicular [three acquisitions]). White color represents non-invertible pixels; red frame indicates the overlapping zone of the three acquisitions (master, opposite, perpendicular). WT=winter triticale, WB=winter barley, WR=winter rye, WW=winter wheat, SO=summer oat. IEEE Copyright.



---

# PART D

## GEOPHYSICAL INVESTIGATIONS

---

---

- <b>SECTION 1:</b> Ground-Based Geophysical Investigations	p. 167
- <b>SECTION 2:</b> Acoustic and Micro-Seismic Monitoring	p. 195
- <b>SECTION 3:</b> Introduction to Offshore Methods	p. 213
- <b>SECTION 4:</b> Stakes of the Airborne Geophysics	p. 218

---

### Section 1

- **Authors:** I. Lecomte<sup>1,2</sup>, S. Bazin<sup>1,3</sup>, G. Grandjean<sup>4</sup>, C. Michoud<sup>5</sup>,
- **Reviewer:** D. Jongmans<sup>6</sup>

<sup>1</sup>. International Center for Geohazards (ICG), Oslo, Norway.

<sup>2</sup>. NORSAR, Kjeller, Norway. [Isabelle.lecomte@norsar.no](mailto:Isabelle.lecomte@norsar.no)

<sup>3</sup>. Norwegian Geotechnical Institute (NGI), Oslo, Norway.

<sup>4</sup>. Bureau de Recherches Géologiques et Minières (BRGM), Paris, France.

<sup>5</sup>. Institute of Geomatics and Risk Analysis (IGAR). Université de Lausanne, Switzerland.

<sup>6</sup>. Laboratoire de Géophysique Interne et de Tectonophysique, Université Joseph Fourier, Grenoble, France.

Lecomte I., Bazin S., Grandjean G., Michoud C., 2010. *Ground-Based Geophysical Investigations*. In the Deliverable 4.1 of the European project SAFELAND: *Review of Techniques for Landslide Detection, Fast Characterization, Rapid Mapping and Long-Term Monitoring*. Edited in 2010 by Michoud C., Abellán A., Derron M.-H. and Jaboyedoff M. Available at <http://www.safeland-fp7.eu>

### Section 2

- **Authors:** A. Tonnellier<sup>1</sup>, J.-P. Malet<sup>1</sup>
- **Reviewer:** M. Roth<sup>2,3</sup>

<sup>1</sup>. Centre National de la Recherche Scientifique (CNRS), Institut de Physique du Globe de Strasbourg (IPGS), France. [alice.tonnellier@unistra.fr](mailto:alice.tonnellier@unistra.fr)

<sup>2</sup>. International Center for Geohazards (ICG), Oslo, Norway.

<sup>3</sup>. NORSAR, Kjeller, Norway.

Tonnellier A., Malet J.-P., 2010. *Acoustic and Micro-Seismic Monitoring*. In the Deliverable 4.1 of the European project SAFELAND: *Review of Techniques for Landslide Detection, Fast Characterization, Rapid Mapping and Long-Term Monitoring*. Edited in 2010 by Michoud C., Abellán A., Derron M.-H. and Jaboyedoff M. Available at <http://www.safeland-fp7.eu>

### Section 3

- **Author:** J.-S. L'Heureux<sup>1,2</sup>, R. Hermanns<sup>1,2</sup>

- **Reviewers:** C. Michoud<sup>3</sup>, M.-H. Derron<sup>3</sup>

<sup>1</sup>. International Center for Geohazards (ICG), Oslo, Norway.

<sup>2</sup>. Geological Survey of Norway (NGU), Trondheim, Norway. [jean.lheureux@ngu.no](mailto:jean.lheureux@ngu.no)

<sup>3</sup>. Institute of Geomatics and Risk Analysis (IGAR). Université de Lausanne, Switzerland.

L'Heureux J.-S., Hermanns R., 2010. *Introduction to Offshore Methods*. In the Deliverable 4.1 of the European project SAFELAND: *Review of Techniques for Landslide Detection, Fast Characterization, Rapid Mapping and Long-Term Monitoring*. Edited in 2010 by Michoud C., Abellán A., Derron M.-H. and Jaboyedoff M. Available at <http://www.safeland-fp7.eu>

### Section 4

- **Author:** R. Supper<sup>1</sup>, I. Baron<sup>1</sup>

- **Reviewer:** A. A. Pfaffhuber<sup>2,3</sup>

<sup>1</sup>. Department of Geophysics, Geological Survey of Austria, Vienna, Austria. [robert.supper@geologie.ac.at](mailto:robert.supper@geologie.ac.at)

<sup>2</sup>. International Center for Geohazards (ICG), Oslo, Norway.

<sup>3</sup>. Norwegian Geotechnical Institute (NGI), Oslo, Norway.

Supper R., Baron I., 2010. *Stakes of the Airborne Geophysics*. In the Deliverable 4.1 of the European project SAFELAND: *Review of Techniques for Landslide Detection, Fast Characterization, Rapid Mapping and Long-Term Monitoring*. Edited in 2010 by Michoud C., Abellán A., Derron M.-H. and Jaboyedoff M. Available at <http://www.safeland-fp7.eu>



# 1. GROUND-BASED GEOPHYSICAL INVESTIGATIONS

## 1.1. INTRODUCTION

Ground-based (also called near-surface) geophysical methods have significantly improved the last 20 years, in terms of method, equipment, and software. The trend is going from 2-dimensional (2D) spatial imaging to 3-dimensional (3D) spatial imaging for site assessment, and further going to time-monitoring modes – the so-called 4D approach, time being the 4th dimension – where acquisition is repeated regularly over time to analyze temporal variations (monitoring mode). Even if geophysical techniques do not directly provide geological and mechanical properties, but instead some physical parameters of soils and rocks (e.g., density, acoustic/elastic parameters, resistivity, etc), ground-based geophysics often give fast and economic information about the subsurface, pending that data are all calibrated with a minimum of ground proofing (e.g., boreholes whenever possible) and that results are interpreted in tight cooperation with other geoscientists, e.g., geologists, hydrogeologists, geotechnicians, glaciologists, etc. Equipment improvement has especially contributed to the application of geophysics for landslides as the corresponding sites are often more challenging (e.g., steep and rough terrain, i.e., leading to difficult work conditions) than in more conventional applications (engineering, environmental, archaeology, etc). For an excellent and recent review of the use of geophysics for landslides, we highly recommend reading Jongmans and Garambois (2007), which contains an extensive analysis of published examples and which was consequently extensively used in the present report. In a slightly wider application range, i.e., geohazards (landslides are major geohazards), Bouillon (2005) goes in some more details – though keeping it simple - through the geophysical methods used and lists also key papers, e.g., Hack (2000) about geophysics for slope stability. For more recent site-specific cases, Maurer et al. (2010) review the use of near-surface geophysics in the Swiss Alps (e.g., frozen-ground issues for slope stability), and Hunter and al. (2010) present Canada's experience in the domain, both offshore and onshore. Finally, the geophysical terms used in the following are according to the dictionary of Sherif (2002).

Before going to field, a geophysicist must get enough information about the site of interest, in order to select the proper methods and estimate a cost; it is indeed always good practice to first visit the site and preferably to test a few methods. As the term of landslide refers to a large variety of mass movements (from very slow slides in soils to rock avalanches), affecting all soil and rock materials and with a large variety of shapes and volumes, it is crucial to understand the key parameters needed for their assessment. Ground modifications due to a landslide are indeed likely to generate changes of physical parameters characterizing the slide mass.

According to the literature review of Jongmans and Garambois (2007), a geotechnical appraisal of landslide stability has to consider three issues: (1) the definition of the 3D geometry of the landslide, in particular failure surfaces; (2) the definition of the hydrogeological regime; and (3) the detection and characterization of the movement. Except in very peculiar cases, a landslide generally results in a modification of the morphology and of the internal structure of the affected ground mass, both in terms of hydrogeological and physical properties. Surface observations and measurements have therefore to be supported by reconnaissance at depth with investigation of the slide mass down to the undisturbed rock or soil. Conventional geotechnical techniques, which mainly include boreholes, penetration tests

and trenching, allow a detailed geological description and mechanical characterization of the material. However, these techniques only give punctual information, at a relatively high cost, and their use is further limited by the difficulty of drilling onto steep and unstable slopes. On the contrary, geophysics can cover rather large surfaces and depths for a lesser or similar cost. The advantages of geophysical techniques are that (1) most are relatively quick and easy to deploy on slopes, (2) they are non-invasive (except for borehole geophysics) while giving information on the internal structure of the soil or rock mass, and (3) they allow a large volume to be investigated. Their main drawbacks are: (1) the decreasing resolution (ability of the method to detect a body of a given size) with depth, (2) the non-uniqueness of the solution for a set of data, hence the need for calibration (e.g., boreholes) and (3) the indirect information they yield (physical parameters instead of geological or geotechnical properties). It is worth noting that almost all the advantages of geophysical methods correspond to disadvantages of the geotechnical techniques, and vice-versa, outlining the complementarities between the two investigation techniques. Geophysics can indeed be first used in a short pilot study (exploration mode) to 1) test the feasibility of the methods and 2) determine the optimal locations of geological/geotechnical coring, hence reducing its cost. After ground proofing, geophysics can in a second stage be used in a more thorough manner to map the relevant properties, both laterally and vertically. Ideally, several geophysical methods should be combined as will be discussed later. Finally, both boreholes and geophysics can be re-used for monitoring of temporal parameter variations, with again the former measurements for calibration and the latter for spatial extent. However, geophysics is far to be systematically used. The limitations of most ancient geophysical methods to adequately investigate a 3D structure, and the problem of linking the measured geophysical parameters to geotechnical properties have probably made many geotechnical engineers reluctant to use geophysical methods. We will come back to that issue in a later discussion.

The geophysical methods to apply depend on their adequacy to the problem to solve and on four controlling factors, which have to be thoroughly considered before any field experiment (Mc Cann and Foster, 1990). The first controlling factor is the existence of a geophysical contrast. The presence of a geological, hydrological or mechanical boundary (e.g., the limit of the sliding mass) does not necessarily imply a variation in terms of geophysical properties. The second issue is the characteristics of the geophysical method itself, namely the penetration depth and the resolution. There is usually a trade-off between resolution and penetration: the deeper the penetration, the poorer the resolution. These limits have to be accounted for during the design of a geophysical survey. Finally, the performance of geophysical techniques is strongly dependent on the signal-to-noise ratio. Landslide material can be highly disturbed and consequently lead to electrical current injection difficulties or strong seismic wave attenuation (hence the need for preliminary tests as indicated earlier).

Through specific processing, geophysical methods provide the distribution of a physical parameter at depth at one given surface location (1D), along a line (2D) or for a grid (3D). 1D information corresponds to a curve function of depth, while 2D and 3D information are geophysical images (vertical sections or cubes). The relevant parameters are obtained through an inversion process, i.e., extraction of the searched parameters from measurements assuming a known model between data and parameters (Menke, 1989). Geophysical inversion (e.g., tomography) has dramatically developed during the last twenty years and has the major advantage to give continuous information of the studied body. But inversion is often a complex and nonlinear mathematical problem and image interpretation has to be done with a

critical mind, considering the already mentioned drawbacks of geophysical techniques and additional limits linked to the inversion process. The necessary condition an image (model) has to fulfil is to explain the data, i.e., the forward modelling of the inverted parameters give results close enough to the data (the so-called data fit). This is usually assessed by a misfit error (RMS) which has to be systematically provided with the image (always ask for that!). However, even if the RMS value is low (e.g., 5% or less), the obtained image may only be one of many solutions explaining the data due to, e.g., the limited measurement coverage and to errors on the data (signal-to-noise ratio). Depending on the inversion technique, different strategies exist to address this problem of non-uniqueness: tests of inversions considering different starting models for sensitivity analyses, introduction of a-priori information (may come from other geophysical results or geological/geotechnical information) in the inversion to constrain the solution, and - ideally - joint inversion of several geophysical data sets. The second issue is the image smoothness caused by most of the inversion techniques used in geophysical tomography, resulting in an inability to detect sharp layer interfaces. New techniques for solving this problem are emerging, using a priori information (Wisén et al., 2005), regularization for favouring sharp boundaries in the inversion process (Zhdanov, 2002) or image processing tools such as crest lines extraction process in gradient images (Nguyen et al., 2005). Finally, most of the existing images are 2D, while a landslide is a 3D phenomenon. 2D images of 3D structures may be affected by strong artefacts which are very hard to detect. A judicious strategy to tackle this problem, i.e., when 3D acquisition is not possible, is to perform 2D and 3D forward modelling to evaluate the robustness and reliability of the obtained image.

After these very general considerations about geophysics and the requirements for landslide assessment, we follow Jongmans and Garambois (2007) to list the most actual geophysical approaches fitting for landslides, reproducing here their review table (Table 14) which relates methods, geophysical parameters, geology, landslide types and applications through several field examples.

*Table 14 (bellow) : Synthesis of geophysical methods used for landslide investigation.  $V_p$  and  $V_s$ : P-wave and S-wave seismic velocity;  $\rho$ : electrical resistivity;  $V$ : electrical potential;  $\epsilon$ : electrical permittivity;  $\gamma$ : density;  $\alpha$ : average slope gradient. The maximum penetration depth is indicated in brackets. From Jongmans and Garambois (2007).*

Method	Parameter information	Geological context	Landslide type	Application	Authors
Seismic reflection	Vp, Vs, 2D vertical sections	Soft sediments (sand to clay)	Earth slide-debris flow ( $\alpha=25^\circ$ )	Geological boundary (80 m)	Bichler <i>et al.</i> (2004)
	Vp, Vs, 2D vertical sections	Gypsum, shale and sandstone	Complex active slide ( $\alpha=10^\circ$ )	Slip surface (50 m) within a gypsum layer	Bruno and Marillier (2000)
	Vp, Vs, 2D vertical sections	Poeylitic rocks, gneiss	Rockslide ( $\alpha=25^\circ$ )	Internal geometry (layering, faults)	Ferrucci <i>et al.</i> (2007)
	Vp, Vs	Weathered marls and limestones	Active complex slide ( $\alpha=1^\circ$ )	Slip surface (3 m)	Glade <i>et al.</i> (2005)
Seismic tomography	Vp, Vs	Limestone, shale and debris	Active rock fall-debris slides	Relief of the bedrock (30 m) and internal structure	Mauritsch <i>et al.</i> (2000)
	Vp, Vs	Black marls	Complex mudslide ( $\alpha=26^\circ$ )	Basal slip surface (9 m)	Carris and Van Asch (1991)
	Vp, 2D vertical sections	Shale	Translational rockslide (vertical cliff)	Geometry of the slide (5-10 m)	Jongmans <i>et al.</i> (2000)
	Vp, 2D vertical sections	Micaschists	Rock slide ( $\alpha=32^\circ$ )	Characterisation of the slide material – lateral boundary	Méhic <i>et al.</i> (2005)
Seismic noise measurements (HVV method)	Vs, 1D vertical profile	Varioloured clays	Complex earth slide-flow ( $\alpha=9^\circ-10^\circ$ )	Thickness of slide (30 m), disk-valued material	Laperina <i>et al.</i> (2005)
	Vs, 1D vertical profile	Black marls	Complex mudslide ( $\alpha=25^\circ$ )	Failure surface (35 m)	Méhic <i>et al.</i> (2006)
	Vs, 1D vertical profile	Varved clays	Translational slide ( $\alpha=10^\circ$ )	Slip surface (27-37 m) and bedrock depths (33-62 m)	Méhic <i>et al.</i> (2006)
	$\rho$ , 1D vertical profile	Clayey arenitic rock	Composite soil-rock slump ( $\alpha=6^\circ$ )	Slip surface (100 m)	Agnesi (2005)
Vertical electrical sounding (VES)	$\rho$ , 1D vertical profile	Black marls	Complex mudslide ( $\alpha=25^\circ$ )	Slip surface and bedrock depths (15 m)	Schmutz <i>et al.</i> (2000)
	$\rho$ , 1D vertical profile	Black marls	Complex mudslide ( $\alpha=25^\circ$ )	Bedrock depth (1.5 m)	Carris and Van Asch (1991)
	$\rho$ , 2D vertical section	Limestone to shale	Rock slide ( $\alpha=22^\circ$ )	Slip surface depth (10 m)	Batayneh and Al-Diabati (2002)
	$\rho$ , 2D vertical section	Soft sediments (sand to clay)	Earth slide-debris flow ( $\alpha=25^\circ$ )	Geological boundary and slip surface depth	Bichler <i>et al.</i> (2004)
Electrical tomography	$\rho$ , 2D vertical section	Alluvia, debris on gneissic rock	Large rockslide ( $\alpha=40^\circ$ )	3D slip surface geometry and water flows	Lebourg <i>et al.</i> (2005)
	$\rho$ , 2D vertical section	Clay and sand	Multiple earth slide ( $\alpha=8^\circ$ )	Geological boundary and slip surface depth	Derouilly <i>et al.</i> (2003)
	$\rho$ , 2D vertical section	Varioloured clays	Complex earth slide-flow ( $\alpha=8^\circ-10^\circ$ )	Slip surface depth (30 m)	Laperina <i>et al.</i> (2005)
	$\rho$ , 2D vertical section	Arenite and clay	Complex earth slide-flow ( $\alpha=10^\circ$ )	Slip surface depth (20 m)	Havenith <i>et al.</i> (2000)
Spontaneous Potential (SP)	$\rho$ , 2D vertical section	Micaschists	Large rockslide	Lateral boundaries and thickness of the rockslide (100 m)	Méhic <i>et al.</i> (2005)
	$\rho$ , 2D vertical section	Clayey sand over crystalline rock		Slip surface depth	Wissen <i>et al.</i> (2003)
	V, 1D horiz. profile and 2D map	Gypsum, shale and sandstone	Complex active slide ( $\alpha=10^\circ$ )	Upward flow of water on the landslide	Bruno (2000)
	V, 1D horiz. profile and 2D map	Varioloured clays	Complex earth slide-flow ( $\alpha=9^\circ-10^\circ$ )	Landslide boundary, and water flows	Laperina <i>et al.</i> (2005)
Electromagnetism (EM31 or TEM)	$\rho$ , 1D horiz. profile and 2D map	Gypsum, shale and sandstone	Complex active slide ( $\alpha=10^\circ$ )	Lateral boundary of the slide	Bruno and Marillier (2000)
	$\rho$ , 1D horiz. profile and 2D map	Micaschists	Large rockslide	Lateral boundary of the slide	Méhic <i>et al.</i> (2005)
	$\rho$ , 1D horiz. profile and 2D map	Black marls	Complex mudslide ( $\alpha=25^\circ$ )	Slip surface and bedrock depths (15 m)	Schmutz <i>et al.</i> (2000)
	$\rho$ , 1D horiz. profile and 2D map	Limestone and shale, debris	Active rock fall-debris slides	Location of saturated areas	Mauritsch <i>et al.</i> (2000)
Ground penetrating Radar (GPR)	$\rho$ , 1D horiz. profile and 2D map	Black marls	Complex mudslide ( $\alpha=26^\circ$ )	Differences in water content	Carris and Van Asch (1991)
	$\rho$ , 2D vertical sections	Soft sediments (sand to clay)	Earth slide-debris flow ( $\alpha=25^\circ$ )	Geological boundary and slip surface depth	Bichler <i>et al.</i> (2004)
	$\rho$ , 2D vertical sections	Limestone	Rock slide	Geometry of the moving mass (5m)	Petrilli <i>et al.</i> (1999)
	$\rho$ , 2D vertical sections	Limestone	Rock slide	Location of fractures (15 m)	Jeanin <i>et al.</i> (2007)
Borehole radar	$\rho$ , 1D Horiz. profile and 2D map	Gneiss		Location of fractures (49 m)	Willenberg <i>et al.</i> (2004)
	$\rho$ , 1D Horiz. profile and 2D map	Flysch		Hollow in bedrock near headscarp	Del Gaudio <i>et al.</i> (2001)

## 1.2. METHODS

Though there is a wide range of methods in ground-based/near-surface geophysics, the scope of the present document does not allow an extended overview and we will therefore concentrate on a few key techniques, specifically used for landslide investigations and mainly following Jongmans and Garambois' review (2007). For more detailed information, we refer to key comprehensive books about near-surface geophysics (e.g., Reynolds, 1997; Butler, 2005), or practical and shorter guides for a quicker/easier reading (e.g., Milsom, 2003). We also highly recommend to check the very good web site of the Swiss Geophysical Commission (see references) and the Code of Practice of Applied Geophysics published by the French AGAP association (1992; see references). These two organisms do not deal only with landslide applications and do list many more geophysical methods, giving both thorough information about the principles and practical guidelines for good practice in the field.

To help non-geophysicist readers of the present report evaluating the use of geophysics for landslides, we will first very briefly review the principles of each selected method, discussing then their applications, advantages and limits with respect to landslide assessment and monitoring. A very few examples were selected here to illustrate some applications of geophysics for landslides and for a more detailed analysis of some landslide-related case studies we refer – again - to Jongmans and Garambois (2007). For a first general and simple overview of geophysical methods, we reproduce below a table from the manuals of the US Army Corps of Engineers (1995 and 2001; Table 15). This table shows that near-surface geophysicists try to measure a wide range of ground parameters. We will see in the following that each method studies a specific type of physical parameters, e.g., elastic properties, resistivity, etc.

Table 15 : Measurements and applications in an engineering context of geophysical methods (US Army Corps of Engineers, 2001).

Method	Basic Measurement	Application	Advantages	Limitations
Seismic				
Reflection seismic	Travel time of compressional waves (P-waves) between layers	Mapping of subsurface of compressional waves through subsurface. Especially useful for mapping interfaces and depths to subsurface of fluid-saturated layers	Depth, geometry, and velocity of compressional waves. Information necessary for understanding subsurface structure and composition	Requires use of high-frequency seismic waves. The resolution is limited by frequency. Interpretation is subjective
Refraction seismic	Travel time of compressional waves (P-waves) from subsurface layers	Mapping of subsurface of compressional waves. Depth, geometry, and velocity of compressional waves	Depth, geometry, and velocity of compressional waves. Information necessary for understanding subsurface structure and composition	Requires use of high-frequency seismic waves. The resolution is limited by frequency. Interpretation is subjective
Highly wave dispersion	Travel time and period of surface seismic waves	Information of shear wave velocity in near-surface materials	Depth, geometry, and velocity of compressional waves. Information necessary for understanding subsurface structure and composition	Requires use of high-frequency seismic waves. The resolution is limited by frequency. Interpretation is subjective
Shear wave tomography	Travel time or wavelength of surface seismic waves	Information of shear wave velocity in near-surface materials	Depth, geometry, and velocity of compressional waves. Information necessary for understanding subsurface structure and composition	Requires use of high-frequency seismic waves. The resolution is limited by frequency. Interpretation is subjective
Reflection seismic (passive seismic)	Travel time of compressional waves (P-waves) and surface seismic waves (S-waves) of reflected signal	Mapping of subsurface of compressional waves. Depth, geometry, and velocity of compressional waves. Information necessary for understanding subsurface structure and composition	Depth, geometry, and velocity of compressional waves. Information necessary for understanding subsurface structure and composition	Requires use of high-frequency seismic waves. The resolution is limited by frequency. Interpretation is subjective
Shear wave tomography	Travel time and period of surface seismic waves	Information of shear wave velocity in near-surface materials	Depth, geometry, and velocity of compressional waves. Information necessary for understanding subsurface structure and composition	Requires use of high-frequency seismic waves. The resolution is limited by frequency. Interpretation is subjective
Acoustic tomography	Travel time and period of surface seismic waves	Information of shear wave velocity in near-surface materials	Depth, geometry, and velocity of compressional waves. Information necessary for understanding subsurface structure and composition	Requires use of high-frequency seismic waves. The resolution is limited by frequency. Interpretation is subjective
Ground Penetrating Radar	Travel time and amplitude of reflected signal	Mapping of subsurface of compressional waves. Depth, geometry, and velocity of compressional waves. Information necessary for understanding subsurface structure and composition	Depth, geometry, and velocity of compressional waves. Information necessary for understanding subsurface structure and composition	Requires use of high-frequency seismic waves. The resolution is limited by frequency. Interpretation is subjective
Gravity	Vertical acceleration field	Mapping of subsurface of compressional waves. Depth, geometry, and velocity of compressional waves. Information necessary for understanding subsurface structure and composition	Depth, geometry, and velocity of compressional waves. Information necessary for understanding subsurface structure and composition	Requires use of high-frequency seismic waves. The resolution is limited by frequency. Interpretation is subjective
Magnetic	Vertical acceleration field	Mapping of subsurface of compressional waves. Depth, geometry, and velocity of compressional waves. Information necessary for understanding subsurface structure and composition	Depth, geometry, and velocity of compressional waves. Information necessary for understanding subsurface structure and composition	Requires use of high-frequency seismic waves. The resolution is limited by frequency. Interpretation is subjective

### 1.2.1. Seismic methods

Seismic methods used elastic waves propagating in solid or liquid media; note that sound waves are elastic waves propagating in the air. Seismic waves correspond to small elastic (i.e., non-permanent) displacements. They can be generated by active sources, e.g., sledge hammer, explosives, and vibrators, or by passive sources, e.g., earthquakes, rockfalls, ocean waves, etc. Receivers are called geophones (hydrophones in water) and may contain on land up to 3 components (3C; orthogonal system with one vertical and 2 horizontal components), though vertical geophones are most used. Seismic waves are grouped in two major categories: body waves and surface waves (Figure 98).



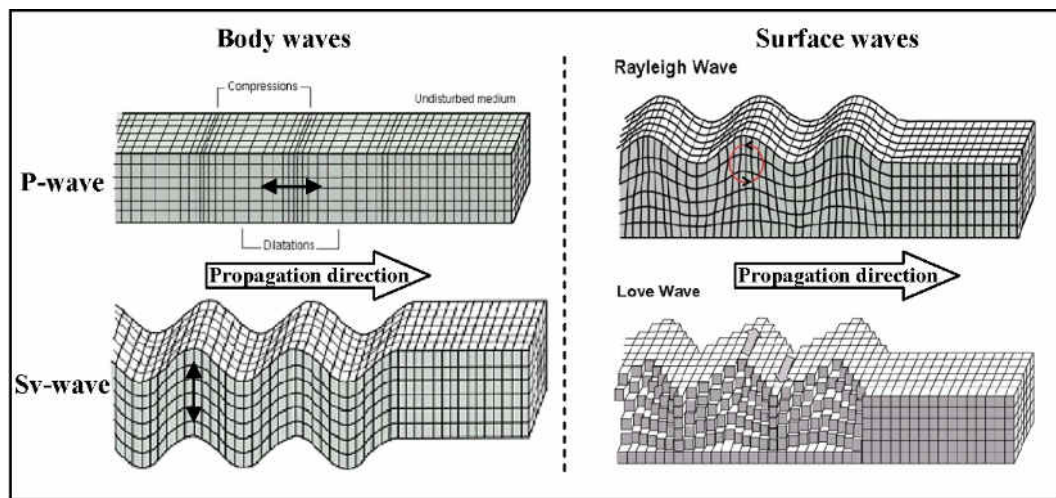


Figure 98 : Elastic waves used in seismic methods. Left) Body waves (adapted from Bolt, 1982): P-waves (top) shake the ground along the propagation direction (black arrow), while S-waves (bottom) shake transverse to that direction (black arrow; here SV-wave illustrated). Right) Surface waves (Wikipedia): two types of surface waves are illustrated: Rayleigh waves (top) and Love waves (below). Their vibration pattern is more complex than for body waves (see arrows on figures).

Body waves are waves passing through layers and are either compressional waves (P-wave; P standing historically for “primary” because the fastest of the body waves) or shear waves (S-wave; S standing historically for “secondary” because slower than P-waves). P-waves vibrate along the direction of propagation while S-waves vibrate perpendicular to that direction. S-waves are often decomposed in 2 components, i.e., an SV-wave (V for vertical) with a vibration in the vertical plane, and an SH-wave (H for horizontal) with a vibration in the horizontal plane, though this is a simplification not really valid in complex 3D media. Ideally, a user of seismic methods should indeed record seismic wavefields with 3C geophones to record all wave modes but this is seldom done. The P-wave velocity is function of the compression (bulk) modulus,  $K$ , the shear modulus,  $G$ , and the density,  $\rho$ , while the S-wave velocity only depends on shear modulus and density, and is lower than the P-wave velocity. S-waves do not propagate in liquid media while P-waves do (acoustics). Examples of P- and S-wave velocities are given in Table 16. In seismics, resolution is defined as a fraction of the wavelength ( $1/4$  is commonly used), which is defined by velocity divided by frequency. Therefore low velocities (and/or high frequencies) contribute to better resolution. Note that the velocity of both body waves may be anisotropic, i.e., even in homogeneous media the velocity may depend of the wave direction due to, e.g., fine layering of a rock formation, fractures, etc. Though such effect is studied and used in other geophysical applications, the authors are not aware of much use of anisotropy in relation to landslide assessment. Dasios et al. (1999) explain 1) that S-waves can offer better vertical resolution than compressional waves due to their lower velocity; 2) they are little affected by changes in fluid saturation, in contrary to P-waves, and are thus more sensitive to lithology, making them more suitable for engineering purposes; and 3) S-waves are less absorbed than P-waves, at least in partially saturated sands, boulder clay and gas-saturated sediments. Though the use of P-waves is still largely dominating in near-surface geophysics, we will see successful examples using S-waves. As for optical laws, elastic body waves have different propagation modes: transmission with refraction (bending of the waves following Snell’s law) at discontinuities, reflection at the same discontinuities, and diffraction. Discontinuities generating reflection and refraction of seismic waves are due to a change in elastic impedance, often called  $Z=\rho V$ ,

which is the product of density  $\rho$  and velocity  $V$ . The reflected wave generated at a discontinuity between a layer of impedance  $Z_1$  and a layer of impedance  $Z_2$  has a strength function of the reflection coefficient  $R$  which is  $(Z_2 - Z_1)/(Z_1 + Z_2)$ . Note that such elastic discontinuities may not be related to geological changes (e.g., water table crossing geological layers) and changes in lithology may not produce impedance contrasts (Table 17). In such cases, other geophysical data, well logs and geological information may help identifying the structures imaged by seismic body waves.

Table 16 : P- and S-wave velocity, and density for soil and rock examples. Modified from Lavergne (1986).

Material	P-velocity $V_p$ (m/s)	S-velocity $V_s$ (m/s)	density $\rho$ (g/cm <sup>3</sup> )
soil	100-600	100-300	1.7-2.4
dry sands	200-1200	100-500	1.5-1.7
wet sands	1500-4000	400-1200	1.9-2.1
glacial maraine	1500-2700	200-700	1.9-2.7
clay	1000-2500	200-800	2.0-2.4
marl/shale	2000-4100	750-1500	2.0-2.7
gneiss	3500-7600	2200-3600	2.7-2.8
sandstone	1400-4500	1200-2800	2.1-2.4
limestone	2800-7000	2000-3300	2.4-2.7
chalk	2300-2600	1100-1300	1.8-2.3
rock salt	4000-5500	2500-3100	2.1-2.3
anhydrite	3500-5500	2200-3100	2.9-3.0
dolomite	2500-6500	1900-3600	2.5-2.9
granite	4500-6200	2500-3300	2.5-2.7
basalt	5000-6500	2800-3400	2.7-3.1
coal	2200-2700	1000-1400	1.3-1.8
ice	3400-4000	1700-1900	0.9
water	1450-1500	-	1.
air	315-350	-	0.001

*Table 17 : Examples of reflection coefficients for some soil and rock mass materials. Note that the reflection coefficient is given here in absolute values. It is however a signed-value, which is positive when the elastic impedance  $Z$  increases across the reflection boundary ( $Z_1 < Z_2$ ), while it is negative when  $Z$  decreases ( $Z_1 > Z_2$ ). From Hack (2000).*

Material	First medium		Second medium		Acoustic contrast	Reflection coefficient
	P-wave (m/s)	Density (kg/m <sup>3</sup> )	P-wave (m/s)	Density (kg/m <sup>3</sup> )	$\delta = Z_1/Z_2$	$R$
Fresh sandstone to fresh limestone	2000	2400	3000	2400	0.67	0.040
Fresh limestone to fresh sandstone	3000	2400	2000	2400	1.50	0.040
Highly weathered sandstone to slightly weathered sandstone	500	2200	1200	2400	0.38	0.20
Fresh sandstone to open discontinuity (air)	2000	2400	360	1.2	11111	0.999
Fresh sandstone to water	2000	2400	1500	1000	3.2	0.27
Clay to slightly weathered sandstone	400	1500	1200	2400	0.21	0.43
Granitic residual soil to fresh granite	600	2000	3500	2500	0.14	0.57
Dense sand to slightly weathered limestone	1000	1800	2500	2400	0.3	0.29

Surface waves travel along/near-to a surface, e.g., the earth's surface or at sea bottom. The amplitudes of surface waves decrease rapidly with depth and their velocities are smaller than S-wave velocities. In seismic exploration, all surface waves are usually referred as “ground roll”, i.e., a high-energy seismic noise a geophysicist wants to get rid of when interested in reflection and transmission of body waves. Though surface waves have proved of great use for a long time in other domains, such as in seismology or engineering, the last decade has seen a sudden increase in their play in near-surface application, including for landslides, as will be described later. More specific terms exist for surface waves, e.g., Rayleigh and Love waves as illustrated in Figure 98.

### 1.2.1.1. Active seismic

## SEISMIC REFRACTION

**Method:** This method is based on the interpretation of first-arrival traveltimes, which are picked (often manually) on seismic records, the resulting curves of traveltimes as function of distance being called hodochrons. A strong assumption in seismic refraction is that the velocity increases with depth. Figure 99 illustrates the path of the seismic waves of concern with source and receivers at the surface. The elastic waves of interest (P or S depending on the source and receiver type, though the use of P-waves is largely dominating) are propagating in a transmission mode, either directly through the top layer or as critically refracted, so-called headwave, recorded at the surface. The usual source for P-waves is a sledge hammer but explosives may be needed for deeper penetration. Shear-wave vibrators are also used but are not as portable as a sledge hammer and S-wave refraction is not that common. To take into account dipping layers with respect to the surface, a minimum of two source locations is needed, i.e., at a certain distance from each extremity of the recording array, the two resulting hodochrons being interpreted together (Figure 100).

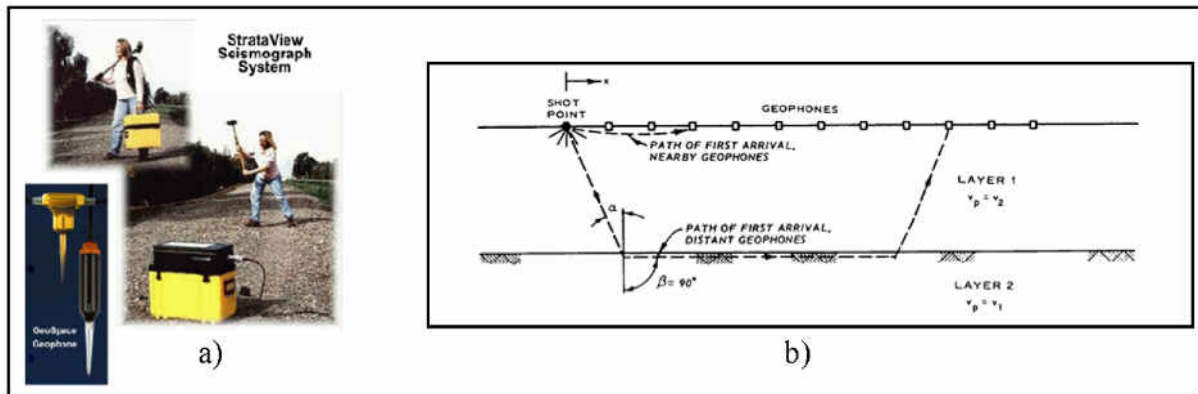


Figure 99 : Refraction seismic. a) acquisition (from [www.fugroinstruments.com](http://www.fugroinstruments.com)) and b) corresponding seismic wavepaths (figure taken from US Army Corps of Engineers, 1995).

**Applications:** Refraction seismic in its traditional form, i.e., processing and interpretation of picked first-arrival traveltimes to map “refractors” and estimate a mean velocity in the layers in between, is still widely used, especially to map clear elastic impedance contracts such as ground-water table and sediments/bedrock. The method has proved to be applicable for landslide investigation, as both P- and S-wave velocities are generally lower in the landslide body than in the unaffected ground below (critically-refracted wave generated at the contact). McCann and Forster (1990) document several case studies showing the use of seismic refraction for locating the undisturbed bedrock below landslides. In recent studies, travelttime data have been interpreted using delay methods (Kearey et al., 2002), like the plus-minus technique or the Generalized Reciprocal Method (GRM), which allow the mapping of an undulating refractor.

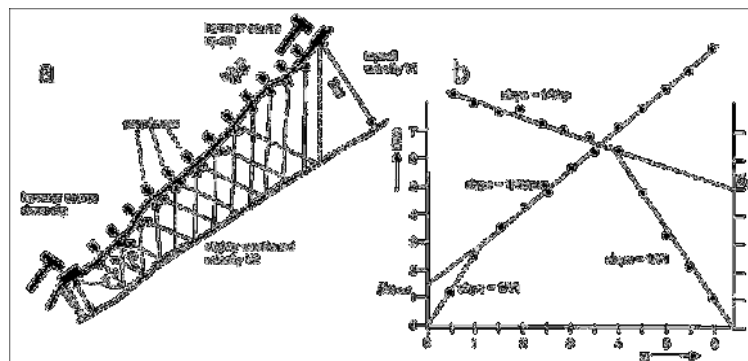


Figure 100 : Refraction seismic on a slope with interface non-parallel to the surface. Acquisition of a direct and reverse recording (a) with the corresponding hodochrons (b).

**Limits:** Refraction seismic requires an increase of elastic impedance with depth so it does not detect low-velocity layers. In the case studies analysed by Jongmans and Garambois (2007), the refraction method was limited to a penetration depth from a few meters to 30 meters. This shallow penetration depth results from the method itself, which requires a relatively long profile (3 to 5 times the penetration depth as a rule of thumb) and from the wave attenuation in the highly disturbed landslide material. Sledge hammer as a source is not sufficient for long profiles and explosives are necessary, but their use is not always allowed, especially on unstable slopes and sensitive sites (e.g., quick clays, see later).

## SEISMIC TOMOGRAPHY

**Method:** Seismic tomography uses first-arrival traveltimes (like refraction) from source to receivers in order to invert for the propagation velocity in 2D or 3D. It is therefore important to acquire as many source/receiver combinations as possible, i.e., with sources both along the recording array and outside on both sides, with different source-receiver distances to cover various depths. This method is not only used for ground-located sources and geophones, but may also be used in boreholes (cross-hole tomography) and in the ocean (air gun as sources, and ocean-bottom seismometers or hydrophones as receivers). The principle of tomography is as in medicine for human bodies: waves travelling across a media accumulate information about a certain parameter and by combining different source-receiver combinations and mapping back that parameter along certain trajectory (e.g., raypaths), an inversion procedure will provide a 2D section or a 3D cube. In seismic or traveltime tomography, traveltime measurements are used to map the velocity model. In a similar manner, we will see later that in resistivity tomography, apparent resistivities measured at the earth's surface are used to map actual resistivities in the ground. In contrary to standard refraction seismic, which maps discontinuities, tomography can compute more or less a smooth velocity model. Therefore, the two methods should be tried together in order to better constrain the resulting model with both clear discontinuities and smoothed velocity fields in between.

**Applications:** For landslide investigation, the technique was used in rock conditions (Jongmans et al., 2000; Méric et al., 2005) and showed a significant decrease of P-wave velocity values (division by at least a factor 2) in a slide-prone or unstable mass. Méric et al. (2005) performed a 300-m long seismic profile across the western limit of the large “Séchilienne” landslide (French Alps) affecting micaschists. Out of the unstable mass, the image showed a strong vertical variation of P-wave velocity, with values ranging from 500 m/s at the surface to 4000 m/s at 25 m depth (intact bedrock). The same profile also pinpointed a significant lateral velocity change from 4000 m/s to 2000 m/s delineating the landslide limit.

**Limits:** The main limits are the efforts (i.e., cost - money and time - and heavy logistics) required to acquire enough sources/receivers for a good coverage of the structures, laterally and vertically, and the rather smooth model finally obtained, though this is not a limit intrinsic to seismic but which will also be found in, e.g., resistivity mapping. Ideally, both P- and S-wave velocity should be mapped but S-sources of sufficient strength are not yet available for difficult ground conditions, though S-wave vibrators start to work well on easier grounds (see under seismic reflection).

## SHALLOW REFLECTION SEISMIC

**Method:** Reflection seismic deals specifically with reflected waves generated at elastic impedance contrasts (Figure 101). In contrary to seismic refraction and tomography, the whole recorded signal is considered but some wave modes and noise have to be removed prior to imaging structures with reflected waves only. Direct and refracted waves as well as surface waves are among the “seismic” noise to remove, even though they may be useful for

other methods. Reflection seismic is a key technique in oil and gas exploration which has greatly contributed to the development of equipments, numerous processing methods and software. The acquisition is usually carried out in a “roll-along” mode, i.e., the receiver lines are moved regularly after shooting at specific locations around them. This means in practice heavy field work though the quite recent use of streamers (geophones mounted at fixed intervals along a towed system with no need to plant them in the ground) does facilitate the acquisition. Though P-waves are mostly used for reflection seismic, S-waves surveys start to emerge, especially for SH-waves (source with vibration perpendicular to the acquisition line and horizontal geophones parallel to the vibration direction; e.g., Pugin et al., 2004).

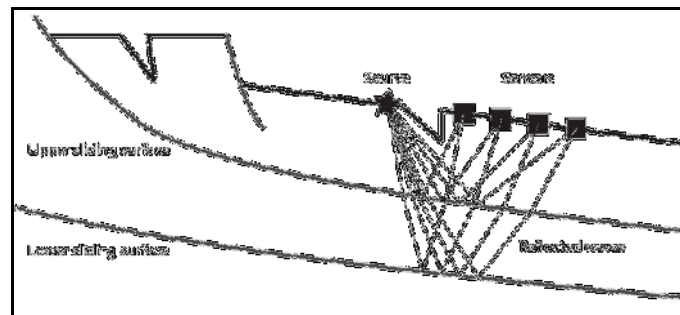


Figure 101 : Principles of seismic reflection acquired in Common Source Gather, imaging two sliding surfaces in a complex translational landslide (courtesy of C. Michoud).

**Applications:** High resolution seismic reflection has been seldom used for landslide investigation (Bruno and Marillier, 2000; Ferrucci et al., 2000; Bichler et al., 2004). The major interests of seismic reflection profiling are its potential for imaging the geometry of the landslide structure, such as the internal bedding or the rupture surface(s), and the robustness/diversity of processing tools compared to tomography. In a recent case study, Polom et al. (2010) describes SH-wave 2D profiling on ground in the harbour of Trondheim, Norway. The very high quality of the seismic profiles (Figure 102) with a 0.5-1.0 m resolution obtained down to 100-150 m (bedrock) is now helping geologists and geotechnicians detecting weak layers, already identified offshore, and assessing the risk for submarine slides which would significantly damage the harbour infrastructures and the nearby train station.

**Limits:** This method requires an even bigger effort to deploy the geophone layouts than seismic tomography, particularly in the conditions of rugged topography, making the acquisition time consuming and costly. The success of shallow seismic reflection requires a good signal-to-noise ratio and the recording of high frequency waves to reach the desired resolution. These two conditions may be difficult to fulfil on landslides where the ground is strongly disturbed and heterogeneous, affecting the geophone-soil coupling, attenuating the seismic waves and generating scattered waves; in such conditions 3D reflection seismic may be necessary for a proper imaging but the cost is often too high. In addition, the processing of these data really requires expert user and takes time.



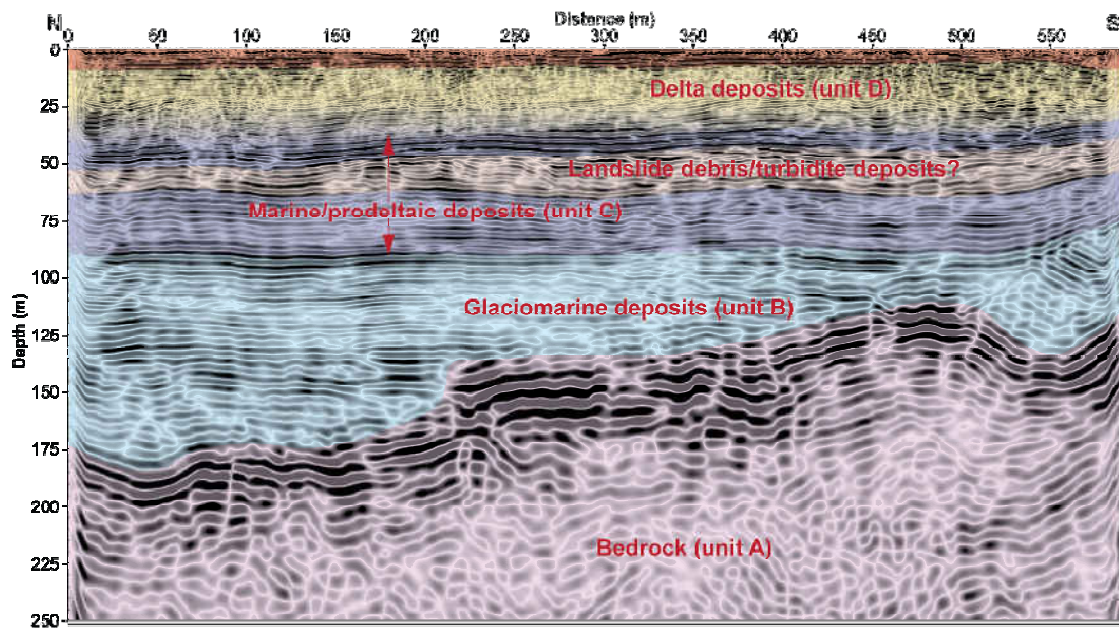


Figure 102 : SH-wave reflection profile (poststack depth migrated) with superimposed geological interpretation, Trondheim harbour, Norway. From Polom et al. (2010).

## SURFACE WAVES

**Method:** Surface waves may show appreciable dispersion in the presence of near-surface velocity layering, i.e., different frequencies of the seismic signal travel with different velocities, while dispersion of body waves is usually very small. During recent years, spectral analysis of surface waves (SASW) has received increasing attention in the geophysical community (Park et al., 1999; Socco and Jongmans, 2004), essentially because it offers a non-invasive means of evaluating the soil shear modulus at depth. In this approach, two or several seismic signals are analyzed in the Fourier domain to interpret phase differences related to Rayleigh-wave (Figure 98) dispersion effects into S-wave velocity variations in depth (vertical sounding). Later, additional developments were performed to use a multichannel recording system to improve signal-to-noise ratio by stacking signals without increasing acquisition times, leading to so-called multichannel analysis of surface waves, MASW (Park et al., 2001). The experiment consists of constructing a seismic antenna, composed of a seismic source and several sensors spaced regularly along the seismic line, then recording the soil particle velocity in time after the source has been activated. An integral transformation converts the time-domain waveform data into a phase velocity–frequency domain called the dispersion image (Figure 103). Because the resulting dispersion image is obtained from the stack of several phase-transformed signals recorded by the sensors, aliasing artefacts are reduced, increasing the resolution of the final image. Consequently, this improvement in resolution makes it possible to distinguish each separate propagation mode. Inverting dispersion properties into shear-wave velocity distributions is generally solved in the 1D approximation (Herrmann, 2002). Another extension of the method, developed by Xia et al. (1999), consists of obtaining a 2D S-wave velocity section through the shallowest layers (Lin and Chang, 2004; Grandjean, 2006) by interpolating contiguous 1D S-wave velocity vertical profiles.



**Applications:** A wide range of applications have demonstrated the use of this method, particularly for landslides studies (Grandjean and Bitri, 2006; Meric et al., 2007). When landslides are the places of highly heterogeneous materials, an adaptation of MASW can be proposed by extending the original method with a summation term, which sums over local dispersion images computed for different receiver windows gathers. This leads to the 2MASW (Multifold MASW) method tested by Grandjean and Bitri (2006) on the Super-Sauze landslide (Figure 103 and Figure 104).

**Limits:** Although MASW methods can provide robust results for imaging landslide structures, it suffers from some limitations. First, the method is based on 1D approximation (no lateral variations) so that 2D complex structures cannot be investigated correctly (Foti, 2000). In addition, the quality of dispersion diagrams are strongly related to the complexity of Rayleigh wave propagation; indeed, diffractions, multiple modes and all seismic patterns caused by sharp velocity variations lead to decrease in dispersion image quality, and thus the quality of inverted models. Regardless of the complexity of the velocity structure, the surface-wave inversion cannot be solved directly, requiring an optimization technique to find the most probable solution in a pool of infinite candidates. This technique can be a deterministic approach, random, or combination of both. The final solution is however not necessarily the exact one and it is highly recommended to display several solutions to better appreciate the sensitivity of the inversion.

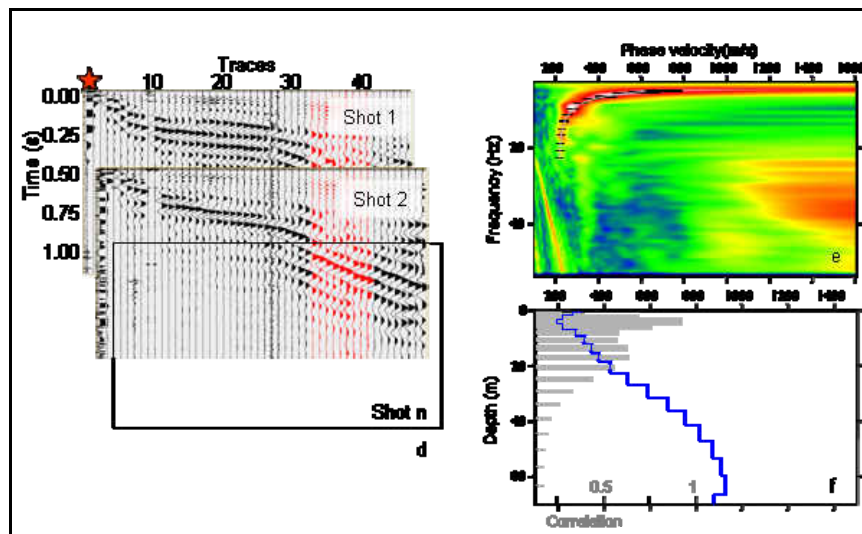


Figure 103 : a) seismic receiver-window gathers (left), dispersion image and resulting S-wave velocity model after inversion in blue and related correlation value in gray (right) indicating the reliability of this model.

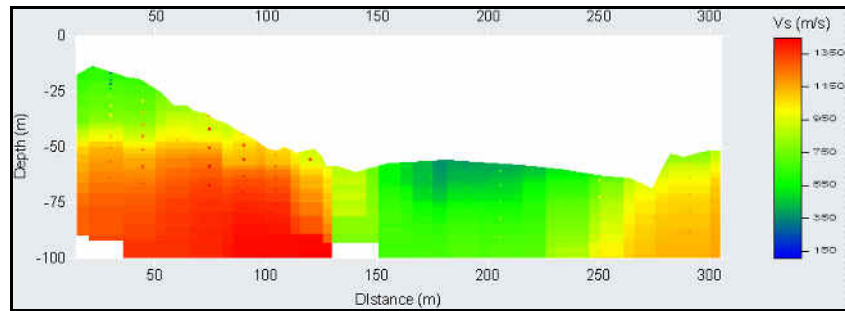


Figure 104 : S-wave velocity field across the Super-Sauze landslide (France) obtained by 2D interpolation of all S-wave velocity models estimated along the seismic section. The landslide appears in green (low velocity values), in the centre part of the section.

### 1.2.1.2. Passive seismic measurements

#### 1D AMBIENT- NOISE MEASUREMENT

**Method:** Passive seismic noise measurements are commonly used in earthquake engineering for determining the geometry and S-wave velocity values of soil layers overlying bedrock (Jongmans and Garambois, 2007). The single-station method (also called the H/V method, as short for Horizontal-to-Vertical spectral ratio method) consists in calculating the horizontal-to-vertical spectral ratio of noise records measured on 3C geophones and allows the resonance frequency of the soft layer to be determined (Nakamura, 1989). For a single homogeneous soft layer, this fundamental frequency is given by  $f = V_s/4h$  where  $V_s$  is the soft layer S-wave velocity and  $h$  is the layer thickness (Figure 105). Knowing an estimate of  $V_s$  allows the thickness of the soft layer to be calculated. The three main assumptions behind the method are that: 1) seismic noise is composed of surface waves; 2) the structure of the soil is 1D and; 3) the  $V_s$  contrast is large enough to generate a clear frequency peak.

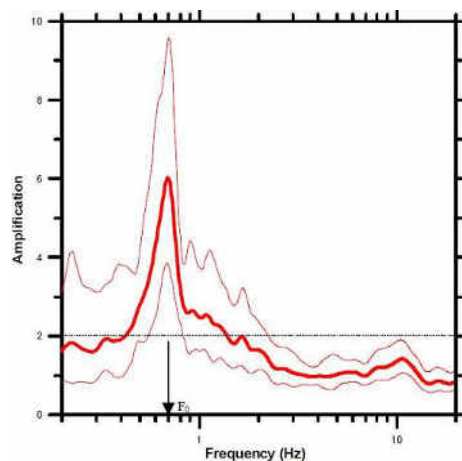


Figure 105 : H/V curve obtained in an elongated alluvial valley. The fundamental frequency of the site may be reliably estimated at 0.7 Hz. Figure from SESAME (2004).

**Applications:** As failure surfaces may generate S-wave velocity contrasts, the method can theoretically directly detect landslide sliding surfaces. It was used on three landslides affecting clayey or marly terrains in the Southern Apennines (Gallipoli et al., 2000) and in the French Alps (Méric et al., 2007). The fundamental frequency was derived from H/V curves

and used for deriving an estimate of the rupture surface depth. This easy-to-perform survey opens interesting perspectives for 3D investigation.

**Limits:** Difficulties appear in heterogeneous soils with strong 2D or 3D effects disturbing the propagation of surface waves (diffraction and diffusion effects) and if various frequencies can be picked due to the presence of unexpected layers or harmonic noise.

### 3D PASSIVE ARRAY

Seismic arrays can be installed near landslides to record local events (Figure 106). Rockfalls and micro-seismicity can be distinguished and classified from their signal characteristics. Triggered and continuous data can be used for this type of seismic monitoring. An example of a successful monitoring network installed since 2005 at Åknes, Norway, is presented in the case study n°12.

More complex techniques using seismic noise arrays instead of one receiver (as the H/V method) can be used to derive consistent S-wave velocity profiles versus depth on soil landslides (e.g., Renalier et al., 2010, in press). A dedicated chapter on acoustic and micro-seismic monitoring is presented in the section 2 of this part (p. 195).

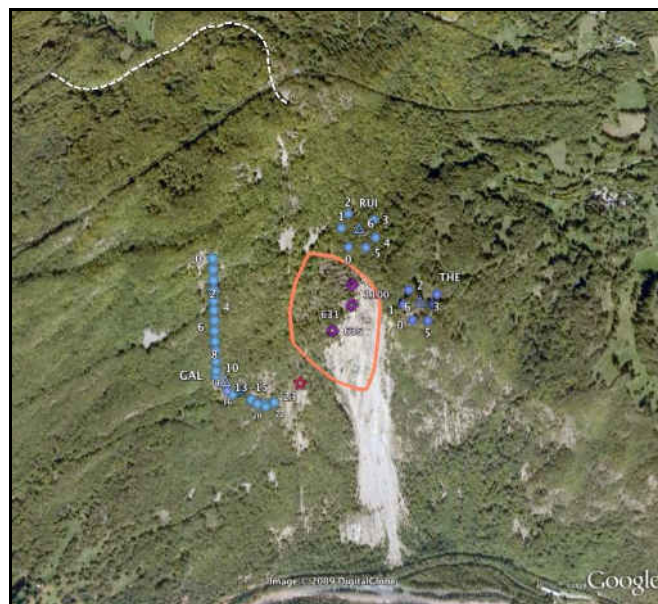


Figure 106 : The Séchilienne rockslide, in the French Alps, about 15 km south west of Grenoble is monitored by a seismic network: vertical sensors (circles) and 3-components seismometers (triangles). Also shown is the location of benchmarks of a displacement network (diamonds) within the most active zone contoured in orange. Figure from Helmstetter and Garambois (2010)

#### 1.2.2. Electrical methods

Electrical measurements are made at the surface of the Earth to investigate electrical resistivity (inverse of electrical conductivity) conditions in an area. The basic measuring equipment consists of two current electrodes and two measuring electrodes, a DC current source, and a measuring device. The two current electrodes are inserted in the ground and

between the electrodes, a DC potential is maintained that causes a DC current to flow through the ground. The resulting potential differences are measured at the surface. Anomalous conditions or heterogeneities within the ground, such as better or poorer conducting layers, are inferred from the fact that they deflect the current and distort the normal potentials. For vertical electric sounding (VES), the spacing between the electrodes is increased with regular steps while the centre of the array is fixed. For horizontal profiling, the array of potential electrodes and current electrodes is moved over the surface and electrical resistivity tomography (ERT) can be performed. ERT vertical profiles along 2D lines or ERT cubes (3D) can be obtained.

### 1.2.2.1. Resistivity

**Method:** The simplest approach to the theoretical study of current flow in the Earth is to consider the case of a completely homogeneous isotropic earth layer of uniform resistivity. The potential difference  $\Delta V$  across a layer of length  $l$  and resistance  $R$ , through which a current,  $I$ , is flowing is  $\Delta V = RI$  (Ohm's law). If we consider a homogeneous half space bounded by the ground surface and let a current of strength  $I$  enter at point  $C1$  on the ground surface, this current will flow away radially from the point of entry (Figure 107). By knowing the input current, the measured voltage  $\Delta V$  and the geometry of the electrode array, the resistance  $R$  can be calculated. The property of the electrical resistance of a material is usually expressed in terms of resistivity ( $\Omega m$ ) or its inverse, the conductivity (mS/m).

As a rule, the more porous or fissured a rock and the larger its ground water salinity, the higher is the conductivity, the lower the resistivity. There is no general correlation of the lithology with resistivity. Nevertheless, a broad classification is possible according to which clays and shales, sands and gravel, compact sandstones and limestones, and unaltered crystalline rocks stand in order of increasing resistivity. Figure 108 shows the approximate resistivity ranges of earth materials.

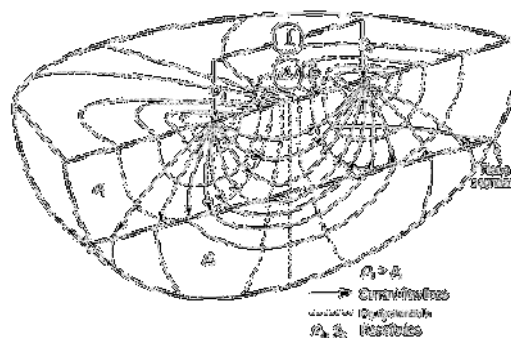


Figure 107 : Basic principle of electrical resistivity imaging. It is possible to determine earth resistivity  $\rho$  by driving a direct current  $I$  (DC signal) into the ground and measuring the resulting potentials (voltages) created in the earth. Figure from Knödel et al. (2007).

Standard resistivity systems use electrodes planted in the ground and linked together with electrical cables (Loke, 1999). Such an installation can be cumbersome on complex grounds but when everything is coupled, the measurements are automatic, in various electrode configuration modes (dipole-dipole, Wenner, Schlumberger, gradient, etc) chosen by the user at the electronic console. This may take a couple of hours depending of the size of the array

and the selected modes. In areas where grounded dipole measurements may be difficult (frozen ground, etc), an alternative system is a towed one working only in dipole-dipole mode and based on a capacitively-coupled resistivity meter. A coaxial-cable array with transmitter and receiver sections is pulled along the ground either by a single person or attached to an all-terrain vehicle. Such towed systems work best on resistive ground and for small-to-intermediate depths compare to traditional electrode-based system. Data collection is faster than with conventional DC resistivity, though a line must be repeated for increasing distances between emitter and receiver in order to increase the penetration depth. In a grid acquisition mode (several parallel lines) a quick surveying may give an idea of the lateral variability of the ground structures. It could be advantageously used in an exploration mode in order to pre-investigate a site and get a first idea of the resistivity and variability of ground structures. But conventional systems are best for reliable measurements.



Figure 108 : Electric resistivity tomography (ERT). a) Electrodes planted in the ground are linked together with electrical cables to an electronic console (courtesy of S. Bazin). b) An alternative system can be towed (picture from [www.geometrics.com](http://www.geometrics.com))

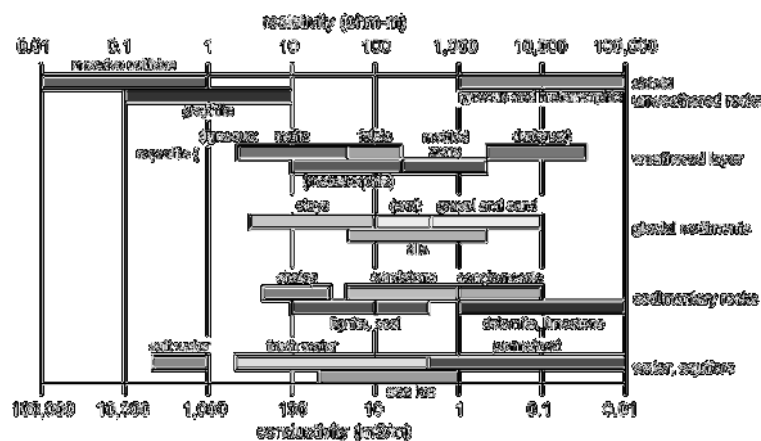


Figure 109 : Typical ranges of electrical resistivities of earth materials after Palacky (1987).



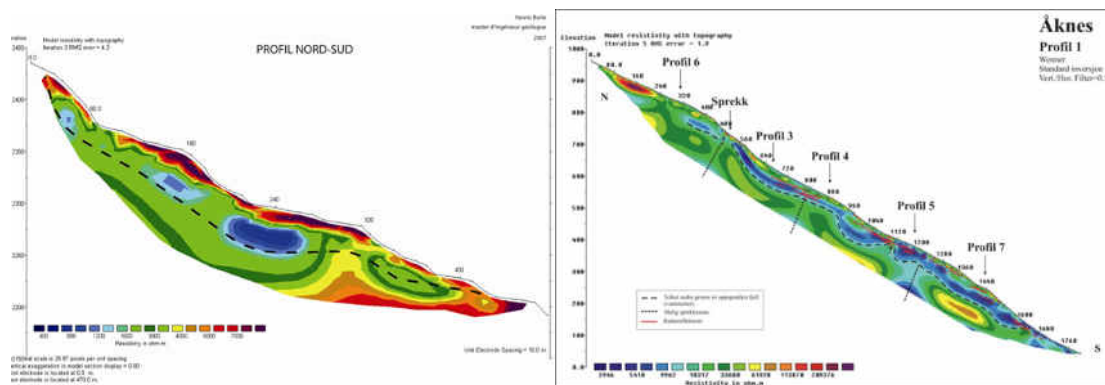


Figure 110 : Examples of ERT profiles in rock slide. Left) Alpine site; the potential sliding plan is in dashed line (Borle and Jaboyedoff, 2007). Right) Åknes site, Norway; the potential sliding plane is in dashed line and correspond to observed GPR reflectors (Rønning et al., 2007).

**Applications:** For landslide investigations, a typical application of ERT is the location of the sliding plan, identifying layers per resistivity contrast (Figure 110). We will also illustrate in the following the use of the resistivity method for 1) quick-clay mapping in Scandinavia and 2) landslide monitoring, this in addition to the detection of sliding plans illustrated above. Note that the use of resistivity tomography has exploded the last year, also for landslides, thanks to significant hardware and software developments, and many other case studies can be found (see, Jongmans and Garambois, 2007).

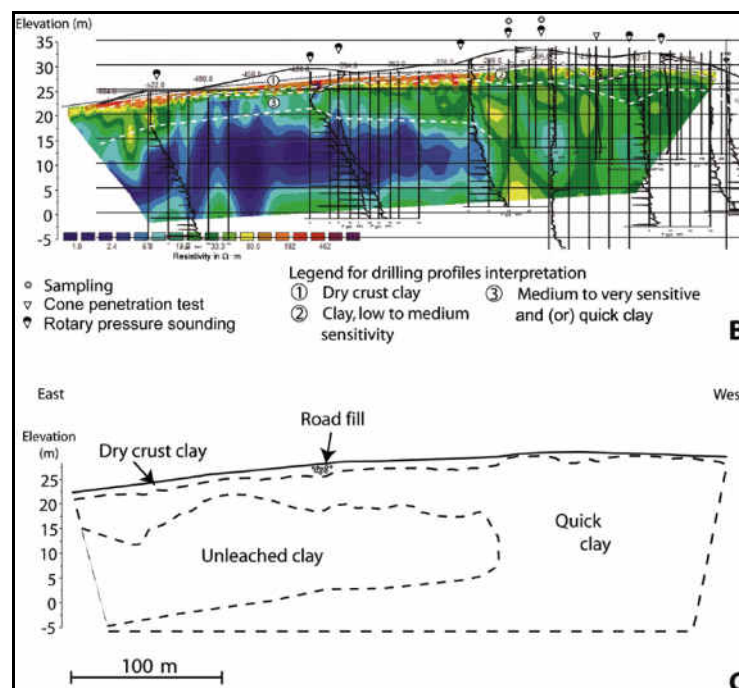


Figure 111 : (Top) 2D ERT profile, Buvika site, Norway, with superimposed geotechnical drilling results and (bottom) interpretation with respect to quick/unleached clay. (from Solberg et al., 2008).

**Quick-clay mapping:** Marine clays in Norway and in Sweden were deposited as the ice cap over Scandinavia retreated some 9000 years ago (Rankka et al., 2004). The clay particles were deposited in sea water creating an open-grain skeleton with high water content. As the isostatic upheaval progressed, the marine clays have been leached by rain water and fresh



groundwater. Pockets/layers of quick clay above/below unleached clay often occur. The bonds between the clay minerals decrease as the salt content decreases, causing a weaker grain structure; eventually the clay becomes unstable (quick). If the quick clay is disturbed, the grain structure collapses and the clay minerals float in their own pore water. Leaching reduces the salt content in the pore water (change in electrical properties). Resistivity measurements are thus very popular for discriminating between unleached and quick clay, though their use should always be controlled by geotechnical drilling at a few key locations due to large variability in salt content (Rankka et al., 2004; Solberg et al., 2008).

**Landslide monitoring:** Time-lapse resistivity imaging (4D ERT) can also show changes associated with seasonal temperature variation, moisture content and ground movement (Figure 112). Note that near-surface changes in resistivity caused by moisture content can be masked by temperature effects so the latter need to be monitored. In addition, initial electrode spacing can be modified by the ground movement and cause artefact in the modelled resistivity. Hence, the geometry of the monitoring system should also be monitored (Wilkinson et al., 2010).

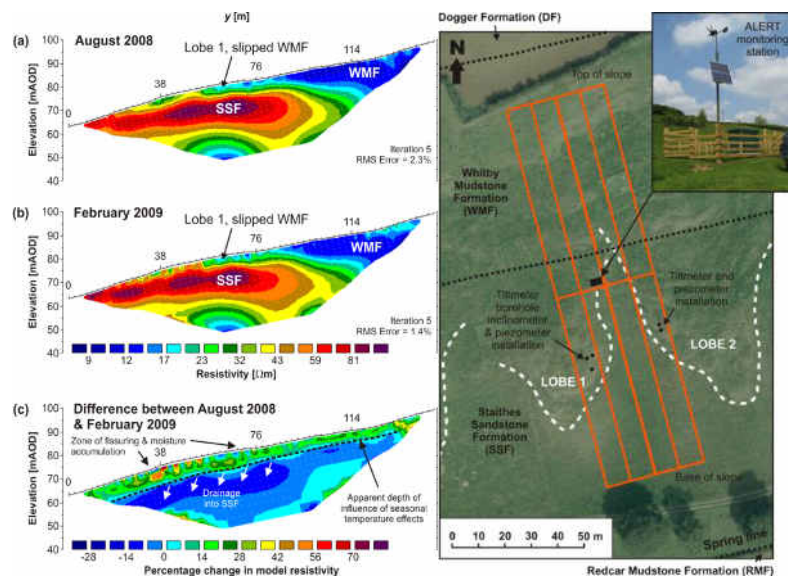


Figure 112 : Time-lapse resistivity results from ALERT monitoring system over an active landslide (Chambers et al., 2009;). a) August 2008, b) February 2009, and c) resulting differential resistivity images.

**Limits:** The smoothness constraint in 2D resistivity inversion needs to be stressed, as in seismics: it tends to “smear out” sharp boundaries such as the basement topography. It is also always difficult to foresee the resolution of a resistivity survey because it depends on several variables: signal-to-noise ratio, topography, resistivity contrast of the materials, electrode contact resistance, etc. Synthetic tests using the survey parameters/geometry are often necessary to illustrate the lateral resolution of a survey and should be provided with the results.

#### 1.2.2.2. Self Potential (SP)

**Method:** Self-Potential surveys are conducted by measuring natural electrical potential difference between pairs of electrodes connected to a high impedance voltmeter. These

natural fields represent the ground surface electric field signature of various charging mechanisms (electrokinetic, thermoelectric, electrochemical, cultural activity) occurring at depth. In absence of electrochemical processes and large telluric current, electrokinetic phenomena, describing the generation of electric fields by fluid flows, is the main source of the recorded electric field. Groundwater and associated flows contained in any landslide body play a major role in slope stability. The level of groundwater determines the supporting hydrostatic pressure, which, together with hydrodynamic pressure of seepage, are factors decreasing the landslide stability. Imaging water level and water flows within the subsurface at a large scale, as well as their fluctuations over time is a challenging problem, which resulted in specific research on hydrogeophysics (Rubin and Hubbard, 2005). Only few hydrogeophysical methods were applied on landslides, except those conducted with the Self-Potential method, which is easy to deploy and monitor.

**Applications:** Bruno and Marillier (2000) measured an SP profile on the “Boup” landslide and observed that high positive SP values (40 to 120 mV) coincide with the boundary between the stable ground and the landslide material and interpret them as the electrical signature of resurgent groundwater flow. Comparable large and stable-over-time positive SP anomalies (up to 350 mV) were acquired by Méric et al. (2005) across the “Séchilienne” landslide. Although they noted that the shape of the SP data was highly correlated with the displacement rate curve, the authors did not conclude whether the source of this anomaly was electrokinetically due to a deep main water flow nearly parallel to the surface or electrochemically due to the geological structure of the movement (fractures, lead-zinc and quartz veins). However, large time varying negative anomalies on the edge of the landslide were attributed to fluid flow variations within major faults and fractures.

Lapenna et al. (2003) presented two SP maps carried out at different climatic conditions on the “Giarossa” landslide. They assume the positive and negative anomalies within the landslide to be due to movements of underground water from the source zone to the accumulation zone within the landslide body. Further, SP changes over time were explained by the lowering of the water level inside the landslide body after the dry summer period. To be more quantitative, they also present SP tomography (Patella, 1997) showing lateral boundaries of the landslide as well as geological heterogeneities. Lapenna et al. (2005) also presented an SP map of the “Varco d’Izzo” landslide which they interpret qualitatively in term of water infiltration and charge accumulation in different zones of the landslide. In the future, increasing number of SP monitoring experiments using networks as well as improvements in numerical simulations and specific signal processing techniques (Gibert and Pessel, 2001; Sailhac and Marquis, 2001) should help understanding the acquired data and improve hydrological information within landslides.

**Limits:** The SP source ambiguity and the lack of quantitative interpretation on the fluid source (depth, extension) are the main limitations of the method, which is still poorly used on landslides.

### 1.2.2.3. Induced Polarization (IP)

**Method:** When a current applied to electrodes is switched off, the voltage between the potential electrodes does not drop to zero immediately (Figure 113). The ground thus acts as a capacitor and stores electrical charges, i.e., becomes electrically polarized. The measurement

of the decaying voltage over a certain time interval is known as time-domain Induced Polarization (IP) surveying (Keary et al., 2002). The measured parameter is the chargeability,  $M$ , defined as the normalized area  $A$  beneath the decay curve over a certain time interval. The IP phenomena occur particularly in presence of metallic (e.g. pyrite, magnetite, native metal, etc.), clay, some coals or graphite particles (US Army Corps of Engineers, 1995).

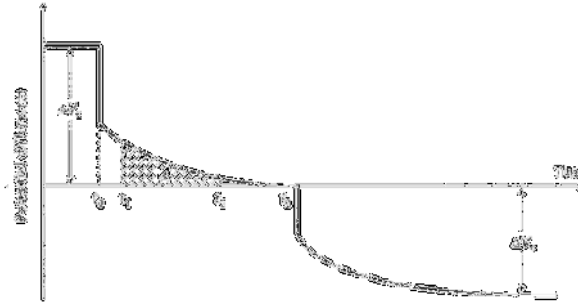


Figure 113 : The phenomenon of induced polarization. At time  $t_0$  the current is switched off and the measured potential difference, after an initial large drop, decays gradually to zero.  $A$  represents the normalized area under the decay curve for a time interval. Figure from Keary et al. (2002).

**Applications:** The IP method can be used to search for disseminated ores, clay minerals, pollution, and groundwater. Even if IP technique can sometimes be used in landslide investigations for specific purposes (Marescot et al., 2008), it is more confidential than resistivity or SP methods. But the IP signal is easily acquired when running resistivity measurements in the field so it is worth recording it as additional information.

**Limits:** IP measurements involve the monitoring of the decaying voltage after the current is switched off, but it cannot distinguish between two polarization effects: the membrane polarization (due to electrolytic flow in the pore fluid) and the electrode polarization (due to metallic minerals present in a rock). The signal-to-noise ratio of chargeability measurements is usually not as good as for resistivity measurements. Quantitative interpretation is considerably more complex than for the resistivity method. Much IP interpretation is only qualitative: simple parameters of the anomalies, such as sharpness, spatial distribution and amplitude may be used to estimate the location, lateral extend, dip and depth of the anomalous zone.

### 1.2.3. Electromagnetic methods

**Method:** Under electromagnetic methods, we consider here very-low frequency (from 800 Hz to 10 kHz) electromagnetic approaches working in a diffusion model in contrary to much higher frequency methods being in wave-propagation mode, as is the case for Ground Penetrating Radar (see next method). The low-frequency electromagnetic methods are based on the transmission of an electromagnetic field from a 'transmission coil' (Hack, 2000). This transmission field (the primary field) will cause a secondary induced field in the materials in the sub-surface. A 'receiver coil' receives the primary electromagnetic field together with the secondary field. The measuring equipment allows for comparison of amplitude and phase shift of the primary and secondary fields. The intensity of the secondary field depends on the conductivity of the materials in the sub-surface. The form of the coils and the distance between the coils depend on the frequencies used and the required depth of the investigation. This also allows for two types of investigation: vertical profiling or also called 'depth

sounding', and horizontal profiling, as in resistivity methods. In vertical profiling, the distance between the coils is increased with regular steps and consequently the received signal is more influenced by deeper buried materials. In horizontal profiling, the distance is kept constant but the whole array of coils is moved and at regular distances, measurements are made. As rule-of-thumb, the penetration depth is not more than about half the spacing between the coils. Vertical profiling or depth sounding can also be achieved by using different frequencies at the same location. Deeper buried materials will have less influence on higher frequency transmissions and vice versa. Low frequency EM surveys are very simple to do, fast, and the equipment is easy to operate. However, the method will virtually never be able to determine boundaries with enough accuracy as the resolution is low. Nonetheless the method works very well for, e.g., determining the extent of a (thick) clay-filled discontinuity in limestone or the presence of rock boulders in clay or sand.

**Applications:** As shown in Table 14, electromagnetic (EM) methods were recently used by several authors for landslide investigation, mainly for determining the geometrical limits of the unstable mass. Except the work of Schmutz et al. (2000) who used TEM (Transient Electromagnetic Method) jointly with VES, EM measurements (Méric et al., 2005; Bruno and Marillier, 2000; Mauritsch et al., 2000) were usually performed in the frequency domain with two horizontal loops and a ground conductivity meter (Geonics EM 34 or EM31). The method, which yields a single apparent electrical resistivity value, allows quick profiling or mapping (Reynolds, 1997). Penetration depth depends on the coil separation (10 m, 20 m or 40 m for the EM34) and ranges from a few meters to a few tens of meters. Méric et al. (2005) and Bruno and Marillier (2000) pointed out a significant variation of apparent resistivity at the limit between the landslide and the stable ground. In rock landslides, Bruno and Marillier (2000) and Mauritsch et al. (2000) interpreted electromagnetic data acquired with different modes and coil separations, assuming a two-layer model (moving mass above stable ground). They found a relatively good agreement between the bedrock depths derived from electromagnetic interpretation and seismic results.

**Limits:** All authors who applied EM methods for landslide investigations stressed out that the results had to be combined with other geophysical techniques for a proper interpretation.

#### 1.2.4. Ground Penetrating Radar

**Method:** Ground Penetrating Radar (GPR) uses electromagnetic waves reflected on discontinuities (dielectric contrasts) after emission from radar antennas positioned along the earth's surface. These discontinuities correspond to changes of electromagnetic impedance  $\eta = \mu c$  where  $\mu$  is the magnetic permeability and  $c = (1/\epsilon\mu)^{1/2}$  is the velocity of electromagnetic waves,  $\epsilon$  being the electric permittivity. It is rather similar in application and processing to seismic reflection using elastic waves reflected at elastic impedance ( $Z = \rho V$ ) contrasts. But in contrary to seismic where velocity  $V$  roughly increases with depth, the electromagnetic wave velocity  $c$  decreases in general with depth with the highest velocity being in the air (0.3 m/ns; Table 18). The frequency range in ground investigations is from 10 Mhz to 1000 MHz. As in seismic, the higher the frequency, the better the resolution, but the lower is the penetration depth. In addition, the penetration capacity is better in resistive materials (e.g., granite, dry sand, ice) than in conductive layers (e.g., clay, saturated soils) (Table 18). GPR measurements can also be carried out in boreholes and used in transmission mode for tomography as in seismic and resistivity.

*Table 18: Relative electric permittivity (called here dielectric constant), velocity and attenuation of electromagnetic waves in different material (From Hack, 2000). The relative electric permittivity is the ratio between the electric permittivity  $\epsilon$  of the considered material and the electric constant  $\epsilon_0$  (electric permittivity of vacuum).*

Material	Dielectric constant	Electric velocity (for frequency 100 MHz) (m/ns)	Attenuation (for frequency 100 MHz) (dB/m)
Air	1	0.3	0
Metal			Infinite
Fresh water	80	0.33	$2 \times 10^{-1}$
Seawater	80	0.01	0.1
Dry sand	3–5	0.15	0.01
Wet sand	20–30	0.06	0.03–3
Limestone	4–8	0.12	0.4–1
Clay	5–40	0.06	1.0–300
Granite	4–6	0.13	0.01–1
Rock salt	5–6	0.13	0.01–1
Shale	5–15	0.09	1.0–100

GPR is a very popular method in near-surface geophysics, as seen during the last 10-15 years, and is widely used by geoscientists thanks to light and portable equipments and the “easy” processing. Beside the considerable development of equipment and software, GPR is popular because of its high resolution (from a few cm to a few m, depending the soil and antennas), its depth of penetration in resistive materials (e.g., ice on glaciers), and its sensitivity to electromagnetic contrasts, especially due to water content. In conventional systems, both the emitting and receiving antennas are moved keeping a fixed distance (offset) between them, this in a profiling mode (Figure 114). Though this acquisition mode allows the quick visualization on field of ground reflectors and diffractors, the intrinsic lack of velocity information prevents proper depth conversion (users usually assumes a mean velocity of 0.1 m/ns to get a rough estimate of depth on field, or use diffractors - if any - to estimate an equivalent velocity). It is therefore highly recommended to acquire a few Common Mid-Point (CMP) gathers at key locations, a technique inherited from seismic acquisition/processing and assuming locally horizontal reflectors. This is done by moving away emitter and receiver from a given location, thus increasing the offset step by step. In GPR, the lower the frequency is, the longer the antennas are (Figure 114a), which may complicate the acquisition on difficult terrain (steep, rough, etc) as the whole antenna surface should be lying on the ground. A more recent development is the use of towed systems which greatly facilitates the acquisition in such cases (Figure 114b). Though such systems may not be as good as conventional ones, their easiness and very fast use is a must, e.g., for landslide investigations.

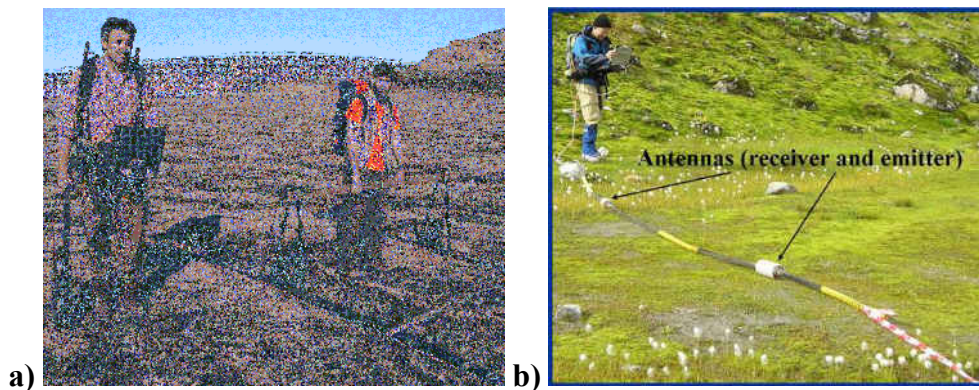


Figure 114 : GPR technology: a) Standard GPR system with a 25 MHz antenna (Svalbard; picture courtesy Geological Survey of Norway); b) towed system with a 50 MHz antenna (4 m offset) (Lecomte et al., 2008).

**Applications:** For rockslide, GPR is particularly useful due to its high resolution (down to a few cm) associated to a deep penetration (several tens of m) when using low frequencies (below 50 MHz). It allows detecting interfaces, such as sliding surfaces, or groundwater table. GPR measurements are also sensitive to fracture properties (filling, aperture). Applications of heavy field GPR investigations in near 3D mode have recently emerged (Maurer et al., 2010; Randa rock slide) and should be followed. The use of towed systems may also largely contribute to more use of GPR on difficult ground (e.g., Lecomte et al., 2008). The use of GPR for time monitoring (4D) of landslides has not yet been documented.

**Limits:** Severe limitations decrease the potential of GPR for landslide investigations, as attested by the very low number of applications in this field (Jongmans and Garambois, 2007). First, GPR utilization in soil slide is limited, due to the classic presence of clay materials and water saturated layers which absorb electromagnetic energy. This is the case for, e.g., quick-clay site investigations in Norway and Sweden, though using GPR first may still be good practice to delimit the clay zones. Second, the high level of diffractions in complex 3D structures such as rock slides may yield poor imaging, though proper processing similar to those used for reflection seismic could probably help. In comparison to seismic, a major drawback of GPR surveys is also the lack of reliable velocity information to constrain the scattering structures in depth as the acquisition is performed in a constant-offset mode, i.e., with fixed distance between emitter and receiver. Without CMP information at different locations, a proper velocity models cannot be derived and only rough estimates are obtained by searching for diffractions patterns to determine mean velocities. Whenever possible, CMP gathers should therefore be acquired.

### 1.2.5. Gravimetry

**Method:** Measuring microgravimetry (range: from 1 to 10  $\mu$ gal) allows to investigate on mass anomalies (US Army Corps of Engineers, 1995). A picture of a microgravimeter is presented in Figure 115.



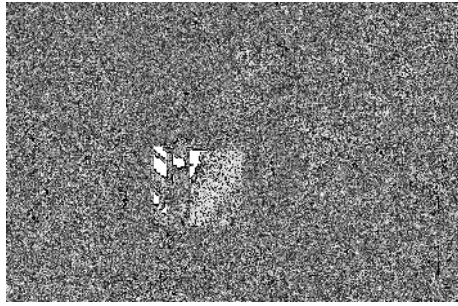


Figure 115 : A high precision gravimeter (picture taken from Seigel, 1995).

**Applications:** Regarding landslides, microgravimetric campaigns are indicated in two situations where a sufficient density contrast may exist (Jongmans and Garambois, 2007): 1) when the sliding surface is located at the interface between two very different materials (e.g., top of the bedrock for an earth slide); and 2) when the sliding mass is very disturbed comparing to the in-place material. The light instrumentation presents big advantages in these circumstances to study landslide geometry, led by fast campaigns requiring less effort on the field than seismic or electric works (Jongmans and Garambois, 2007). A dense coverage can be acquired and gravimetric anomalies generated by sufficient density contrast are detected (at least a few tenths of  $\text{g/cm}^3$ ). This condition is fulfilled when the surface failure coincides with the bedrock top or when the landslide reduces the compactness and therefore density of the moving mass. Del Gaudio et al. (2000) underlined that together with the support of limited other subsurface data (mechanical, geophysical, DTM), gravimetric surveys are able to provide useful information for slope stability analysis: 1) estimation of landslide body thickness and density contrasts between the moving and stable mass and, 2) location and geometry of heterogeneities within the moving mass. Bláha et al. (1998) also claimed that gravimetric surveys provided an effective contribution to the description of the structures (deformation, particular blocks, zones under tensile stress) and their dynamic control over time (by gravimetric monitoring).

**Limits:** As noted by del Gaudio et al. (2000), the use of gravimetric surveys in slope stability investigations is rather uncommon, mainly due to the long and difficult data processing and to the strong non-uniqueness of interpretation (Reynolds, 1997). The major problem is separating anomalies of interest from the overlapping effects of other features. In the example of the “Senerchia” slump-earthflow (Southern Apennines), del Gaudio et al. (2000) performed two microgravimetric surveys in order to evaluate the potential of gravimetry to detect possible spatial-temporal density variations observed at surface. They showed that this method was able to provide information on lithological heterogeneities that may control the dynamic of landslide enlargement, if borehole measurements are available. The surveys did not show enough sensitivity to detect any temporal density changes.

#### 1.2.6. Borehole geophysics

**Method:** Though the present guidelines mostly intends to cover non-intrusive geophysical techniques, when boreholes are first planned in a site investigation, it is highly recommended to design them for geophysical logging as well if the cost allows it (boreholes could also be used for various tomographies, e.g., seismic, resistivity and GPR). All physical parameters measured by the geophysical methods mentioned earlier can thus be measured in details as function of depth and later linked to surface-related measurements. The main advantage of

borehole geophysics with regards to surface geophysics is the constant and detailed resolution versus depth.

**Applications:** The literature about borehole geophysics for landslides is not extensive, probably due to the cost of the borehole in the 1st place. But a few examples of various geophysical logs, combined with geological and hydrological ones, can be found in Rønning et al. (2006) and Ganerød et al. (2008) at the Åknes rockslide site in Norway.

**Limits:** Borehole measurements are obtained at a much finer vertical scale (a few cm) than surface-based measurements and the retrieved parameters of the two approaches may be difficult to relate to each other. A careful upscaling of the borehole data may therefore be needed for a proper comparison, as well as calibration, with the surface-related data. In addition to the scale issue, such measurements are very local and may not be representative of the main structures. Ideally, the locations of boreholes should be planned according to preliminary surface-based investigation to secure a proper sampling of the geological structures of interest.

### 1.3. DISCUSSION

Jongmans and Garambois (2007) showed that geophysical prospecting is applied on various types of landslides for slope varying from a few degrees (earth slide) to vertical (rock fall) (Table 15). The penetration depth of the surveys may range from a few to several hundreds of meters and the targets of the surveys are often two. The dominant one is the location of the vertical and lateral boundaries of the slip mass (failure surface). An additional and wished target is the mapping of the internal structure of the landslide. Four main different situations can occur. In the first case, geophysical contrasts are due to lithological changes (layering, tectonic contact or pre-slide weathering) and the failure surface mainly coincides with a geological interface or layer. In the second case, geophysical contrasts are also controlled by lithological variations, but the failure surface cuts the structure in a more complex way and may be or not deduced from the geophysical image, depending on the landslide velocity, the heterogeneity of the material and the resolution of the technique. Exceptionally (third situation), the failure surface (or potential failure) is directly detected, mainly by propagation methods (Petinelli et al., 1996; Bichler et al., 2004; Willenberg et al., 2004; Jeannin et al., 2005). In the fourth case, the landslide develops in a globally homogeneous layer and alters its characteristics. The geophysical contrast then arises between the slide and the unaffected mass from the cumulative or separate action of the mechanical dislocation, the weathering and an increase of water content (Caris and van Asch, 1991; Bruno and Marillier, 2000; Schmutz et al., 2000; Méric et al., 2005; Lapenna et al., 2005; Lebourg et al., 2005). The second target of geophysical prospecting is the detection of water within the slip mass, for which electrical (Bruno and Marillier, 2000; Lebourg et al., 2005; Lapenna et al., 2005) and electromagnetic (Caris and van Asch, 1991; Mauritsch et al., 2000) methods were most applied.

A landslide category not highlighted before is the one of debris flows (and other flows of rock or soil) if we follow Cruden and Varnes (1996), as done in the present project. Among the large variety of debris flows, we will briefly mention here the use of geophysics for those generated by glacial hazards, e.g., so-called Glacial Lake Outburst Flows (GLOFs), due to their potentially huge threat to population and infrastructures (Reynolds, 1992). The most devastating events happened so far in the Himalaya and in Peru; to give an order, over 32 000

people were killed by glacially-related sliding phenomena in Peru during the 20th century (e.g., 1941: about 7000 people died in one event in Cordillera Blanca). However, global warming with glacier melting/retreat may pose problems elsewhere (Alpes, Caucasus, etc). In such cases, it is not possible to investigate the “slide” part itself as it comes brutally but the source of such debris flows may correspond to zones where geophysics can bring lots of information (Reynolds, 2006). Several flood scenarios are possible in glacial hazards with, e.g., the presence of lakes at the front end of glaciers and dammed by moraines, etc. A very recent example (summer 2010) is a large pocket of melt water, blocked by frozen channels, detected by GPR measurements and others, and located under a glacier in French Alpes near the Mont Blanc; if the ice roof collapses in the water pocket (happened in 1892), a huge flood wave will rush down the valley carrying lots of boulders and soil, and destroying everything on its way to the city of St Gervais. Mitigation of this huge risk is underway but without detection by geophysics, such risk prevention would not have been possible. While GPR was used here to detect the pocket, repeating such measurements over time (monitoring) would also permit to follow the development of the water pocket. GPR is a very favourable technique on glacier and frozen grounds (e.g., permafrost) because ice is a very resistive material in contrary to water. For the same reasons, resistivity methods may be very useful too. In a joint interpretation (if not inversion), the contrasts detected by GPR complete nicely the smooth resistivity structures as imaged by electrical tomography in such cases (Lecomte et al., 2008).

The design of a geophysical survey for landslide recognition is still a much debated question and no unique strategy came out from Jongmans and Garambois (2007), especially considering the wide range of landslide types around the world. In such heterogeneous structures, the combination of different geophysical techniques anyway appeared as a necessary condition for obtaining reliable results (e.g., geophysical investigations at Åknes, Norway, as reported by Rønning et al., 2006, 2007). The choice of the techniques is clearly guided by the expected contrasts in physical parameters. Other parameters, like the required penetration depth, as well as the volume and the morphology of the landslide, may also have a significant effect on the survey strategy, including for economical reasons. The major difficulty of applying geophysical techniques to landslides is probably the complex relationship between the measured geophysical parameters and the desired geotechnical and hydrogeological properties, which prevents from giving a straightforward interpretation in terms of engineering properties. In other domains, several attempts were made, e.g., in engineering geology, to derive soil or rock properties from geophysical measurements, using experimental relationships. In soils, correlations were developed between the small-strain shear wave velocity ( $V_s$ ) and penetration resistance from CPT, mainly in geotechnical earthquake engineering. Recently, Ghose (2004) proposed a model-based integration of seismic and CPT data to derive soil parameters for sandy material. In rocks, most of the geophysical studies were aimed at characterizing the rock quality or fracturing (e.g., GPR techniques to determine the fracture geometry). Apart from radar imaging, seismic methods play a more and more important role in characterizing rock sites for geotechnical purpose. As an example, a relationship between S-wave velocity and the Rock Mass Rating, which is a geotechnical factor used for tunnel design, was recently proposed by Barton (2006) and Cha et al. (2006). In landslide investigation, similar relationships, linking for instance geophysical parameters to the displacement rate (Méric et al., 2005) should be studied more deeply. Beside geotechnical parameters, assessing hydrogeological properties from geophysical data is a necessity and outstanding results have been obtained in recent years in a new

interdisciplinary field (hydrogeophysics), combining the integration of multiple sources of data and the development of comprehensive petrophysical models. The application of these methods allows hydrogeological parameters of the subsurface, like porosity, water content, and hydraulic conductivity to be estimated from high-resolution fluid-sensitive geophysical data (seismic, electrical, electromagnetic): a recent state-of-the-art can be found in Rubin and Hubbard (2005). Both experimental relationships and quantitative approaches should be developed in the future for landslide investigations, incorporating under-used techniques, such as spontaneous potential and induced polarization, and including numerical modelling, data inversion and fusion.

## **1.4. CONCLUSIONS**

Areas affected by landslides usually exhibit dramatic spatial and temporal variations of lithological and hydrogeological conditions. The development of 2D, and very recently 3D, geophysical imaging techniques has been a first major advance forward for investigating the complex structure of landslide areas. A second one will be the installation of permanent arrays of geophysical sensors as a part of monitoring systems of landslides. Such geophysical time-lapse surveys have recently been initiated on some landslides (Supper and Romer, 2003; Lebourg et al., 2005), mainly with a multi-electrode electrical array. Coupled with high resolution remote-sensing techniques (Van Westen, 2004) and SP monitoring systems for hydrological purposes (Méric et al., 2006), these permanent geophysical imaging systems give a new insight into the 4D deformation mechanism of a landslide. However, geophysical techniques may suffer severe drawbacks, as listed earlier, and they need to be combined and calibrated against geological and geotechnical data to give reliable information. The complexity of landslides also requires using a combination of different geophysical techniques. Geophysicists have to make an effort in the presentation and discussion of their results. Resolution and penetration issues are not systematically discussed in an understandable manner and the geological/geotechnical interpretation of geophysical data should be more clearly and critically explained. Lack of communication and explanation in early multi-disciplinary projects (not only for landslides) may partly explain the reluctance of the engineering community to use geophysical techniques. It will be a challenge for geophysicists in the following years to convince geologists and engineers that 3D and 4D geophysical imaging techniques can be valuable tools for both investigating and monitoring landslides. Finally, efforts should also be done towards more quantitative information from geophysics in term of geotechnical parameters and hydrological properties.

## **2. ACOUSTIC AND MICRO-SEISMIC MONITORING**

### **2.1. INTRODUCTION**

#### **2.1.1. Definitions: Acoustic Emission (AE) and micro-seismic monitoring**

The macroscopic deformation of rocks, debris and soils, at scales ranging from laboratory samples (cm) to hillslopes and earth crust (hm to km), is associated with local irreversible processes (cracks/faults propagation and shearing, crack/fissure opening, material friction along discontinuities, etc). These movements involve propagation of acoustic waves which can be observed by remote sensing. Passive seismic monitoring during strain progression can help our understanding of mass movement behaviour and lead to the recognition of possible failure precursors. Although of significant potential, this observational tool has had only

limited application in the analysis geohazards such as glaciers, volcanoes, and mass movements such as landslides, rockfalls and debris flows.

Recording “seismic noise” consist in using seismic sensors (e.g. seismometers, geophones, accelerometers, acoustic emission transducers, hydrophones) to monitor passively potential events, also called “Acoustic Emission (AE)” events. The extent of the investigated area varies from some centimetres to thousands of kilometres, depending on (1) the magnitude and depth of the events, (2) the possible attenuation of the waves by the material, and (3) the type of seismic devices and the design of the seismic array. In the case of natural events, seismic noise monitoring may provide information on the characteristics of regional earthquakes to small material instabilities observed within a local slope failure.

AE is generated by an event source which converts localised stress accumulation of elastic energy into the release and the propagation of elastic waves that are transmitted within a material. AE sources may characterize several types of material behaviours such as failure, friction, shearing and sliding, crack propagation, impact, and cavitation processes. For the monitoring of geohazards, AE is also referred to as “micro-seismicity” or “rock noise”.

To understand the failure processes and to search for precursory patterns to material failure, the micro-seismicity tool has been extensively used at laboratory rock sample scale (Lockner, 1993) and at an intermediate scale between the laboratory scale and the large tectonic earthquake for studies of seismicity and rock burst in mines or tunnels (Obert, 1977; Nicholson, 1992). Most of these research activities have been conducted following the initial ideas of Obert et al. (1941; 1942; 1945a; 1945b; 1957) who have studied sub-audible noise associated to mining activities. Later, Goodman et al. (1965) and Cadman et al. (1967) demonstrated from field acquisitions and laboratory experiments that rock and earth slopes generate possible forerunners of acceleration by emitting acoustic signals. These sub-audible noises can be detected over distances of several tens of meters in hard rocks but are attenuated below detectable level into less than 30m in soft rocks and soils. These results suggested that installing arrays of conventional seismic geophones on the ground surface near the most active parts of mass movements should provide information about their geometry and dynamic. A few application of micro-seismic monitoring for slope stability are related either to open mines and quarries (Hardy et al., 1991; Kennedy et al., 1971). Concerning natural mass movements, some rare experiments have been carried out mainly in rocky cliffs (Kolesnikov et al., 2003, Amitrano et al., 2004; Willenberg et al., 2004, Eberhardt et al., 2004; Amitrano et al., 2005). The micro-seismic monitoring technique has also been used for the monitoring and the warning of debris flows (Arratano, 1999; Itakura et al., 2005). In the last case, the amplitude of seismic noise appears to be correlated to the volume and velocity of the debris flow and can be used to trigger an alarm or a video recording (Lavigne et al., 2000). For mass movements developed in soft rocks and deforming continuously (such as mudslides), the high attenuation of the material generally avoids the use of micro-seismic monitoring. Some authors have overcome this difficulty by using passive or active waveguides (Novosad et al., 1977; Dixon et al., 1996; Kousteni et al., 1999; Dixon et al., 2003). The passive waveguide is used to provide a shorter path for transmitting the elastic waves directly to the sensor, whereas the active waveguide generates AE signals by deforming itself within the moving mass (as the principle of vertical inclinometers). The system of waveguide allows using the micro-seismic monitoring technique even for very attenuating material such as clayey soils.

### 2.1.2. Objective and structure of the state-of-the-art

This section of deliverable D.4.1 aims at presenting a current state-of-art on passive seismic applications carried out to monitor and characterize mass-movements. In order to illustrate this state-of-the-art, a synthesis of the more recent applications of seismic noise monitoring, among probably many others, is summarized in Table 19. It illustrates AE monitoring applications for all types of mass movements (falls, slides, flows) and for several types of objectives (e.g. observation and characterization of the AE signals in terms of amplitude, frequency, duration and magnitude, to more advanced analyses of AE signals spatial localization). Nowadays, most of the research activities in micro-seismic monitoring of mass movements are to develop pattern recognition analysis tools, characterization of the sources of the AE signals and correlation of the signals to internal and external triggers (earthquake, rainfall).

The state-of-the-art is organized by presenting successively the different methodologies of AE monitoring that have been introduced chronologically by different authors.

While first applications of AE monitoring aimed at detecting and identifying the temporal and frequency domain of event sources, progress is nowadays carried out towards providing more details on the dynamics and mechanisms of mass movements (source event localisation and characterisation). With time, long-term monitoring (LTM) of AE aims at developing forecasting tools based on pattern recognition techniques for mass-movement early warning systems.

*Table 19 (bellow) : AE signals monitoring used on unstable slopes during the last 20 years (non-exhaustive list). The colours indicates the different types of geological material (successively from white to dark grey: ice, rock, debris, and soil materials) and the numbers indicated in the 3<sup>rd</sup> column ("category of study") correspond to the hereafter sections of the state-of-the-art.*



References	Geohazard type	Objective of the monitoring / investigation	Seismic acquisition device and other monitoring equipment used for the analysis
Rouse <i>et al.</i> , 1991a; 1991b	Landslide	Catalogue, rain correlation	Accelerometer
Weichert <i>et al.</i> , 1994	Mine failing, rockslide	Landslide dynamics, comparison from earthquake	passive seismic monitoring
Harp <i>et al.</i> , 1995	Landslide	Landslide dynamics, response to earthquake	3C strong-motion accelerometers, extensometers, piezometers
Dixon <i>et al.</i> , 1996	Landslide, cliff collapse	Landslide dynamics, event occurrence, displacement	AH transducers, wave-guide, inclinometers
Kishimura <i>et al.</i> , 1997	Snow avalanche	Snow avalanche characteristics	seismometers, video camera
Zlatev <i>et al.</i> , 1998	Landslide	Landslide mechanism, waves polarisation	local network for earthquake monitoring
Arattano, 1999	Debris flow	Debris flow characteristics, velocity, occurrence	seismometers
Surinrach <i>et al.</i> , 2000	Snow avalanche	Snow avalanche characteristics	3C geophones, video camera
Surva <i>et al.</i> , 2000	Debris flow	Debris flow characteristics, peak discharge, volume	seismometers
Brotscholl <i>et al.</i> , 2000	Pyroclastic flow	Lahar characterization, temporal localisation	broadband seismometers
Surinrach, 2001	Snow avalanche	Snow avalanche characteristics, size, signal phases	3C seismic stations
Marchi <i>et al.</i> , 2002	Debris flow	Debris flow characteristics, volume, velocity, discharge	seismic detectors, sonic sensors, video-camera, velocimeters
Kolesnikov <i>et al.</i> , 2003	Landslide	Landslide mechanism, waves polarisation, source direction	3C broadband seismometers
Brotsky <i>et al.</i> , 2003	Volcanic landslide	Landslide mechanism, rheology	teleseismic and regional seismic records
Uuang <i>et al.</i> , 2004	Debris flow	Catalogue	hydrophone
La Rossa <i>et al.</i> , 2004	Volcanic landslide	Landslide mechanism, polarisation, failure force	broadband and short-period seismic station
Amitrano <i>et al.</i> , 2005	Rockfall, cliff collapse	Landslide mechanism, occurrence of AE signals before collapse	geophones, accelerometers
Arattano <i>et al.</i> , 2005	Debris flow	Debris flow characteristics, front velocity	seismic sensors, geophones, sonic sensors (hydrograph), video-camera
Surinrach <i>et al.</i> , 2005	Landslide	Landslide catalogues, automatic detections	different types of 3C seismometers (spectrogram)
Stuart <i>et al.</i> , 2005	Ice glacier	Glacier dynamics, catalogue, location of AE signals	array of 1C geophones and accelerometers
Ge, 2005	Mining activity	Quarry activity, catalogue, location of AE signals	sensors arrays
Roth <i>et al.</i> , 2005	Rockslide	Landslide characteristics, catalogue	mini-arrays
Brückl <i>et al.</i> , 2006	Rockslide	Landslide characteristics, catalogue	3C seismometers (and broadband) (spectrogram)
Shibani, 2006	Rockslide	Landslide mechanism, direction of the sources	AH sensors, WI-AD wave-guide
Esposito <i>et al.</i> , 2006	Volcanic landslide	Landslide characteristics, automatic discrimination	3C broadband seismometers network (spectrogram)
Wüst-Bloch <i>et al.</i> , 2006	Sinkhole	Landslide characteristics, catalogue	SNRs (spectrogram)
de Angelis <i>et al.</i> , 2007	Pyroclastic flow	Lahar characteristics, catalogue	3C broadband network and 2 short-period 1C (spectrogram), aerial pictures
Bessiam <i>et al.</i> , 2007	Rockfall, debris flow	Rockfall and debris flow characteristics, automatic detection, catalogue	seismometer and 3C accelerometers
Cole <i>et al.</i> , 2008	Lahar	Lahar dynamics, rheology	3C seismometers
Mério <i>et al.</i> , 2007	Landslide	Landslide characterization, internal structure	3C seismometers

References	Geohazard types	Objective of the monitoring activity	Seismic acquisition device and other monitoring equipment used for the analysis
Ambrano <i>et al.</i> , 2007	Landslide	Landslide dynamics, frequency band identification, rain correlation	3C broadband seismometer (spectrogram), extensometer
Unggel <i>et al.</i> , 2007	Volcanic lee-rock slide	Landslide dynamics	short-period seismometer network (spectrogram), space and airborne
Spillmann <i>et al.</i> , 2007	Rockslide	Landslide dynamics, location of sources, automatic detection	3C geophones (spectrogram)
Yang <i>et al.</i> , 2007	Mining activity	Landslide dynamics, location of sources, occurrence	3C seismometers
Wang <i>et al.</i> , 2007	Mining activity	Landslide dynamics, location of sources, occurrence	1C geophones
Mourot, 2008	Rockfall	Landslide mechanism, processes before collapse	1C geophones
Walter <i>et al.</i> , 2008	Landslide	Landslide characteristics, catalogue, rain correlation	Mini-arrays of SNs (3C seismometers, 1C seismometers), spectrogram
Suwa <i>et al.</i> , 2008	Quarry exploitation	Landslide characteristics, occurrence of events before collapse	1C geophones
Deparis <i>et al.</i> , 2008	Rockslide	Landslide mechanism, catalogue, waves polarisation, events phase	Signalp seismological network
Zimmer <i>et al.</i> , 2008	Rockslide	Landslide characteristics, catalogue	geophone and accelerometer
Walter <i>et al.</i> , 2009a	Landslide	Landslide characteristics, catalogue	Mini-arrays of SNs (3C seismometers, 1C seismometers), spectrogram, UAV-based remote-sensing
Walter <i>et al.</i> , 2009b	Landslide	Landslide characteristics, catalogue, location of sources	Mini-arrays of SNs (3C seismometers, 1C seismometers), spectrogram
Helmstaedt, 2009	Rockslide	Landslide characteristics, catalogue, location of sources, rain correlation	1C and 3C seismometers network (spectrogram)
Borini <i>et al.</i> , 2009	Debris flow	Debris flow characteristics, catalogue, location of sources, rain correlation	broadband seismometers, spectrogram, meteorological data
Zobin <i>et al.</i> , 2009	Lahar, pyroclastic flow	Lahar characteristics, catalogue	broadband seismometers
Cole <i>et al.</i> , 2009	Lahar	Lahar characteristics, catalogue	3C broadband seismometer (spectrogram)
Senfaute <i>et al.</i> , 2009	Rockfall, cliff collapse	Landslide mechanism, processes before collapse	geophones, accelerometers

## 2.2. THE PIONEERING PERIOD – IDENTIFICATION OF AE SIGNALS AND LIMITATIONS OF THE TECHNIQUE

### 2.2.1. Identification of AE signals

The first information that can be obtained from AE signals properly acquired is the amplitude, the duration and the frequency content of the plotted signals considered as events. First studies by Obert in the 1940s, and Goodman and Cadman in the 1960s highlighted the variations of signals in the temporal and frequency domains with the load and the induced response within a rocky slide (Figure 116).

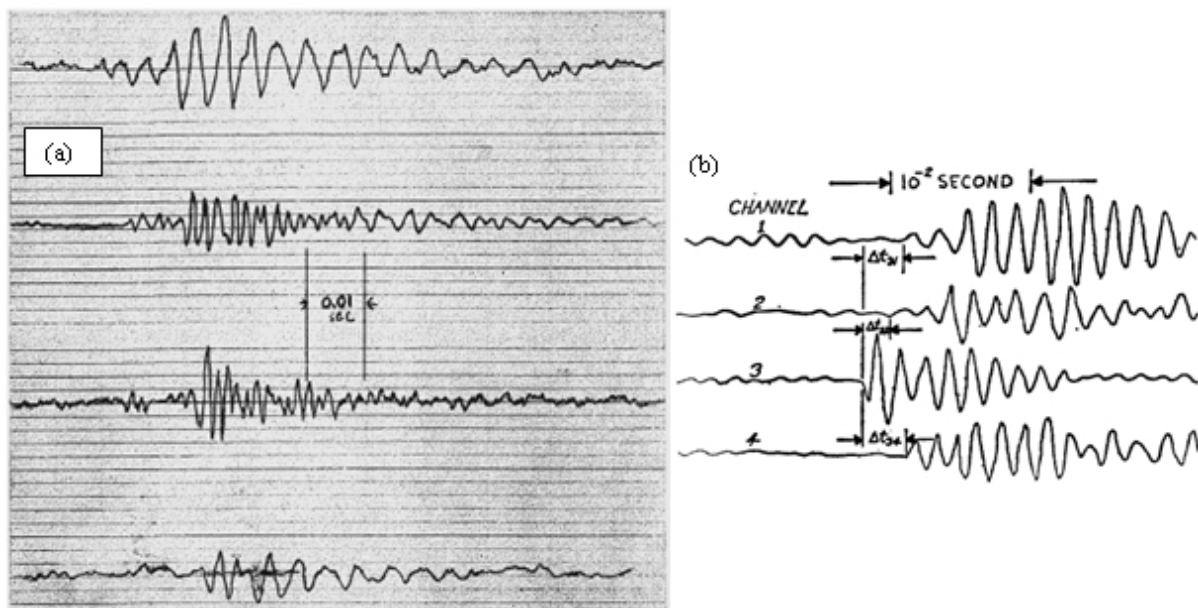


Figure 116 : a) Oscillations of rock noise received at four different detectors at different times (Goodman et al., 1965); b) Recording of a subaudible event generated within a small-scale landslide and received by four piezoelectric transducers, showing the three time delays (Cadman et al., 1967).

Cadman et al. (1967) carried out flume tests in the laboratory with partially saturated sand in order to observe the sliding mass and to record the movement noises with four piezoelectric transducers placed within the sandy slope at known coordinates, and whose output was recorded on a magnetic tape. These studies proved the increase of AE emission before failure and the possibility of localising the events through non-linear resolution systems (Newton-Raphson) from the understanding of the compression wave velocity, the coordinates of the geophones and the time delays between them.

### 2.2.2. Frequency domain observations: spectrum and spectrogram/sonogram

With the digitalization of the seismographs, it became easier to study the signal spectra in the frequency domain through several transformations. Spectral representation actually allows discriminating signal from low signal-to-noise ratio (SNR) recordings because it highlights the frequency content of the signal and consequently helps in applying filters and discriminate the interesting AE events from the ones induced by external disturbing noises.

By the same way, for interesting AE signals that appears to be confused in the temporal domain, the frequency content pattern can be a useful tool to discriminate the characteristics of different events.

Rouse et al. (1991a) for instance observed four distinct types of AE signals within a muddy landslide in South Wales, each type being characterized by different peaks in frequency (Figure 117 left).

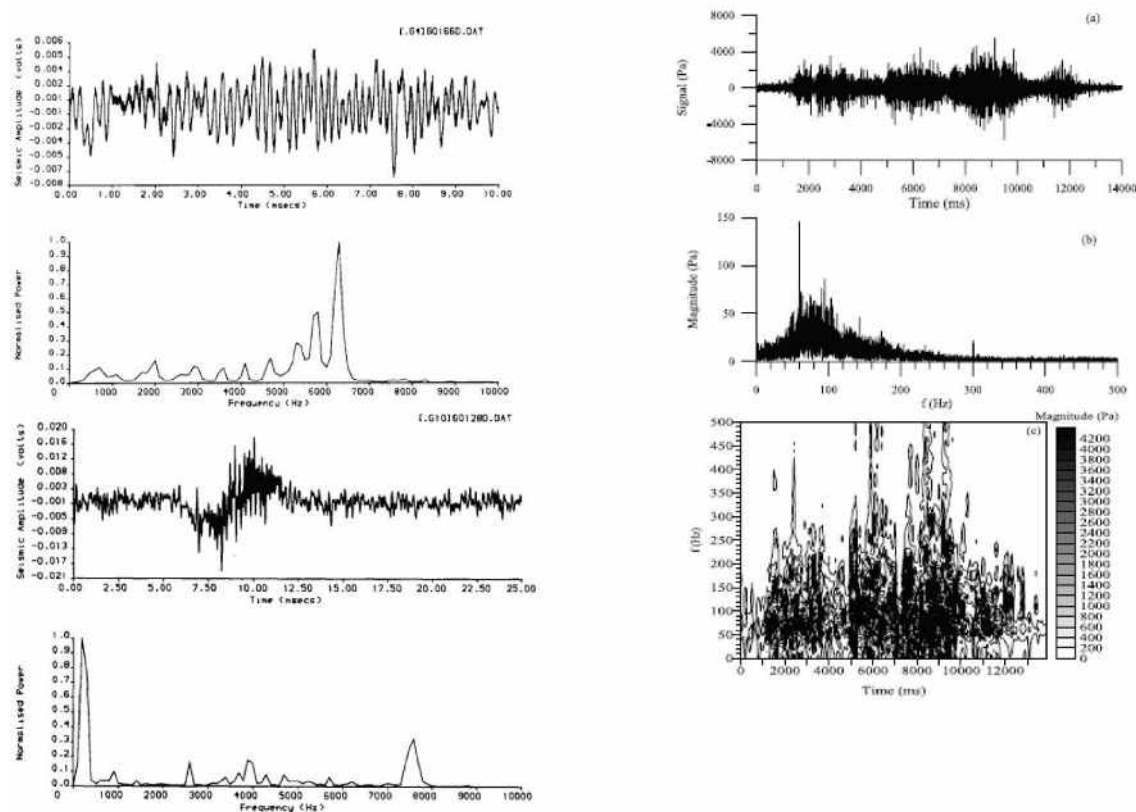


Figure 117 : (left) Time series and power spectrum of two identified events at Glynrhigos (South Wales) (Rouse et al., 1991a) . (right) Seismic noise generated by a debris flow: (a) time series; (b) signals in the frequency domain obtained using FFT; (c) spectrum obtained using Gabor transform (Huang et al., 2004).

In addition to the application of numerous transform operators (Fourier, Gabor; eg. Huang et al., 2004; Figure 117 right), the use of spectrograms and sonograms has been developed in the recent years. A spectrogram is an image that shows the variations of the spectrum of the signal with time. For this reason, combination of classical seismogram analysis with spectrogram/sonogram analysis is now a useful tool to point out with precision the located events and to extract their characteristics in time and frequency. Some examples are detailed in Section 3 as a useful application to discriminate different AE signals induced on landslides.

### 2.2.3. Limitations of the technique: identification of attenuation and noise problems

Under stress conditions, geological materials can induce a broad range of frequency extending from 10Hz to 500kHz. In the field, low frequencies can be contaminated by background noises (electrical noise, wind and tide waves, human disturbance) while higher frequencies

are affected by the high attenuations of the material. Therefore, a choice has to be made in order to minimize the loss of information.

To prevent material attenuations, metal wave guides have been used to conduct signals from the soil or rock body to the AE sensors (Lord et al., 1982; Hardy, 1992; Dixon, 1996 and 2003; Kousteni, 1999; Shiotani, 2006). According to Figure 118, iron and steel provide very low attenuated responses with respect to the geological ones (Koerner et al., 1981). An example of such an acquisition instrument is illustrated in Figure 119. The steel bar is more sensitive to the deformation process, and also compensates the attenuations of the material.

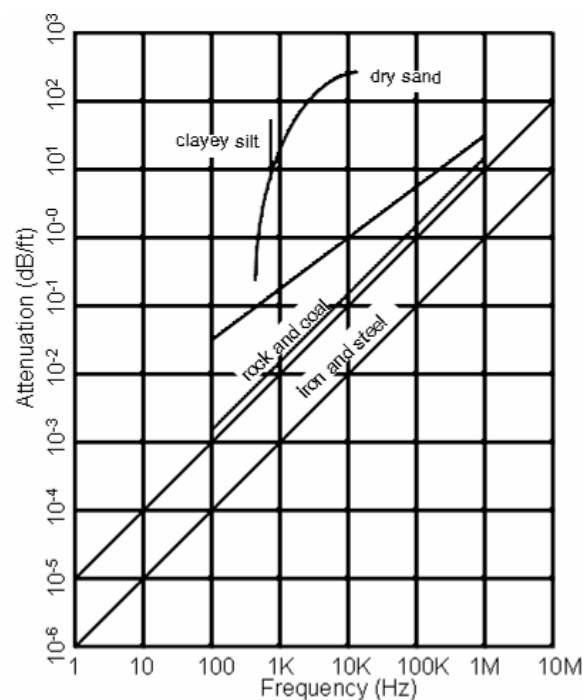


Figure 118 : Attenuation response of different soil types, rock, coal and iron/steel (Koerner et al., 1981).

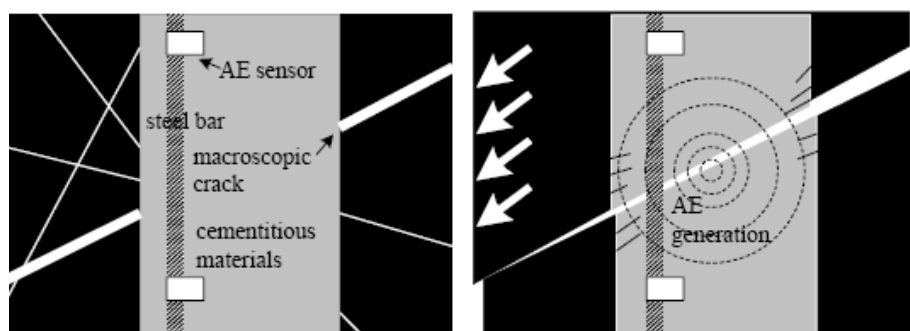


Figure 119 : Schematic behavior of the WEAD waveguide during the deformation process of rock (left: intact state, right: AE signals generated along with rock deformation) (Shiotani, 2006).

### 2.3. THE RECENT PERIOD – MICRO-SEISMIC MONITORING AND CHARACTERIZATION OF AE SIGNALS

In this part, we tried to distinguish ambient noise listening applications from micro-seismic monitoring for event source location and characterization.

#### 2.3.1. Low-amplitude seismic noise listening for landslide structure characterisation

Nakamura (1989) adapted a method introduced in the early 1950s, which used microtremors for estimating dynamic characteristics of surface layers. Microtremors are low amplitude ambient vibrations of the ground caused by man-made or atmospheric disturbances. Nakamura explained that the study of the H/V (horizontal on vertical components, recorded simultaneously at a given location with a 3D seismometer placed on the ground surface) spectral ratio of the ambient noise can be used to detect the sedimentary zones within surface layers that could amplify seismic ground motion.

After experimental and numerical validation of the H/V method, Méric et al. (2007) applied it to muddy landslides (Super-Sauze, Saint-Guillaume) composed of stratified soil profiles (e.g. a soft layer on top of stiff bedrock). Méric et al. used the H/V spectral ratio method to detect first the slip surfaces (Figure 120, Figure 121), and second to derive S-wave velocity profiles. However, they encountered difficulties in the interpretation because of multiple resonance frequencies probably due to deeper interfaces, heterogeneities or bad coupling with the ground during the acquisition.

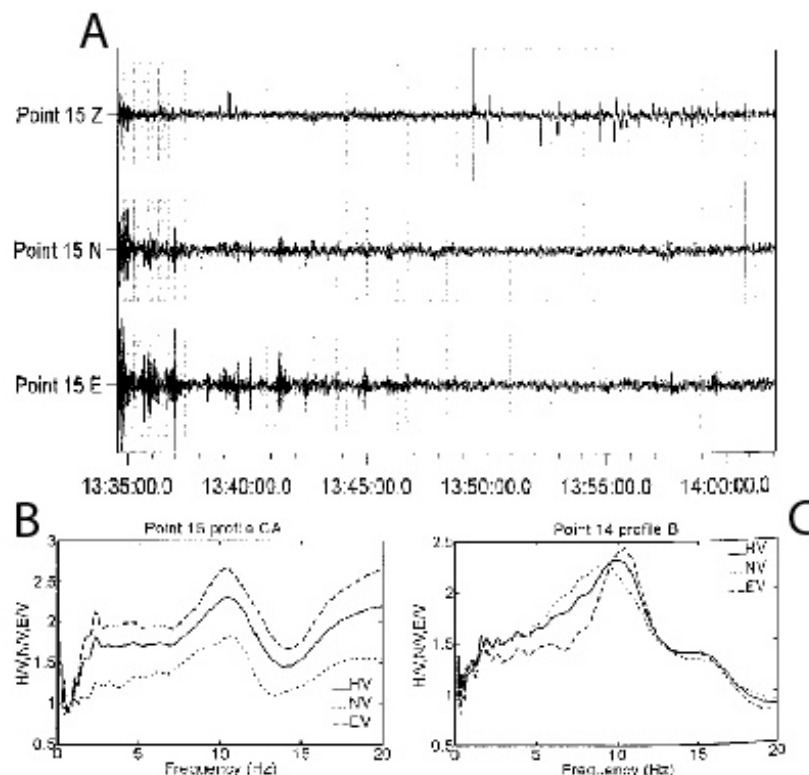


Figure 120 : Example of ambient vibration data acquired on the Super-Sauze landslide: a) Ambient vibration data sampled at 200 Hz and recorded for 30 min, b) Spectral ratio computed using the E-W component, the N-S



component and the  $H$  component (square root of  $E$ - $W$  and  $N$ - $S$  components) for point 15 of profile  $CA$ ; c) Spectral ratio computed using the  $E$ - $W$  component, the  $N$ - $S$  component and the  $H$  component (square root of  $E$ - $W$  and  $N$ - $S$  components) for point 14 of profile  $B$  (Fig. 7) (Méric et al., 2007).

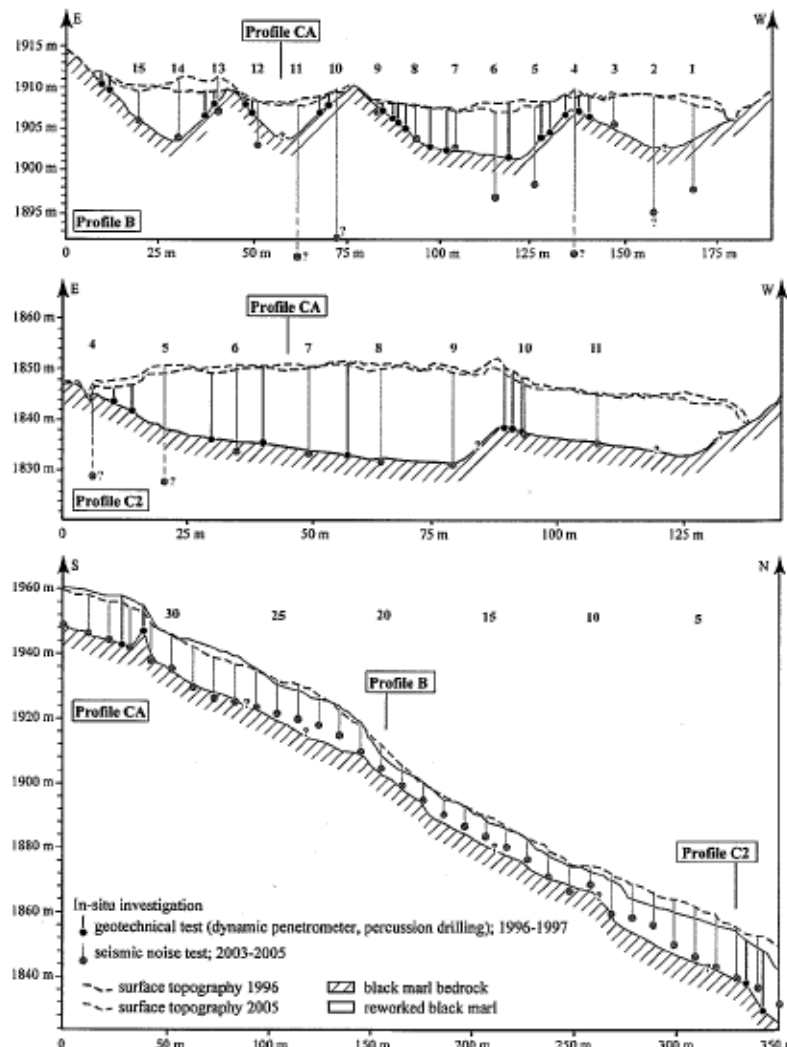


Figure 121 : Interpretation of  $H/V$  picked spectral frequencies on the Super-Sauze mudslide for three profiles  $B$ ,  $C1$  and  $CA$ , assuming an average ( $S$ )-wave velocity of  $260 \text{ m.s}^{-1}$ . Results from geotechnical and electrical data are also shown for comparison. The interface between the sliding material and the stable bedrock was drawn considering all the results. The presence of two peaks in some  $H/V$  ratio (Fig. 6b and 6c) resulted into two possible interpretations, although lower frequencies are expected to be due to the presence of deeper interfaces (former coarse mudslide), acquisition problems or local heterogeneity (Méric et al., 2007).

A critical review of microtremor  $H/V$  technique has been proposed by Mucciarelli et al. (2001), who synthesized several case studies between 1990 and 2000. Thanks to its low-cost and fast deployment on a site, the  $H/V$  method is convenient for landslide characterisation.

### 2.3.2. High-frequency seismic noise listening for landslide velocity/volume estimation

Other studies carried out on mass movements are related to the use of seismometers or geophones for landslide volume estimation or velocity estimation. For instance, Arattano et al. (1999) and Marchi et al. (2002) studied the velocity and the volume of debris flows in the

North East Italian Alps by installing geophones in debris flow prone torrents. Suwa et al. (2000), Zhang et al. (2004) and Huang et al. (2007) calculated the volume and the kinetic energy (e.g. loading) of debris flows in Japan and China. Suriñach et al. (2000) determined a relationship between seismic signals and avalanches paths and volumes and Brodsky et al. (2003) calculated the coefficient of friction of lahars. All these results are based on the analysis of high-frequency seismic noise using spectral analysis of the continuous seismic recordings. Such an example of analysis is presented on Figure 122 with the detection of a granular debris flow that occurred on 15/08/2003 in the Himalaya mountain range (Burtin et al., 2009).

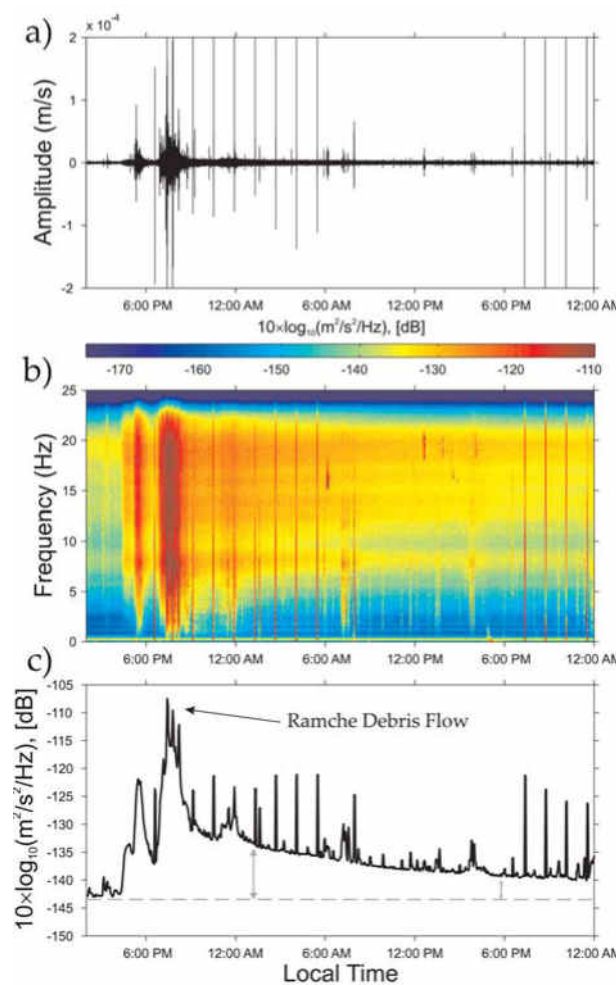


Figure 122 : Example of seismic monitoring of a large granular debris flow that occurred on 15/08/2003 in the Himalaya mountain range. a) Vertical seismogram recorded at station H0390. The seismic signal is bandpass filtered between 0.1 and 20 Hz. The recording starts at 2:00 pm on the 15/08/2003 (local time). b) Spectrogram calculated from the vertical seismic recording at station H0390, using a multi-taper method with 50% overlap between time segments of 5 min. Amplitudes are given in decibels (dB), red and blue colors stand for high and low amplitudes, respectively. (c) 1-hr-smoothed mean high frequency seismic energy at station H0390 for the vertical component (b) in the 2-22 Hz frequency band. Amplitudes are given in dB. (Burtin et al., 2009).

### 2.3.3. Micro-seismic monitoring and correlation of the AE signal catalogues to possible triggers

Other studies involve micro-seismic monitoring in order to detect all type of AE signals within long periods of time and without any frequency trigger. A first application consists in developing catalogues of landslide events to observations of possible triggers such as earthquakes, rainfalls or explosions. The goal is also to discriminate the mass-induced AE from the direct acoustic emission generated by these external events. For instance, observations carried out by Rouse et al. (1991a, b), Walter et al. (2008) and Helmstetter et al. (2009) during and after long rainfall periods on landslides demonstrated the marked change in the number of AE signals which occurs during and after the rain. Walter et al. (2008) observations are referred to the Heumös clayey landslide in Vorarlberg (Austria); according to Figure 123, they concluded that the events are generated from a few minutes to one day after intense rainfalls, which let them conclude that these AE signals were generated by precipitation-induced material failure within the landslide. Clusters of AE signals can also be clearly observed over the period.

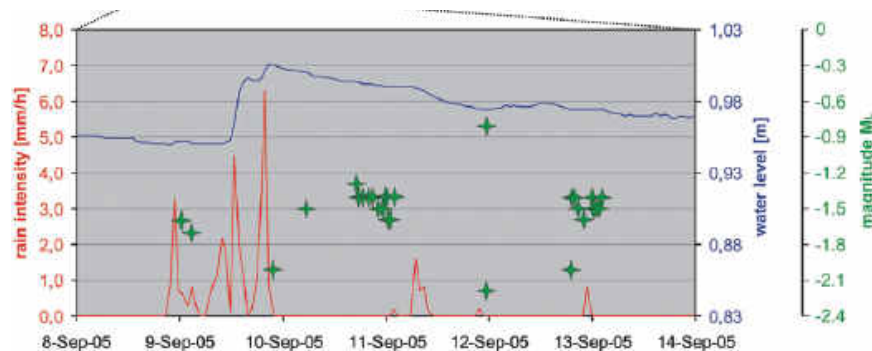


Figure 123 : Micro-seismic monitoring at the Heumös landslide in Vorarlberg (Austria). Example of correlation among rain intensity (red), ground water level (blue) and temporal occurrence of the recorded fracture events (with their magnitude ML) during 7 days in September 2005. Clusters of AE signals can be clearly observed over the period, and associated to the changes in ground water levels with some delays (10-11/09/2005) or to rainfall (13/09/2005). (Walter et al., 2008).

### 2.3.4. Micro-seismic monitoring and temporal behaviour of AE signals at the onset of large failures

Other studies have been carried out in order to characterize the temporal pattern of AE signals at the onset of major failures.

Senfaute et al. (2009) examined the micro-seismic signal recorded 15h prior to a rockfall that occurred at Mesnil-Val in France in a chalky cliff; the results lead to the hypothesis that several phases of failure mechanisms contributed to the rockfall (Figure 124). These encouraging results offered the possibility of using micro-seismic systems to possibly forecast large failures in hard rock slopes.

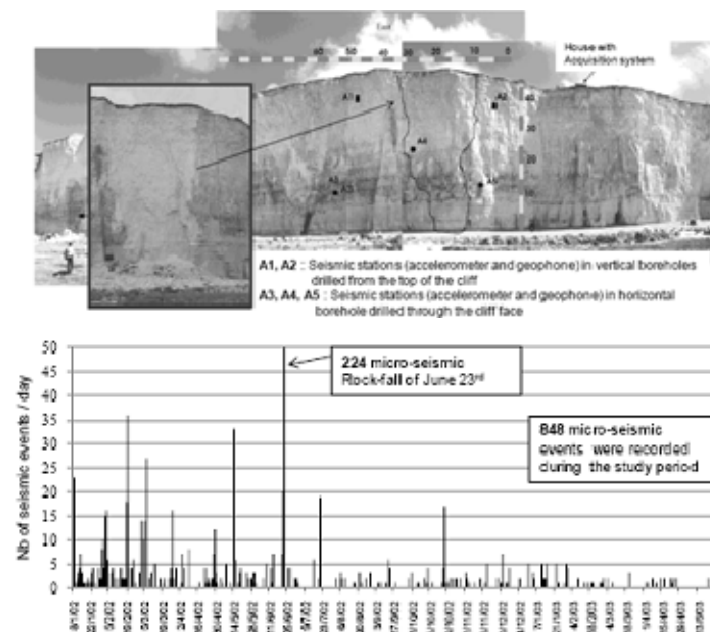


Figure 124 : Micro-seismic monitoring of a cliff collapse at Mesnil-Val (North-West France). a) Location of the sensors (A1, A2, A3, A4, A5) on the cliff and photograph of the rockfall on 23/06/2002 that occurred at the centre of the monitored zone; b) Number of micro-seismic events per day recorded only during low tides (the number of events increase during tides) and during the 18 months of the monitoring period. (Senfaute et al., 2009).

Correlation among large earthquakes and the dynamic response of a landslide can also be found in Harp et al. (1995) who proposed a method to anticipate critical failures that may occur in already unstable slopes. The same type of temporal pattern of AE events has been observed at the Valoria landslide (Northern Apennines, Italy) in soft marls, during the failure of the upper part of the landslide that occurred in November 2009 (Tonnellier et al., 2010); the first results indicated the increase of AE signals until failure (Figure 125).

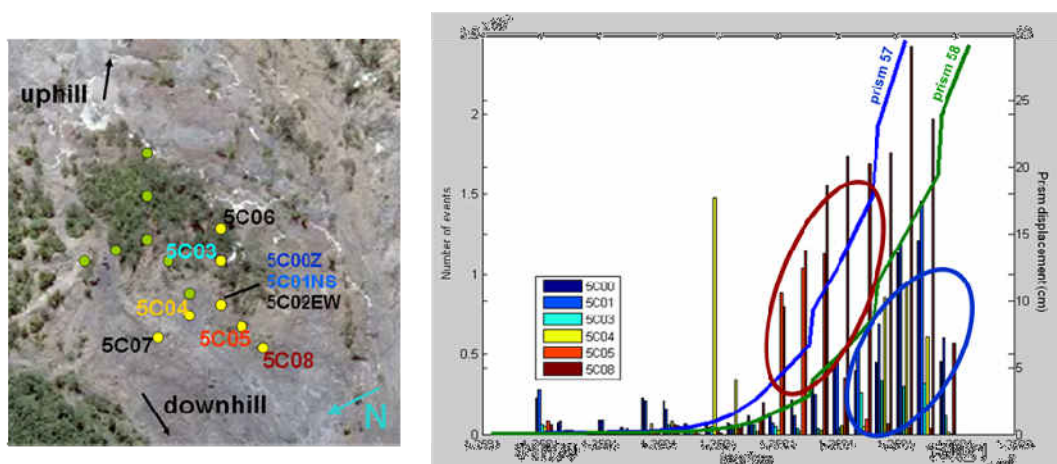


Figure 125 : Micro-seismic monitoring of the Valoria landslide (Northern Apennines) in November 2010. An increase in landslide displacement rate and in the number of seismic events recorded by station IHR05 during the day before the failure is observed. The number of events started to increase in the seismic station located downhill and then progressively migrate uphill. (Tonnellier et al., 2010)

### 2.3.5. Micro-seismic monitoring and spatial pattern of AE signals for landslide mechanism understanding

Up to now, few studies have investigated the source location of the AE signals within a landslide. Further information on the source should help to understand better the mechanisms that control the dynamics of the landslide. Accuracy of detection of the source location is affected by many factors, such as the characteristics of the sensors, the geometry of the array, the previous knowledge on the investigated slope (layering, location of slip surfaces), the petrophysical characteristics of the material (seismic velocity model, ambient noise) and the type of recorded AE events (Ge, 2005).

As explained in § 2.3, Cadman (1967) was successful to locate the AE events between the uphill, the middle and the downhill parts of a small-scale man-made slope in laboratory tests. Using waveguides, Novosad et al. (1977) were able to characterize the direction of the sources. Such pioneering results proved that spatial location of low energy AE on slopes could be foreseen using the same type of location techniques used for high energy earthquakes.

Near Tomsk (West Siberia, Russia), Zyatev et al. (1998) observed strongly differing polarisation patterns of microseisms on active and inactive parts of landslides. These polarisation patterns were confirmed thanks to numerical simulations and several processing tests in a landslide site in the Northern Tien-Shan (Kirgizstan) with the conclusion that cracks that develop in the vicinity of a forming slip surface often have preferred orientations due to stress conditions in rocks (Figure 126; Kolesnikov et al., 2003). Polarisation analysis also appears to be a useful tool for providing the orientation of the sources generated within landslides.

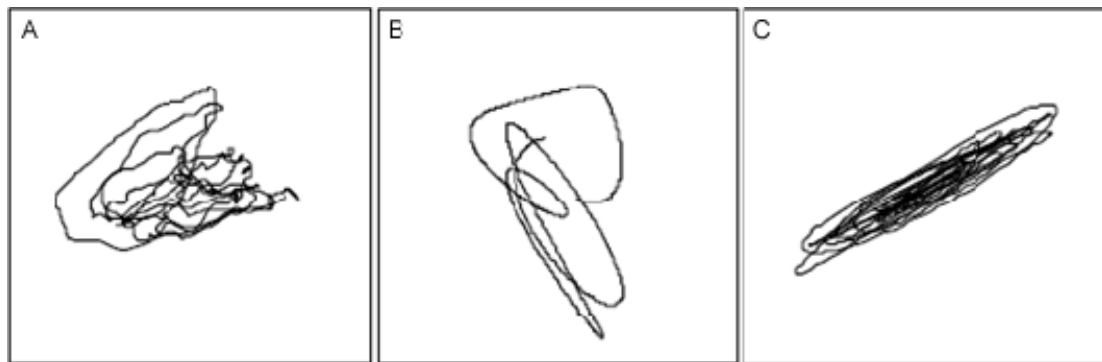


Figure 126 : Detection of AE signals polarisation on a landslide in Western Russia. Horizontal projections of possible particle trajectories in a point on the slope: a) from the original record, b) after 10-45Hz band pass filtering, c) after 120-210Hz band pass filtering. (Kolesnikov, 2003).

After an efficient pattern recognition of the events recorded at the S  chilienne rockslide in the French Alps, Helmstetter et al. (2009) highlighted that a better location of the sources for rockfall-induced events is still difficult because most recorded AE signals did not present impulsive waves, which hindered the time picking of first arrivals (Figure 127), as well as the differentiation among P and S waves because of the small distance between the sources and the receivers. They also used the cross-correlation of signals recorded at different sensors in order to precisely measure the time delays between the sensors. They also used the beam-

forming methods proposed by Almendros et al. (1999) in order to search for the best source point which maximises the intertraces correlation, averaged over all couples of sensors, and after shifting the traces in time by the travel time. However, the sources of these AE signals were not precisely located and the authors concluded that the array of sensors should be completed.

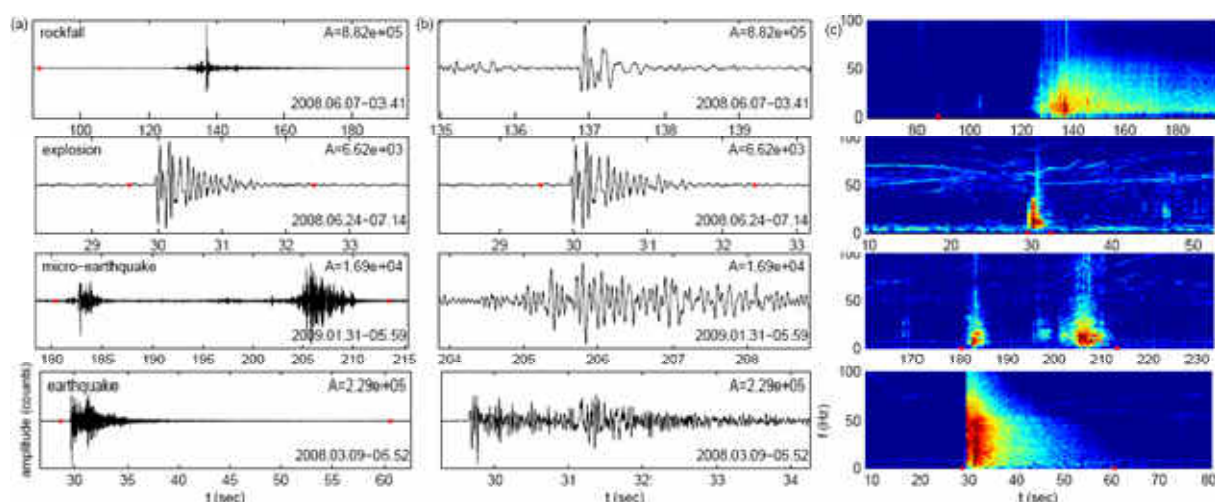


Figure 127 : A selection of different types of signals. (a) Seismograms, (b) zoom for a window of 5 seconds around the peak of amplitude. The maximum amplitude (in counts) is given in the upper-right corner of each plot. (c) Spectrograms (log amplitude scale). Dots indicate the onset and end of each event (Helmstetter et al., 2009).

Applying the ‘nanoseismic method’ (Joswig, 2005), Walter et al. (2008, 2009b) analyzed waveforms and spectrograms to detect and partly locate distinct types of events caused by the dynamics of the Heumös (Walter et al., 2008) and Super-Sauze (Walter et al., 2009b; Tonnellier et al., 2010) landslides. Some signals correspond to collapses of brittle material from the upper parts of the landslides; other are generated by micro-cracks propagating within the landslide. Such events are recorded by all the stations which is a criteria to discern them from potential noise. They concluded that more precise location of the sources should be obtained thanks to a denser distribution of the seismic arrays, and that a detailed catalogues of events with a quantitative description of the signals are the basis of a sound analysis.



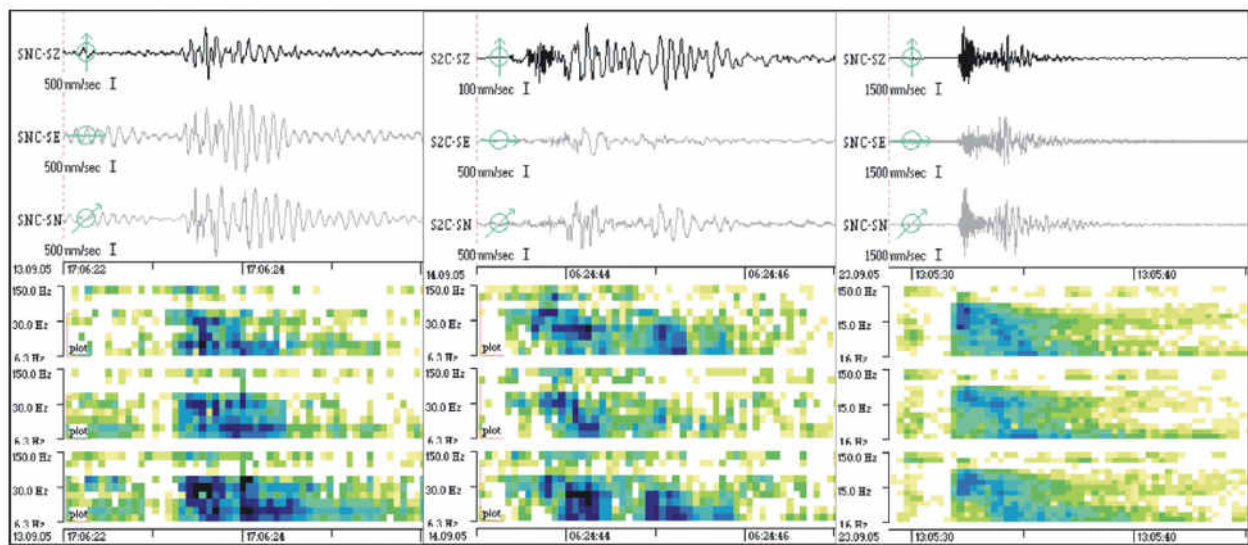


Figure 128 : Waveforms and sonograms of three events that were recorded during the seismic monitoring on the Heumös landslide in Vorarlberg (Austria): a) Fracture process  $ML=-2.0$  in 160 m distance, b) fracture process  $ML=-1.4$  in 350 m distance and c) local earthquake  $ML=1.3$  in 10 km distance. (Walter et al., 2008).

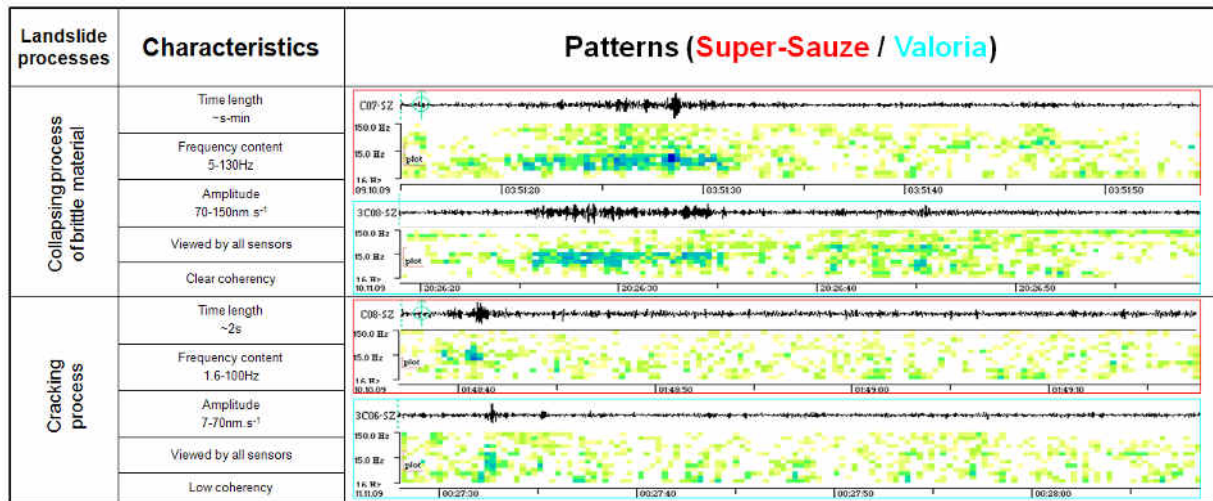


Figure 129 : Waveforms and sonograms of common AE events observed at the Super-Sauze and Valoria landslides directly induced by the landslide mechanisms. (Tonnellier et al., 2010).

**2.3.6. Towards mechanical description of the AE signals observed on landslides**

The discrimination of the AE signals observed within a landslide provides information on its mechanism because it helps in decomposing its evolution into several phases. Such information can be completed by the results obtained from other monitoring devices such as (a) ortho-photographs obtained from the use of an Unmanned-Aerial-Vehicle (UAV) to combine evolution of the ground surface of the landslide (e.g. displacement, development of the fissure pattern) and micro-seismic monitoring (Walter et al., 2009a), (b) displacement and ground water level monitoring (Walter et al., 2010) and (c) 3D geometrical models of the landslide to locate a priori the main possible sources of AE signals (Figure 130; Walter et al., 2009b).



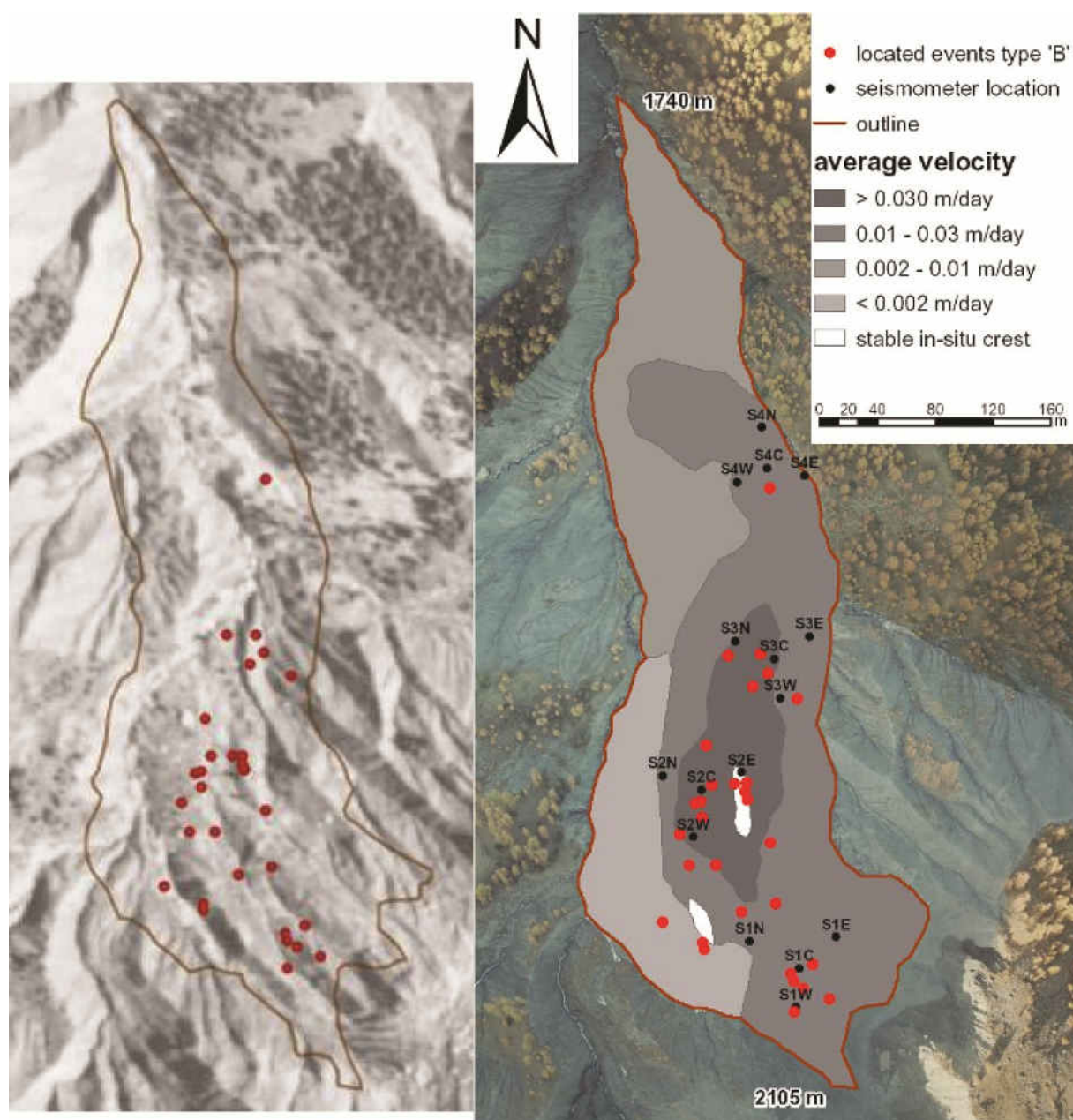


Figure 130 : Location (in planimetry) of the main sources events detected at the Super-Sauze landslide in July 2008. Most event sources are located along crests buried below the landslide mass where friction and sliding processes are maximized, in the most active part of the landslide where the surface displacement rates are high, in intensively fissured areas and in the upper part near the main scarp where small amplitudes rockfall are observed. (Walter et al., 2009b).

Using the same type of approach, de Angelis et al. (2007) demonstrated the advantage at considering together seismograms and spectrograms in order to better identify the AE signals induced by the travel of rapid pyroclastic flows at the Soufrière Hills Volcano, and to characterize the phases of the signals during the propagation of the flow (Figure 131).

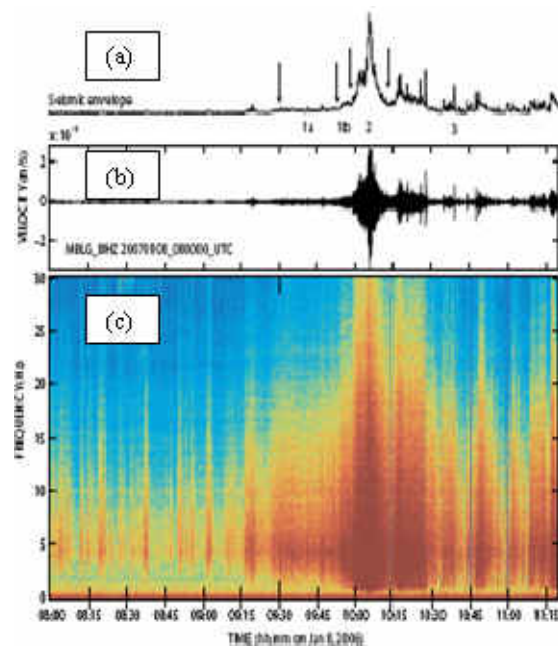


Figure 131 : a) Seismic envelope, b) velocity seismogram, c) Spectrogram from the signal recorded during pyroclastic flows at the Soufrière Hills Volcano, Montserrat (de Angelis et al., 2007).

## 2.4. CONCLUSIONS

Using acoustic seismic methods to characterize the structure, define the dynamics and understand the mechanism of mass movements is not as recent as one could have thought. This review on the application of passive seismic monitoring techniques has shown that they can be exploited for a wide range of issues and objectives, chronologically focused on ‘simple’ seismic noise content characterization (amplitude, duration, frequency) to more detailed analyses in terms of catalogues and accurate location of the sources. The introduction of waveguides and above all the digitalization of seismic data increased the feasibility of characterizing AE signals within unstable slopes using spectral approaches.

Studies have been carried out on a variety of geohazard types in a broad range of geological contexts: soft rock landslides, rocky slopes, rock quarries, mining activities, granular and muddy debris flows, lahars, snow avalanches, ice glaciers (Table 19). These exercises provided successful information about the definition and the dynamics of the mass movements. Based on these experiences, Suriñach et al. (2005) and Spillman et al. (2007) have started to investigate the possibility of automate the recognition of AE signals on respectively snow avalanches and rockslides. On a longer term, the main issue will be to characterize the source mechanisms, and to detect of possible seismic forerunners of mass movement acceleration and define the potentialities of using seismic noise observations as a predictive-tool for early-warning of all kinds of mass movement failures.

For that purpose, dense AE monitoring devices have been set up at several landslides for long term observations (e.g. Super-Sauze and Avignonet mudslides in soft clays, Séchilienne, Aknes and Randa rockslide in hard rocks).

### 3. INTRODUCTION TO OFFSHORE METHODS

Submarine and coastal landslides are of major concern for coastal communities and infrastructures but also for the safe development and exploitation of seafloor resources. Because of their unique geological settings, these landslides can be up to two orders of magnitude bigger than those that occur on land. Hazards related to such landslides may be catastrophic and range from destruction of offshore facilities to collapse of coastal infrastructures and the generation of tsunamis (e.g., Longva et al. 2003, Bondevik et al. 2005, Dan et al. 2007). During the last two decades, researchers have shown the great potential of combining multi-beam bathymetric surveys and high resolution seismic methods for studying landslides processes in the submarine environment and also for mapping the risk related to such natural hazards (e.g., Locat and Lee 2002, Haflidason 2004).

#### 3.1. MULTI-BEAM SYSTEMS

Seabed topography is conventionally mapped using vessel-based acoustic echo-sounding devices, such as multi-beam bathymetric systems. Through digital processing techniques and with help of differential positioning systems the data provides precise shaded relief topographic maps of near air-photographic quality (Figure 132). Such maps are now routinely used for detailed morphological mapping of the seabed, for mapping of landslide scars and deposits, and also as a prerequisite to slope stability analysis. Most swath bathymetry systems also acquire backscatter data, which can be used for mapping local changes in morphology and also for the production of sediment maps.

Multi-beam systems use acoustic signal emitted from a series of transmitter mounted on the hull of a vessel (Figure 133). The beams are transmitted at different angles from the same transducer unit, creating a fan perpendicular to the vessel direction. The angle of the fan is termed swath angle, which along with the water depth determines the width of the corridor mapped (Table 20). As a rule of thumb, a wider swath angle and deeper water increases the corridor mapped but reduces the resolution as the distance between the individual beams increase. The greater the number of transmitters and higher frequencies will provide more precise bathymetric coverage. Since multi-beam systems acquire dense sounding data both along the ship's track and between the track lines, they can provide 100% coverage of the seafloor.

The many multi-beam systems that are currently on the market utilise two differing technologies to achieve bathymetry measurements across a “swath” of the seabed: 1) multiple narrow-beam swath bathymetric systems (Hughes Clarke, 1996) and 2) multiple-beam interferometric or phase discrimination systems (Green and Cunningham, 1998). Both of these techniques have their merits; however the same end results can be achieved. Bathymetry data from various sources can also be merged together (Figure 132).



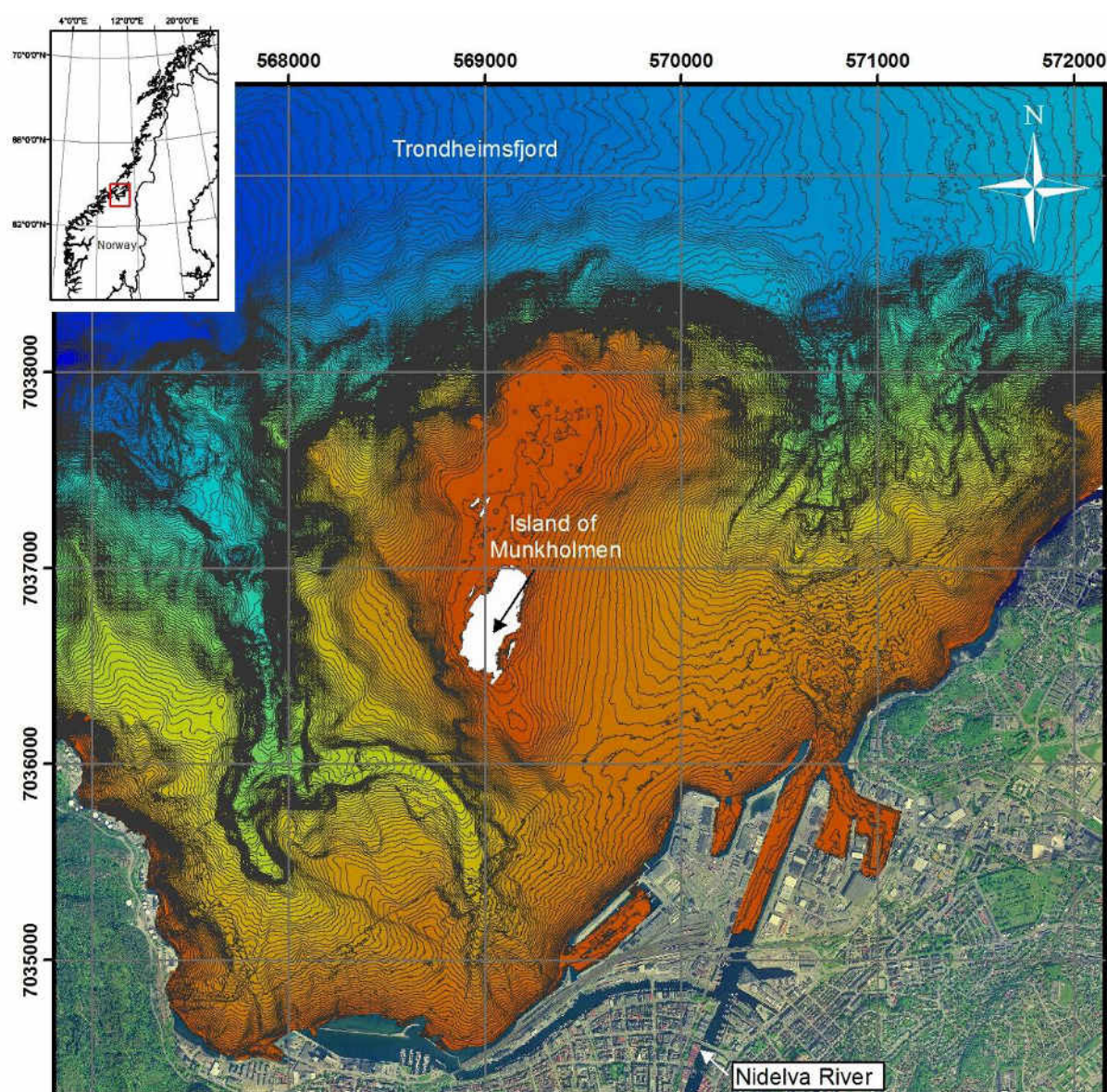


Figure 132 : Example of shaded relief bathymetric contour map (2 m interval) within the bay of Trondheim, central Norway (L'Heureux et al. 2010). Bathymetry data were collected using a GeoSwath 250 kHz system from GeoAcoustics and a multi-beam echo sounder EM 2000 from Kongsberg.

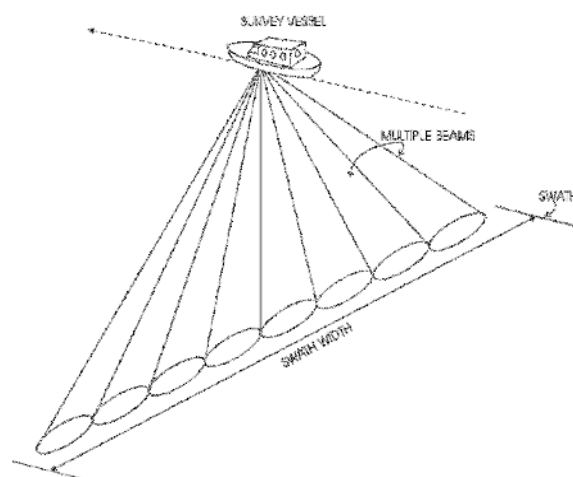


Figure 133 : Examples showing a multi-beam sonar swath (from SeaBeam, 1999).

Multi-beam echo sounders (MBES) collect bathymetric soundings by measuring the depth to the sea floor in discrete angular increments or sectors across the swath (Hughes-Clarke et al. 1996). The bathymetry is calculated from the two way travel time that is corrected for the traveling patch and measured properties of the seawater. Modern MBES systems use frequencies spanning from a few kHz to several hundred kHz depending on the sea floor depth (Table 20). For example, low frequency (12 kHz) systems can collect swath soundings at full ocean depths, i.e., up to 30,000 meters. In contrast, high frequency MBES systems (300+ kHz) are utilized for collecting swath bathymetry in depths of 200 meters or less. Table 20 shows some general characteristics of MBES available for seabed mapping, including depth range and swath coverage. Such details must be taken into consideration when planning a survey for a given environment.

In contrast, the term interferometry is generally used to describe multi-beam techniques that use the phase content of the sonar signal to measure the angle of a wave front returned from a sonar target. In general, interferometry systems have a slower ping rate than MBES system thus they are primarily used in shallow water operations. The along line density of data in interferometry systems is restricted by vessel speed, however, cross line data is only restricted by the quality of the data and processor, thus small targets can be readily observed. MBES have higher ping rates and so the along line density is not so restricted by speed but cross line density can vary depending on the number of fixed or variable beams available.

Table 20 : Typical multi-beam echo sounder systems.

Type of system	Manufacturer / Model	Frequency (kHz)	Depth range (m)	Swath coverage	Depth resolution
<b>Multi-beam echosounders (MBES)</b>	Kongsberg EM 2000	200	1-300	7 x depth or 250 m	8 cm
	Kongsberg EM 3002	300	0.5-200	10 x depth or 200 m	cm
	Kongsberg / EM 122	12	20-11,000	6 x depth or 30,000 m	cm
	Kongsberg / EM 302	30	10-7000	5.5 x depth or 8 km	cm
	Kongsberg / EM 710	70-100	3-2000	5.5 x depth or 2.5 km	cm

---

<b>Interferometric systems</b>	R2Sonic LLC / Sonic 2024	200-400	200	11 x depth	< cm
	RESON/ SeaBat8125	455	0.5-120	400 m	6 mm
	GeoAcoustics / GeoSwath +	125	200	12 x depth	6 mm
	GeoAcoustics / GeoSwath +	250	100	12 x depth	3 mm
	GeoAcoustics/ GeoSwath +	500	50	12 x depth	mm

### 3.2. 2D AND 3D HIGH RESOLUTION SEISMIC

In combination with multi-beam bathymetric surveys, 2D high resolution seismic data is routinely acquired for investigating submarine mass movements and other offshore geohazards. A source, generating an acoustic signal which can vary from MHz to 10 Hz, and receivers (hydrophones) recording the reflected sound, constitute the basic setup of seismic acquisition systems (Figure 134). The interpretation of features mapped using a seismic data set is based on acoustic impedance differences of subsurface material. The transmitted acoustic energy is reflected from boundaries between mediums of different acoustic impedances (e.g. the water-sediment interface). The interface between different materials is displayed graphically in a seismic section and these are used to analyse the structure of a basin. As an example, seismic data can be used to capture lateral variability in sediment properties and to identify the presence of weak geotechnical layers on which a mass movement may initiate (Figure 134). High resolution seismic data are also well suited for mapping buried landslide deposits (e.g., Hermanns et al. 2006).



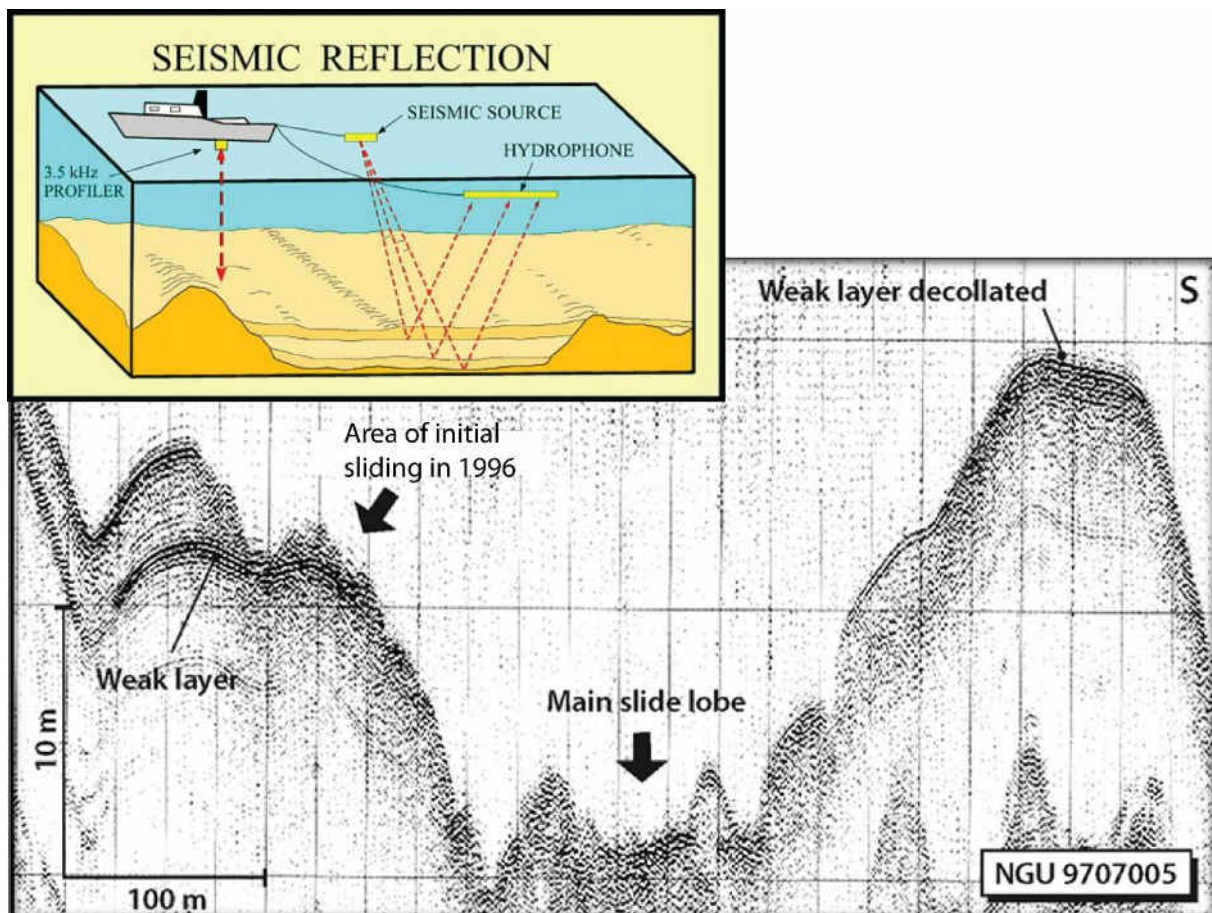


Figure 134 : Example showing a high resolution seismic line through the 1996 landslide in Finneidfjord, Norway (Longva et al. 2003). Note the distinct high amplitude reflection (weak layer) correlating with the initial sliding plane.

Like seismic data that are collected for the petroleum industry, high resolution seismics use reflected acoustic energy to image the subsurface structure and stratigraphy. The two techniques differ in that the petroleum industry seismic data typically penetrate several kilometres and have resolution on the order of 10s of meters, whereas high resolution seismic data for marine geohazard purposes might penetrate several 10s of metres but resolve features that are 10s of centimetres thick. High resolution seismics can be obtained using several source systems such as airguns, 'boomer' and 'sparker'. The configuration can vary greatly, depending on the source signal, distance from source to receivers, and amount of receivers as some of the main parameters that can be adjusted. The settings vary according to the target of the investigation; deeper investigations require lower frequencies and generally give lower resolution. Collection of sub-bottom profiler (SBP) data (e.g. TOPAS system) is often done simultaneously with heavier equipment (airguns, 'boomer', 'sparker'). SBP gives better resolution than seismic data, but poorer penetration.

In more recent years, 3D high resolution seismic data has become available to the academia and has had a tremendous impact on our understanding of offshore mass-wasting processes. Such data allow for accurate visualization of modern and buried landslide events in comparable (or superior) resolution to that achieved by multi-beam systems (Figure 135). One of the greatest strengths of the 3D seismic method is the dense, regular sampling of data over

the region of interest. The high-spatial resolution provided by 3D seismic data allows for a detailed seafloor analysis and an exceptional visualization of the internal geometry mass transport deposits. This increases the possibility to erect sophisticated kinematic and dynamic models for mass-wasting processes. Application of 3D seismic interpretation has also proven to be a powerful tool for geohazard identification and assessment of slope failure in offshore deepwater areas (e.g., Steffens et al. 2004; Heiniö and Davies 2006; Frey-Martínez et al. 2009). A current and promising research field in the study of offshore geohazards is the integration of 3D seismic attributes (e.g., instantaneous frequency, reflection strength, coherency) with borehole log data and insitu geotechnical tests to make predictions of subsurface physical properties over wide areas (e.g., Pinson et al. 2008).

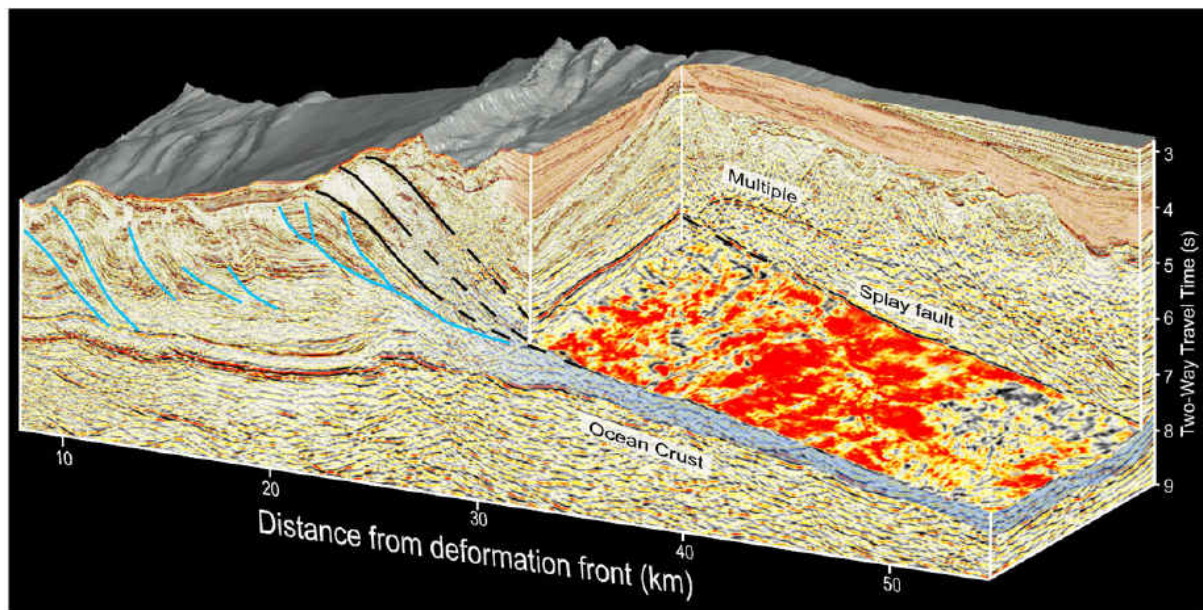


Figure 135 : Perspective view of a 3-D seismic volume with cut-out from the Kumano Basin 3D seismic reflection survey (from Bangs et al. 2009).

### 3.3. SUMMARY AND CONCLUSIONS

During the last two decades the development of high quality seafloor imaging techniques, differential global positioning systems and high resolution seismics have given us the opportunity to view the underwater morphology in a realistic way. These techniques are now routinely used in order to build precise geological and geotechnical models, to conduct detail morphological analyses of the seafloor and to map factors of importance for slope instability. Because of this the use of multi-beam techniques and high resolution seismic data is today essential to any offshore geoscientific activity and positively impact on any research planning.

## 4. STAKES OF THE AERIAL GEOPHYSIC

Airborne geophysics has been intensively applied for exploration of raw materials within the last decades. Recently it developed into a promising approach for landslide investigations and rapid mapping (Nakazato et al. 2006, Pfaffhuber et al. 2010, Sasaki & Nakazato 2004, Supper et al. 2008). An applied example is shown within the case study 13. One reason for this is the significant technology improvement during the last 10-15 years, providing accurate and well calibrated data.

The airborne geophysical technology uses sensors that are either mounted on an aircraft or dragged on a cable several tens of meters below the aircraft (Figure 136). Commonly used platforms are fixed wing airplanes or helicopters. Due to the fact that mass movements are usually located in rugged terrains and that a maximum distance between sensor and topography has to be kept due to the rapid signal decay, helicopters are in most cases the only choice for the acquisition platform for such surveys.



*Figure 136 : Helicopter borne electromagnetic system of the Geological Survey of Austria.*

One of the big advantages of airborne geophysical measurements is that large areas can be surveyed within relatively short survey times. Additionally it is the only remote sensing method with which not only information about the surface but also of the internal structure can be derived. Although the use of helicopters seems to be quite expensive the method is very effective since several different sensor systems of different kind can be combined, which acquire all data at the same time and at the same location. Further, if a comparable amount of data had to be acquired on the ground, the costs would be magnitudes higher as with airborne geophysics.

Due to the significant improvements in data acquisition as well as in data processing and interpretation during the last years more delicate results could be expected by incorporating latest improvements in airborne technology. Therefore several test studies are planned within the SafeLand project to advance interpretation for landslide mapping and to explore the

prospects of this methodology and evaluate the usability of the results for fast detection and mapping of landslides. Results, interpretations and implications will be shown in the deliverable 4.5 of the SafeLand project, “*Evaluation report on innovative monitoring and remote sensing methods and future technology*”.

---

# PART E

## GEOTECHNICAL GROUND-BASED MONITORING SYSTEMS

---

---

- <b>SECTION 1:</b> Extensometers	p. 222
- <b>SECTION 2:</b> Inclinometers	p. 224
- <b>SECTION 3:</b> Piezometers	p. 229
- <b>SECTION 4:</b> Contact Earth Pressure Cells	p. 235
- <b>SECTION 5:</b> Multi-parametric In-Place Systems	p. 236

---

### Sections 1, 2, 3, 4 and 5

- **Author:** E. Abbiate<sup>1</sup>, M. Lovisolo<sup>1</sup>
- **Reviewer:** J. Gilli<sup>2</sup>, C. Michoud<sup>3</sup>

<sup>1</sup>. Centro Servizi di Geoingegneria S.r.l., Acqui Terme, Italia. [mario.lovisolo@csgsrl.eu](mailto:mario.lovisolo@csgsrl.eu)

<sup>2</sup>. Department of Geotechnical Engineering and Geosciences, Universitat Politècnica de Catalunya, Barcelona, Spain.

<sup>3</sup>. Institute of Geomatics and Risk Analysis (IGAR). Université de Lausanne, Switzerland.

Abbiate E., Lovisolo M., 2010. *Geotechnical Ground-Based Monitoring Systems*. In the Deliverable 4.1 of the European project SAFELAND: *Review of Techniques for Landslide Detection, Fast Characterization, Rapid Mapping and Long-Term Monitoring*. Edited in 2010 by Michoud C., Abellán A., Derron M.-H. and Jaboyedoff M. Available at <http://www.safeland-fp7.eu>



## **1. INTRODUCTION**

Geotechnical instrumentation plays an important role in monitoring field performance. It allows to identify ground geomorphologic evolution with the following goals:

- Evaluate current and future stability condition for monitoring works at risk through the study and prediction of movements and stress evolution;
- Use warning systems;
- Choose the best consolidation works
- Evaluate mitigation interventions
- Observational method (earth structures application)

In this part will be described some specific geotechnical ground-based monitoring systems that provide measurements of deformation (extensometers and inclinometers), groundwater pressure (piezometers) and total stress in soil (contact earth pressure cells).

## **2. EXTENSOMETERS**

### **2.1. PROBE EXTENSOMETERS**

Probe extensometers are used to measure the change in distance between two or more points within a drilled hole in soft ground, by means of a portable probe containing a reed switch. The probe is inserted into a casing in the drill hole in which the reference points, each of which contains an array of bar magnets, have been fixed in a way to surround the casing on the outside. The distance between the two points is determined by measurements of probe position. For determination of absolute deformation data either one measuring point must be at a location not subject to deformation or its position must be determined by surveying methods. The pipe may be vertical (providing measurements of settlement or heave), horizontal (providing lateral deformation measurements) or inclined. Typical applications of probe extensometers are monitoring vertical compression within embankments, settlement alongside excavations, heave at the base of open cut excavations and lateral deformation of embankments. They are alternatives to fixed borehole extensometers, allowing for more measuring points and minimizing the cost of permanently installed instrumentations, but measurements are less precise.

To go further, please read Dunnicliff (1988-1993).

### **2.2. FIXED BOREHOLE EXTENSOMETERS**

Fixed borehole extensometers installed from ground surface may be used in soft ground or rock and may be Single Position (SPBX) for settlement measurements at one specific elevation or Multiple Position (MPBX) for measurements at several elevations. They monitor the changing distance between two or more points along the axis of the borehole, without use of a movable probe. When the location of one measurement point is determined with respect to a fixed reference datum, the devices also provide absolute deformation data. Typical



applications are monitoring deformations around underground excavation in rock and behind the faces of excavated slopes. Fixed borehole extensometers are also used for monitoring consolidation settlements in soil, bottom heave in open cut excavations and strain in concrete structures. The distance from the face of the collar anchor to the end of the rod is measured using either a mechanical or an electrical transducer (Figure 137).

To go further, please read Burland et al. (1972) and Dunnicliff (1988-1993).

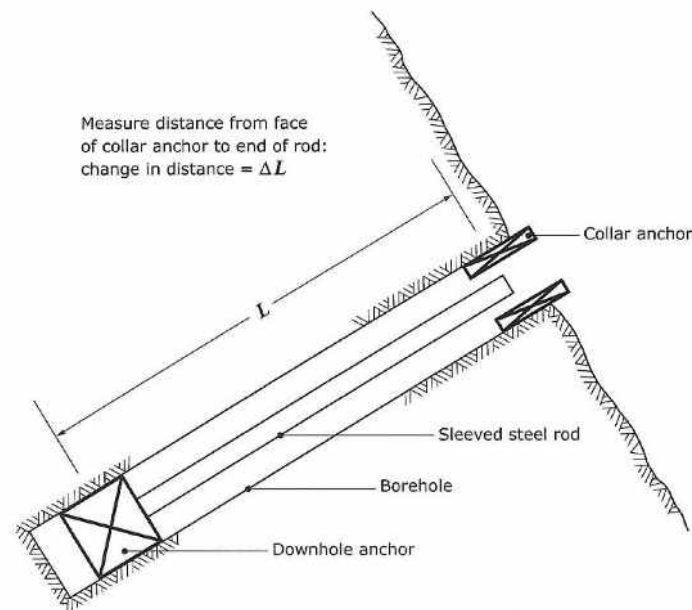


Figure 137 : Fixed borehole extensometer (Dunnicliff et al., 2005).

### 2.3. WIRE EXTENSOMETERS

The wire extensometer is a simple and low-cost device that allows the measurement of the relative displacement between two points, one in the landslide mass that is in motion and the other in stable ground (the borehole has been drilled vertically through the landslide body and crosses the surface of failure). In Figure 138, we can observe instrumentation functioning. At the left is visualized the device as installed; at the right it's illustrated the situation after some sliding displacement of the upper mass downhill. The device consists of a protected steel wire anchored to a fixed point inside the borehole below the slip surface of the landslide. The opposite end of the wire is attached to a frame outside the borehole that is anchored to the landslide surface and holds a pulley. The wire is placed around the pulley and is kept in tension by means of a counterweight. The movement of the landslide displaces the wire with the consequent rotation of the pulley. The amount of wire displacement is measured by a potentiometer which provides an electrical signal that is transmitted to a data logger. One advantage of the system application is in combination with inclinometric probe measurements in active landslides, extending the technical limitation of the probe inclinometer (typically a few centimetres of displacement along the slide surface could stop the probe lowered inside the pipe, requiring a new drilling activity). In the description of Vallcebre case study, (Corominas et al., 2000) give exhaustive explanations about wire extensometer functioning.

To go further, please read also Kovari (1985; 1988).

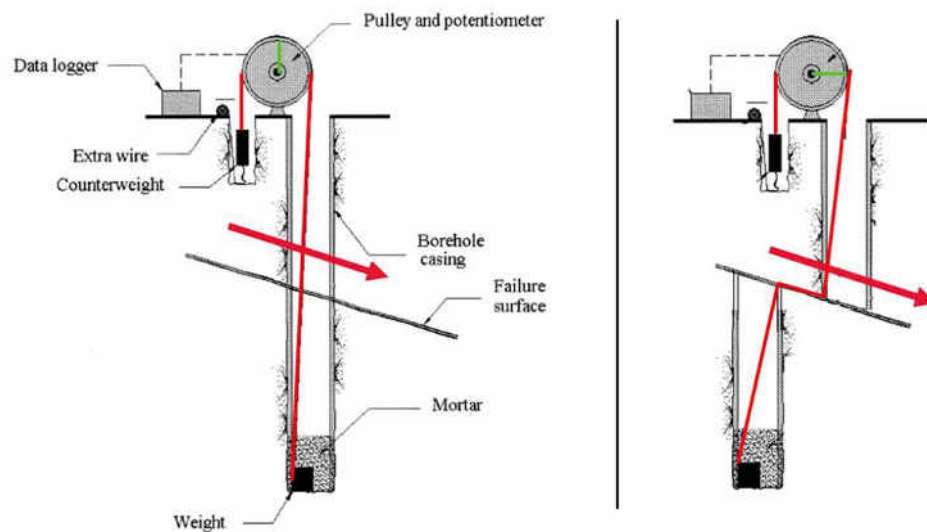


Figure 138 : Scheme of the wire extensometer (modified from Corominas et al., 2000).

### 3. INCLINOMETERS

#### 3.1. PROBE INCLINOMETERS

Probe inclinometers are defined as devices for monitoring deformation normal to the axis of a pipe by means of a probe passing along the pipe (Figure 139). The casing has tracking grooves to guide the sensing probe for orientation both parallel to and at right angles to the axis of the excavation. After the installation of the casing, the probe (containing a gravity-sensing transducer designed to measure inclination with respect to the vertical) is lowered on a graduated cable to the bottom of the hole and winched upward, with stops at (1m, 0.5 m, or 2-foot) intervals for collection of inclination data by means of a readout unit at the ground surface. Typical applications of the inclinometers are:

- The determination of the zone of a landslide movement; however, the probe inclinometers do not allow continuous recording of the displacements and cannot work after displacements of only a few centimetres;
- Monitoring of horizontal movements of earth dams, embankments in soft soil and along excavations or tunnels;
- Monitoring of deviations from vertical of bulkheads or retaining walls.

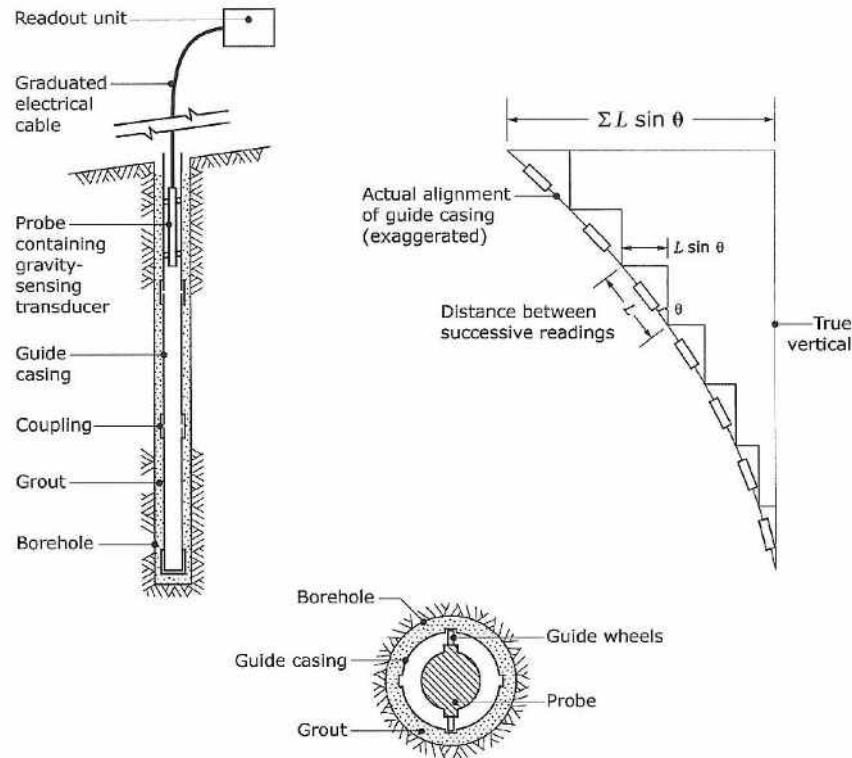


Figure 139 : Inclinator (Dunncliff et al., 2005).

The probe of the inclinometers has wheels that allow it to lowering parallel the pipe stretch. Executing two measures in the orthogonal planes it's possible to determine the components of horizontal movement of any section. After the pipe installation, a first sequence of measures is made to define pipe's inclination. Comparing these first values with successive inclinometric measures inclination variations can be measured.

Inclinometer data measures the tilt of the probe and determines the shape of the inclinometer casing. Figure 140 presents schematics of the inclinations that are being measured. Changes in shape could represent ground deformation or movement.

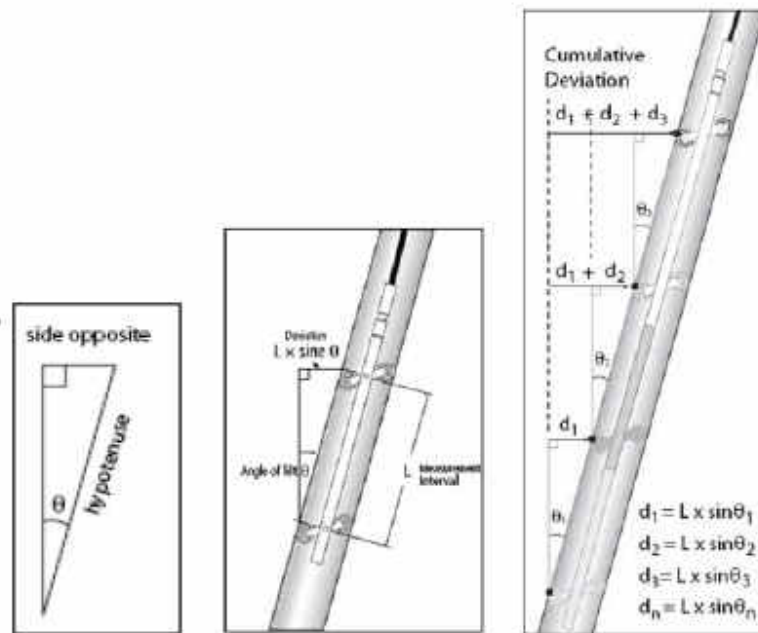


Figure 140 : Measurement principles (Machan & Bennett, 2008).

The field accuracy of the instrument has been evaluated on a large scale project based on measurements taken in USA and Canada (Mikkelsen) is  $\pm 7.8$  mm in 30 m depth. This value is the sum of random and systematic error (Figure 141). Random error accumulates at a rate of square roots of the number of readings, typically is  $\pm 0.16$  mm for each reading. The systematic error cumulates arithmetically with an indicative 0.11 mm per reading.

The main factors that influence data error are:

- Bias shift and sensitivity drift of the transducer;
- Mechanical coupling of the combination wheels and casing;
- Rotation error (orientation of pipe's grooves if not compensated regularly can be significant in long boreholes);
- Positioning error (depth)
- Temperature drift of transducer and analog reading units.

To go further, please read Mikkelsen (2003 b).

A good indication to increase accuracy in general is considering also in the design stage, inclinometric pipe with larger diameters available: deformations of pipe along the time could open or break soon the gooves and the casing will be unusable.

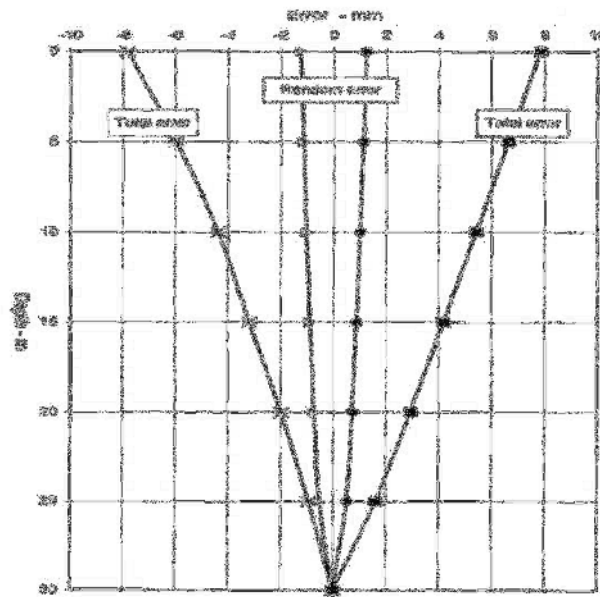


Figure 141 : Total and random errors in inclinometer data. (Mikkelsen, 2003 b)

### 3.2. AUTOMATIC PROBE INCLINOMETER SYSTEM

The system developed by CNR-Italy represents a technological evolution of Automated Inclinometer System, developed to measure a more accurate and reliable depth displacements in a landslide areas and to determine the speed of movement (Figure 142). The System, controlled by a PC, consists of a biaxial inclinometric probe with the novelty by a integration of a electronics for data acquisition and storage, an electric motor with encoder for precision driving and control in continuous position of the probe. By suitably programming the electronic controller, the probe periodically goes down into the tube, then goes up, making some stops for the measures at the desired levels. The data is acquired and stored by electronics on board the probe and at the end of the cycle of measurement are transmitted wireless mode (other news) at PC for data processing. This involves the elimination of expensive cables connecting the probe at the PC (large section) and especially susceptible to wear (for the high number of cycles of measurements). These major technological innovations have led to a significant reduction in size, weight and consumption, which can lead to electricity through solar panels and battery. The system is also designed for remote control and you can set thresholds to alert / alarm system including the speed of displacements recorded.

To go further, please read Lollino (1992) and datings.



*Figure 142 : Automatic probe inclinometer (courtesy of Ing Lollino, CNR-IRPI Italy).*

### **3.3. IN-PLACE INCLINOMETERS**

In-place inclinometers are typically used for monitoring subsurface deformations around excavations when rapid monitoring is required or when instrumented locations are difficult to access for continued manual readings and also is used to monitor landslide areas. The device consists of a series of gravity-sensor transducers (uniaxial or biaxial), joined by articulated rods, positioned at intervals along the borehole axis or concentrated in zones of expected movement (Figure 143). The main advantages include rapid automatic data logging and real-time monitoring, while a disadvantage is the great complexity and expense of the hardware.

To go further, please read Dunnicliff and La Fonta (2001) and La Fonta and Beth (2002), Machan G. and Bennett V.G. (2008).

In-place inclinometers can be used in combination with a conventional inclinometer in two possible modes:

- a) In-place version is installed before the conventional inclinometer to define the location of any transverse deformation, with minimal labour costs for reading. If deformation occurs, the in-place version is removed and the zone is monitored by a conventional inclinometer probe.
- b) Conventional inclinometer is first installed to indicate any deformation and the in-place system is installed later to minimize subsequent effort and to provide an alarm trigger.



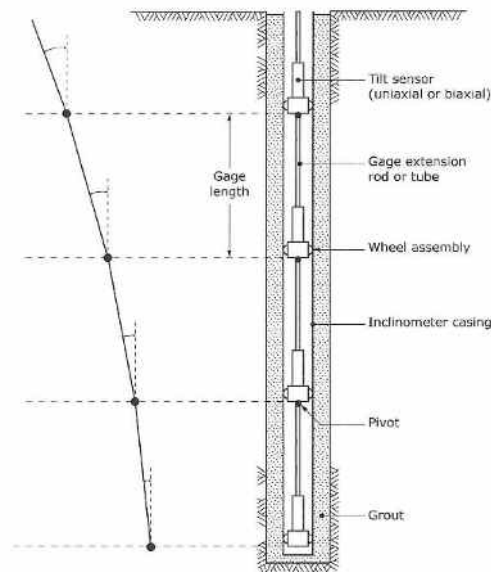


Figure 143 : In-place inclinometer (Dunnicliff et al., 2005).

## 4. PIEZOMETERS

Piezometers are instruments used to monitor water level in the ground and to determine the value of pore water pressure. To measure the pressure the piezometers are sealed within the ground so that they respond only to groundwater pressure around themselves. Piezometers should ideally have a very short screen and filter zone: if this is located at a specific isolated depth, the piezometer is defined punctual, while, if the piezometer has a filter on all its length, is defined windowed. Piezometers can be grouped into those that have a diaphragm between the transducer and the pore or joint water and those that do not. Instruments in the first group are piezometers with pneumatic, vibrating wire and electrical resistance strain gage transducers; instruments in the second group are open standpipe and twin-tube hydraulic piezometers. Generally the term “piezometer” indicates a device that measures the interstitial water pressure in a specific ground layer; otherwise it will be used the term “observation well” that suggests an instrument that has no subsurface seals and that creates a vertical connection between strata. When we want to define the groundwater level we use observation wells and open piezometers, while, when we want determine the pressure of interstitial fluid, piezometers with pressure transducers are applied. The main problem with the piezometers is the time-lag between the variation of piezometric level in the aquifer and the respective variation in the piezometer.

To go further, please read Dunnicliff (1988-1993) and Mikkelsen (2003 a).

### 4.1. OBSERVATION WELLS

An observation well consists in a plastic or steel pipe, installed in a borehole, that is slotted (“windowed”) in the lower section (Figure 144). The cavity between the pipe and the borehole is filled with sand/gravel, creating a vertical connection with the strata. So, to prevent water infiltration from the surface, the upper part is sealed with concrete and bentonite or quarry- clay. For the same reason it is placed at the top of the pipe a cap that has a hole of connection with the outside in other that air pressure overtopping water level is same

as atmospheric pressure. Applications of observation wells are limited at the case of continuously permeable ground in which groundwater pressure increases uniformly with depth. If the well crosses rock or soil strata with different hydraulic conductivity, it will be registered the layer with maximum value of conductivity. To obtain the piezometric level a measure dipmeter probe suspended to a marked cable, is lowered in the pipe. When the probe contacts the surface of the water, a led illuminates and the beeper sounds; the operator then can read the depth-to-water measurement (a reference point on top of the pipe or on surface should be selected for multiple readings). The resolution is 1cm.

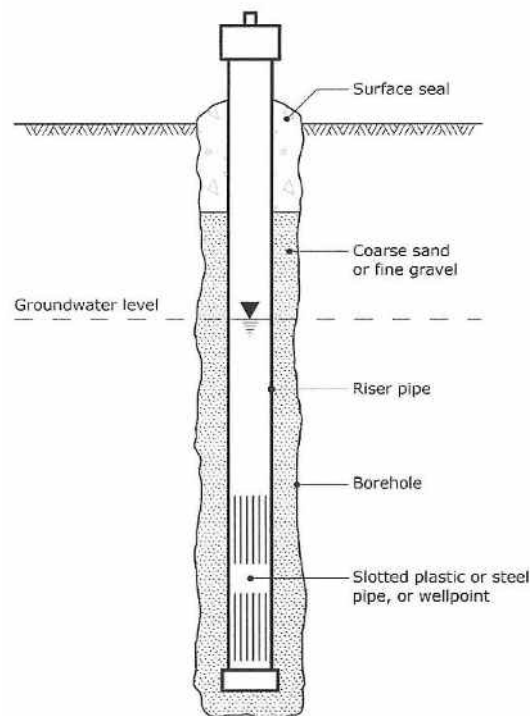


Figure 144 : Observation well (Dunnicliff et al., 2005).

## 4.2. OPEN STANDPIPE PIEZOMETERS

They are different from observation wells because, to measure the interstitial pressure of a specific layer, the cavity is sealed with concrete and bentonite over the monitoring layer (Figure 145). When there is the possibility of undesired infiltrations from the bottom it is placed under the layer an impermeable pad.

The components are identical in principle to components of an observation well, with the addition of seals. Also an appropriate stopcock cover can be used, ensuring that venting of the standpipe is not obstructed.

The main advantages of open standpipe piezometer are:

- Reliability of collected data;
- Long term monitoring;

- Can be used to evaluate the hydraulic conductivity;
- Integrity of the seals can be evaluate after the installation;
- It can be converted to diaphragm piezometer;

The main limitations of open standpipe piezometer are:

- Long time lag;
- The device is subject to damage during the installation and by vertical compression of soil around standpipe.

To obtain a more rapid answer in soils with permeability lower then  $10^{-6}$  m/s is employed a Casagrande piezometer. It is always an open standpipe piezometer, but it is composed by a filter element, consisting in cylinder of porous stone, linked with the surface by the means of a tube with a little section.

Various methods are available for reading open standpipe piezometers, most of which involve sounding the elevation of the water surface with a probe. The most commonly used probe is an electrical dipmeter, described before.

Moreover a pneumatic, vibrating wire or electrical resistance strain gage pressure transducer can be inserted into the open standpipe piezometer below the lowest possible piezometric level, thereby allowing continuous readings to be made.

The transducer can be connected to a acquisition system (data collector) and downloaded in field manually by a notebook (RS 232 serial port or wireless) or downloaded with a GSM-GPRS modem connection by a remote location (monitoring centre).

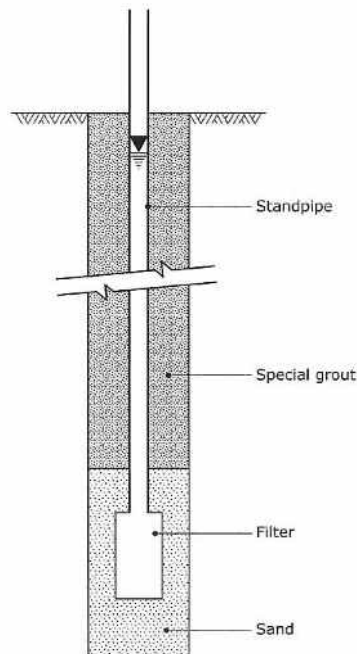


Figure 145 : Open standpipe piezometer (Dunnicliff et al., 2005).

### 4.3. TWIN-TUBE HYDRAULIC PIEZOMETERS

This device was developed for installation in the foundations and fill during construction of embankment dams. It consists of a porous filter element connected to two plastic tubes that allow, through water circulation, the elimination of gas bubbles eventually penetrated within the piezometer. Gas bubbles tend to get together both in the filter element and in the tubes: the creation of discontinuity in the liquid caused not realistic pressure readings. The gas must be removed by flushing: this is the reason for requiring two tubes. Plastic tubes are connected with pressure measure instruments like manometers and electric transducers. The piezometric elevation is determined by adding at the filter elevation a quantity corresponding at the register pressure.

The main advantages of twin-hydraulic piezometer are:

- Inaccessible components have no moving parts;
- It is reliable;
- Long successful performance record;
- When installed in fill, integrity can be checked after the installation;
- Piezometer cavity can be flushed;
- It can be used to measure permeability.

The main limitations are:

- Application generally limited to long-term monitoring of pore water pressure in embankment dams;
- Tubing must not be significantly above minimum piezometric elevation;
- Periodic flushing may be required.

#### 4.4. PNEUMATIC, VIBRATING WIRE AND ELECTRICAL RESISTANCE PIEZOMETERS

Their installation is analogue to open standpipe installation. In these piezometers the difference is that the water crosses the porous filter entering in a cavity where it acts on a rubber or metal membrane.

##### 4.4.1. Pneumatic piezometer

In this type of piezometer introducing gas behind the membrane (by the means of a tube), when gas pressure is just higher than pore water pressure, there is an extroversion of the membrane that allow to gas to enter in a tube connected with the surface. Obtaining the gas presence in this tube it is possible to measure balance pressure. In some models oil is used instead of gas (Figure 146).

The main limitation of these devices is that membrane extroversion reduces volume available to interstitial water: consequently pore water pressure increases. If the gas pressure increase is not slow and gradual we can carry out wrong pore water pressure readings. This problem is bigger in clay soils.

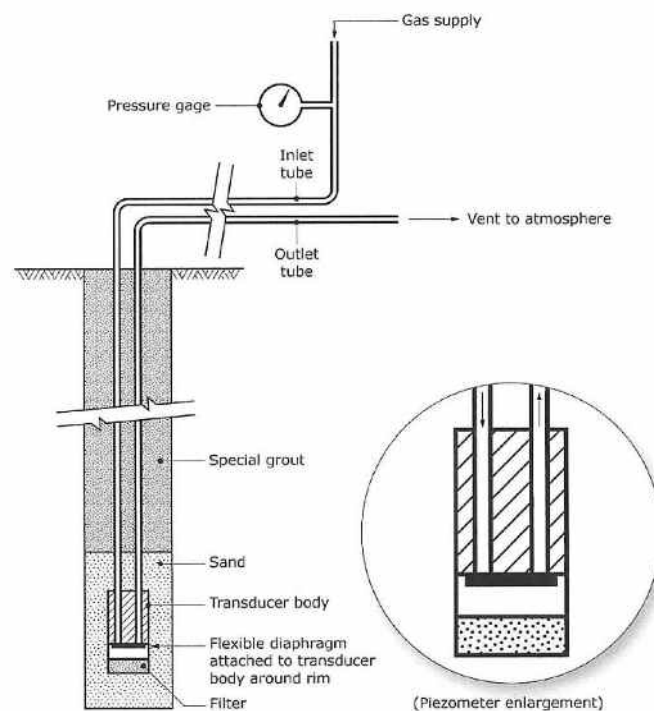


Figure 146 : Pneumatic piezometer (Dunnicliff et al., 2005)

#### 4.4.2. Vibrating wire piezometer

The vibrating wire piezometer has a metallic diaphragm separating the pore water from the measuring system. A tensioned wire is attached to the midpoint of the diaphragm: the diaphragm deflection causes changes in wire tension (Figure 147). Since the oscillation frequency wire exchanges with its tension, pinching with an electromagnet the wire in midpoint and measuring with another coil oscillation frequency we can determine wire tension and then pore water pressure.

The principal limitation consists in fact that wire can work loose causing a variation of vibration frequency. Also, the wire can be subject to corrosion phenomena.

Instead, the advantage of vibrating wire piezometer are:

- easy readings;
- short time lag;
- no freezing problems;
- independence of reading elevation from the height where is placed the piezometer;
- possibility to measuring negative pore water pressure.

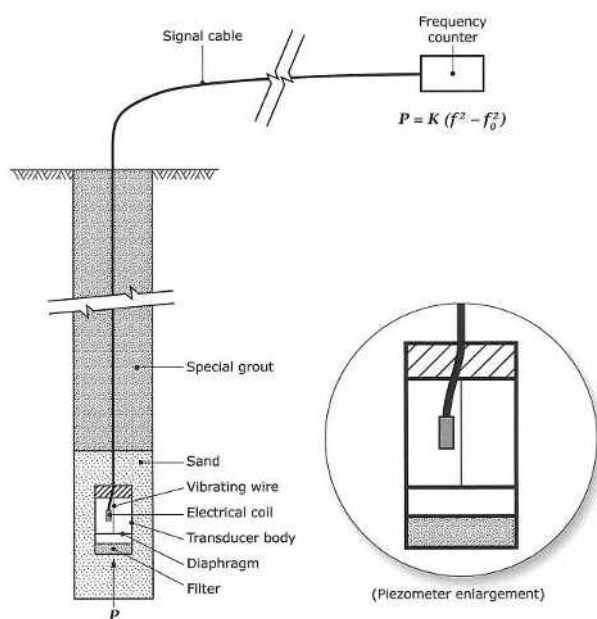


Figure 147 : Vibrating wire piezometer (Dunnicliff et al., 2005).

#### 4.4.3. Electrical resistance piezometer

These devices are based on the concept that the resistance exchanges with length which in turn exchanges with the vary of stress affecting the conductor. There are used especially for in situ tests when there is the necessity to have little instruments and it is possible to remove



periodically the device. They are dividing in two categories on the base of wire installation: bonded and unbonded electrical resistance strain gage piezometers.

The advantages of electrical piezometer are the same of vibrating wire piezometer advantages, but unbonded version can provides temperature and dynamic measurements.

## 5. CONTACT EARTH PRESSURE CELLS

Earth pressure cells are used to determine distribution, intensity and direction of total stress. On the base of their employ in different kind of measurements they are subdivided in:

- Embedment earth pressure cells (measurements within a soil mass, like embankment dam or fill overlying a tunnel);
- Contact earth pressure cells (measurements at the interface of a structural element, like retaining walls, tunnels, piles and below shallow foundations).

There are two models of cells that can be used for measurements within the ground: diaphragm cells and hydraulic cells. The first type is characterized by a rigid circular membrane that is deflected from external soil pressure: the deformation is captured by an electrical resistance transducer directly linked to the interior surface of the cell or by a vibrating wire transducer. The two faces in diaphragm cells are independent and can be active or not. If either the faces are active and are in similar contact with the soil, the measurements are important to understand the quality of the installation. The hydraulic type, instead, is constructed from two circular or rectangular stainless steel plates welded together around their periphery and separated by a narrow gap filled with hydraulic fluid. It is very important that the cell is filled with de-aired liquid and that no gas bubbles are trapped during the filling. External pressure squeeze the two plates together creating an equal pressure in the internal fluid. A length of stainless steel tubing connects the fluid filled cavity to a pressure transducer that converts the fluid pressure into an electrical signal transmitted by cable to the readout location. The active faces of hydraulic cells can be thin (when either the faces are active) or more thick (in the case of only an active face).

The types of contact earth pressure cells are similar to those utilize within a soil mass (Figure 148). In fact, some embedment earth pressure cells can be used directly as contact cells. However there are some exceptions. First, a hydraulic cell with a thin active face couldn't use because it's not possible to install the cell completely sticking to the structure. Second, a cell must be used with two active faces because the measurements collected from the external surface are more subject to errors. Contact earth pressure cells provide a direct means of measuring total pressures, for example the combination of effective soil stress and pore water pressure. Measurements of total stress at the face of the structural elements are not plagued by so many errors associated with measurements within a soil mass; however, cell stiffness and the influence of temperature are often critical. The principal requirement for the installation of a cell at the interface of a structure is that the sensitive face of the cell is absolutely flush with the surface of structural element.

To go further, please read Dunnicliff (1988-1993).

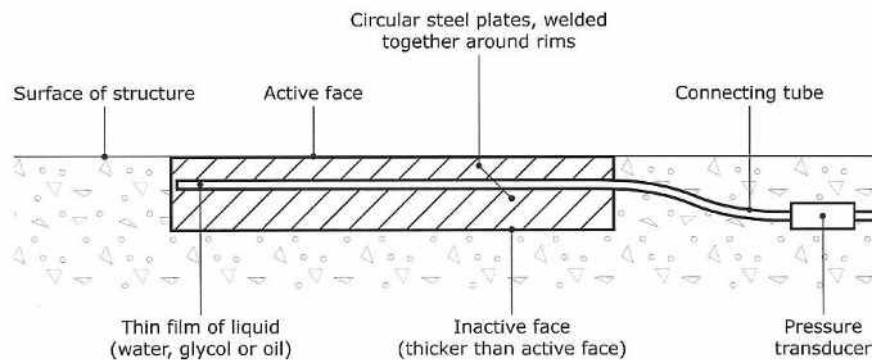


Figure 148 : Contact earth pressure cell (Dunnicliff et al., 2005).

## 6. MULTIPARAMETRIC IN PLACE SYSTEMS

Although in the environmental field several applications are known about multiparametric devices (probe for water quality, chemical and physical parameters) in the geotechnical field there are only a few applications. One of the main advantage is the correlation of the geoindicators in the same time and site conditions with a significative cost reduction for the drilling activities, control units/transmission systems specially when piezometric, inclinometric and extensometric measurements are required in the same area.

### 6.1. DMS SYSTEM

The DMS is an in place system specifically designed for the real time stability control of landslides, cuttings, engineering works. It allows the differential monitoring of the major physical and mechanical parameters of the soil-bedrock and of the structures in 2D/3D as well as of the piezometric level, accelerometric variations, temperature.

DMS column is like a “spiral cord” composed of a sequence of hard tubular modules (hosting sensors and AD control), connected with each other by special joints, endowed with the degree of freedom specific for the type of measurement performed (Figure 149). Depending on the instrumentation version, vertical, horizontal and inclined installations are possible.

D.M.S. 3D system has been specifically studied for 3D measurement in drilling holes, so as to record deformations directly on rocks or soils, and to execute multipiezometric measurements in the same monitoring hole. The system is composed of modules (E.D. 80 millimeter, with packers for direct hole anchorage), linked by special 3D flexible joints with high traction resistance (up to 100 KN) and maximal extension  $> \pm 100$  mm/module.

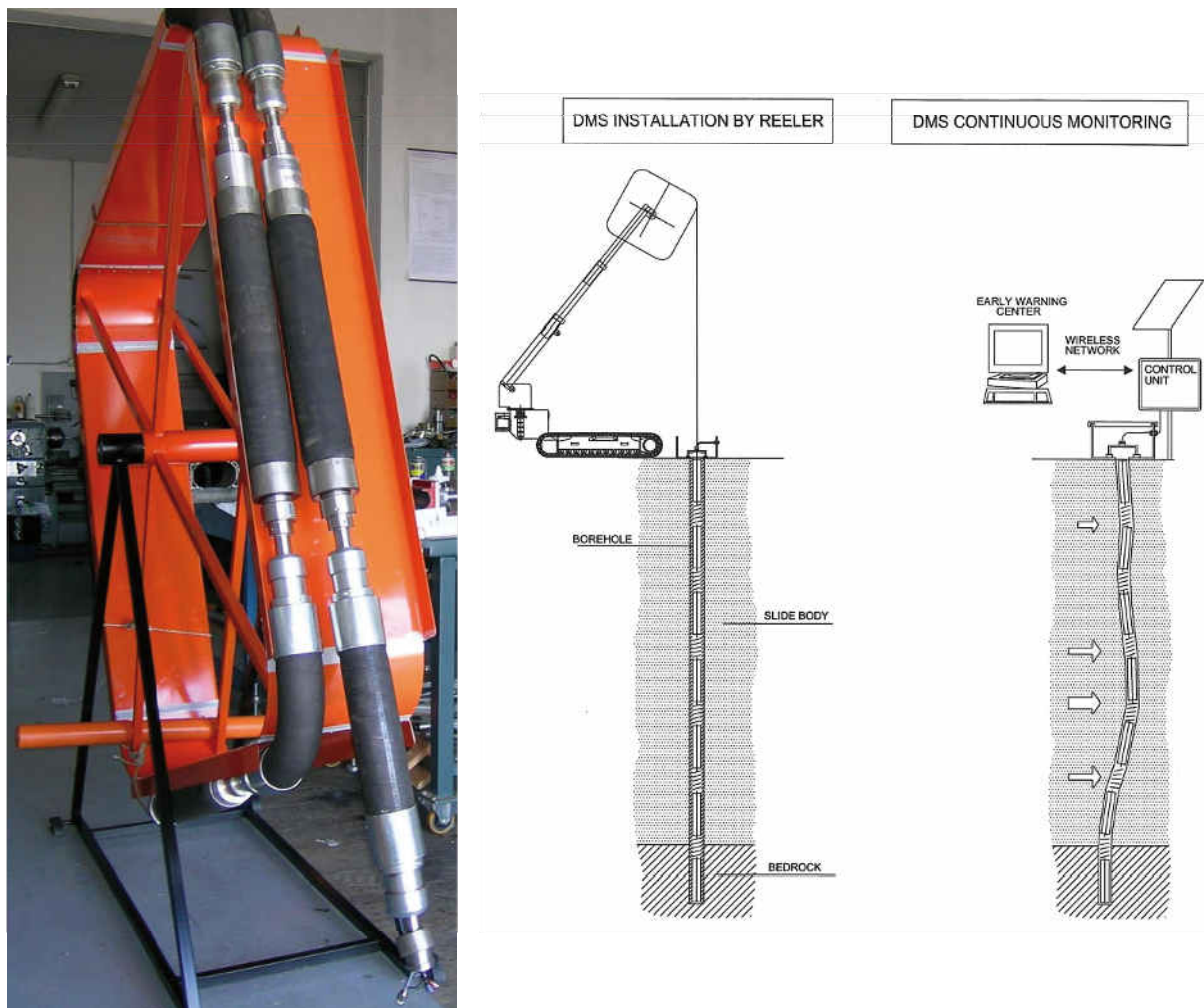


Figure 149 : Left - D.M.S. 3D column. Right - Installation and continuous monitoring of D.M.S. column.

Thanks to the modular structure DMS can operate in harsh environments with continuous adaptability to bend and twist of the casing (or borehole), also with high deformations rate. It is possible to use a wide range of transducers on a modular basis that may be interfaced with the same digital control unit: mono/biaxial inclinometers, extensometers, accelerometers, piezometers, thermometers, digital compasses.

Advantages compared to traditional instrumentation are:

- Simultaneous multiparametric monitoring in the same casing/borehole
- 2D/3D deformation analysis
- Continuous in place monitoring H24 suitable for Early Warning applications (self tests on board and functionality checks guarantee a reliable monitoring)
- High adaptability of the monitoring column to deformations
- High space resolution of measurements

- Easy installation in place, and possibility to recover the instrumentation after the monitoring period
- Modularity and cost reduction

For column with considerable length ( $>30\text{m}$ ) installation is made easier by means of a DMS reeler, which allows to install and retrieve the column inside the drilling hole/casing. The robust structure of the columns allows also to transport and install the system directly inside the casing by means of a helicopter (mountain areas and harsh environments).

To go further, please read Lovisolo and Della Giusta (2005).

---

# PART F

## OTHERS TECHNIQUES

---

- 
- **SECTION 1:** Global Navigation Satellite Systems (GNSS, GPS ...) p. 240
  - **SECTION 2:** Introduction to Core Logging p. 247
- 

### Sections 1

- **Author:** J. Gili<sup>1</sup>
- **Reviewer:** T. Eiken<sup>2,3</sup>

<sup>1</sup>. Department of Geotechnical Engineering and Geosciences, Universitat Politècnica de Catalunya, Barcelona, Spain. [j.gili@upc.edu](mailto:j.gili@upc.edu)

<sup>2</sup>. Department of Geosciences, Universitetet i Oslo, Norway.

<sup>3</sup>. International Center for Geohazards (ICG), Oslo, Norway.

Gili J., 2010. *Global Navigation Satellite Systems*. In the Deliverable 4.1 of the European project SAFELAND: *Review of Techniques for Landslide Detection, Fast Characterization, Rapid Mapping and Long-Term Monitoring*. Edited in 2010 by Michoud C., Abellán A., Derron M.-H. and Jaboyedoff M. Available at <http://www.safeland-fp7.eu>

### Section 2

- **Authors:** C. Michoud<sup>1</sup>, L.H. Blikra<sup>2</sup>, A. Abellán<sup>1</sup>, M.-H. Derron<sup>1</sup>, M. Jaboyedoff<sup>1</sup>
- **Reviewer:** M. Levisolo<sup>3</sup>

<sup>1</sup>. Institute of Geomatics and Risk Analysis (IGAR). Université de Lausanne, Switzerland. [clement.michoud@unil.ch](mailto:clement.michoud@unil.ch)

<sup>2</sup>. Åknes/Tafjord Early Warning Centre, Stranda, Norway.

<sup>3</sup>. Centro Servizi di Geoingegneria S.r.l., Acqui Terme, Italia.

Michoud C., Blikra L.H., Abellán A., M.-H. Derron, Jaboyedoff M., 2010. *Introduction to Core Logging*. In the Deliverable 4.1 of the European project SAFELAND: *Review of Techniques for Landslide Detection, Fast Characterization, Rapid Mapping and Long-Term Monitoring*. Edited in 2010 by Michoud C., Abellán A., Derron M.-H. and Jaboyedoff M. Available at <http://www.safeland-fp7.eu>

# **1. GLOBAL NAVIGATION SATELLITES SYSTEMS (GNSS, GPS...)**

## **1.1. INTRODUCTION**

The GPS is a radionavigation, timing and positioning system with a wide set of applications: from air, sea and terrestrial navigation, to environmental studies, natural resources management, GIS data capture, surveying and geodetic global measurements. By tracking the electromagnetic waves that the GPS satellites are sending continuously to the world, the system can obtain the antenna position (Longitude, Latitude, and Height, or X, Y, Z coordinates).

In 1995 the Global Positioning System (GPS) became fully operational. Nowadays, at least four satellites are available worldwide, day and night. The equipment is reliable, light, cheap and easy to use. New procedures, methods and software have been developed to assist in the field data capture and in the post-processing. As a consequence, the GPS equipment is progressively more and more used for a wide range of engineering applications, such as the establishment of control points for photogrammetry and remote sensing images, positioning and levelling of boreholes and wells, off-shore surveys, environmental studies and monitoring.

The GPS is based on the NAVSTAR constellation of satellites, deployed by the Department of Defence (DoD) of the United States of America, for strategic purposes. There is a parallel development, by Russia (from the former Soviet Union), based on the GLONASS constellation; although it is not fully deployed, the GLONASS system has been reactivated in the last years. Nevertheless, receivers able to track satellites of both constellations already exist. Nowadays, the European navigation and positioning system, called GALILEO, is under implementation and advanced deployment. It will be interoperable and complementary with GPS and GLONASS. The Chinese Beidou system is also partially deployed. Other satellite navigation systems are announced. The common acronym for all these satellite positioning systems is GNSS (Global Navigation Satellite Systems). Fortunately, all the GNSS systems are very similar in concept and in operation. It is a matter of fact that most of the users speak about GPS even when they are using also other satellites. Step by step, we may evolve to the use of the general acronym (GNSS).

Although the GPS was first conceived for military purposes, the civilian use of the systems is allowed and very common. In the last decade the GNSS has been used extensively for Geodesy and Surveying, modifying and enhancing the conventional survey procedures.

## **1.2. BASIC PRINCIPLE**

The satellites compose the spatial sector. When fully deployed, each GNSS constellation has a basic setup of 24 to 30 satellites, deployed in several orbital planes. The orbits have mean altitudes between 20000 and 23000 Km over the Earth surface and are approximately circular. Each satellite completes approximately two turns around the Earth per day. They send continuously electromagnetic sinusoidal waves to the Earth, in several carrier frequencies within the L band (i.e., for the GPS the carrier waves are L1 and L2, with wavelengths  $\lambda_1 \approx 19$  cm,  $\lambda_2 \approx 24.4$  cm). These carrier waves are modulated according to digital binary codes that have an overall appearance of randomly distributed zeroes and ones. For this reason, they are



called pseudo-random codes. For instance, the GPS satellites send two codes: the C/A or Coarse Acquisition code, only on the L1 carrier, and the P or Precise code (usually encrypted), on both L1 and L2. New GPS satellites will have a C code also on L2.

The GNSS system calculates the user position using a set of measurements called the observables. They consist of data derived from the electromagnetic waves received from each satellite. Dependent on the type of receiver and purpose, the computations can be made using either the code or the phase of the carrier, or a combination of both. Positioning can be in real time or with post-processing. The codes are widely used in navigation and in coarse positioning (10 m typical precision, Figure 150).

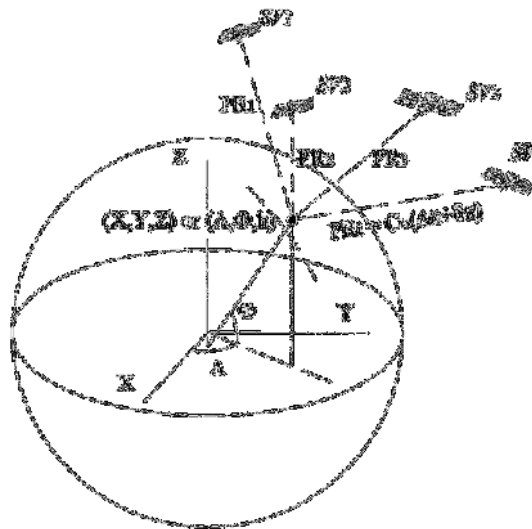


Figure 150 : GPS/GNSS three-dimensional spatial multilateration of a point based on pseudo-ranges (PRi) derived from code observation with different satellites (SVi). ( $\lambda$ ,  $\Phi$ ,  $h$ ) are respectively Longitude, Latitude and the height of the point above the reference ellipsoid. ( $X$ ,  $Y$ ,  $Z$ ) are the global geocentric cartesian co-ordinates (Gili et al., 2000)

Sophisticated geodetic receivers are used when higher accuracy is required, as in monitoring. The computations are based in the phase of the carrier wave, no longer in the pseudorange measured from the code. Additionally, double frequency or “dual frequency” receivers are advised. Several (two or more) receiver + antenna have to track simultaneously the carrier waves, and register the change in phase (phase angle) between the satellite and the antenna with time. The calculations are more involved, with algorithms (single differences, double differences, etc.) extending over observation time, usually from several minutes to several hours. The clue point is the ambiguity resolution, that is, the determination of the integer number of complete wavelengths,  $N$ , that fits between a given satellite and the antenna (see Figure 151). This operation can be identified with an initialization period that has to be spent in some kinematic methods. The most common processing procedures actually compute relative positions of the points in the space. The vector that links two station points is called *baseline* (Figure 151). A new point (R) is positioned by adding the *baseline* to the co-ordinates of a previously known one, called *base point* (B). Often, these calculations are carried out after the fieldwork, during the post-processing, merging the data files from several user receivers. Thus, the results may achieve very high precision, up to few mm.

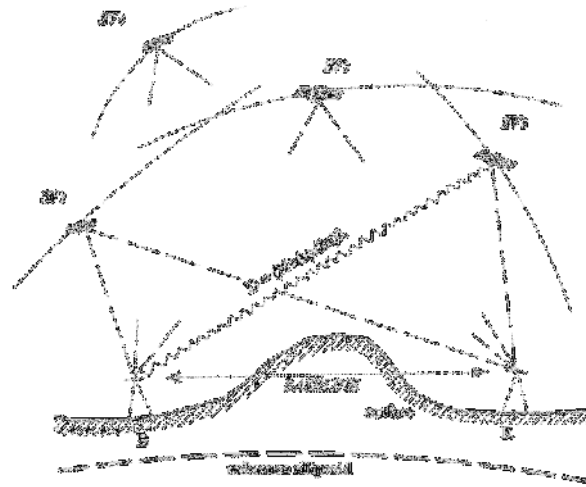


Figure 151 : GPS/GNSS carrier phase measurements.  $D$  is the distance between the antenna and a given satellite,  $\lambda$  the wavelength,  $\phi$  the phase angle and  $N$  an integer number (Gili et al., 2000).

### 1.3. FIELD PROCEDURES

There are several procedures or methods for data capture and treatment depending on the purpose and precision required for the GNSS survey:

- Considering the *number* of receivers involved, the positioning may be *absolute* or *autonomous* positioning, when using one single unit (low precision), and *relative* positioning when two or more units are used coordinately (observing at the same time and sharing data). The term *differential* GPS (DGPS) refers to a medium precision mode based on the coarse code: the user's receiver derives the position as in the Figure 150, but enhancing the pseudo-ranges with a set of corrections supplied by an infrastructure of reference stations that covers the area.

But, in all the applications requiring high precision, two or more units (receiver plus antenna) observing the carrier phase are needed. In some surveying cases, the reference stations might belong to a network of base stations, public or commercial, spread over the territory. For monitoring applications, however, it is preferred to have the base station(s) in a stable outcrop, very close to the site, as the precision degrades with the distance between stations.

- According to the receiver *movement*, the surveys may be *static*, *kinematic*, or a combination of both. Several procedures are available, the Static method, the Fast-Static, the Pseudo-Kinematic, the Stop-and-Go, and others. Measurement of landslide displacements can be undertaken by means of either static and/or kinematic methods. The choice depends on practical local considerations, namely, the accessibility, the number of points, the precision, the obstacles and the distance from point to point.

The first precision GPS method was the *Static* one, used for the observation of geodetic networks covering hundreds of kilometres; the logging sessions last for several hours in order to achieve the target precision. Nowadays, the most productive methods available for determining single points with precision of millimetres or

centimetres, are the *Fast-Static* (FS, also called *Rapid-Static*) and the *Real Time Kinematic* (RTK), see Figure 152. The first one is a method with post-processing, an evolution of the former Static positioning. In a typical case, with baselines around 1 km and 6, 5 or 4 common satellites in the sky, each session of logging needs around 10, 15 or 20 minutes respectively (although it is advisable to register some time in excess). In the RTK method, the information of code and carrier phase observables received at both ends of the baseline (Base station and Rover station, Figure 152) is merged to compute the precise position on the spot. For this, our Base must transmit some information for each observation epoch to the Rover. The communication Base-to-Rover can be by radio (i.e. a UHF/VHF data link, quite directional), or via GSM, GPRS or internet.

The main characteristics of the quoted methods are summarized in the Table 21.

It is also available the *RTK-Network* method: the local Base is substituted by several permanent stations that constitute a network surrounding the area. Through GSM/GPRS or via the internet, the rover can connect to this general network to obtain some net-interpolated solutions (from the so-called Virtual Reference Station, VRS). However, with the present networks density and availability, this quite new method is less suitable for a precise monitoring as the precision degrades with the distance to the *real* Base.

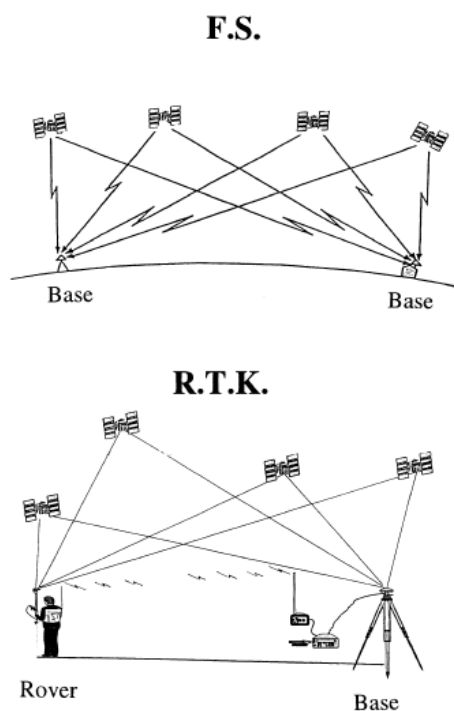


Figure 152 : Fast-Static (F.S., or Rapid Static) and Real Time Kinematic (R.T.K.) GNSS methods. The station over a known fixed point is referred as Base, and the receiver that moves from point to point as Rover (Gili et al., 2000).

Table 21 : Main characteristics of main GNSS/GPS methods (modified from Kahmen, 1997, and Gili et al., 2000).

Method	Obs.time, per point, after initialisation	Post-process	Strength against lost of signal	Typical max. baselines (km)	Typical baseline planimetric error <sup>b, c</sup>
General Static	1 to several hours	Yes	robust	50 to 100 <sup>a</sup>	(5–1)mm+(1–0.1)ppm
Fast-Static or Rapid-Static	8 to 20 min	Yes	robust	15 to 20	5mm+1ppm
R.T.K.	1 to 10 s	No	sensitive	10	10mm+2ppm

<sup>a)</sup> Easily baselines can reach about 50 km. Depending on observation time, type of post-processing and required precision, it may be extended up to thousands of km. <sup>b)</sup> The vertical or elevation error is roughly 1.5 times the planimetric one. This factor can increase up to 3 or 4 with the latitude. <sup>c)</sup> 1 ppm means one part per million, or one additional millimetre per kilometre of measured baseline.

- Depending on *when* the solution is obtained, the procedure may be in *real time* (when the position is obtained in the field, the RTK for instance), or with *post-process* (as the FS). As discussed previously, the post-processing methods are used only in certain precision procedures; special software (with appropriate algorithms, time averaging, filters and network adjustment) is run in order to obtain the final position.

#### 1.4. SOME CONSIDERATIONS ON THE USE OF GNSS IN LANDSLIDE MONITORING AND ITS PRECISION

Field surveys are usually carried out with a given frequency (i.e. monthly, weekly) with removable GPS-GNSS stations. The difference between the present values and the initial coordinates, gives the movement of the target. The main results of a GNSS positioning are the coordinates of the occupied points at a certain time. Then, we can obtain displacements as differences of positions along the time; velocities by derivatives; accelerations by double derivatives, etc. The results are discontinuous over time, and related to the cumulative movements of surface points.

Although the costs is still high, it is also possible to automate the procedure for the continuous monitoring of the displacements with GPS stations working permanently on the slide area (Malet et al., 2002). This solution, among others, is however justified to ensure the monitoring of sites with high risk for the people downhill, and is the only GPS setup eligible as an early warning system.

In the usual ‘manual’ GPS surveys for monitoring, the precision of the positions is highly dependent on both the equipment and, fundamental, the selected method. When using a relative GPS high precision method we can reach cm to mm accuracy, depending on the total log time, the number of satellites under tracking, their geometry (the spatial distribution on the user’s horizon...), and on the network configuration (number of receivers working together, redundancy of the net, fixed base points...). Usually, atmospheric delays, the orbital parameters and the co-ordinate transformation are the most important factors in terms of

positioning error. Fortunately, the effect of these factors can be avoided or reduced when measuring *displacements* with GPS. Using two or more receivers -relative positioning-, at points located, for instance, up to 20 km, these errors have a similar influence in both baseline ends, and cancel.

When working with centimetre precision at several tents of kilometres, and without direct line of sight, even in the night or raining, it is clear that the advantage of satellite positioning over conventional surveying increases as the working area enlarges. On the other hand, the antenna must have a good view of the sky: the buildings, the forest and the slopes of narrow step valleys are obstructions to the direct reception of the radio signal that might difficult the positioning.

Another important source of error is the setting-up of the antennas over the physical marks in the field. Due to access, to environmental considerations and/or budget constraints, the marking of the control points is quite light. The geodetic-type concrete cylinders are seldom used. Instead, some special antenna mountings can be used to allow the forced centring (Schäfer 2008). In other situations, it is better to station the antenna over a surveying tripod than sustaining it over the telescopic pole (Figure 153).



Figure 153 : Different antenna set-up: antenna directly over a rock outcrop; setting-up with tripod and optical plummet; antenna over a telescopic pole.

Another issue when talking about precision of the results is the postprocessing software in use. There are two fundamental approaches. The first one are the *Standard or commercial* GNSS software, provided by the Receiver manufacturer, like TGO from Trimble, the LGO from Leica, the TopconTools from Topcon, etc. They use to provide excellent results for small and medium networks as the ones deployed usually around the landslide area. They are quite user friendly, but the baselines are processed with the default parameters and the user has few chances to choice or change them. On the other hand, we have the *scientific* GNSS software like BERNESSE (Univ. of Berna) or GIPSY (JPL) or the PPP (Precise Point Positioning) techniques. There, the user might select hundreds of parameters and models (troposphere, ionosphere, meteo, precise orbits, antenna offsets, etc). However, this kind of software must be run by highly skilled operators, besides they need very long logging sessions (day to week). Fortunately, this high level software is only essential for long baselines (>30 km), and wide networks.

No big networks of control points are usually observed around a landslide monitored with satellite positioning. A common situation, due to accessibility, personnel and equipment

limitations is to use a set of radiations from one base point. It is suggested, if possible, to set-up a second base receiver in another fixed point; this will considerably strengthen the results. The reoccupation (at different hour of the day) and the incorporation of some fixed points (for result checking) are also advisable strategies.

In the Table 22, the actual planimetric (X-Y) and elevation errors for a typical landslide monitoring setup are given, when using the FS or the RTK method (Gili et al., 2000).

*Table 22 : Example of planimetric and elevation errors for a typical GPS landslide monitoring (modified from Gili et al., 2000)*

GPS method	RMS (1 $\sigma$ , 68%)	
	Planimetry	Elevation
FS or Rapid Static	12 mm	18 mm
RTK	16 mm	24 mm

<sup>a)</sup> The GPS observation consists in a single radiation from one base point. The baselines range between 1 and 1.5 km. The errors are distributed normally. The setting-up methods considered are: tripod in the base, and telescopic pole with bubble in the rover side.

## 1.5. EXAMPLES

In the last decade landslide monitoring with GPS has experienced a rapid development because it has demonstrated to be a reliable technique to follow the slide motion especially for slow movements.

An early result was reported by Bonnard et al. (1996) in instrumented landslides located in the Swiss Alps: using several receivers simultaneously, they obtained a precision of about one centimetre. This precision was higher than that achieved there using ordinary surveying techniques of triangulation.

Brunner et al. (2007) describes a long experience of monitoring a deep seated mass movement in Gradenbach (Austria) with relative GPS. The authors reported motion discrepancies (1  $\sigma$ ) of  $\pm 4$  mm in horizontal direction and  $\pm 8$  mm in vertical direction during the last seven years (17 GPS surveying campaigns with at least 48 hours of observation; choke-ring antennas, post-processing software Bernese 5.0, etc).

## 1.6. TRENDS

As previously quoted, it is possible nowadays to install permanent GPS stations in the landslide acquiring continuously the GPS observables (Malet et al., 2002). The data can be remotely transmitted to the Early Warning Centre, where it can be processed in near real time (hourly sessions, for instance).

According to ClimChalp (2008), continuous monitoring with low-cost GPS receivers is currently object of research. Another way to adjust the installation budget is to implement a multi-antenna scheme, where one receiver is able to sequentially log or process the GPS signal acquired by several antennas spread in the area (Chen et al., 2005).

## 2. INTRODUCTION TO CORE LOGGING

All techniques described in the previous chapters are employed to investigate landslide surfaces and sub-surfaces by geophysical measurements from plane or at the ground surface. In most cases, there are arising a series of questions regarding the interpretation of such data, and there will be a need for confirmation and comparison by direct measurements in the subsurface. This part gives a short introduction of different methods and instrumentation for subsurface investigations (cf. Table 23). Three main references on this topic are recommended: McGuffey et al, in Turner and Schuster (1996), the US Army Corps of Engineers (2001) and Bell (2007).

Borings should be performed in order to obtain the following main data:

- Rock or soil description and characteristics
- Sliding surfaces
- Geomechanical characteristics
- Hydrogeological parameters
- Displacements

Following techniques can be used:

- Drilling registrations and observations (Figure 156)
- Core logging (Figure 154 and Figure 155)
- Geophysical borehole logging
- In situ testing, for example hydrological pumping
- In place equipments.

Table 23 resumes some of the data that can be collected in connection with boreholes. The US Army Corps of Engineers (2001) gives details on the listed techniques and tests, such as the famous Standard or Cone Penetration Test (SPT, CPT) which assess the shear strength of soils. McGuffey et al, in Turner and Schuster (1996), provides more details on geophysical well logging, such as the Neutron-Neutron log which gives information on natural moisture content above water table and porosity below water table. Other geophysical logging sensors give data on P and S velocity, resistivity, conductivity, density, gamma and temperature.

Borehole investigations are one of the most important datasets for investigating large landslides, and are crucial for detecting subsurface deformation and sliding surfaces. In addition to geophysical logging and hydrological testing, two areas of investigations are important:

- Core description and logging



- In-place equipment for investigating deformations and pore pressure (inclinometers, extensometers and piezometers)

Ideally one should perform core drilling giving rock cores, where the rock characteristics and possible sliding planes can directly be documented and studied. Examples of two sliding planes at the Åknes rockslide are shown in Figure 154 and Figure 155 (Ganerød et al., 2007). Destructive drillings are often performed in landslide studies, and then rock characteristics can be studied by camera or televiewer equipment.



*Figure 154 : Core logging in Åknes. Lower borehole shows a crushed zone at 115 m depth, possible representing a sliding zone.*



*Figure 155 : Core logging in Åknes. Middle borehole, 32 m depth: crushed and brecciated zone with silt and clay which represents the upper sliding zone, also documented by displacement in DMST<sup>TM</sup> column (Differential Monitoring of Stability, in place instrumentation).*

The documentation of the subsurface displacements is the next important step in the subsurface investigations. This can be done by different approaches (cf. chapters 2.F.):

- Manual inclinometric probes, Inclinometer casing are established in the borehole and measurements are taken manually at different time periods.
- In-place inclinometers or extensometers measuring continuous. This can be combined also with piezometers measuring at different levels. The challenge is to find the best localization of sensors in order to measure the displacements.
- DMS columns. It allows the differential monitoring of displacement 2D/3D along the overall landslide/rockslide domain as well of the major physical and mechanical parameters piezometric level, pore pressure, accelerometric variations, temperature. System is installed in place and measurements are in continuous.

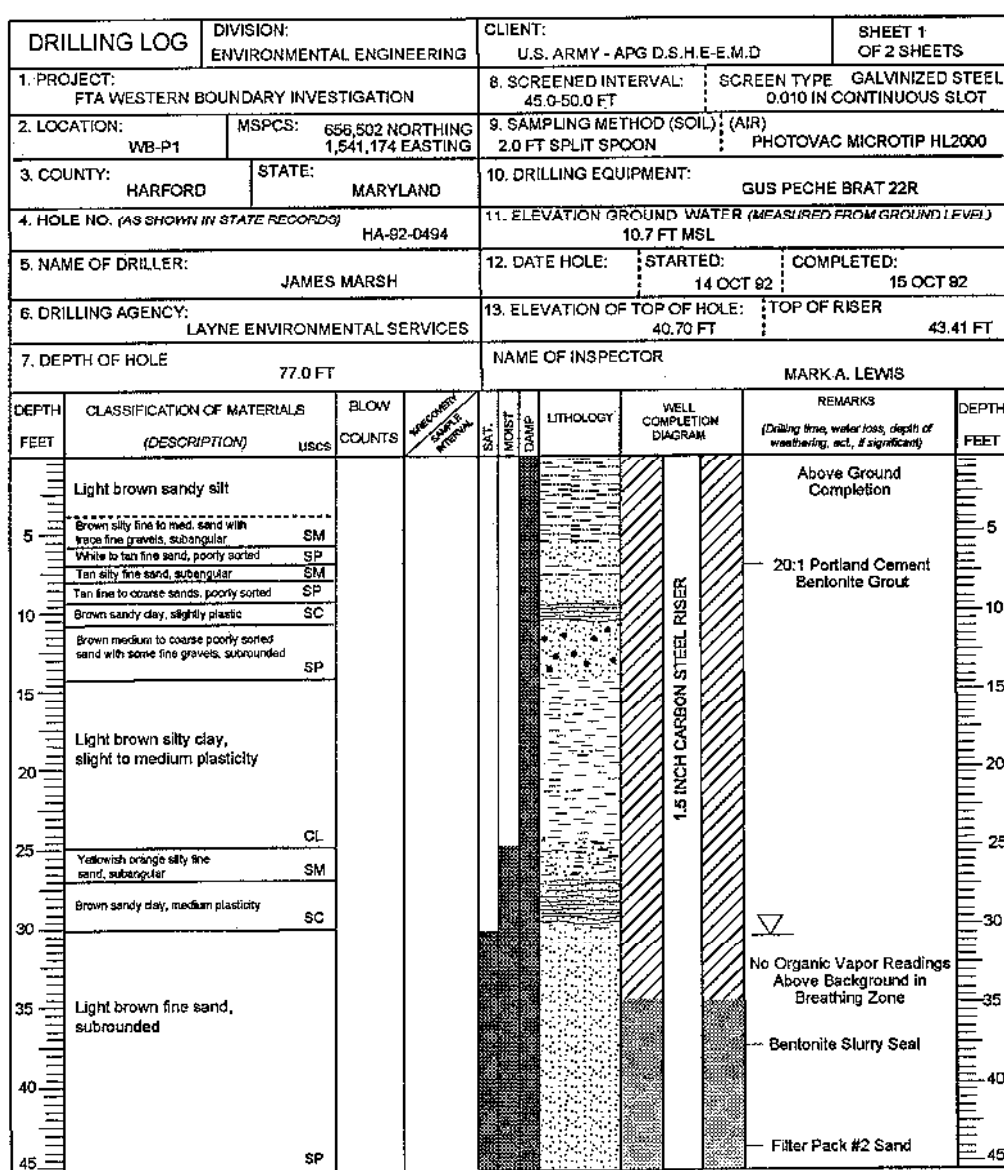


Figure 156 : example of drilling report. The header indicates technical information on the boring, as the sampling method and the equipment. Then drillers reported lithologies, moistures, voids and water tables. (US Army Corps of Engineers, 2001)

Table 23 : Methods and type of data that can be achieved by performing boreholes.

Topic	Argument	Methods			
		Drilling observations	In situ testing	Core logging	Geophysical well logging
Instability	Sliding areas	+		+	
					+
Rock description	Lithology	+	+	+	+
	Bedding			+	
	Discontinuities			+	
	Weathering			+	
	Texture, Structure			+	
	Surface roughness	+		+	
	Solutions, Void conditions	+		+	+
	Nature of infilling			+	
	Inclusions and fossils			+	
	Staining			+	
Geomechanical settings	RQD, Stress conditions		+	+	
	Strength		+	+	
	Plasticity		+	+	
	Liquefaction susceptibility		+	+	
	Bearing capacity		+		
	Density		+	+	+
	Permeability		+	+	
	Porosity			+	+
	Temperature				+
Hydrogeological parameters	Situation of aquifers	+			+
	Drainage systems	+			+
	Saturation				+
	Moisture			+	+
Monitoring	Displacement				+
	Water table				+

# **APPLICATION TO LANDSLIDES: CASE STUDIES**



### 3. APPLICATION TO LANDSLIDES: CASE STUDIES

#### Passive optical sensors

1. Landslide monitoring - *Monitoring Tessina landslide, Italy, from optical remotely sensed imagery.*
2. Landslide mapping - *Landslide mapping by textural analysis of ATM data: a case study from the LOS Vélez district, south eastern Spain.*

#### Active optical sensors

3. Landslide characterization and monitoring; displacement detection; collapse characterization - *Using TLS for rockslide monitoring. Case study of the Eiger collapse, Swiss Alps.*
4. Structural analysis; Discontinuity orientation - *Structural analysis using color coded information derived from 3D point clouds.*
5. Rock face monitoring; rockfall detection; Spatial prediction - *Using TLS for rockfall detection and prediction.*
6. Susceptibility assessment at regional scale - *Susceptibility assessment at regional scale based on areal LIDAR datasets. Application to the canton of Vaud, western Switzerland.*
7. Landslide inventory and susceptibility mapping at regional scale - *The application of LIDAR-derived images for landslide inventory and susceptibility mapping in the Flemish Ardennes, Belgium.*

#### Active microwave sensors

8. Landslide detecting - *Characterization and analyses of surface deformation, mass movements and alpine region lifting with PSInSAR techniques/methods.*
9. Landslide detection and mapping at regional scale - *Landslide detection and mapping at the basin scale by means of radar-interpretation.*
10. Landslide characterization and monitoring at local scale - *Integration of PSInSAR data and ground-based instrument measurements for landslide characterization and monitoring at the local scale.*
11. Slow-moving landslide detection, mapping, characterization, monitoring - *A new approach to the use of DInSAR data in landslide studies at different scales: the case study of National Basin Authority of Liri-Garigliano and Volturno rivers.*

## **Geophysical investigations**

12. Rock slope monitoring - *Microseismic monitoring at the unstable rock slope at Åknes, Norway.*
13. Landslide investigations - *Landslide of Rindberg / Sibratsgfäll investigated with airborne geophysical survey.*

## **Geotechnical investigations**

14. Geotechnical investigations and instrumentation - *Site-specific geotechnical investigations for landslide characterization and detection. Application at the Åknes rockslide, western Norway.*
15. Landslide monitoring - *From early warning to site-specific kinematic analysis: the case of Bagnaschino landslide.*

## **Multidisciplinary approaches**

16. Ground surface displacement measurement - *Detecting and mapping landslides in Salazie area, La Réunion Island, using remote sensing techniques.*
17. Long term monitoring, characterization and modelling - *Vallcebre landslide, Spain, monitoring, from wire extensometers to GB-InSAR.*



## CASE STUDY 1:

**Title:** Monitoring Tessina landslide, Italy, from optical remotely sensed imagery.

**Application:** Landslide monitoring.

**Technique:** Multi-temporal image change detection.

**Main references:** This case study is based on following publication: Hervás et al. (2003).

**Contributors:** JRC (Hervás J., Barredo J.I., Rosin P.I., Van Den Eeckhaut M.).

### ABSTRACT

In this study an image-processing method to map and monitor landslide activity using multitemporal optical imagery is proposed. The method entails automatic change detection of suitably pre-processed (geometrically registered and radiometrically normalised) sequential images, followed by thresholding into landslide-related change pixels. Subsequent filtering based on the degree of rectangularity of regions followed to eliminate pixel clusters corresponding to man-made land use changes.

The application of this method is illustrated in the complex Tessina landslide in the Eastern Italian Alps. The study focused on discriminating the changes caused by the major reactivation of April 1992. The method has been devised for optical remote sensing imagery in general, but due to the absence of high-resolution satellite imagery covering that period, digital images derived by scanning existing aerial photograph diapositives at 1 m x 1 m resolution have been used. The results show that the tested threshold method is able to classify image pixels according to landslide activity conditions.

### 1. INTRODUCTION

Collecting information on landslide activity over wide areas is a crucial task for landslide hazard assessment. Field techniques, despite being very precise, are usually not sufficient to achieve this goal, since they mostly provide point-based measurements. Mainly because of its synoptic view and its capability for repetitive observations, optical (visible-infrared) remotely sensed imagery acquired at different dates and at high spatial resolution can be considered as an effective complementary tool for field techniques to derive such information (Soeters and van Westen, 1996).

The insufficient spatial resolution provided until very recently by most spaceborne earth observation systems inhibited the use of satellite remote sensing in the optical region of the electromagnetic spectrum (Soeters and van Westen, 1996; Mantovani et al., 1996). On non-stereoscopic digital imagery, efforts have mainly concentrated on extracting possible indirect landslide indicators such as land cover disruption patterns, specific sun-shading features of hummocky surfaces and scarps and atypical lithological occurrence patterns (e.g. McKean et al., 1991; Hervás and Rosin, 1996; Hervás et al., 1996). Therefore the launch of e.g. IKONOS, Quickbird, Eros and ALOS, Geoeye satellite imagery at very high spatial resolution had opened new perspectives for monitoring landslides.

The objective of this study was to test and image processing method to map ground-surface changes caused by landsliding, using multitemporal high-

resolution optical remotely sensed imagery. The method

includes change detection and thresholding of suitably pre-processed images acquired before and after the landslide event.

For this test, the Tessina landslide in Belluno province, Northeast Italy, initiated in 1960 and reactivated several times afterwards (Pasuto et al., 1993; Angeli et al., 1994; Turrini et al., 1994; Mantovani et al., 2000) has been selected. The Tessina landslide has a large source area with rotational slides and mudflows depositing the material onto a wide flat area making up the upper accumulation zone. From there, the material feeds downstream through a narrow and steep canal filling up the valley and approaching the villages of Funès and Lamosano. The landslide developed in the Tessina valley between altitudes of 1220 and 625 m asl, with a total longitudinal extension of nearly 3 km and a maximum width of about 500 m. This study focusses on the latest major reactivation in 1992 when the easternmost part (area 70,000 m<sup>2</sup> with a volume of 3.10<sup>6</sup> m<sup>3</sup>) of the source area collapsed as a result of high precipitation and snow melting.

### 2. MATERIAL AND METHODS

Since high spatial resolution satellite imagery was not available at the time of this event, simulated IKONOS digital imagery at 1 m x 1 m resolution from existing aerial photographs acquired in 28/9/88 and 7/10/94 at 1:75,000 scale has been used in this experiment. The images were orthorectified and radiometrically corrected (Hall et al., 1991; Hill and Sturm, 1991). We

refer to Hervás et al. (2003) for more detailed information.

In remote sensing, a number of methods for land cover change detection are possible (Singh, 1989). In general, two basic approaches can be considered: either analysis of independently classified images (i.e. post-classification techniques) or simultaneous analysis of multitemporal images (i.e. pre-classification techniques) followed by thresholding to discard differences possibly related to non-surface changes (Singh, 1989). For panchromatic imagery, the latter approach appears more suitable. Although a number of image processing techniques can be applied to derive the simple pixel intensity change image, it is usually accomplished either by image differencing or image ratioing. Image ratioing involves a simple ratio operation between the values of corresponding pixels of two registered images of different dates (on a band-by-band basis if images are multispectral). With this operation, more weight is progressively given to pixel differences closer to zero. As a result, the numeric scale is neither symmetrical nor linear, thus making the subsequent thresholding process difficult. To facilitate thresholding, a log transformation can be applied to the ratio image to make the scale linear and symmetrical about zero. Image differencing in turn involves the subtraction of pixel values between both images. Unlike the ratio technique, the difference method highlights all cases of change to the same extent. To map ground surface changes due to landsliding using radiometrically normalised, multitemporal remotely sensed orthoimagery, we have developed a method based on digital change detection techniques. The method encompasses two main steps: image differencing and subsequent thresholding into classes of changes in connection with landslide activity. The thresholding procedure here is essential to discriminate “true change” image pixels by filtering out from the change image most of the noise due to scene changes between the image acquisitions and residual differential illumination and geometric misregistration effects.

Bilevel image thresholding into simple “change” and “no change” classes most often requires the occurrence of two distinct modes in the image intensity histogram. In addition, these two peaks should not be too similar in size and they should have approximately normal distributions (Rosin, 2002). However, in change detection analysis of remotely sensed images over inland areas, the image histogram may often contain only one obvious peak, as is the case for the Tessina images. This causes difficulties for most popular thresholding algorithms (Rosin, 2002). In order to correctly threshold difference images with unimodal histograms, Rosin et al. (2000) tested a number of algorithms on images of the Tessina area. From these, the best results were obtained with a relatively simple thresholding algorithm proposed earlier by Rosin (2001). The algorithm consists of thresholding at the corner of the histogram. To find this corner, a straight line is first drawn from the peak (largest bin) to the

high end (first empty bin following the last filled bin) of the histogram (Fig. 1). The threshold point is selected at the pixel intensity value that maximises the perpendicular distance between the line and the histogram distribution. The distance along the perpendicular from a histogram point  $(x_i, y_i)$  to the line  $(x_1, y_1) \rightarrow (x_2, y_2)$  is derived as follows.

$$\frac{(y_1 - y_2)x_i - (x_1 - x_2)y_i - x_2y_1 + x_1y_2}{\sqrt{(x_1 - x_2)^2 + (y_1 - y_2)^2}} \quad \text{eq.1}$$

Not only is this algorithm simple and robust, but it has been shown to work effectively in a variety of applications such as edge, motion and texture thresholding. The thresholding is applied to the absolute pixel difference values (i.e. negative values are made positive). The resulting binary image can then be classified into positive and negative categories of change by checking for each above threshold value the sign of the original signed difference image. Depending on the spectral characteristics of land cover and underlying soil/bedrock on unstable slopes, such a classification may enable a better identification and monitoring of slide masses.

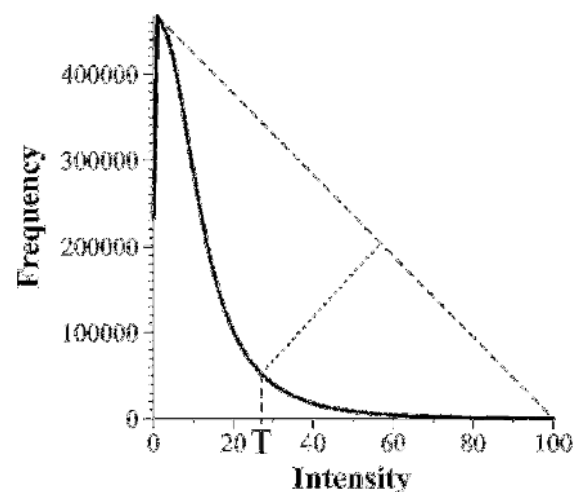


Fig. 1. Difference image histogram showing threshold value (T) corresponding to the detected corner.

Simple thresholding may often not be sufficient to identify changes truly caused by landsliding. An additional processing step is needed to eliminate undesirable noise. Possible polygonal-shaped manmade features (e.g. random land use changes, crop parcels, buildings and road segments) were filtered out using rectangularity filtering preceded by area filtering to avoid selection of very small pixel groups as perfectly rectangular (Rosin et al., 2000).

### 3. RESULTS

The method entailed: (1) the creation of an image expressing the differences in pixel brightness between the two input images, (2) preliminary thresholding of such an image using the histogram corner algorithm (Rosin, 2001; Fig. 1), (3) splitting the thresholded image into positive changes (i.e. increase in pixel brightness from the older image to the newer one) and negative changes (i.e. decrease in pixel brightness) and (4) filtering out rectangular-shaped image blobs (that is, clusters of adjacent pixels).

The final result of the image processing sequence is shown in Fig. 2. Here, positive pixel intensity changes are colored in red. Within the Tessina landslide, these represent ground change patterns mostly associated with the reactivation occurred in 1992, as documented by Pasuto et al. (1993) and Angeli et al. (1994), and illustrated by both on-site photographs and low-altitude aerial photographs taken at the time of the reactivation.

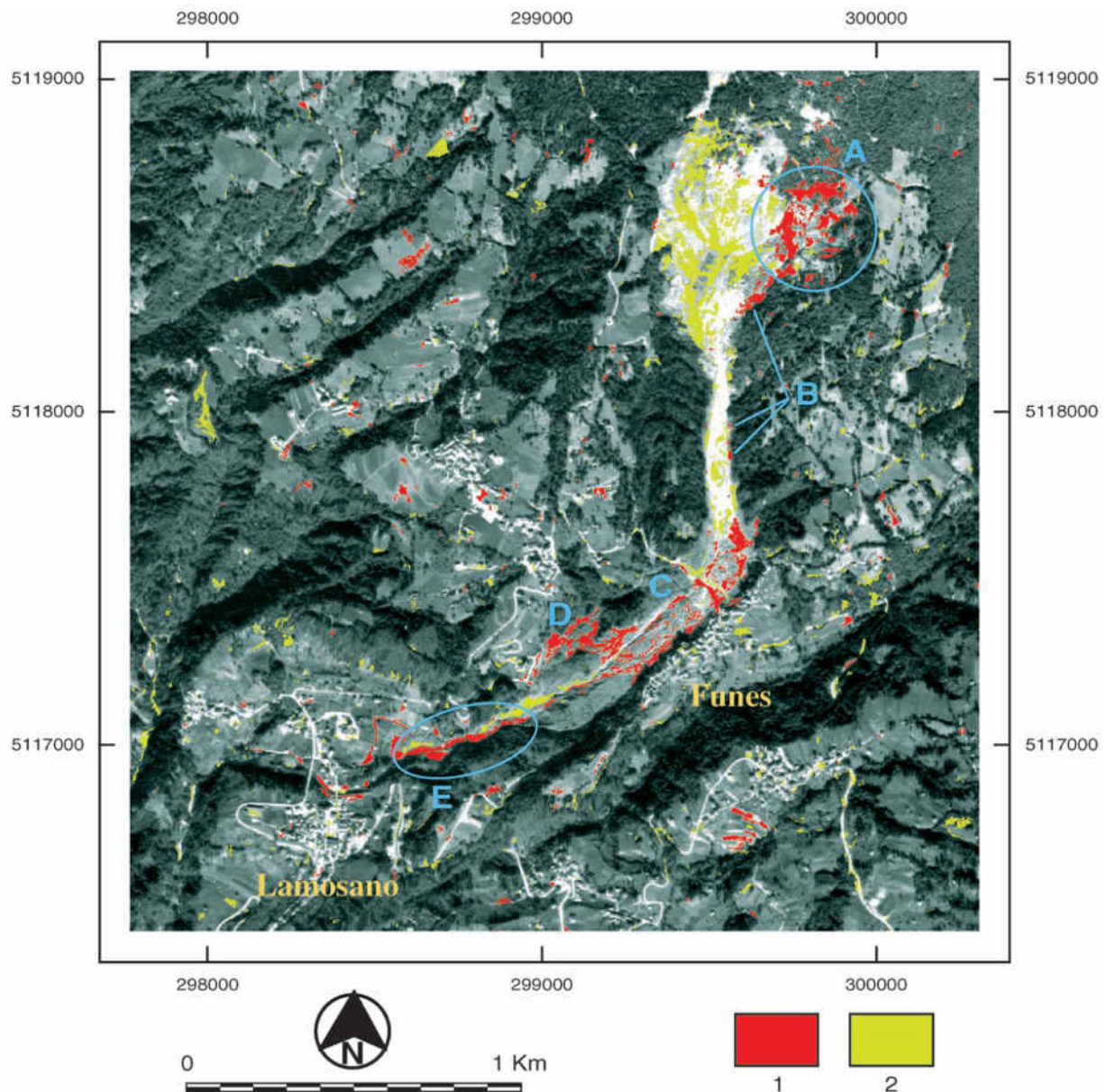


Fig. 2. Surface changes in the Tessina landslide between 1988 and 1994 illustrated on the 1994 orthophotograph. Legend: (1) within the landslide body, positive pixel intensity changes represent both new soil outcrops and remobilised soil as a result of landslide reactivation; zones highlighted are explained in the text; (2) negative pixel intensity changes due to vegetation growth or soil moisture increase. Most changes outside the landslide correspond to land use change. Coordinates in UTM.

Five major change zones can be observed. First, the zone detached in 1992 from the northeastern landslide crown, which produced a landslide surface increase of 70,000 m<sup>2</sup> (zone A in the figure), thus showing fresh soil outcrops with higher pixel intensity in the 1994 image. New soil outcrops together with fresh remobilised material can also be observed along the flanks of the narrow steep canal (zone B) because of remobilisation and depletion of the previous mudflow in this zone and subsequent minor sliding of the main flanks. Zone C, adjacent to Funès, appears irregularly reworked by small mudflows and remobilisation of the former mudflow, as well as by man-made drainage channels (depicted as linear blobs) dug following the 1992 event. Zone D shows a mudflow running off the right flank of the landslide body, opposite to the village of Funès. Here, the higher brightness fresh slide mass partly filled a vegetated small depression originally made up by a side stream, after breaching a levee. Much of the former mudflow zone southwest of Funès appears, however, not affected by the 1992 movements. In this zone, the remobilised material, already highly fluidised, was funneled along the previously dug central drainage channel into the narrower valley section below, near the village of Lamosano, where the new runout material is clearly shown (zone E). New linear structures consisting of protection walls and concrete partly paving the Tessina stream floor, built in 1992, are also apparent at the north end of Lamosano because of their significant pixel brightness increase in the 1994 image.

Areas in yellow, which represent negative pixel intensity changes, appear mostly associated with either soil moisture increase or simple land cover changes, including the growth of natural vegetation on temporarily stable sectors of the landslide body. While vegetation growth may be an indicator of ground stability, soil moisture conditions (which can change dramatically over short periods of time) may conceal the brightness properties of the underlying ground, especially on panchromatic images.

Apparent changes detected outside Tessina landslide are for example changes related to vegetation regrowth on stable sectors of gully walls northwest of Lamosano.

#### 4. CONCLUSIONS

A method based on automatic digital image change detection and thresholding techniques using optical remotely sensed imagery has been successfully applied for monitoring landslide-related ground surface changes (mainly land cover and exposed soil conditions). Although tested with very high resolution aerial photographs, the method is suited to monitor landslide occurrence and activity over extensive areas using the latest generation of very high resolution satellite imagery. It is particularly useful for monitoring surface changes caused by moderate-velocity landslides, even if involving high internal deformation,

in humid and heavily vegetated areas, where the application of more accurate radar interferometry techniques is often not possible.

#### REFERENCES

- Angeli, M.-G., Gasparetto, P., Menotti, R.M., Pasuto, A., Silvano, S., 1994. A system of monitoring and warning in a complex landslide in Northeastern Italy. *Landslide News* 8, 12–15.
- Hall, F.G., Strebel, D.E., Nickenson, E., Goetz, S.J., 1991. Radiometric rectification: toward a common radiometric response among multirate multisensor images. *Remote Sensing of Environment* 35, 11 – 27.
- Hervás, J., Rosin, P.L., 1996. Landslide mapping by textural analysis of Daedalus ATM data. *Proc. Eleventh Thematic Conf. Applied Geologic Remote Sensing*, Las Vegas, Nevada, vol. 2. ERIM, Ann Arbor, Michigan, USA, pp. 394–402.
- Hervás, J., Rosin, P.L., Fernández-Renau, A., Gómez, J.A., León, C., 1996. Use of airborne multispectral imagery for mapping landslides in Los Ve'lez district, south-eastern Spain. In: Chacon, J., Irigaray, C., Fernández, T. (Eds.), *Landslides*. Balkema, Rotterdam, pp. 353–361.
- Hervás, J., Barredo, J.I., Rosin, P.L., Pasuto, A., Mantovani, F., Silvano, S., 2003. Monitoring landslides from optical remotely sensed imagery: the case history of Tessina landslide, Italy. *Geomorphology* 54, 63–75.
- Hill, J., Sturm, B., 1991. Radiometric correction of multitemporal Thematic Mapper data for use in agricultural land-cover classification and vegetation monitoring. *International Journal of Remote Sensing* 12, 1471–1491.
- Mantovani, F., Pasuto, A., Silvano, S., Zannoni, A., 2000. Data collection aiming at the definition of future hazard scenarios of the Tessina landslide. *International Journal of Applied Earth Observation and Geoinformation* 2 (1), 33–40.
- McKean, J., Buechel, S., Gaydos, L., 1991. Remote sensing and landslide hazard assessment. *Photogrammetric Engineering and Remote Sensing* 57 (9), 1185–1193.
- Pasuto, A., Silvano, S., Bozzo, G.P., 1993. The Tessina landslide (Belluno, Italy). In: Panizza, M., Soldati, M., Barani, D. (Eds.), *Proc. First European Intensive Course on Applied Geomorphology*, Pubblicazioni Istituto di Geologia, Università degli Studi di Modena, Italy, pp. 63–69.
- Pasuto, A., Silvano, S., Tecca, P.S., Zannoni, A., 1999. Convenzione tra la Regione del Veneto e l'IRPI-CNR per lo studio della frana del Tessina in Comune di Chies d'Alpago (BL). *Relazione finale*. IRPI-CNR, Padova, Italy.
- Rosin, P.L., 2001. Unimodal thresholding. *Pattern Recognition* 34 (11), 2083–2096.

- Rosin, P.L., Hervás, J., Barredo, J.I., 2000. Remote sensing image thresholding for landslide motion detection. Proc. 1st Int. Workshop on Pattern Recognition Techniques in Remote Sensing, Andorra, 10– 17.
- Singh, A., 1989. Digital change detection techniques using remotely sensed data. International Journal of Remote Sensing 10, 989– 1003.
- Soeters, R., van Westen, C.J., 1996. Slope instability recognition, analysis and zonation. In: Turner, K., Schuster, R.L. (Eds.), Landslides Investigation and Mitigation, Transportation Research Board, Special Report 247, National Research Council, Washington DC, pp. 129– 177.
- Turrini, M.C., Abu-Zeid, N., Semenza, E., Semenza, P., El-Naqa, A., 1994. New studies on the Tessina landslide (Belluno, Italy). Proc. 7th Int. IAEG Congress. Balkema, Rotterdam, pp. 1667– 1675.





## CASE STUDY 2:

**Title:** Landslide mapping by textural analysis of ATM data: a case-study from the Los Vélez district, south eastern Spain.

**Application:** Landslide mapping.

**Technique:** Semi-automated texture enhancement using band 11 (8.5  $\mu\text{m}$  - 13.5  $\mu\text{m}$ ; capturing thermally emitted energy) from Daedalus AADS 1268 Airborne Thematic Mapper (ATM) data.

**Main references:** This case study is based on following publication: Hervás and Rosin (1996), Hervás et al. (1996) and Hervás and Rosin (2001).

**Contributors:** JRC (Hervás J., Rosin P.I., Van Den Eeckhaut M.).

### ABSTRACT

In this study two statistical approaches to semi-automated texture enhancement and discrimination for landslide mapping in semi-arid, sedimentary terrain from Daedalus ATM data were evaluated. A supervised texture discrimination technique was applied, based on calculating similarity between a reference texture spectrum obtained from training samples and spectra from moving image windows. The results are compared with those from interpreting a set of popular texture measures from the literature, derived from grey level co-occurrence matrix statistics. In this comparison, interpretation is facilitated by statistical selection of the best combination of three measures using a sequential forward search algorithm. It is concluded that the texture spectrum based discrimination technique proves superior to using pre-defined sets of texture measures, since it is able to highlight areas on imagery which are often associated with disrupted, displaced land masses.

## 1. INTRODUCTION

Landslides may produce complex slope surface patterns not readily distinguished visually on remotely sensed data. Therefore approaches to landslide mapping with remotely sensed digital imagery, are commonly based on a combination of textural and spectral enhancements (Eyers et al, 1995). Automatic texture analysis has been successful in discriminating regular patterns in many machine vision applications. However, a more serious challenge is posed when it is applied to remotely sensed data because of the irregular and less distinctive patterns usually occurring in nature.

In this study we evaluate two statistical approaches to texture enhancement and discrimination for semi-automated mapping hummocky slid terrain from Daedalus ATM data. The first approach regards the use of texture measures (Haralick et al, 1973; Haralick 1979; Baraldi and Parmiggiani, 1995). These measures contain information about the spatial distribution of local grey-level variations within a band. In the second approach, image texture is defined in terms of frequency distribution of local intensity variation by means of its "texture spectrum" (Wang and He, 1990). From this, a supervised texture discrimination technique is applied to identify areas with possible slides. Statistical and empirical methods to select the best texture measures and algorithm parameters, as well as the introduction of subtle variations to the original algorithms are also discussed.

## 2. MATERIAL AND METHODS

### 2.1 Study area

The semi-arid moderate-relief area of Los Vélez in SE Spain was selected for this study. This site includes complex terrain patterns in terms of both landforms and land use, which are very representative of the various natural conditions found in extensive areas of south and south-east Spain (Hervás and Rosin, 1996; Hervás et al., 1996).

Landslides occur mainly on dark green and greenish-brown clays and marls of Lower Miocene age, which often includes gypsum crystals and some sandstone layers locally. They appear at the foot of the limestone and dolomite ridges and hills, and at gully sides. Often these formations are capped by cemented conglomerate colluvium which slides together with the underlying materials. Using the nomenclature from UNESCO (1993) and IAEG (1990), the slope movements correspond to rotational slides, both single and multiple, and composite rotational-slides rock-falls. Scarps are only apparent in some slides. The surface dimensions of the displaced masses range from 100 to 800 metres either along or across the major movement direction. Most slides show a characteristic hummocky surface made up of an irregular succession of depletion and accumulation zones.

### 2.2 Digital data



For this study Daedalus AADS 1268 Airborne Thematic Mapper (ATM) data were used. The ATM sensor acquires imagery in 11 spectral bands from the visible to the thermal infrared. A number of swaths were flown by INTA of Torrejón, Spain, on 26th April 1994 just before noon. A 6051 × 883 pixel swathe with a nominal pixel size of 3.5 m at nadir was then selected. This covers an area approximately 16 km long by 2.5 km wide. A ground survey was undertaken simultaneously with the ATM flights.

The wide field of view of the ATM causes some panoramic distortion across the swath, which was corrected during pre-processing, as were the roll effects (see Hervás et al., 1996). No further geometric correction was attempted since it was not regarded relevant for this kind of investigation. Possible across-track differential sun illumination effects were reduced to a minimum by flying swaths at a time when high sun elevation angle is relatively high, while its azimuth is far from the across-track scanning direction. This effect was not immediately apparent in the data, therefore no attempt was made to correct for it.

We further refer to Hervás and Rosin (2001) where the same methods were adopted to SPOT panchromatic images of 10 m x 10 m resolution and IRS-1C panchromatic images of 5 m x 5 m.

### 2.3 Texture measure approach

Statistical texture measures are concerned with the spatial distribution and spatial dependence among the image pixel values in a local area. These measures are extracted from grey-level co-occurrence matrices (Haralick et al, 1973; Haralick, 1979). In this work we evaluate the usefulness for landslide mapping of 14 textural measures selected from among those reported successful in the literature for various remote sensing applications. Some of these have been originally proposed by Haralick et al (1973), such as Angular Second Moment, Contrast, Correlation, Variance, Inverse Difference Moment, Sum Average, Sum Variance, Sum Entropy, Entropy, Difference Variance, Difference Entropy and Second Measure of Correlation. Others such as Recursivity and Inverse Recursivity were proposed by Baraldi and Parmiggiani (1995).

Because it was impossible to test the 14 texture features for all bands, it was decided after both visual inspection and preliminary processing of the ATM data (see Hervás et al., 1996) to use only band 11 (8.5 µm - 13.5 µm). This band captures thermally emitted energy with dominant effect of surface temperature. Daytime thermal imagery in the area is sensitive to topography and therefore to geomorphology while is less sensitive to land use and lithological variations. Basic spectral enhancement techniques for characterising possible variations of vegetation patterns, soil moisture or lithologies between the slid and surrounding non-slid areas using other bands generally proved inefficient. This was mainly due to the steady drought conditions in the area, the single time acquisition and the lack of

significant lithological changes around the displaced mass.

### 2.4 Texture spectrum approach

The texture spectrum approach (Wang and He, 1990) first considers texture units ( $E_i$ ) by analysing each 3×3 window. The central value  $V_c$  is compared to its 8 nearest neighbours  $V_i$  or, alternately, to longer distance neighbours, which are assigned one of three values  $E_i$  determined by

$$E_i = \begin{cases} 0 & \text{if } V_i < V_c \\ 1 & \text{if } V_i = V_c \\ 2 & \text{if } V_i > V_c \end{cases}$$

From  $E_i$  the texture unit number is generated by

$$N_{TU} = \sum_{i=1}^8 3^{i-1} E_i \quad \text{with } N_{TU} \in \{0, 1, 2, \dots, 656\}$$

For each  $w \times w$  window in the image a texture spectrum is generated by histogramming the texture unit numbers that occur within the window (Figure 1). Similarity between textures can now be compared by taking the absolute differences between their texture spectra. Thus, for two texture spectra  $A_i$  and  $B_i$  where  $i \in \{0, 1, 2, \dots, 656\}$ , the similarity is

$$S = \sum_{i=0}^{656} |A_i - B_i|$$

For our purposes we generate the training texture spectrum  $T_i$  from the area(s) of interest (of arbitrary size and shape), corresponding to known landslide(s), over ATM band 11. This spectrum is normalised to a frequency by dividing each element of the histogram by the area of the region. Supervised texture discrimination is then carried out by assigning to each pixel in the image the similarity  $S$  calculated from the difference between  $T_i$  and the image texture spectrum  $W_i(x,y)$ , calculated in the  $w \times w$  window centred at  $(x,y)$

$$S_{x,y} = \sum_{i=0}^{656} |T_i - W_i(x,y)|$$

Since in most cases pixels do not have precisely identical values to their neighbours a more efficient version is to generate texture units using only two values

$$E_i = \begin{cases} 0 & \text{if } V_i < V_c \\ 1 & \text{if } V_i > V_c \end{cases}$$

while in the situation that  $V_i = V_c$  either the texture unit number can be discarded, or  $E_i$  can be randomly

assigned either 0 or 1, and the resulting texture unit number retained. We take the latter approach. Using 2 rather than 3 values means that much shorter texture spectra are generated (containing 256 rather than 6561 values), providing a substantial improvement in efficiency for only a slight degradation in quality. In either version image pixels are subsequently normalised to [0, 255].

to discriminate between rough and smooth surfaces. However, in the study area the distinction between known landslides, small gullies and cultivation terraces is generally not possible in any of these texture images. The Entropy image (Figure 2c), as first-ranked by the SFS algorithm, does not appear in general superior to Recursivity and Second Measure of Correlation for mapping possible sliding. Nonetheless, these measures are proved superior to other randomly-selected measures.

### 3. RESULTS

The 3 statistically-selected texture measures are able

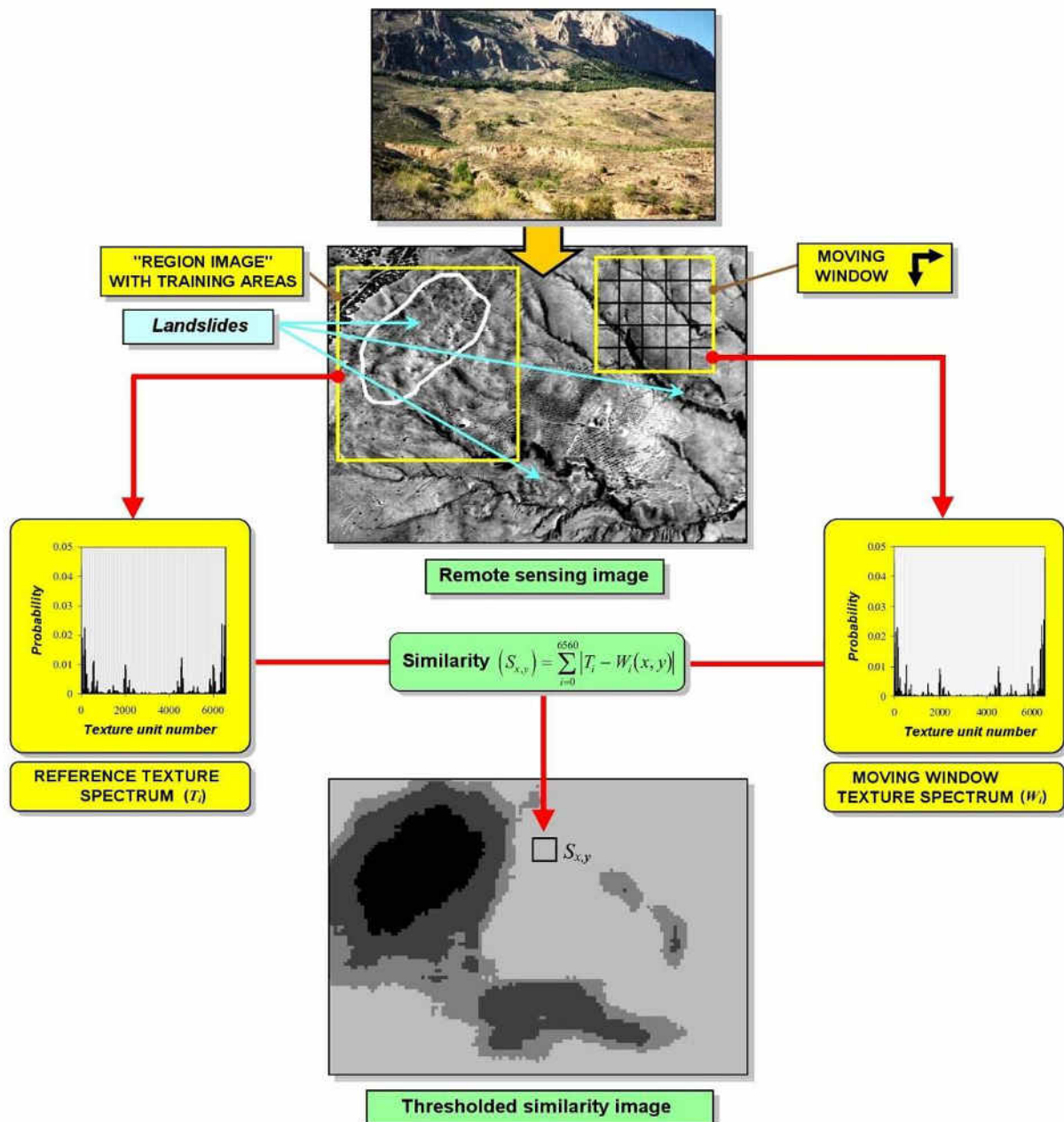


Fig. 1. Schematic flow chart of the texture spectrum approach with training texture spectrum  $T_i$  and image texture spectrum  $W_i$

In a false colour composite of these three texture images discrimination of gullies and slides is improved with respect to single measures, but this is not yet a very useful product to differentiate slides by its own. Furthermore, hummocky slid terrain cannot be distinguished from closed pine trees stands. These texture measures can be useful for landslide mapping only as a preliminary image segmentation technique. The texture spectrum method outputs an image where very low pixel value areas are often associated with landslides and disrupted terrain. From testing a few variations of the possible texture spectrum algorithm

parameters, it was found that selecting a minimum of 2 training sites, a moving window ( $w \times w$ ) of  $81 \times 81$  pixels and a pixel increment of 4 for moving the window both in the row and column directions, resulted in a satisfactory image to map potential and existing slide areas. In this density-sliced image (Figure 2b), forest stands and regularly spaced trees crops are clearly discriminated from known displaced land masses. Incipient badlands and some area with irregular limestone exposures appear undifferentiated from landslides. The former may hinder detecting existing instability on gully sides.

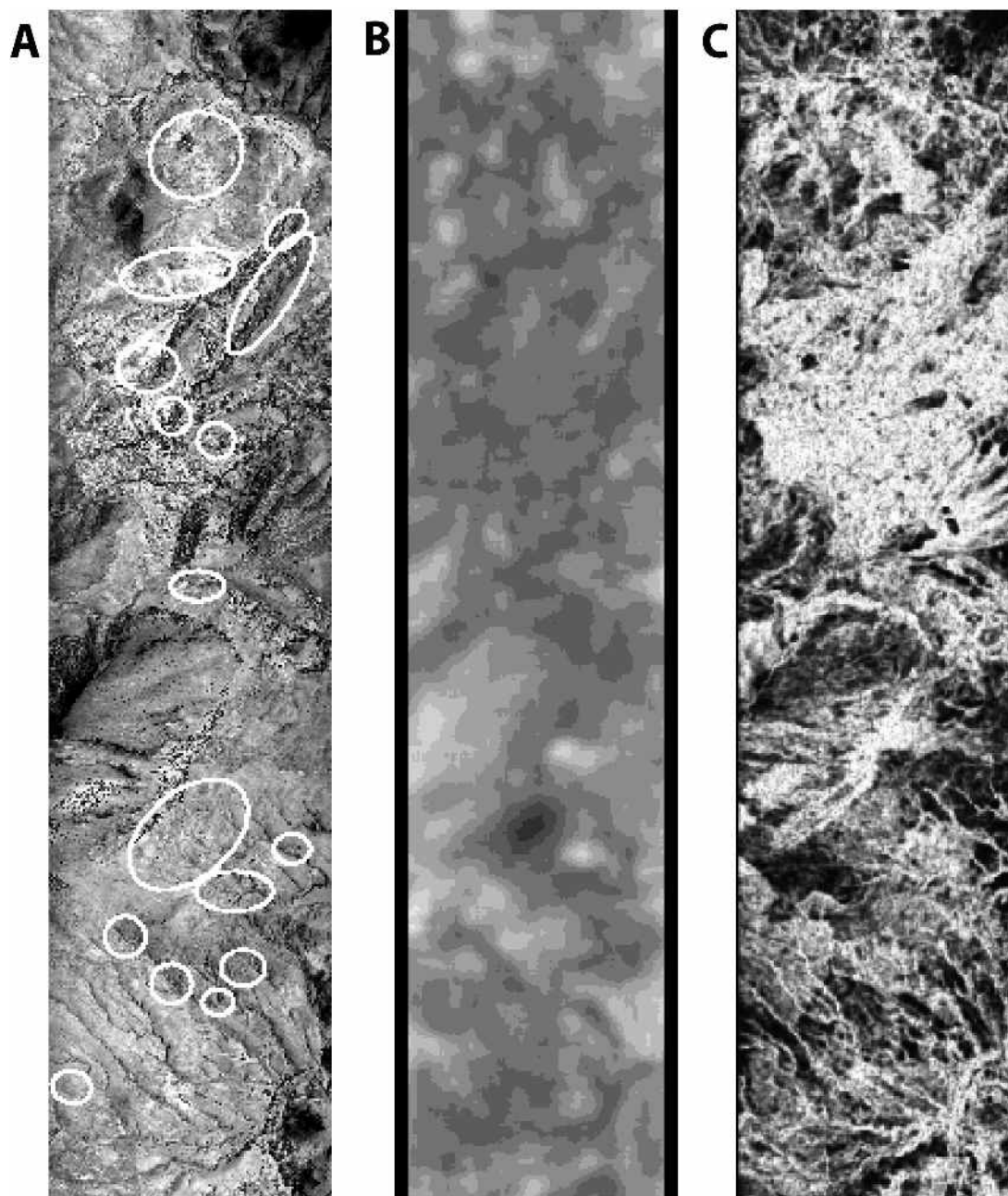


Fig. 2. (a) ATM Band 11. Known landslide sites are circled. (b) Texture Spectrum Based Segmentation. (c) Entropy Image

In our data, larger algorithm window sizes and pixel increments tend to smooth the image, making the site discrimination more difficult. Smaller windows and pixel increments can result in relatively noisy images, enhancing non-relevant spatial frequency content.

#### 4. CONCLUSIONS

Two semi-automated, statistical texture approaches for mapping landslide geomorphologic features in semi-arid terrain have been analysed using single acquisition, high spatial resolution optical data.

Some predefined texture measures can be useful in this type of research for preliminary image segmentation. In addition, the ability of some of the local statistics properties as edge enhancers becomes apparent. Selected measures using a discriminant function prove to be a more objective approach, and can thus be used irrespective of the study area. This approach can be fairly automated, although it requires substantial computer processing. Texture spectrum based discrimination proves a more suitable and cost-effective method, since it is able to highlight areas on imagery often associated to sliding, and suspect areas where detailed site investigations are needed. However, in both approaches landslides are not easily differentiated from dense erosion patterns. Investigations are continuing to test the methodology to lower spatial resolution images and further tune the algorithm parameters.

#### REFERENCES

- Devijver, P.A., Kittler, J., 1982. Pattern Recognition. A Statistical Approach, Prentice-Hall, Englewood Cliffs, New Jersey, USA.
- Eyers, R., J. Moore, J. Hervás, Liu, J.G., 1995. "Landslide mapping using digital imagery: a case history from south east Spain", Proc. 31st Annual Conf.: Geohazards and Engineering Geology, Coventry, UK, 10-14 September 1995. The Geological Society, pp. 379-388.
- Haralick, R.M., Shanmugan, K., Dinstein, I., 1973. Textural features for image classification, IEEE. Trans. Syst. Man, Cybern. Vol. SMC-3, 6, 610-621.
- Haralick, R.M., 1979. Statistical and structural approaches to texture, Proc. IEEE 67, 786-804.
- Hervás, J., Prieto, C., 1981. Estudio de movimientos del terreno en la provincia de Granada, Ministerio de Obras Públicas, Transportes y Medio Ambiente, Dirección General de Carreteras, Madrid, Spain. Internal Report, 3.
- Hervás, J., Rosin, P.L., 1996. Landslide mapping by textural analysis of Daedalus ATM data. Proc. Eleventh Thematic Conf. Applied Geologic Remote Sensing, Las Vegas, Nevada, vol. 2. ERIM, Ann Arbor, Michigan, USA, pp. 394-402.
- Hervás, J., Rosin, P.L., Fernández-Renau, A., Gómez, J.A., León, C., 1996. Use of airborne multispectral imagery for mapping landslides in Los Ve'lez district, south-eastern Spain. In: Chacon, J., Irigaray, C., Fernández, T. (Eds.), Landslides. Balkema, Rotterdam, pp. 353-361.
- Hervás, J., Rosin, P.L., 2001. Tratamiento digital de imágenes de teledetección en el espectro óptico para el reconocimiento y control de deslizamientos. Proc. V Simposio Nacional sobre Taludes y Laderas Inestables. Madrid, 27-30 November 2001. CEDEX, Ministerio de Fomento, Madrid, pp. 63-74.
- IAEG Commission on Landslides, 1990. Suggested nomenclature for landslides. Bull. International Association of Engineering Geology 41, 13-16.
- UNESCO Working Party on World Landslide Inventory, 1993. A suggested method for describing the activity of a landslide. Bull. International Association of Engineering Geology 43, 53-57.
- Wang, L. He, D.C., 1990. A new statistical approach for texture analysis. Photogram. Eng. Remote Sensing 56, 61-66.



## CASE STUDY 3:

**Title:** Using TLS for rockslide monitoring. Case study of the Eiger collapse, Swiss Alps.

**Application:** Landslide characterization and monitoring; Displacement detection; Collapse characterization.

**Technique:** Terrestrial Laser Scanner (TLS); Terrestrial LIDAR.

**Main references (text extracted from):** Oppikofer et al. (2008); Oppikofer (2009).

**Contributor:** NGU (Oppikofer, T.) and UNIL (Jaboyedoff, M.).

### ABSTRACT

Landslides are a significant natural hazard in mountainous regions and are often triggered by external factors, such as earthquakes, rainfall, permafrost thawing or retreat of glaciers. A large landslide occurred in the Swiss Alps on 13 July 2006, when portions of an immense rock spur on the eastern flank of the Eiger peak collapsed. Here we use field observations and terrestrial laser scanning data to record and quantify the relative motion along the various blocks of rock that form this spur. The data show that during two years of observation the blocks moved relative to one another by up to tens of metres along fractures that can be related to pre-existing discontinuities. Rates of motion and deformation were high throughout July 2006, particularly in the northern part of the spur that partially collapsed on 13 July. The rates decreased considerably during the subsequent months, although a slight increase was noted in June and July 2007, but disintegration of the rock mass continued until Summer 2009, when the last remnants of the rock spur collapsed. These observations are consistent with instability of the spur initiated by subsidence of a single block at the rear, which acted as a wedge and disintegrated over time owing to loss of lateral confinement.

### 1. INTRODUCTION

High-resolution digital elevation models obtained from aerial or terrestrial laser scanning (ALS and TLS, respectively) are used to detect landslides and rockfalls (Slob and Hack, 2004; Rosser et al., 2005; Abellán et al., 2006; Bitelli et al., 2004; Rosser et al., 2007; Bauer et al., 2005; Derron et al., 2005; Schulz, 2007; Agliardi and Crosta, 2003; McKean and Roering, 2004). Most landslide monitoring techniques provide information on only a few selected points and not the whole landslide surface. Sequential terrestrial laser scanning, on the other hand, allows for analysis of movement direction and velocity, displacement and volume change. These three-dimensional data open new perspectives in predicting mass wasting and deciphering failure mechanisms.

In this case study, we focus on a collapse at the Eiger's eastern flank (Fig. 1), one of Switzerland's most famous peaks. The instability of this 2 million m<sup>3</sup>, compact Jurassic limestone mass, was caused by the Lower Grindelwald glacier's retreat, which has been accelerated since 1935 by global warming. At the last glacier maximum in 1860, the ice reached the back scar's level. The instability was subject to particularly high glacial compression due to its position on a topographic ridge. The removal of the glacier buttress and subsequent decompression allowed the spur to fail. On 10 June 2006 rockfalls of several hundred m<sup>3</sup>, first slope movements and two steep 250-m-long valley-parallel open cracks were observed. One of

these fractures forms the back-crack of the spur, and the other separates the spur into a front and a rear block (Fig. 1b,c). In addition, these blocks are separated into a main part and a northern part by a subvertical bedding plane that is nearly perpendicular to the open cracks (Fig. 1c).

Fig 2a (20 June 2006) shows the scar one week after the opening of the back-crack (dashed red line). Only small displacements are visible in this figure, besides some rockfall activity on the southeastern part. Fig. 2b (13 July 2006) shows that the rear part moved downwards by several meters and started to break up, while a partial collapse occurred in the northern part (before the first terrestrial laser scans). Fig 2c (17 July 2006) shows the scar of the 13 July 2006 collapse in the northern part of the rock spur. Fig 2d (2 August 2006) shows the continuation of the movement in the rear part. The last free standing column in the northern part also collapsed, and a small rockfall scar is visible on the front block (dashed red line). Figs 2e to g (30 August 2006, 22 September 2006 and 1 December 2006, respectively) show ongoing displacements, break-up of the rear block and the opening of a new middle fracture (dashed red line) within the front block. Figs 2h and i (11 June 2007 and 14 August 2008) show the dismantling of the front block with an increase of rockfall activity and several partial collapses. Finally, Fig 2j shows one of the final stages of this rockslide, where only small parts of the rear block and a 90 m high, blade-shaped needle remained until it collapsed in summer 2009.





Fig. 1. a) Situation map of the Eiger rockslide; b) Picture of the back-crack at the beginning of the monitoring campaign (Picture: Geotest AG); c) Frontal view of the Eiger rockslide showing the division of the spur into a front and a rear block separated by a steep middle fracture (green line) and the northern rear and front blocks are separated from the main blocks by a bedding plane (blue line).

At the beginning of the monitoring campaign, slope movements were very fast (several dm per day) and caused frequent rockfalls and partial collapses. Initially, the back-crack opening was measured by perilous hand measurements, followed by total station surveys. As the installed reflective targets were rapidly destroyed due to collapses and rockfalls, a contactless and reflectorless monitoring technique – terrestrial laser scanning (TLS) – had to be used. On 11 July 2006, we deployed a long-range terrestrial laser scanner to monitor the rockslide and acquired sequential TLS point clouds on 12, 13, 17 and 25 July, 22 September and 1 December 2006, on 11 June and 17 July 2007 and on 14 August and 21 October 2008. The comparison of sequential point clouds reveals the instability's displacements and enables the calculation of rockfall volumes. A more detailed explanation of this case study can be found in Oppikofer et al., 2008 and Oppikofer, 2009.

## 2. MATERIAL AND METHODS

TLS is based on the reflectorless and contactless acquisition of a point cloud of the topography using the pulsed laser time-of-flight technique (Slob and Hack, 2004). For this study, we used an Optech ILRIS3D terrestrial laser scanner system. TLS point clouds, were acquired from two viewpoints located on the opposite side of the valley (Sites A and B in Fig. 1a), at a distance of 600m and 530m respectively. From both viewpoints the resulting point cloud has an average resolution of 18.0 cm on the rock face and 20.0 cm at the back-crack. This spacing is approximately twice the magnitude of the laser spot size (11.4 cm at a distance of 600 m), which is significantly more than the proposed ideal spacing of 0.859 times the beamwidth (Lichti and Jamtsho, 2006). This however has the advantage of drastically reducing acquisition time and data file size by still providing high-resolution point clouds.

We aligned the scans from both viewpoints with Innovmetric PolyWorks software using first manual point-pair matching and afterwards the surface-to-surface iterative closest point algorithm implemented in PolyWorks. We progressively reduced the maximum distance between the two scans to minimize the alignment errors ( $1\sigma_a < 2.5$  cm). This error is mainly due to the spot spacing and the fact that consequently not always the same points of the quite irregular rock surfaces were measured. In comparison, the instrument's precision is given by the manufacturer as 7 mm on the range and 8 mm on the position at a distance of 100 m. Georeferencing is achieved by alignment of the TLS point cloud onto the high-resolution aerial digital elevation model with a cell size of 2m (DEM-CS provided by swisstopo), with an absolute positioning error of 14.5 cm ( $1\sigma_{gr}$ ). We used the same alignment procedure for the alignment of sequential TLS point clouds, but restraining the iterative alignment to the stable part around the rockslide only ( $1\sigma_a < 2.5$  cm). Thus, the overall alignment error of sequential scans is equal to approximately 6 cm on single points. The displacements measured in the 2006 Eiger rockslide are much bigger than instrumental and data treatment errors. Considering entire point clouds, for example by interpolated surfaces, errors are significantly lower than on single points.

Pre- and postfailure three-dimensional models on the basis of the interpolated TLS point clouds permitted us to obtain precisely the volume of rockfalls by calculating the volume contained between the two surfaces using PolyWorks. The comparison of the aligned sequential TLS point clouds reveals differences (expressed as shortest distance) between the two topographic surfaces. These positive or negative differences are interpreted as slope movements: positive differences stand for an advance of the rockslide and debris accumulation on the scree slopes, whereas negative differences are related to subsidence or rockfalls.



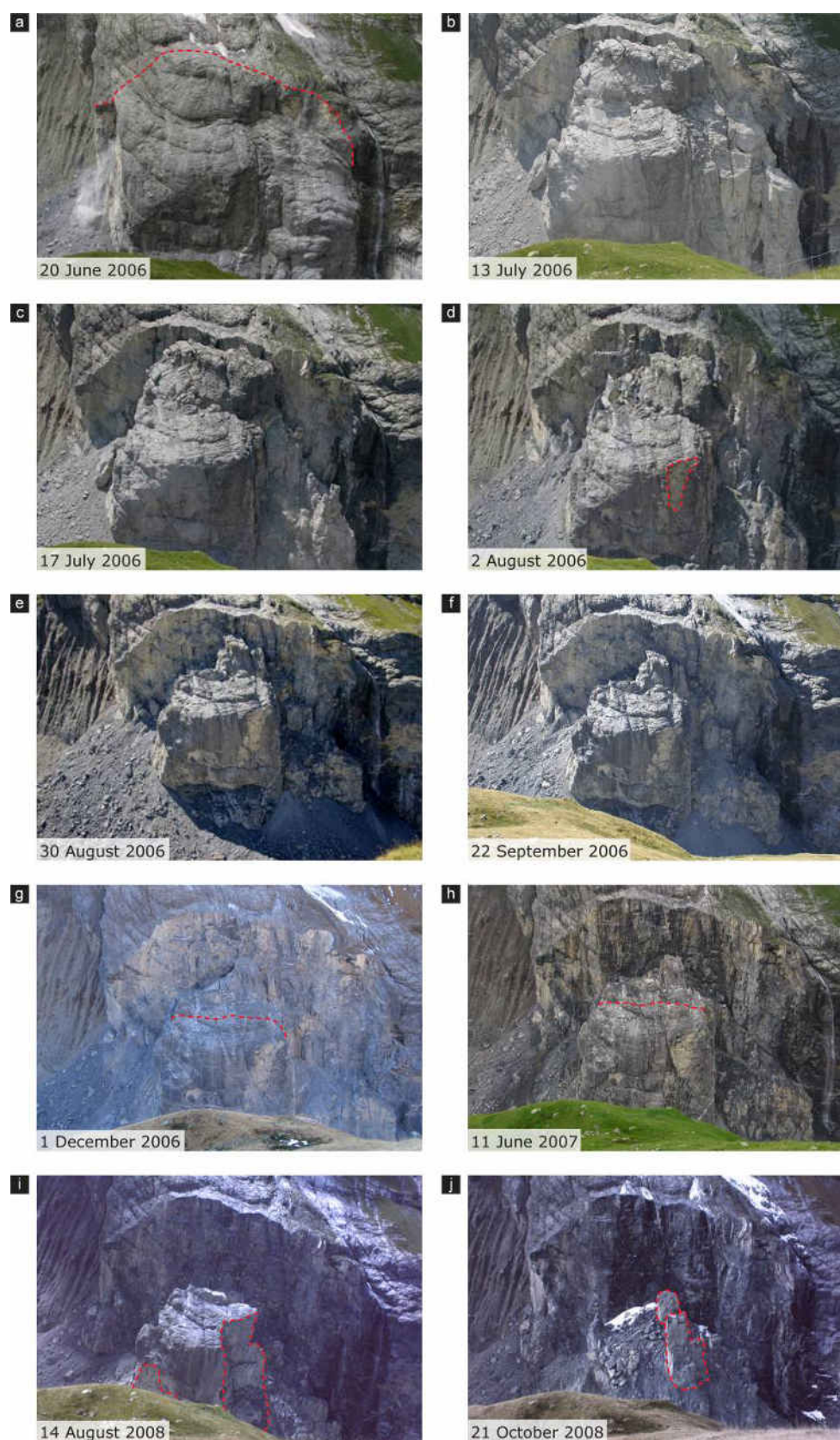


Fig. 2. From a to j, photographs of the evolution of the Eiger collapse. See text for a detailed explanation.

More precise information on the slope movements is obtained from displacement vectors of different rockslide parts. They are calculated by manually identifying corresponding points on view-shaded representations of both point clouds. Ideal point pairs are summits of blocks or small spurs, intersections or end points of discontinuity traces and so on. The vector between a point pair provides the displacement direction and velocity of the point. Multiple vectors on each rockslide compartment provide the mean displacement vector and error. The errors in the average displacement length and orientation are obtained by dividing the standard deviations by the square root of the number of vectors and are equal to 10.1 cm and 2.7 (aperture of cone centred on the mean orientation and including 68% of the values), respectively. The relatively high error is due to the high point spacing (~18 cm), the measurement error on a single point and the fact that the slope is breaking apart.

### 3. RESULTS

Sequential TLS point clouds permitted to follow the slope movements in 3D using shortest distance comparisons with displacements of 80 cm/d for the rear block, 20 cm/d for the front block and locally even up to 125 cm in 24 hours (between 12 and 13 July 2006). This movement monitoring provided a first assessment of the slope movements and highlighted the different displacement directions and velocities of the rear relative to the front block, with mainly negative differences in the rear (downward displacements) and positive differences at the front block (advances on basal sliding surface). After the very fast initial displacement rates in summer 2006, the velocities decreased in the following months (4 cm/d and 1.5 cm/d for the rear and front blocks, respectively, during winter 2006/2007). In one year, the total displacements reached 15 m for the front block and 50 m for the rear parts. These high displacements went along with the progressive lateral dismantling and break-up of the rear block.

A detailed explanation of the rockslide evolution, using the comparison between two consecutive TLS point clouds, is shown in Fig 3:

TLS comparison between 11 and 12 July 2006 (Fig 3a) displays the downward movement of the rear part (~80 cm/day), the advance by 125 cm/day of two columns in the northern block, as well as the 2530 m<sup>3</sup> large rockfall on the northern block and the scree deposits on the southern side.

a) TLS comparison between 12 and 13 July 2006 (Fig 3b) highlights the ongoing downward movement of the rear part (~75 cm/day) and the fast movement of the columns in the northern block (up to 150 cm/day) accompanied by two rockfalls of 118 and 329 m<sup>3</sup>. These higher movement rates on these

columns and the small rockfalls can be interpreted as precursory signs for the partial collapse on 13 July 2006. Photographs of this collapse indicate that it started with the failure of this fast-moving column, which is valuable information for rockslide monitoring and especially spatial and temporal failure prediction through the possibility to detect areas with high displacement rates by TLS, as discussed in Abellán et al. (2009).

b) TLS comparison between 13 and 17 July 2006 (Fig 3c) reveals the extent of the northern flank's partial collapse that occurred at 19h35 on 13 July 2006 (grey area in Fig 3c) and the associated scree deposits in the valley. Furthermore the continuous downward movement of the rear block can be quantified to 65 cm/year.

c) TLS comparison between 17 and 25 July 2006 (Fig 3d) shows the ongoing advance of the northern part, besides the advance of the front block (~1.25 m; ~15 cm/day) and the downward movement of the rear part (~4 m or 50 cm/day in average, up to 10 m on the left flank). A 4460 m<sup>3</sup> large rockfall on the front block and the associated deposits can also be seen in this comparison of sequential TLS point clouds.

d) TLS comparison between 25 July and 22 September 2006 (Fig 3e) displays the dismantling of the southern flank of the rear block and the breaking-up of the northern part. A small collapse along the vertical fracture separating the northern front block from the front block led to the accumulation of up to 15 m-high scree deposit. The front block advanced by 6 to 7 m (~12 cm/day), while the rear block moved downwards by more than 15 m (~30 cm/day).

e) TLS comparison from 22 September to 1 December 2006 (Fig 3f) shows the downward movement by about 8 m (~11 cm/day) of the rear block and rear of the northern block, together with the advance of the front block advanced (~2.5 m; ~4 cm/day). A new subvertical fracture, parallel to the back-crack, separated the front block into two parts, but no differential movement is detected between the two. Note also the 3280 m<sup>3</sup> rockfall of an overhanging block on the back-crack.

f) TLS comparison from 1 December 2006 to 17 July 2007 (Fig 3g) shows the continuation of the movement of the rear block (~15 m; ~7 cm/day) and its breaking-up, while the displacement of the front block reached up to 6 m (~2.5 cm/day). The comparison with a TLS dataset acquired on 11 June 2007 reveals that during winter 2006/2007 the movement rates were 3-4 times smaller than in the beginning of summer 2007, indicating possible seasonal variations in the rockslide activity.



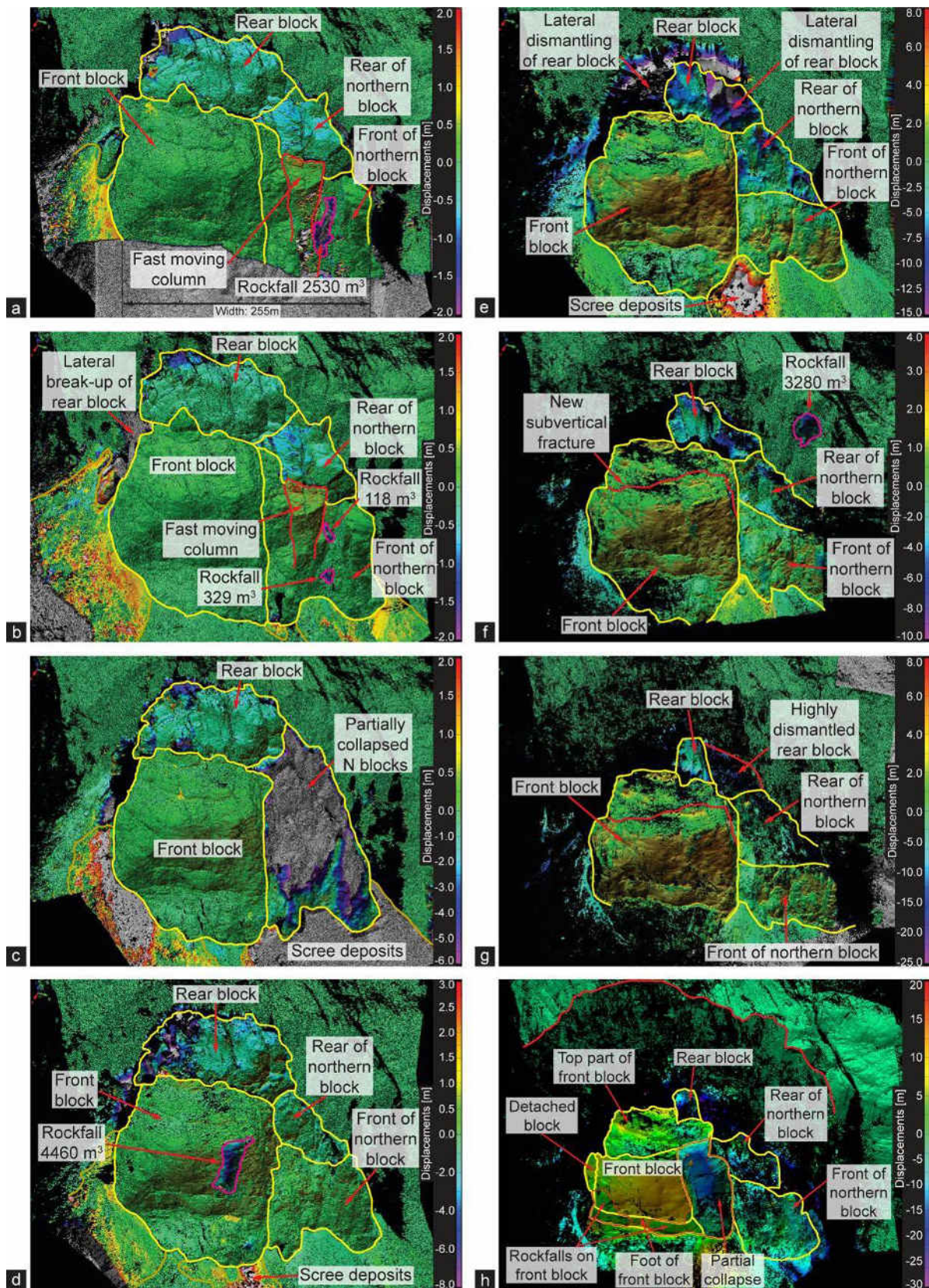


Fig. 3. Sequential comparison of TLS point clouds. Negative values equal downward displacements and/or detachment of material. Positive values equal outward displacement and/or debris accumulation

g) Finally, TLS comparison from 17 July 2007 to 14 August 2008 (Fig 3h) displays the slope displacements for both blocks with up to 30 m for the rear block that continued to break-apart laterally and approximately 10 m for the front block. This comparison also testifies the increase in rockfall activity with two large rockfalls on the front block, as well as a partial collapse of approximately 60'000 m<sup>3</sup> on its north-eastern corner (Fig 3h). Until 21 October 2008, the front block continued its break-up with several smaller and larger events – according to eye-witnesses – and only a blade-shaped, 90 m high needle remained.

Displacement vectors measured for the different blocks provide a more precise analysis of the slope movements. The sliding directions remained fairly constant until autumn 2006, but the velocities decreased. Since autumn 2006, the rear block's sliding direction turned more to the East owing to the lateral dismantling of the rock mass. Based on these 3D displacement data and on a structural analysis of the spur, a coherent geometrical model for the 2006 Eiger rockslide was proposed. In the early stages of the rockslide, its mechanism was a bilinear wedge failure (Norris and Willey, 1996). The downward-moving rear block acted as an active wedge splitting the front block from the stable rock mass and pushing it passively along a complex sliding surface with an average dip angle of ~33° (see Oppikofer et al., 2008 for more details).

#### 4. CONCLUSIONS

The study of the 2006 Eiger rockslide demonstrates the necessity of a global analysis of 3D displacements on the entire rockslide, in order to better understand the failure mechanism and construct a consistent structural and geometrical instability model. Such knowledge is crucial for landslide hazard assessment, because it opens new perspectives in characterizing and understanding the slope movements and helps in designing continuous monitoring techniques. The ability to predict failure is crucial to hazard assessment and monitoring of landslides (Crosta and Agliardi, 2003). Comparisons of sequential TLS data enable the detection of areas with the highest displacement rates, which are more susceptible to future failure. The partial collapse of 13 July 2006 underlines the link between maximum velocities and failure locations. Knowing the most active zones on a landslide, permanent survey techniques can be designed for precise temporal failure prediction.

#### REFERENCES

- Abellán, A., Jaboyedoff, M., Oppikofer, T., Vilaplana, J.M. Detection of millimetric deformation using a Terrestrial Laser Scanner: Experiment and application to a rockfall event. *Natural Hazards and Earth System Science*, 9, 365-372 (2009).
- Abellán, A., Vilaplana, J. M. & Martínez, J. Application of a long-range terrestrial laser scanner to a detailed rockfall study at Vall de Núria (Eastern Pyrenees, Spain). *Eng. Geol.* 88, 136–148 (2006).
- Agliardi, F. & Crosta, G. B. High resolution three-dimensional numerical modelling of rockfalls. *Int. J. Rock Mech. Min.* 40, 455–471 (2003).
- Bauer, A., Paar, G. & Kaltenböck, A. in *Geo-information for Disaster Management* (eds van Oosterom, P., Zlatanova, S. & Fendel, E. M.) 393–406 (Springer, Berlin, 2005).
- Beniston, M. August 2005 intense rainfall event in Switzerland: Not necessarily an analog for strong convective events in a greenhouse climate. *Geophys. Res. Lett.* 33, L05701 (2006).
- Bitelli, G., Dubbini, M. & Zanutta, A. *Proc. XXth ISPRS Congress, Istanbul Vol. 35*, 246–251 (International Society for Photogrammetry and Remote Sensing, Istanbul, Turkey, 2004).
- Coe, J. A. et al. Seasonal movement of the Slumgullion landslide determined from Global Positioning System surveys and field instrumentation, July 1998–March 2002. *Eng. Geol.* 68, 67–101 (2003).
- Crosta, G. B. & Agliardi, F. Failure forecast for large rock slides by surface displacement measurements. *Can. Geotech. J.* 40, 176–191 (2003).
- Derron, M.-H., Jaboyedoff, M. & Blikra, L. H. Preliminary assessment of rockslide and rockfall hazards using a DEM (Oppstadhornet, Norway). *Nat. Haz. Earth Syst. Sci.* 5, 285–292 (2005).
- Eberhardt, E., Stead, D. & Coggan, J. S. Numerical analysis of initiation and progressive failure in natural rock slopes—the 1991 Randa rockslide. *Int. J. Rock Mech. Min.* 41, 69–87 (2004).
- Evans, S. G. & Clague, J. J. Recent climatic change and catastrophic geomorphic processes in mountain environments. *Geomorphology* 10, 107–128 (1994).
- GK/SCNAT & VAW/ETHZ. *The Swiss Glaciers, Yearbooks of the Glaciological Commission of the Swiss Academy of Science (SAS)*. (<http://glaciology.ethz.ch/swiss-glaciers>) (Laboratory of Hydraulics, Hydrology and Glaciology (VAW) of ETH Zürich, 2006).
- Guarnieri, A., Pirotti, F., Pontin, M. & Vettore, A. 3rd IAG/12th FIG Symp., Baden, Austria (International Association of Geodesy & International Federation of Surveyors, Baden, Austria, 2006).
- Hopkin, M. Eiger loses face in massive rockfall. *News@Nature* <<http://www.nature.com/news/2006/060717/full/060717-3.html>> (2006).
- Jaboyedoff, M., Baillifard, F., Bardou, E. & Girod, F. The effect of weathering on Alpine rock instability. *Q. J. Eng. Geol.* 37, 95–103 (2004).
- Lichti, D. D. & Jamtsho, S. Angular resolution of terrestrial laser scanners. *The Photogrammetric Record* 21, 141–160 (2006).



- Lindembergh, R. & Pfeifer, N. Proc. 7th Conf. Optical 3D Measurement Techniques, Vienna, Austria Vol. 2, 61–70 (Vienna University of Technology, Vienna, Austria, 2005).
- Liniger, M. Die Herausforderung der Gefahrenprognose bei Massenbewegungen: Rutsch- und Sturzprozesse Markus Liniger. Bull. Appl. Geol. 11, 75–88 (2006).
- McKean, J. & Roering, J. Objective landslide detection and surface morphology mapping using high-resolution airborne laser altimetry. *Geomorphology* 57, 331–351 (2004).
- Menzl, V. Mechanics of landslides with non-circular slip surfaces with special reference to the Vaiont slide. *Geotechnique* 16, 329–337 (1966).
- Messerli, B., Messerli, P., Pfister, C. & Zumbuhl, H. J. Fluctuations of climate and glaciers in the Bernese Oberland, Switzerland, and their geoecological significance, 1600 to 1975. *Arct., Alp. Res.* 10, 246–260 (1978).
- Munich, Re. Topics Geo - Annual Review: Natural Catastrophes 2005 (Munich Reinsurance Company, Munich, Germany, 2006).
- Norrish, N. I. & Wyllie, D. C. in *Landslides Investigation and Mitigation* (eds Turner, A. K. & Schuster, R. L.) 391–425 (Transportation Research Board, National Research Council, National Academy Press, Washington DC, 1996).
- OcCC. Climate Change and Switzerland in 2050. Impacts on Environment, Society and Economy (OcCC/ProClim-, Bern, Switzerland, (2007).
- Oppikofer T., Detection, analysis and monitoring of slope movements using high-resolution digital elevation models. PhD thesis, Institute of Geomatics and Analysis of Risk, University of Lausanne, Switzerland, 191 p. (2009)
- Oppikofer T., Jaboyedoff M., Keusen H.-R., Collapse at the eastern Eiger flank in the Swiss Alps. *Nature Geosciences* 1(8), 531–535 (2008).
- Petrascheck, A. & Hegg, C. (eds) *Hochwasser 2000 - Les crues 2000* (Federal Office for Water and Geology, Berne, Switzerland, 2002).
- Rosser, N. J., Petley, D. N., Dunning, S. A., Lim, M. & Ball, S. Rock mechanics: Meeting society's challenges and demands. in *Proc. 1st Canada–U.S. Rock Mechanics Symposium*, Vancouver, Canada, May 27–31, 2007 (eds Eberhardt, E., Stead, D. & Morrison, E.) 113–120 (Taylor and Francis, London, 2007).
- Rosser, N. J., Petley, D. N., Lim, M., Dunning, S. A. & Allison, R. J. Terrestrial laser scanning for monitoring the process of hard rock coastal cliff erosion. *Q. J. Eng. Geol.* 38, 363–375 (2005).
- Sartori, M., Baillifard, F., Jaboyedoff, M. & Rouiller, J. D. Kinematics of the 1991 Randa rockslides (Valais, Switzerland). *Nat. Haz. Earth Syst. Sci.* 3, 423–433 (2003).
- Schulz, W. H. Landslide susceptibility revealed by LiDAR imagery and historical records, Seattle, Washington. *Eng. Geol.* 89, 67–87 (2007).
- Slob, S. & Hack, R. in *Engineering Geology for Infrastructure Planning in Europe. A European Perspective* (eds Hack, R., Azzam, R. & Charlier, R.) 179–190 (Springer, Berlin, 2004).
- Wieczorek, G. F. in *Landslides Investigation and Mitigation* (eds Turner, A. K. & Schuster, R. L.) 76–90 Transportation Research Board, National Research Council, National Academy Press, Washington DC, (1996).



## CASE STUDY 4:

**Title:** Structural analysis using colour coded information derived from 3D point clouds.

**Application:** Structural analysis; Discontinuity orientation.

**Technique:** Aerial Laser Scanner (ALS); Terrestrial Laser Scanner (TLS).

**Main references (text extracted from):** Metzger et al., 2008 ; Jaboyedoff et al., 2007.

**Contributor:** UNIL (Metzger, R., Jaboyedoff, M.)

### ABSTRACT

Current laser scanning systems, either mounted over aerial or terrestrial sensors, allow for massive acquisition of million 3D points. One of the main current issues in laser scanner processing is the managing of this information and its transformation into a certain parameter, e.g. dip direction and dip angle. In this case study, we present the application of Coltop 3D software developed by our group (Metzger et al., 2008; Jaboyedoff et al., 2007) for structural analysis purposes. Each point of the point cloud dataset can be represented through its colour defined by the local dip and strike direction. The method for the basically in a three step process: (1) the spatial indexing of massive unstructured point clouds; (2) the computation of the local dip and strike direction, by means of Eigen values analysis; (3) the unique data representation according to their dip and strike direction, by means of a lower Schmidt projection. Such analysis allows for the quick identification of structural features that may condition landslide occurrence, such as the different joints sets, foliation, faults, etc.

### 1. INTRODUCTION

The use of LIDAR derived High Resolution Digital Elevation Models (HRDEM) is currently widely used on landslide detection, characterization, monitoring and modelling.

Although GIS tools allow the analysis of topography using slope, slope aspect, second derivative, curvature, flow paths, etc., only a few softwares are dedicated to the analysis of the relief structure. A pioneering attempt of merging slope angle and slope aspect in a single map was made by Brewer and Marlow (1993), representing slope angle and slope aspect with different colours. Using the dip and strike direction of each cell, a DEM can be theoretically represented with a map having a unique colour for each spatial orientation. The application of this colour code information may help in the 3D characterization of geological structures.

### 2. METHOD

#### 2.1 Principles of the software

Basically, the software allows for the visual representation of dip and strike directions using a HSI (Hue Saturation Intensity) wheel. The color displayed in the screen is linked to the normal pole of the surrounding points, as depicted in figure 1.

In order to deal with the huge number of datasets, a structure based on octrees (an index based on spatial portioning) is used, which allows for fast localization of points within a given region, low consumption of RAM, and hard drive access minimization. The covariance

matrix C is defined over a local neighborhood surrounding a point of interest as:

$$C = COV(X) = \begin{bmatrix} \sigma_{xx} & \sigma_{xy} & \sigma_{xz} \\ \sigma_{xy} & \sigma_{yy} & \sigma_{yz} \\ \sigma_{xz} & \sigma_{yz} & \sigma_{zz} \end{bmatrix}$$

where the entries for a neighborhood containing k points are defined as:

$$\sigma_x^2 = \text{var}(x) = E(x^2) - E(x)^2 = \frac{1}{k} \sum_{i=1}^k (x_i - \bar{x})^2$$

$$\sigma_{xy} = \text{cov}(x, y) = E(xy) - E(x)E(y) = \frac{1}{k} \sum_{j=1}^k (x_i - \bar{x})(y_i - \bar{y})$$

with E(value) being the expected value or the mean value,  $E(x)=\bar{x}$ , and var(x) and cov(x,y) denoting the variance of x and the covariance between x and y respectively (Belton and Lichti, 2002). Since C is a symmetric and positive semidefinite, its associated eigenvalues  $\lambda_i$  are greater than (or equal) to zero. The local normal vector is given by the associated eigenvector  $e_i$  with the smallest eigenvalue. The direction of the normal vector is the same as the one found by least squares plane fitting, since the two methods are equivalent (Shakarji, 1998).

#### 2.2 Outputs

Following information is extracted from the LIDAR point cloud using COLTOP 3D software:



- Dip angle and dip direction of a given point of the point cloud.
- Histogram of the orientations of a given area of the point cloud.
- Vegetation extraction, based on the high surface variability of the point cloud on certain areas.

All the extracted information can be visualized either in a stereonet plot or in a table with the numerical values.

### 3. DISCUSSION AND CONCLUSIONS

3D point clouds acquired from airborne or ground-based Lidar permit a rapid structural analysis. This is useful since joints and instabilities are often in inaccessible zones. The colors obtained from grid DEMs using the Hue Saturation Index in COLTOP-3D permit an easy detection of the main features of a relief, such as the main joint sets shaping rock faces. The colored surfaces and their interactivity, allow for a

detailed structural analysis. Unstructured clouds of 3D data points can serve as a basis for surface reconstruction by triangulation. Thus, the color representation, based on the dip direction and the dip angle of the surface, can be assigned to each triangle. This color representation forms a simple way to quickly obtain information for slope analysis. COLTOP-3D has shown its efficiency using square DEM grids. The difficulty to implement a true 3D version comes from: (1) storage and access of huge Lidar data sets; (2) octree classification and triangulation of data points; (3) extraction of 3D surface resulting from the triangulation, and; (4) representation of the 3D surface according to a Hue Saturation Index wheel using the dip direction and dip angle. The promising preliminary results presented here indicate that these new DEM analysis tools will greatly help structural geologists and rock mechanics engineers by supplementing part of the classical field work and permitting to contribute to more quantitative field work analysis.

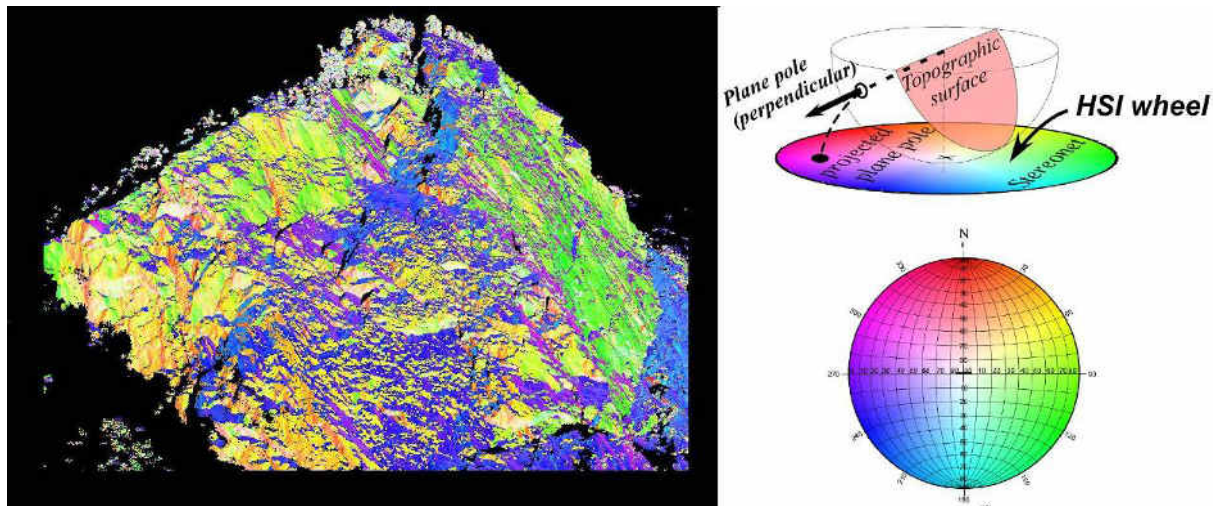


Fig. 1. Principle of the COLTOP 3D software. The color of each sector is defined using the normal vector of the surface terrain; the HIS wheel is also plotted over a stereonet projection.

### REFERENCES

- Belton, D. and Lichti, D. 2005. Classification and Feature Extraction of 3D Point Clouds from Terrestrial Laser Scanners, in SSC2005: Spatial Intelligence, Innovation and Praxis: Proceedings of National Biennial Conference of the Spatial Sciences Institute 2005, Melbourne, Vic, pp. 39-48, CD Publication.
- Brewer, C. A. and Marlow, K. A. 1993, Color representation of aspect and slope simultaneously. Proceedings, Eleventh International Symposium on Computer-Assisted Cartography (Auto-Carto-11), Minneapolis, 328-337.
- Metzger, R., and Jaboyedoff, M.: COLTOP 3-D: A software dedicated to analyze relief using large DEM and massive 3-D imaging cloud points, Geophysical Research Abstracts, 10, 08785, 2008.
- Jaboyedoff, M., Metzger, R., Oppikofer, T., Couture, R., Derron, M.-H., Locat, J., and Turmel, D.: New insight techniques to analyze rock-slope relief using DEM and 3D-imaging cloud points: COLTOP-3D software, in: Rock mechanics: Meeting Society's challenges and demands, Proc. of the 1st Canada-U.S. Rock Mechanics Symposium, ed by: Eberhardt, E., Stead, D., and Morrison, T., Taylor & Francis, 1, 61-68, 2007.
- Shakarji, C. 1998. Least-Squares Fitting Algorithms of the NIST Algorithm Testing System. Journal of Research of the National Institute of Standards and Technology. Vol. 103, 6.

## CASE STUDY 5:

**Title:** Using TLS for rockfall detection and prediction.

**Application:** Rock face monitoring; Rockfall detection; Spatial prediction.

**Technique:** Terrestrial Laser Scanner (TLS); Terrestrial LIDAR.

**Main references:** Abellán et al. (2010); Abellán et al., 2009; Abellán, 2009.

**Contributor:** UNIL (Abellán, A.); Univ. Barcelona (Vilaplana, J.M.; Calvet, J.)

### ABSTRACT

This case shows an application of a Terrestrial Laser Scanner (TLS) for rock face monitoring. The pilot study area corresponds to the main scarp of an old slide located at Puigcercós (Pallars Jussà, Spain). Five different point clouds of the slope were acquired between 2007 and 2009 in an ongoing project. The first part of this research shows the main rockfalls that occurred during the time span: geometry, frequency, volume, etc... The second deals with the spatial prediction of rockfalls through the detection of a rockfall precursory indicator (small scale pre-failure deformation). The spatial location of different rockfall events were predicted through the developed methodology. This research offers interesting prospects in rockfall risk management: the TLS instrumental offer interesting prospects not only for the spatial location of rockfalls but also for their spatial prediction.

### 1. INTRODUCTION

The possibility of acquiring datasets with high accuracy and spatial resolution are currently opening up new ways to visualize, model and interpret Earth surface processes. One of these new remote sensing tools, a Terrestrial Laser Scanner (TLS) was used in this study for the detection and spatial prediction of rockfalls. Minor scale rockfalls are the most frequent type of landslides on cliffs and steep slopes in mountain areas. Since this phenomena is the fastest type of landslide, its impact energy and geological hazard can reach very high values.

The monitored rock face (Fig.1) is the main scarp of a landslide that took place in January 1881. This event was described as a complex roto-translational slide, evolving into an earth flow in its zone of accumulation (Vidal 1881; Corominas and Alonso, 1984). The displaced material occupied an area of 80,000 m<sup>2</sup>. The scar consists on an alternation of grey marls, sandstones, silt and clays. Minor rockfalls currently constitute the main geomorphological process.

This scar was selected as a pilot area for rockfall monitoring using a TLS.

### 2. MATERIAL AND METHODS

#### 2.1 Terrestrial Laser Scanner (TLS)

A TLS ILRS3D (Optech) was employed in this study. This instrument consists of a transmitter/receiver of infrared laser pulses and a scanning device. Distance measurement (range,  $\rho$ ) is based on the *time-of-flight* ( $\Delta t$ ) of the laser pulse. A complete explanation of the material and method is described in chapter 3 of this deliverable.

#### 2.2 Data acquisition

Data acquisition was performed from a single station. First dataset was acquired on September 2007; subsequent datasets were acquired 59, 135, 303 and 409 days after the first data acquisition.



Fig. 1. Study area: main scarp of an old landslide. The monitored rock face consists in an alternation of grey marls, silt and sandstones.

Three scans were collected in each fieldwork campaign in order to totally cover the rock face. Main range distances are comprised between 125 and 175 meters. The mean point spacing ranged from 4 to 6 cm. The standard deviation of the instrumental at the specific condition of the study area was assessed as a 1.68cm.

### 2.3 Comparison of sequential scans

3D variations of the terrain on different time periods were detected through a comparison of sequential TLS datasets. The method for alignment (ICP) and comparison (point to surface method) is described in chapter 3 of this deliverable. Using this approach, two different type of slope processes were recorded using this approach: rockfalls and pre-failure deformation.

### 2.4 Rockfall detection

The detection of the different rockfalls occurred during the monitoring period is based on the methodology described in Lim et al., 2006 and Rosser et al., 2005. It basically consists in a non-continuous acquisition of TLS datasets, alignment in a common reference system, difference calculation and volume extraction.

### 2.5 Detection of the pre-failure deformation

The pre-failure deformation on certain sectors of the rock face may be used as a precursory indicator prior to the failure (Abellán, 2009). This deformation is quantified in our study through the displacement measured at each point of the TLS point cloud. Millimetric displacements cannot be detected with certainty using the original, unprocessed TLS datasets. Nevertheless, a nearest neighbour (NN) filtering technique can be applied to the original dataset, enabling the accurate detection of these displacements (Abellán et al., 2009).

## 3. RESULTS

### 3.1 Rockfall detection

Rockfalls occurred during the time span can be accurately detected using TLS. The rockfall events occurred in the study area are shown in Fig. 2. Volumes of events A, B, C, D and E range from 1 to 100m<sup>3</sup>. Event A is the event of the highest magnitude (87m<sup>3</sup>). A more detailed description of the rockfall frequency and magnitude during the different periods analysed is shown in Blanchard et al., (2008) and Abellán et al. (accepted).

### 3.2. Spatial prediction of rockfall

As stated above, the spatial prediction of rockfall is based on the detection of the pre-failure deformation. In order to spatially detect this precursory indicator over the rock face, a detailed mesh was generated (resolution: 5cm). The scattering of the differences calculation was reduced by applying the NN filtering technique described in Abellán et al. (2009). During the time span, two areas showed a centimetric deformation: areas B and F. These areas showed the following characteristics: (a) a vertical discontinuity delimiting the moving block from the stable part of the slope, (b) an increase in the horizontal displacement upwards, which is characteristic of a toppling deformation and (c) a centimetric value of the pre-failure deformation lower than 10 cm.

The pre-failure deformation in area B was detected in period i, being followed by a failure in this area (Event B) during the next period of the study, meaning that this pre-failure deformation can be used as a precursory indicator or rockfall events.

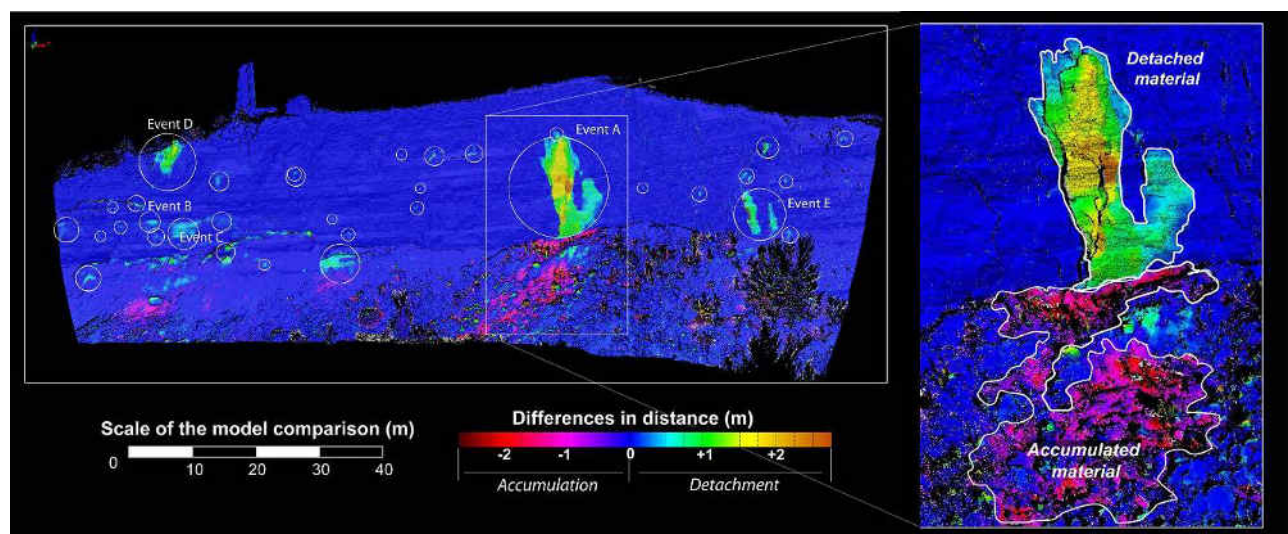


Fig. 2. Rockfall detection using TLS. The detached and accumulated materials of all the rockfalls that occurred during the time span are encircled with a white line. The higher magnitude (Event A) rockfall is enlarged.



Similarly, the pre-failure deformation in area F was detectable during periods ii and iii. The maximum value of the pre-failure deformation in this sector of the rock face has the same value as the deformation that preceded the event B, with the result that a failure is very likely in area F. New datasets acquired in November 2009 confirmed the failure of this area.

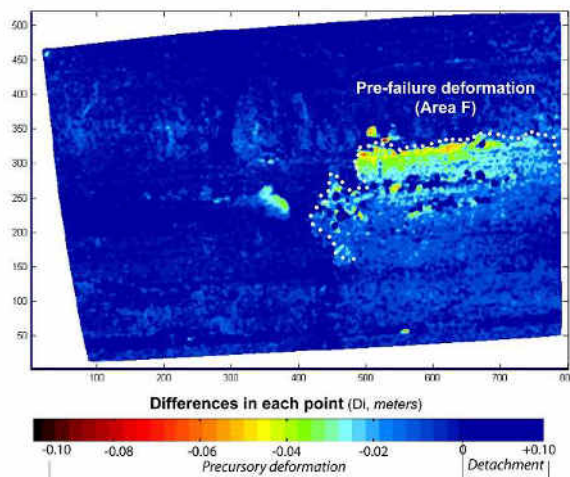


Fig. 3. Pre-failure deformation in area F during period iii. As predicted, a rockfall event occurred in the area few months later.

#### 4. DISCUSSION

The first part of the research deals with the detection of the main rockfalls that occurred during the time span: rockfall frequency, magnitude, geometry, etc. The subvertical discontinuities generated after the 1881 landslide constitute the surface of detachment of the current rockfalls. Toppling is the main failure mechanism of these rockfalls. A direct relationship between the intensity of the rainfall and rockfall frequency is discussed in Abellán et al., (2010).

The second part of this case study deals with the spatial prediction of rockfalls. This detection was performed through the detection of the pre-failure deformation over the whole rock face. Terzaghi (1950) pointed out the importance of detecting slow surface movements preceding catastrophic landslides in soils, even if this deformation is not always detectable using conventional techniques.

There is scant literature on coupling spatial and temporal prediction of minor scale rockfalls, such as those discussed in this study. Rosser et al., (2007) demonstrated that rockfall frequency may be used as a precursory indicator of greater failures. One question that remains to be resolved is as follows: are all rockfalls preceded by a precursory indicator? Drawing an analogy with the observations of Terzaghi (1950) on soil slides: are we currently failing to detect the phenomena that precede minor rockfalls?

In our case study, the relationship between pre-failure deformation and rockfall failure was proved in two different examples (Areas B and F). Furthermore, new datasets acquired during 2009 confirmed new rockfall events preceded by precursory deformation. Nevertheless, no precursory indicator was detected prior to some metric scale rockfalls (events A,C,D and E). This could be due either to an insufficient temporal resolution (no detection is possible if temporal resolution of the study is lower than the temporal length of the pre-failure deformation) or to an insufficient accuracy of the method for detecting the precursory deformation.

New cases studies are needed in order to validate the hypothesis stated in this case study: the applicability of the method over different study areas should be tested. Different materials, failure mechanisms and maximum range may influence the reliability of the method for detecting rockfall pre-failure deformation.

#### 5. CONCLUSION

The frequency and magnitude of the main rockfalls that occurred during the time span was analyzed. Furthermore, the spatial prediction of events B and F was carried out through the detection of the pre-failure deformation over the whole rock face. These results proved that TLS instrumental can be used not only for detection but also for prediction of minor scale rockfall.

#### REFERENCES

- Abellán, A. 2009. Improvements in our understanding of rockfall phenomenon by Terrestrial Laser Scanning. Emphasis on change detection and its application to spatial prediction. PhD Thesis, RISKINAT group, Faculty of Geodynamics and Geophysics, University of Barcelona, Spain, 185pp.
- Abellán, A. Jaboyedoff, M., Oppikoffer, T., Vilaplana, J.M., 2009. Detection of millimetric deformation using a Terrestrial Laser Scanner: Experiment and application to a rockfall event. *Natural Hazards and Earth System Science*, 9, 365-372.
- Abellán, A., Calvet, J., Vilaplana, J.M., Blanchard, J., 2010. Detection and spatial prediction of rockfalls by means of terrestrial laser scanning monitoring. *Geomorphology*. doi:10.1016/j.geomorph.2010.03.016
- Blanchard, J., Calvet, J., Abellán, A., García, D., Khazaradze, G., Vilaplana, J.M., 2008: Estudio del escarpe del deslizamiento de Puigcercós mediante láser escáner terrestre. *Conca de Tremp, Catalunya. Geotemas* 10, 1389-1392.
- Corominas, J., Alonso, E., 1984. Inestabilidad de laderas en el Pirineo catalán. Tipología y causas. Inestabilidad de laderas en el Pirineo. Ponencias y Comunicaciones. ETSICCP-UPC, C.1-C.53.

- Crosta, G.B., Agliardi, F., 2004. Failure forecast for large rock slides by surface displacement measurements. *Canadian Geotechnical Journal*, 40(1), 176-191
- Lim, M., Petley, D.N., Rosser, N.J., Allison, R.J., Long, A. J., Pybus, D., 2006. Combined digital photogrammetry and time-of-flight laser scanning for monitoring cliff evolution. *Photogrammetric Record*, 20(1), 109-129.
- Rosser, N.J., Petley, D.N., Lim, M., Dunning, S.A. & Allison, R.J., 2005. Terrestrial laser scanning for monitoring the process of hard rock coastal cliff erosion. *Quarterly Journal of Engineering Geology and Hydrogeology*, 38(4), 363-375.
- Rosser, N.J., Lim, N, Petley, D.N., Dunning, S. & Allison, R.J., 2007. Patterns of precursory rockfall prior to slope failure. *Journal of Geophysical Research*, Vol. 112, No. F4.
- Vidal, L.M., 1881. Nota acerca de los hundimientos ocurridos en la Cuenca de Tremp (Lérida) en Enero de 1881. *Boletín de la Comisión del Mapa Geológico de España*, Tomo VIII:113-129.

## CASE STUDY 6:

**Title:** Susceptibility assessment at regional scale based on areal LIDAR datasets. Application to the canton of Vaud, western Switzerland.

**Application:** Susceptibility assessment at regional scale.

**Technique:** Aerial Laser Scanner (ALS) ; Aerial LiDAR.

**Main references:** Jaboyedoff et al., 2008; Horton et al., 2008 (*Section 3, debris flow*); Loye et al., 2009 (*Section 4, rockfalls*).

**Contributor:** UNIL (Jaboyedoff, M., Pedrazzini, A., Loye, A., Horton, P., Abellán, A., Michoud, C., Derron, M.H.).

### ABSTRACT

This case study shows a susceptibility assessment at regional scale. The goal of the study was to develop and apply different methods in order to provide a fast overview of potential events related to slope mass movement (landslides, rockfalls and debris flows) at regional scale. The present method was developed for the Canton of Vaud (2'800 km<sup>2</sup>), western Switzerland. A summary of the methodology for the different phenomena is showed as follows: (a) LANDSLIDES: Landslide inventory was performed based on the geomorphological observations of High Resolution DEM, orthophotos and field work campaigns through expert criteria; (b) ROCKFALLS: susceptibility analysis was performed through the identification of potential rock fall source areas based on a geomorphometric analysis of DEM together with the calculation of the run-out assessment according to the 3D shallow angle method; (c) DEBRIS FLOWS: susceptibility analysis was divided into two main steps: source area identification and spreading area assessment. Both analyses were carried out based on HRDEM. The estimation of the spreading area was carried out coupling flow direction and run-out distance calculations. The results of this study allow a quick overview of areas potentially reached by the specific hazard. Results were validated using datasets from the historical record, showing good agreement with past events and the knowledge of the local geologists and guides. These susceptibility maps will help the decision-makers of the Vaud canton to prioritize area of interest for the creation of more detailed, site specific hazard maps.

### 1. INTRODUCTION

During the last decade, innovative applications in remote sensing techniques have been developed. The possibility of acquiring datasets with high accuracy and spatial resolution mounted on terrestrial, aerial and/or satellite instrumentals is currently opening up new ways of visualizing, modelling and interpreting Earth surface processes. In this case study, High resolution Digital Elevation Models (HRDEM) acquired from Aerial Laser Scanner (ALS) was used for a multi-hazard susceptibility assessment.

Landslides, debris flows and rockfalls, which occur mainly in mountainous regions, are a severe potential danger for inhabited regions. Landslide risk in mountainous areas is increasing as the population and economic activity increase. The results of this study allow a quick overview of areas potentially reached by the specific hazard: landslides, rockfalls or debris flows. The identification of the most susceptible areas at regional scale plays a key role for the prioritization of more detailed, site specific studies. Susceptibility maps indicate the potentially unstable area, in order to assess whether an area is potentially endangered or not by slope. Nevertheless, such maps do not give any information on the intensity and/or the frequency of occurrence of the slope movements. This kind of map

belongs to the first step of the working process leading toward detailed local danger maps (Lateltin, 1997).

This case study introduces an overview of the methodologies applied for the following slope processes: Landslides, debris flows and rockfalls. A more detailed explanation of the proposed approach can be found in Jaboyedoff et al., (2008), Horton et al., (2008); Loye et al. (2009).

### 2. LANDSLIDE INVENTORY AND SUSCEPTIBILITY

#### 2.1 Method

The method focused on the use of GIS tools and GIS Data (i.e. LiDAR-DEM of 1m x 1m cell size). The potential instabilities (deep landslides) were identified by means of a systematic approach over the 3200 km<sup>2</sup> of the canton of Vaud, based on LiDAR-DEM analysis, information provided from the 1:25,000 geological maps as well as orthophotos. The validation of the results was based on a review of geological data, field observations and comparison with available historical inventories (Noverraz, 1995).

### 2.1.1 Landslide inventory

A landslides inventory was performed using following information: (a) previous inventories (DUTI program; Noveraz, 1995); (b) a detailed investigation of the 1:25,000 topographic map; (c) geological maps; (d) LiDAR-DEM (MNT-MO, © 2005 SIT) hillshade; (e) morpho-structural analysis of LiDAR-DEM data; (f) orthophotos.

### 2.1.2 Landslide susceptibility

The potential landslide areas were obtained by: (a) the mapping of geomorphic traces visually analyzed using the LiDAR-DEM hillshade; (b) the mapping of the landslide activity carried out through the analysis of the orthophotos and (c) the use of the historical record, including previous landslide inventory maps. As described by Ardizzone et al., (2007), such fine-scale morphological topographic analysis is a relevant approach for delineating potential landslides. According to a systematic approach based on morphological features (slope failures, scars, deposits, sagging) all kinds of topographic irregularities (slope statistics, etc.) were taken as evidence to delineate current and ancient landslide prone areas. Moreover, this approach was associated with the analysis of the 1:25'000 geological maps ([www.swisstopo.ch](http://www.swisstopo.ch)), using the sensitivity of lithologies to landsliding, structural elements such as fault systems and tectonic lines. The slopes at rivers edges were also considered because of the effect of enhanced erosion in such a context (distortion of watercourses, occurrence of natural dams, etc.) and were therefore used as criterion to detect landslide activity. Then, the landslide susceptibility was subdivided in three categories from proven landslides (clear geomorphologic signatures) to zones that possess one or more criteria susceptible to contain landslides, but without any clear features.

The three main susceptibility classes are described as follow: (i) *Class 1*: Zone characterized by the occurrence of landslides detected by a typical and complete set of morphological landslide features or based on previous inventories; (ii) *Class 2*: Zone characterized by the occurrence of possible landslides deduced by some of the morphological evidence but which cannot be verified without a detailed field work; (iii) *Classes 3*: This class was subdivided in three sub-classes: 3a) areas characterized by an important fluvial erosion; 3b) areas showing a rugged topography (depression, scars, etc.); 3c) areas characterized by a mean slope value between 18°-37°, which define a range of slope suitable to develop landslides (Van Westen et al, 1997).

## 3. DEBRIS FLOWS

### 3.1 Methodology

A new model was developed for a regional debris flow susceptibility assessment using Matlab environment. The methodology results in a 2 steps work: source

area identification and debris flow propagation. Both the sources identification and the spreading area assessment are based on a regular grid with a resolution of 10 meters, which is needed to capture the variability of the topographic form for hillslopes (Wilson 1996). A more detailed explanation can be found in (Horton et al., 2008).

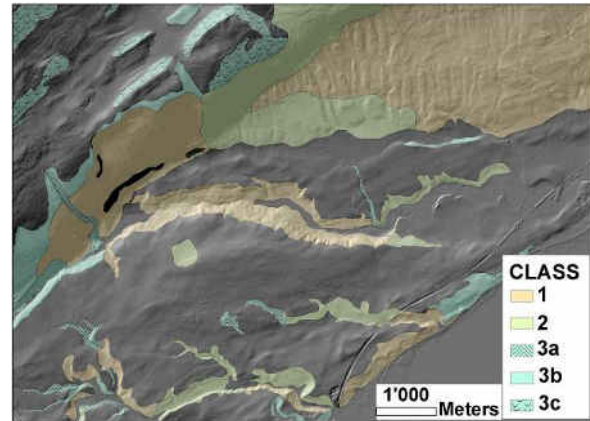


Fig. 1. Close up of the landslide prone areas map based on DEM (MNT-MO, © 2005 SIT), orthophotos and geological map analysis. Each class corresponds to different morphological evidence and to different types of processes, as is described in the text. Figure from Horton et al., 2008

### 3.1.1 Source area identification

Three main criteria are relevant for a debris flow initiation: sediment availability, water input and geometry of the slope (Takahashi, 1981; Rickenmann and Zimmermann 1993, Delmonaco et al., 2003): (i) Sediment availability was linked to the lithology, as some geological units produce more or less debris and fine particles prone to be eroded, such as flysch and marls; (ii) Water input was estimated using the upslope contributing area; (iii) Geometry of the slope: the inclination of each cell (slope angle) is a key parameter in the triggering of the Debris Flow. Finally, the plan curvature and the land use map were added to increase the detection quality.

### 3.1.2 Spreading area assessment

The debris flow spreading was mathematically estimated by two types of algorithms: flow direction algorithms and run-out distance calculations:

- (i) Flow direction algorithms: these algorithms apportion the flow from one cell to its eight neighbours. The final probabilities are function of the slope and the persistence. Best fitting with occurred debris flows was observed using Holmgren's (1994) algorithm.
- (ii) Run-out distance calculations: these algorithms control the distance reached by the debris flow and reduce their divergence, influencing the flow direction. The probable maximum run-out is characterized by an average slope angle of 11° (Huggel et al. 2002).



### 3.2 Results

The results are based on the extreme events threshold for the source areas previously identified (see Horton et al., 2008). The spreading areas of all sources are combined by keeping the maximum probability values. The result is the total area exposed to debris flow spreading, with an associated qualitative probability qualifying the susceptibility potential, as shown in figure 2. A surface with a red colour has a higher probability to be reached by a debris flow than a yellow one. More accurate identification of the source and spreading areas are obtained using a HRDM derived from LIDAR datasets. A good coherence between the simulation results and field observations was observed on specific catchments where major debris flow events occurred.

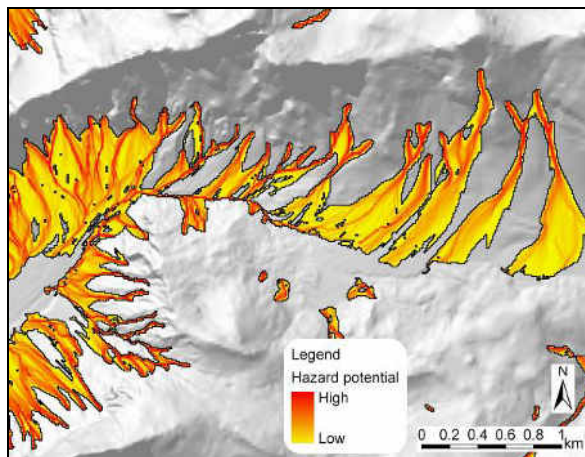


Fig. 2. Spreading results for extreme events for the Anzeindaz – Solalex (Switzerland) region, with representation of the probability values. (DEM by SITVD. Figure from Horton et al., 2008)

## 4. ROCKFALLS

One of the most challenging tasks for rockfall prediction is to define the potential rockfall source areas and the accurate determination of the reach susceptibility. The methodology developed in this section (Loye et al., 2009) results in a 2 steps work: source area identification and block propagation.

### 4.1 Source area Identification

Unstable rockfall source areas are found in most cases in unstable, rocky steep slopes. Rockfall phenomenon is assumed to be controlled by rock type, structural conditions (discontinuities, foliation, etc.) and slope gradient.

It can be considered that the type of relief (e.g. glacial, alluvial, plains, etc.) and the mechanical properties of the rocks are characteristic for a given morphotectonic setting (Strahler, 1950). Hence, main morphological units of the topography (varying randomly around its mean slope gradient) such as steep slopes, cliffs, etc., can be expressed in a unique Slope Angle Distribution

(SAD), characteristic of the main morphological units (see Loye et al., 2009 for a further explanation).

As regards the interpretation, the peak of each fitted curve can be correlated to major morphological units. Two thresholds slope angle were encountered: (a) the intersection between cliff and steep slopes and (b) the cliff outcrop only. The maximum of the Gaussian distribution can be assumed as an apparent stable slope angle.

The slope angle frequency histogram was performed on a DEM of 1m x 1m cell size (MNT-MO, © 2005 SIT). For each of the five geologically-based units areas of the Canton of Vaud, a slope angle frequency distribution was computed and plotted (see Loye et al., 2009). Slope gradients steeper than the angle defined at the intersection between the estimated “Cliffs” and “Mountain sides” population were also considered as potential rockfall source areas, independently of the lithology and surface cover. This corresponds to the slope above which the “Cliffs” data distribution becomes dominant over the other morphometric classes (“Cliff” slope angle limit).

### 4.2 Run-out zones assessment.

Assessment of the runout zones from the potential source areas described above was performed by means of the CONEFALL software (Jaboyedoff and Labieuse, 2003), which simply implements shallow angle method (Toppe, 1987; Evans and Hungr, 1988) computed in a GIS environment with software CONEFALL (Jaboyedoff and Labieuse, 2003). Thus, this software allows the estimation of the maximum runout length in 3D by assuming a given aperture angle ( $90^\circ - \phi_p$ ) centred on the source point (See Jaboyedoff et al., 2008).

Critical angles for each major unit are listed in Loye et al. (2009). CONEFALL was applied to each potential source zone with an aperture angle of  $33^\circ$  for all units. This was established by comparison with rockfall events observed on orthophotos and fieldwork undertaken on test zones. Figure 3 shows the results of the rockfall source and propagation areas.

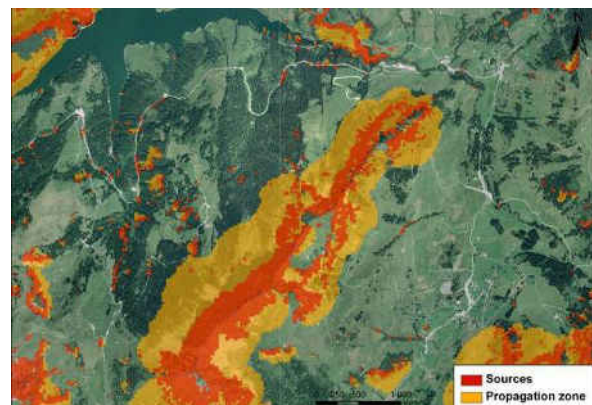


Fig. 3. Close-up of the Indicative rockfall hazard map. Rockfall source zones are drawn in red and the runout perimeter in orange SWISSIMAGE © 2004 swisstopo (DV012716). Figure from Horton et al., 2008

## 5. RESULTS AND DISCUSSION

Currently, modern acquisition techniques (Airborne Laser Scanning, Photogrammetry) enable to obtain a regional scale DEM with a resolution as high as 1m making the topographical analysis more and more relevant since the modelled slope angles are very close to reality. The quality of the results depends on the DEM resolution and on the availability of other different spatial information: the higher the accuracy and resolution of a given DEM, the more accurate the results. All the information related to the landslide susceptibility classes were stored in a GIS database and form an interactive landslides susceptibility map all over the territory, which consist of a complete description of information (distinctive morphological sign, class, etc.). These characteristics enable an overview of the state of knowledge of the landslide prone areas.

ALS proved useful for the updating of previous landslide inventories (section 2). The limiting factor in interpreting LIDAR derived DEM hillshade 2D and its 3D visualization depends principally to the data artifacts. They are mostly related to the occurrence of locally very dense vegetation cover or occurrence of clouds during the data acquisition as well as some steep rugged topography that truncates the laser signal during the data acquisition. Displaying hillshade can have some kind of shading effects as well, which creates inaccurate or even incorrect morpho-structural features.

Process based modelling of debris flow is difficult because of the complexity of the phenomenon and the variability of controlling factors. The automatic identification of sources areas and the estimation of debris flow spreading, based on GIS tools, provide a substantial basis for a preliminary susceptibility assessment at a regional scale.

The method used in section 4 for source detection areas is a rather conservative way to consider cliff faces and slopes surfaces to be potentially instable over a certain slope gradient. Likewise, CONEFALL allows quick but accurate delineation of potential rockfall prone perimeters, resembling with a 3D trajectography model, although it doesn't require physically-based parameters acquired on field.

## 6. GENERAL CONCLUSION

Nowadays, the availability of LiDAR-DEM represents an important tool either to obtain a rapid overview of potential unstable areas or to perform more detailed studies as well. The methods analyzed in this case study show the potential of the DEM-based analysis for the estimation of the susceptibility of common slope process phenomena in mountain areas. These methods, relatively easy to use, allow a quick overview of the potential hazard affecting a large territory by using LIDAR-DEM. As a result, significant

information of the zones where a more detailed analysis must be carried out is provided.

## REFERENCES

- Ardizzone, F. Cardinali, M., Galli, M., Guzzetti, F., and P. Reichenbach 2007. Identification and mapping of recent rainfall-induced landslides using elevation data collected by airborne Lidar. *Nat. Hazards Earth Syst. Sci.*, 7, pp. 637-650.
- Delmonaco, G., Leoni, G., Margottini, C., Puglisi, C. and Spizzichino, D. 2003. Large scale debris-flow hazard assessment: a geotechnical approach and GIS modelling. *Natural Hazards and Earth System Sciences*, Vol. 3, pp. 443-455.
- Holmgren, P. 1994. Multiple flow direction algorithms for runoff modelling in grid based elevation models: An empirical evaluation. *Hydrological Processes*, Vol. 8(4), pp. 327-334.
- Horton, P., Jaboyedoff, M., Bardou, E. 2008. Debris flow susceptibility mapping at a regional scale. In Locat, J., Perret, D., Turmel, D., Demers, D., and Leroueil, S., 2008. *Proceedings of the 4<sup>th</sup> Canadian Conference on Geohazards. From Causes to Management*. Presse de l'Université Laval, Québec, 594p.
- Huggel, C., Kaab, A., Haeberli, W., Teyssie, P. and Paul, F. 2002. Remote sensing based assessment of hazards from glacier lake outbursts: a case study in the Swiss Alps. *Canadian Geotechnical Journal*, Vol. 39(2), pp. 316-330.
- Hungr O. and Evans S. G. 1988. Engineering evaluation of fragmental rockfall hazard. *Proceedings of the 5th International Symposium on Landslides*, Lausanne, pp. 685-690.
- Jaboyedoff, M. and Labiouse, V. 2003. Preliminary assessment of rockfall hazard based on GIS data. *ISRM 2003 - Technology roadmap for rock mechanics*, South African Institute of Mining and Metallurgy.
- Jaboyedoff, M., Pedrazzini, A., Horton, P., Loye, A., Surace. 2008. Preliminary slope mass movements susceptibility mapping using LIDAR DEM. *Proceedings, 61st Canadian Geotechnical Conference and 9th Joint CGS/IAH-CNC Groundwater Conference*. Edmonton, AB.
- Lateltin, O., 1997. *Recommandations - Prise en compte des dangers dus aux mouvements de terrain dans le cadre des activités de l'aménagement du territoire*. Office fédéral de l'Environnement, des forêts et du paysage.
- Loye, A., Jaboyedoff, M., and Pedrazzini, A. 2009. Identification of potential rockfall source areas at a regional scale using a DEM-based geomorphometric analysis, *Nat. Hazards Earth Syst. Sci.*, 9, 1643-1653.
- Noverraz F. 1995. *Carte des instabilités de terrain du Canton de Vaud*. Ecole Polytechnique Fédérale de Lausanne 33p.
- Rickenmann, D. and Zimmermann, M. 1993. The 1987 debris flows in Switzerland: documentation and analysis. *Geomorphology*, Vol. 8(2-3), pp. 175-189.

- Strahler, A. N. 1950. Equilibrium theory of erosional slopes approached by frequency distribution analysis, *Am. J. Sci.*, 248, 673–696, 800–814.
- Takahashi, T. 1981. Estimation of potential debris flows and their hazardous zones: Soft countermeasures for a disaster. *Natural Disaster Science*, Vol. 3(1), pp. 57-89.
- Toppe, R. 1987. Terrain models – a tool for natural hazard mapping. In Salm, B. and Gubler, H., editors, *Avalanche formation, movement and effects*. IAHS Publication no. 162, 629–38.
- Van Westen, C.J., Rengers, N., Terlien, M. and Soeters, R. 1997. Prediction of slope instability phenomena through GIS-based hazard zonation. *Geol. Rundschau*, 86, pp. 404-414.
- Wilson, J.P. 1996. GIS-based land surface/subsurface modeling: new potential for new models, Third International Conference / Workshop on Integrating GIS and Environmental Modeling, Santa Fe, New Mexico, pp. 21-26.



## CASE STUDY 7:

**Title:** The application of LiDAR-derived images for landslide inventory and susceptibility mapping in the Flemish Ardennes, Belgium.

**Application:** Landslide inventory and susceptibility mapping at regional scale.

**Technique:** Aerial LiDAR.

**Main references:** This case study is based on following publications: Van Den Eeckhaut et al. (2006; 2007a,b; in press).

**Contributor:** JRC (Van Den Eeckhaut M., Poesen J., Vandekerckhove L., Hervás J.).

### ABSTRACT

Large, deep-seated soil slides are common features in the Flemish Ardennes (Belgium). As many of these old (> 100 years) landslides are located under forest in this hilly region, aerial photo interpretation is not an appropriate landslide mapping method. Van Den Eeckhaut et al. (2007a) tested the potential of airborne LiDAR images for mapping old active and dormant landslides in a 125 km<sup>2</sup> test area in the Flemish Ardennes, and concluded that that large-scale LiDAR-derived hillshade and contour line maps analyzed by experienced geomorphologists can significantly improve field survey-based inventories of landslides with a subdued morphology in hilly regions. In the same area LiDAR-derived slope and aspect maps were applied successfully, together with lithological maps, for statistical landslide susceptibility mapping (Van Den Eeckhaut et al., 2006). This study presents the LiDAR-derived landslide inventory and susceptibility map of the complete Flemish Ardennes (720 km<sup>2</sup>), and is a good example of “science meeting policy” as the scientific results are used by qualified authorities to inform local people. On the website of the Environment, Nature and Energy Department of the Flemish Government (<http://www.lne.be/themas/bodem/grondverschuivingen>) the landslide inventory and landslide susceptibility maps are available and prevention and mitigation measures are presented.

### 1. INTRODUCTION

The Flemish Ardennes is a hilly region marked by old, large, deep-seated landslides with an affected area of at least 1 ha and an assumed shear plane depth of more than 3 m (Van Den Eeckhaut et al., 2005). Due to the vicinity of cities such as Brussels and Ghent (Figure 1), the forested hills of this region have become attractive residential areas, and it appears that the expansion of settlements and human interference has increased vulnerability to landsliding. Indeed, reactivations of old landslides, causing damage to public and private property have been documented, mostly during winter and spring, after periods of persistent rainfall. This has resulted in an increased interest in the process of landsliding and its related problems by the local and regional authorities. Optimal approaches to reduce landslide risk generally comprise a mix of four strategies (Schuster and Kockelman, 1996), among which reduction of development in landslide-prone areas, is the most effective and economical. To apply this strategy, the locations of landslide-prone areas must be known. As it is believed that past and present landslide locations are the key to prediction of future landslide locations (Carrara et al., 1995), a detailed landslide inventory map is indispensable for the production of landslide susceptibility maps (Ardizzone et al., 2002). Therefore this study provides an overview of the LiDAR-derived

landslide inventory and susceptibility map of the complete Flemish Ardennes (720 km<sup>2</sup>).

### 2. MATERIALS AND METHOD

#### 2.1 LiDAR and landslide inventory mapping

A detailed description of the LiDAR-data can be found in Van Den Eeckhaut et al. (2007a). For the complete Region of Flanders, LiDAR data was collected in 2001 and 2002. The original laser pulses had an average pulse density of 1 per 4 m<sup>2</sup> and the post-processing was conducted by the vendor. The Terrascan software was used to automatically remove undesired returns and to create the bald earth DEM. Afterwards a manual check followed. The database finally provided (AGIV, 2004) has a uniform point density of at least 1 per 20 m<sup>2</sup>. The accuracy of the altitude depends on the soil cover and decreases with increasing vegetation heights from 7 cm for freshly cut lawns to 20 cm for forests and pastures (GIS-Vlaanderen, 2003). A DEM with a 2 m x 2 m resolution was derived from the LiDAR data using TIN interpolation. Production artifacts were removed with low pass filtering. Then, a slope map, contour line map (2 m interval) and two hillshade maps were created. The two hillshade maps had a sun elevation angle of 30° and a sun azimuth angle of 315° and 45°. No vertical exaggeration was used.



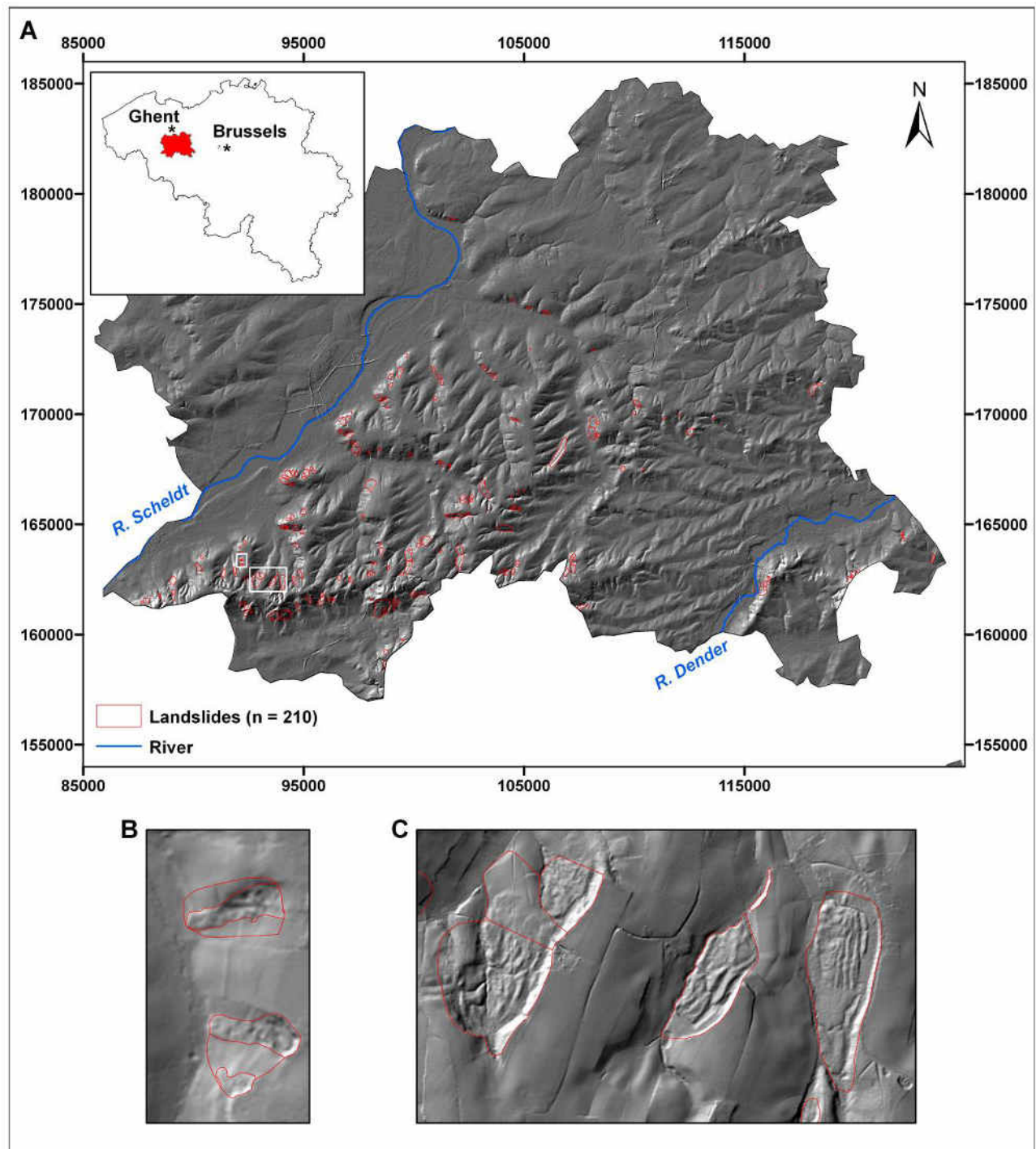


Fig. 1. Study area in the Flemish Ardennes (720 km<sup>2</sup>): (A) Landslide inventory overlain on LiDAR-derived hillshade map. White rectangles show excerpts of (B) and (C); (B) Excerpt of the hillshade map showing shallow active landslides under pasture; (C) Excerpt of the hillshade map showing three deep-seated rotational earth slides under forest.

The identification of landslides on hillshade and contour line maps is based on the recognition of landslide characteristics (e.g. main scarps, reverse slopes, convex landslide foots) and alterations of the drainage system (e.g. a main valley stream pushed away by a landslide; Wills and McCrink, 2002; Van Den Eeckhaut et al., 2007a).

Therefore between three and seven experts were asked to digitize the presumed landslides on a vector map which could be overlain with the LiDAR-derived maps.

Afterwards, the LiDAR-derived landslide inventory map was compared with the landslide inventory produced from intensive field surveys before LiDAR data



became available for the study area (Van Den Eeckhaut et al., 2005).

## 2.2 LiDAR-derived maps for landslide susceptibility mapping

Understanding the role of individual factors controlling landslide location is important for predicting 'where' landslides can occur in the future, i.e. to ascertain landslide susceptibility. In the past three decades, a large number of qualitative and quantitative methods were applied and tested to assess landslide susceptibility (e.g. Carrara et al., 1995; Guzzetti et al., 1999; Glade and Crozier, 2005). For modeling landslide susceptibility on a regional scale, logistic regression is nowadays a common statistical modeling technique (e.g. Carrara et al. 1995; Greco et al., 2007). We adopted logistic regression to find the best-fitting model describing the relationship between the dependent variable (i.e. the presence or absence of depletion areas of large, deep-seated landslides) and a set of independent variables (i.e. terrain height, slope gradient, aspect, plan and profile curvature, Tertiary geology, soil drainage, distance to rivers and distance to faults). A 10 m x 10 m resolution was used and all topographical data was derived from LiDAR.

## 3. RESULTS AND DISCUSSION

### 3.1 Internal morphology of landslides

On the LiDAR-derived hillshade map, the internal morphology of the landslides is clearly visible. Figure 1C shows three deep-seated rotational earth slides, all located under forest with the main scarps and several reverse slopes clearly distinguishable. The main scarps are indicated in white, because they are oriented to the light source located in the northwest. The reverse slopes, which are oriented towards the east and thus lying in the shadow. Also several ditches draining ponding water from some of the reverse slopes are visible, and the curved form of the brook at the foot of the most eastern landslide indicates that it has been pushed to the west by the displaced slope material.

### 3.2 Landslide inventory

The regional inventory (Figure 1A) shows 210 landslides, equivalent to a density of one landslide every 3.4 km<sup>2</sup>. However, landslides are not equally distributed throughout the area. 77.6% (n=163) of the total number of observed landslides are deep-seated, i.e. the shear surface was estimated to be deeper than 3 m, and larger than 1 ha (average 4 ha; e.g. Figure 1C). The estimation of shear surface depth is based upon the deformation of the terrain and the height and shape of the main scarp. These deep-seated landslides are mainly classified as rotational earth slides (Cruden and Varnes 1996) Shallow landslides represent 22.3% (n=47) of all landslides in the inventory, and individually occupy an area of less than

1 ha (average 0.5 ha; Figure 1B). They have an estimated depth of less than 3 m, and are classified chiefly as rotational slides with a flow component at the toe. Many of the shallow failures occurred inside pre-existing deep-seated landslides.

Important here is that the analysis of the LiDAR-derived maps resulted in an improvement of the field survey-based landslide inventory map. First, the boundaries of landslides under forest could be mapped more accurately and secondly LiDAR derivatives allowed experts to have a complete overview of the large landslides.

### 3.3 Landslide susceptibility map

Several models based on different combinations of independent variables were evaluated with the same evaluation parameters as explained in Van Den Eeckhaut et al. (2006; i.e. Area under Receiver Operating Characteristic Curve; Kappa value and other parameters calculated from confusion matrices). From this evaluation procedure, we found that the best landslide susceptibility model can be written as:

$$\log\left(\frac{\hat{p}}{1-\hat{p}}\right) = -13.418 + (0.386 \times \text{slope gradient}) + (2.520 \times \text{NW}) + (2.948 \times \text{W}) + (2.043 \times \text{SW}) + (2.399 \times \text{S}) + (1.653 \times \text{SE}) + (2.337 \times \text{GeVI}) + (2.407 \times \text{GeMe}) + (1.488 \times \text{Tt}) + (1.381 \times \text{KoAa}) \quad (1)$$

where  $\hat{p}$  is a value between 0 and 1 reflecting the probability of occurrence of a landslide depletion (initiation) area. Slope gradient, the presence of northwest (NW), west (W), southwest (SW), south (S) and southeast (SE) oriented hillslope sections, and the presence of lithological formations with an important clay content (GeVI, GeMe, Tt and KoAa) are the independent variables influencing landslide occurrence. Slope gradient is the most important environmental factor controlling landslide occurrence, and landslides are expected to occur on hillslopes with a slope gradient above 0.10 m.m<sup>-1</sup> and a southeast to northwest orientation where a lithology rich in swelling clays is located at relatively shallow depth. Landslide accumulation zones are difficult to delineate by this model as the landslide debris is sometimes deposited on slope sections with a 0.05 m.m<sup>-1</sup> slope gradient. Figure 2 shows the classified landslide susceptibility map produced from model (1). 7% of the study area (i.e. ca. 7 times the area mapped as affected by landslides) is classified with very high to moderate susceptibility to landslides and 84% of the mapped landslide grid cells are correctly classified susceptible.

## 4. CONCLUSIONS

The results of this study revealed that for hilly regions affected by active and dormant landslides high-quality landslide inventory maps can be obtained through the combination of the analysis of LiDAR-derived maps in

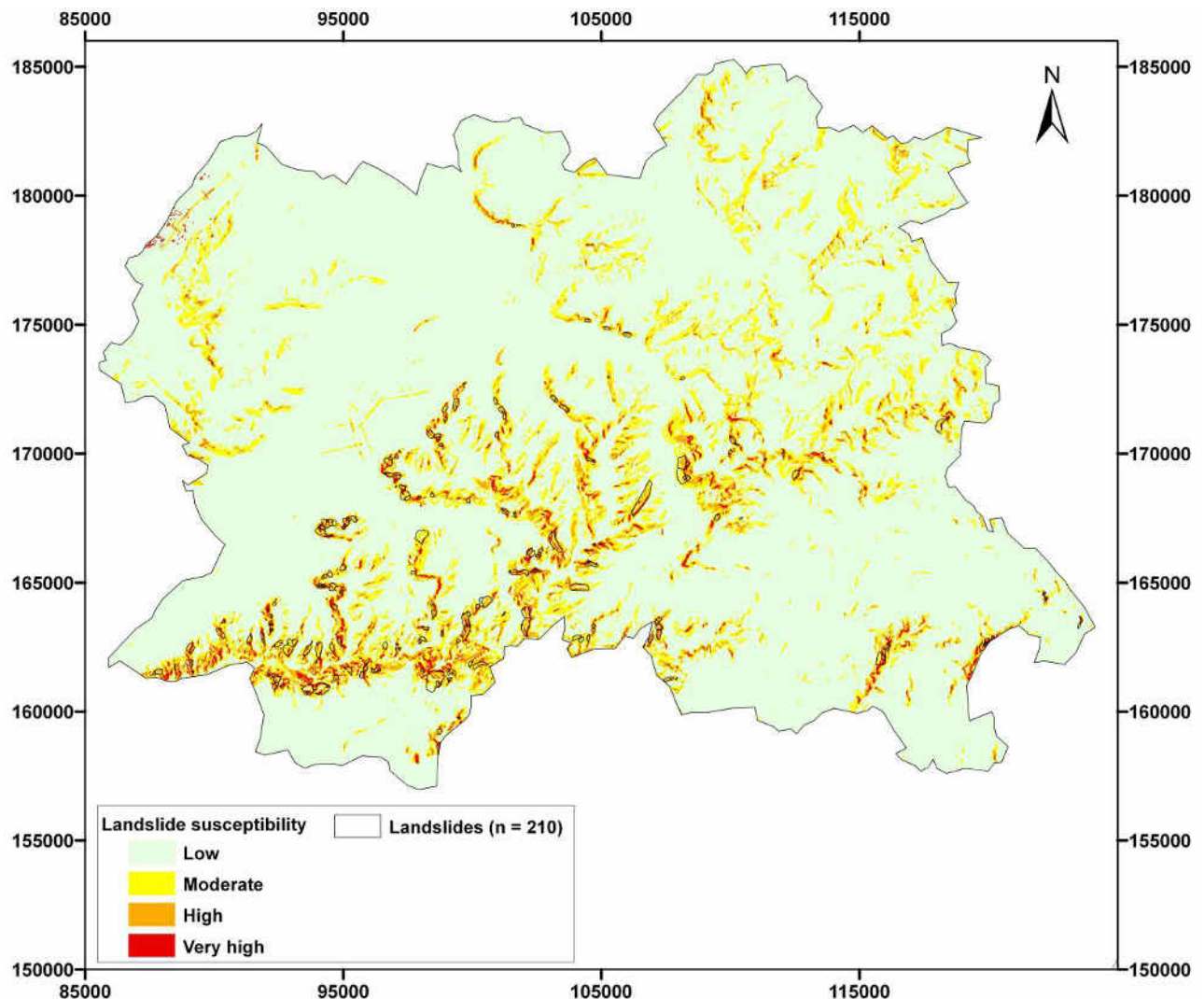


Fig. 2. Landslide susceptibility map of the Flemish Ardennes (720 km<sup>2</sup>)

a GIS environment, where possible by different experts, and detailed field checks. Indeed, for landslide inventory mapping the analysis of LiDAR derivatives and field surveys is complementary. Field checks remain necessary to exclude false positives (e.g. quarries) and to map small and shallow landslides, and landslides that occurred after LiDAR-data was collected.

The results further show that high resolution slope and aspect maps derived from LiDAR represent important tools for landslide susceptibility mapping.

## REFERENCES

- AGIV, 2004. DHM Vlaanderen, LIDAR hoogtepunten – brondata, GIS-Vlaanderen, AGIV.
- Ardizzone F, Cardinali M, Carrara A, Guzzetti F, Reichenbach P. 2002. Impact of mapping errors on the reliability of landslide hazard maps. *Natural Hazards and Earth System Sciences* 2: 3-14.
- Carrara A, Cardinali M, Guzzetti F, Reichenbach P. 1995. GIS technology in mapping landslide hazard. In *Geographical Information Systems in Assessing Natural Hazards*, Carrara A, Guzzetti F (eds). Kluwer Acad. Publ.: Dordrecht; 135-176.
- Cruden DM, Varnes DJ. 1996. Landslide Types and Processes. In *Landslides, Investigation and Mitigation*, Transportation Research Board. National Research Council, Special Report 247, Turner AK, Schuster RL (eds). National Academy Press: Washington, DC; 36-71.
- GIS-Vlaanderen, 2003; <http://www.gisvlaanderen.be/gis/diensten/geo-vlaanderen/?artid=240>

- 
- Glade, T. and Crozier, M. J., 2005. The nature of landslide hazard impact. In: Glade, T, Anderson, M.G. and Crozier, M. J., (Eds.) *Landslide Hazard and Risk*. Wiley, Chichester, pp.43-74
- Greco, R., Sorriso-Valvo, M., Catalano, E., 2007. Logistic Regression analysis in the evaluation of mass movements susceptibility: The Aspromonte case study, Calabria, Italy. *Engineering Geology* 89, 47-66.
- Guzzetti, F., Carrara, A., Cardinali, M., Reichenbach, P., 1999. Landslide hazard evaluation: a review of current techniques and their application in a multi-scale study, Central Italy, *Geomorphology*, 31, 181-216.
- Schuster, R.L., Kockelman, W.J., 1996. Principles of landslide hazard reduction. In *Landslides Investigation and Mitigation*, National Research Council, Special Report 247, Turner AK, Schuster RL (Eds.). National Academy Press: Washington, DC; pp. 91-103.
- Van Den Eeckhaut, M., Poesen, J., Verstraeten, G., Vanacker, V., Moeyersons, J., Nyssen, J., Van Beek, L.P.H., 2005. The effectiveness of hillshade maps and expert knowledge in mapping old deep-seated landslides. *Geomorphology* 67: 351-363.
- Van Den Eeckhaut, M., Vanwalleghem, T., Poesen, J., Govers, G., Verstraeten, G., Vandekerckhove, L., 2006. Prediction of landslide susceptibility using rare events logistic regression: a case-study in the Flemish Ardennes (Belgium). *Geomorphology* 76, 392-410.
- Van Den Eeckhaut, M., Poesen, J., Verstraeten, G., Vanacker, V., Nyssen, J., Moeyersons, J., Van Beek, L.P.H., Vandekerckhove, L., 2007a. The use of LIDAR-derived images for mapping old landslides under forest. *Earth surface processes and landforms* 32, 754-769.
11. Van Den Eeckhaut, M., Poesen, J., Verstraeten, G., 2007b. Vervolgproject - Opstellen van een gevoeligheidskaart met betrekking tot grondverschuivingen voor de Vlaamse Ardennen. Rapport In opdracht van Vlaamse Overheid, Dpt LNE, ALBON, Brussel, pp. 97. <http://www.lne.be/themas/bodem/grondverschuivingen/grondverschuivingen>
- Van Den Eeckhaut, M., Poesen, J., Vandekerckhove, L., Van Gils, M., Van Rompaey, A., in press. Human-environment interactions in residential areas susceptible to landsliding: the Flemish Ardennes case-study. *Area*.
- Wills CJ, McCrindle TP. 2002. Comparing landslide inventories, the map depends on the method. *Environmental and Engineering Geoscience* 8: 279-293.



## CASE STUDY 8:

**Title:** Characterization and analyses of surface deformations, mass movements and alpine region lifting with PSInSAR method in NW Slovenia.

**Application:** Landslide detecting.

**Technique:** PSInSAR™.

**Main references:** This case study is based on following publications: Komac and Bavec, 2007a, Komac and Bavec, 2007b.

**Contributor:** GeoZS (Carman, M., Kumelj, S., Jemec, M.).

### ABSTRACT

PSInSAR method was used for mass movement detection on an area which spreads over 700km<sup>2</sup> and lies in the NW part of Slovenia. The research area forms the eastern flank of the Alpine arch and is tectonically still active. For the analytical purposes 57 images of descending orbit from satellites ERS 1 and ERS 2 were used. The time span of the acquired images was from April 1992 to December 2000. The average signal reflector (PS) density for the area was 23 per km<sup>2</sup>. Altogether 16304 permanent scatters were detected. For the best 10 % (1646 PS), time series of displacements were acquired. The results also show a constant uplift of Alps and they indicate that the uplift is of higher magnitude than it was considered until now. The relative uplift in relation to the reference point in the Alpine foreland ranges up to 3.35 mm per year.

### 1. INTRODUCTION

Slovenia lays in the eastern flank of Alpine arch and an active tectonics present are main driving forces for mass movements in the region, especially the north-western part of Slovenia. The research area was chosen as the study area due to its neotectonic activity (Poljak et al., 2000; Zupančič et al., 2001; Grenerczy et al., 2005) and due to a number of landslide, rockfall and debris flow occurrences (Komac et al., 2005). The proved active tectonics of the region is a consequence of compression field with approximate tension field  $\sigma_1$  in N-S direction (Placer, 1998; Grenerczy et al., 2005; Weber et al., 2006; Rižnar et al., 2007). There are several major active faults (Idrija, Sava and Ravne fault) and an active South Alps thrust (Poljak, 2000). These faults are most probably right displacement faults, at least this can be stated for Ravne fault (Zupančič et al., 2001; Bajc et al., 2001). The area is subdivided into several nappes (Julian nappe, Tolmin nappe, Trnovski nappe; after Placer, 1998). Wider area is classified as of middle seismic activity area (Poljak et al., 2000). During the InSAR data acquisition, between April 1992 and December 2000, a major earthquake occurred in the research area with magnitude of MW = 5.6 (Bajc et al., 2001; Gosar et al., 2001; Zupančič et al., 2001).

The research area consists mainly of Mesozoic carbonate rocks, some flysch clastites, in the northern part of Paleozoic clastic and carbonate rocks. The net of fluvial and glacial valleys is filled with Quaternary sediments. (Buser, 1987; Jurkovšek, 1987).

Modern satellite radar permanent (also persistent) scatterer interferometric technique (PSInSAR) enables very accurate monitoring of relative vertical

displacement velocities of observed surfaces and grounds (Ferretti et al., 2001; Ferretti et al., 2005; Bürgmann et al., 2006; Dixon et al., 2006; Ferretti & Cresp, 2006). Technique is also very useful in geology for monitoring coseismic and aseismic tectonic displacements (Massonnet et al., 1993; Massonnet et al., 1994; Dixon, 1995; Peltzer et al., 1996; Massonnet et al., 1996; Peltzer et al., 1999), slow moving landslides (Ferretti et al., 2001; Colesanti et al., 2003a; Hilley et al., 2004), and swelling of ground or subsidence (Carnec and Delacourt, 2000; Ferretti et al., 2000; Colesanti et al., 2003b; Vasco & Ferretti, 2005).

### 2. RESEARCH AREA

PSInSAR technique is also very useful in geology for monitoring coseismic and aseismic tectonic displacements, slow moving landslides and swelling of ground or subsidence. The research area is located in the NW part of Slovenia, bordering the Italy and covering the south-eastern flank of Alps, the area of Julian Alps (Figure 1).

To assess the tectonic and landslide mass movements in the research area, geological (Buser, 1987; Jurkovšek, 1987), structural data, digital elevation model (SMA, 2001), landslide occurrences (Komac et al., 2005), seismic (Placer, 1998; Poljak et al., 2000; Bajc et al., 2001; Gosar et al., 2001; Zupančič et al., 2001; Grenerczy et al., 2005; Weber et al., 2006; Živčič, 2006; Rižnar et al., 2007), rainfall (ARSO, 2006) and "geophysical" (Permanent Scatterer InSAR; T.R.E., 2006) data were used. Analyses were focused into assessment of applicability of PSInSAR technique for monitoring the uplifts or subsidence of

masses, either as a consequence of endogenic (tectonics) or exogenic (gravitation, climate...) forces.

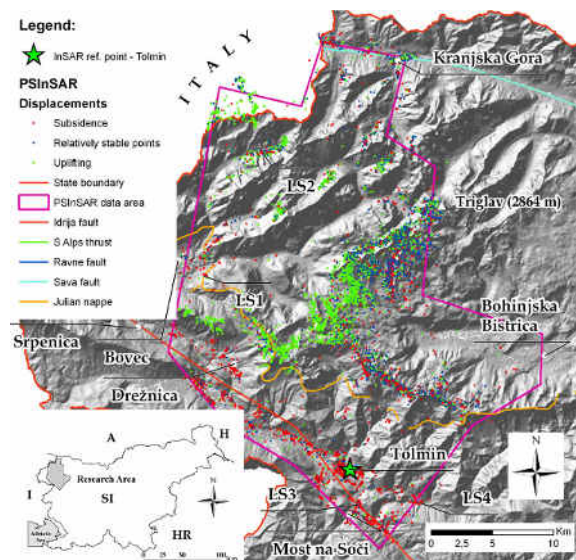


Fig. 1. The research area. The reference was set in the town of Tolmin represented in the Figure 1 with the star. Landslide sites are marked with LS 1 to LS 4.

### 3 SLOPE MASS MOVEMENTS

Slope mass movements in the research area, detected with the PSInSAR, are more related to tectonic activity than to other triggering factors (i.e. rainfall, human activity...). A general overlook of the research area indicates that majority of the "subsiding" PS indicate their connection to scree deposits and gravitational processes related to them. Analyses of average displacements have been conducted on several sites, Jablenca (6 PS), Koritnica (2 PS), Modrej (6 PS), and Ilovica (1 PS), marked as sites LS1, LS2, LS3, and LS4 respectively in Figure 1. From the movements of observed sites, trends of environs have been deduced to eliminate aseismic displacements in the surrounding areas. Displacement results have been compared to rainfall and seismic data to assess the causes of displacements. In case of Jablenca landslide it can be concluded that displacements are more governed by seismic activity than by rainfall, while for Koritnica and Ilovica sites the rainfall seems to be the main triggering factor, in case of later with a delay of one to two months, most probably due to its geological setting (shale with sandstone and limestone). In case of Modrej movements are most probably a combination of several factors, since neither seismic activity or rainfall are evidently related to displacements. Figure 2 represents the comparison of landslide displacements with monthly rainfall cumulative values.

### 4 CONCLUSIONS

The PSInSAR method shown as important tool for characterisation and detecting the landslides. The research was primarily focused on tectonic uplifting.



Fig. 2. Vertical displacements (mm) related to mass movements on four sites, Jablenca (LS 1), Koritnica (LS 2), Modrej (LS 3), and Ilovica (LS 4). Monthly rainfall cumulative values are represented with bars.

In case of uplifting the reasons are more or less clear, it is the consequence of active tectonics and those extreme ones are probably the result of locally limited conditions. On the contrary, the "subsidence" or moving downwards is more of a complex character. It is probably the combination of simultaneous influence of tectonics and gravitation. Most extreme movements are most probably indications of gravitational mass movements – landslides. To a certain degree mass displacements in form of landslides can be monitored, although same problems as with tectonic activity exist. The uplifting velocity values have to be interpreted very carefully, since the horizontal displacements can blur real vertical displacements noticeably.

Further investigations would have to be upgraded with ground measurements and with InSAR data from ascending orbits to cover the south-facing slopes where majority of landslides in the area occur. Also more precise geological assessment of individual PS would have to be conducted.

### REFERENCES:

- Bajc, A., Aoudia, A. Sarao, P. Suhadolc, 2001. "The 1998 Bovec-Krn mountain (Slovenia) earthquake sequence", *Geophys. Res. Lett.*, vol 28, p.p. 1839–1842.
- Buser, S., 1987. "Basic geological map of SFRY, sheet Tolmin and Udine, 1:100.000", Federal Geological Survey, Belgrade.
- Bürgmann, G. Hilley, A. Ferretti and F. Novali, 2006. "Resolving vertical tectonics in the San Francisco Bay Area from permanent scatterer InSAR and GPS analysis", *Geology*, Vol 34/3, p.p. 221-224.
- Colesanti, A. Ferretti, C. Prati and F. Rocca, 2003a. "Monitoring Landslides and Tectonic Motion with the Permanent Scatterers Technique", *Engineering Geology*, vol 68, p.p. 3-14.
- Carnec and C. Delacourt, 2000. "Three years of mining subsidence monitored by SAR interferometry, near Gradane, France", *Journal of Applied Geophysics*, vol 43, p.p. 43-54.



- Colesanti, A. Ferretti, F. Novali, C. Prati and F. Rocca, 2003b. "SAR Monitoring of Progressive and Seasonal Ground Deformation Using the Permanent Scatterers Technique", IEEE Transactions on Geoscientific Remote Sensing, vol 41, p.p. 1685-1700.
- Dixon, F. Amelung, A. Ferretti, F. Novali, F. Rocca, R. Dokka, G. Sella, S.W. Kim, S. Wdowinski and D. Whitman, 2006. "Subsidence and flooding in New Orleans", Nature, vol 441, p.p. 587-588.
- Ferretti, M. Bianchi, C. Prati and F. Rocca, "Higher-Order Permanent Scatterers Analysis", EURASIP Journal on Applied Signal Processing, vol 20, p.p. 3231-3242, 2005
- Ferretti, C. Prati and F. Rocca, 2001. "Permanent Scatterers in SAR Interferometry", IEEE Transactions On Geoscience And Remote Sensing, vol 39/1, p.p. 8-20.
- Ferretti and S. Crespia, 2006. "Advances in Differential SAR Interferometry: from DInSAR to PSInSARTM", CSTARS "Height" Workshop October, 24th 2006, Miami, Florida.
- Gosar, R. Stopar, M. Car and M. Mucciarelli, 2001. "The earthquake on 12 April, 1998 in Krn mountains (Slovenia): Ground motion amplification study using microtremors and modelling based on geophysical data", Journal Appl. Geophys., vol 47/2, p.p. 153-167.
- Grenerczy, G. Sella, S. Stein and A. Kenyeres, 2005. "Tectonic implications of the GPS velocity field in the northern Adriatic region", Geophys. Res. Lett., vol 32, article L16311, doi: 10.1029/2005GL022947.
- Jurkovšek, B., 1987. "Basic geological map of SFRY, sheet Beljak and Pontebba, 1:100.000", Federal Geological Survey, Belgrade.
- Komac, M., Bavec, M., 2007a. Detection of mass movements in Alpine Slovenia using PSInSAR data. 32nd International Symposium on Remote Sensing of Environment, San José, 25-29 June 2007. Sustainable development through global earth observations.
- Komac, M., Bavec, M., 2007b. PSInSAR data analysis - an insight into active tectonics and mass movements in west Slovenia. V: Mednarodna konferenca "Gospodarjenje z odpadki, okoljska geotehnologija in trajnostni razvoj": ICWMEGGSD'07 - GzO'07, Avgust 28.-30., 2007, Ljubljana, Slovenija. Ljubljana: Naravoslovnotehniška fakulteta, Oddelek za geotehnologijo in rudarstvo, 2007, 10 p.
- Komac, J. Šinigoj, M. Krivic, Š. Kumelj, K. Hribernik and A. Vehovec, 2005. "Pregled in analiza podatkov v obstoječih bazah plazov za novelacijo baze gis\_ujME", Geološki zavod Slovenije, 51 str., Ljubljana.
- Massonnet, D., M. Rossi, C. Carmona, F. Adragna, G. Peltzer, K. Feigl and T. Rabaute, 1993. "The displacement field of the Landers earthquake mapped by radar interferometry", Nature, vol 364.
- Massonnet, D., K.L. Feigl, M. Rossi and F. Adragna, 1994. "Radar interferometric mapping of deformation in the year after the Landers earthquake", Nature, vol 369.
- Massonnet, D., W. Thatcher and H. Vadon, 1996. "Detection of post-seismic fault zone collapse following the Landers earthquake", Nature, vol 382.
- Placer, L., 1998. "Contribution to the macrotectonic subdivision of the border region between southern Alps and External Dinarides", Geologija, vol 41, p.p. 223-255, 1998.
- Poljak, M., 2000. Structural-Tectonical Map of Slovenia 1 : 250.000, Geological Survey of Slovenia.
- Poljak, M. Živčič and P. Zupančič, 2000. "The seismotectonic characteristics of Slovenia", Pure Applied Geophysics, vol 157, p.p. 27-55.
- Rižnar, B. Koler and M. Bavec, 2007. "Recentna aktivnost regionalnih geoloških struktur v zahodni Sloveniji", Geologija, vol 50/1 (in press), Ljubljana.
- Vasco & Ferretti, 2005. "On the use of quasi-static deformation to understand reservoir fluid flow", Geophysics, vol 70/4, p.p. O13-O27.
- Zupančič, I. Ceci, A. Gosar, L. Placer, M. Poljak and M. Živčič, 2001. "The earthquake of 12 April 1998 in the Krn Mountains (Upper Soča valley, Slovenia) and its seismotectonic characteristics", Geologija, vol 44/1, p.p. 169-192.
- Weber, M. Vrabec, B. Stopar, P. Pavlovčič Prešeren and T. Dixon, 2006. "The PIVO-2003 experiment: a GPS study of Istria peninsula and Adria microplate motion, and active tectonics in Slovenia", In: Pinter, N., Grenerczy, G., Weber, J., Stein, S., Medak, D. (eds): The Adria microplate: GPS geodesy, tectonics and hazards. NATO Science Series, IV, Earth and Environmental Sciences, vol 61, p.p. 305-320, Springer.



## CASE STUDY 9:

**Title:** Landslide detection and mapping at the basin scale by means of PSI technique. The case study of the Arno River Basin, Italy.

**Application:** Landslide detection and mapping at regional scale.

**Technique:** PSI (Persistent Scatterers Interferometry).

**Main references:** This case study is based on the following publications: Lu et al., 2009; Farina et al., 2006; Canuti et al., 2008.

**Contributor:** UNIFI (Tofani V., Catani F., Casagli N.)

### ABSTRACT

SAR interferometry (InSAR) has already shown its significance for landslide mapping. However, temporal decorrelation and atmospheric disturbances limit the usefulness of traditional differential InSAR techniques. The recently developed Permanent Scatterers (PS) technique removes the temporal decorrelation and atmospheric artifacts by generating radar benchmarks derived from a multi-interferogram analysis of SAR images. PS are suitable for investigating slow moving landslides because they are able to detect ground displacements with the accuracy of millimeters.

The PS analysis was applied at a regional scale for the integration of the PS measurements within a landslide inventory for the presence of a high number of mass movements. About 350 ERS 1/ERS2 SAR images have been interferometrically processed by means of the PS technique, with the detection of about 600,000 PS.

However, because of the large number of PS that can be identified, the effective extraction of information useful for landslide studies from this PS technique sometimes remains difficult. With the aim of mapping landslides rapidly and (semi-) automatically, the hotspot analysis on the PS present within the Arno river basin (Italy) using spatial statistics approach has been performed. Four years (2003-2006) of RADARSAT SAR images within the basin have been processed so as to identify slow moving landslides.  $G_i^*$  statistics for the local test on PS datasets and the kernel function for PS density estimation based on the  $G_i^*$  values have been applied. The output is the hotspot map which emphasizes the existing mass movement. This methodology offers an innovative tool for extracting useful information from PS, thus providing an effective way of landslide rapid mapping.

### 1. INTRODUCTION

Remote sensing is useful for landslide studies. SAR interferometry (InSAR) is an important branch of remote sensing (Bamler & Hartl 1998) and is a valuable tool for landslide mapping and monitoring (Corsini et al. 2006). Combined with both amplitude and phase parameters, an interferogram can be generated with the radar images of the same area. After unwrapping interferogram fringes, it is capable to detect ground movement with millimetric accuracy (Massonnet & Feigl 1998). However, the usefulness of traditional differential InSAR (DInSAR) techniques is limited by factors such as temporal decorrelation and atmospheric disturbances (Fruneau et al. 1996, Massonnet & Feigl 1998, Kimura & Yamaguchi 2000, Ferretti et al. 2001).

The multi-image Persistent Scatterers SAR Interferometry (PSI) technique (Ferretti et al. 2001, Colesanti et al. 2003, Mora et al. 2003, Werner et al. 2003, Duro et al. 2005), has showed its capability to provide information about ground deformations over wide area with millimetric precision, making this technique suitable for both regional and slope scale mass movements investigations. In particular the Permanent Scatterers (PS) technique patented by the Politecnico di Milano and is commercially available

through the POLIMI spin-off company Tele-Rilevamento Europa (TRE). PS technique produces radar benchmarks derived from a multi-interferogram analysis of SAR images. The temporal decorrelation and atmospheric artifacts can be meanwhile estimated and removed (Ferretti et al. 2001). Some successful cases have shown the suitability of PS for investigating slow moving landslide (Colesanti et al. 2003, Casagli et al. 2005, Farina et al. 2006).

In this contribution examples of the application of the PS technique to landslide mapping at regional scale are described. The study area is the Arno river basin located in the Northern Apennines, Italy.

In particular the updating of the landslide inventory map carried by means of the ERS and ENVISAT PS processed from 11 years (1992-2001) is described. The methodology adopted relies on the possibility of assigning a spatial meaning to the point-wise ground displacement measurements provided by the PS technique, through the interpretation aerial-photos and optical satellite imagery, topographic maps and ancillary data.

Besides with the intention of developing an effective and semi-automatic procedure for landslide mapping from PS, a spatial statistical approach on the PS analysis in the same area is described. The aim is to

employ PS processed from 4 years (2003-2006) of RADARSAT SAR images to identify slow moving landslides within the basin. We consider this spatial statistics approach as an effective way for landslide mapping, thus providing an innovative approach for the rapid extraction of useful information from PS.

## 2. STUDY AREA

The Arno river basin is located in the central Italy (Figure 1). The total area of the whole basin is about 9130 km<sup>2</sup>. The basin is across of Apennines chain. As a result, 7190 km<sup>2</sup> of the basin is situated in the mountainous and hilly area. The basin is very susceptible to landslides. More than 27,000 landslides were mapped. The affected landslide area is more than 800 km<sup>2</sup>. These landslides are dominated by earth slides and flows (about 74%) as well as shallow landslides and creeps (Catani et al. 2005a, Farina et al. 2006). Most of these slide movements are slow and intermittent, accompanied with accelerations due to the prolonged and intensive rainfall. The concentration of precipitation periods also accounts for the landslides activity transition from dormant to active (Catani et al. 2005b). Considering the high density population within the basin, the prevalence of landslides in the Arno river basin poses an high risk. More than 16,000 civil buildings, 460 industrial areas and 350 km roads are affected by landslides. In addition, ca. 6 billions Euro losses are expected in the upcoming 30 years (Catani et al. 2005b).

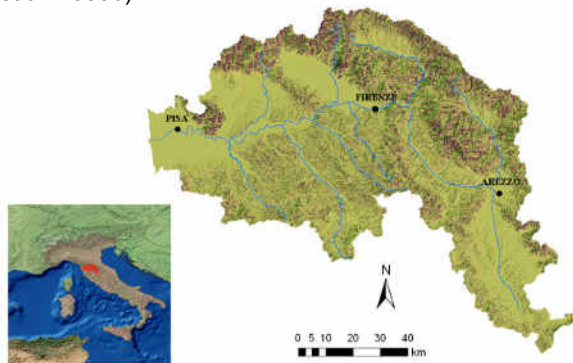


Fig. 1. The location of the Arno river basin.

## 3. UPDATING OF LANDSLIDE INVENTORY MAP

### 3.1 Methodology

Landslide inventories report the spatial distribution of existing slope movements, frequently including details about the landslides typologies and their state of activity (Wieczorek, 1984). Today the most common methodology for their compilation is based on aerial-photo interpretation, on field surveys and on the collection of local databases (Crozier, 1984, Soeters and Van Westen 1996). The Arno River Basin Authority produced an inventory map of active, dormant and

inactive landslides at a reference mapping scale of 1:10,000, dating back to 2003. The map follows the landslide classification and the terminology proposed by Cruden and Varnes (1996), with a few slight changes due to the scope and to the extent of the analyzed basin. Within the Arno river basin more than 27,000 landslides have been mapped. Based on this inventory map, PS have been used for discovering previously undetected landslides and to redefine the perimeter and state of activity of the existing ones.

By interferometrically processing more than 350 ERS-1 and ERS-2 SAR images spanning 10 years (1992-2002), approximately 600,000 PS have been detected within the whole basin. 44.8% of the derived PS are located in the hilly and mountain areas with a density of 37 PS/km<sup>2</sup>.

By combining PS information with optical images such as SPOT5, color aerial photos, and a 10-meter resolution digital elevation model (DEM) we performed a geomorphologic analysis for landslide detection. Attention was focused on the spatial distribution and the state of activity (active, dormant or inactive, according to Cruden and Varnes (1996)) of both already mapped landslides and new unstable areas (Fig. 1). In particular the main benefits obtained from the application of the PS technique to landslides regard:

- Better defined boundaries of already detected mass movements and/or;
- Better defined states of activity and/or;
- The detection of previously unmapped unstable areas.

The first effort was devoted to the detection of the presence of PS within or close to mapped mass movements. Once that the PS information have confirmed the boundaries and state of activities of the mapped landslides a new field with the average velocities, computed on the two different time intervals (1992–2002 and 1999–2002), has been added in the attributes table. In case of differences in the spatial distribution, e.g. PS in movement close to the landslide boundaries, or in the state of activity, e.g. PS stable within an active landslide, the support of multi-temporal aerial-photos or SPOT5 image was employed. The interpretation of these data was aimed at detecting morphological or vegetation features indicative of a variation of the landslide boundaries or a change of its state of activity (Figure 2).

Furthermore, a strong effort was spent on the interpretation of moving PS located far from any mapped landslide. To limit possible misinterpretations, attention was focused only on groups of PS characterized by displacement rates (over 3–4 mm/year) that are significant with respect to the technique precision. Sparse radar benchmarks showing lower rates were neglected.

The support of photo-interpretation and contour lines analysis for detecting diagnostic morphologies induced by slope instabilities was fundamental at this phase, as were field surveys for particularly problematic areas.

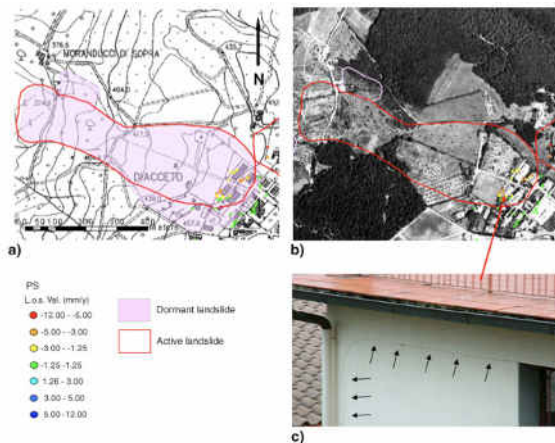


Fig. 2. Example of landslide inventory map modification with the PS-based methodology: (a) the pink polygon represents the originally mapped landslide while the red outline indicates the updated boundary from the PS method; (b) the aerial-photo (1996) of the mapped landslide; (c) cracks on a building located within the unstable area, where the PS record velocities up to 5 mm/year.

Table 1. Statistical data about the results of PS-methodology applied on the Arno basin landslide inventory map (AdBA is the acronym of Autorità di Bacino del F. Arno).

Number of landslides mapped by AdBA	27,270
Number of landslides mapped by AdBA with PS information	1664
% for number of landslides mapped by AdBA with PS information	6.1%
Area of AdBA landslides (km <sup>2</sup> )	802.9
Area of landslides mapped by AdBA with PS information (km <sup>2</sup> )	151.3
% of area of landslides mapped by AdBA with PS information	18.9%
Landslides density (km <sup>2</sup> /km <sup>2</sup> as a percentage of whole river basin)	8.8%

### 3.2 Results

In order to highlight the percentage of information coming from the proposed methodology and to also evaluate its effectiveness, a simple statistical analysis of the final landslide inventory map was performed (Table 1).

223 new landslides have been mapped while 1660 existing landslides have been modified regarding the state of activity or the boundary throughout the whole basin for the new landslide inventory. The newly mapped landslides through PS information represent 6.8% of the total landslides in the final inventory.

## 4. HOT SPOT ANALYSIS

### 4.1 Methodology

The effective extraction of useful information from PS technique for landslide studies is sometimes difficult due to the large number of PS that can be present, thereby entailing long interpretation times. In the places where there are a lot of stable reflectors such as buildings and bared rocks, the PS density is higher than 500 PS/km<sup>2</sup>. Large number of PS calls for an efficient approach of data processing. Still, with the quick development of new SAR sensors and efforts of increasing PS density, the PS data is expected to be updated more frequently with higher density. Thus, an effective approach of data interpretation is needed.

With the intention of developing an effective procedure for landslide mapping from PS, a spatial statistical approach on the PS analysis is introduced. The aim is to employ PS processed from 4 years (2003-2006) of RADARSAT SAR images to identify slow moving landslides within the basin. We consider this spatial statistics approach as an effective way for landslide mapping, thus providing an innovative approach for the rapid extraction of useful information from PS.

The purpose of the hotspot analysis is to identify concentrations of high velocity PS. The analysis is based on the two statistics approaches: Getis-Ord Gi\* statistics and kernel density estimation.

The Getis-Ord Gi\* statistics is a kind of local spatial statistics which represents the association up to a specified distance. In the study we apply Gi\* statistics to evaluate the spatial clustering of neighboring PS. The Gi\* index is defined as follows (Getis & Ord 1996):

$$G_i^*(d) = \frac{\sum_j w_{ij}(d)x_j - W_i^* \bar{x}}{s^* \left\{ \left[ (nS_{1j}^*) - W_i^{*2} \right] / (n-1) \right\}^{0.5}}$$

While in the Equation 1,

$$W_i^* = \sum_j w_{ij}(d) + w_{ij}, S_{1j}^* = \sum_j w_{ij}^2 \text{ and}$$

$$s^{*2} = \frac{\sum_j x_j^2}{n} - \bar{x}^2$$

wij(d) is the spatial weights vector. It is defined within the searching distance d from the PS whose velocity is x. Each single PS is at a site i with its neighbours j within the distance d. In the study, all the PS are treated as the same weight, namely 1.

In order to define the searching distance of d, for each pixel (10m) of the DTM of the Arno river basin, both the shortest path to a channel (d1) and the ridge (d2) are calculated based on steepest descent direction.



The searching distance of each pixel ( $d_i$ ) is calculated as the mean value of  $d_1$  and  $d_2$ , simulated as a measure of landslide length along the slope. The estimation of the searching distance  $d$  is based on the mean value of all DTM pixels. In the case of the Arno River basin, the searching distance  $d$  is 114m compared with a DTM of 10m resolution.

We apply the  $G_i^*$  statistics in our study and perform the local test on PS datasets. We choose the velocity of PS as the weighting factor and calculate  $G_i^*$  index for each single PS. The  $G_i^*$  index measures concentrations of high velocity PS for the entire study area. The larger (positive) the  $G_i^*$  index is, the more intense the clustering of high velocity values, with the PS moving direction towards Line-of-Sight (LOS) of the satellite. The smaller (negative) the value is, the more intense the clustering of low velocity values (negative), with the PS moving direction away from LOS.

The following procedure is to estimate PS density using kernel calculation. The kernel density estimation (Silverman 1986) uses a kernel estimator which is defined as:

$$f(x) = \frac{1}{nh} \sum_{i=1}^n K\left(\frac{x - X_i}{h}\right)$$

where  $h$  is the window width,  $x - X_i$  is the distance to each PS  $i$ .  $K$  is the quadratic kernel function defined as:

$$K(x) = \frac{3}{4}(1 - x^2), |x| \leq 1$$

$$K(x) = 0, x > 1$$

We employ this kernel function for PS density estimation, choosing the previous derived  $G_i^*$  index as the weight. The output is a smooth density map adding the values of kernel function. It indicates the existing hotspot of high velocity mass movement.

## 4.2 Results

Figure 3 shows one part of the hotspot map derived from the same SAR image frame. The area is within the Arno river basin covering the Pistoia-Prato-Firenze and the Mugello basin. Both the ascending (Fig 3a) and descending (Fig 3b) hotspot map are displayed based the result of kernel density estimation. Clustering of positive velocity PS (moving towards LOS) is rendered with blue hotspot while clustering of negative velocity PS (moving away from LOS) is rendered with red color. The deeper color it displays, the more intense clustering of higher velocity PS. The radius of the hotspot implies the dimension of the potential landslide-affected area. Figure 4 is the hotspot map with the overlay of both ascending and descending hotspot map. The magenta areas are the combination of red and blue hotspots. They indicate the different moving directions of PS from different ascending and descending orbits. Still, the deep blue and deep red hotspot indicate the same moving directions detected from the ascending and descending PS.

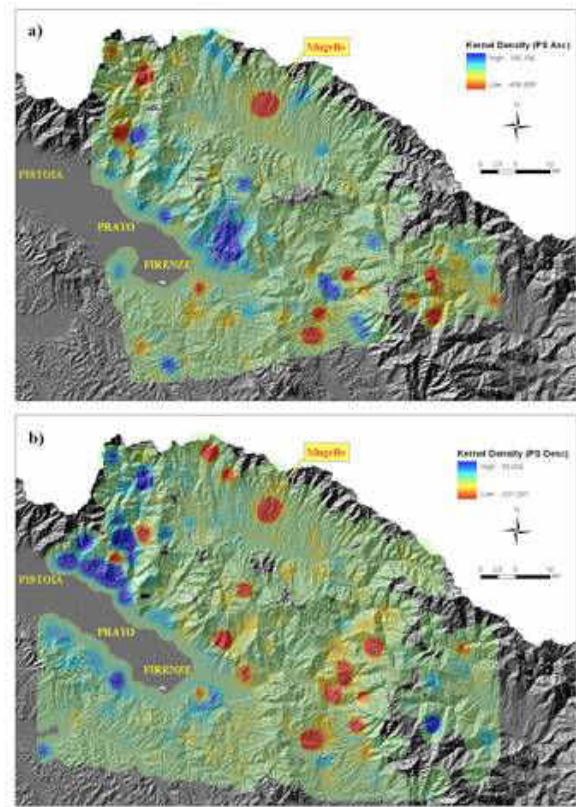


Fig. 1. Part of the hotspot map of the Arno river basin, including the Pistoia-Prato-Firenze and Mugello basin area: a) hotspot map derived from kernel density estimation using ascending RADARSAT PS; b) hotspot map derived from kernel density estimation using descending RADARSAT PS. Red Hotspot (low negative kernel density) indicates the clustering of high velocity PS moving away from satellite along LOS whereas blue hotspot (high positive kernel density) implies the clustering of high velocity PS moving towards satellite along LOS.

The clustering of high velocity PS is able to detect landslide considering LOS of satellite and down-slope landslide movement can especially be detected from PS moving away from sensor. According to the previous studies and existing landslide inventory map, some of the detected hotspots are confirmed to be the mass movements resulting from slow moving landslides. Hence, the hotspot map is expected to be an important source for the following study of landslide inventory updating. However, detection errors exist when such mass movement is related to other geophysical processes that PS can identify. The major errors are attributed to uplift and ground subsidence. Moreover, the hotspot sometimes shows the limitations in separating landslide movement from other geo-processes. For example, if an area is subject to both landslide and subsidence, the hotspot analysis possibly only yields the result of one big hotspot. This hotspot however fails to separate these two kinds of mass movement. Such problems are mainly resulted from the current limitations of PS technology for detailed interpretation of mass movement.



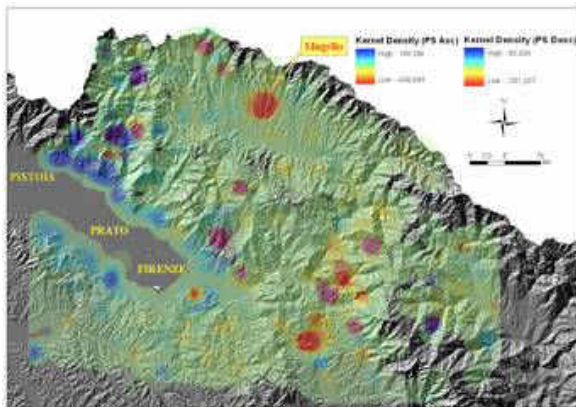


Fig. 4. The hotspot map overlaid with ascending and descending data. The magenta hotspot indicates the clustering of high velocity PS detected by both ascending and descending PS, with one moving direction away from LOS and another moving towards LOS. The deep red and blue hotspots imply the clustering of high velocity PS detected by both ascending and descending data, with the same moving direction along LOS.

## 5. DISCUSSION AND CONCLUSION

In this contribution the usefulness of the PS technique for landslide detection and mapping at regional scale is discussed.

The application of this method at the regional scale, as a support for the production of a landslide inventory map, was performed on the Arno river basin, in Central Italy.

The main benefit of the methodology regards the capability to perform ground displacement measurements over urbanized areas where risk conditions are usually higher. The positive feedback implies that within the next years, due to the imminent launch of the space-borne SAR missions with a acquisition parameters better tuned for landslides investigations, the methodology has the potential to become a fully operational tool for landslide mapping.

On the other hand the effective extraction of useful information from PS technique for landslide studies is sometimes difficult due to the large number of PS that can be present. Large number of PS calls for an efficient approach of data processing.

At this regard the hotspot analysis employs the spatial statistics analysis of PS in order to emphasize the landslide-affected area. The output map is the hotspot visualization emphasizing the clustering of high velocity PS. The approach is considered to be an example of effectively extracting useful information from large number of PS. The derived hotspot is considered to be useful for the further landslide inventory mapping and risk management.

## REFERENCES

Bamler, R. & Hartl, P. 1998. Synthetic aperture radar interferometry. *Inverse Problems* 14: 1-54.

- Canuti P., Casagli N., Catani F., Falorni G., Farina P. 2007. Integration of Remote Sensing Techniques in different stages of landslide response. In *Progress in Landslide Sciences* Eds. Kyoji Sassa, Hiroshi Fukuoka, Fawu Wang, Gonghui Wang
- Casagli, N., Guerri, L., Righini, G., Ferretti, A., Colombo, D. & Prati, C. 2005. Integrated use of PS and very high resolution optical images for supporting landslide risk management. *URSI, Symposium on Microwave Remote Sensing of the Earth, Oceans, Ice and Atmosphere*, 20-21 April 2005, Ispra, Italy.
- Catani, F., Farina, P., Moretti, S., Giovanni, N. & Strozzi, T. 2005a. On the application of SAR interferometry to geo-morphological studies: estimation of landform attributes and mass movements. *Geomorphology* 66: 119-131.
- Catani, F., Casagli, N., Ermini, L., Righini, G. & Menduci, G. 2005b. Landslide hazard and risk mapping at catchment scale in the Arno River basin. *Landslides* 2: 329-342.
- Colesanti, C., Ferretti, A., Prati, C. & Rocca, F. 2003. Monitoring landslides and tectonic motions with the Permanent Scatterers Technique. *Engineering Geology* 68: 3-14.
- Corsini, A., Farina, P., Antonello, G., Barbieri, M., Casagli, N., Coren, F., Guerri, L., Ronchetti, F., Sterzai, P. & Tarchi, D. 2006. Space-borne and ground-based SAR interferometry as tools for landslide hazard management in civil protection. *International Journal of Remote Sensing* 27: 2351-2369.
- Crozier, M.J., 1984. Field assessment of slope instability. In: Brundsen, D., Prior, D. (Eds.), *Slope Instability*. John Wiley and Sons, Chichester, pp. 103-140.
- Cruden, D. M. & Varnes, D. J. 1996. Landslides types and processes. In: *Landslides Investigation and Mitigation: Transportation Research Board*, A.K. Turner and R.L. Schuster (eds.), US National Research Council, Special Report 247, Washington DC, p. 36-75.
- Farina, P., Colombo, D., Fumagalli, A., Marks, F. & Moretti, S. 2006. Permanent Scatterers for landslide investigations: outcomes from the ESA-SLAM project. *Engineering Geology* 88: 200-217.
- Ferretti, A., Prati, C. & Rocca, F. 2000. Non-linear subsidence rate estimation using Permanent Scatterers in Differential SAR interferometry. *IEEE Transactions on Geoscience and Remote Sensing* 38: 2202-2212.
- Ferretti, A., Prati, C. & Rocca, F. 2001. Permanent Scatterers in SAR interferometry. *IEEE Transactions on Geoscience and Remote Sensing* 39: 8-20.
- Fruneau, B., Achache, J. & Delacourt, C. 1996. Observation and modeling of the Saint-Etienne-de-Tinée landslide using SAR interferometry. *Tectonophysics* 265(3): 181-190.
- Getis, A. & Ord J.K. 1996. Local spatial statistics: an over-view. In John Wiley and Sons (eds), *Spatial Analysis: Modeling in a GIS Environment* : 261.

- Kimura, H. & Yamaguchi, Y. 2000. Detection of landslide areas using satellite radar interferometry: Photogrammetric Engineering and Remote Sensing 66(3): 337-344.
- Lu P., Casagli N., Catani F., Tofani V. (2009) Hotspot analysis of Permanent Scatterers (PS) for slow moving landslides detection. In: Landslide Processes: From Geomorphological Mapping To dynamic Modelling. Proceedings of the Landslide Processes Conference, A tribute to Dr. Theo van Asch, Strasbourg, 6-7 February 2009.
- Mora, O., Mallorquí, JJ, Broquetas, A. (2003). Linear and nonlinear terrain deformation maps from a reduced set of interferometric SAR images. IEEE Transactions on Geoscience and Remote Sensing, 41(10), 2243-2253.
- Massonnet, D. & Feigl, K. L. 1998. Radar interferometry and its application to changes in the earth's surface. Reviews of Geophysics 36(4): 441-500.
- Soeters, R. & Van Westen C. J. 1996. Slope instability recognition, analysis and zonation. Turner AK, Schuster RL (eds) Landslides: investigation and mitigation. Sp. Rep.247, Transportation Research Board, National research Council, National Academy Press, Washington, DC, pp129-177.
- Werner, C.L., Wegmuller, U., Wiesmann, A., Strozzi, T., (2003). Interferometric Point Target Analysis for Deformation Mapping. IGARSS Proceedings 2003, Toulouse.
- Wieczorek, G (1983). Preparing a detailed landslide-inventory map for hazard evaluation and reduction. Bulletin of the Association of Engineering Geologists, 21(3), 337 – 342.

## CASE STUDY 10:

**Title:** Integration of PS-InSAR data and ground-based instrument measurements for landslide monitoring at the local scale.

**Application:** Landslide characterization and monitoring at local scale.

**Technique:** PSI (Persistent Scatterers Interferometry).

**Main references:** This case study is based on the following publications: Casagli et al., 2009; Farina et al., 2006.

**Contributor:** UNIFI (Tofani V., Catani F., Casagli N.)

### ABSTRACT

Interferometric SAR, whether satellite- or ground-based (InSAR and DInSAR) are the techniques most researched during the last decade for slope motion monitoring and characterization. In particular the multimage Persistent Scatterers SAR Interferometry (PSI) technique (Ferretti et al. 2001, Colesanti et al. 2003, Mora et al. 2003, Werner et al. 2003, Duro et al. 2005), has showed its capability to provide information about ground deformations over wide area with millimetric precision, making this technique suitable for both regional and slope scale mass movements investigations. The PSI analysis has been applied for the monitoring of single well-known slope movement, the Carbonile landslide, located in the Arno river basin, Northern Apennines. In this case study the use of InSAR for the monitoring of single slow landslides threatening built-up areas has provided satisfactory results, allowing the measurement of superficial deformations with high accuracy on the landslide sectors characterized by a good radar reflectivity and coherence. Besides the PS-InSAR™ technique has been integrated with classic ground-based monitoring techniques in order to facilitate the interpretation of landslide behaviour and kinematics.

### 1. INTRODUCTION

Monitoring means the comparison of landslide conditions like areal extent, speed of movement, surface topography and soil humidity from different periods in order to assess landslide activity (Mantovani et al., 1996).

The measurement of superficial displacements induced by a slope movement often represents the most effective method for defining its behavior, allowing the observation of response to triggering factors and the assessment of effectiveness of corrective measures (Farina et al., 2006).

Different techniques are available for measurements of the ground displacements, starting from the traditional inclinometers, extensometers, topographic surveys, until more recent applications such as GPS, aerial photogrammetry, LIDAR measurements (Angeli et al., 2000; Gili et al., 2000; Kaab, 2000; Hervas et al., 2003; McKean and Roering, 2004).

Interferometric SAR, whether satellite or ground-based (InSAR and DInSAR) are the techniques most researched during the last decade for slope motion monitoring (Metternicht et al., 2005).

In particular the multi-image Persistent Scatterers SAR Interferometry (PSI) technique (Ferretti et al. 2001, Colesanti et al. 2003, Mora et al. 2003, Werner et al. 2003), has showed its capability to provide information about ground deformations over wide area with millimetric precision, making this technique suitable for both regional and slope scale mass movements investigations. In particular the

Permanent Scatterers (PS-InSAR™) technique patented by the Politecnico di Milano and is commercially available through the POLIMI spin-off company Tele-Rilevamento Europa (TRE). PS technique produces radar benchmarks derived from a multi-interferogram analysis of SAR images. The temporal decorrelation and atmospheric artifacts can be meanwhile estimated and removed (Ferretti et al. 2001).

The InSAR technique, by providing an accurate measurement of ground displacements without the necessity of positioning any targets on the ground and without any physical contact with the slope, is best suited for assessing the temporal evolution of slow landslides (up to a few centimeters per year). Unfortunately, incidence angle, spatial resolution, wavelength, and revisiting time interval of the operational sensors are not optimal compared to the particular spatial and temporal pattern of all the types of movement we are dealing with.

In this contribution an example of monitoring of the Carbonile slow moving landslide by means of PS technique is reported. This example provides the combined use of underground and superficial data for a better understanding of the landslide geometry and its deformation pattern.

### 2. CARBONILE LANDSLIDE

Carbonile, a small village located in Northern Apennines, Tuscany and it has been affected by

different slope instability problems since 1984. This site has been selected as case study in the project ESA-SLAM (Farina et al., 2006). These movements have seriously endangered the village and its 200 residents. Damage to cultivated areas, buildings and infrastructures have been recorded since 1984. For these reasons the whole zone was mapped as exposed to the highest landslide hazard level within the Hydrogeological Setting Plan of the River Basin Authority.

The landslides correspond to complex movements dominated by earth-slides with translational and rotational components occurring on multiple shear surfaces and with non-uniform distribution of velocities. The inclinometric readings show displacement rates ranging from slow to very slow (IUGS/WGL, 1995).

The advanced PS processing performed on the ERS1-ERS2 descending dataset has allowed the detection of 310 radar benchmarks within the study site (2.7 km<sup>2</sup>) resulting in a PS spatial density of 114 PS/ km<sup>2</sup> (Figure 1).

The PS velocities indicate that the central part of the ancient landslide is stable, while three zones, two on the sides of Carbonile and one in the upper part of the slope, are characterized by significant movements, with deformation rates up to 12 mm/year.

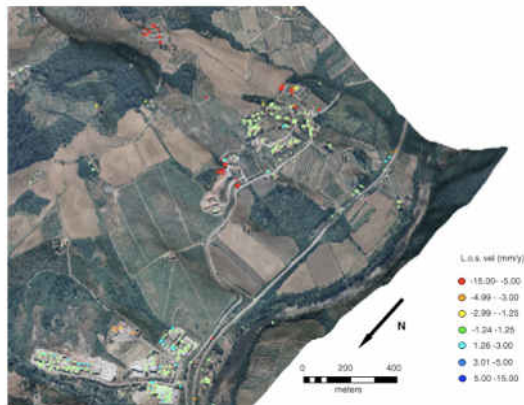


Fig.1. Aerial-photo of the Carbonile landslide with the location of the Permanent Scatterers. The colors of the PS are related to the average annual velocity along the satellite line of sight, estimated between 1992 and 2002.

In order to assist the geological interpretation of the main landslides present in the Carbonile area, an integration of PS data with inclinometric readings and borehole samplings was attempted. The analysis was performed along different profiles. The main rupture surfaces, placed at depths ranging from 3 to 13 m, were interpreted from the inclinometric readings, while boreholes provided the stratigraphic information.

Profile BB (Figure 2) represents an example of the combined use of underground and superficial data for a better understanding of the slope instability geometry. Down-slope movements with velocities of up to 15 mm/ year were recorded by the inclinometers between 1987 and 1992 (tubes 4 and 22) along a main

failure surface. The PS located in the lower part of the slope also indicate ground displacements compatible with the movement measured by the inclinometer, in terms of both line of sight velocity (about 7–10 mm/year) and direction of movement. The PS have negative velocities, meaning that they are moving away from the satellite sensor, which is compatible with the SW down-slope direction of movement recorded by the inclinometric tubes.

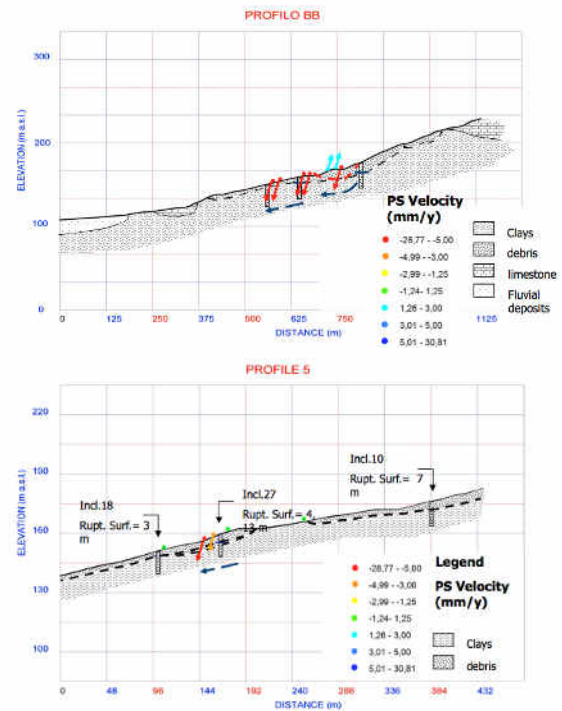


Fig.2. Cross-sections of the Carbonile area showing both subsurface information from inclinometric readings and borehole samplings and superficial movement from the PS analysis. Dashed lines indicate the main sliding surfaces, as inferred from the inclinometric measurements. Continuous arrows represent the PS displacement vectors as measured along the satellite line of sight (L.O.S.). Arrow's length is proportional to the average PS velocity (computed over the period 1992–2002) and the vector versus indicates the velocity sign. The upper image shows profile B–B and while the bottom profile 5–5.

A quantitative comparison of PS and inclinometric measurements was performed using inclinometric tube 27 (by considering the average deformations along the tube), located along profile 5 (Figure 2), and the three closest PS. For the comparison all the data were projected along the E–W movement direction recorded by the inclinometer, with a 10° gradient equal to local slope of the terrain. Even though the overlap in the time interval covered by the two datasets was not complete (the PS analysis ranges from 1992 up to 2002, while inclinometric readings were acquired from 1990 to 1996), the radar measurements are of the same order of magnitude as the inclinometric readings. The projected average velocity (obtained

from the linear fitting of the displacement measurements) recorded by the inclinometric tube between 1992 and 1996 is 3.4 mm/year, while velocities measured by the PS range from 7.0 to 13.7 mm/year, with an average value of 9.5 mm/year. The difference between the two sets of measurements was ascribed to the different types of movement measured by the two techniques (superficial vs. deep deformations) and to the low sensitivity of PS measurements to horizontal movements.

### 3. CONCLUSION

The Carbonile case study illustrates how it is possible to use Permanent Scatterers for the monitoring of single landslides inducing high risk scenarios.

The advanced processing of ERS1-ERS2 descending dataset spanning a time interval from 1992 to 2002 has allowed an accurate analysis of temporal and spatial displacement fields as well as the identification of the most hazardous areas.

In order to assist the geological interpretation of the landslide both concerning the landslide geometry and deformation pattern, a comparison of the PS measurements and inclinometers measurements was carried out. The quantitative comparison has demonstrated that the measurements acquired by the two instrumentations are of the same order of magnitude thus proving that SAR interferometry is a powerful tool for landslide monitoring.

### REFERENCES

- Angeli M., Pasuto A., Silvano S. (2000), A critical review of landslide monitoring experiences. *Engineering Geology* 55, 133-147.
- Casagli N., Tofani V., Adler R. (2009), A look from space. In *Landslides, Disaster Risk Reduction*, Sassa K. and Canuti P. eds.
- Colesanti, C., Ferretti, A., Prati, C. & Rocca, F. (2003). Monitoring landslides and tectonic motions with the Permanent Scatterers Technique. *Engineering Geology* 68: 3-14.
- Farina, P., Colombo, D., Fumagalli, A., Marks, F. & Moretti, S. (2006). Permanent Scatterers for landslide investigations: outcomes from the ESA-SLAM project. *Engineering Geology* 88: 200-217.
- Ferretti, A., Prati, C. & Rocca, F. (2001). Permanent Scatterers in SAR interferometry. *IEEE Transactions on Geoscience and Remote Sensing* 39: 8-20.
- Gili J.A., Corominas J., Rius J. (2000) Using Global Positioning System techniques in landslide monitoring. *Engineering Geology* 55, 95-113.
- Hervas J., Barredo J., Rosin P., Pasuto A., Mantovani F., Silvano S. (2003). Monitoring landslides from optical remotely sensed imagery: The case story of Tessina landslide, Italy. *Geomorphology*, 54, 63 – 75.

- Kaas A. (2002). Monitoring high-mountain terrain deformation from repeated air and spaceborne optical data: examples using digital aerial imagery and ASTER data ISPRS, *Journal of Photogrammetry and Remote Sensing*, 57(1-2), 39-52
- Mantovani F., Soeters R., Van Westen C. J. (1996) Remote sensing techniques for landslide studies and hazard zonation in Europe, *Geomorphology*, 15( 3-4): 213-225.
- McKean J., Roering J. (2004). Objective landslide detection and surface morphology mapping using high-resolution airborne laser altimetry. *Geomorphology*, 57, 331 – 351.
- Metternicht, G., Hurni L., Gogu R. (2005) Remote sensing of landslides: An analysis of the potential contribution to geo-spatial systems for hazard assessment in mountainous environments. *Remote Sensing of Environment*, Vol. 98, n°2-3, pp. 284-303.





## CASE STUDY 11:

**Title:** A new approach to the use of DInSAR data in landslide studies at different scales: the case study of National Basin Authority of Liri-Garigliano and Volturno rivers.

**Application:** Slow-moving landslide detection; Mapping; Characterization; Monitoring.

**Technique:** DInSAR.

**Main references:** This case study is based on the following publications: Cascini et al., 2010; Cascini et al., 2009; Cascini et al., 2008.

**Contributors:** UNISA (Cascini L., Peduto D., Fornaro G.)

### ABSTRACT

Within the general framework of the landslide risk analysis, in the last decades significant efforts have been made by the scientific community towards the development of topics dealing with the hazard analysis (including the landslide characterization and the analysis of frequency) and the consequence analysis.

With reference to slow-moving landslide characterization, the contribution deriving from remote sensing techniques can be helpful in detecting large areas and in analyzing both the state of activity and the kinematical characteristics of the instability phenomena. In particular, the use of remote sensing techniques such as Differential SAR Interferometry (DInSAR) has been already dealt with in the scientific literature via a number of case studies. However, standardized procedures for the proper interpretation and the confident use of DInSAR data have not been fully investigated and validated, although algorithms for image processing have become more and more sophisticated. Moreover, the diffusion of these data when they are not validated can dangerously bring to misleading interpretations and unjustified warnings.

Starting from current limits of the applicability to landslide, this contribution shows the potential of innovative procedures based on the joint use of DInSAR data, at both full- and low- resolution, with the help of considerations on the acquisition geometry of sensors, simplified landslide kinematical models and landslide-induced damage to structures/infrastructures.

### 1. INTRODUCTION

This study has been carried out jointly by the group of Geotechnical Engineering of Salerno University (Italy) and IREA-CNR (Italy) as a development of the expertise achieved in the exploitation of DInSAR data for the analysis of subsidence phenomena at different scales (Cascini et al., 2006; 2007). The passage from subsidence to landslides is not straightforward due to the complexity of instability phenomena and current limitations in both the sensor acquisition geometry and the availability/interpretation of DInSAR data on slopes (Cascini et al., 2010). To this end, the present analysis introduces a new methodology for DInSAR data interpretation in areas for which a proper geomorphological and topographic knowledge is available.

The first step is the generation of the a priori DInSAR landslide visibility map (described in details in Cascini et al., 2009). Then, DInSAR data interpretation is based on the joint use of remote sensed data and simplified geomorphological models. The reported procedure is tested at both medium (i.e. 1:25,000 scale according to Fell et al., 2008) and large scales (i.e. 1:5,000 scale, Fell et al., 2008) within a sample area extending for around 500 km<sup>2</sup> in the territory of National Basin Authority of Liri-Garigliano and Volturno (NBA-LGV) rivers (Central-Southern Italy) (Fig.1).

### 2. THE TEST AREA AND THE USED DATASET

Thirty-three images (track 308 - frame 2765), acquired over descending orbits of the ERS1-ERS2 satellite systems (period March 1995 - February 2000), have been processed via the Enhanced Spatial Differences (ESD) approach (Fornaro et al., 2009a,b), which represents an upgrading of the original SBAS algorithm (Berardino et al., 2002). These algorithms allow the generation of both low-resolution DInSAR maps (with pixel on the ground of approximately 80 x 80 m) and full-resolution maps (with pixel on the ground of approximately 10 x 10 m).

For the test area both base and thematic maps are available at 1:25,000 scale. The base maps were produced in 2001 as results of the activities of the PSAI project (Piano Stralcio per l'Assetto Idrogeologico), carried out by a group of experts and technicians working for NBA-LGV in accordance with the Act of Italian Parliament (L. 365/2000), aimed to zone both landslide hazard and risk all over the Italian territory (Cascini, 2008). The geological map highlights that the bedrock mainly consists of Upper Miocene arenaceous units mantled by Quaternary Age superficial deposits, characterized by talus and alluvial fans. Landslide phenomena cover around 5% of the whole territory as it can be noticed in the available

landslide inventory map, derived from aerial photographs and surface surveys. This map furnishes detailed information for each mapped phenomena with reference to location, typology, state of activity and areal extension (Cascini et al., 2005).

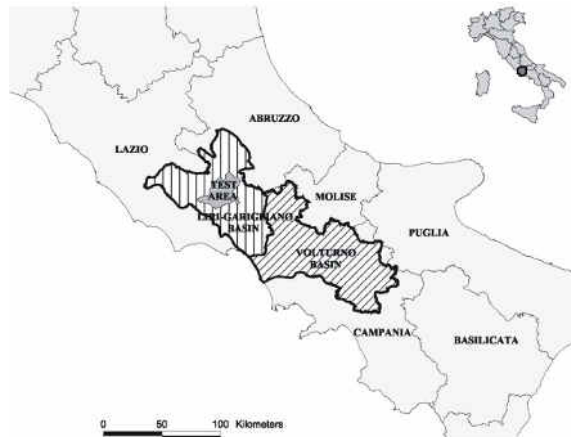


Fig. 1. The test area.

Owing to the phase ambiguity limitation of DInSAR data processing (for more details refer to Cascini et al., 2010), the analysis of landslides focuses on the typology of phenomena ranging from extremely to very slow velocity classes (i.e. lower than 1,6m/year according to Cruden and Varnes, 1996). In the study area a total number of 897 slow-moving landslides are mapped (Peduto, 2008; Cascini et al., 2009); according to Varnes (1978) they are classified as: 204 rotational slides, 238 earth flows, 78 rotational slides-earth flows, 336 creeps, 33 earth flows - creeps, 8 deep-seated gravitational movements. On the basis of geomorphological criteria, three different states of activity are distinguished for these landslides, defined as follows: "active" (including active, reactivated and suspended), "dormant" and "inactive" (relict) phenomena (Cruden and Varnes, 1996). The selected landslide typologies exhibit a significant predominance of dormant phenomena (428) on active ones (92). This is confirmed by the available dataset on damage to buildings and roads interacting with the displaced masses that includes: 557 phenomena (around 62% of the total) interacting with properties; 183 damage surveys and only 40 damaged facilities inventoried in the study area (Cascini et al., 2008), corresponding to 30% of surveyed buildings and 24% of investigated roads.

### 3. THE PROCEDURE PROPOSED FOR DINSAR APPLICABILITY TO LANDSLIDES

The framework sketched in Fig. 2 describes the procedure developed for DInSAR data analysis at different scales. The first step consists of the generation of the a priori DInSAR landslide visibility map (Peduto, 2008; Cascini et al., 2009), which can be

used to distinguish in advance whether an area is expected to be visible from space-borne SAR sensors thus driving data-users through the image dataset selection. Once SAR images have been processed, if an adequate knowledge of landslide phenomena is available, a procedure for 1D-LOS DInSAR data projection can be implemented to generate the advanced DInSAR landslide velocity map.

As for the scale of the study, low-resolution DInSAR data can be used for landslide analyses at 1:25,000 scale, according to the dimension of both the landslide phenomena and the coherent DInSAR pixels on the ground; whereas full-resolution DInSAR data allow studies at more detailed scale (i.e. 1:5,000) according to the almost point-wise information and the dimension of single portions of landslides and structures/infrastructures.

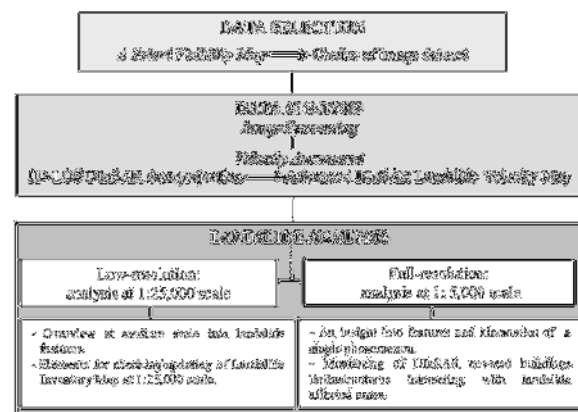


Fig. 2. The framework of DInSAR data analyses for landslide studies (Cascini et al., 2010).

#### 3.1 A priori visibility map

The choice of the most suitable SAR image dataset represents a key step for DInSAR data exploitation in landslide studies, since the visibility of a certain portion of a slope depends on several factors such as slope aspect and inclination, vegetation cover, presence of buildings/infrastructures.

The role played by the aspect angle and the slope inclination, which have direct impact on the feasibility of DInSAR deformation monitoring, has been already discussed in Colesanti & Wasowski (2006); Peduto (2008); Cascini et al. (2009).

Following the procedure described in details in Peduto (2008) and Cascini et al. (2009) here an example of the a-priori DInSAR landslide visibility map over a portion of the study area, obtained via low-resolution ESD DInSAR data, is presented at 1:25,000 scale (Fig.3). The input data consist of the following available maps: landslide inventory map; aspect map; slope angle map; land-use map; urbanised area map. Particularly, by intersecting the aspect map and the slope angle map *visible/ visible with difficulty/ not visible areas* are zoned.

By merging the land-use map and the urbanised area map, vegetated areas are removed from those portions classified as visible according to geometric considerations, thus obtaining the so called "a priori DInSAR landslide visibility map". The validation of the map for the whole test area (partially shown in Fig. 3) proves that 67% out of a total of 215 low-resolution DInSAR coherent pixels intersecting landslide affected areas concentrate on *visible areas*; 19% lay on areas visible with difficulty; only 14% can be found in areas assumed as *not visible*. The described procedure can be easily applied at 1:5,000 scale if base and derived maps are available at this scale.

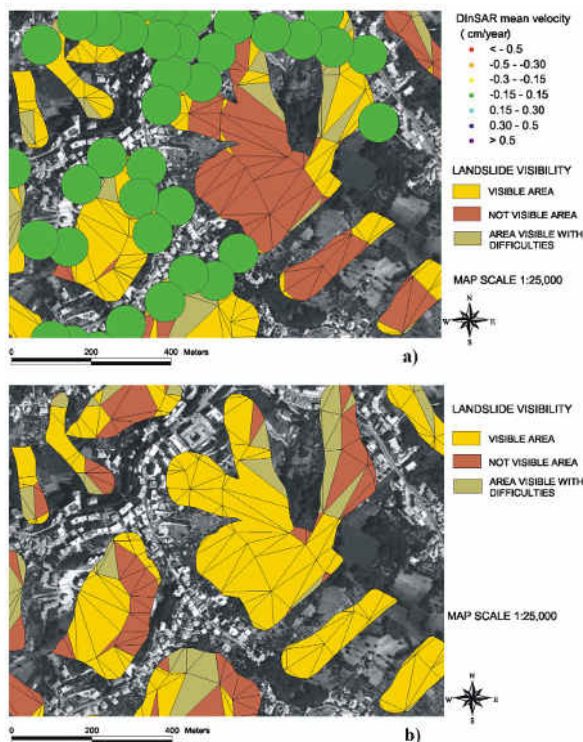


Fig. 3. The "a priori DInSAR landslide visibility map": (a) on descending orbits with low-resolution DInSAR coherent pixel distribution; (b) on ascending orbits (Cascini et al., 2009).

### 3.2 1D LOS DInSAR data projection and the generation of the advanced DInSAR landslide velocity map

The procedure for the projection of 1D LOS DInSAR velocity vectors, based on both geomorphological and DEM models, is described in Peduto 2008 and Cascini et al., 2010. The flow-chart for the generation of the advanced DInSAR landslide velocity map is shown in Fig. 4.

On this map DInSAR coherent pixels are represented depending on several factors to be taken into account. Particularly, conditions of movement/no-movement depend on whether the mean velocity of the DInSAR coherent pixel exceeds the fixed velocity threshold (Cascini et al., 2010). Moreover, the direction of movement is assumed consistent with the

geomorphological scheme of the landslide (see Cascini et al., 2010) on which each DInSAR coherent pixel is located. Finally, the projected velocity value is assumed as a reliable value if the condition number (see the Appendix in Cascini et al., 2010) does not exceed the fixed threshold.

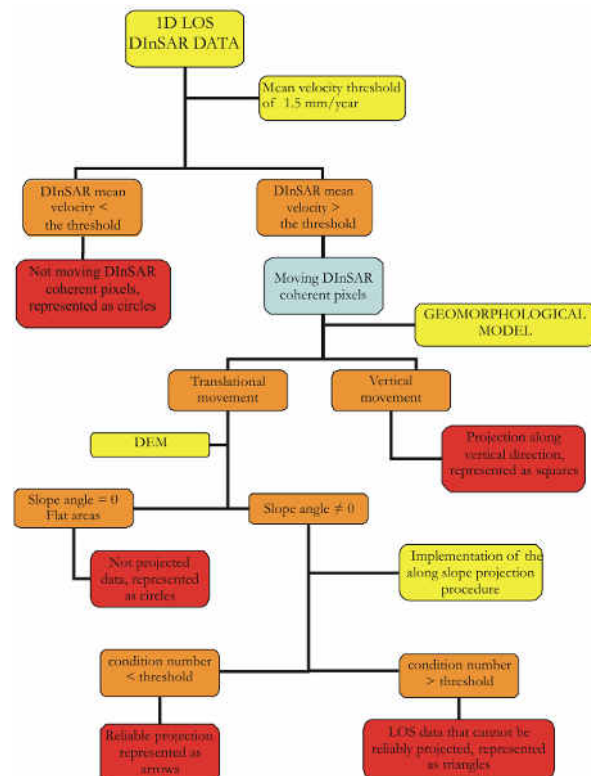


Fig. 4. Flow-chart for the generation of the advanced DInSAR landslide velocity map (Cascini et al., 2010).

## 4. LOW-RESOLUTION LANDSLIDE ANALYSIS

The advanced low-resolution DInSAR landslide velocity map was developed at 1:25,000 scale for all the test area in ADB-LGV according to the schemes in Fig. 4 so as to analyse rotational slides, earth flows and rotational slides-earth flows, whose total amount is 553; 185 (around 33%) of those resulted covered by DInSAR data. Moreover, the map highlighted that almost 84% of the DInSAR covered dormant landslides (144) exhibit evidence of no-movement. On the other hand, the percentage of active landslides (25) with moving coherent DInSAR pixels is about 24%, on the average (Cascini et al., 2008). An example is reported with reference to the municipalities of Frosinone and Torrice (Lazio Region) in Fig. 5 where very few moving low-resolution DInSAR pixel are detected over an area of about 3 km x 6 km where dormant phenomena prevail.

Within this area, the directions of movement (see the four red arrows), derived by modelling the available 1D LOS DInSAR data, seem congruent with the



assumption of the geomorphological schemes (downward direction along slope).

Moreover, over the test area the highest projected mean velocities are attained in the main body, independently of the landslide typology (Fig. 6).

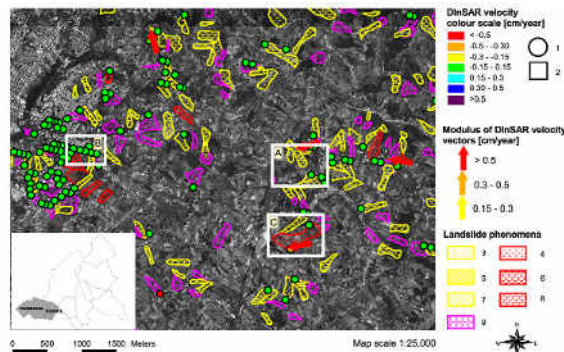


Fig. 5. An example of advanced low-resolution DInSAR landslide velocity map for the municipality of Frosinone and Torrice (Lazio Region, Italy). 1) Not moving DInSAR coherent pixel or on flat areas; 2) DInSAR coherent pixel moving on vertical direction; 3) dormant rotational slide; 4) active rotational slide; 5) dormant earth flow; 6) active earth flow; 7) dormant rotational slide – earth flow; 8) active rotational slide – earth flow; 9) creep phenomenon (Cascini et al., 2010).

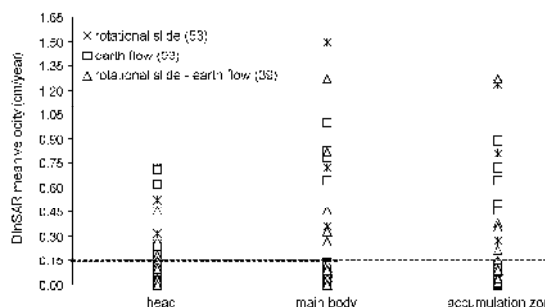


Fig. 6. DInSAR mean velocities recorded within covered landslides: 53 rotational slides; 93 earth flows; 39 rotational slides – earth flows (Cascini et al., 2010).

The advanced low-resolution map were then used to detect new landslide phenomena within the test area in ADB-LGV by extending the analysis of moving/not moving coherent pixels on those portions of the territory mapped as hollows in the geomorphological map at 1:25,000 scale (Cascini et al., 2009). These zones (1263 in the investigated area) are characterized by geomorphological settings quite similar to landslide-affected areas, also exhibiting the same landslide predisposing factors. Indeed, as for 63 hollows a clear evidence of movement was recorded; this can provide elements for a check/update of the landslide inventory map that represents the starting point for the landslide risk analysis as described in Fell et al.(2008).

## 5. FULL-RESOLUTION LANDSLIDE ANALYSIS

Analyses of landslide phenomena at more detailed scale (i.e. 1:5,000) can exploit full-resolution DInSAR data following the flow-chart in Fig. 4. However, since these analyses call for significant computational efforts they should be concentrated on limited areas. Taking this in mind two main goals were pursued: the preliminary analysis of landslide features (i.e. check of mapped boundaries; detection of ground displacement out of mapped areas); an insight into different kinematic behaviour characterizing different portions of the same phenomenon.

### 5.1 Analysis of landslide features

In order to check possible changes in landslide boundaries, the entire full-resolution coherent pixel dataset was projected assuming translational movements along the steepest slope direction for the pixels out of the mapped landslides. Several examples are reported in Cascini et al. (2010); here, a portion of the municipality of Frosinone (Fig. 7) highlighting evidences of movements both inside and outside the landslide boundaries is shown. Particularly, special attention is worth being paid to full-resolution DInSAR coherent pixels exhibiting mean velocity values exceeding 0.3 cm/year within two dormant earth flows (labelled with letters A and D) and creep zones (labelled with letters B and C) as well as the areas framed with the circle and the square, respectively. As for the zone framed with the circle, a cross check via the geomorphological map shows that the buildings in the area were built on an hollow on which the DInSAR data show evidences of movement for the period 1995-2000. The area framed by a rectangle highlights the presence of moving full-resolution DInSAR coherent pixels in proximity of a landslide classified as active earth flow in the landslide inventory map at 1:25,000 scale.

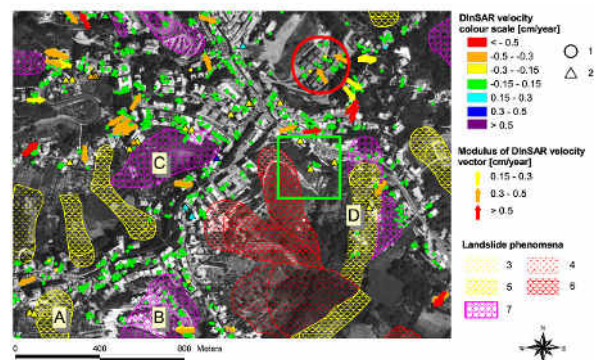


Fig. 7. Overview of Advanced full-resolution DInSAR landslide velocity map for a portion of the municipality of Frosinone (Lazio Region, Italy). 1) Not moving DInSAR coherent pixel or on flat areas; 2) not projected translational displacement owing to high condition number; 3) dormant rotational slide; 4) active rotational slide; 5) dormant earth flow; 6) active earth flow; 7) creep phenomenon (Cascini et al., 2010).

In this case further analyses carried out via a map at 1:5,000 scale of the landslide affected areas (see Cascini et al., 2010) allowed to point out that the moving coherent pixel falls within a small active rotational slide – earth flow; on the contrary, the stable coherent pixels are located within the head of the dormant rotational slide – earth flow. This highlights that full-resolution DInSAR data reliability must be necessarily checked via thematic and topographic maps at 1:5,000 scale.

## 5.2 The case study of La Consolazione landslide

“La Consolazione” landslide is a rotational slide – earth flow, located within Torrice municipality, which twice reactivated in the last decades (1986; 1990). The landslide (around 12 ha) exhibits the typical shape of rotational slide – earth flow with a width ranging from 100-150m (in the head where the rotational mechanism develops) up to 250m (in the accumulation zone where the enlarging earth flow prevails). Furthermore, in the upper accumulation zone (between the elevations of 200 and 220 m. a.s.l.)

evidence of creep phenomena (e.g. ripples on the ground surface) can be distinguished.

The available documents report that in 1986 only the narrow upper portion (Fig. 8a) reactivated; then, in the 90s subsequent reactivations involved the portion of the landslide that stretches from the creeping zone down to the toe.

The above information allows the identification of three main portions: the old main scarp and the old terraced accumulation zone with evidence of cracks; the recent minor scarp (215 m a.s.l.) bordering the reactivated earth flow; the old accumulation zone.

Referring to the state of activity, the upper portion of the landslide, as well as the old accumulation zone appears as dormant; whereas the remaining portion corresponds to the reactivated earth flow.

Fig. 8a shows the advanced full-resolution DInSAR velocity map superimposed to both the building map and the landslide map at 1:5,000 scale. Full-resolution DInSAR data concentrate on 4 buildings within the landslide affected area.

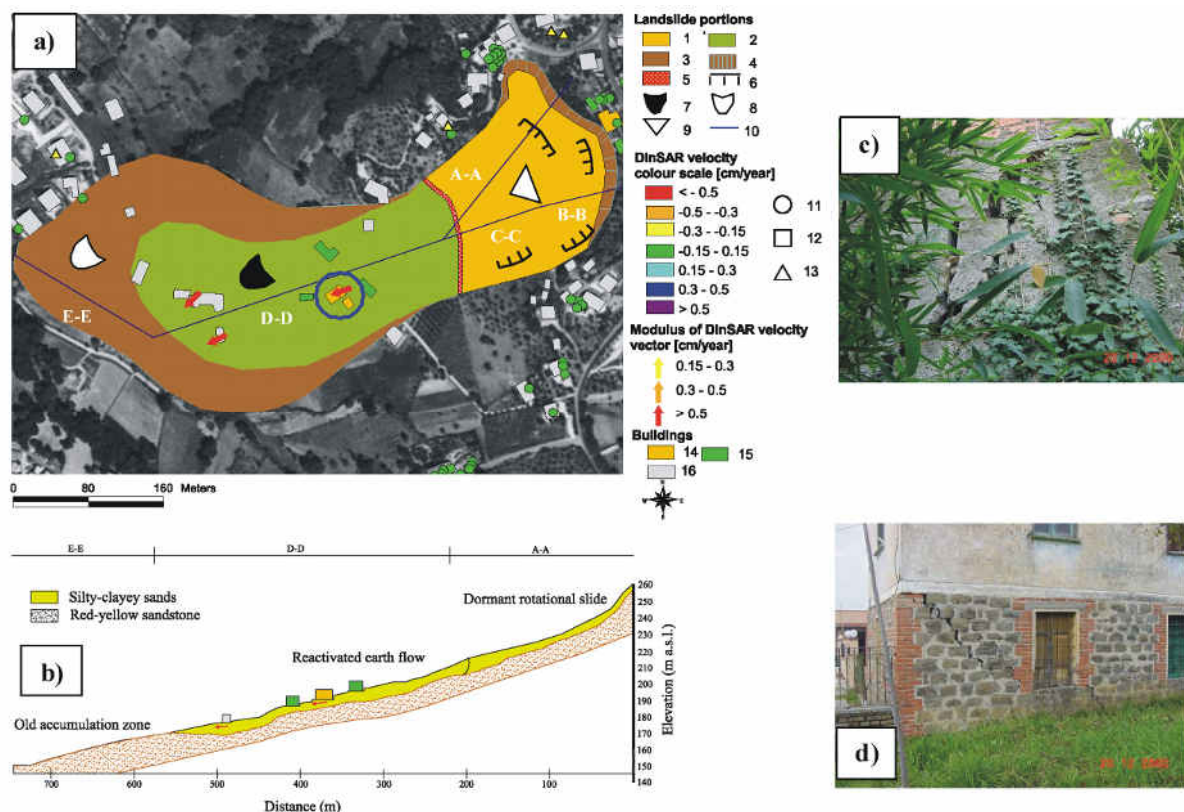


Fig. 8. La Consolazione landslide: a) Map of the landslide with buildings and Advanced full-resolution DInSAR velocity data; b) Longitudinal cross section of the landslide with buildings and DInSAR velocity vectors; c) and d) photo of two damaged buildings framed in the circle and corresponding to the orange one in the section: 1)terraced old accumulation zone; 2)reactivated old accumulation zone; 3) old accumulation zone; 4) old scarp; 5) recent scarp; 6)cracks; 7)reactivated earth flow; 8) dormant earth flow; 9) dormant rotational slide; 10) cross-section; 11) not moving DInSAR coherent pixel or moving coherent pixel on flat areas; 12) DInSAR coherent pixel moving on vertical direction; 13) not projected translational displacement owing to high condition number; 14) damaged building; 15) building without damage survey; 16)building without damage survey (Cascini et al., 2010).

The analysis of mean velocity values for 1995-2000 period highlights that the full-resolution coherent pixels located near of the old scarp exhibit no evidence of movement, whereas those located within the reactivated portion are moving with mean velocity values higher than 0.5 cm/year (Fig. 8a and b). As for the landslide mechanism, Fig. 11b shows the longitudinal cross section of the instability phenomenon and the DInSAR velocity vectors. Finally, referring to the buildings in the area, it can be noticed that: i) the evidence of movement recorded to two buildings, framed with the circle in Fig. 9a and located in the central portion of the reactivated landslide, matches the damage occurrence as observed by the damage survey (Figs. 9 c and d); ii) the unchecked buildings located in the lower portion of the landslide exhibiting evidence of movement need a damage survey in order to assess their structural integrity.

## 6. CONCLUSIONS

In the last decade the use of remote sensing data derived from DInSAR techniques has rapidly grown thanks to the development of enhanced image processing algorithms and their increased availability that, as in the case of the Italian territory, can reach the total coverage. Consequently, there is the need of a confident use of these data so as to overcome some problems that still arise in the analysis of slow-moving landslides. In this regard, this research introduces an innovative procedure that allows a significant improvement of the common 1D LOS velocity maps at both low- and full-resolution.

The results obtained seem particularly appealing considering the enhanced capabilities of the newest sensor (e.g. TerraSAR X, COSMO/SKYMED, etc) which will offer high resolution DEMs also allowing improved spatial resolution, three times higher data acquisition frequency and an increase in the sensitivity to temporal decorrelation via the reduction of the wavelength.

## REFERENCES

- Berardino P., Fornaro G., Lanari R. and Sansosti E. (2002). A New Algorithm for Surface Deformation Monitoring based on Small Baseline Differential SAR Interferograms. *IEEE Trans. Geosci. and Remote Sens.*, 40 (11), 2375-2383.
- Cascini L., Bonnard Ch., Corominas J., Jibson R., Montero-Olarte J. (2005). Landslide hazard and risk zoning for urban planning and development. State of the Art Report (SOA7). Proceedings of the International Conference on "Landslide Risk Management", Vancouver (Canada). O. Hungr, R. Fell, R. Couture and E. Eberhardt (eds.). Taylor and Francis, London, 199-235.
- Cascini L., Fornaro G., Peduto D. (2010). Advanced low- and full-resolution DInSAR map generation for slow-moving landslide analysis at different scales. In press on *Engineering Geology*, doi:10.1016/j.enggeo.2010.01.003. now available online at: <http://dx.doi.org/10.1016/j.enggeo.2010.01.003>
- Cascini L., Fornaro G., Peduto D. (2009). Analysis at medium scale of low-resolution DInSAR data in slow-moving landslide-affected areas. *ISPRS Journal of Photogrammetry and Remote Sensing*, 64(6),598-611. doi:10.1016/j.isprsjprs.2009.05.003
- Cascini L., Ferlisi S., Peduto D., Pisciotta G., Di Nocera S., Fornaro G. (2008) – Multitemporal DInSAR data and damages to facilities as indicators for the activity of slow-moving landslides. In: *Landslides and Engineered Slopes. From the Past to the Future*. Chen Z., Zhang J., Li Z., Wu F., Ho K. (eds.). Proceeding of the 10th International Symposium on Landslides and Engineered Slopes, 30 June-4July 2008, Xi'an (China), Taylor and Francis Group, London. Vol. II, pp. 1103-1109. ISBN 978-0-415-41196-7.
- Cascini L., Ferlisi S., Peduto D., Fornaro G., Manunta M. (2007) Analysis of a subsidence phenomenon via DInSAR data and geotechnical criteria. *Italian Geotechnical Journal*, 4, 50-67.
- Cascini L., Ferlisi S., Fornaro G., Lanari R., Peduto D., Zeni G. (2006).Subsidence monitoring in Sarno urban area via multitemporal DInSAR technique. *International Journal of Remote Sensing* Vol.27, No. 8, 20 April 2006, 1709-1716. Taylor and Francis. ISSN 0143-1161, DOI: 10.1080/01431160500296024.
- Fell R., Corominas J., Bonnard C., Cascini L., Leroi E., Savage W.Z. (2008). Guidelines for landslide susceptibility, hazard and risk zoning for land-use planning. *Engineering Geology*, 102 (3-4), pp. 99-111.
- Fornaro G., Pauciuolo A., Serafino F. (2009a) Deformation monitoring over large areas with multipass differential SAR interferometry: A new approach based on the use of spatial differences, *International Journal of Remote Sensing*, 30 (6), 1455 - 1478.
- Fornaro G., Reale D., Serafino F. (2009b). Four-Dimensional SAR Imaging for Height Estimation and Monitoring of Single and Double Scatterers", *IEEE Trans. Geosci. Remote Sens.*, 47 (1), 224-237.
- Peduto D. (2008). Analysis of ground deformations related to subsidence and landslide phenomena via DInSAR techniques. Ph.D.Thesis (In English). University of Salerno, Italy, May 2008. Tutor: Cascini L.; co-tutor: Fornaro G..



## CASE STUDY 12:

**Title:** Microseismic monitoring at the unstable rock slope at Åknes, Norway.

**Application:** Rock slope monitoring.

**Technique:** Microseismic monitoring.

**Main references:** mainly based on Roth et al., 2006 and Roth and Blikra, 2009.

**Contributors:** NORSAR (Roth, M.).

### ABSTRACT

The unstable rock slope at Åknes has an estimated volume of about 70 million m<sup>3</sup>, and parts of the slope are moving at a rate between 2-15 cm/year. Amongst many other direct monitoring systems we have installed a small-scale seismic network in order to monitor microseismic events related to the movement of the slope. The network has been operational since November 2005 with only a few short-term outages. Seismic data are transferred in real-time from the site to NORSAR for automatic detection processing. The resulting detection lists and charts and the associated waveform are forwarded immediately to the early warning centre of the Municipality of Stranda.

Seismic monitoring provides independent and complementary data to the more direct monitoring systems at Åknes. We observe increased seismic activity in periods of heavy rain fall or snow melt, when laser ranging data and extensometer readings indicate temporary acceleration phases of the slope. The seismic network is too small and the velocity structure is too heterogeneous in order to obtain reliable locations of the microseismic events. End of 2009 we installed a high-sensitive broadband seismometer (60 s - 100 Hz) in the middle of the unstable slope. This will allow us to better constrain the locations of the microseismic events and to monitor local/regional and global seismicity.

### 1. INTRODUCTION

Microseismic monitoring is a well-established technique for risk evaluation and production optimization in mines. During production the stress field in the subsurface changes and sudden stress releases in form of microearthquakes occur. Similar we expect to observe microseismic events at a moving rock slope. There might be microseismic events associated directly with the movement in form of stick-slip movements on a sliding plane or shear-failures of intact rock during the formation of a sliding plane. Furthermore, we expect secondary microseismic events in form of individual rock-falls and small-scale slides induced by the movement of the slope.

Microseismic monitoring is an indirect tool in that one measures effects of the movement and not directly the movement itself as done for instance by extensometers etc. However, in contrary to point measurements, a seismic monitoring system can provide an overview over the seismic activity in the entire volume of interest. Depending on the instrument sensitivity, the installation, the site and the ambient noise conditions even the tiniest signals can be detected (on a rocky subsurface for instance a hammer blow can be easily detected in 100 m distance).

Changes of the seismic activity can be indicative for changes of the slope dynamic or the slope movement rate. The seismic systems at Åknes are considered as an important part of the overall monitoring system providing independent and complementary input to the National centre for rock slide monitoring at Stranda.

### 2. AKNES ROCKSLOPE

The Åknes rock slope is located in the county of Møre og Romsdal, Norway approximately halfway between Bergen and Trondheim (Figure 1). Already in 1985 geological mapping revealed the instability of the site and continuous extensometer measurements showed an opening of fractures in the upper part of the slope with a rate of several centimeters per year. The volume of the instability was estimated to be about 6 million m<sup>3</sup> at that time.

Later investigations based on additional field studies, high-resolution aerial photography and detailed mapping concluded that the volume is much larger, i.e. 40 – 70 million m<sup>3</sup>, and that a sudden failure of the slope could generate a local tsunami in the Storfjord system.

The upper part of the instability is clearly defined by distinct back-scarps and fractures some of them several meters wide and 20 - 30 m deep. The lower limit of the unstable slope is more difficult to identify, because it is covered with boulders and dense vegetation. However, several springs can be found at about 150 m above sea level, which may represent the outlets of water running along detachment faults. The area of the unstable part is about one km<sup>2</sup> (Figure 2). Core drillings in summer 2005 revealed fault gauges in a depth of 30 to 40 m in the centre of the slope and in the upper part of the site fault gauges could be found even down to 100 m depth.



Fig. 1. Location of the Åknes rock slope.



Fig.2. Outline of the unstable area (picture taken from the opposite shore of the fjord).

### 3. INSTRUMENTATION

There are several real-time monitoring systems (e.g. optical total station, GPS, laser ranging system, extensometers, crackmeters, tiltmeters, borehole DMS), installed at Åknes. In addition to those instruments we installed a small-scale geophone network in 2005 and a broadband seismic station in 2009.

The seismic network consists of 8 three-component geophones (4.5 Hz) covering an area of about 250 x 150 m in the upper part of the slope (Figure 3). The geophones are connected by armored cables with the central acquisition system (Figure 4) in Bunker I. The acquisition system customized by NORSAR engineers includes a 24-channel digitizer (Geode, Geometrics), a GPS clock, an industry computer with low power

consumption and a GSM telephone relay. It is powered by a set of batteries which in turn is charged by a diesel generator. Data are transmitted via radio link and internet to NORSAR for automatic processing. During the first 9 months of operation data were recorded in continuous mode and in August 2006 the system was switched to triggered-mode recording with higher sampling rate (1000 Hz).

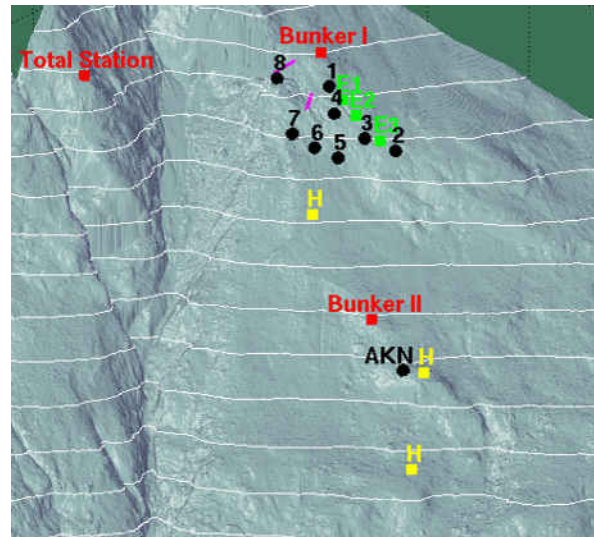


Fig.3. Digital elevation map with the positions of the geophone network and the seismic station AKN (black), helicopter pads (yellow), three extensometers (green), two laser ranges (magenta) and the bunkers with power supply and radio communication (red).



Fig. 4. Up: Data acquisition system of geophone network installed in the upper bunker. Down: Installation of a 3-component geophone.

The broadband station AKN (international registry of seismograph stations) has been installed on an outcrop in the middle of the unstable area (Figure 5). The station is connected to Bunker II and provides continuous real-time data to the early warning centre in Stranda (<http://www.aknes.no/>) and to NORSAR. The sensor is a Guralp ESPC with a frequency band from 1/60 to 100 Hz in order to monitor the local microseismic activity as well as the global/regional seismicity. The broadband seismometer has a sensitivity which is about 65 times higher than that of the installed geophones and the sensor will be able to record the same microseismic events as seen by the geophone network. Both systems are synchronized by GPS clocks and therefore we expect to obtain better constraints for the locations of the observed microseismic events.



Fig.5. Up: Installation of the broadband seismic station AKN. Down: Seismometer pit with sensor, power/communication module and data acquisition module.

#### 4. PERFORMANCE AND DATA PROCESSING

The robustness of the system is a very important issue, because the Åknes site is remote and can only be accessed by helicopter. The seismic network has been operational without major outages since 2005 (Figure 6) and it is performing very stable. So far only two complete outages happened: one due to a failure of the central power supply, the other due to a failed software update. Partial outages have been caused by cable damages from rock falls and water leakage into the geophones.

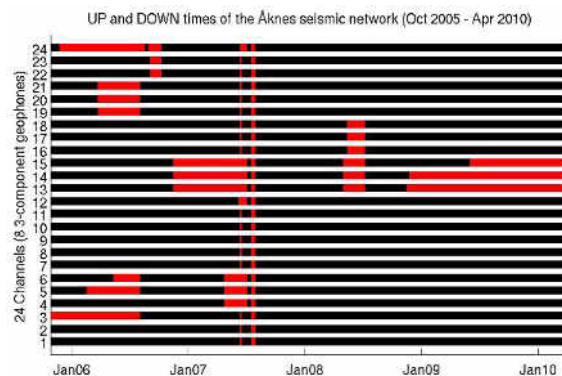


Fig. 6. Up (black) and Down (red) times of the 24 channels of the geophone network for the time period Oct 2005 - Apr 2010.

The state-of-health of the geophone network is being checked continuously and seismic data are transferred automatically from Åknes to NORSAR using ftp. In triggered-mode the average daily data volume is about 250 MByte. The data are submitted to an automatic event detection (Signal-to-noise ratio > 2 on at least 10 channels within a common time window of 1 s). The results are displayed in near real-time (~10-15 min delay) on <http://www.norsar.no/pc-47-48-Latest-Data.aspx>. In addition we automatically generate plots of the event waveforms and make them available to the Åknes/Tafjord data base.

The broadband station AKN has been online without any data outage so far. The waveform data are publicly available from NORSAR or from ORFEUS (<http://www.orfeus-eu.org/>) and waveform plots can be accessed at <http://www.norsardata.no/NDC/heliplots/>. A real-time data stream is forwarded to the early warning centre in Stranda, Møre og Romsdal.

#### 5. OBSERVATIONS

Figure 7 displays an example for a microseismic event (left) and a rock fall (right) recorded with the geophone network. The plots show the 24 channels of the 8 three-component geophones for a time window of 17 seconds. The microseismic event has a duration of about 1-3 seconds and it is relatively strong with a high signal-to-noise ratio on all channels. The rock fall has a total duration of more than 10 seconds with multiple signal arrivals.

Figure 8 shows the signal amplitudes of reviewed events for the time period from January 2006 until March 2009. The data base has been inspected visually and all obvious non-local events, man-made events and other noise events have been removed. The signal amplitudes vary over a range of about 3 magnitudes with most of the events having amplitudes less than 1 mm/s.



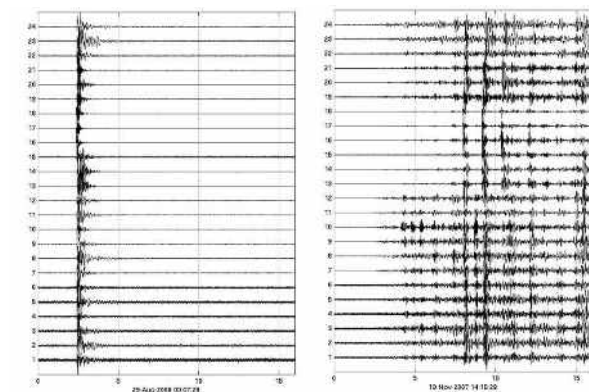


Fig. 7. Left: Microseismic event, Right: rockfall.

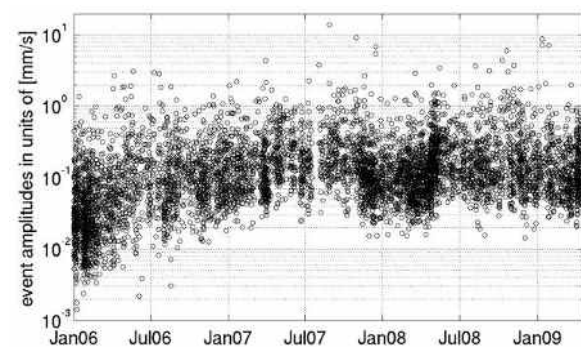


Fig. 8. Signal amplitudes of reviewed events.

Another way to illustrate the seismic activity is to plot the cumulative signal amplitudes (Figure 9). A constant slope of this curve is indicative for a constant rate of seismic activity. Kinks and steps in this curve are changes of the slope are the result of temporal clusters of small events and/or the occurrence of larger individual events. The change of seismic activity might be indicative for acceleration phase of the Åknes slope. We observe changes in seismicity mainly during autumn (2007, 2008), when heavy rainfalls occurred and during spring (2007, 2008, 2009) seasons, when air temperature stays above 0 degrees (Figure 10) and snow melt starts.

During this periods we also have indications for slope acceleration from the extensometer (Figure 11) and laser measurements (Figure 12).

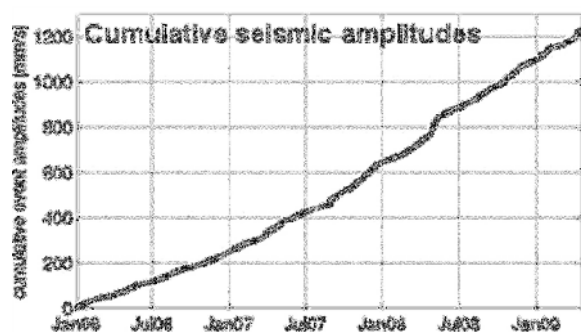


Fig. 9. Cumulative signal amplitudes.

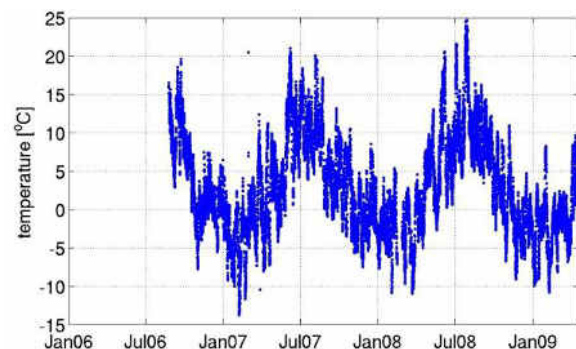


Fig. 10. Air temperature measurements.

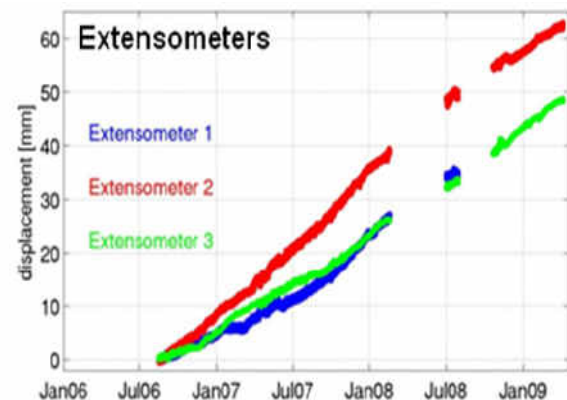


Fig. 11. Extensometer measurements. Acceleration phases in autumn 2007 at extensometer 2 and 3. Instrument outages spring and summer 2008.

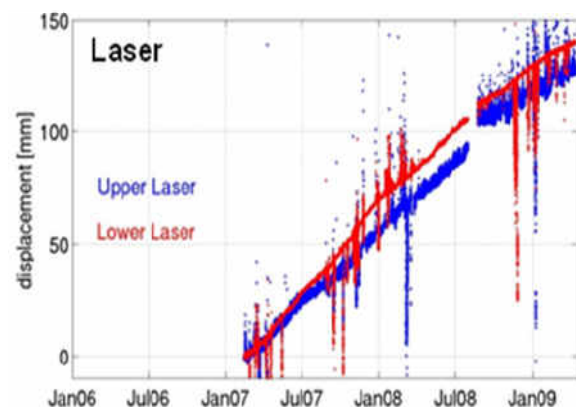


Fig. 12. Laser measurements. Acceleration phase in spring 2008 on lower laser.

## 6. CONCLUSIONS

The seismic monitoring systems at Åknes are operating reliable and provide independent real-time input to the early warning centre in Stranda. We observe a higher level of microseismicity during snow

melt, which coincides with temporary acceleration phases of the slope. Microseismic monitoring is complementary to the direct measurements at the unstable rock slope, but it is important. All measurements have uncertainties and systems can fail. Therefore, an early warning system that is based on different technologies and that correlates observations from independent real-time data will perform more stable and reliable.

## REFERENCES

- Roth, M., Dietrich, M., Blikra, L. H. & I. Lecomte 2006. Seismic monitoring of the unstable rock slope site at Åknes, Norway. 19th annual Symposium on the Application of Geophysics to Engineering and Environmental Problems, Seattle, USA
- Roth, M. & L. H. Blikra 2008. Microseismic monitoring at the Åknes rock slope, Norway. EGU General Assembly 2008, Vienna, Austria.
- Roth, M. & L. H. Blikra 2009. Seismic monitoring of the unstable rock slope at Åknes, Norway. EGU General Assembly 2009, Vienna, Austria.
- Roth, M. and L. H. Blikra (2009): Seismic Monitoring of the Unstable Rock Slope at Åknes, Norway. Geophysical Research Abstracts, 11, EGU2009-3680, Vienna, Austria

## WEBPAGES

Seismic network latest automatic processing results:  
<http://www.norsar.no/pc-47-48-Latest-Data.aspx>.

Broadband station AKN current data:  
<http://www.norsardata.no/NDC/heliplots/>

Broadband station AKN historic data:  
<http://www.norsardata.no/NDC/data/>  
<http://www.norsardata.no/NDC/lpdata/>

Early warning centre Stranda (in Norwegian):  
<http://www.aknes.no/>





## CASE STUDY 13:

**Title:** Landslide of Rindberg / Sibratsgfall investigated with airborne geophysical survey.

**Application:** Landslide investigations.

**Technique:** Airborne geophysical survey.

**Main references:** Based on the paper: Supper et al. 2008.

**Contributors:** GSA (Supper R., Baron I.).

### ABSTRACT

After a large landslide event in Sibratsgfall/Austria several exploration methods were evaluated on their applicability to investigate and monitor landslide areas. The resulting optimised strategy consists of the combined application of airborne electromagnetics, ground geoelectrical measurements and geoelectrical monitoring combined with hydrological and geological mapping and geotechnical modeling. Interdisciplinary communication and discussion was the primary key to assess this complicated hazard situation.

### 1. INTRODUCTION

In spring 1999, after a short period of heavy precipitation and the rapid melting of snow, a catastrophic landslide was triggered on the South-flank of the Rubach Valley near Sibratsgfall in the province of Vorarlberg (Austria). Shortly after the first slide activity was observed, the State Department of Avalanche and Torrent Control authorized preliminary geological investigations. As a follow up of this first phase of investigation, a complex research program was initiated. The final goal of this study was to develop an operative strategy to optimise measures in case of future events. The applied methods incorporated geo-morphological, hydro-geological and geophysical surveys of the area. It was determined that airborne geophysical measurements are a valuable tool to obtain a quick overview of the geological situation. Furthermore they can help to detect areas susceptible to a high sliding risk, to assist the follow up geological and hydrological mapping program and to optimise further ground-geophysical surveys. In a second step, ground geoelectrical surveys were used to achieve advanced understanding of the internal structure of the landslide. The location of survey lines was planned according to the resistivity pattern derived from the airborne electromagnetic survey. Based on these findings and on the results of the geo-hydrological mapping program, boreholes were drilled to calibrate the geoelectrical results. Laboratory tests were performed on soil and rock samples to determine the geotechnical parameters the main subsurface units. Additionally, geophysical and hydrophysical logging were carried out. Based on these results a geotechnical subsurface model was created and parameters and conditions of safety and failure were calculated. Finally a multi parameter monitoring network was installed and has been operated since

2002. In this paper we focus on the geophysical aspects of the strategy.

### 2. THE GEOLOGICAL FRAMEWORK

The research area is entirely located within the "Feuerstätter Unit", which is characterized by extensive rock disruption. The landslide area itself is mainly composed of rocks of the Junghansen and Schelpen series. These sub-units consist of marl and schist with highly variable stability as a result of tectonic fracturing. Due to their low resistance against weathering, rocks degrade under the influence of water into deeply weathered granular soils. Within these areas, all primary scarps are located. The Junghansen and Schelpen series are embedded into the more stabile Feuerstätter sandstones and limestones of the Aptychen series. Fig.1 shows the results of the geological mapping of the landslide area (Jaritz et al, 2004) and surroundings.

### 3. THE AIRBORNE GEOPHYSICAL SURVEY

Soon after the landslide event, a high resolution, multi-parameter airborne survey was performed. The main part of the airborne system (Motschka, 2001) consisted of a GEOTECH-"Bird" of 5.6 m length and 140 kg weight.. For the "Sibratsgfall" survey, electromagnetic alternating fields with frequencies of 3200Hz (coaxial coil) and 7190Hz (coplanar coil) were used, thus allowing investigation depths up to 70 m below ground surface. The electromagnetic bird was supplemented by a laser altimeter, two differential GPS sensors, one of them located in the "bird" and the other one in the helicopter, a Cs-magnetometer, a gamma spectrometer and a passive microwave soil moisture sensor.

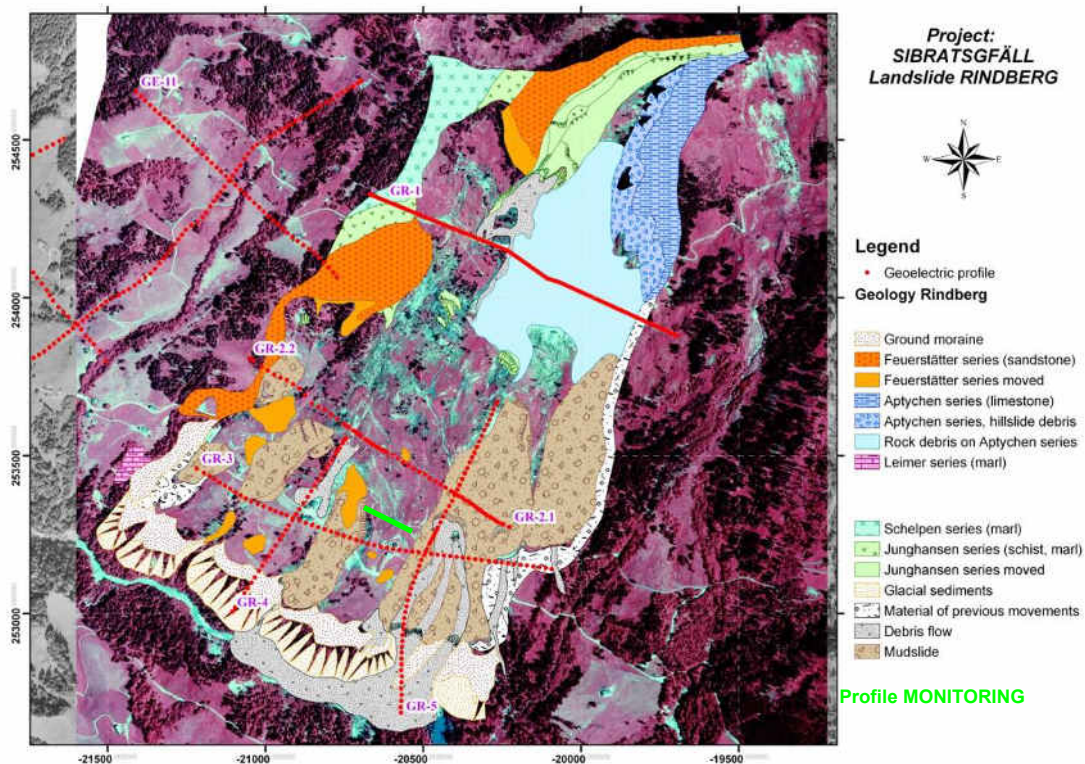


Fig. 1. Geological overview map of the landslide Rindberg.

Out of the set of different airborne techniques, the electromagnetic method was expected to deliver the most useful results for the investigation of landslide areas. This is due to the fact that with this method depth-specific sounding can be performed. Moreover the derived parameter, namely the electrical bulk resistivity of the subsurface, directly depends on fluid content, soil porosity and clay content. These parameters describe indirectly the internal lithological composition of the landslide. Using the results of a two-layer inversion cross-correlated with remote sensing data (satellite images, ortho-photographs and digital terrain data from airborne laser scanning) and results from geological mapping, a conceptual model of the subsurface structure was derived.

Fig. 2 shows the results of the inversion of the electromagnetic data using a homogenous halfspace model (Ahl, 2007). This approach is very useful in providing a first overview over geological structures in a research area.

The territory affected by movement of clay and marl material is clearly detectable in the central zone of the landslide, exhibiting medium to low resistivities (35-100 Ohmm). Sandstones (resistivity > 175 Ohmm) of the Feuerstätter series, building up the unmoved frame of the landslide on the western side, can be delineated laterally with high resolution due to their contrast in resistivity to the surrounding materials.

However, ground moraines, defining the south-western border of the landslide, and limestone material from

the Aptychen series, dominating the north-eastern part of the landslide, show the same resistivity signature. Therefore they cannot be distinguished from the sandstone using only electromagnetic results.

Incorporating additionally results from the gamma ray mapping, particularly the potassium distribution (fig.3), a more accurate differentiation between Aptychen series (low potassium content) and sandstones (medium potassium values) was possible.

It is remarkable that the distribution of maximum potassium content follows the main flow track of the landslide (fig.3). The reason for that is not obvious. This might be due to the fact that the top layers in the landslide material are mainly mixtures of marl and schist originating from Junghansen and Schelpen series, which show also high potassium contents at in-situ position. Destruction of the vegetation cover and dehiscing of the sward by high movement rates could be other causes. Within a second processing step, the geoelectric results as well as information from core drillings were used to constrain the inversion of the airborne electromagnetic data. This improved resistivity model was consequently used to refine the subsurface structural model, based on the complex interpretation of all available data.

Furthermore it has to be pointed out that all airborne geophysical results had been very valuable for mapping geologists as they helped to optimize the follow-up mapping procedures. Additionally it helped to minimize actual field work, which is often very difficult and time consuming in the rugged terrain of unstable slopes.



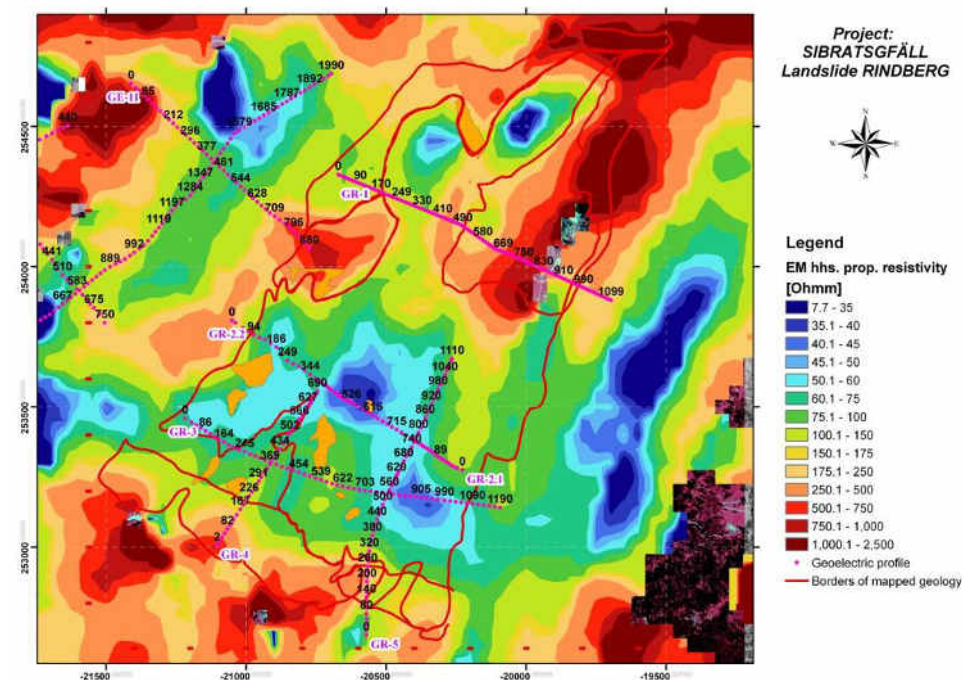


Fig. 2. Results of the inversion of airborne electromagnetic mapping: homogenous halfspace inversion - Parameter: Resistivity [Ohmm].

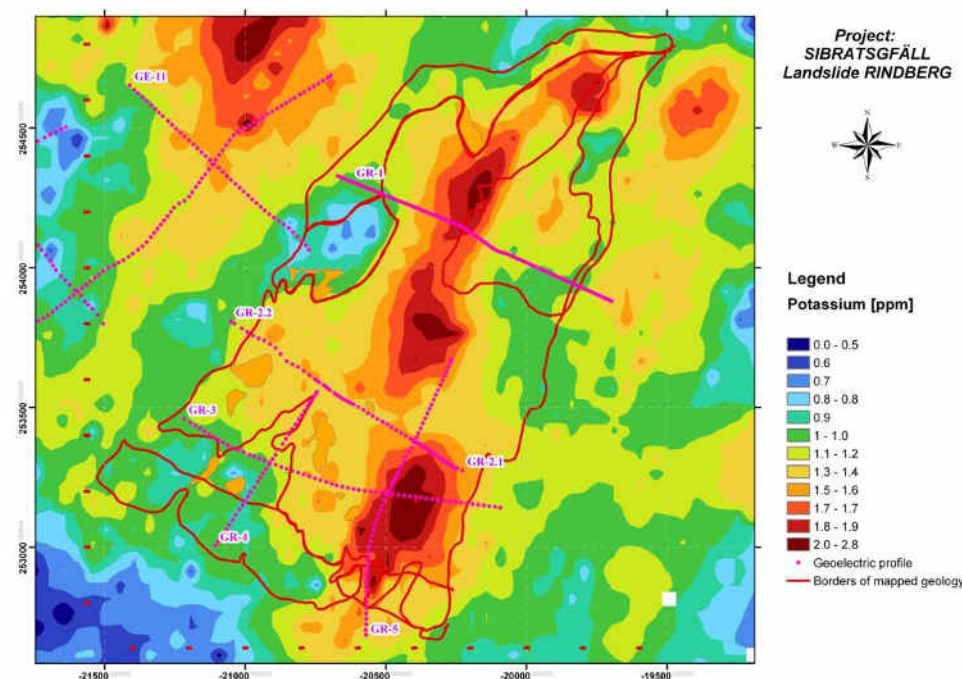


Fig. 3. Results of the inversion of airborne mapping: – Parameter: Gamma ray spectroscopy – Potassium [ppm].

#### 4. CONCLUSIONS

Several methods were evaluated to design an improved interdisciplinary strategy for immediate measures to be applied in case of future landslide events. The strategy allows to quickly assess the

prevailing hazard situation and to develop and recommend effective mitigation measures.

The resulting optimised approach consists of the application of airborne electromagnetics, ground geoelectrical measurements and geoelectrical monitoring combined with hydrological and geological mapping and geotechnical modeling. Interdisciplinary

communication and discussion was the primary key to access the complicated hazard situation in the case of the large-scale landslide event evaluated at Rindberg.

### **Acknowledgements.**

This study was financed by grants from the State Department of Torrent and Avalanche Control (WLV), the Federal Ministry of Transport, Innovation and Technology (BMVIT), the Federal Ministry of Science and Research (BMWF), the State of Vorarlberg and internal research funds of the Geological Survey of Austria. We further like to thank Grete Wöhrer –WLV (logistical support), Martina Mittelberger – Land Surveying Office Feldkirch (GPS) and Robert Hofmann (geotechnical consulting) for fruitful cooperation.

Winkler, E., Seiberl W., Ahl A.: Interpretation Of Airborne Electromagnetic Data with Neural Networks: In Geophysical Applications of Artificial Neural Networks and Fuzzy Logic, Sandham,W. and Leggett M. (Eds.), Kluwer Academic Publishers, 2003.

### **REFERENCES**

- Ahl, A., Winkler E., Bieber G., Römer A.: Probabilistic inversion of aereoelectromagnetic data with a homogeneous halfspace model: Journal of Applied Geophysics, submitted, 2007.
- Avdeev A.: Three dimensional electromagnetic modelling and inversion from theory to practice, Surveys in Geophysics 26:767-799, 2005.
- Jaritz W, Reiterer A, Supper R.: Landslide Rindberg (Vorarlberg): Multidiscipline Research, Proceedings of the 10th Interpraevent Congress, Riva del Garda, 2004.
- Motschka, K.: Aerogeophysics in Austria: Bulletin of the Geological Survey of Japan Vol. 52 No. 2/3, pp. 83–88, Tsukuba, Japan, 2001.
- Pedler, W. H., Head, C. L., and Williams, L. L.: Hydrophysical Logging: A New Wellbore Technology for Hydrogeologic and Contaminant Characterization of Aquifers, Proceedings of National Groundwater Association 6th National Outdoor Action Conference, pp 1701-1715, 1992.
- Seiberl, W., Ahl A., Winkler E.: Interpretation of airborne electromagnetic data with neural networks: Exploration Geophysics, 29, 152-156, 1998.
- Sengpiel, K., Siemon B.: Examples of 1-D inversion of multifrequency HEM data from 3-D resistivity distributions: Expl. Geophys., 29, 133-141, 1998.
- Supper, R.; Ahl, A. ; Römer, A.; Jochum, B.; Bieber, G.: A complex geo-scientific strategy for landslide hazard mitigation – from airborne mapping to ground monitoring, Advances in Geosciences, 14, 1-6, 2008.

## CASE STUDY 14

**Title:** Site-specific geotechnical investigations for landslide characterization and detection. Application at the Åknes rockslide, western Norway.

**Application:** Geotechnical investigations and instrumentation.

**Technique:** Core drilling; Bedrock core logging and testing; Geophysical borehole logging; Hydrological testing; Borehole inclinometers (DMS).

**Main references:** See references list at the end of the case study.

**Contributor:** Åknes/Tafjord Early Warning Centre (Blikra L.H. & Kristensen L.); ICG - Geological Survey of Norway (Oppikofer T.)

### ABSTRACT

Site-specific geotechnical data are essential for the design and implementation of monitoring systems and early-warning of large landslides. This data gives us important information about the characterization and strength of geological structures and the kinematics of the unstable areas. The case study shows some of the investigation methods used for the Åknes rockslide in western Norway. The methods used include geological field mapping, geophysical surface measurements and measurements of deformations. One of the most important investigations is coming borehole drilling. Bedrock-core logging and testing, geophysical logging and instrumentation in order to investigate subsurface deformations are crucial data in order to understand geometry, volumes and kinematics of the rockslide. Large efforts have also been on the investigations of the hydrological system. The full understanding of the geological model and the kinematics will only be achieved by doing detailed subsurface investigations and instrumentation in boreholes.

### 1. INTRODUCTION

Site-specific geotechnical data are essential for the design and implementation of monitoring systems and early-warning of large landslides. This data gives us important information about the characterization and strength of geological structures and the kinematics of the unstable areas. They are key data in order to perform reliable numerical models and to construct geological models.



Fig. 1. The location of the Åknes rockslide in the inner part of Storfjorden, western Norway

The case presented here is the Åknes rockslide, situated on the north-western flank of the Sunnylvsfjord in Western Norway (Fig. 1). The Åknes/Tafjord project initiated in 2004 was a large investigation, monitoring and early-warning project

focusing on the Åknes rockslide and other large unstable slopes (Blikra, 2008). The Åknes rockslide with an estimated volume of 30 to 54 Mm<sup>3</sup> is moving with a velocity of up to 8 cm/year, and its failure may trigger a devastating tsunami in the fjord.

The case study gives an overview of the geotechnical investigations and instrumentation that have been performed in order to be able to construct a reliable geological model and as an important basis for the design of monitoring systems.

### 2. GEOLOGICAL SETTING

Åknes rockslide is located in the Western Gneiss Region and the bedrock is constituted of medium grained granitic gneisses and granodiorite gneisses of Proterozoic age (Ganerød et al., 2008) with bands and lenses of mafic material. These gneisses have generally well developed foliation surfaces and mineral banding (Braathen et al., 2004) and numerous centimetric to decametric, close to tight folds are visible in the field. At Åknes there occur biotite-rich layers up to 20 cm thick and coincide with zones of high fracture frequencies and sliding surfaces is likely located within these mica-rich layers (Ganerød et al., 2008).

The morphological investigations show several characteristic features (Fig. 2):



- An about 500m more or less continuous back crack (Upper tension fracture).
- A large depression in the upper western corner of the rockslide, developed into a graben structure. The total vertical displacement is from 20-30 m.
- A series of tension fractures from the upper to the middle part of the slope.
- Prominent slide scars along the southwestern canyon. Historical data indicates a slide in the upper part in the late 1800, and slides also in 1940 and 1960.
- Small slide scars in the lower part of the rockslide.
- Large blocks or parts of the rocks is coming out of the slope at two particular areas, one in the middle part and one area in the lowermost part.
- Distinct water springs at the lowermost part of the slope at about 100masl. However, there are also smaller springs in the middle part of the slide area.

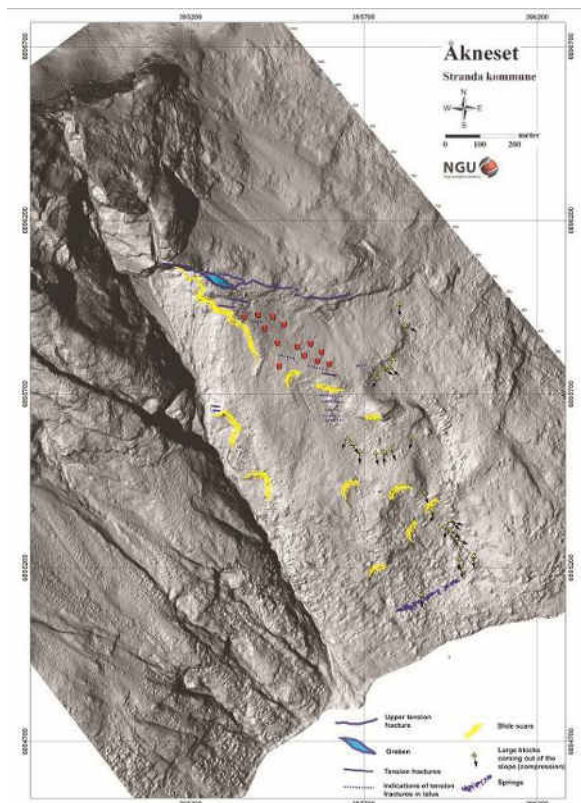


Fig. 2. Morphological features of the Åknes rockslide (Blikra, 2008).

### 3. SURFACE DISPLACEMENTS

The movement of the Åknes area has been measured by a series of different methods, including GPS, total station, ground-based radar, extensometers and single lasers (Fig. 3). The large tension cracks in the upper part are more than 500 m long and limit the total volume which is moving. The movement data

measured by periodic GPS and total station demonstrates that there is a movement of between 2 and 4 cm/year. The south-western flank has a much larger movement with a general trend of 6-8 cm a year, but locally up to 15 cm/year. The same trend can also be seen on the measurements done by ground-based radar campaigns placed in Oaldsbygda on the other side of the fjord.

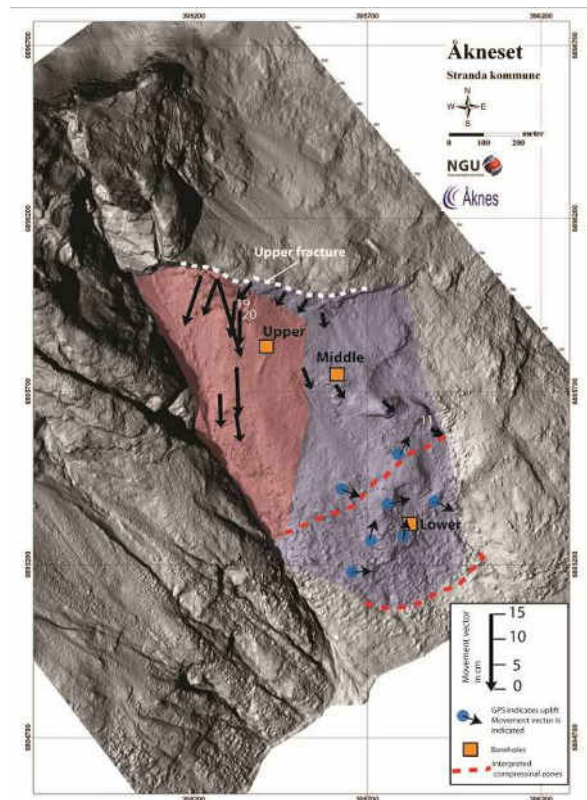


Fig. 3. Shaded relief map of the Åknes area showing movement data measured by periodic GPS and total station. The extent of the possible unstable area is shown in colour. The fast moving upper western part is indicated by red colours, and the interpreted compressional zones are indicated.

### 4. DRILLING AND CORING

An important part of the investigations at Åknes has been the core drilling, including 7 deep boreholes at 150-200 m depth at three different locations (Fig. 3). Logging of different types of data was performed during the drilling operation. Important are especially the water pressure, water flow, the system pressure and the penetration velocity (Fig. 4). These data are important information at an early stage and gives information about the hydrological conditions and the occurrence of large fractures. Note for example the reduced water pressure and system pressure at 35-50 m depth due to large open fractures. Similar reduced water pressure can be seen at 120 m depth.



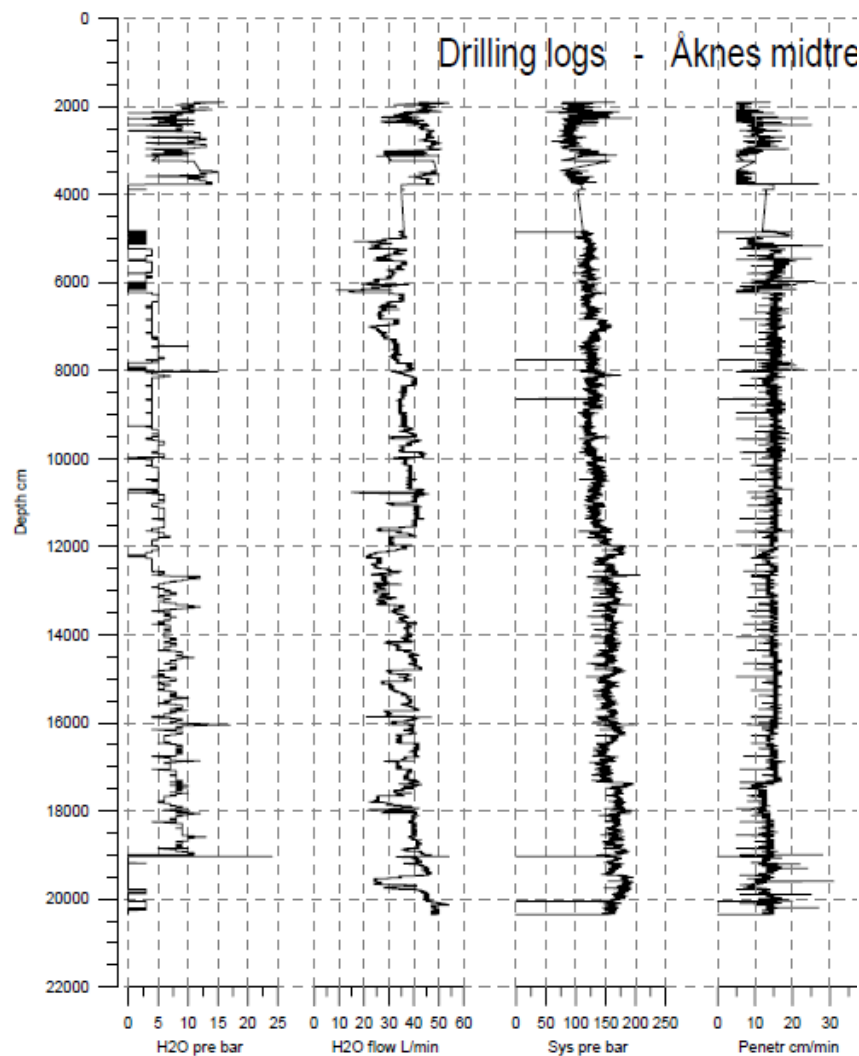


Fig. 4. Data from the drilling operation at the middle site showing water pressure, water flow, system pressure, and penetration velocity.

The bedrock cores were of excellence quality and gave important information about the rock quality and the characteristics of fractures and weak zones (Ganerød et al., 2007). Some zones were totally crushed, while others have well-defined breccias with silt and clay (Fig. 5). We experienced some core loss at zones characterized by crushed rocks. All cores were carefully logged, and the fracture frequency gives a good picture of the down-hole variation (Fig. 6, right).

## 5. GEOPHYSICAL LOGGING

All boreholes were logged by different methods before the in-place instrumentation (Fig. 6). The resistivity data gives good indications of the water conditions in fractures and the seismic P-velocity gives overview of the rock quality and fractures. The seismic velocity from just below the water level (52 m depth) and down to about 105 m is characterized by large variations in velocity indicating many fractures. Below this zone, a

higher velocity with less change is documented until 125 m depth.



Fig. 5. Drilling core at 34 m depth at the middle borehole at Åknes, showing a crushed and brecciated zone with silt and clay, representing the upper sliding zone. This sliding plane is also documented by displacement in DMS™ column (Differential Monitoring of Stability, in place instrumentation).

## 6. HYDROLOGICAL TESTING

A vital part of stability considerations of large landslides is the hydrological conditions. An integrated approach combining heat pulse flowmeter logging with a new protocol of dynamic fluid electric conductivity (DFEC) were performed by ETH (Switzerland) for the identification and characterization of groundwater flow (Thöny, 2008). A pulse flow-meter logging was also performed, in addition to large-scale tracer experiments.

The dynamic fluid electric conductivity logging was performed in the following way:

1. The borehole were first flushed with water with a higher salinity that the water in the system
2. The conductivity were logged several times after the flushing in order to observe the time changes

The test gives very interesting data showing clearly were we have stagnant conditions and were we distinct water circulation (Fig. 7). The profile shows generally stagnant flow conditions above 87 m and below 119 m, but with downward oriented flow in between, and upward directed flow in the uppermost 10 meters of the logged section. The loss of drilling fluid pressure from 87 to 115 m depth and the highly conductive outflow at 119 m depth clearly indicate the

occurrence of highly permeable rock masses between 87 and 120 m depth (Thöny, 2008).

## 7. SUBSURFACE DISPLACEMENTS

Tree of the boreholes has been instrumented by the DMS (Differential Monitoring of Stability) system. The DMS is a multiparametric column for investigations and permanent monitoring of subsurface movements; temperature and water pressure, and have been developed and patented by the Italian company **CSG srl**. The DMS column is like a sensorized spiral cord or "snake" composed of a sequence of hard tabular modules connected to each other by special 2D/3D joints. The present system at Åknes composes 3 continuous columns 50, 100 and 120 m long measuring the movement in 2D. The 120 m long column consists of totally 245 sensors. The sensors composes inclinometers, temperature sensors and in selected modules piezometers and digital compass. Figure 8 show example of data from the first campaign at the middle location. It clearly documents the sliding zone at 33-34 m depth, but also movement at deeper parts.

The instrumentation in boreholes is essential for both the investigations of subsurface characteristics (sliding planes, volumes etc) and for operative early-warning.

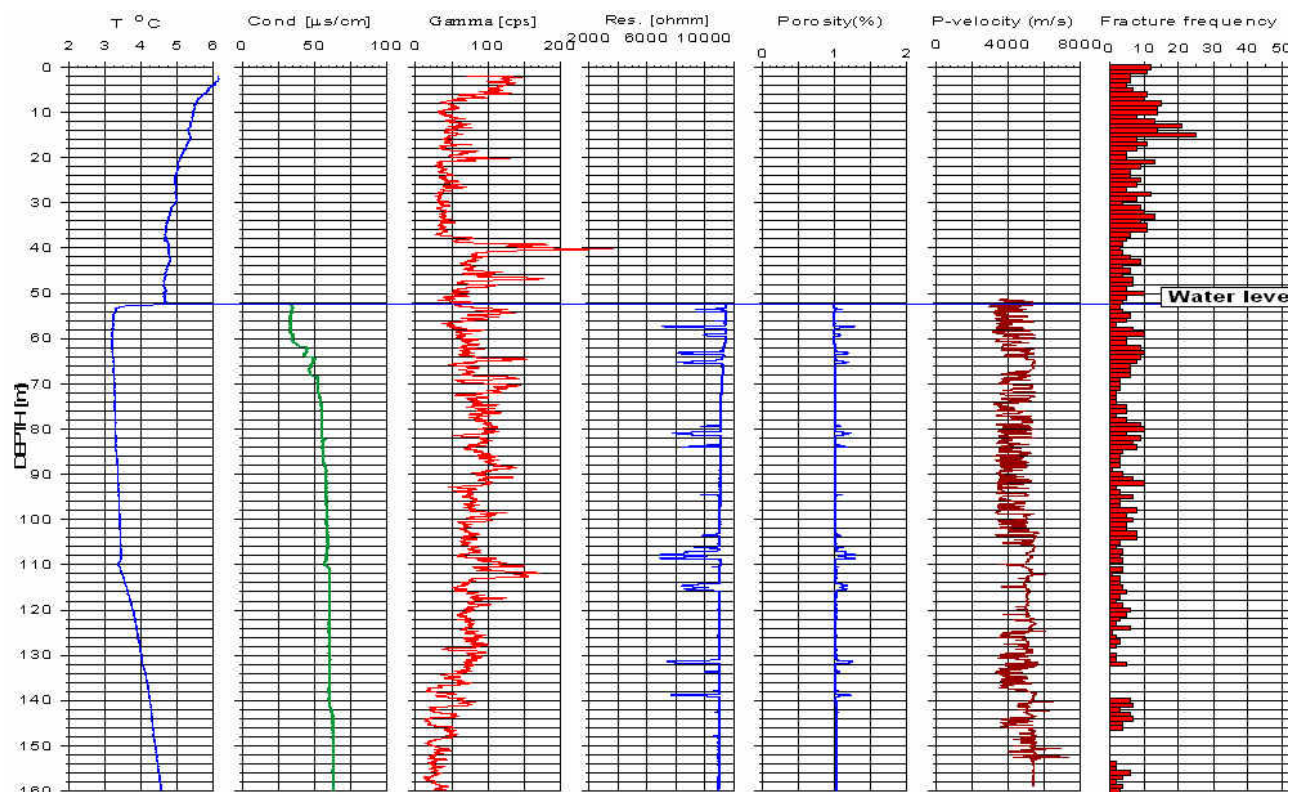


Fig. 6. Geophysical logging upper borehole (Rønning et al., 2006).

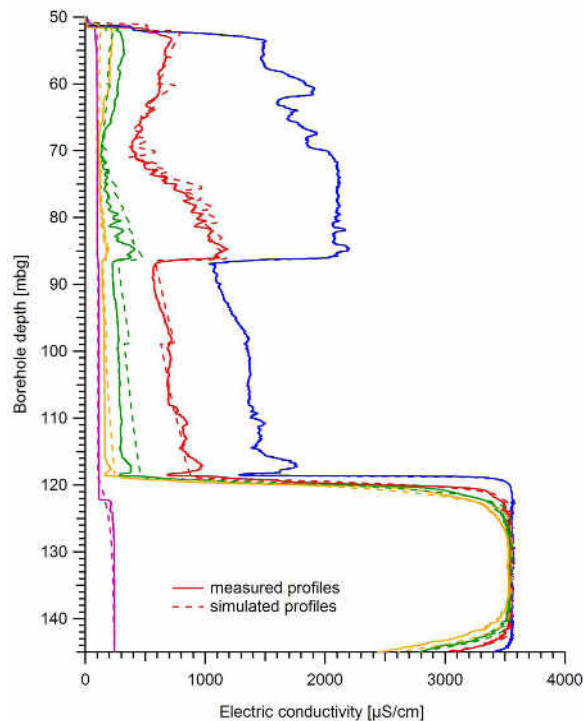


Fig. 7. Measured and simulated electric conductivity profiles in upper borehole. From Thöny (2008).

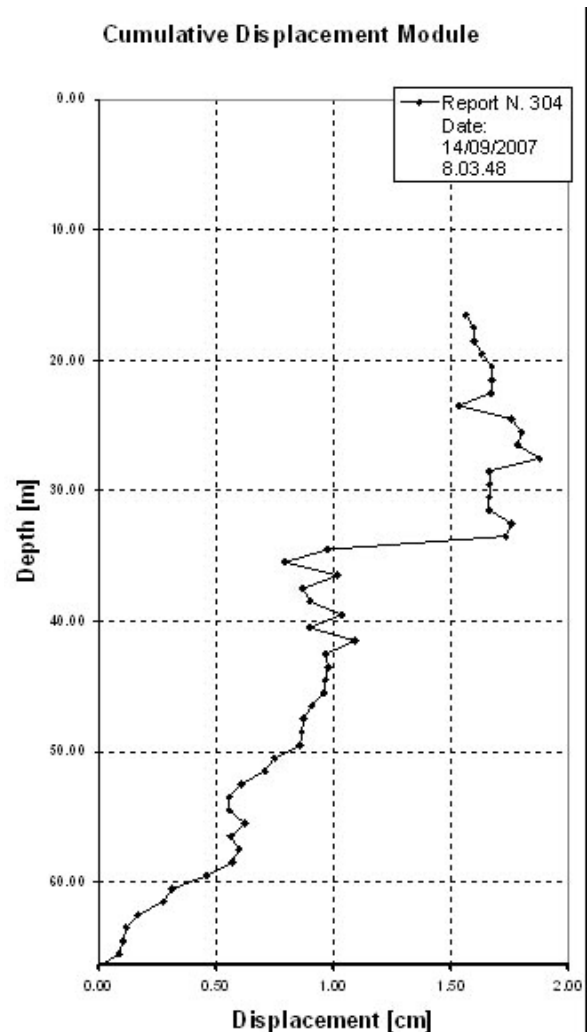


Fig. 8. Displacement in upper part of middle borehole from a 10 month campaign. Data is from a DMS system of 50 in-place inclinometric sensors.

## 8. GEOLOGICAL MODEL

Numerous geological, geophysical and geotechnical studies were made on the Åknes rockslide to better understand its mechanism and to locate sliding surfaces (e.g. Rønning et al., 2006; Blikra, 2008; Ganerød et al., 2008). The slope movements are monitored by GPS, total station, extensometers, laser distance meters, ground-based radar, InSAR and terrestrial laser scanning (Kveldsvik et al., 2006; Blikra, 2008). A detailed summary of these studies can be found in Oppikofer (2009). The geological model is not yet totally understood, but the instability is clearly controlled by the structural pattern of the gneissic rocks, with the step back fracture following a sharp fold, and the sliding zones being parallel to the foliation planes further down slope. The upper part of the rockslide is characterized by tension, while several parts in the lower area show compression features (Fig. 2 and 9). However, this only gives the general picture, as the geometry and subsurface deformation

is much more complex (e.g. Jaboyedoff, 2010). The rockslide is composed of several individual blocks with different surface movement directions, and also differential movement at different depths.

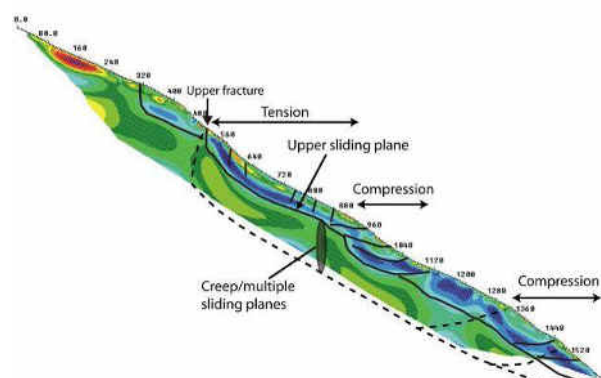


Fig. 9. A proposed general geological model for a 2D length profile at Åknes. The colours show the 2D resistivity data, with blue codes reflecting low resistivity.

## 9. CONCLUSIONS

Monitoring and early-warning related to large landslides requires detailed investigations with the use of different methods. These include geological field mapping, geophysical surface measurements and measurements of deformations. One of the most important data is coming from borehole drilling. Bedrock-core logging and testing, geophysical logging and instrumentation in order to investigate subsurface deformations are crucial data in order to understand geometry, volumes and kinematics of the rockslide. Large efforts have also been on the investigations of the hydrological system.

Thöny, R.2008: Dynamic fluid electric conductivity logging for identification and characterization of preferential groundwater flow in the Åknes rockslide (Norway). MSc Thesis, Engineering Geology, ETH Zurich.

Ganerød, G.V., Grøneng, G., Aardal, I.B., Kveldsvik, V., 2007. Core logging of seven boreholes from Åknes, Stranda municipality, Møre and Romsdal County. NGU report no. 2007.020, pp. 222.

## REFERENCES

- Blikra, L.H. (2008): The Åknes rockslide; monitoring, threshold values and early-warning. In: ZUYU Chen; Jian-Min Zhang; Ken Ho; Fa-Quan Wu; Zhong-Kui Li (Eds). Landslides and Engineered Slopes. From the Past to the Future. Proceedings of the 10<sup>th</sup> International Symposium on Landslides and Engineered Slopes, 30 June - 4 July 2008, Xi'an, China. Taylor and Francis. ISBN: 978-0-415-41196-7.
- Ganerød, G., Grøneng, G., Rønning, J.S., Dalsegg, E., Elvebakk, H., Tønnesen, J.F., Kveldsvik, V., Eiken, T., Blikra, L.H. and Braathen, A. (2008). Geological model of the Åknes rockslide, western Norway. *EngineeringGeology*102, 1–18.
- Braathen, A., Blikra, L.H., Berg, S.S. and Karlsen, F. 2004: Rock-slope failures of Norway; type, geometry, deformation mechanisms and stability. *Norwegian Journal of Geology (NGT)* 84, 67-8.
- Kveldsvik, V. (2008). Static and dynamic stability analyses of the 800 m high Åknes rock slope, western Norway. Ph. D. thesis, Norwegian University of Science and Technology (NTNU), Dept. of Geology and Mineral Resources Engineering. 128.
- Oppikofer, T. 2009: Detection, analysis and monitoring of slope movements by high-resolution digital elevation models. Ph.D. thesis, University of Lausanne.
- Jaboyedoff, M., Oppikofer, T., Derron, M-H., Böhme, M., Blikra, L.H. & Saintot, A. 2010. Complex landslide behavior and structural control: a 3D conceptual model of Åknes rockslide, Norway. Special Publications of the Geological Society of London (in press).
- Rønning et al., 2006 Rønning, J.S., Dalsegg, E., Elvebakk, H., Ganerød, G. & Tønnesen, J.F. 2006: Geofysiske målinger Åknes og Tafjord, Stranda og Nordal kommuner, Møre og Romsdal. Norges geologiske undersøkelse Rapport 2006.002 (in Norwegian).



## CASE STUDY 15:

**Title:** From early warning to site-specific kinematic analysis: the case of Bagnaschino landslide.

**Application:** Landslide monitoring.

**Technique:** Differential Monitoring of Stability (D.M.S.) system.

**Main references:** Unpublished report, specific for the Safeland project.

**Contributors:** CSG S.r.l. (Levisolo, M).

### ABSTRACT

This case study shows the capabilities of a technique for landslide monitoring: Differential Monitoring of Stability (D.M.S.) system.

The instrumentation is installed on Bagnaschino landslide that is located in the Municipality of Torre Mondovì (Cuneo, Piedmont) and is characterized by a composite movement. During the observation period (28<sup>th</sup> October 2008 – 13<sup>th</sup> July 2009) it was possible to monitor different kinematics and different weather conditions in continuous. D.M.S. column allowed to investigate 5 triggering events and their relative period of stasis. In spite of a displacement of approximately 60 cm that occurred at 7 m blg, the integrity of D.M.S. column was preserved. Continuous monitoring of the landslide allowed to notice weak deep creep in the interval 30-44 m blg in addition to considerable shallow movements. The system was efficient also with the presence of elevated displacements unfitting with the functionality of the traditional borehole instrumentation.

### 1. HISTORY OF THE SITE

#### 1.1 Characteristics of the landslide

During the flood event occurred in Piedmont in 1994 the highway n. 194 was seriously damaged by a landslide activated in Bagnaschino site (Torre Mondovì, Cuneo) (fig. 1-2).

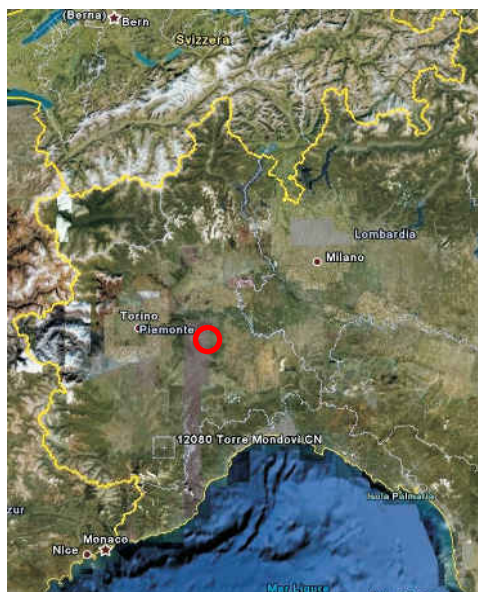


Fig. 1. Localization of Bagnaschino site (Google Earth).



Fig. 2. DEM of Bagnaschino landslide and D.M.S. position.

In a first time, Casotto Torrent strongly damaged the road with wide erosions and, in a second time, in proximity of km 1+400, a large landslide invaded the carriage way. The phenomenon is classified as a complex landslide movement. It was considered as a reactivation of a deep-seated gravitational slope deformation. The estimated value of area and volume involved in the phenomenon are respectively 150.000 m<sup>2</sup> and 1.2 million m<sup>3</sup>. Geotechnical investigations allowed to understand the stratigraphy of the landslide. At the top there is a thick layer of eluvial-colluvial overburden (up to 20-30 m in the upper part) composed by heterogeneous debris inside an abundant sandy clay loam matrix. Below this layer, there is a strongly alterate bedrock mainly composed by laminated micaschistes overlapping on metabasites and prasinites. Because of heavy rainfalls of flood

event of 1994, there was a saturation of overburden's material that slid over the bedrock, overflowing in the slope lower part.

## 1.2 Projects and works

In 1998 it was made a General Project relative to the reconstruction of the road sections damaged during the flood event of 1994.

After a first analysis it was hypothesized to divert the highway on opposite slope by means of two bridges. However this solution was much onerous and also the opposite slope was characterized by unacceptable geotechnical and global stability characteristics.

So the attention has been focused on the slope on landslide with further investigations through boreholes with piezometers and inclinometers. Following there are the main works realized:

- modelling of detachment part of the landslide;
- regularization and profiling of the upper slope of landslide zone for the formation of a single sloping plane;
- excavation of unstable material with the creation of n°4 benches;
- building of draining trenches and sub-horizontal drains on the slope;
- natural engineering works;
- creation of little channels for water draining;
- profiling of the most steep areas;
- realization of monitoring and control works (piezometers and inclinometers).

Finally, it was realized an artificial gallery with the aim of road protection against the material that could come from the slope.

## 2. MONITORING SYSTEM WITH D.M.S. COLUMN

In order to monitor in continuous the stability conditions, the province of Cuneo (Civil Protection Office) established in 2008 a slope monitoring plan with a D.M.S. system. The monitoring instrumentation is composed of n°1 multiparametric D.M.S. column 60 m long installed in inclinometric pipe DN 80 mm. The column is connected to a local control unit equipped with solar cell power supply and to a GSM data transmission. The column is composed of a sequence of rigid tubular modules containing various sensors, connected each other by means of special 2D/3D flexible joints having 2 or 3 freedom degrees: this allows to single units to adapt with borehole characteristics and soil movements and to conserve azimuth direction compared with an external reference system.

In order to monitor the conditions of the groundwater, there were installed n°2 piezometric sensors.

The instrumentation was installed on 28<sup>th</sup> October 2008 (fig. 3) and immediately linked in situ in wireless remote mode through a GSM network.



Fig. 3. Installation of D.M.S. column.

The acquisition unit performs in continuous:

- transducers energization;
- sensorial data acquisition;
- data storage;
- alarm thresholds management on 4 levels.

Following there are described the technical characteristics of sensors, control unit and data transmission applied for the monitoring of Bagnaschino landslide:

### *Biaxial inclinometric sensors*

Range (deg)	± 20°
Resolution (deg)	0.005°
Accuracy (deg)	0.02°
Linearity (25% range)	0.2
Access time (ms)	160
Power (V)	7-12 DC
Temp. op. range (°C)	+70°/-20°
Temp. storage (°C)	+90°/-40°

### *Piezometric sensors*

Range (psi)	0-30-100
Resolution (% FS)	0.01
Linearity (% FS)	0.02
Power (V)	7-12 DC
Temp. op. range (°C)	+70°/-20°
Temp. storage (°C)	+90°/-40°

### *Control unit and data transmission unit* Communication

Applicable sensors	Remote control with GSM-GPRS/wireless in situ with serial RS 232 or RS 485
Data storage ability	Max n°128 DIGITAL-ANALOGICAL
Power (V)	Circular buffer
Case	7-12 DC
Battery	IP68
	12 V, 5 years duration

The data in binary format of D.M.S. column are transmitted by communication protocol RS 485 to the control and recording unit, where they can be acquired in continuous or at regular intervals defined by the user by means of the GEOMASTER management software.

The program allows remote control of the D.M.S. monitoring, real-time data visualization, data download (memory buffer) and the setting of alarms and phone



numbers of the control staff on duty. Remote control, download, storage and processing of data can be executed through a server unit in the monitoring centre or, in emergency conditions, through a mobile remote control unit equipped with integrated GSM-GPRS wireless transmission (fig. 4).

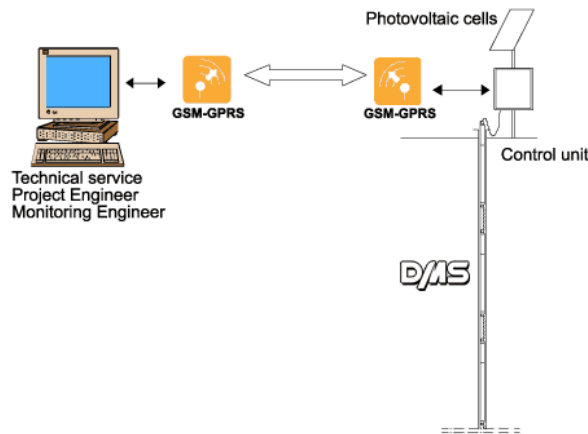


Fig. 4. Remote control of D.M.S. system.

### 3. MONITORING RESULTS AND DISCUSSION

#### 3.1 Contribute for the triggering thresholds study

Correlation between precipitations data and D.M.S. displacement allowed to identify critical events that have reactivated the landslide on the sliding surface at 7 meters blg, with direction 30° NE. During the observation period it was possible to monitor in continuous different kinematics and different weather conditions. D.M.S. column allowed to investigate 5 triggering events and their relative period of stasis, with a clear delay time after rain events or snow melting. Weather data are been taken from database of two climatic station in proximity of Bagnaschino site

(Viola and Pamparato). Following there are described the characteristics of each event:

- *First event:* on 28<sup>th</sup> November 2008 there was the first snowfall (one of the most intense of the last century in the area) that was followed by some rainy days and finally by another snowfall on 13-19<sup>th</sup> December. In the same days there was a temperature rise that caused the partial snow melting and subsequently the first movement read by D.M.S. column.
- *Second event:* on 1<sup>st</sup> March 2009 there was a light rainfall following by a strong temperature rise (thermal zero at 1500 m asl) that caused the second landslide activation on 2<sup>nd</sup> March 2009 at 20:03, 37 hours after the rainfall beginning.
- *Third event:* on 31<sup>st</sup> March 2009 at 06:00 a strong rainfall began and lasted for some days. After 30 hours, the landslide moved.
- *Fourth event:* this event is linked to more rainfalls occurred in the days 16<sup>th</sup>-22<sup>nd</sup> April 2009 and is different from the previous events because of a lower movement velocity (displacement about 10 mm).
- *Fifth event:* on 26<sup>th</sup> April 2009 the strongest spring rainfall started and after about 29 hours (27<sup>th</sup> April, 08:00) the landslide moved. This heavy rainfall lasted for some days: the cumulative displacement was 299.7 mm in only two days. The roll axis on the involved D.M.S. module reached its saturation angle (tilt>20°): the further displacement is calculated with the interpolation of its pitch axis, still active.

In the following table (table 1) and diagram (fig. 5) each triggering event has been described in detail considering also rain, cumulative rain, snow events and temperature.

	1 <sup>st</sup> EVENT	2 <sup>nd</sup> EVENT	3 <sup>rd</sup> EVENT	4 <sup>th</sup> EVENT	5 <sup>th</sup> EVENT
<b>Rainfalls start</b>	12/12/2008 0.00	01/03/2009 6.00	31/03/2009 6.00	16/04/2009 6.00	26/04/2009 3.00
<b>Displacement start</b>	16/12/2008 6.00	02/03/2009 20.00	01/04/2009 12.00	22/04/2009 0.00	27/04/2009 8.00
<b>Rainfalls type</b>	Snow	Rain/snow	Rain	Rain	Rain
<b>Snow at ground</b>	Yes	Yes	Yes	No	No
<b>Temperature rise</b>	Yes	Yes	No	No	No
<b>Concomitant factors</b>	Snow melting 90 mm	Snow melting 120 mm	-	-	-
<b>Rainfall [mm]</b>	70	44	63	160	77.6
<b>Rainfalls duration [h]</b>	84	96	30	138	29
<b>Critical intensity [mm/h]</b>	1.786	1.708	2.100	1.159	2.676
<b>Total cumulative rainfall [mm]</b>	190	354	480	590	800
<b>Cumulative rainfall event [mm]</b>	150	164	180	110	220
<b>Total cumulative displacement [mm]</b>	11.5	160.6	209.0	225.0	524.7
<b>Cumulative displacement event [mm]</b>	11.5	149.1	48.4	10.0	299.7

Table 1. Rainfall thresholds events.

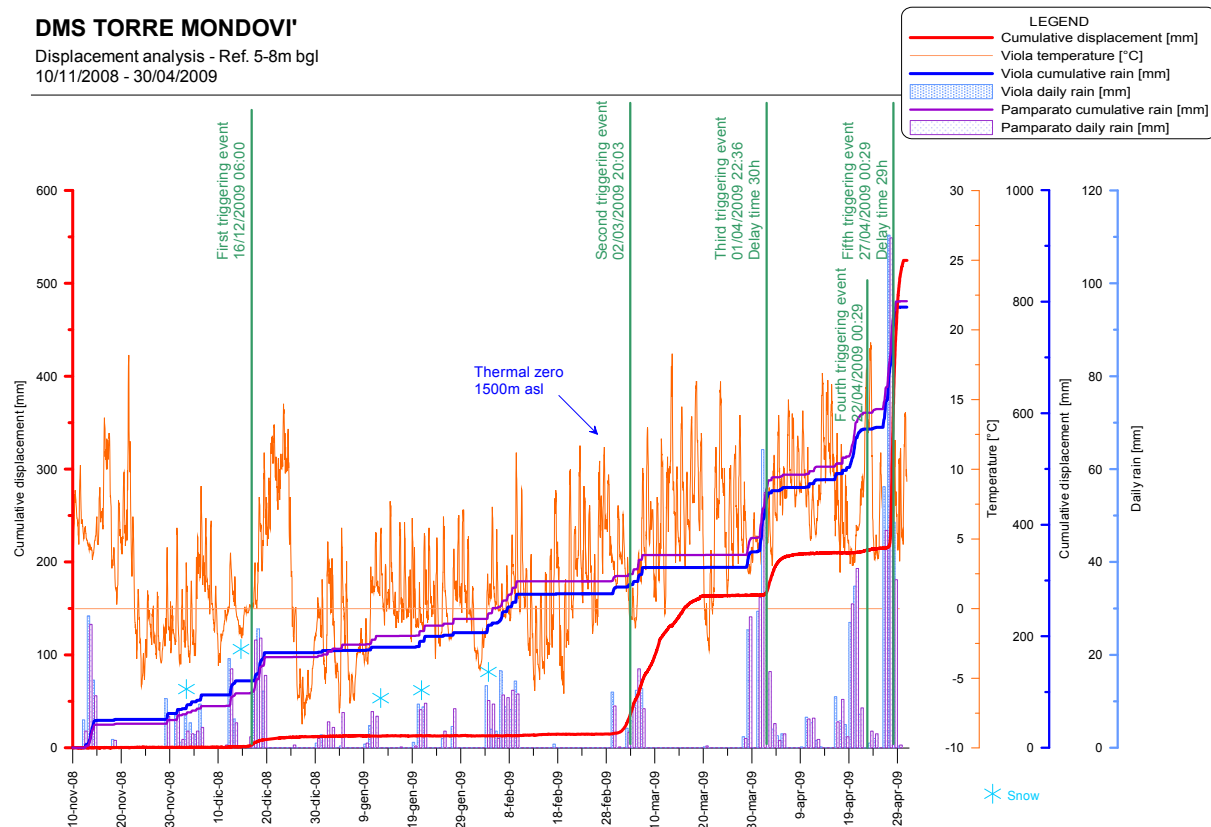


Fig. 5. Displacement analysis with the individuation of 5 triggering events.

For each event it was calculated a particular value, the *critical intensity*, that correspond to the ratio between precipitation quantities (calculated in mm) that caused triggering movement and its duration (calculated in hours). The interpolated line in the following bi-logarithmic plot (fig. 6) can be considered a site-specific deterministic approach to the limit equilibrium threshold that separates the stability and instability field.

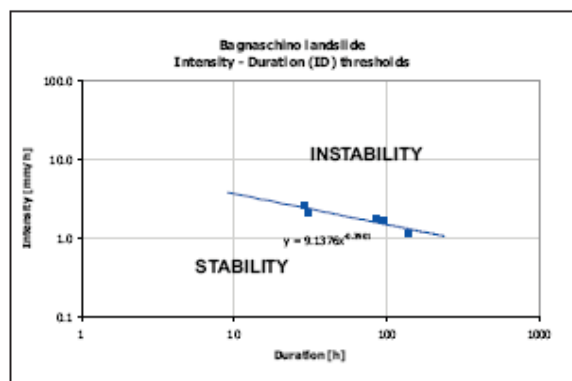


Fig. 6. Plot of intensity-duration thresholds.

The relation that links precipitation intensity and duration can be represented with the following equation:

$$I = c + a \cdot D^{-b}$$

where, in this case:

$$\begin{aligned} c &= 0 \\ a &= 9.1376 \\ b &= 0.3901 \end{aligned}$$

The next graph (fig. 7) shows the trend of threshold elaborated, by means of real field monitored displacement data, on Bagnaschino landslide compared to a review of empirical/statistical thresholds resulted in slope failures, run out (Caine, 1980; Cancelli & Nova, 1985; Ceriani et al., 1994; Crosta & Frattini, 2001, etc).

Continuous monitoring of the landslide allowed to notice weak deep creep in the interval 30-44 m bgl in addition to considerable shallow movements. The activation of deep movements is delayed in respect to shallow movements, with not unambiguous behaviour.

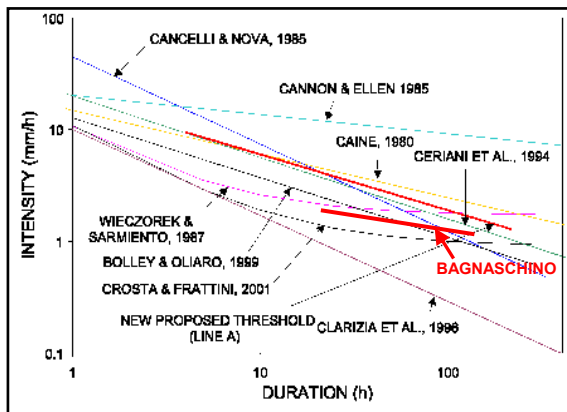


Fig. 7. Comparison of Bagnaschino threshold with literature empirical/statistic thresholds approach.

### 3.2 Relationship between rainfalls and displacement

The following plot showing the relationship between cumulative rainfall for each event and the relative displacement.

In the graph we can notice two *outlier* points: its rainfall value, in default of certain data, has been calculated assuming the total contribute of snow melting at ground previous the event..

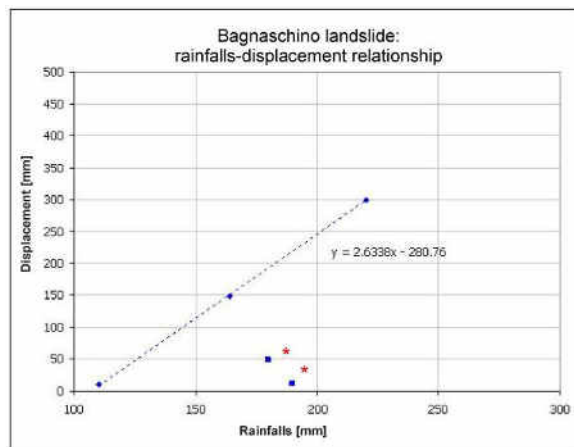


Fig. 8. Plot showing relationship between rainfalls and displacement (\* these points are obtained considering the total snow melting at ground).

In rainfall interval included between 100 and 300 mm, data interpolation can be a line whose equation is:

$$y = 2.6338x - 280.76$$

To ensure the linear behaviour in the first part of the curve rainfalls-displacements, it will be necessary to individualize at least a significant triggering event characterized only by rainfalls not snowy.

### 3.3 Removal of D.M.S. column

On 13<sup>th</sup> July 2009 the D.M.S. column was removed. The D.M.S. column allowed to obtained with continuity the kinematics of the landslide in action, not only limited to the initial stages of trigger, but also during the evolution up to achievement of stasis conditions.

The integrity of D.M.S. column is preserved in spite of the displacement of 60 cm occurred at 7 m blg (fig. 9-10). The excavation realized subsequently to release the column confirmed depth, direction and extent of the displacement, allowing the complete recovery of the instrumentation and the repair of the inclinometric pipe that is replaced and protected by another pipe with a larger diameter.



Fig. 9. Removal of D.M.S. column.



Fig. 10. The deformed module of D.M.S. column showing the displacement of about 60 cm.

## 4. CONCLUSIONS

This case study shows the potential of the D.M.S. system for landslides continuous monitoring. The Bagnaschino landslide monitoring shows that D.M.S. column allowed to investigate 5 triggering events multilevel and their relative period of stasis.

Moreover D.M.S. system allowed to obtain with continuity the kinematics of the landslide in action, (initial stages of triggering, evolution and achievement of stasis conditions). The registration of several triggering events in a short monitoring period is a particularity of D.M.S. system. In fact, in spite of a displacement of about 60 cm, the integrity of D.M.S. column is preserved and the involved modules are still active. Elevated displacements influence the functionality of the traditional borehole instrumentation after only a few centimetres.

## REFERENCES

- Baldesi, L. 2006. Studio cinematico dei dissesti ed analisi dei fattori di innesco nella media ed alta Val Nure (Piacenza); I casi di monitoraggio in continuo di Farini e Casale-Colla. Università degli Studi di Milano-Bicocca, unpublished thesis.
- Cannon, S.H., Ellen, S.D., 1988. Rainfall that resulted in abundant debris-flow activity during the storm of January 3–5, 1982, in the San Francisco Bay region, California: U.S. Geological Survey Professional Paper 1434, 27–33.
- Caine, N. 1980. The rainfall intensity-duration control of shallow landslides and debris flows. *Geogr. Ann. A*, vol. 62, pp. 23-27.

## CASE STUDY 16:

**Title:** Detecting and mapping landslides in Salazie area, La Réunion Island, using Remote Sensing techniques.

**Application:** Ground surface displacement measurement.

**Technique:** Remote Sensing: radar interferometry, image correlation.

**Main references:** Delacourt et al., 2009; Cruchet, 1994.

**Contributors:** BRGM (Raucoules D., de Michele M.).

### ABSTRACT

This case study shows the capabilities of a technique for landslide monitoring: Differential Monitoring of Stability (D.M.S.) system.

The instrumentation is installed on Bagnaschino landslide that is located in the Municipality of Torre Mondovì (Cuneo, Piedmont) and is characterized by a composite movement. During the observation period (28<sup>th</sup> October 2008 – 13<sup>th</sup> July 2009) it was possible to monitor different kinematics and different weather conditions in continuous. D.M.S. column allowed to investigate 5 triggering events and their relative period of stasis. In spite of a displacement of approximately 60 cm that occurred at 7 m blg, the integrity of D.M.S. column was preserved. Continuous monitoring of the landslide allowed to notice weak deep creep in the interval 30-44 m blg in addition to considerable shallow movements. The system was efficient also with the presence of elevated displacements unfitting with the functionality of the traditional borehole instrumentation.

### 1. INTRODUCTION

Due to its specific geological and climatic conditions, landslides are a major hazard affecting La Réunion Island in the Indian Ocean (Cruchet 1994). Several large landslides (up to several square kilometres) severely affect infrastructures (especially roads) and

habitations mostly in the region of “les Cirques”. The presented study (carried out in the framework of MVterre-1 project, 2001-2002, funded by EU, Reunion region and BRGM) focuses on Cirque de Salazie and more precisely on the Hellbourg Landslide (figures 1 and 2).

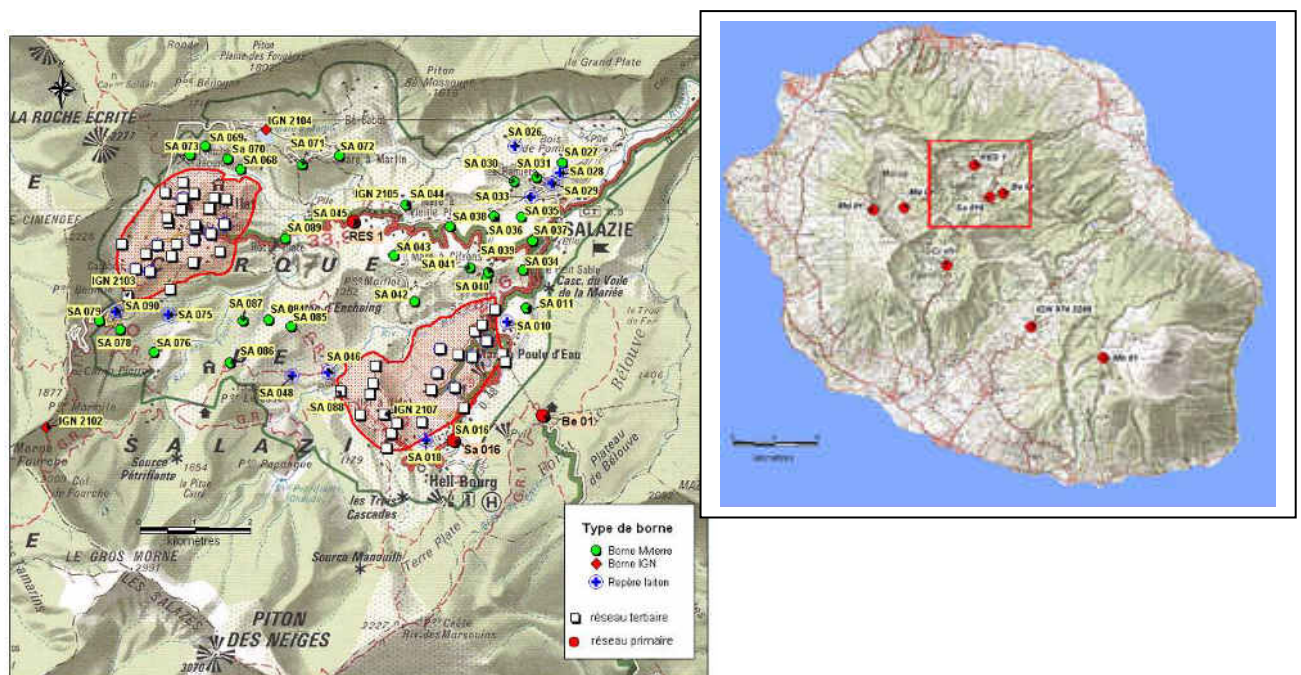


Fig. 1. La Réunion Island. The red frame locates the Salazie circle. The main GPS network is located.



Presently, most of the techniques for monitoring landslide displacements are derived from measurements of reference stations. Conventional geodetic techniques and extensometry techniques are the most commonly used. GPS measurements are an alternative (figure 1 shows the current GPS network installed by the Regional Geological Survey of la Réunion on the study area). Moreover, due to spatial and temporal heterogeneities of the displacements, such ground based measurements are not sufficient to fully describe the velocity field of a landslide.

Remote sensing imagery is a powerful tool for landslide monitoring because it offers synoptic views that can be obtained at different time intervals. Differential SAR interferometry (DINSAR) of ERS (C band) has shown its capability for deriving high accuracy maps (at centimeter level –Massonnet and Feigl, 1998) of landslide displacement. However, this technique is affected by severe geometrical and environmental limitations. Due to the dense vegetation cover of the study site, coherence of C-band (i.e. Radarsat data) interferograms is poor: we therefore assessed L-band JERS-1 data because the band is more penetrative.

In the recent years, new techniques based on correlation of optical images for the production of deformation maps have been developed. Those techniques have been successfully applied to the measurement of coseismic deformation (Michel et al., 1999) and more recently on landslides by combining both aerial photographs and Quick-Bird Images (Delacourt et al, 2004). For our test site, we used aerial photographs and SPOT 5 optical images.

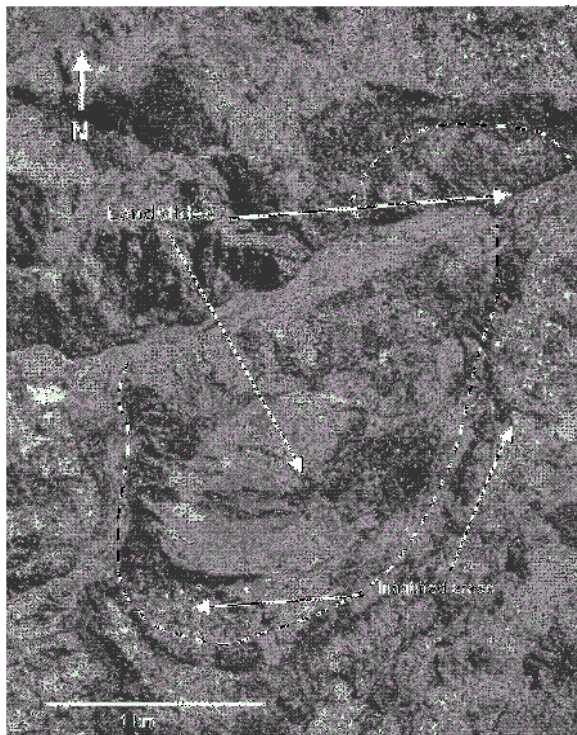


Fig. 2. Airborne photograph of the Hellbourg Landslide.

## 2. RESULTS

We have therefore tested two remote sensing techniques to observe landslides in the La Réunion Island (Hellbourg area, Cirque de Salazie).

The INSAR analysis, carried out with a reduced set of 6 JERS-1 scenes, shows the interest of the L-band SAR interferometry (figure 3). Both the shape and rate of the Hellbourg landslide have been obtained. Deformations larger than one fringe (i.e. about 11.5 cm) were observed. These results show the interest of using L-band data in a context where C-band is not relevant due to the vegetation cover.

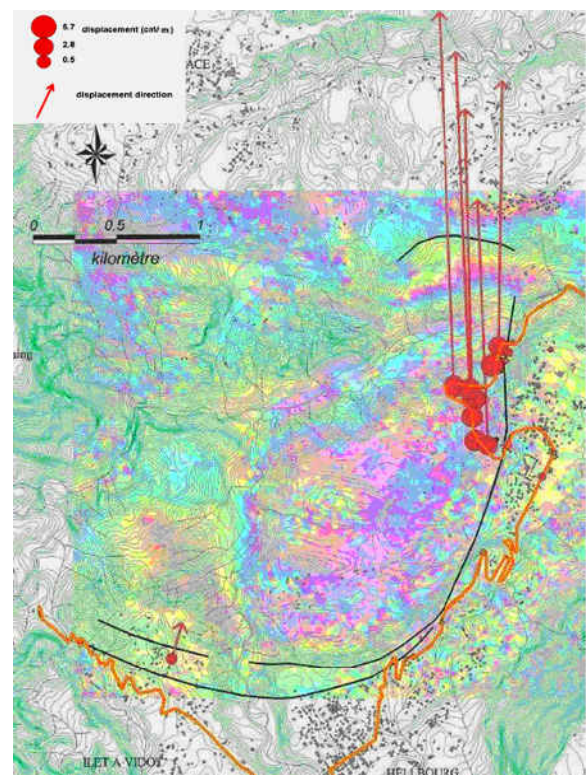


Fig. 3. Sum of two 3 months JERS-1 interferograms (1 fringe = 5.6 cm in line of sight) overlain on the topographic map of the landslide. In red, GPS displacements for the period 1995-1999. Black lines represent positions of observed crack boundaries of the landslide. Orange line shows the position of the Hellbourg road severely affected by the landslide.

Correlation of optical data can be used for deriving deformation maps of landslides that have a nearly constant displacement rate over several years. This technique can be applied either with two scenes acquired at two periods by the same type of sensor, or with different sensors (for example aerial photography combined to very high resolution satellite imagery). This technique allows the mapping of a large displacement field. Our preliminary results in correlating of SPOT 5 and aerial optical images have permitted the detection of displacements of about 5m over a period of five years (figure 4).



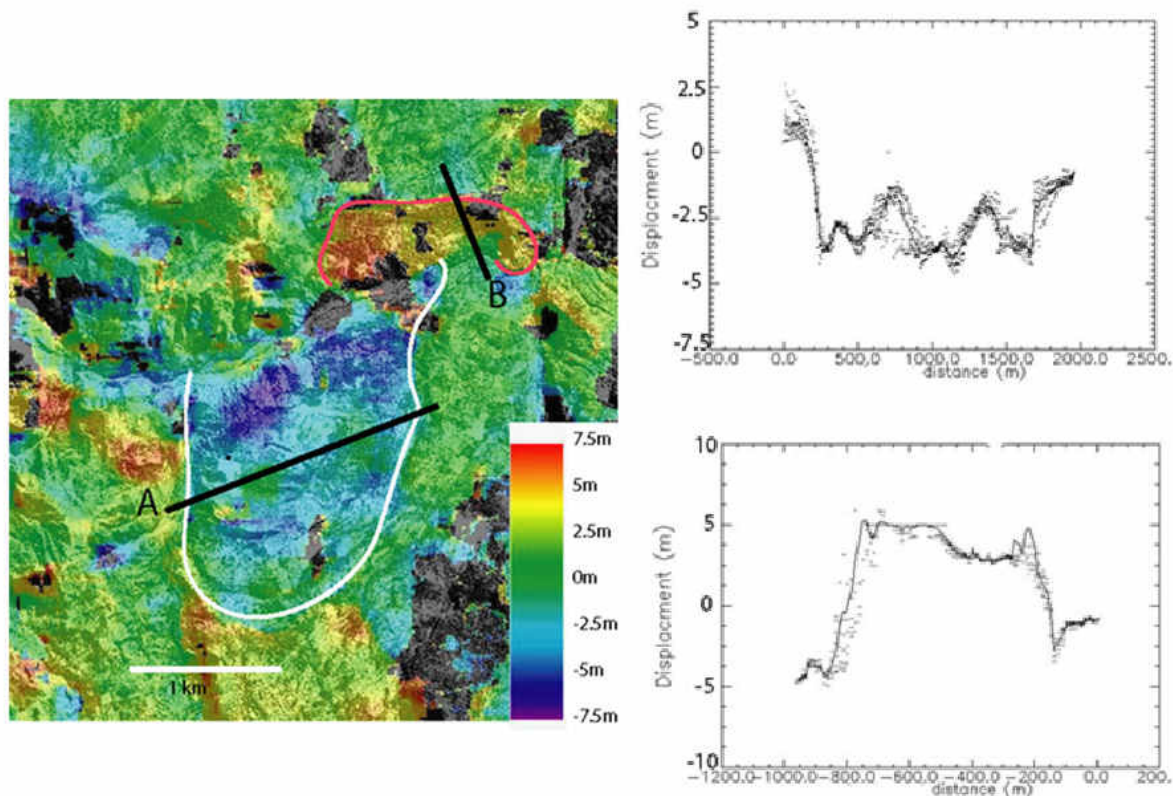


Fig. 4. a) Correlation Spot 5 and air-borne image (1997-2002) b) N-S displacement along profile A c) N-S displacement along profile B.

Both the geometry and cinematic evolution of the two landslides studied in the Hellbourg area by optical correlation are compatible with the InSAR results.

### 3. PERSPECTIVES

In further works (to be carried out in the framework of Mvterre-2 project, 2009-2013), we plan to use the presented techniques to the whole Cirque de Salazie and in particular Grand Ilet and Hellbourg landslides. For this second step of the MvTerre Project we have a particular interest for the data provided by new sensors: Formosat (optical), TerraSAR-X and Cosmo-Skymed (X-band radar).

Although (due to the vegetated cover of the area) we do not expect exploitable results with X-band interferometry, the high resolution and repeativity of those sensors should be suitable for multi-temporal image correlation in a displacement monitoring perspective.

The combination of results from the different sensors should provide 3D displacements and their evolution with time. Validation using the GPS network data and interpretation will be carried out, in particular in order to correlate the results with displacement acceleration in relation with seasonal conditions.

### REFERENCES

- Cruchet, M., 1994, p. 57. Approche des problèmes de stabilité des pentes à la Réunion. Rapport BRGM/RR-37962-FR.
- Delacourt, C., Allemand, P., Casson, B., Vadon, H., 2004, Velocity field of the "La Clapière" landslide measured by the correlation of aerial and QuickBird images, *Geophys. Res. Lett.*, 31, p. 15.
- Delacourt, C., Raucoules, D., Mouélic, S.L., Carnec, C., Feurer, D., Allemand, P., Cruchet, M., 2009, Observation of a large landslide on la reunion island using differential sar interferometry (JERS and Radarsat) and correlation of optical (Spot5 and aerial) images, *Sensors*, Volume 9, Issue 1, January 2009, Pages 616-630
- Massonnet, D., Feigl, K., 1998, Radar interferometry and its application to the changes of the Earth's surface, *Review of Geophysics*, 36 (4), pp 441-500.
- Michel, R., Avouac, J.-P., 2002, Deformation due to the 17 August 1999 Izmit, Turkey, earthquake measured from SPOT images, *Journal of Geophysical Research B: Solid Earth*, 107 (4), pp. 2-1.



## CASE STUDY 17

**Title:** Monitoring the Vallcebre landslide, Spain: from wire extensometers to GB-InSAR.

**Application:** Long term monitoring, characterization and modelling.

**Technique:** Surveying; Photogrammetry; GPS; Inclinometers; Wire-extensometers; Piezometers; Rain-gages; DInSAR; GBSAR.

**Main references:** This case study is based mainly in Corominas et al., 2005.

**Contributors:** UPC (Gili, J.)

### ABSTRACT

This case study presents the work carried out for monitoring the displacements of Vallcebre landslide (Eastern Pyrenees, Spain). The landslide, which extends over an area of 0,8 Km<sup>2</sup> and involves more than 20 million cubic meters, has experienced displacements as large as 1 m per year in some points. It has been periodically monitored since 1987, using a wide range of surface and in-hole techniques, successively along time: triangulation with theodolite, Terrestrial Photogrammetry, Electronic Distance Measurement, GPS, inclinometers and wire extensometers, piezometers, rain gages, satellite based DInSAR, and GBSAR. Somehow, the Vallcebre monitoring is a showroom of the evolution along the last decades of the measuring technologies, which have been applied in the landslide as a natural laboratory or as a demonstration site. After the cross-checking of the different systems and the assessment of their advantages and drawbacks, we conclude that, even though wire extensometers and inclinometers may have the highest precision, in practice, all the systems have their own role in giving meaningful data for the monitoring. When possible, the complementary use of some of them is strongly recommended..

### 1. INTRODUCTION

The Vallcebre landslide is located in the Eastern Pyrenees, 140 Km north of Barcelona, Spain. The situation, geological context of the landslide, and a complete geomorphological description can be found in Corominas et al. (2005). The mobilized material consists of a set of shale, gypsum and claystone layers gliding over a thick limestone bed. The average slope of the whole landslide is about 10°. The movement affects an area of 0.8 km<sup>2</sup>, which shows superficial cracking and distinct ground displacements.

The landslide is a translational slide with a stair-shape profile. Fig.1 shows a geomorphologic sketch of the landslide and the location of the monitored points and boreholes. The most active area is the lower unit, the toe of which is being eroded continuously by the Vallcebre torrent. Fig. 2 presents a geological cross-section of the landslide

As in most of real landslides, the structure and behaviour is not simple. Very often, the measurement of displacements is the simplest way to observe the evolution of a landslide and to analyze either the kinematics of the movement, the response to the triggering conditions (i.e. rainfall) or the efficiency of corrective measures. In certain situations, remedial works are not feasible for budget, technical or social constraints, and monitoring is one of the few mitigation actions that can be adopted. Several measuring techniques of these methods have been used in Vallcebre since 1987, beginning with

“classical” surveying and photogrammetry, and using GPS from 1995. In 1996, this site was included in the frame of the NEWTECH Project funded by the European Commission.

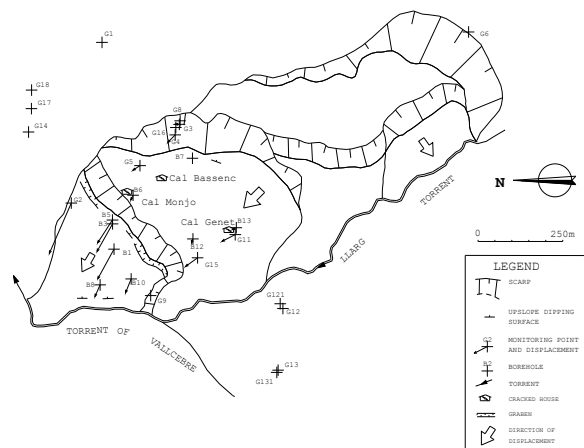


Fig. 1. Geomorphologic scheme and monitoring network of Vallcebre landslide. Base points (E3, E4 and E5) are outside this map, around 1 Km to the NW. Sample mean yearly rates of displacement are shown (enlarged by a factor of 100).

Fourteen boreholes were drilled in the slope and equipped with inclinometers, wire extensometers and piezometers. Recently, Radar Interferometry is being tested in the “Vallcebre natural Lab”.

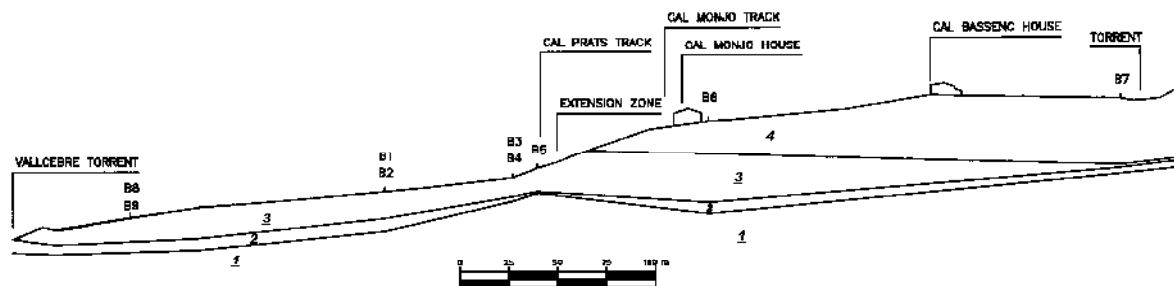


Fig. 2. Geological cross-section showing B1 to B9 instrumented boreholes. The materials are: (1) Limestone (bedrock), (2) Laminated clay siltstone, (3) Clay siltstone with gypsum micro-modules, (4) Gravel with silty matrix (superficial formation).

## 2. MONITORING SYSTEMS USED IN VALLCEBRE

In this section, a general overview of the monitoring techniques that have been used consecutively along the years in Vallcebre is described.

### 2.1 Terrestrial photogrammetry

The first monitoring network established on the landslide was based on terrestrial (or “close-range”) photogrammetry. A total of seven campaigns were performed at the landslide foot between 1987 and 1992.

Stereopairs were taken with a Wild P32 metric camera (fig.3). The ground control surveys were carried out by triangulation with Wild T2 theodolite, with an expected error of 2 mm. The stereocompilation was done with an analytical stereo-plotter Wild AC1 at the Institut Cartogràfic de Catalunya. The residuals after the least squares adjustment were around 9 mm (RMS), giving an error-to-distance ratio of 9 mm / 45 m (1/5000) for well defined points (as clear as pointing targets).

The results for each survey were the change in the coordinates of main points (displacements) and maps with contour lines. In general, the application of this method is not straight forward because of the difficulty to found the proper set-up with an adequate view over the hill slope. Also, dedicated and costly equipment has to be available. Regardless of that, the terrestrial photogrammetry provides information continuous over the space, but very scarce along time.

### 2.2 Triangulation and EDM

Since 1987, geodetic measurements with theodolite and EDM (Electronic Distance Measurement) were carried out. Since 1987 until 1992, triangulation was undertaken in the same area than the photogrammetry (lower unit, fig. 4 a). In the period 1988-1994, three

additional points in the middle unit were monitored with single distance variation measurements (fig. 4 b). During 1994 and 1995, a “triangulation” (fig. 4 c) from new base points E1 and E2 was extended to 16 points spread out through the whole landslide. The angle measurements were carried out with a Wild T2 theodolite, and the EDM with a Wild DIOR 3002S.

During the period 1987-1995, displacements as large as 8 m were observed at the lower unit, decreasing uphill. The rate of movement was strongly dependent on the rainfall. Rates of about 4 m per year were observed at certain points near the toe in the rainy years, while almost no displacement occurred during periods of drought. In the upper landslide units, the rate of displacement was significantly smaller, in the range of 10 to 30 cm/year. This stage allowed the identification of the most active sectors within the landslide and a rough assessment of the relation between rainfall and surface displacements was envisaged (Fig. 5).



Fig. 3. Wild P32 camera for terrestrial photogrammetry over a theodolite.

### 2.3 The GPS surveys

The GPS technology has been used since the early 1990s to monitor structural and terrain deformations (see i.e. Lovse et al., 1995). An overview of the applications of GPS to structural and terrain monitoring can be found in Gili et al. (2000).

Theoretically, GPS a priori errors have to be more balanced in the three axes, when compared to theodolite and EDM ellipses of error. This point was confirmed by the results of several monitoring campaigns, and led us to check the feasibility of using GPS techniques to perform systematic monitoring of the Vallcebre landslide. GPS preliminary tests were made in July 1994. Five baselines, from 800 to 1500 m, were observed with two Topcon Geodetic Receivers GP-R1, following the Static method. The results were promising due to easy-to-use, precision and matching with surveying measurements. Also, a movement simulation test was made in July 1994. A displacement of 10 mm North was imposed to the antenna, and the static observation repeated. The new computations gave a "movement" vector of  $\{\Delta E = 0 \text{ mm}, \Delta N = 16 \text{ mm}\}$ .

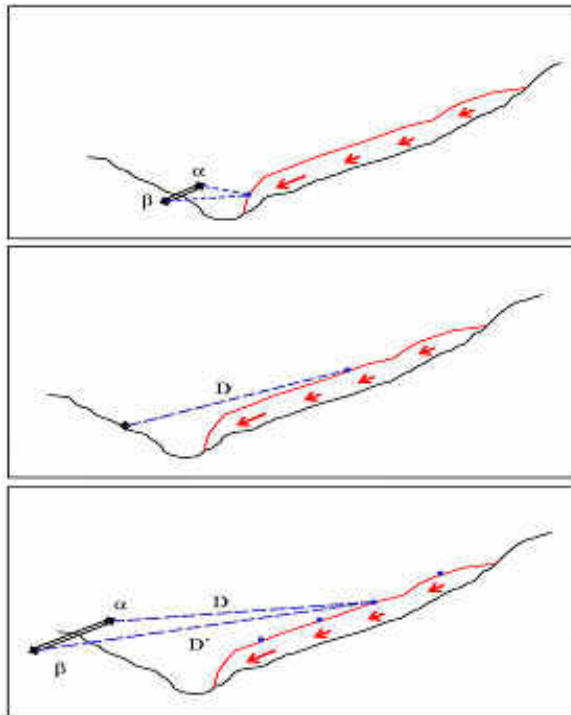


Fig. 4. Triangulation, single distance variation and triangulation schemes.

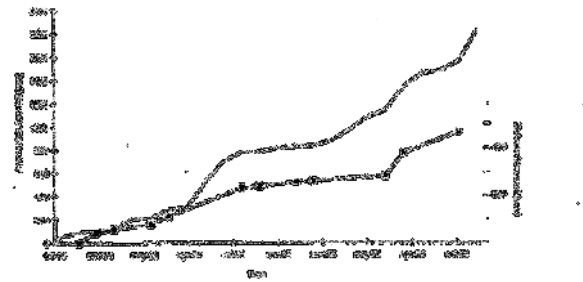


Fig. 5. First Relationship between accumulated rainfall (mm, solid line) and displacements (mm, right scale, line with dots).

The observed discrepancy (0 mm, 6 mm) falls within the expected error.

In December 1995, a complete EDM and GPS survey was carried out, to link the measurements taken with classical methods with the first campaign with GPS. Two Trimble 4000 SSI dual frequency receivers were used (Fig. 6).



Fig. 6. Examples of Vallcebre monitoring points with different antenna set-up methods: telescopic pole (left); tripod with optical plummet over an inclinometer borehole (right).

New base points were established (E3, E4 and E5, engraved directly on stable surface of the limestone layer) for stability and visibility requirements, and most of the old targets were recovered with minor modifications. As new points have been added since 1996, the monitoring network has now 40 points (Fig. 1 and 7): most of them are points engraved in rock blocks outcropping in the hillside or the top of the casing of the inclinometric boreholes; several steel rods, stakes and poles have been used as well. Four additional points are on the limestone around the sliding zone. These points were the fixed points used to check the GPS accuracy. This network allowed both the measurement of displacements and the comparison with movements obtained with the borehole equipment (inclinometers and wire extensometers).



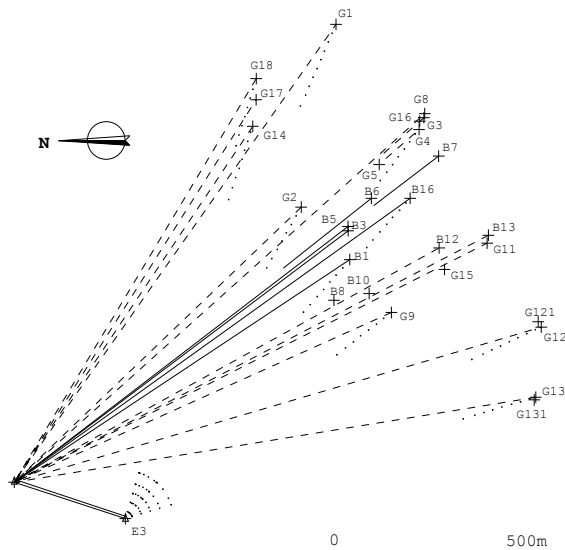


Fig. 7. Part of Vallcebre landslide GPS monitoring network: solid and dashed lines are respectively GPS-FS and GPS-RTK baselines during a given campaign.

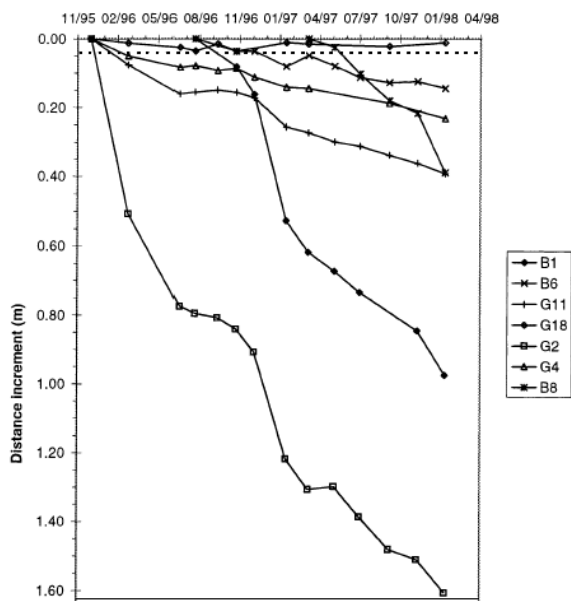


Fig. 8. Partial view of the GPS monitoring in Vallcebre. Displacement in plan from the initial position. A maximum error fringe (horizontal dotted line) has been added to highlight the tolerance threshold. Target numbers correspond to those indicated in figure 1.

The GPS methods used are either static (Fast-Static or Quick-Static) or kinematic (Real Time Kinematic), depending on the sky visibility of the points (the FS method is more robust against temporary signal interruption).

24 GPS campaigns have been carried out since 1995, with Trimble (4000 SSi) and Topcon (Hyper Pro) receivers. Part of the results can be appreciated in fig. 8.

## 2.4 In-hole measurements

Between July 1996 and April 1998, 16 boreholes were drilled in the slope, and equipped with inclinometers, wire extensometers and open standpipe piezometers. In 2004-2005 multipoint piezometers were installed in three additional boreholes.

Inclinometers and piezometers were standard devices. As an example, Fig. 9 shows a typical record from inclinometer B7, where the slip surface is clearly marked. Measurements were made every 2-3 weeks until they went out of order. On the other hand, a wire extensometer equipment was especially built following a previous design of Angeli et al. (1988). It consists of a protected steel wire anchored to the bedrock, below the slip surface, inside a piezometric pipe (fig. 10). The wire is kept in tension by means of a pulley and a counterweight of which rotation is continuously recorded using a potentiometer. This system has proven to work properly with landslide displacements much larger than those required to broken inclinometric pipes. Full details of the wire extensometer and the correction of the reading of the wire to derive the landslide displacement can be found in Corominas et al. (2000).

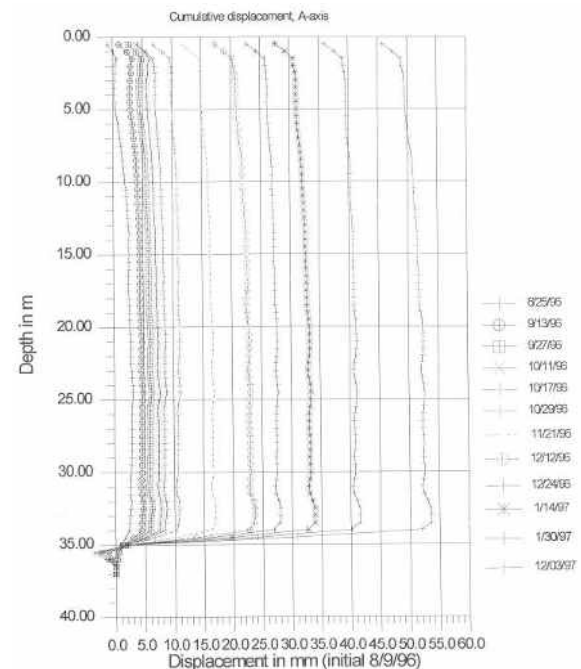


Fig. 9. Horizontal displacement profile obtained from inclinometer B7.

A main advantage is that the piezometers and wire extensometers were installed with an automatic recording system.



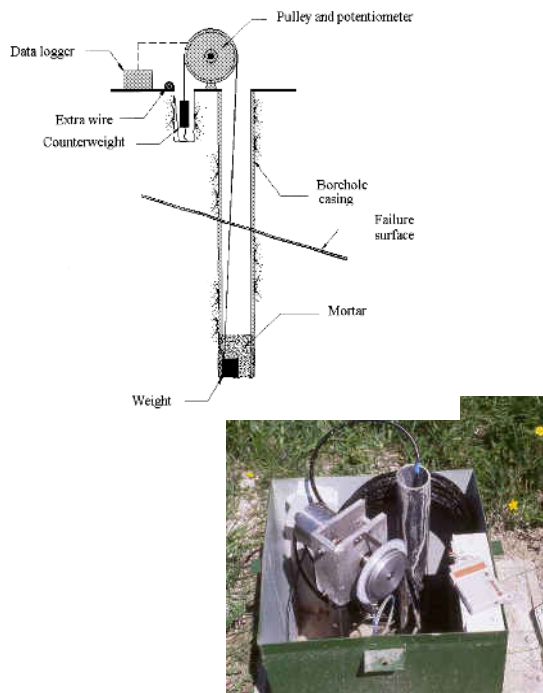


Fig. 10. Sketch of the borehole wire extensometer (Corominas et al., 2000). In the picture, the black cable for the piezometer can also be appreciated.

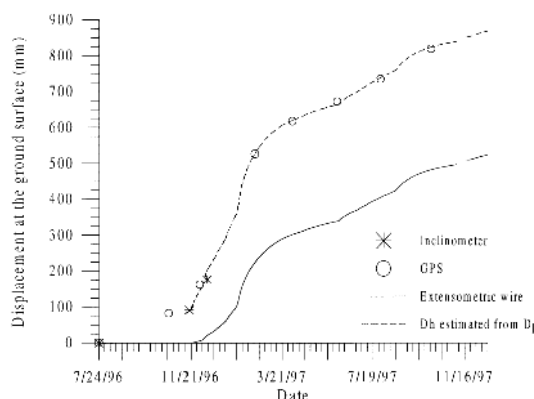


Fig. 11. Wire extensometer measurements at borehole B2. Each minor tick in the time axis corresponds to 1 week.

The readings were taken every 20 min and stored until they were downloaded: each month, manually, in the beginning; by GSM data transmission nowadays. Without a continuous measurement (fig. 11), crucial information would be lost near the concentrated rainfall periods characteristics of the Mediterranean climate. In Vallcebre it has been possible to establish that there is a perfect synchronism between changes in displacements and the groundwater level inside the slope.

### 2.5 Radar Interferometry

We are in the firsts steps for the application of both the DInSAR and the GBSAR techniques to landslide

monitoring, although some previous experiences exists (i.e. Squarzoni et al., 2003; Tarchi et al., 2003).

DInSAR: In November 2006 we installed seven corner reflectors to enhance the performance of DInSAR techniques (figure 12) with SAR data of the ASAR sensor within the ESA Envisat satellite mission. The cross-checking of the DInSAR results versus the displacements derived from the wire extensometers has been carried out along 2007 and 2008, and some preliminary results have been obtained (Gili et al., 2009).

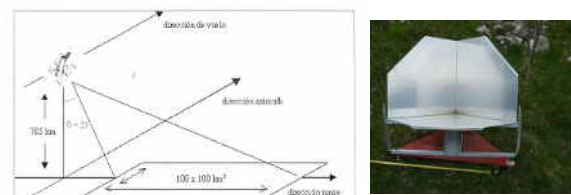


Fig. 12. The DInSAR technique (left, Crosetto et al, 2009) has been used to compute the displacements of several corner reflectors (right) since November 2006.

GBSAR first surveys: The Institute of Geomatics owns a GBSAR (Ground Based Synthetic Aperture Radar) system (IBIS-L model from Ingegneria Dei Sistemi – IDS; working in the Ku band, 17.1 GHz). Although the 2009/2010 wintertime has been quite crude, two preliminary GBSAR campaigns (February 9th and April) have been carried out in Vallcebre (figure 13), in order to start the GBSAR monitoring. This will help the SAFELAND project to assess the advantages and drawbacks of this technique as landslide monitoring and early warning system.



Fig. 13. The IBIS-L-IDS GBSAR system installed in front of the Vallcebre landslide by the Institute of Geomatics for the first tests. A number of mini-corners (right) were deployed in the scene.

## 3. SUMMARY AND CONCLUSION

It is out of the scope of this extended abstract to present all the cross-checks and precision evaluation for the different methods installed in Vallcebre. Some of these analyses can be found in the references. Only a few conclusions will be highlighted here.

The GPS measurements show better trends and stability than the EDM, at least with the Vallcebre conditions and equipment. The expected error ( $1\sigma$ ) established for a single GPS Fast Static positioning is 12 mm in plan and 18 mm in elevation.

The precision achieved with the GPS set-up in Vallcebre, although enough for the monitoring goals, may be increased using improved setting up of the antennas over the benchmarks and/or extended observation times.

On the other hand, the inclinometric measurements are precise within the 1-2mm, but the readings were only possible until 5 to 20 cm of total displacement for the top of the boreholes, due to the casing deformation in the failure zone. For the extensometers, the results show an excellent match with the inclinometers and the GPS (fig. 11). Compared with the GPS, the wire extensometer technique has the advantage of being an automatic and continuous measuring system which can be correlated with rainfall and piezometric heads. But the installation of in-hole devices had been possible only when additional funding was obtained in order to drill the boreholes and to instrument them. All the piezometers and the wire extensometers installed in Vallcebre are still operational. The wire cumulative displacements are of several meters since the installation in 1996. With readings each 20 minutes, especially during critical rainy events when other systems are not in operation, it is a very valuable data for the correlation with the rain and the water pressure inside the slope.

Regarding the SAR interferometry first results: the DInSAR computations in the 7 corner reflectors have exhibited a nice relationship with the wire extensometer measurements. The terrestrial GBSAR is only in the first phase and it needs some additional campaigns to establish their strengths and weaknesses.

Rates of displacement of the Vallcebre landslide were up to 130 mm/month at the lower unit during rainy periods, with an average of 30 mm/month. These figures fall to zero during the drought periods.

All the results are in fairly good accordance when adequate corrections and error considerations are done. The redundancy between methods is very advisable to detect malfunctions of the devices or to cover gaps with no data. The different methods should not be considered as excluding alternatives but as complementary systems to be applied progressively or in different areas.

## REFERENCES

Angeli, M.G., Gasparetto, P., Silvano, S., Tonetti, G. (1988). "An automatic recording system to detect the critical stability of slopes". Proc. 5th Int. Symposium on Landslides, Lausanne, Vol. 1. A.A. Balkema, Rotterdam, pp.375-378.

Corominas, J., Moya, J., Lloret, A., Gili, J.A., Angeli, M.G., Pasuto, A. and Silvano, S. (2000). "Measurement of landslide displacements using a wire extensometer". Engineering Geology 55, pp. 149-166.

Corominas, J., Moya, J., Ledesma, J., Lloret, J., Gili, J.A. (2005). "Prediction of ground displacements and velocities from groundwater level changes at the Vallcebre landslide (Eastern Pyrenees, Spain)". Landslides 2, pp. 83-96.

Crosetto M., Monserrat O., Pozzoli A. & Gili J.A. (2009). "Detección y medida de deformaciones del terreno utilizando interferometría diferencial SAR" (in Spanish). Proceed. VII Simposio Nacional sobre Taludes y Laderas Inestables, Barcelona, oct. 2009.

Gili, J.A.; Corominas, J., Rius, J. (2000). "Using Global Positioning System Techniques in landslide monitoring". Engineering Geology 55, pp. 167-192.

Gili, J.A., Crosetto, M. & Serral, D. (2009). "Reflectores Radar en el deslizamiento de Vallcebre. Validación y primeros resultados" (in Spanish). Proceed. VII Simposio Nacional sobre Taludes y Laderas Inestables, Barcelona, oct. 2009.

Lovse, J.W., Teskey, W.F., Lachapelle, G., Cannon, M.E. (1995). "Dynamic Deformation Monitoring of Tall Structure Using GPS Technology". Journal of Surveying Engineering - ASCE. Vol. 121, No. 1, pp. 35-40.

Squarzoni, C., C. Delacourt, P. Allemand (2003). "Nine years of spatial and temporal evolution of the La Valette landslide observed by SAR interferometry". Engineering Geology, Vol. 68, 1-2, pp. 53-66.

Tarchi, D, N. Casagli, R. Fanti, D.D. Leva, G. Luci, A. Pasuto (2003). "Landslide monitoring by using ground-based SAR interferometry: an example of application to the Tessina landslide in Italy". Engineering Geology, Vol. 68, 1-2, pp. 15-30.

## **DISCUSSION**



## 4. DISCUSSION

### 4.1. ADVANTAGES AND LIMITATIONS OF EACH METHOD

The main advantages and limitations of each of the techniques described in previous chapters are discussed in this section. These characteristics are basically mentioned in terms of spatial and temporal resolution, accuracy, spatial coverage, cost, etc. This chapter is intended to be a link or an introductory section to the deliverable 4.4 (*“Guidelines for the selection of appropriate remote sensing technologies for monitoring different types of landslides”*) of the SafeLand project.

Table 24 : Advantages and limitations of passive optical sensors.

	Advantages	Limitations
Ground based imaging	<ul style="list-style-type: none"> <li>- High spatial and temporal resolution (on demand, e.g. 50 pixels per m2 at 1 picture per day)</li> <li>- Large coverage on steep slopes</li> <li>- Images obtained at a low cost</li> <li>- High flexibility (i.e. easy data acquisition and high portability)</li> </ul>	<ul style="list-style-type: none"> <li>- Limited coverage in gentle slopes</li> <li>- Inter-visibility is required (optical line of sight)</li> <li>- Others: Solar illumination affects datasets, e.g. presence of shadows in the pictures; data acquisition is not possible during night.</li> </ul>
Airphotos	<ul style="list-style-type: none"> <li>- Very large coverage on gentle slopes</li> <li>- Historical record available: Images since the middle of the XX century</li> <li>- Very high spatial resolution</li> </ul>	<ul style="list-style-type: none"> <li>- Limited temporal resolution</li> <li>- Inter-visibility is required (optical line of sight)</li> <li>- Others: reduced coverage in steep slopes and cliffs (steep slopes are misrepresented)</li> </ul>
Satellite imaging	<ul style="list-style-type: none"> <li>- Very large spatial coverage (up to several thousand km2)</li> <li>- Cost: low resolution images (e.g. landsat, ASTER) can be obtained at a low price</li> <li>- Short revisit times with very high resolution pointable sensors</li> <li>- Others: Historical record available: Images since 70's; Panchromatic / multispectral images are frequently used</li> </ul>	<ul style="list-style-type: none"> <li>- Low spatial resolution of historical images (pixels at meter or decameter level)</li> <li>- In some sensors, low temporal resolution (monthly acquisition)</li> <li>- Low accuracy (depending on the sensor)</li> <li>- Inter-visibility is required (optical line of sight)</li> <li>- Others: low coverage in steep slopes and cliffs (i.e., steep slopes are misrepresented); Post processing is needed (filtering)</li> <li>- Image quality depends on atmospheric conditions</li> <li>- Very high resolution images from commercial satellites (e.g. QuickBird, IKONOS, GeoEye) are very expensive</li> <li>- Geometric distortions due to different view angles of pointable sensors.</li> </ul>

Table 25 : Advantages and limitations of active optical sensors.

	Advantages	Limitations
<b>Electronic Distance Meter</b>	<ul style="list-style-type: none"> <li>- High accuracy (millimeter level).</li> <li>- Temporal and spatial resolution on demand</li> <li>- Considerable maximum range (up to several km)</li> <li>- Others: 3D information; High flexibility (i.e., easy set-up and portability); Feasibility of automation of the process (e.g. using a robotic total station); suitable for early warning systems</li> </ul>	<ul style="list-style-type: none"> <li>- Low resolution (singular measurements do not provide a complete image of the object)</li> <li>- Others: Intervisibility is required (optical line of sight)</li> </ul>
<b>Terrestrial Laser Scanners</b>	<ul style="list-style-type: none"> <li>- High resolution (e.g. 200 point per m2).</li> <li>- Good accuracy (centimeter level)</li> <li>- Large coverage on steep slopes.</li> <li>- Others: 3D information; High flexibility (i.e., easy set-up and portability)</li> </ul>	<ul style="list-style-type: none"> <li>- Relatively low maximum range (&lt; 700m)</li> <li>- Others: Post processing is needed (aligning, filtering, etc.); intervisibility is required (optical line of sight)</li> </ul>
<b>Aerial Laser Scanners (ALS)</b>	<ul style="list-style-type: none"> <li>- High resolution in gentle surfaces</li> <li>- Very large coverage (thousand km2)</li> <li>- Others: 3D information; fast data acquisition; considerable maximum range (few thousand km)</li> </ul>	<ul style="list-style-type: none"> <li>- Centimeter to decimeter accuracy level</li> <li>- Post processing is needed (filtering)</li> <li>- Others: Post processing is needed (aligning, filtering, etc.); reduced coverage in steep slopes (cliffs are misrepresented)</li> </ul>

Table 26 : Advantages and limitations of active microwave sensors.

	Advantages	Limitations
<b>Interferometric Radar Distance Meters</b>	<ul style="list-style-type: none"> <li>- Very high accuracy: sub millimeter level.</li> <li>- High range (up to 5km)</li> <li>- High temporal resolution (on demand, up to 1 measurements each 10 sec.)</li> <li>- Others: not affected by atmospheric artifacts; suitable for early warning systems</li> </ul>	<ul style="list-style-type: none"> <li>- Low spatial resolution (singular measurements do not provide a complete image of the object)</li> <li>- Others: a heavy setup is needed in case of real time monitoring</li> </ul>
<b>Ground Based InSAR</b>	<ul style="list-style-type: none"> <li>- Very high temporal resolution (on demand) when using a fixed GB-SAR (e.g. 1 measurement each 10min), allowing for real time monitoring</li> <li>- Very high accuracy (millimeter level)</li> <li>- Range up to 3 km</li> <li>- High spatial resolution (pixels at a meter level); Ability to monitor movements over a long period; suitable for early warning systems</li> </ul>	<ul style="list-style-type: none"> <li>- Others: Loss of coherence in vegetated areas; Atmospheric artifacts are possible; Post processing is needed. A heavy setup is needed in case of real time monitoring</li> </ul>



<b>DInSAR</b>	<ul style="list-style-type: none"> <li>- Large coverage</li> <li>- Others: Historical record: images available since 1991; Ability to monitor movements over a long period; Only 2 timages are needed; No cost installation and maintenance of equipment on the ground</li> </ul>	<ul style="list-style-type: none"> <li>- Low spatial resolution, specially in areas with steep slopes or presence of vegetation</li> <li>- Low temporal resolution (monthly values). Not suitable for fast movements</li> <li>- Others: Loss of coherence in vegetated areas and when dealing with fast movements; Atmospheric artifacts are possible; Post processing is needed; A Digital elevation model is needed; Time decorrelation problems</li> </ul>
<b>Advanced DInSAR</b>	<ul style="list-style-type: none"> <li>- Application to different scales of study</li> <li>- High accuracy in the measurement of the displacements (mm level).</li> <li>- Others: Historical record: images available since 1991; Ability to monitor movements over a long period; No cost installation and maintenance of equipment on the ground</li> </ul>	<ul style="list-style-type: none"> <li>- Low spatial resolution, specially in areas with steep slopes or presence of vegetation</li> <li>- Low temporal resolution (monthly values). Not suitable for fast movements</li> <li>- Others: Requires the presence of fixed points on several sequences of radar images; Landslide displacements are measured parallel to the satellite Line Of Sight; Loss of coherence in vegetated areas; Atmospheric artifacts are possible; Post processing is needed; The cost can be substantial when dealing with high resolution datasets; Requires a large set of images</li> </ul>

Table 27 : Advantages and limitations of geophysical investigations.

	<b>Advantages</b>	<b>Limitations</b>
<b>Ground-Based</b>	<ul style="list-style-type: none"> <li>- Higher resolution than aerial approaches.</li> <li>- Cheaper than boreholes and most methods are non-intrusive.</li> <li>- Derives from the surface information about subsurface structures and provides either curves (1D), vertical sections (2D), or cubes (3D) of the mapped parameters.</li> <li>- Can gather several types of parameters (elastic, electrical, electromagnetic, etc).</li> <li>- Wide range of portable and light instruments nowadays and several standardized software.</li> <li>- Should be used to plan location of boreholes for ground proofing (cost reduction).</li> <li>- Should be used to interpolate structures between boreholes for 2D-3D mapping and in order to catch the lateral variability of the ground.</li> <li>- Hydrogeophysics is in full expansion and geophysics can help understand the hydrology of a site.</li> <li>- Can be used for monitoring.</li> </ul>	<ul style="list-style-type: none"> <li>- May be difficult to relate measured parameters (elastic, electrical, etc) to soil/rock properties.</li> <li>- Measurements should always be calibrated with borehole testing and geophysical logging.</li> <li>- Often non-uniqueness of the results which should always be provided with errors and modeling controls. Not sufficient to produce “nice” color maps and state that one color is one type of soil: not that simple.</li> <li>- Some approaches are still heavy to carry out and may be challenging on difficult ground (e.g., some landslide sites).</li> <li>- Still heavy equipment and requires electrical power (batteries, etc).</li> <li>- Application for site monitoring is still a subject of research for several methods, though some are quite standard already (e.g., micro-seismics).</li> <li>- Geophysical results are difficult to interpret if not done in tight cooperation with other geoscientists (geology, geotechnique, hydrogeology, glaciology, etc).</li> </ul>

<b>Aerial</b>	<ul style="list-style-type: none"> <li>- Wide coverage, several parameters recorded at the same time</li> <li>- Only remote sensing technique that can look into the subsurface (not just surface)</li> </ul>	<ul style="list-style-type: none"> <li>- Application for site monitoring is still a subject of research</li> </ul>
---------------	---	--

Table 28 : Advantages and limitations of geotechnical methods.

	<b>Advantages</b>	<b>Limitations</b>
<b>Extensometer</b>	<p><b>Probe:</b></p> <ul style="list-style-type: none"> <li>- Low cost survey</li> </ul> <p><b>Fixed borehole:</b></p> <ul style="list-style-type: none"> <li>- High accuracy</li> </ul> <p><b>Wire:</b></p> <ul style="list-style-type: none"> <li>- High accuracy</li> <li>- Others: simple device; real time monitoring is possible; low-cost device</li> </ul>	<p><b>Probe:</b></p> <ul style="list-style-type: none"> <li>- Measurements are less precise than using a fixed borehole;</li> <li>- A borehole with casing is required</li> </ul> <p><b>Fixed borehole:</b></p> <ul style="list-style-type: none"> <li>- A borehole with casing is required</li> </ul> <p><b>Wire:</b></p> <ul style="list-style-type: none"> <li>- A borehole with casing is required</li> </ul>
<b>Inclinometer</b>	<p><b>Manual probe:</b></p> <ul style="list-style-type: none"> <li>- Low cost survey</li> </ul> <p><b>In-place:</b></p> <ul style="list-style-type: none"> <li>- Rapid automatic data logging; real time monitoring is possible</li> <li>- Remote control</li> </ul> <p><b>Automatic probe:</b></p> <ul style="list-style-type: none"> <li>- High accuracy</li> <li>- Remote control; real time monitoring is possible</li> </ul>	<p><b>Manual probe:</b></p> <ul style="list-style-type: none"> <li>- Post processing is needed, correction of systematic errors</li> <li>- No continuous recording of the displacement</li> <li>- Access limited due to a localized deformation of the casing of only a few centimeters</li> <li>- A borehole with 4 grooves casing is required</li> </ul> <p><b>In-place:</b></p> <ul style="list-style-type: none"> <li>- Great complexity; Cost of the instrumentation</li> <li>- Long term stability</li> <li>- A borehole with 4 grooves casing is required</li> </ul> <p><b>Automatic Probe:</b></p> <ul style="list-style-type: none"> <li>- Costs of the instrumentation</li> <li>- Access limited due to a localized deformation of the casing of only a few centimeters</li> <li>- A borehole with 4 grooves casing is required</li> </ul>

<p style="text-align: center;"><b>Piezometer</b></p>	<p><b>Observation well:</b></p> <ul style="list-style-type: none"> <li>- Can be more economic</li> </ul> <p><b>Open standpipe:</b></p> <ul style="list-style-type: none"> <li>- High accuracy</li> <li>- Reliability of collected data</li> <li>- Long-term monitoring</li> <li>- Can be used to evaluate the hydraulic conductivity</li> <li>- Can be converted to diaphragm piezometer</li> </ul> <p><b>Twin-tube hydraulic:</b></p> <ul style="list-style-type: none"> <li>- High accuracy</li> <li>- Inaccessible components have no moving parts</li> <li>- Reliable</li> <li>- Long successful performance record</li> <li>- Piezometer cavity can be flushed</li> <li>- Can be used to measure permeability</li> </ul> <p><b>Pneumatic:</b></p> <ul style="list-style-type: none"> <li>- High accuracy</li> </ul> <p><b>Vibrating wire:</b></p> <ul style="list-style-type: none"> <li>- Easy readings</li> <li>- Short time lag</li> <li>- No freezing problems</li> <li>- Independence of reading elevation from the height where is placed the piezometer</li> <li>- Possibility to measure negative pore water pressure</li> </ul> <p><b>Electrical resistance:</b></p> <ul style="list-style-type: none"> <li>- Easy readings</li> <li>- Short time lag</li> <li>- No freezing problems</li> <li>- Independence of reading elevation from the height where is placed the piezometer</li> <li>- Possibility to measure negative pore water pressure</li> </ul>	<p><b>Observation well:</b></p> <ul style="list-style-type: none"> <li>- Single layer aquifer</li> <li>- Time-lag between the variation of piezometric level in the aquifer and the respective variation in the piezometer</li> <li>- A borehole with casing is required</li> </ul> <p><b>Open standpipe:</b></p> <ul style="list-style-type: none"> <li>- Device subject to damage during the installation and vertical compression</li> <li>- A borehole is required (+standpipe)</li> </ul> <p><b>Twin-tube hydraulic:</b></p> <ul style="list-style-type: none"> <li>- Application generally limited to long-term monitoring of pore water pressure in embankments dams</li> <li>- Tubing must not be significantly above minimum piezometric elevation</li> <li>- Periodic flushing may be required</li> <li>- A borehole is required (+twin tubes)</li> </ul> <p><b>Pneumatic:</b></p> <ul style="list-style-type: none"> <li>- Membrane extroversion reduces volume available to interstitial water (pore water pressure increases)</li> <li>- A borehole is required (+twin tubes)</li> </ul> <p><b>Vibrating wire:</b></p> <ul style="list-style-type: none"> <li>- Wire subject to corrosion phenomena</li> <li>- Zero drift</li> <li>- A borehole is required</li> </ul> <p><b>Electrical resistance:</b></p> <ul style="list-style-type: none"> <li>- A borehole is required</li> </ul>
<p style="text-align: center;"><b>Earth pressure cells</b></p>	<ul style="list-style-type: none"> <li>- High accuracy</li> <li>- Direct measurement</li> <li>- Not post processing is needed.</li> </ul>	<ul style="list-style-type: none"> <li>- Low spatial resolution (singular measurements do not provide a complete image of the object)</li> </ul>

<b>Multiparametric in place systems (DMS)</b>	<ul style="list-style-type: none"> <li>- Multiparametric continuous monitoring in the same casing/borehole</li> <li>- 2D/3D deformation analysis</li> <li>- Early Warning applications</li> <li>- High adaptability of the monitoring column to larger deformations</li> <li>- Easy installation (set-up);</li> <li>- The instrumentation can be recover after the monitoring period</li> <li>- Modularity</li> </ul>	<ul style="list-style-type: none"> <li>- Cost of the instrumentation (in particular 3D versions of the DMS)</li> <li>- A borehole is required</li> </ul>
---	---	--

Table 29 : Advantages and limitations of other techniques.

	<b>Advantages</b>	<b>Limitations</b>
<b>GNSS</b>	<ul style="list-style-type: none"> <li>- High positioning accuracy is possible (mm level) with precision GNSS</li> <li>- Spatial and temporal resolution on demand</li> <li>- Others: Intervisibility is not required.; low cost; easy data acquisition; suitable for early warning systems</li> </ul>	<ul style="list-style-type: none"> <li>- Low spatial resolution (singular measurements do not provide a complete image of the object)</li> <li>- Others: low signal when data acquisition performed in narrow valleys or close to buildings, trees, etc.; More elaborated signal post processing is required for millimeter level accuracy</li> </ul>
<b>Core Logging</b>	<ul style="list-style-type: none"> <li>- Direct observation of subsurface materials</li> <li>- Direct observation of shear surface; allows for geological and geotechnical investigations (see section 5.1.5)</li> </ul>	<ul style="list-style-type: none"> <li>- Low spatial resolution (singular measurements do not provide a complete image of the object)</li> <li>- Very high cost</li> </ul>

## 4.2. APPROPRIATE TECHNIQUES ACCORDING TO LANDSLIDE SITUATION

Landslides occur within different soil and rock contexts, destabilized by different internal settings, triggered by different external factors including human activities (Terzaghi, 1950; Jaboyedoff & Derron, 2005; and more generally the Deliverable 1.1 of the SafeLand project).

With the case studies presented in this document, the reader will get an idea of the effective implementation, the results that can be obtained and the reliability of these techniques in specific situations. In addition to this document, Deliverable 4.4 of the SafeLand project (*“Guidelines for the selection of appropriate remote sensing technologies for monitoring different types of landslides”*) is specifically dedicated to this topic.

### 4.3. INNOVATIVE TECHNIQUES AND FURTHER DEVELOPMENTS

Researchers always aim to increase the level of the knowledge to overcome the actual technical limitations, either by developing new (1) algorithms, (2) softwares or (3) instrumentations. One or two examples of innovative techniques for each of these categories are presented below.

The innovative applications (e.g. methods, algorithms, hardware or software) will be discussed in detail in Deliverable 4.5 of the SafeLand project (*“Evaluation report on innovative monitoring and remote sensing methods and future technology”*).

#### (a) Algorithm developments

An important challenge in DInSAR for landslide studies is to increase the number of permanent scatterers or targets in non-urban areas, and much of the research is focused on development of algorithms that can process and interpret the increased volume of data more efficiently. For example, the development of the SqueeSAR™ algorithm by T.R.E. (Novali et al., 2009) allows to drastically increase the density of points in mountainous areas (Figure 157), keeping a very high spatial resolution.

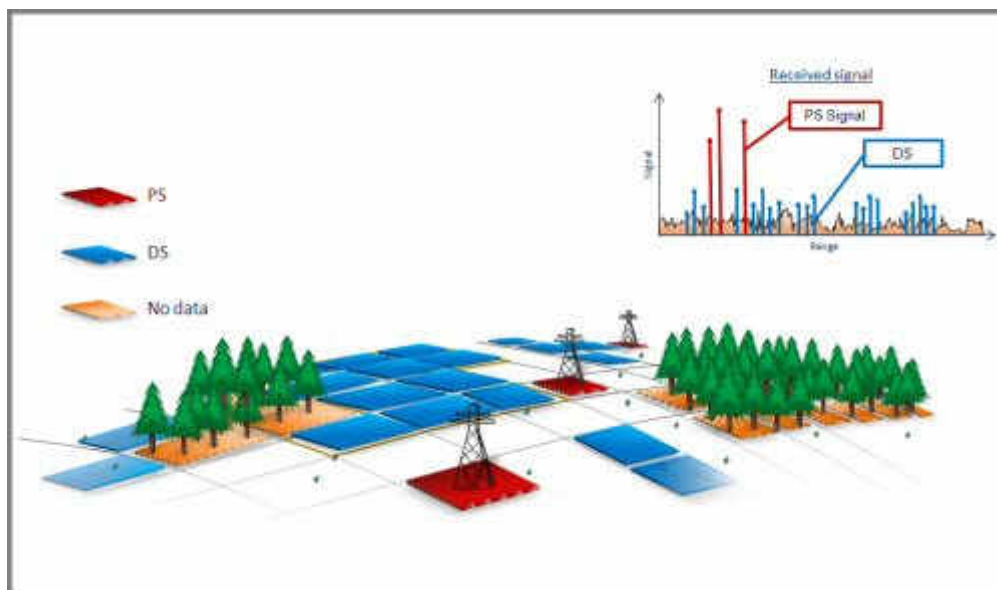


Figure 157: Localization of scatterers, using the SqueeSAR™ algorithm (from Novali et al., 2009). The high density of points allows for a better delimitation and interpretation of SAR data for landslide investigations in non-urban areas (T.R.E. website, 2010. Available at <http://www.treuropa.com/treuropa/tabid/178/Default.aspx>).

#### (b) Software developments

Softwares for radar images and interferometry processing have also experienced rapid development during the last decade. Current efforts are focused on creating more user-friendly softwares, allowing a democratization of methods by non-specialists. For instance, ESA in collaboration with the Delft University of Technology is currently developing a complete toolbox for radar images and interferometry processing, which will soon be available for free, NEST-DORIS (Figure 158, Marinkovic et al., 2009).

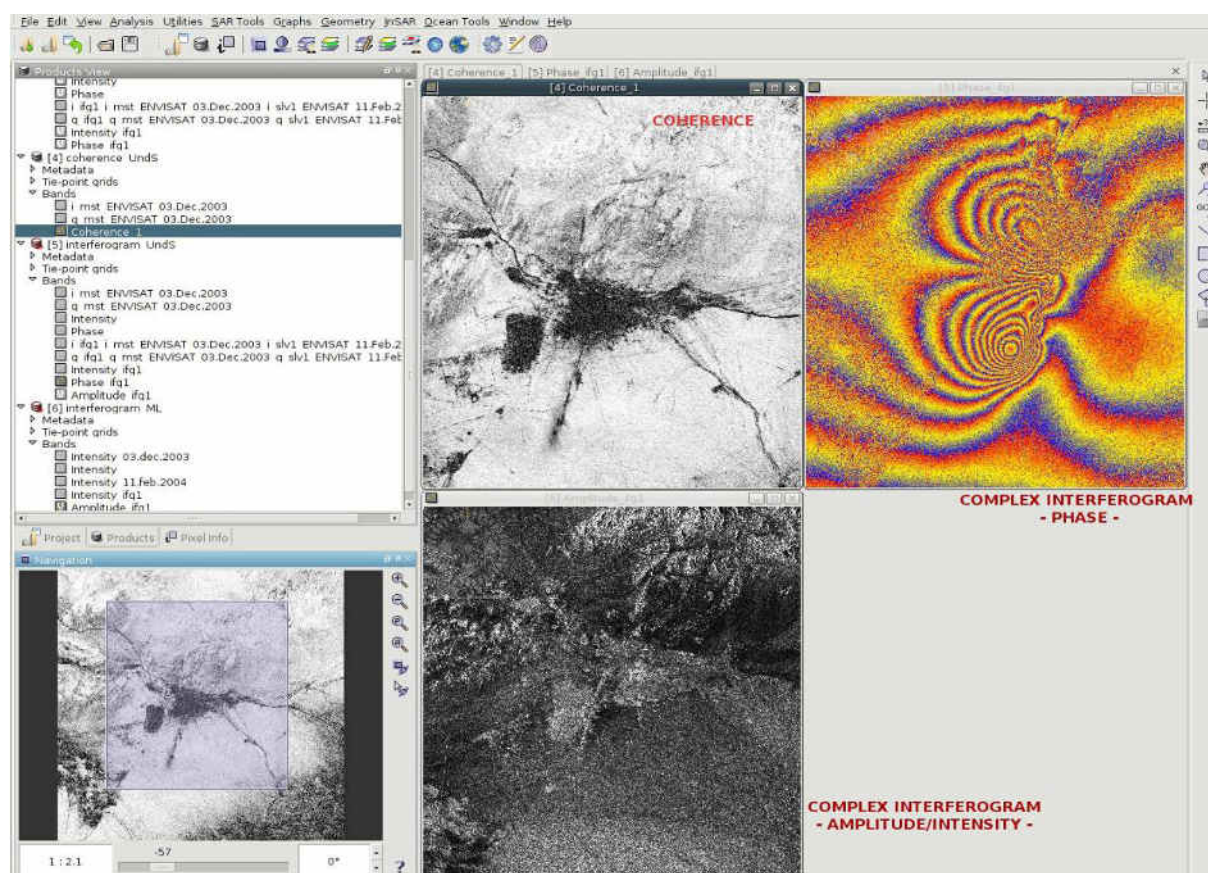


Figure 158 : Early version of the software NEST-DORIS, demonstrated during the Fringe 2009 (Marinkovic et al., 2009)

Another example is the new software Coltop 3D, developed at the IGAR (University of Lausanne) for post-processing of TLS datasets and now available in its commercial version (contact: <http://www.terranum.ch>). It allows one to work on huge dataset (up to 200 million of points) and to perform structural analysis, providing discontinuities identification, dips measurement and color coding of rock face (Jaboyedoff et al., 2007).

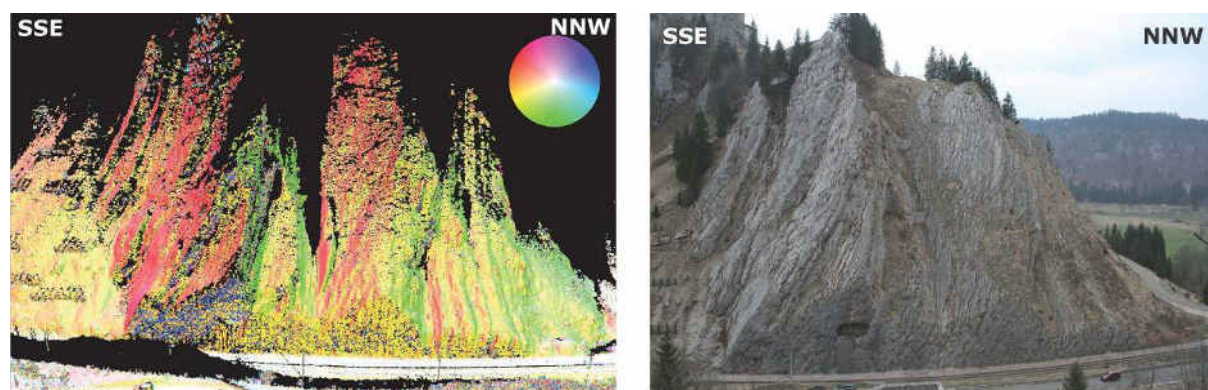


Figure 159 : Illustration of a TLS dataset imported in Coltop 3D (left) and the field corresponding (right) (Carrea et al., 2010)



### (c) Instrumental developments

Hardware and tools for remote sensing and monitoring are continuously being improved. For example, a new TLS developed by Optech, the LYNX Mobile Mapper, allows scanning transportation corridors from a car by simply scanning along the road (Figure 160 and Figure 161). It can be very useful to assess the rockfall susceptibility along transportation corridors, saving a lot of time for the point cloud acquisition and post-processing (Carrea et al., 2010).



Figure 160 : Up. Point cloud acquired thanks to LYNX Mobile Mapper, highlighting main discontinuity sets. Low. Corresponding outcrop on field. (Carrea et al., 2010)



Figure 161 : LYNX Mobile Mapper apparel on the roof of the car. (Optech website, 2010. Available at [http://www.optech.ca/press\\_LYNX\\_Release.htm](http://www.optech.ca/press_LYNX_Release.htm))



## CONCLUSIONS



## 5. CONCLUSIONS

Since the 90's, innovative applications in monitoring and remote sensing techniques have been developed. The possibility of acquiring terrain information (height, displacement, land use, etc.) with high accuracy and high spatial resolution is currently opening up new ways of visualizing, modelling and interpreting Earth surface processes such as landslides, debris flows, rockfalls, etc. These new sensors can be mounted on terrestrial, aerial and/or satellite instrumentals, covering a full spectra of accuracies, resolutions, points of view, etc. Geophysical and geotechnical investigations can also bring additional information on sub-surface processes and movements, which are essential for monitoring and early-warning systems.

The main part of this deliverable provides a comprehensive review of the state of the art for different techniques (remote sensing and ground-based) used for landslide detection, fast characterization, rapid mapping and long-term monitoring. Together with the technical information, an effort was made to provide examples of applications of each technique to specific landslide case studies, as described in chapter 3.

This Deliverable attempts to provide useful information not only to researchers, but also to stakeholders who look for a better understanding of important questions related to landslide hazard and risk, namely *where, how and when a landslide will occur?*





## REFERENCES



## 6. REFERENCES

### 6.1. GENERAL REFERENCES WITHIN THE DELIVERABLE

- Carrea, D., Longchamp, C., Jaboyedoff, M., Choffet, M., Derron, M.-H., Michoud, C., Pedrazzini, A., Conforti, D., Leslar, M., Tompkinson, W., 2010. Fast rockfall hazard assessment along a road section using the new LYNX Mobile Mapper Lidar. EGU General Assembly, EGU2010-5178.
- Jaboyedoff, M. & Derron, M.-H. 2005. Hazard assessment within an Integrated Risk Assessment Process for Landslides (IRAPL). Proc., International Conference on Landslide Risk Management, Vancouver, Balkema. in press.
- Jaboyedoff M., Metzger R., Oppikofer T., Couture R., Derron M.-H., Locat J. Turmel D., 2007. New insight techniques to analyze rock-slope relief using DEM and 3D-imaging cloud points: COLTOP-3D software. In Eberhardt, E., Stead, D and Morrison T. (Eds.): Rock mechanics: Meeting Society's Challenges and demands (Vol. 1), Taylor & Francis. pp. 61-68.
- Marinkovic, P., Hanssen, R., Minchella, A., Engdahl, M., 2009. NEST-DORIS: InSAR extension for NEST. In: Fringe 2009 Workshop. Advances in the Science and Applications of SAR Interferometry. Organized by the European Space Agency. ESA ESRIN Frascati (Italia), 30<sup>th</sup> November – 4<sup>th</sup> December 2009.
- Novali, F., Ferretti, A., Fumagalli, A., Rocca, F., Prati, C., Rucci, A., 2009. The Second Generation PSInSAR approach: SqueeSAR. In: Fringe 2009 Workshop. Advances in the Science and Applications of SAR Interferometry. Organized by the European Space Agency. ESA ESRIN Frascati (Italia), 30<sup>th</sup> November – 4<sup>th</sup> December 2009.
- Optech website, 2010. Available at [http://www.optech.ca/press\\_LYNX\\_Release.htm](http://www.optech.ca/press_LYNX_Release.htm)
- SafeLand deliverable 1.1, 2010. Landslide triggering mechanisms in Europe – Overview and State of the Art. Deliverable 1.1 of the European project SafeLand. Edited in 2010 by Crosta G., Agliardi F., Frattini P., Sosio R.
- Terzaghi, K., 1950. Mechanism of Landslides. The Geological Society of America, Engineering Geology (Berkley) Volume. Pp 83-123
- T.R.E. website, 2010. Available at <http://www.treuropa.com/treuropa/tabid/178/Default.aspx>

### 6.2. SPECIFIC REFERENCES FOR THE CHAPTER 2A

- Aizu, Y., and T. Asakura (1987), Principles and development of spatial filtering velocimetry, *Applied Physics B: Lasers and Optics*, 43(4), 209-224.
- Ando, S. (1986), A velocity vector field measurement system based on a spatio-temporal image derivative, *Transactions of the Society of Instrument and Control Engineers*, 22(12), 1330-1336.
- Arattano, M., and P. Grattoni (2000), Using a fixed video camera to measure debris flow surface velocity, in *Debris-Flow Hazards Mitigation: Mechanics, Prediction, and Assessment*, edited by G. F. Wieczorek and N. D. Naeser, pp. 273-281, Balkema., Rotterdam.
- Arattano, M., and L. Marchi (2000), Video-derived velocity distribution along a debris flow surge, *Physics and Chemistry of the Earth, Part B: Hydrology, Oceans and Atmosphere*, 25(9), 781-784.
- ASTER-GDEM-VALIDATION-TEAM (2009), *ASTER Global DEM Validation Summary ReportRep.*, 28 pp, METI/ERSDAC NASA/LPDAAAC USGS/EROS.
- Avrithis, Y. S., A. D. Doulamis, N. D. Doulamis, and S. D. Kollias (1999), A Stochastic Framework for Optimal Key Frame Extraction from MPEG Video Databases, *Comput Vis Image Und*, 75(1-2), 3-24.
- Batz, M., C. Hoffmann, and G. Willhauck (2008), *Progressing from object-based to object-oriented image analysis*, edited, pp. 29-42.
- Baldi, P., M. Fabris, M. Marsella, and R. Monticelli (2005), Monitoring the morphological evolution of the Sciara del Fuoco during the 2002-2003 Stromboli eruption using multi-temporal photogrammetry, *ISPRS Journal of Photogrammetry and Remote Sensing*, 59(4), 199-211.
- Baltsavias, E. P. (1999), On the performance of photogrammetric scanners, in *Photogrammetric Week 99'*, edited by D. Fritsch and E. Spiller, pp. 155-173, Wichmann, Heidelberg, Stuttgart, Germany.

- Barlow, J., S. Franklin, and Y. Martin (2006), *High spatial resolution satellite imagery, DEM derivatives, and image segmentation for the detection of mass wasting processes*, *Photogrammetric Engineering and Remote Sensing*, 72(6), 687-692.
- Barron, J. L., D. J. Fleet, and S. S. Beauchemin (1994), *Performance of optical flow techniques*, *International Journal of Computer Vision*, 12(1), 43-77.
- Bendjebbour, A., Y. Delignon, L. Fouque, V. Samson, and W. Pieczynski (2001), *Multisensor image segmentation using Dempster-Shafer fusion in Markov fields context*, *Geoscience and Remote Sensing, IEEE Transactions on*, 39(8), 1789-1798.
- Berthier, E., H. Vadon, D. Baratoux, Y. Arnaud, C. Vincent, K. L. Feigl, F. Rémy, and B. Legrésy (2005), *Surface motion of mountain glaciers derived from satellite optical imagery*, *Remote Sensing of Environment*, 95(1), 14-28.
- Bitelli, G., M. Dubbini, and A. Zanutta (2004), *Terrestrial Laser Scanning and Digital Photogrammetry techniques to monitor landslide bodies*, in *ISPRS*, edited, Istanbul.
- Blaschke, T. (2010), *Object based image analysis for remote sensing*, *ISPRS Journal of Photogrammetry and Remote Sensing*, 65(1), 2-16.
- Borghuis, A. M., K. Chang, and H. Y. Lee (2007), *Comparison between automated and manual mapping of typhoon-triggered landslides from SPOT-5 imagery*, *International Journal of Remote Sensing*, 28, 1843-1856.
- Bovolo, F., L. Bruzzone, L. Capobianco, A. Garzelli, S. Marchesi, and F. Nencini (2010), *Analysis of the Effects of Pansharpening in Change Detection on VHR Images*, *Geoscience and Remote Sensing Letters, IEEE*, 7(1), 53-57.
- Brady, B. T., and G. A. Rowell (1986), *Laboratory investigation of the electrostatics of rock fracture*, *Nature*, 321, 488-492.
- Brandes, J. (2003), *Further Developments of Film Emulsions*, in *Photogrammetric Week 2003*, edited by D. Fritsch, pp. 89-93, Stuttgart, Germany.
- Brückl, E., F. K. Brunner, and K. Kraus (2006), *Kinematics of a deep-seated landslide derived from photogrammetric, GPS and geophysical data*, *Engineering Geology*, 88(3-4), 149-159.
- Bubenzer, O., and A. Bolten (2008), *The use of new elevation data (SRTM/ASTER) for the detection and morphometric quantification of Pleistocene megadunes (draa) in the eastern Sahara and the southern Namib*, *Geomorphology*, 102(2), 221-231.
- Büyüksalih, G., and K. Jacobsen (2007), *Comparison of DEM Generation by Very High Resolution Optical Satellites*, in *New Developments and Challenges in Remote Sensing*, edited by EARSeL, pp. 627-637, Millpress, Rotterdam, Warschau.
- Canty, M. J., A. A. Nielsen, and M. Schmidt (2004), *Automatic radiometric normalization of multitemporal satellite imagery*, *Remote Sensing of Environment*, 91(3-4), 441-451.
- Cardenal, J., E. Mataa, J. L. Perez-Garcia, J. Delgado, M. A. Hernandez, A. Gonzalez, and J. Diaz-de-Teran (2008), *CLOSE RANGE DIGITAL PHOTOGRAMMETRY TECHNIQUES APPLIED TO LANDSLIDES MONITORING* paper presented at ISPRS Congress 2008, Commission VIII, Beijing, 3-11 July 2008.
- Carr, L., and E. Rathje (2008), *The Use of Remote Sensing to Identify Landslides Caused by the 2004 Niigata-ken Chuetsu Earthquake in Japan*, in *6th International Workshop on Remote Sensing for Disaster Management Applications*, edited, Pavia, Italy.
- Casson, B., C. Delacourt, and P. Allemand (2005), *Contribution of multi-temporal remote sensing images to characterize landslide slip surface. Application to the La Clapière landslide (France)*, *Nat. Hazards Earth Syst. Sci.*, 5(3), 425-437.
- Chandler, J., P. Ashmore, C. Paola, M. Gooch, and F. Varkaris (2002), *Monitoring River-Channel Change Using Terrestrial Oblique Digital Imagery and Automated Digital Photogrammetry*, *Annals of the Association of American Geographers*, 92(4), 631-644.
- Chandler, J. H., J. G. Fryer, and A. Jack (2005), *Metric capabilities of low-cost digital cameras for close range surface measurement*, *The Photogrammetric Record*, 20(109), 12-26.
- Chang, L.-W. (2006), *Combining Feature Extraction and Contextual Classification for Landslide Identification based on Multispectral Imagery*, 65 pp, National Cheng Kung University, Tainan.

- 
- Chang, Y.-L., L.-S. Liang, C.-C. Han, J.-P. Fang, W.-Y. Liang, and K.-S. Chen (2007), *Multisource Data Fusion for Landslide Classification Using Generalized Positive Boolean Functions*, *IEEE Transactions on Geoscience and Remote Sensing*, 45(6), 1697-1708.
- Chavez, P. S. (1988), *An improved dark-object subtraction technique for atmospheric scattering correction of multi-spectral data*, *Remote Sensing of Environment*, 24(459-479).
- Chavez, P. S. (1996), *Image-Based Atmospheric Corrections - Revisited and Improved*, *Photogrammetric Engineering & Remote Sensing*, 62(9), 1025-1036.
- Chen, X., L. Vierling, and D. Deering (2005), *A simple and effective radiometric correction method to improve landscape change detection across sensors and across time*, *Remote Sensing of Environment*, 98(1), 63-79.
- Cheng, K. S., C. Wei, and S. C. Chang (2004), *Locating landslides using multi-temporal satellite images*, *Advances in Space Research*, 33(3), 296-301.
- Cheng, P., and C. Chaapel (2008), *Automatic DEM Generation-Using WorldView-1 Stereo Data with or without Ground Control*, *Geoinformatics*, Oktober/November 2008.
- Choudhary, A., M. Pal, S. Banerjee, and S. Chaudhury (2008), *Unusual Activity Analysis Using Video Epitomes and pLSA*, in *Indian Conference on Computer Vision, Graphics & Image Processing*, edited, pp. 390-397.
- Clark, R. N., G. A. Swayze, K. E. Livo, R. F. Kokaly, T. V. V. King, J. B. Dalton, J. S. Vance, B. W. Rockwell, T. Hoefen, and R. R. McDougal (2002), *Surface reflectance calibration of terrestrial imaging spectroscopy data: A tutorial using AVIRIS*, in *10th Airborne Earth Science Workshop*, edited, p. 21, JPL Publication.
- Coe, J. A., J. P. McKenna, J. W. Godt, and R. L. Baum (2009), *Basal-topographic control of stationary ponds on a continuously moving landslide*, *Earth Surface Processes and Landforms*, 34(2), 264-279.
- Coimbra, M. T., and M. Davies (2005), *Approximating optical flow within the MPEG-2 compressed domain*, *Circuits and Systems for Video Technology*, *IEEE Transactions on*, 15(1), 103-107.
- Costa, J. E., and G. P. Williams (1984), *Debris-flow dynamics (videotape)*, in *Open File Report*, edited, United States Geological Survey.
- Cramer, M. (2001), *On the use of direct georeferencing in airborne photogrammetry*, in *3rd International Symposium on Mobile Mapping Technology*, edited, p. 13, Cairo, digitale Publikation auf CD, 13 Seiten.
- Cramer, M. (2009), *Digital Photogrammetric Camera Evaluation – The Initiative of the German Society of Photogrammetry, Remote Sensing and Geoinformation (DGPF)*, *ISPRS Highlights*, 7(March 2009 Issue), [http://www.isprshighlights.org/nieuws/item.php?nieuws\\_id=89](http://www.isprshighlights.org/nieuws/item.php?nieuws_id=89).
- Cramer, M., H. Krauß, K. Jacobsen, M. von Schönermark, and N. S. Haala, V. (2009), *Das DGPF-Projekt zur Evaluierung digitaler photogrammetrischer Kamerasysteme*, in *DGPF Yearly Conference*, edited by E. Seyfert, DGPF, Jena, Germany.
- Crippen, R. E. (1992), *Measurement of Subresolution Terrain Displacement using SPOT Panchromatic Imagery*, *Episodes*, 15(1), 56-61.
- Crosta, G. (1997), *Evaluating rock mass geometry from photographic images*, *Rock Mechanics and Rock Engineering*, 30(1), 35-58.
- Danneels, G., E. Pirard, and H.-B. Havenith (2007), *Automatic landslide detection from remote sensing images using supervised classification methods*, in *Geoscience and Remote Sensing Symposium*, edited, IGARSS, Barcelona, Spain.
- Datcu, M., H. Daschiel, A. Pelizzari, M. Quartulli, A. Galoppo, A. Colapicchioni, M. Pastori, K. Seidel, P. G. Marchetti, and S. D'Elia (2003), *Information mining in remote sensing image archives: system concepts*, *Geoscience and Remote Sensing*, *IEEE Transactions on*, 41(12), 2923-2936.
- Delacourt, C., P. Allemand, B. Casson, and H. Vadon (2004), *Velocity field of the "La Clapière" landslide measured by the correlation of aerial and QuickBird satellite images*, *Geophys. Res. Lett.*, 31.
- Delacourt, C., D. Raucoules, S. L. Mouélic, C. Carnec, D. Feurer, P. Allemand, and M. Cruchet (2009), *Observation of a Large Landslide on La Reunion Island Using Differential Sar Interferometry (JERS and Radarsat) and Correlation of Optical (Spot5 and Aerial) Images*, *Sensors*, 9(1), 616-630.
- Delacourt, C., P. Allemand, E. Berthier, D. Raucoules, B. Casson, P. Grandjean, C. Pambrun, and E. Varel (2007), *Remote-sensing techniques for analysing landslide kinematics: a review*, *Bulletin de la Societe Geologique de France*, 178(2), 89-100.
-

- 
- Dewitte, O., J. C. Jasselette, Y. Cornet, M. Van Den Eeckhaut, A. Collignon, J. Poesen, and A. Demoulin (2008), *Tracking landslide displacements by multi-temporal DTMs: A combined aerial stereophotogrammetric and LIDAR approach in western Belgium*, *Engineering Geology*, 99(1-2), 11-22.
- Dong, J., D. Zhuang, Y. Huang, and J. Fu (2009), *Advances in Multi-Sensor Data Fusion: Algorithms and Applications*, *Sensors*, 9(10), 7771-7784.
- Du, Y., P. M. Teillet, and J. Cihlar (2002), *Radiometric normalization of multitemporal high-resolution satellite images with quality control for land cover change detection*, *Remote Sensing of Environment*, 82(1), 123-134.
- Du, Y., J. Cihlar, J. Beaubien, and R. Latifovic (2001), *Radiometric normalization, compositing, and quality control for satellite high resolution image mosaics over large areas*, *IEEE Transactions on Geoscience and Remote Sensing*, 39, 623-634.
- Dymond, J. R., A.-G. Ausseil, J. D. Shepherd, and L. Buettner (2006), *Validation of a region-wide model of landslide susceptibility in the Manawatu-Wanganui region of New Zealand*, *Geomorphology*, 74(1-4), 70-79.
- Ebert, A., N. Kerle, and A. Stein (2009), *Urban social vulnerability assessment with physical proxies and spatial metrics derived from air- and spaceborne imagery and GIS data*, *Natural Hazards*, 48(2), 275-294.
- Eckardt, A., A. Börner, and F. Lehmann (2009), *The Bright Future of High Resolution Satellite Remote Sensing – Will Aerial Photogrammetry Become Obsolete?*, in *Photogrammetric Week 09*, edited by D. Fritsch, pp. 127-134, Wichmann, Stuttgart, Germany.
- Eckhardt, D. W., J. P. Verdin, and G. R. Lyford (1990), *Automated update of an irrigated lands GIS using SOPT HRV imagery*, *Photogrammetric Engineering and Remote Sensing*, 56(11), 1515-1522.
- Elvidge, C. D., D. Yuan, R. D. Werackoon, and R. S. Lunetta (1995), *Relative radiometric normalization of Landsat Multispectral Scanner (MSS) data using an automated scattergram controlled regression*, *Photogrammetric Engineering and Remote Sensing*, 61(10), 1255-1260.
- Enet, F., and S. T. Grilli (2007), *Experimental Study of Tsunami Generation by Three-Dimensional Rigid Underwater Landslides*, *Journal of Waterway, Port, Coastal, and Ocean Engineering*, 133(6), 442-454.
- Ergun, B., T. Kavzoglu, I. Colkesen, and C. Sahin (2010), *Data filtering with support vector machines in geometric camera calibration*, *Opt. Express*, 18(3), 1927-1936.
- Euroconsult (2008), *Earth Observation Remote Sensing Trends*, in *Advisory Committee on Commercial Remote Sensing*, edited by A. Keith.
- Euroconsult (2009), *Satellite-Based Earth Observation, Market Prospects to 2018*, edited.
- Eyers, R., J. M. Moore, J. Hervas, and J. G. Liu (1998), *Integrated use of Landsat TM and SPOT panchromatic imagery for landslide mapping: case histories from southeast Spain*, *Geological Society, London, Engineering Geology Special Publications*, 15(1), 133-140.
- Fernández, T., J. Jiménez, P. Fernández, R. E. Hamdouni, F. J. Cardenal, J. Delgado, C. Irigaray, and J. Chacón (2008), *Automatic Detection of Landslide Features with Remote Sensing Techniques in the Betic Cordilleras (Granda, Southern Spain)*, paper presented at ISPRS Congress 2008, Commission VIII, Beijing, 3-11 July 2008.
- Ferrier, G. (1995), *Evaluation of apparent surface reflectance estimation methodologies*, *International Journal of Remote Sensing*, 17(12), 2291-2297.
- Fourniadis, I. G., J. G. Liu, and P. J. Mason (2007), *Landslide hazard assessment in the Three Gorges area, China, using ASTER imagery: Wushan-Badong*, *Geomorphology*, 84(1-2), 126-144.
- Fujisawa, K., and J. Ohara (2008), *Simultaneous monitoring of a collapsing landslide with video cameras*, *Advances in Geosciences*, 14, 183-187.
- Galli, M., F. Ardizzone, M. Cardinali, F. Guzzetti, and P. Reichenbach (2008), *Comparing landslide inventory maps*, *Geomorphology*, 94(3-4), 268-289.
- Gao, B.-C., M. J. Montes, C. O. Davis, and A. F. H. Goetz (2009), *Atmospheric correction algorithms for hyperspectral remote sensing data of land and ocean*, *Remote Sensing of Environment*, 113(Supplement 1), S17-S24.
- Garzelli, A., F. Nencini, and L. Capobianco (2008), *Optimal MMSE Pan Sharpening of Very High Resolution Multispectral Images*, *Geoscience and Remote Sensing, IEEE Transactions on*, 46(1), 228-236.
-



- 
- Genevois, R., A. Galgaro, and P. R. Tecca (2001), *Image analysis for debris flow properties estimation*, *Physics and Chemistry of the Earth, Part C: Solar, Terrestrial & Planetary Science*, 26(9), 623-631.
- Gianinetto, M. (2008), *Multi-Scale Digital Terrain Model Generation Using Cartosat-1 Stereo Images for The Mausanne Les Alpilles Test Site*, in *The International Archives of the Photogrammetry, Remote Sensing and Spatial Information Sciences*, edited, pp. 1331-1336.
- Gianinetto, M., and M. Scaioni (2008), *Automated Geometric Correction of High Resolution Pushbroom Satellite Data*, *Photogrammetric Engineering and Remote Sensing*, 74, 107-115.
- Gislason, P. O., J. A. Benediktsson, and J. R. Sveinsson (2006), *Random Forests for land cover classification*, *Pattern Recognition Letters*, 27(4), 294-300.
- Haeberlin, Y., P. Turberg, A. Retière, O. Senegas, and A. Parriaux (2005), *Validation of Spot-5 Satellite Imagery for Geological Hazard Identification and Risk Assessment for Landslides, Mud and Debris Flows in Matagalpa, Nicaragua*, in *XXth ISPRS Congress*, edited, Istanbul, Turkey.
- Hall, F. G., D. E. Strebel, J. E. Nickeson, and S. J. Goetz (1991), *Radiometric rectification: Toward a common radiometric response among multirate, multisensor images*, *Remote Sensing of Environment*, 35(1), 11-27.
- Haralick, R. M., and L. Shapiro (1985), *Survey: Image segmentation techniques.*, *Computer Vision, Graphics, and Image Processing* 29(100-132).
- Haralick, R. M., K. Shanmugam and I. H. Dinstein (1973), *Textural Features for Image Classification.*, *IEEE Transactions on Systems, Man and Cybernetics*, 3(6), 610-621.
- Hervás, J., and P. L. Rosin (1996), *Landslide mapping by textural analysis of ATM data*, in *11th Thematic Conference on Applied Geologic Remote Sensing*, edited, pp. 394-402, Las Vegas, USA.
- Hervás, J., and P. Bobrowsky (2009), *Mapping: Inventories, Susceptibility, Hazard and Risk*, in *Landslides – Disaster Risk Reduction*, edited by K. Sassa and P. Canuti, pp. 321-349, Springer, Heidelberg.
- Hervás, J., P. L. Rosin, A. Fernandez-Renau, J. A. Gomez, and C. Leon (1996), *Use of airborne multispectral imagery for mapping landslides in Los Velez, south eastern Spain*, in *Landslides: 8th International Conference and Field Trip on Landslides*, edited by J. Chacon, C. Irigaray and T. Fernandez, Balkema. Rotterdam. , Granada, Spain.
- Hervás, J., J. I. Barredo, P. L. Rosin, A. Pasuto, F. Mantovani, and S. Silvano (2003), *Monitoring landslides from optical remotely sensed imagery: the case history of Tessina landslide, Italy*, *Geomorphology*, 54(1-2), 63-75.
- Hild, F., B. Raka, M. Baudequin, S. Roux, and F. Cantelaube (2002), *Multiscale Displacement Field Measurements of Compressed Mineral-Wool Samples by Digital Image Correlation.*, *Applied Optics*, 41, 6815-6828.
- Hirschmugl, M., H. Gallaun, R. Perko, and M. Schardt (2005), *Pansharpening - Methoden für digitale, sehr hoch auflösende Fernerkundungsdaten*, in *Angewandte Geoinformatik*, edited by J. Strobl, T. Blaschke and G. Griesebner, pp. 270-276, Wichmann, Salzburg, Austria.
- Holzer-Popp, T., M. Bittner, E. Borg, S. Dech, T. Erbertseder, B. Fichtelmann, and M. Schroedter (2001), *Das automatische Atmosphärenkorrekturverfahren „DurchBlick“*, in *Fernerkundung und GIS. Neue Sensoren - innovative Methoden*, edited by T. Blaschke, Herbert Wichmann Verlag, Heidelberg.
- Honda, K., and M. Nagai (2002), *Real-time volcano activity mapping using ground-based digital imagery*, *ISPRS Journal of Photogrammetry and Remote Sensing*, 57(1-2), 159-168.
- Hong, G. (2007), *Image Fusion, Image Registration, and Radiometric Normalization for High Resolution Image Processing*, Department of Geodesy and Geomatics Engineering, University of New Brunswick, New Brunswick, Canada.
- Hong, G., and Y. Zhang (2008), *A comparative study on radiometric normalization using high resolution satellite images*, *Int. J. Remote Sens.*, 29(2), 425-438.
- Honkavaara, E., et al. (2009), *Digital Airborne Photogrammetry—A New Tool for Quantitative Remote Sensing?—A State-of-the-Art Review On Radiometric Aspects of Digital Photogrammetric Images*, *Remote Sensing*, 1(3), 577-605.
- Hovius, N., C. P. Stark, and P. A. Allen (1997), *Sediment flux from a mountain belt derived by landslide mapping*, *Geology*, 25(3), 231-234.
- Hsieh, C.-C. (2006), *Subpixel Change Detection and Identification Based on Spectral Unmixing: An Application to Change Detection of Landslide*, 65 pp, National Cheng Kung University, Tainan.
-

- 
- Hu, Y., and C. V. Tao (2002), *Updating Solutions of the Rational Function Model Using Additional Control Information*, *Photogrammetric Engineering & Remote Sensing*, 68(7), 715-723.
- Ilstad, T., F. V. De Blasio, A. Elverhøi, C. B. Harbitz, L. Engvik, O. Longva, and J. G. Marr (2004), *On the frontal dynamics and morphology of submarine debris flows*, *Marine Geology*, 213(1-4), 481-497.
- Imaizumi, F., S. Tsuchiya, and O. Ohsaka (2005), *Behaviour of debris flows located in a mountainous torrent on the Ohya landslide, Japan*, *Canadian Geotechnical Journal*, 42(3), 919-931.
- Inaba, H., Y. Itakura, and M. Kasahara (2000), *Surface velocity computation of debris flows by vector field measurements*, *Physics and Chemistry of the Earth, Part B: Hydrology, Oceans and Atmosphere*, 25(9), 741-744.
- Itakura, Y., H. Inaba, and T. Sawada (2005), *A debris-flow monitoring devices and methods bibliography*, *Nat. Hazards Earth Syst. Sci.*, 5(6), 971-977.
- Jacobsen, K. (2006), *Pros and cons of the orientation of very high resolution optical space images*, *International Archives of Photogrammetry, Remote Sensing and Spatial Information Science/ISPRS Symposium*, 36(1), 7.
- Janzen, D. T., A. L. Fredeen, and R. D. Wheate (2006), *Radiometric correction techniques and accuracy assessment for Landsat TM data in remote forested regions*, *Canadian Journal of Remote Sensing*, 32(5), 330-340.
- Jarvis, A., H. I. Reuter, A. Nelson, and E. Guevara (2008), *Hole-filled SRTM for the globe Version 4*, available from the CGIAR-CSI SRTM 90m Database, edited.
- Jensen, J. R. (1983), *Urban/Suburban Land Use Analysis*, in *Manual of Remote Sensing*, edited by R. N. Colwell, pp. 1571-1666, American Society of Photogrammetry, Falls Church, VA.
- Jensen, J. R. (2005), *Introductory digital image processing : a remote sensing perspective*, Third edition ed., 526 pp., Prentice-Hall, Upper Saddle River.
- Jibson, R. (2006), *The 2005 La Conchita, California, landslide*, *Landslides*, 3(1), 73-78.
- Joyce, K. E., G. D. Dellow, and P. J. Glassey (2008), *Assessing image processing techniques for mapping landslides*, in *IEEE International Geoscience and Remote Sensing Symposium*, edited, pp. 1231-1234, Boston, USA.
- Joyce, K. E., S. E. Belliss, S. V. Samsonov, S. J. McNeill, and P. J. Glassey (2009), *A review of the status of satellite remote sensing and image processing techniques for mapping natural hazards and disasters*, *Progress in Physical Geography*, 33(2), 183-207.
- Kääb, A. (2002), *Monitoring high-mountain terrain deformation from repeated air- and spaceborne optical data: examples using digital aerial imagery and ASTER data*, *ISPRS Journal of Photogrammetry and Remote Sensing*, 57(1-2), 39-52.
- Kääb, A. (2004), *Mountain glaciers and permafrost creep. Methodical research perspectives from earth observation and geoinformatics technologies. Habilitation thesis*, , 205 pp, University of Zurich.
- Kääb, A. (2005), *Combination of SRTM3 and repeat ASTER data for deriving alpine glacier flow velocities in the Bhutan Himalaya*, *Remote Sensing of Environment*, 94(4), 463-474.
- Kalantari, M., A. Hashemi, F. Jung, and J. P. Guedon (2009), *A New Solution to the Relative Orientation Problem using only 3 Points and the Vertical Direction*, doi: arXiv:0905.3964v1 [cs.CV].
- Kandawasvika, A. M. (2009), *On Interoperable Management of Multi-Sensors in Landslide Monitoring Applications*, 172 pp, Universität der Bundeswehr, Erlangen.
- Kaufman, Y. J. (1989), *The atmospheric effect on remote sensing and its corrections*, in *Theory and Applications of Optical Remote Sensing*, edited by G. Asrar, Wiley New York.
- Kaufman, Y. J., A. E. Wald, L. A. Remer, G. Bo-Cai, L. Rong-Rong, and L. Flynn (1997), *The MODIS 2.1- $\mu$ m channel-correlation with visible reflectance for use in remote sensing of aerosol*, *Geoscience and Remote Sensing, IEEE Transactions on*, 35(5), 1286-1298.
- Kavzoglu, T., and I. Colkesen (2009), *A kernel functions analysis for support vector machines for land cover classification*, *International Journal of Applied Earth Observation and Geoinformation*, 11(5), 352-359.
- Kennedy, R. E., P. A. Townsend, J. E. Gross, W. B. Cohen, P. Bolstad, Y. Q. Wang, and P. Adams (2009), *Remote sensing change detection tools for natural resource managers: Understanding concepts and tradeoffs in the design of landscape monitoring projects*, *Remote Sensing of Environment*, 113(7), 1382-1396.
-

- 
- Korup, O., M. J. McSaveney, and T. R. H. Davies (2004), *Sediment generation and delivery from large historic landslides in the Southern Alps, New Zealand*, *Geomorphology*, 61, 189–207.
- Koyama, T., H. Inaba, Y. Itakura, and M. Kasahara (2000), *Detection of Debris Flow Based on MPEG Video*, *Transactions of the Society of Instrument and Control Engineers*, 36(11), 1047-1049.
- Kraus, K. (2007), *Photogrammetry : geometry from images and laser scans*, Second edition ed., 459 pp., De Gruyter, Berlin.
- Ladstädter, R., and V. Kaufmann (2005), *Terrestrisch-photogrammetrische Dokumentation des Blockgletschers im Äußeren Hochebenkar.*, in *Internationale Geodätische Woche*, edited by G. Chesi and T. Weinhold, pp. 92-101, Wichmann, Heidelberg, Obergurgl, Austria.
- Laliberte, A., and A. Rango (2009), *Texture and Scale in Object-Based Analysis of Subdecimeter Resolution Unmanned Aerial Vehicle (UAV) Imagery*, *IEEE Transactions on Geoscience and Remote Sensing*, 47(3), 761-770.
- Laliberte, A., C. Winters, and A. Rango (2008), *A procedure for orthorectification of sub-decimeter resolution imagery obtained with an unmanned aerial vehicle (UAV) in American Society for Photogrammetry and Remote Sensing Annual Conference*, edited, Portland, OR.
- Leprince, S. (2008), *Monitoring Earth Surface Dynamics With Optical Imagery*, 252 pp, California Institute of Technology, Pasadena.
- Leprince, S., S. Barbot, F. Ayoub, and J. P. Avouac (2007a), *Automatic and Precise Orthorectification, Coregistration, and Subpixel Correlation of Satellite Images, Application to Ground Deformation Measurements*, *Geoscience and Remote Sensing, IEEE Transactions on*, 45(6), 1529-1558.
- Leprince, S., F. Ayoub, Y. Klinger, and J.-P. Avouac (2007b), *Co-Registration of Optically Sensed Images and Correlation (COSI-Corr): an Operational Methodology for Ground Deformation Measurements*, in *Geoscience and Remote Sensing Symposium*, edited, pp. 2700–2702, Institute of Electrical and Electronics Engineers, Barcelona, Spain.
- Lim, M., N. J. Rosser, R. J. Allison, and D. N. Petley (2010), *Erosional processes in the hard rock coastal cliffs at Staithes, North Yorkshire*, *Geomorphology*, 114(1-2), 12-21.
- Lu, D., P. Mausel, E. Brondizio, and E. Moran (2004), *Change detection techniques*, *International Journal of Remote Sensing*, 25(12), 2365-2401.
- Luhmann, T., S. Robson, S. Kyle, and I. Harley (2006), *Close range photogrammetry : principles, techniques and applications*, 500 pp., Whittles, Caithness.
- Mantovani, F., R. Soeters, and C. J. Van Westen (1996), *Remote sensing techniques for landslide studies and hazard zonation in Europe*, *Geomorphology*, 15(3-4), 213-225.
- Mantovani, F., A. Pasuto, S. Silvano, and A. Zannoni (2000), *Collecting data to define future hazard scenarios of the Tessina landslide*, *International Journal of Applied Earth Observation and Geoinformation*, 2(1), 33-40.
- Marcelino, E. V., A. R. Formaggio, and E. E. Maed (2009), *Landslide inventory using image fusion techniques in Brazil*, *International Journal of Applied Earth Observation and Geoinformation*, 11(3), 181-191.
- Marcelino, E. V., L. M. G. Fonseca, F. Ventura, and A. N. C. S. Rosa (2003), *Evaluation of HIS, PCA and Wavelet Transform fusion techniques for the identification of landslide scars using satellite data*, in *IX Simpósio Brasileiro de Sensoriamento Remoto*, edited, pp. 487–494, Belo Horizonte, Brasil.
- Marchi, L., M. Arattano, and A. M. Deganutti (2002), *Ten years of debris-flow monitoring in the Moscardo Torrent (Italian Alps)*, *Geomorphology*, 46(1-2), 1-17.
- Marpu, P. R., I. Niemeyer, S. Nussbaum, and R. Gloaguen (2008), *A procedure for automatic object-based classification*, edited, pp. 169-184.
- Martha, T., N. Kerle, C. J. van Westen, and K. Kumar (2009a), *Characterising spectral, spatial and morphometric properties of landslides for semi-automatic detection using object-oriented methods*, *Geomorphology*, In Press, Corrected Proof.
- Martha, T., N. Kerle, J. V. Jetten, C. v. Westen, and K. V. Kumar (2009b), *Landslide Volumetric Analysis Using Cartosat-1 Derived DEMs*, in *Geoscience and Remote Sensing Letters*, edited.
- Martha, T., N. Kerle, C. van Westen, V. Jetten, and K. Vinod Kumar (2010a), *Effect of Sun Elevation Angle on DSMs Derived from Cartosat-1 Data.*, *Photogrammetry and Remote Sensing*, Article In Press.
-

- 
- Martha, T. R., N. Kerle, V. Jetten, C. J. van Westen, and K. Vinod Kumar (2010b), *Landslide Volumetric Analysis Using Cartosat-1-Derived DEMs*, *Geoscience and Remote Sensing Letters, IEEE*, PP(99), 1-5.
- Maruya, M., and H. Ohyama (2008), *Accurate DEM and Ortho-Rectified Image Production from ALOS/PRISM*, paper presented at *Geoscience and Remote Sensing Symposium, 2008. IGARSS 2008. IEEE International*.
- Mason, P. J., M. S. Rosenbaum, and J. M. Moore (1998), *Digital image texture analysis for landslide hazard mapping*, *Geological Society, London, Engineering Geology Special Publications*, 15(1), 297-305.
- Mavrantza, O., and D. Argialas (2008), *An object-oriented image analysis approach for the identification of geologic lineaments in a sedimentary geotectonic environment*, edited, pp. 383-398.
- Moine, M., A. Puissant, and J.-P. Malet (2009), *Detection of landslides from aerial and satellite images with a semi-automatic method*.
- Application to the Barcelonnette basin (Alpes-de-Haute-Provence, France)*, in *International Conference 'Landslide Processes'*, edited by J.-P. Malet, A. Remaitre and T. Bogaard, pp. 63-68, Strasbourg, France.
- Murphy, M. A., and W. P. Burgess (2006), *Geometry, kinematics, and landscape characteristics of an active transtension zone, Karakoram fault system, Southwest Tibet*, *Journal of Structural Geology*, 28(2), 268-283.
- Nagasubramanian, V., P. Radhadevi, R. Ramachandran, and R. Krishnan (2008), *3D Reconstruction with Rational Function Model*, *Journal of the Indian Society of Remote Sensing*, 36(1), 27-35.
- Nelson, T., H. G. Wilson, B. Boots, and M. A. Wulder (2005), *Use of ordinal conversion for radiometric normalization and change detection*, *International Journal of Remote Sensing*, 26(3), 535 - 541.
- Nichol, J., and M. S. Wong (2005), *Satellite remote sensing for detailed landslide inventories using change detection and image fusion*, *International Journal of Remote Sensing*, 26(9), 1913 - 1926.
- Nichol, J. E., A. Shaker, and M.-S. Wong (2006), *Application of high-resolution stereo satellite images to detailed landslide hazard assessment*, *Geomorphology*, 76(1-2), 68-75.
- Niethammer, U., S. Rothmund, and M. Joswig (2009), *UAV-based remote sensing of the slow-moving landslide Super-Sauze*, paper presented at *International Conference Landslide Processes: from geomorphologic mapping to dynamic modelling*, CERIG Editions, Strasbourg, February 6 to 7, 2009.
- Niethammer, U., M. R. James, S. Rothmund, J. Travelletti, and M. Joswig (forthcoming), *Very high spatial resolution monitoring of the Super-Sauze landslide with an UAV-based remote sensing technique*, *Engineering Geology*.
- Ochiai, H., Y. Okada, G. Furuya, Y. Okura, T. Matsui, T. Sammori, T. Terajima, and K. Sassa (2004), *A fluidized landslide on a natural slope by artificial rainfall*, *Landslides*, 1(3), 211-219.
- Over, M., B. Schottker, M. Braun, and G. Menz (2003), *Relative radiometric normalisation of multitemporal Landsat data-a comparison of different approaches*, paper presented at *Geoscience and Remote Sensing Symposium, 2003. IGARSS '03. Proceedings. 2003 IEEE International*.
- Owen, L. A., U. Kamp, G. A. Khattak, E. L. Harp, D. K. Keefer, and M. A. Bauer (2008), *Landslides triggered by the 8 October 2005 Kashmir earthquake*, *Geomorphology*, 94(1-2), 1-9.
- Pal, R., Pal, K. (1993), *A review on image segmentation techniques*, *Pattern Recogn*, 26(9), 1277-1294.
- Paolini, L., F. Grings, J. A. Sobrino, J. C. J. Muñoz, and H. Karszenbaum (2006), *Radiometric correction effects in Landsat multi-date/multi-sensor change detection studies*, *International Journal of Remote Sensing*, 27(4), 685 - 704.
- Park, N.-W., and K.-H. Chi (2008), *Quantitative assessment of landslide susceptibility using high-resolution remote sensing data and a generalized additive model*, *Int. J. Remote Sens.*, 29(1), 247-264.
- Petley, D. N., W. D. O. Crick, and A. B. Hart (2002), *The use of satellite imagery in landslide studies in high mountain area*, in *23rd Asian Conference on Remote Sensing* edited, Kathmandu, Nepal.
- Petrie, G. (2008), *paceborne Digital Imaging Sensors and Systems*, in *Advances in Photogrammetry, Remote Sensing and Spatial Information Sciences*, edited by Z. Li, J. Chen and E. Baltsavias, pp. 29-43, CRC Press, London.
- Pierrot-Deseilligny, M., and N. Paparoditis (2006), *A multiresolution and optimization-based image matching approach: An application to surface reconstruction from SPOT5-HRS stereo imagery*, in *ISPRS Workshop On Topographic Mapping From Space (With Special Emphasis on Small Satellites)*, edited, Ankara, Turkey.
- Poon, J. (2007), *Spatial Information Generation from High-Resolution Satellite Imagery*, 160 pp, University of Melbourne, Melbourne.
-

- 
- Popp, T. (1995), *Correcting atmospheric masking to retrieve the spectral albedo of land surfaces from satellite measurements*, *International Journal of Remote Sensing*, 16(18), 3483 - 3508.
- Proske, H., K. Granica, M. Hirschmugl, and M. Wurm (2008), *Landslide Detection and Susceptibility Mapping using innovative Remote Sensing Data Sources*, in *Intraprevent*, edited, pp. 219 - 229, Dornbirn, Austria.
- Puymbroeck, N. V., R. Michel, R. Binet, J.-P. Avouac, and J. Taboury (2000), *Measuring Earthquakes from Optical Satellite Images*, *Appl Optics*, 39(20), 3486-3494.
- Quénot, G. M., J. Pakleza, and T. A. Kowalewski (1998), *Particle image velocimetry with optical flow*, *Experiments in Fluids*, 25(3), 177-189.
- Rahman, H., and G. Dedieu (1994), *SMAC: A simplified method for the atmospheric correction of satellite measurements in the solar spectrum*, *International Journal of Remote Sensing*, 15(1), 123–143.
- Rau, J.-Y., L.-C. Chen, J.-K. Liu, and T.-H. Wu (2007), *Dynamics Monitoring and Disaster Assessment for Watershed Management Using Time-Series Satellite Images*, *Geoscience and Remote Sensing, IEEE Transactions on*, 45(6), 1641-1649.
- Reulke, R. (2003), *Film-based and Digital Sensors – Augmentation or Change in Paradigm?*, in *Photogrammetric Week 2003*, edited by D. Fritsch, pp. 41-52, Stuttgart, Germany.
- Richards, J. A., and X. Jia (2006), *Remote Sensing Digital Image Analysis*, Springer, Berlin, Germany.
- Richter, R. (1990), *A fast atmospheric correction algorithm applied to Landsat TM images*, *International Journal of Remote Sensing*, 11(1), 159 - 166.
- Richter, R. (1998), *Correction of Satellite Imagery Over Mountainous Terrain*, *Appl Optics*, 37(18), 4004-4015.
- Richter, R., T. Kellenberger, and H. Kaufmann (2009), *Comparison of Topographic Correction Methods*, *Remote Sensing*, 1(3), 184-196.
- Riedel, T., C. Thiel, and C. Schmullius (2008), *Fusion of multispectral optical and SAR images towards operational land cover mapping in Central Europe*, edited, pp. 493-511.
- Robson, S., and M. James (2007), *Photogrammetric image sequence processing to determine change in active lava flows*, in *Annual Conference of the Remote Sensing & Photogrammetry Society*, edited, Newcastle upon Tyne.
- Roessner, S., H.-U. Wetzel, H. Kaufmann, W. Kornus, M. Lehner, P. Reinartz, and R. Mueller (2000), *Landslide investigations in Southern Kyrgyzstan based on a Digital Elevation Model derived from MOMS-2P data*, in *IAPRS*, , edited, pp. 1259-1266, Amsterdam.
- Roncella, R., G. Forlani, and F. Remondino (2005), *Photogrammetry for geological applications: automatic retrieval of discontinuity in rock slopes*, in *SPIE-IS&T Electronic Imaging*, edited, pp. 17-27, San Jose, California.
- Sadasiva Rao, B., A. S. R. K. V. M. Mohan, K. Kalyanaraman, and K. Radhakrishnan (2006), *Evaluation of Cartosat-I Stereo Data of Rome*, in *International Symposium on Geospatial Databases for Sustainable Development*, edited, Goa, India.
- Sarkar, A., A. Banerjee, N. Banerjee, S. Brahma, B. Kartikeyan, M. Chakraborty, and K. L. Majumder (2005), *Landcover classification in MRF context using Dempster-Shafer fusion for multisensor imagery*, *Image Processing, IEEE Transactions on*, 14(5), 634-645.
- Scherler, D., S. Leprince, and M. R. Strecker (2008), *Glacier-surface velocities in alpine terrain from optical satellite imagery--Accuracy improvement and quality assessment*, *Remote Sensing of Environment*, 112(10), 3806-3819.
- Schmidt, S., and M. Nüsser (2009), *Fluctuations of Raikot Glacier during the past 70 years: a case study from the Nanga Parbat massif, northern Pakistan*, *Journal of Glaciology*, 55(194), 949-959.
- Schneevoigt, N. J., S. van der Linden, H.-P. Thamm, and L. Schrott (2008), *Detecting Alpine landforms from remotely sensed imagery. A pilot study in the Bavarian Alps*, *Geomorphology*, 93(1-2), 104-119.
- Schöpfer, E., S. Lang, and F. Albrecht (2008), *Object-fate analysis - spatial relationships for the assessment of object transition and correspondence*, edited, pp. 785-801.
- Schott, J. R., C. Salvaggio, and W. J. Volchok (1988), *Radiometric scene normalization using pseudoinvariant features*, *Remote Sensing of Environment*, 26(1), 1-16.
- Schowengerdt, R. A. (2007), *Remote Sensing - Models and Methods for Image Processing*, 3rd ed., 509 pp., Academic Press, Burlington.
-

- Schroeder, T. A., W. B. Cohen, C. Song, M. J. Canty, and Z. Yang (2006), Radiometric correction of multi-temporal Landsat data for characterization of early successional forest patterns in western Oregon, *Remote Sensing of Environment*, 103(1), 16-26.
- Serpico, S. R., and G. Moser (2007), MRF-based remote sensing image classification with automatic model parameter estimation. , in *Signal and Image Processing for Remote Sensing*, edited by C. H. Chen, CRC Press, Boca Raton, FL.
- Sertel, E., S. H. Kutoglu, and S. Kaya (2007), Geometric correction accuracy of different satellite sensor images: application of figure condition, *International Journal of Remote Sensing*, 28(20), 4685 - 4692.
- Singhroy, V., K. E. Mattar, and A. L. Gray (1998), Landslide characterisation in Canada using interferometric SAR and combined SAR and TM images, *Advances in Space Research*, 21(3), 465-476.
- Song, C., C. E. Woodcock, K. C. Seto, M. P. Lenney, and S. A. Macomber (2001), Classification and Change Detection Using Landsat TM Data: When and How to Correct Atmospheric Effects?, *Remote Sensing of Environment*, 75(2), 230-244.
- Stewénius, H., C. Engels, and D. Nistér (2006), Recent developments on direct relative orientation, *ISPRS Journal of Photogrammetry and Remote Sensing*, 60(4), 284-294.
- Strang, G. a. N., and T. Nguyen (1996), *Wavelets and Filterbanks*, Wellesley Press, Cambridge.
- Sturzenegger, M., and D. Stead (2009), Quantifying discontinuity orientation and persistence on high mountain rock slopes and large landslides using terrestrial remote sensing techniques, *Natural Hazards and Earth System Sciences*, 9, 267–287.
- Take, W. A., M. D. Bolton, P. C. P. Wong, and F. J. Yeung (2004), Evaluation of landslide triggering mechanisms in model fill slopes, *Landslides*, 1(3), 173-184.
- Tatem, A. J., S. J. Goetz, and S. I. Hay (2008), Fifty Years of Earth Observation Satellites: Views from above have lead to countless advances on the ground in both scientific knowledge and daily life, *American Scientist*, 96(5), 390-398.
- Tenenbaum, D. E., L. E. Band, S. T. Kenworthy, and C. L. Tague (2006), Analysis of soil moisture patterns in forested and suburban catchments in Baltimore, Maryland, using high-resolution photogrammetric and LIDAR digital elevation datasets, *Hydrological Processes*, 20(2), 219-240.
- Tokumaru, P. T., and P. E. Dimotakis (1995), Image correlation velocimetry, *Experiments in Fluids*, 19(1), 1-15.
- Toutin, T. (2004), Review article: Geometric processing of remote sensing images: models, algorithms and methods, *International Journal of Remote Sensing*, 25(10), 1893 - 1924.
- Toutin, T. (2006), Comparison of 3D Physical and Empirical Models for Generating DSMs from Stereo HR Images, *Photogrammetric Engineering & Remote Sensing*, 72(5), 597–604.
- Travelletti, J., C. Delacourt, G. Koval, J.-P. Malet, J. Schmittbuhl, and D. B. v. Dam (2009), A multi-temporal image correlation method to characterize landslide displacement fields, *Geophysical Research Abstracts*, 11.
- Tsutsui, K., S. Rokugawa, H. Nakagawa, S. Miyazaki, T. Chin-Tung Cheng Shiraishi, and S.-D. Yang (2007), Detection and Volume Estimation of Large-Scale Landslides Based on Elevation-Change Analysis Using DEMs Extracted From High-Resolution Satellite Stereo Imagery *IEEE Transactions on Geoscience and Remote Sensing Letters*, 45(6), 1681 - 1696
- van Asselen, S., and A. C. Seijmonsbergen (2006), Expert-driven semi-automated geomorphological mapping for a mountainous area using a laser DTM, *Geomorphology*, 78(3-4), 309-320.
- van Westen, C. J., and F. L. Getahun (2003), Analyzing the evolution of the Tessina landslide using aerial photographs and digital elevation models, *Geomorphology* 54(1–2), 77–89.
- Velloso, M. L. F., F. J. de Souza, and M. Simoes (2002), Improved radiometric normalization for land cover change detection: an automated relative correction with artificial neural network, paper presented at Geoscience and Remote Sensing Symposium, 2002. IGARSS '02. 2002 IEEE International.
- Vermote, E. F., D. Tanré, J. L. Deuzé, M. Herman, and J. J. Morcrette (1997), Second simulation of the satellite signal in the solar spectrum, 6S: An overview, *IEEE Trans. Geoscience and Remote Sensing*, 35(3), 675–686.
- Walstra, J., J. H. Chandler, N. Dixon, and T. A. Dijkstra (2007), *Aerial photography and digital photogrammetry for landslide monitoring*, Geological Society, London, Special Publications, 283(1), 53-63.



- 
- Wang, Z. H. (2004), *RS+GCPs select basic information of landslide*, *The Chinese Journal of Geological Hazard and Control*, 15(1), 94-101.
- Weber, D., and A. Herrmann (2000), *Contribution de la photogrammétrie numérique à l'étude spatio-temporelle de versants instables: l'exemple du glissement de Super-Sauze (Alpes-de-Haute-Provence)*, *Bulletin de la Société géologique de France*, 171(6), 637-648.
- Wen, G., S.-C. Tsay, R. F. Cahalan, and L. Oreopoulos (1999), *Path radiance technique for retrieving aerosol optical thickness over land*, *Journal of Geophysical Research*, 104(D24), 31321-31332.
- White, D. J., W. A. Take, and M. D. Bolton (2003), *Soil deformation measurement using particle image velocimetry (PIV) and photogrammetry*, *Géotechnique*, 53(7), 619-631.
- Whitworth, M., D. Giles, and W. Murphy (2002), *Identification of landslides in clay terrains using Airborne Thematic Mapper (ATM) multispectral imagery*, *SPIE*.
- Whitworth, M., D. Giles, and W. Murphy (2005), *Airborne remote sensing for landslide hazard assessment: a case study on the Jurassic escarpment slopes of Worcestershire, UK*, *Quarterly Journal of Engineering Geology and Hydrogeology*, 38(3), 285-300.
- Whitworth, M., D. Giles, and I. Anderson (2006), *Landslide imaging techniques for urban geoscience reconnaissance in 10th IAEG Congress - Engineering geology for tomorrow's cities*, edited, Nottingham, United Kingdom.
- Wills, C. J., and T. P. McCrink (2002), *Comparing Landslide Inventories: The Map Depends on the Method*, *Environmental and Engineering Geoscience*, 8(4), 279-293.
- Wolff, K., and A. Gruen (2008), *Up to Date DSM Generation Using High Resolution Satellite Image Data*, in *21th ISPRS Congress*, edited, pp. 1103-1108, *International Archives of Photogrammetry, Remote Sensing and Spatial Information Sciences*, Beijing.
- Xu, J.-F., and J.-F. Huang (2008), *Empirical Line Method Using Spectrally Stable Targets to Calibrate IKONOS Imagery*, *Pedosphere*, 18(1), 124-130.
- Ya'allah, S. M., and M. R. Saradjian (2005), *Automatic normalization of satellite images using unchanged pixels within urban areas*, *Information Fusion*, 6, 235-241.
- Yamaguchi, Y., S. Tanaka, T. Odajima, T. Kamai, and S. Tsuchida (2003), *Detection of a landslide movement as geometric misregistration in image matching of SPOT HRV data of two different dates*, *International Journal of Remote Sensing*, 24(18), 3523-3534.
- Yang, X., and C. P. Lo (2000), *Relative Radiometric Normalization Performance for Change Detection from Multi-Date Satellite Images*, *Photogrammetric Engineering & Remote Sensing*, 66(8), 967-980.
- Yin, H.-Y., Y. Lin, J.-C. Lien, B.-J. Lee, T.-Y. Chou, Y.-M. Fang, H.-P. Lien, and Y.-H. Chang (2007), *The Study of On-site and Mobile Debris Flow Monitoring Station*, in *2nd International Conference on Urban Disaster Reduction*, edited, Taipei, Taiwan.
- Youssef, A., N. Maerz, and A. Hassan (2009), *Remote sensing applications to geological problems in Egypt: case study, slope instability investigation, Sharm El-Sheikh/Ras-Nasrani Area, Southern Sinai*, *Landslides*, 6(4), 353-360.
- Yuan, D., and C. D. Elvidge (1996), *Comparison of relative radiometric normalization techniques*, *ISPRS Journal of Photogrammetry and Remote Sensing*, 51(3), 117-126.
- Zakeri, A., K. Høeg, and F. Nadim (2008), *Submarine debris flow impact on pipelines -- Part I: Experimental investigation*, *Coastal Engineering*, 55(12), 1209-1218.
- Zhang, H., J. E. Fritts, and S. A. Goldman (2008a), *Image segmentation evaluation: A survey of unsupervised methods*, *Comput Vis Image Und*, 110(2), 260-280.
- Zhang, L. (2005), *Automatic Digital Surface Model (DSM) Generation from Linear Array Images*, 219 pp, *Swiss Federal Institute of Technology Zurich*.
- Zhang, L., L. Yang, H. Lin, and M. Liao (2008b), *Automatic relative radiometric normalization using iteratively weighted least square regression*, *International Journal of Remote Sensing*, 29(2), 459 - 470.
- Zhang, Z., G. H., Z. W., and Y. Zhang (2005), *Application of remote sensing to study of landslide*, paper presented at *Geoscience and Remote Sensing Symposium, 2005. IGARSS '05. Proceedings. 2005 IEEE International*.
-

Zitová, B., and J. Flusser (2003), *Image registration methods: a survey*, *Image Vision Comput.*, 21(11), 977-1000.

### 6.3. SPECIFIC REFERENCES FOR THE CHAPTER 2B

- Abellán, A. 2009. *Improvements in our understanding of rockfall phenomenon by Terrestrial Laser Scanning. Emphasis on Change detection and its application to spatial prediction*. PhD Thesis RISK-NAT group, University of Barcelona, 185 pp.
- Abellán, A., Calvet, J., Vilaplana, J.M., Blanchard, J., 2010. *Detection and spatial prediction of rockfalls by means of terrestrial laser scanner monitoring*. *Geomorphology* vol. 119(3-4), 162-171. doi:10.1016/j.geomorph.2010.03.016.
- Abellán, A., Vilaplana, J.M., Martínez, J., 2006. *Application of a long-range Terrestrial Laser Scanner to a detailed rockfall study at Vall de Núria (Eastern Pyrenees, Spain)*. *Engineering Geology* 88, 136–148.
- Abellán, A., Jaboyedoff, M., Oppikofer, T., Vilaplana, J. M., 2009. *Detection of millimetric deformation using a terrestrial laser scanner: experiment and application to a rockfall event*, *Nat. Hazards Earth Syst. Sci.*, 9, 365-372.
- Agliardi, F., Crosta, G.B., 2003. *High resolution three-dimensional numerical modelling of rockfalls*. *International Journal of Rock Mechanics and Mining Sciences* 40, 455–471.
- ASPRS LiDAR Committee, 2004. *ASPRS Guidelines Vertical Accuracy Reporting for LiDAR Data*. Available at [http://www.asprs.org/society/committees/lidar/Downloads/Vertical\\_Accuracy\\_Reporting\\_for\\_Lidar\\_Data.pdf](http://www.asprs.org/society/committees/lidar/Downloads/Vertical_Accuracy_Reporting_for_Lidar_Data.pdf).
- ASPRS LIDAR committee, 2004. *ASPRS Guidelines: Vertical Accuracy Reporting for Lidar Data*. Ed: M. Flood
- Baillifard, F., Jaboyedoff, M., Rouiller, J.-D., Robichaud, G., Locat, P., Locat, J., Couture, R., Hamel, G., 2004. *Towards a GIS-based rockfall hazard assessment along the Quebec City Promontory, Quebec, Canada*. Pages 207–213 of: Lacerda, W.A., Ehrlich, M., Fontoura, A.B. & Sayão, A. (eds), *Landslides: Evaluation and Stabilization*. London: Taylor & Francis.
- Baillifard, F., Jaboyedoff, M., Sartori, M., 2003. *Rockfall hazard mapping along a mountainous road in Switzerland using a GIS-based parameter rating approach*. *Natural Hazards and Earth System Sciences*, 3(5), 435–442.
- Baltsavias, E. P., 1999. *Airborne laser scanning: basic relations and formulas*. *ISPRS Journal of Photogrammetry & Remote Sensing* 54:199-214.
- Bauer, A, Paar, G., Kaltenböck, A., 2005. *Mass movement monitoring using terrestrial laser scanner for rock fall management*, *Proceedings of the First International Symposium on Geo-Information for Disaster Management*, pp. 393–406 Delft, The Netherlands.
- Besl, P., McKay, N., 1992. *A method for registration of 3-D shapes*. *IEEE Transactions on Pattern Analysis and Machine Intelligence* 14:239-256.
- Bornaz, L., Rinaudo, F., 2004. *Terrestrial Laser Scanner Data processing*. *Proceedings of XX ISPRS Congress*, 12-23 July 2004, Istanbul, Turkey, IAPRS vol. XXXXV, part B5: pp. 514-519.
- Chandra, A.M., 2005. *Higher surveying. Chapter 1: Triangulation and trilateration*. New age international publishers, 424 pp.
- Chen, Y., Medioni, G., 1992. *Object Modelling by Registration of Multiple Range Images*. *Image and Vision Computing* 10, 145–155.
- Dallaire E. E., 1974. *Electronic distance measuring revolution well under way*. *Civil Engineering* 44(10): 66-71.
- Delacourt C., Allemand P, Casson B., Vadon H., 2004. *Velocity field of the "La Clapière" landslide measured by the correlation of aerial and QuickBird satellite images*. *Geophysical Research Letters* 31, No. 15, L15619, 10.1029/2004GL020193.
- Dorren, L.K.A., Seijmonsbergen, A.C., 2003. *Comparison of three GIS-based models for prediction rockfall runout zones at a regional scale*. *Geomorphology* 56, 49–64.
- Frattini, P., Crosta, G., Carrara, A. & Agliardi, F. 2008. *Assessment of rockfall susceptibility by integrating statistical and physically-based approaches*. *Geomorphology*, 94(3-4), 419–437.

- Gokceoglu, C., Sonmez, H., Ercanoglu, M., 2000. Discontinuity controlled probabilistic slope failure risk maps of the Altindag (settlement) region in Turkey. *Engineering Geology*, 55(4), 277–296.
- Günter, A., 2003. Slopemap: programs for automated mapping of geometrical and kinematical properties of hard rock hill slopes, *Computer & Geosciences* 29/7, 865–875.
- Guzzetti, F., Reichenbach, P. & Wieczorek, G. F. 2003. Rockfall hazard and risk assessment in the Yosemite Valley, California, USA. *Natural Hazards and Earth System Sciences*, 3(6), 491–503.
- Habib, A., Van Rens, J. 2008. *Quality Assurance and Quality Control of LiDAR Systems and Derived Data*. American Society for Photogrammetry and Remote Sensing (ASPRS) committee, 15pp. <[http://www.asprs.org/society/committees/lidar/AKAM\\_LiDAR\\_Calibration.pdf](http://www.asprs.org/society/committees/lidar/AKAM_LiDAR_Calibration.pdf)>
- Harding, D., 2009. Pulsed Laser Altimeter Ranging Techniques and Implications for Terrain Mapping, in *Topographic Laser Ranging and Scanning: Principles and Processing*, Jie Shan and Charles Toth, eds., CRC Press, Taylor & Francis Group, pp. 173 – 194.
- Heritage GL, Large ARG. 2009. *Laser scanning for the environmental sciences*. Wiley-Blackwell, London.
- Hiremagalur J, Yen KS, Akin K, Bui T, Lasky, TA, Ravani B (2007) *Creating Standards and specifications for the use of Laser Scanning in CalTrans projects*. Technical report n° F/CA/RI/2006/46, California Department of Transportation, US.
- Hoek, E., 2000. Analysis of rockfall hazards. *Rock Engineering: course notes*, p. 115-136. Rocscience. Available at <[www.rocsience.com](http://www.rocsience.com)>.
- Hoek, E., Bray, J., 1981. *Rock Slope Engineering*. 3rd edn. London: E & FN Spon.
- Horton, P., Jaboyedoff, M., Bardou, E. 2008. Debris flow susceptibility mapping at a regional scale. In Locat, J., Perret, D., Turmel, D., Demers, D., and Leroueil, S., 2008. *Proceedings of the 4th Canadian Conference on Geohazards. From Causes to Management*. Presse de l'Université Laval, Québec, 594p.
- Ingensand, H., 2006. Metrological aspects in terrestrial laser-scanning technology. In *Proceedings of the 3rd IAG/12th FIG Symposium*, Baden, Austria.
- Jaboyedoff, M. & Labiouse, V. 2003. Preliminary assessment of rockfall hazard based on GIS data. Pages 575–578 of: *10th International Congress on Rock Mechanics ISRM 2003 - Technology roadmap for rock mechanics*. South African Institute of Mining and Metallurgy, Johannesburg, South Africa.
- Jaboyedoff, M., Baillifard, F., Couture, R., Locat, J. & Locat, P. 2004c. New insight of geomorphology and landslide prone area detection using Digital Elevation Model(s). Pages 191–198 of: *Lacerda, W.A., Ehrlich, M., Fontoura, A.B. & Sayão, A. (eds), Landslides: Evaluation and Stabilization*. London: Taylor & Francis.
- Jaboyedoff, M., Baillifard, F., Couture, R., Locat, J., Locat, P. 2004. New insight of geomorphology and landslide prone area detection using Digital Elevation Model(s). Pages 191–198 of: *Lacerda, W.A., Ehrlich, M., Fontoura, A.B. & Sayão, A. (eds), Landslides: Evaluation and Stabilization*. London: Taylor & Francis.
- Jaboyedoff, M., Metzger, R., Oppikofer T., Couture, R., Derron, M.-H., Locat, J., Turmel, D., 2007. New insight techniques to analyze rock-slope relief using DEM and 3D-imaging cloud points: COLTOP-3D software. In: *Eberhardt, E., Stead, D., Morrison, T. (Eds.) Rock Mechanics: Meeting Society's Challenges and Demands (Vol. 2)*. Taylor & Francis, pp. 61-68.
- Jaboyedoff, M., Pedrazzini, A., Loye, A., Horton, P. & Surace, I. 2008. Preliminary slope mass movements susceptibility mapping using Lidar DEM. Pages 419–426 of: *Proceedings of the 61st Canadian Geotechnical Conference*, vol. 1.
- Jaboyedoff, M., Choffet, M., Derron, M.-H., Horton, P., Loye, A., Longchamp, C., Mazotti, B., Michoud, C., Pedrazzini, A., 2010. Preliminary slope mass movements susceptibility mapping using DEM and LiDAR DEM. Submitted in march 2010. 58p.
- Kamerman, G. W., 1993. Laser radar (chapter 1). In: *Fox CS (ed) The Infrared and Electro-Optical Systems Handbook*. Infrared Information Analysis Center, Ann Arbor, Michigan, 1–76.
- Kemeny, J., Turner, K. Norton, B., 2006. *LIDAR for Rock Mass Characterization: Hardware, Software, Accuracy and Best-Practices*, *Proceedings of the Workshop on Laser and Photogrammetric Methods For Rock Mass Characterization: Exploring New Opportunities*, Golden, CO.
- Kemeny, J., Turner, K., 2008. *Ground-Based LiDAR: Rock Slope Mapping and Assessment*. Federal Highway Administration report, FHWA-CFL/TD-08-006. Available at <http://www.iaeg.info/portals/0/Content/Commissions/Comm19/GROUND-BASED LiDAR Rock Slope Mapping and Assessment.pdf>

- Lan, H., Martin, C. D.; Zhou, C.; Lim, C.H., 2010. Rockfall hazard analysis using LiDAR and spatial modeling. *Geomorphology*, 118(1-2), 213-223. doi:10.1016/j.geomorph.2010.01.002.
- Lato, M., Diederichs, M., Hutchinson, D.J., Harrap., R., 2009. Optimization of LiDAR scanning and processing for automated structural evaluation of discontinuities in rockmasses. *International Journal of Rock Mechanics & Mining Sciences* 46, 194–199.
- Lichti D.D., Jamtsho M., 2006. Angular resolution of terrestrial laser scanners. *Photogrammetric Record* 21(114), 141–160.
- Lichti, D.D., 2005. Spectral filtering and classification of terrestrial laser scanner point clouds, *Photogrammetric Record* 20, pp. 218–240
- Lichti, D.D., 2007. Error modelling, calibration and analysis of an AM-CW terrestrial laser scanner system, *ISPRS Journal of Photogrammetry and Remote Sensing* 61 (5), 307–324.
- Lindenbergh, R. and Pfeifer, N., 2005. A statistical deformation analysis of two epochs of terrestrial laser data of a lock. *Proceedings of the 7th Conference on Optical 3D. Measurement Techniques*, Vienna, Austria, 61-70.
- Loye, A., Jaboyedoff, M., and Pedrazzini, A.: Identification of potential rockfall source areas at a regional scale using a DEM-based geomorphometric analysis, *Nat. Hazards Earth Syst. Sci.*, 9, 1643-1653, doi:10.5194/nhess-9-1643-2009, 2009.
- Malet, J.P., Maquaire, O., Calais, E., 2002. The use of Global Positioning System techniques for the continuous monitoring of landslides: application to the Super-Sauze earthflow (Alpes-de-Haute-Provence, France). *Geomorphology* 43, 33-54.
- Manetti L., Steinmann G., 2007. 3DeMoN ROBOVEC – Integration of a new measuring instrument in an existing generic remote monitoring platform. 7th International Symposium on Field Measurements in Geomechanics, 24-27 September 2007, Boston, MA, USA.
- McKean, J., Roering, J., 2004. Objective landslide detection and surface morphology mapping using high-resolution airborne laser altimetry. *Geomorphology*, 57, pp.331–351.
- Meentemeyer, R. K., Moody, A., 2000. Automated mapping of conformity between topographic and geological surfaces. *Computers & Geosciences*, 26(7), 815–829.
- Mikoš, M., Vidmar, A., and Brilly, M.: Using a laser measurement system for monitoring morphological changes on the Strug rock fall, Slovenia, *Nat. Hazards Earth Syst. Sci.*, 5, 143-153, 2005
- Monserat, O., Crosetto, M., 2008. Deformation measurement using terrestrial laser scanning data and least squares 3D surface matching. *ISPRS Journal of Photogrammetry and Remote Sensing*, 63(1), 142-154.
- Oppikofer T., 2009. Detection, analysis and monitoring of slope movements using High-Resolution Digital Elevation Models. PhD thesis, Institute of Geomatics and Analysis of Risk, University of Lausanne, Switzerland, 191 pp.
- Oppikofer, T., Jaboyedoff, M., Blikra, L., Derron, M.-H., Metzger, R., 2009. Characterization and monitoring of the Åknes rockslide using terrestrial laser scanning. *Nat. Hazards Earth Syst. Sci.*, 9, 1003-1019, 2009
- Oppikofer, T., Jaboyedoff, M., Keusen, H.-R., 2008. Collapse of the eastern Eiger flank in the Swiss Alps. *Nature Geosciences* 1(8), 531-535.
- Optech, 2009. ILRIS-3D Intelligent Laser Ranging and Imaging System, from Optech, <http://www.optech.ca/i3dprodline-ilris3d.htm>, access 12 June 2009.
- Pedrazzini, A. Abellan, A., Oppikofer, T., Ambrosi, C., Spataro, A., Jaboyedoff, M., 2010. Retrogressive landslide monitoring by TLS: precursory displacements and final collapse. Case study at Val Canaria (Ticino, Switzerland). *Geophysical Research Abstracts Vol. 12*, EGU2010-12160, 2010
- Petrie and Toth, 2008. Introduction to laser ranging, profiling and scanning. In *Topographic Laser Ranging and Scanning: principles and processing*. Edited by: Shan, J., Toth, C. K., CRC Press, Taylor & Francis, 590p.
- Rosser, N.J., Lim, N., Petley, D.N., Dunning, S., Allison, R.J., 2007. Patterns of precursory rockfall prior to slope failure. *Journal of Geophysical Research*, Vol. 112, No. F4, doi:10.1029/2006JF000642.
- Rosser, N.J., Petley, D.N., Lim, M., Dunning, S. A., Allison, R.J., 2005. Terrestrial laser scanning for monitoring the process of hard rock coastal cliff erosion. *Quarterly Journal of Engineering Geology and Hydrogeology*, 38(4), 363-375.
- Rouiller, J., Jaboyedoff, M., Marro, Ch., 1998. *Pentes instables dans le penique valaisan*. Ed V/d/f. Zurich. 239p.

- Settles, E., Göttle, A., Von Poschinger, A., 2008. *Slope Monitoring Methods - A State of the Art Report. ClimChalp, Interreg III B, Alpine Space, Work package 6, Munich, 165pp.*
- Shan J, Toth K., 2008. *Topographic laser ranging and scanning – principles and processing. CRC Press, Taylor & Francis Group, LLC.*
- Slob, S., Hack, R., 2004. *3D Terrestrial Laser Scanning as a new Field Measurement and Monitoring Technique. In: Hack, R., Azzam, R., Charlier, R. (eds), Engineering Geology for Infrastructure Planning in Europe: A European perspective. Springer, Berlin. Lecture notes in Earth Sciences, n.104, pp179-189.*
- Sturzenegger, M., Stead, D., 2009. *Quantifying discontinuity orientation and persistence on high mountain rock slopes and large landslides using terrestrial remote sensing techniques. Nat. Hazards Earth Syst. Sci., 9, 267–287.*
- Teza, G., Galgaro, A., Zaltron, N., Genevois, R., 2007. *Terrestrial laser scanner to detect landslide displacement fields: a new approach. International Journal of Remote Sensing, Volume 28, Issue 16, pages 3425 – 3446.*
- Travelletti, J., Oppikofer, T., Delacourt, C., Malet, J.P., Jaboyedoff, M. 2008. *Monitoring landslide displacements during a controlled rain experiment using a long-range terrestrial laser scanning (TLS). International Archives of Photogrammetry and Remote Sensing, 37 (B5), 485–490.*
- USACE, 2002. *Engineering and Design - Structural Deformation Surveying. U.S. Army Corps of Engineers Manual EM 1110-1-1804, 292pp*
- USACE, 2007. *Control and topographic surveying. U.S. Army Corps of Engineers Manual EM 1110-1-1005, 498pp.*
- Van Den Eeckhaut, M., Poesen, J., Verstraeten, G., Vanacker, V., Moeyersons, J., Nyssen, J., and van Beek, L. P. H. (2005). *The effectiveness of hillshade maps and expert knowledge in mapping old deep-seated landslides, Geomorphology, 67(3–4), 351–363.*
- Vilajosana, I., Suriñach, E., Abellán, A., Khazaradze, G., Garcia, D., Llosa, J., 2008. *Rockfall induced seismic signals: case study in Montserrat, Catalonia, Nat. Hazards Earth Syst. Sci., 8, 805-812.*
- Voegtli, T., Schwab, I., Landes, T., 2008. *Influences of different materials on the measurement of a Terrestrial Laser Scanner (TLS). Proc. of the XXI Congress, The International Society for Photogrammetry and Remote Sensing, ISPRS2008, Vol. XXXVII, Commission V, 3-11 July 2008, Beijing, China, 1061-1066.*
- Vosselman, G., Maas, H.-G., 2009. *Airborne and terrestrial laser scanning. Whittles. Publishing, Dunbeath, Caithness, Scotland. 336 p*
- Wehr, A., Lohr, U., 1999. *Airborne laser scanning - an introduction and overview. ISPRS Journal of Photogrammetry and Remote Sensing 54:68-82.*

#### 6.4. SPECIFIC REFERENCES FOR THE CHAPTER 2C

- Adam, N., B. Kampes, M. Eineder, J. Worawattanamatekul, and M. Kircher., *The development of a scientific permanent scatterer system, paper presented at ISPRS Hannover Workshop, Inst. for Photogramm. and Geoinf., Hannover, Germany. 2003.*
- Allievi, J., Prati, C., Rocca, F., Savio, G., Arrigoni, M., Zanoletti, L. *Combined use of artificial and permanent scatterers. Proceedings of the ESA Envisat Symposium, 6-10 September 2004, Salzburg (Austria). 2004.*
- Antonello, G., Casagli, N., Farina, P., Guerri, L., Leva, D., Nico, G., Tarchi, D. *SAR interferometry monitoring of landslides on the Stromboli Volcano. Proceedings of FRINGE 2003 Workshop, 1-5 December 2003, ESA/ESRIN, Frascati, Italy. 2003.*
- Arnaud A., Adam N., Hanssen R., Inglada J., Duro J., Closa J., and Eineder M. *ASAR ERS interferometric phase continuity. International Geoscience and Remote Sensing Symposium, 21-25 July 2003, Toulouse (France). 2003.*
- Atzori S., Manunta M., Fornaro G., Ganas A., Salvi S., *"Postseismic displacement of the 1999 Athens earthquake retrieved by the Differential Interferometry by Synthetic Aperture Radar time series", J. Geophys. Res., 113, B09309, doi:10.1029/2007JB005504. 2008.*
- Bamler, R., Hartl, P. *Synthetic aperture radar interferometry. Inverse Problems 14. 54p. 1998.*
- Bamler, R. *A Comparison of Range-Doppler and Wavenumber Domain SAR Focussing Algorithms. IEEE Trans. Geosci. Remote Sens., 30, pp. 706-713. 1992.*

- Beckmann P. and A. Spizzichino, *The Scattering of Electromagnetic Waves from Rough Surfaces*, Norwood, MA: Artech House. 1987.
- Berardino, P., Fornaro, G., Lanari, R., Sansosti, E. A new algorithm for surface deformation monitoring based on Small Baseline Differential SAR Interferograms. *IEEE Trans. Geosci. Remote Sens.* 40 (11), 2375-2383. 2002.
- Berardino, P., Costantini, M., Franceschetti, G., Iodice, A., Pietranera, L., Rizzo, V. Use of differential SAR interferometry in monitoring and modelling large slope instability at Maratea (Basilicata, Italy). *Engineering Geology* 68, pp 31-51. 2003.
- Bernardini G., Ricci, P., Coppi, F. A Ground Based Microwave Interferometer with imaging capabilities for remote sensing measurements of displacements, 7th Geomatic Week/3rd Int. Geotelematics Fair, Barcelona, Spain, 2007 February 20-23. 2007.
- Blanco-Sanchez P., Mallorqui J., Duque S., Monnells D. The Coherent Pixels Technique (CPT): An Advanced DInSAR Technique for Nonlinear Deformation Monitoring. *Pure and Applied Geophysics*, vol. 165, n. 6, pp. 1167-1193. 2008.
- Bovenga, F., Nutricato, R., Refice, A., Wasowski, J. Application of multi-temporal differential interferometry to slope instability detection in urban/peri-urban areas. *Eng. Geol.* 88, 219-240. 2006.
- Bürgmann, R., Hilley, G.E., Ferretti, A. Resolving vertical tectonics in the San Francisco Bay Area from Permanent Scatterer InSAR and GPS Analysis. *Geology*. 34, 221-224. 2006
- Canadian Center for Remote-Sensing. <http://cct.rncan.gc.ca>. 2008.
- Canuti, P., Casagli, N., Farina, P., Ferretti, A., Marks, F., Menduni, G. Land subsidence in the Arno river basin studied through SAR interferometry. *Proc. of SISOLS 2005, 7th Int. Symp. on Land Subsidence*. Shanghai, China, 23-28 Oct. 2005. 1, 407-416. 2005.
- Carnec, C., Massonnet, D., King, C. Two examples of the use of SAR interferometry on displacement fields of small spatial extent. *Geophysical Research Letters*, vol. 23 no. 4. pp 3579-3582. 1996.
- Casagli N., Tibaldi A., Merri A., Del Ventisette C., Apuani C., Guerri L., Fortuny-Guasch J., Tarchi D. Deformation of Stromboli Volcano (Italy) during the 2007 eruption revealed by radar interferometry, numerical modelling and structural geological field data. *Journal of Volcanology and Geothermal Research* 182 (2009) 182-200. 2003.
- Casu F., Manzo M., Lanari R. A quantitative assessment of the SBAS algorithm performance for surface deformation retrieval from DInSAR data. *Remote Sens. Of the Environment*, vol. 102, pp. 195-210. 2006.
- Casu, F., Manzo, M., Pepe, A., Lanari R. SBAS-DInSAR Analysis of Very Extended Areas: First Results on a 60,000 km<sup>2</sup> Test Site. *IEEE Geosci. and Remote Sens. Letters*, vol. 5, no. 3, pp 438-442. 2008
- Catani, F., Farina, P., Moretti, S., Nico, G., Strozzi, T. On the application of SAR interferometry to geomorphological studies: Estimation of landform attributes and mass movements. *Geomorphology* 66. pp 119-131. 2005
- Catani, F., Casagli, N., Ermini, L., Righini, G., Menduni, G. Landslide hazard and risk mapping at catchment scale in the Arno River basin. *Landslides*. 2, 329-342. 2005b
- Colesanti, C., and Wasowski, J. Satellite SAR interferometry for wide-area slope hazard detection and site-specific monitoring of slow landslides. *Proc. 9th Int. Symp. on Landslides*, 28 Jun. - 2 Jul., 2004, Rio de Janeiro, 795-802. 2004.
- Colesanti, C., and Wasowski, J. Investigating landslides with space-borne Synthetic Aperture Radar (SAR) interferometry. *Eng. Geol.* 88, 173-199. 2006.
- Colesanti, C., Le Mouélic, S., Bennani, M., Raucoules, D., Carnec, C., Ferretti, A. Detection of mining related ground instabilities using the Permanent Scatterers technique - A case study in the east of France. *Int. J. Remote Sens.* 26 (1), 201-207. 2005.
- Colesanti, C., Ferretti, A., Prati, C., Rocca, F. Monitoring landslides and tectonic motions with the Permanent Scatterers Technique. *Eng. Geol.* 68, 3-14. 2003.
- Colombo, D., Farina, P., Moretti, S., Nico, G., Prati, C. Land subsidence in the Firenze-Prato-Pistoia basin measured by means of spaceborne SAR interferometry. *Proc. IGARSS 2003*, Toulouse, France. 2003.
- Costantini, M., Iodice, A., Magnapane, L., Pietranera L. Monitoring terrain movements by means of sparse SAR differential interferometric measurements. *Proc. IGARSS 2000*, Honolulu, Hawaii, USA. 7, 3225-3227. 2000.



- 
- Costantini, M., S. Falco, F. Malvarosa, F. Minati, A new method for identification and analysis of persistent scatterers in series of SAR images. in *Proc. Int. Geosci. Remote Sensing Symp. (IGARSS)*, Boston MA, 7-11 July 2008, pp. 449-452. 2008.
- Costantini, M., S. Falco, F. Malvarosa, F. Minati, F. Trillo. Method of Persistent Scatterers Pairs (PSP) and High Resolution SAR Interferometry. *Proc. Int. Geosci. Remote Sensing Symp. (IGARSS)*, Cape Town, South Africa, 12-17 July 2009. 2009.
- Crosetto M. and Pasquali P. DSM generation and deformation measurement from SAR data. Chapter 12 in *Advances in Photogrammetry, Remote Sensing and Spatial Information Science*, ISPRS Congress Book, edited by P. Aplin, 2008. 2008.
- Crosetto M., Crippa B., Biescas E. Early detection and in-depth analysis of deformation phenomena by radar interferometry. *Eng Geol.* 79 (1-2), pp. 81-91. 2005a.
- Crosetto M., Crippa B., Biescas E., Monserrat O., Agudo M. State-of-the-Art of Land Deformation Monitoring Using Differential SAR Interferometry. *ISPRS Hannover Workshop 2005. High Resolution Earth Imaging for Geospatial Information 17-20 May 2005, XXXVI, Part 1/w3*. 2005b.
- Crosetto, M., A. Arnaud, J. Duro, E. Biescas, and M. Agudo. Deformation monitoring using remotely sensed radar interferometric data, paper presented at 11th FIG Symposium on Deformation Measurements, Patras Univ., Santorini, Greece. 2003.
- Crosetto, M., Biescas, E., Duro, J., Closa, J., and Arnaud, A. Generation of Advanced ERS and Envisat Interferometric SAR Products Using the Stable Point Network Technique, *Photogramm. Eng.*, 74(4), 443–451, 2008.
- Czuchlewski, K., Weissel, J.K., Kim, Y. Polarimetric synthetic aperture radar study of the Tsaoling landslide generated by the 1999 Chi-Chi earthquake, Taiwan. *J. Geophys. Res.*, 108. 2003.
- De Maio, A., Fornaro G., Pauciuolo A. Detection of Single Scatterers in Multidimensional SAR Imaging. *IEEE Trans. Geosci. Remote Sens.*, July 2009, 47 (7), pp. 2284-2997. 2009.
- Dixon, T.H., Amelung, F., Ferretti, A., Novali, F., Rocca, F., Dokka, R., Sella, G., Kim, S.W., Wdowinski, S., Whitman, D. Subsidence and flooding in New Orleans - A subsidence map of the city offers insight into the failure of the levees during Hurricane Katrina. *Nature*. 441, 587-588. 2006.
- Dubois, P.C., van Zyl, J.J., and Engman, E.T.. An Empirical Soil Moisture Estimation Algorithm Using Imaging Radar. *IEEE Trans. Geosci. Remote Sens.*, Vol. 33, No. 4, pp. 915-926, 1995.
- Dubois, P.C., van Zyl, J.J., and Engman, E.T., Measuring Soil Moisture with Imaging Radars. *IEEE Trans. Geosci. Remote Sens.*, Vol. 33, No. 4, pp. 915-926. 1995.
- Duro J., Closa J., Biescas E., Crosetto M., Arnaud A. High resolution differential interferometry using time series of ERS and Envisat SAR data. *Actes del congrés 6a. Setmana Geomàtica*” (CD-ROM). Barcelona (ES), 2005.2.8-11.. 2005.
- Duro, J., Inglada, J., Closa, J., Adam, N., Arnaud, A. High resolution differential interferometry using time series of ERS and ENVISAT SAR data. *Proc. of FRINGE 2003*, 1-5 Dec. 2003, Frascati, Italy. 2003.
- ESA Radar courses. [http://earth.esa.int/applications/data\\_util/SARDOCS/spaceborne/Radar\\_Courses/](http://earth.esa.int/applications/data_util/SARDOCS/spaceborne/Radar_Courses/). 2010.
- Farina, P., Casagli, N., Ferretti, A. Radar-interpretation of InSAR measurements for landslide investigations in civil protection practices. *Proc. 1st North American Landslide Conference*, Vail, Colorado, 3-8 Jun. 2007. 272-283. 2008.
- Farina, P., Colombo, D., Fumagalli, A., Gontier, E., Moretti, S. Integration of Permanent Scatterers Analysis and High Resolution Optical Images within Landslide Risk Analysis. *Proc. of FRINGE 2003*, 1-5 Dec. 2003, Frascati, Italy. 2003.
- Farina, P., Colombo, D., Fumagalli, A., Marks, F., Moretti, S. Permanent Scatterers for landslide investigations: outcomes from the ESA-SLAM project. *Eng. Geol.* 88, 200-217. 2006.
- Ferretti, A., Prati, C., Rocca, F. Nonlinear subsidence rate estimation using Permanent Scatterers in Differential SAR Interferometry. *IEEE Trans. Geosci. Remote Sens.* 38, 2202-2212. 2000.
- Ferretti, A., Prati, C., Rocca, F. Permanent Scatterers in SAR interferometry. *IEEE Trans. Geosci. Remote Sens.* 39 (1), 8-20. 2001.
- Ferretti, A., Monti-Guarnieri, A., Prati, C., Rocca, F., Massonnet, D. Lichtenegger, J. *InSAR Principles : Guidelines for SAR Interferometry Processing and Interpretation*. ESA Publications, 234p. 2007.
-

- Fornaro, G., Monti Guarnirei, A. Minimum Mean Square Error Space-Varying Filtering of Interferometric SAR Data. *IEEE Trans. Geosci. Remote Sens.*, 40, pp. 11-21. 2002.
- Fornaro G., Pauciullo A., Serafino F. Deformation Monitoring over large areas with Multipass Differential SAR Interferometry: a new approach based on the use of Spatial Differences. *Int. Journal of Remote Sens.*, vol. 30, no. 6, April 2009, pp 1455-1478. 2009.
- Fornaro G., Reale D., Serafino F. Four-Dimensional SAR Imaging for Height Estimation and Monitoring of Single and Double Scatterers. *IEEE Trans. Geosci. Remote Sens.*, vol. 47 (1), pp. 224-237. 2009.
- Fornaro G., Serafino F., Reale D. 4D SAR Imaging: the Case Study of Rome. doi 10.1109/LGRS.2032133. 2009.
- Fortuny-Guash, J., Sieber, A.J. Fast algorithm for near-field synthetic aperture radar processor. *IEEE Trans. Antennas Propagat.*, vol. 42, pp. 1458–1460. Oct. 1994.
- Fortuny-Guasch J. A Fast and Accurate Far-Field Pseudopolar Format Radar Imaging Algorithm, *IEEE Trans. Geosci. Remote Sens.* 47 (4), 1187–1196. April 2009.
- Fruneau, B., Apache, J., Delacourt, C. Observation and modeling of the Saint-Etienne-de-Tinée landslide using SAR interferometry. *Tectonophysics* 265. pp 181-190. 1996.
- Gamma Remote Sensing. GammaSar user manual, Bern. 2008.
- Hajnsek, I., Pottier, E., and Claude, S. Inversion of Surface Parameters From Polarimetric SAR. *IEEE Trans. Geosci. Remote Sens.*, Vol. 41, No. 4, pp. 727-744, 2003.
- Hajnsek, I., Jagdhuber, T., Shon, H., and Papathanassiou, K.P. Potential of Estimating Soil Moisture Under Vegetation Cover by Means of PolSAR. *IEEE Trans. Geosci. Remote Sens.*, Vol. 42, No. 2, pp. 442-454, 2009.
- Hanssen, R.F. *Radar Interferometry: Data Interpretation and Error Analysis*. Kluwer Academic Publishers. 308p. 2001.
- Hanssen, R.F. Satellite radar interferometry for deformation monitoring: a priori assessment of feasibility and accuracy. *International Journal of Applied Earth Observation and Geoinformation* 6, pp 253-260. 2005.
- Herrera G., Davalillo J. C., Mulas J., Cooksley G., Monserrat O. and Pancioli V. (2009b) - Mapping and monitoring geomorphological processes in mountainous areas using PSI data: Central Pyrenees case study. *Nat. Hazards Earth Syst. Sci.*, 9, 1587–1598, 2009.
- Herrera, G., Fernandez, J.A., Tomas, R., Cooksley, G., Mulas, J., (2009a). Advanced interpretation of subsidence in Murcia (SE Spain) using A-DInSAR data - modelling and validation. *Nat. Hazards Earth Syst. Sci.*, 9, 647-661.
- Hilley, G.E., Burgmann, R., Ferretti, A., Novali, F., Rocca, F., (2004). Dynamics of slow-moving landslides from Permanent Scatterer analysis. *Science*. 304 (5679), 1952-1955.
- Hooper A. and Pedersen R. (2007) - Deformation due to Magma Movement and Ice Unloading at Katla Volcano, Iceland, Detected by Persistent Scatterer InSAR. *Proceedings ENVISAT Symposium*, Montreux 2007.
- Hooper A., Segall P., Zebker H. (2007) - Persistent Scatterer InSAR for Crustal Deformation Analysis, with Application to Volcán Alcedo, Galápagos. *J. Geophys. Res.*, 112, B07407, doi:10.1029/2006JB004763.
- Hooper, A., Zebker, H., Segall, P., Kampes, B. (2004). A new method for measuring deformation on volcanoes and other natural terrains using InSAR persistent scatterers. *Geophys. Res. Lett.*, 31 (23), 5, 2004.
- Jagdhuber, T., Hajnsek, I., Papathanassiou, K.P., and Bronstert, A., “Soil Moisture Estimation Using A Multi-Angular Modified Three-Component Polarimetric Decomposition”, *Proc. of the IEEE Geosci. and Remote Sens. Symposium, IGARSS'09*, Cape Town, 2009.
- Lanari R., Casu F., Manzo M., Lundgren P. Application of the SBAS-DInSAR technique to fault creep: a case study of the Hayward fault, California. *REMOTE SENSING OF ENVIRONMENT*, vol. 109, pp.20-28. 2007.
- Lanari, R., Berardino, P., Borgström, S., Del Gaudio, C., De Martino, P., Fornaro, G., Guarino, S., Ricciardi, G.P., Sansosti, E., Lundgren, P. The use of IFSAR and classical geodetic techniques for caldera unrest episodes: application to the Campi Flegrei uplift event of 2000. *J. Volcanol. Geotherm. Res.*, 133, 247-260. 2004.
- Lauknes, T.R. Long-Term Surface Deformation Mapping using Small-Baseline Differential SAR Interferograms. *Faculty of Science, University of Tromsø*. 88p. 2004.

- 
- Le Mouélic, S., Raucoules, D., Carnec, C., King, C. A least squares adjustment of multi-temporal InSAR data: application to the ground deformation of Paris. *Photogrammetric Engineering and Remote Sensing*, 71 (2), pp. 197-204. 2005.
- Le Toan, T. Beaudoin, A. and Guyon, D. Relating Forest Biomass to SAR Data. *IEEE Trans. Geosci. Remote Sens.*, Vol. 30, No. 2, pp. 403-411. 1992.
- Lemoine, G.F., Hoekman, D.H., and Sieber, A.J. Polarimetric Contrast Classification of Agricultural Fields using MESTRO-1 AIR-SAR Data. *Int. J. Remote Sensing*, Vol. 15, No. 14, pp. 2851-2869. 1994.
- Leva, D., Nico, G., Tarchi, D., Fortuny-Guasch, J., Sieber, A.J. Temporal analysis of a landslide by means of a ground-based SAR Interferometer. *IEEE Trans. Geosci. Remote Sens.*, vol. 41, no 4, Part 1, pp.745 – 752. April 2003.
- Lin, D.S., Wood, E.F., Beven, K. and Saatchi, S. Soil Moisture Estimation over Grass-covered Areas Using AIRSAR. *Int. J. Remote. Sensing*, Vol. 15, No. 11, pp. 2323-2343. 1994.
- Luzi, G., Pieraccini, M., Mecatti, D., Noferini, L., Guidi, G., Moia, F., Atzeni C. Ground-Based Radar Interferometry for Landslides Monitoring: Atmospheric and Instrumental Decorrelation Sources on Experimental Data. *IEEE Trans. Geosci. Remote Sens.*, vol. 42, no 11, pp 2454 – 2466. November 2004.
- Luzi, G., Pieraccini, M., Mecatti, D., Noferini, L., Macaluso, G., Galgaro, A., Atzeni, C. Advances in ground based microwave interferometry for landslide survey: a case study. *International Journal of Remote Sensing*, Vol. 27, No. 12 / 20, pp. 2331 – 2350. June 2006.
- Luzi, G., Pieraccini, M., Mecatti, D., Noferini, L., Macaluso, G., Tamburini, A., Atzeni, C. Monitoring of an Alpine Glacier by Means of Ground-Based SAR Interferometry. *Geoscience and Remote Sensing Letters* , Vol. 4, No 3, pp. 495-499. July 2007.
- Luzi, G., Noferini, L., Mecatti, D., Macaluso, G., Pieraccini, M., Atzeni, C., Schaffhauser, A., Fromm, R., Nagler, T. Using a Ground-Based SAR Interferometer and a Terrestrial Laser Scanner to Monitor a Snow-Covered Slope: Results From an Experimental Data Collection in Tyrol (Austria). *IEEE Transaction on Geoscience and Remote Sensing*, vol.47, no.2 , February 2009, Page(s): 382-393. 2009.
- Luzi, G. Ground based SAR interferometry: a novel tool for Geoscience. In: *Geoscience and Remote Sensing, New Achievements*, edited by: P.Imperatore & D. Riccio, ISBN: 978-953-7619-97-8. In print.
- Lyons, S., and D. Sandwell. Fault creep along the southern San Andreas from interferometric synthetic aperture radar, permanent scatterers, and stacking, *J. Geophys. Res.*, 108(B1), 2047, doi:10.1029/ 2002JB001831. 2003.
- Massonnet, D., Feigl, K.L. Radar interferometry and its application to changes in the Earth's surface. *Reviews of Geophysics* 36. pp 441-500. 1998.
- Mensa, D. High Resolution Radar Cross-Section Imaging. Artech House, Boston. 1991.
- Metternicht, G., Hurni, L., Gogu, R. Remote sensing of landslides: An analysis of the potential contribution to geo-spatial systems for hazard assessment in mountainous environments. *Remote Sens. Environ.* 98 (2), 284-303. 2005.
- Michoud, C., Jaboyedoff, M., Pedrazzini, A. Application de l'interférométrie différentielle Radar dans la surveillance du glissement de La Frasse, Suisse. *Mémoire de Master ès Sciences de l'Ecole Lémanique des Sciences de la Terre et de l'Environnement*. 95p. 2009.
- Mora, O., Mallorqui, J., Broquetas, A. Linear and non-linear terrain deformation maps from a reduced set of interferometric SAR images. *IEEE Trans. Geosci. Remote Sens.* 41 (10), 2243-2253. 2003.
- Musson, R.M.W., Haynes, M., Ferretti, A. Space-based tectonic modelling in subduction areas using PSInSAR. *Seismol. Res. Lett.* 26 (9), 1913-1926. 2004.
- Noferini, L., Pieraccini, M., Mecatti, D., Luzi, G., Tamburini, A., Broccolato, M., Atzeni, C. Permanent scatterers analysis for atmospheric correction in Ground Based SAR Interferometry. *IEEE Trans. Geosci. Rem. Sens.*, vol. 43, no 7, pp. 1459-1471. 2005.
- Norland, R. Differential Interferometric Radar for Mountain Rock Slide Hazard Monitoring. Technical report, 4p. Available on the Åknes/Taffjord Beredskap IKS website: <http://www.aknes-taffjord.no>. 2006.
- Oh, Y., Sarabandi, K. and Ulaby, F.T. An Empirical Model and an Inversion Technique for Radar Scattering from Bare Soil Surfaces. *IEEE Trans. Geosci. Remote Sens.*, Vol. 30, No. 2, pp. 370-381. March 1992.
- Peckham, G. Instrumentation and measurements in atmospheric remote sensing. *Reports on Progress in Physics* 54, pp. 531-577. 1991.
-

- 
- Pepe A., Lanari L. *On the Extension of the Minimum Cost Flow Algorithm for Phase Unwrapping of Multitemporal Differential SAR Interferograms*. *IEEE Trans. Geosci. Remote Sens.*, vol. 44, no. 9, pp. 2374-2383. 2006.
- Pieraccini, M., Casagli, N., Luzi, G., Tarchi, D., Mecatti, D., Noferini, L., Atzeni, C. *Landslide monitoring by ground-based radar interferometry: a field test in Valdarno (Italy)*. *International Journal of Remote Sensing*, 24 6, pp. 1385-1391. 2002.
- Pipia, L., Fabregas, X., Aguasca, A., Lopez-Martinez, C., Mallorqui, J., Mora, O. *A Subsidence Monitoring Project using a Polarimetric GB-SAR Sensor*. *The 3rd Int. Workshop POLinSAR 2007 Frascati, Italy on 22-26 January 2007*.
- Prati, C. *Introduction to SAR and InSAR*. *4e Conférence canadienne sur les géorisques : des causes à la gestion. Workshop, Université Laval*. 2008.
- Preissner, J. *The influence of the atmosphere on passive radiometric measurements*. *Proceedings of the Symposium on Millimeter and Submillimeter Wave Propagation Circuits: AGARD Conference, Vol. 245*, pp. 1-13. 1978.
- Reale, D., Pascasio, V., Schirinzi, G., Serafino, F. *3D Imaging of Ground based SAR Data*. *Geoscience and Remote Sensing Symposium, 2008 IGARSS2008. IEEE International Volume 4, 7-11 July 2008*.
- Righini, G., Casagli N., Del Ventisette, C., Costantini, M., Malvarosa, F., Minati, F. *Space-borne SAR Analysis for Landslides Mapping in the Framework of the PREVIEW Project*. *Proc. 1st World Landslide Forum, Tokyo, Japan*. 26-27. 2008.
- Rignot, E., Zimmerman R., and van Zyl, J.J. *Spaceborne Applications of P. Band Imagin Radars for Measuring Forest Biomass*. *IEEE Trans. Geosci. Remote Sens.*, Vol. 33, pp. 1162-1169. 1995.
- Rudolf, H., Leva, D., Tarchi, D., Sieber, A.J., *A mobile and versatile SAR system*. *Proc. IGARSS'99, Hamburg*, pp. 592-594. 1999.
- Salvi, S., Atzori, S., Tolomei, C., Allievi, J., Ferretti, A., Rocca, F., Prati, C., Stramondo, S., Feillet, N. *Inflation rate of the Colli Albani volcanic complex retrieved by the permanent scatterers SAR interferometry technique*. *Geophys. Res. Lett.* 31, 1-4. 2004.
- Sansosti, E., Berardino, P., Manunta, M., Serafino, F., Fornaro, G. *Geometrical SAR Image Registration*. *IEEE Trans. Geosci. Remote Sens*, vol. 44, no.10, pp. 2861-2870. 2006.
- SARMap courses. Synthetic Aperture Radar, SARscape – The SAR Guidebook*. 268p. 2008
- Shi, J., Wang, J., Hsu, A. Y., O'Neill, P.E. and Engman, E.T. *Estimation of Bare Surface Soil Moisture and Surface Roughness Parameter Using L-band SAR Image Data*. *IEEE Trans. Geosci. Remote Sens.*, Vol. 35, No. 5, pp. 1254-1266. 1997.
- Shi, J., and Dozier, J. *Estimation of Snow Water Equivalence Using SIR-C/X-SAR, Part I: Inferring Snow Density and Subsurface Properties*. *IEEE Trans. Geosci. Remote Sens.*, Vol. 38, No. 6, pp. 2465-2474, November 2000.
- Squarzoni, C. *Mesure des champs de déplacement de surface et modélisation numérique des glissements de terrain*. *Diplôme de doctorat de l'Université Claude Bernard – Lyon 1 et l'Universita degli Studi di Padova*. 221p. 2003.
- SRTM factsheet*. <http://www2.jpl.nasa.gov/srtm/factsheets.html>. 2005.
- Stramondo, S., Bozzano, F., Marra, F., Wegmüller, U., Cinti, F.R., Moro, M., Saroli, M. *Subsidence induced by urbanisation in the city of Rome detected by advanced InSAR technique and geotechnical investigations*. *Remote Sens. Environ.* Vol. 112, 3160-3172. 2008.
- Strozzi, T., Matzler, C. *Backscattering Measurements of Alpine Snowcovers at 5.3 GHz and 35 GHz*. *IEEE Trans. on Geoscience and Remote Sensing*, Vol. 36, No. 3, pp. 838-848. May 1998.
- Strozzi, T., Wegmüller, U., Mätzler, C. *Mapping Wet Snowcovers with SAR Interferometry*. *Int. J. Remote Sens.*, Vol. 20, No. 12, pp. 2395-2403. 1999.
- Strozzi T., Wegmüller U., Keusen H.R., Graf K., Wiesmann A. *Analysis of the terrain displacement along a funicular by SAR interferometry*. *IEEE Geoscience and Remote Sensing Letters*, January 2006, vol. 3, no. 1, pp.15-18. 2006.
- Tarchi, D., Ohlmer, E., Sieber, A.J. *Monitoring of structural changes by radar interferometry*. *Res. Nondestruct. Eval.* 9, 213- 225. 1997.
-

- Tarchi, D., Rudolf, H., Luzi, G., Chiarantini, L., Coppo, P., Sieber, A.J. SAR interferometry for structural changes detection: a demonstration test on a dam. *Proc. IGARSS'99, Hamburg*, pp. 1522–1524. 1999
- Tarchi, D., Casagli, N., Fanti, R., Leva, D., Luzi, G., Pasuto, A., Pieraccini, M., Silvano, S. Landside Monitoring by Using Ground-Based SAR Interferometry: an example of application to the Tessina landslide in Italy, *Engineering Geology* 68, pp.15-30. 2003a.
- Tarchi, D., Casagli, N., Moretti, S., Leva, D., Sieber, A.J. Monitoring landslide displacements by using ground-based radar interferometry: Application to the Ruinon landslide in the Italian Alps, *J. Geophys. Res.*, 108, 10.1-10.14. 2003b.
- Tizzani, P., Berardino, P., Casu, F., Euillades, P., Manzo, M., Ricciardi, G.P., Zeni, G., Lanari, R. Surface deformation of Long Valley caldera and Mono Basin, California investigated with the SBAS-InSAR approach. *Remote Sens. Environ.* 108, 277-289. 2007.
- Tsang, L., J.A.Kong, and R.T.Shin, *Theory of Microwave Remote Sensing*, New York: John Wiley, 1985.
- Ulaby, F.T., R.K.Moore, and A.K.Fung, *Microwave Remote Sensing*, vol. II, Reading, MA: Addison-Wesley, 1982.
- Vilardo, G., Ventura, G., Terranova, C., Matano, F., Nardò, S. Ground deformation due to tectonic, hydrothermal, gravity, hydrogeological, and anthropic processes in the Campania Region (Southern Italy) from Permanent Scatterers Synthetic Aperture Radar Interferometry. *Remote Sens. Environ.* 113 (1), 197-212. 2009.
- Wasowski J., D. Casarano, C. Lamanna, F. Bovenga, D. Conte, R. Nutricato, P. Berardino, M. Manzo, A. Pepe, G. Zeni, R. Lanari, A. Refice. A comparative analysis of DInSAR results achieved by the SBAS and SPINUA techniques: the Maratea valley case study, Italy. *Proc. 'Envisat Symposium 2007'*, Montreux, Switzerland 23–27 April 2007 (ESA SP-636, July 2007). 2007.
- Wegmuller U., Werner C., Strozzi T., Wiesmann A. Monitoring mining induced surface deformations. *Proc. of IGARSS 2004, Anchorage (USA)*. Sept. 2004.
- Wegmuller U., Werner C., Strozzi T., Wiesmann A. Application of SAR interferometric techniques for surface deformation monitoring. *3rd IAG / 12th FIG Symposium, Baden*, May 22-24, 2006.
- Werner C., Wegmuller U., Strozzi T., Wiesmann A. Interferometric Point Target Analysis for deformation mapping. *Proc. of IGARSS 2003, Toulouse (Francia)*, Luglio 2003. 2003a.
- Werner C., Wegmuller U., Strozzi T., Wiesmann A. Interferometric Point Target Analysis with JERS L-band data. *Proc. of IGARSS 2003, Toulouse (Francia)*, Luglio 2003. 2003b.
- Werner, C., Strozzi, T., Wesmann, A., Wegmuller, U. Gamma's portable radar interferometer. *13th FIG Symposium on Deformation Measurements and analysis, LNEC, Lisbon* May 12-16 2008. 2008.
- Wiley, C.A. Pulsed Doppler Radar Methods and Apparatus. United States Patent No. 3196436. 1954.
- Woodhouse, I.H. *Introduction to Microwave Remote Sensing*. CRC Taylor & Francis, 370p. 2006.
- Zebker, H.A., Rosen, P.A., Hensley, S. Atmospheric effects in interferometric synthetic aperture radar surface deformation and topographic maps. *Journal of Geophysical research* 102. pp 7547-7563. 1997.

## 6.5. SPECIFIC REFERENCES FOR THE CHAPTER 2D

- Agnesi, V., Camardab, M., Conoscentia, C., Di Maggio, A., Dilibertoc, I., Madoniac, P., Rotiglianoa, E., 2005. A multidisciplinary approach to the evaluation of the mechanism that triggered the Cerda landslide (Sicily, Italy). *Geomor.*, 65, 101-116.
- Almendros, J. Ibáñez, G. Alguacil, E. Del Pezzo, 1999. Array analysis using circular-wave-front geometry: an application to locate the nearby seismo-volcanic source. *Geophys. J. Int.*, 136,159-170.
- Amitrano D., Gaffet S., Malet J.P., Maquaire O., 2007. Understanding mudslides through micro-seismic monitoring: the Super-Sauze (South-East French Alps) case study. *Bull. Soc. Géol. Fr.*, 178 (2), 149-157.
- Amitrano D., Grasso J.-R., Senfaute G., 2005. Seismic precursory patterns before a cliff collapse and critical-point phenomena. *Geophysical Research Letters*, 32, 8, L08314, doi:10.1029/2004GL022270.
- Amitrano D., Senfaute G., Grasso J.R., Got J.L., Gaffet S., Clement C., 2004. Potential of the seismic monitoring for the understanding of gravitational instability. *AGU Fall Meeting*, paper n°H44A-06, San Francisco.

- Arattano M., 1999. On the use of seismic detectors as monitoring and warning systems for debris flows. *Natural Hazards*, 20, 197-213.
- Arattano M., Marchi L., 2005. Measurements of debris-flow velocity through cross-correlation of instrumentation data. *Natural Hazards and Earth System Sciences*, 5, 137-142.
- Bangs, N.L.B., Moore, G.F., Gulik, S.P.S., Pangborn, E.M., Tobin, H.J., Kuramoto, S., Taira, A., 2009: Broad, weak regions of the Nankai Megathrust and implications for shallow coseismic slip. *Earth and Planetary Science Letters* 284: 44-49.
- Barnhardt, W.A. and Kayen, R.E., 2000. Radar structure of earthquake-induced coastal landslides in Anchorage, Alaska. *Environ. Geosciences*, 7, 38-45.
- Barton, N., 2006. *Rock Quality, Seismic Velocity, Attenuation and Anisotropy*. Taylor and Francis, UK and Netherlands, 729p.
- Batayneh, A.T. and Al-Diabat, A.A., 2002. Application of a two-dimensional electrical tomography technique for investigating landslides along the Amman-Dead Sera Highway, Jordan. *Env. Geol.*, 42, 399-403.
- Besson B., Eiriksson G., Thorarinsson O., Thorarinsson A., Einarsson S., 2007. Automatic detection of avalanches and debris flows by seismic methods. *Journal of Glaciology*, 53, No 182, 461-472.
- Bichler A., Bobrowsky P., Best M., Douma M., Hunter J., Calvert T., Burns R., 2004. Three-dimensional mapping of a landslide using a multi-geophysical approach: the Quesnel Forks landslide. *Landslides*, 1 (1), 29-40.
- Bláha P., Mrlina J., Nešvara J., 1998. Gravimetric investigation of slope deformations. *Expl. Geophys, Remote-Sens. and Env. J.*, 1, 21-24.
- Bolt, B. A., 1982. *Inside the Earth*. San Francisco: W.H. Freeman.
- "Bondevik, S., Løvholt, F., Harbitz, C., Mangerud, J., Dawson A., Svendsen, J.I., 2005: The Storegga Slide tsunami; comparing field observations with numerical simulations. *Marine and Petroleum Geology*, 22: 195-208. "
- Borle, Y., and Jaboyedoff, M., 2007. Phénomènes érosifs dans le bassin versant de Lourtier (Valais, Suisse): étude d'une instabilité rocheuse et établissement d'un bilan sédimentaire à l'aide d'une cartographie de terrain détaillée : méthodologie et application. Master thesis in Engineering Geology. IGAR-UNIL.
- Bouillon, A.-L., 2005. Geophysics for geohazards on land: state-of-the-art, case studies and education: Dipl. Eng. Geophysics, University of Strasbourg, ICG Report 2005-T1-1, NGI Report 20051108-1, [http://www.geohazards.no/projects/geophys/ICG\\_ALB\\_Report.pdf](http://www.geohazards.no/projects/geophys/ICG_ALB_Report.pdf)
- Brodsky E. E., 2003. Landslide basal friction as measured by seismic waves. *Geophysical Research Letters*, 30, No. 24, 1-5.
- Brückl E., Mertl S., 2006. Seismic monitoring of deep-seated mass movements. In: *Disaster Mitigation of Debris Flows. Slope Failures and Landslides*, 571-580.
- Bruno, F. and Marillier, F., 2000. Test of high-resolution seismic reflection and other geophysical techniques on the Boup landslide in the Swiss Alps. *Surveys in Geophys.*, 21, 333-348.
- Burtin A., Bollinger L., Cattin R., Vergne J., Nabelek J. L., 2009. Spatio-temporal sequence of Himalayan debris flow from analysis of high-frequency seismic noise. *J. Geophys. Res.*, 114, 1-15.
- "Butler, D., 2005. *Near Surface Geophysics, SEG investigations in geophysics series; no. 13*, Ed. Butler, ISBN 1-56080-130-1."
- Cadman J.D., Goodman R.E., 1967. Landslide noise. *Science*, 158, 1182-1184.
- Caris, J.P.T. and Van Asch, Th.W.J., 1991. Geophysical, geotechnical and hydrological investigations of a small landslide in the French Alps. *Eng. Geol.*, 31, 249-276.
- Cha, Y., Kang, J., Jo, C.H., 2006. Application of linear-array microtremor surveys for rock mass classification in urban tunnel design. *Expl. Geophys.*, 37, 108-113.
- Chambers, J.E., Meldrum, P.I., Gunn, D.A., Wilkinson, P.B., Kuras, O., Weller, A.L., Ogilvy, R.D., 2009. *Hydrogeophysical Monitoring of Landslide Processes Using Automated Time-Lapse Electrical Resistivity Tomography (ALERT)*. Extended abstract, Near Surface Conference, Dublin.
- Cole S. E., Cronin S. J., Sherburn S. and Manville V., 2009. Seismic signals of snow-slurry lahars in motion: 25 September 2007, Mt Ruapehu, New Zealand. *Geophysical Research Letters*, 36, 1-5.



- 
- Cole S. E., Cronin S. J., Sherburn S., Manville V., 2008. Seismic signals associated with the 2007 lahars of Mt. Ruapehu, New Zealand. AGU, San Francisco, USA, Fall Meeting 2008, Abstract-based Poster.
- Cruden, D.M. and Varnes, D.J., 1996. Landslide types and processes. In: *Landslides investigation and mitigation*, Transportation Research Board, Special Report 247, National Academy of Sciences. Washington DC., USA, 36-75.
- Dan, G., Sultan, N. & Savoye, B. 2007: The 1979 Nice harbour catastrophe revisited: Trigger mechanism inferred from geotechnical measurements and numerical modeling. *Marine Geology* 245, 40-64.
- Dasios, A., McCann, C., Astin, T.R., McCann, D.M., Fenning, P., 1999. Seismic imaging of the shallow subsurface: shear-wave case histories. *Geophysical Prospecting*, 47, 565-591.
- De Angelis S., Bass V., Hards V., Ryan G., 2007. Seismic characterization of pyroclastic flow activity at Soufrière Hills Volcano, Montserrat, 8 January 2007. *Nat. Hazards Earth Syst.*, 7, 467-472.
- Del Gaudio, V., Wasowski, J., Pierri, P., Mascia, U., Calcagnile, G., 2000. Gravimetric study of a retrogressive landslide in Southern Italy. *Surveys in Geophys.*, 21, 391-399.
- Demoulin, A., Pissart, A., Schroeder, C., 2003. On the origin of late Quaternary palaeolandslides in the Liège (E Belgium) area. *Int. J. Earth Sci. (Geol Rundsch)*, 92, 795-805.
- Deparis J., Jongmans D., Cotton F., Baillet L., Thouvenot F., Hantz D., 2008. Analysis of rock-fall and rock-fall avalanche seismograms in the French Alps. *Bull. of the Seism. Soc. of America*, 98-4, 1781-1796.
- Dixon N., Hill R., Kavanagh J., 2003. Acoustic emission monitoring of slope instability: development of an active waveguide system. *Geotech. Eng.*, 156, 83-95.
- Dixon N., Kavanagh J., Hill R., 1996. Monitoring landslide activity and hazard by acoustic emission. *J. Geol. Soc. China*, 39, 437-464.
- Eberhardt E., Spillmann T., Maurer H., Willenberg H., Loew S., Stead D., 2004. The Randa Rockslide Laboratory: Establishing brittle and ductile instability mechanisms using numerical modelling of microseismicity. *Proc. 5th Int. Symp. on Landslides*, Rio de Janeiro, Brazil – Balkema, Rotterdam, 481-487.
- Esposito A. M., Giudicepietro F., Scarpetta S., D'Auria L., Marinaro M. And Martini M., 2006. Automatic Discrimination among Landslide, Explosion-Quake, and Microtremor Seismic Signals at Stromboli Volcano Using Neural Networks. *Bulletin of the Seismological Society of America*, 96, No. 4A, 1230-1240.
- Ferrucci, F., Amelio, M., Sorriso-Valvo, M., Tansi, C., 2000. Seismic prospecting of a slope affected by deep-seated gravitational slope deformation: the Lago Sackung, Calabria, Italy. *Eng. Geol.*, 57, 53-64.
- Foti, S., 2000, Multistation methods for geotechnical characterization using surface waves: PhD thesis, Politecnico di Torino, Italy.
- French Association for quality of applied geophysics, *Applied Geophysics, Code of Practice*, 1992. <http://www.agapqualite.org/>
- Frey-Martinez, J. 2009: 3D Seismic Interpretation of Mass Transport Deposits: Implications for Basin Analysis and Geohazard Evaluation. In D.C. Mosher et al. (eds.), *Submarine Mass Movements and Their Consequences*, *Advances in Natural and Technological Hazards Research*, Vol 28: 667-684.
- Gallipoli, M., Lapenna, V., Lorenzo, P., Mucciarelli, M., Perrone, A., Piscitelli, S., Sdao, F. 2000. Comparison of geological and geophysical prospecting techniques in the study of a landslide in southern Italy. *European J. Env. Eng. Geophys.*, 4, 117-128.
- Ganerød, G.V., Grøneng, G., Aardal, I.B., Kveldsvik, V., 2007. Logging of drill cores from seven boreholes at Åknes, Stranda municipality, Møre and Romsdal County. Geological Survey of Norway, report 2007.020.
- Ge M., 2005. Efficient mine microseismic monitoring. *International Journal of Coal Geology*, 44-56.
- Ghose, R., 2004. Model-based integration of seismic and CPT data to derive soil parameters. In: (Ed.) *Proc. 10th European Meeting of Environmental and Engineering Geophysics*, Utrecht, The Netherlands, EAGE Publications, Houten, The Netherlands, paper B019, 4 p.
- Gibert, D. and Pessel, M., 2001. Identification of sources of potential fields with the continuous wavelet transform: Application to self-potential profiles. *Geophys. Res. Lett.*, 28, 1863-1866.
- Glade, T., Stark, P., Dikau, R., 2005. Determination of potential landslide shear plane depth using seismic refraction. A case study in Rheinhessen, Germany. *Bull. Eng. Geol. Environ.*, 64, 151-158.
- Goodman R. E., Blake W., 1965. An investigation of rock noise in landslides and cut slopes. In: *Rock Mechanics and Engineering geology Supplementum II, Safety in Rock Engineering*, 15th Symposium of the Austrian Regional group (i. f.) of the International Society for Rock Mechanics, Salzburg, 24-25 September 1964.
-

- Grandjean, G. 2006. *A seismic multi-approach method for characterizing contaminated sites. Journal of Applied Geophysics.*, 58, 2, 87-98.
- Grandjean, G., and Bitri, A., 2006. 2M-SASW: Multifold multichannel seismic inversion of local dispersion of Rayleigh waves in laterally heterogeneous subsurfaces: application to the Super-Sauze earthflow, France. *Near Surface Geophys.*, 367-375.
- Green, M., and Cunningham, D. 1998: *Seabed imaging techniques. Hydro International*, 2(1): 4 pp.
- Hack, R. , 2000. Geophysics for slope stability. *Surveys in Geophys.*, 21, 423-448.
- Haflidason H., Sejrup H.P., Nygård A., Mienert J., Bryn .P, Lien R., Forsberg C.F., Berg K., Masson D. 2004: *The Storegga Slide: architecture, geometry and slide development. Mar Geol* 213:201–234.
- Hardy H. R. Jr., 1992. Laboratory studies relative to the development of mechanical waveguides for acoustic emission monitoring of geological structures: *Int. J. of Non-destructive Testing and Diagnostics*, XIII, 2, 32-38.
- Hardy, H.R. and E.J. Kimble. 1991. Application of high-frequency AE/MS techniques to rock slope monitoring. *Vth Conf. AE/MS Geol. Str. and Mat.*, edited by Hardy, Trans Tech Publication, Germany, The Pennsylvania State University, 457-477.
- Harp E. L. and Jibson R. W., 1995. Seismic instrumentation of landslides: building a better model of dynamic landslide behavior. *BSSA*, 85, No. 1, 93-99.
- Havenith, H.B., Jongmans, D., Abdrakmatov, K., Trefois, P., Delvaux, D., Torgoev, A. 2000. Geophysical investigations on seismically induced surface effects, case study of a landslide in the Suusamyr valley, Kyrgyzstan. *Surveys in Geophys.*, 21, 349-369.
- Helmstetter A., Garambois S., 2009. Seismic monitoring of Séchilienne Rockslide (French Alps): analysis of seismic signals and their correlation with rainfalls. *J. Geophys. Res.*, submitted paper.
- Helmstetter, A., and Garambois, S., 2010. Seismic monitoring of Séchilienne Rockslide (French Alps): analysis of seismic signals and their correlation with rainfalls, *J. Geophys. Res.*, 115, F03016, doi:10.1029/2009JF001532.
- Hermanns, R.L., Blikra, L.H., Naumann, M., Nilsen, B., Panthi, K.K., Stromeyer, D., Longva O., 2006: Examples of multiple rock-slope collapses from Köfels (Ötztal valley, Austria) and western Norway. *Engineering Geology*, 83: 94-108.
- Herrmann, R.B., 2002. *Computer programs in seismology. Department of Earth and Atmospheric Sciences, Saint Louis University.*
- Huang C.-J., Shieh C.-L., Yin H.-Y., 2004. Laboratory study of the underground sound generated by debris flows. *J. Geophys. Res.*, 109, 1-11.
- Huang, C.-J., Yin H.-Y., Chen C.-Y., Yeh C.-H., Wang C.-L. 2007. Ground vibrations produced by rock motions and debris flows, *J. Geophys. Res.*, 112, F02014, doi:10.1029/2005JF000437.
- Huggel C., Caplan-Auerbach J., Waythomas C. F., Wessels R. L., 2007. Monitoring and modeling ice-rock avalanches from ice-capped volcanoes: A case study of frequent large avalanches on Iliamna Volcano, Alaska. *J. of Volcanology and Geothermal res.*, 168, 114-136.
- Hughes-Clarke, J.E., Mayer, L.A., and Wells, D.E. 1996: *Shallow-water imaging multibeam sonars: A new tool for investigating sea floor processes in the coastal zone and on the continental shelf. Marine Geophysical Researches*, 18: 607-629.
- Hunter, J. A., Burns, R. A., Good, R. L., Oullan, S. E., Pugin, A., Crow, H., 2010. Near-surface geophysical techniques for geohazards investigations: some Canadian examples, *The Leading Edge*, August, 964-975.
- International Centre for Geohazards (ICG), Oslo, *Geophysics for Geohazards Theme.* <http://www.geohazards.no/projects/geophys.htm>
- Itakura M., Kaburaki H. And Arakawa C., 2005. Branching mechanism of intergranular crack propagation in three dimensions. *Physical Review E*, 71, 055102(R) 1-4.
- Jeannin, M., Garambois, S., Gregoire, S., Jongmans, D., 2006. Multi-configuration GPR measurements for geometrical fracture characterization in limestone cliffs (Alps). *Geophysics*, 71, 885-892.
- Jongmans, D., and Garambois, S., 2007. Geophysical investigation of landslides: A review. *Bulletin Société Géologique de France* 178, 2. Pp 101-112.
- Jongmans, D., Hemroulle, P., Demanet, D., Renardy, F., Vanbrabant, Y., 2000. Application of 2D electrical and seismic tomography techniques for investigating landslides. *European J. Env. Eng. Geophys.*, 5, 75-89.
-

- 
- Joswig M., 2005. *Nanoseismic Monitoring: Method and First Applications, Elaborate Tutorial on Nanoseismic Monitoring*.
- Kearey, Ph., Brooks, M., Hill I., 2002. *An introduction to geophysical exploration*. Wiley-Blackwell Publishing, 262p.
- Kennedy, B.A., and K.E. Niermeyer, 1971. *Slope monitoring systems used in the prediction of a major slope failure at the Chuquicamata Mine, Chile*. In: *Proceedings of the Conference on Planning Open Pit Mines*, Balkema, Johannesburg, 215-225.
- Kishimura K. and Izumi K., 1997. *Seismic signals induced by snow avalanche flow*. *Natural Hazards*, 15, 89-100.
- Knödel, K., G. Lange, H.-J. Voigt, 2007. *Environmental geology, Handbook for field methods and case studies*, Ed: *Bundesanstalt für Geowissenschaften und Rohstoffe*, ISBN 978-3-540-74669-0 Springer Berlin Heidelberg New York, 1357p.
- Koerner R. M., Mc Cabe W. M., Lord A. E., 1981. *Acoustic emission behaviour and monitoring of soils: Acoustic Emission in Geotechnical Practice*, ASTM STP 750, American Society for Testing and Materials, 93-141.
- Kolesnikov Y.I., Nemirovich-Danchenko M.M., Goldin S.V., Seleznev V.S., 2003. *Slope stability monitoring from microseismic field using polarization methodology*. *Nat. Haz. Earth Sys. Sc.*, 3, 515-521.
- Kousteni A., Hill R., Dixon N., Kavanagh J., 1999. *Acoustic emission technique for monitoring soil and rock slope instability*. *Proc. Int. Symp. On Slope Stability Engineering: Geotechnical and Geoenvironmental Aspects*, Matsuyama, Shikoku, Japan – Balkema, Rotterdam, 151-156.
- L'Heureux, J.-S., Hansen, L., Longva, O., Emdal, A., Grande, L. 2010: *A multidisciplinary study of submarine slides at the Nidelva fjord delta, Mid-Norway - Implications for hazard assessments*. *Norwegian Journal of Geology*.
- La Rocca M., Galluzzo D., Saccorotti G. Tinti S., Cimini G. B. and Del Pezzo E., 2004. *Seismic signals associated with landslides and with tsunamis at Stromboli Volcano, Italy*. *Bulletin of Seismological Society of America*, 94, No. 5, 1850-1867.
- Lapenna, V., Lorenzo, P., Perrone, A., Piscitelli, S., Rizzo, E., Sdao F., 2005. *2D electrical resistivity imaging of some complex landslides in Lucanian Apennine chain, southern Italy*. *Geophysics*, 70, B11-B18.
- Lapenna, V., Lorenzo, P., Perrone, A., Piscitelli, S., Rizzo, E., Sdao F., 2003. *High-resolution geoelectrical tomographies in the study of the Giarrossa landslide (Potenza, Basilicata)*. *Bull. Eng. Geol. Env.*, 62, 259-68.
- Lastras, G., Canals, M., Urgeles, R., Hughes-Clarke, J. E. & Acosta, J. 2004: *Shallow slides and pockmark swarms in the Eivissa Channel, western Mediterranean sea*. *Sedimentology* 51, 1–14.
- Lavergne, M., 1986. *Méthodes Sismiques*, Ed : TECHNIP, Paris, 207p.
- Lavigne F., 2000. *Lahars hazard micro-zonation and risk assessment in Yogyakarta city, Indonesia*. *GeoJournal*, 49, No 2, 131-138.
- Lebourg, T., Binet, S., Tric, E., Jomard H., El Bedoui, S., 2005. *Geophysical survey to estimate the 3D sliding surface and the 4D evolution of the water pressure on part of a deep seated landslide*. – *Terra Nova*, 17, 399-406.
- Lecomte, I., Thollet, I., Juliussen, H., Hamran, S.-E., 2008. *Using geophysics on a terminal moraine damming a glacial lake: the Flatbre debris flow case, Western Norway*, *Advances in Geosciences*, 14, 301-207, ICG contribution 191.
- Lin, C.-P., and Chang T.-S., 2004. *Multi-station analysis of surface wave dispersion*. *Soil Dynamics and Earthquake Engineering* 24, 877–886.
- Locat J. & Lee, H.J. 2002: *Submarine landslides: advances and challenges*. *Canadian Geotechnical Journal* 39, 193-212.
- Lockner D.A., 1993. *The role of acoustic emission in the study of rock fracture*. *Int. J. Rock Mech. Min. Sci. and Geomech. Abstr.*, 30, No 7, 883-899.
- Loke, M. H., 1999, *Electrical imaging surveys for environmental and engineering studies: A practical guide to 2-D and 3-D surveys*, [www.geometrics.com](http://www.geometrics.com), copyright by Dr. M.H. Loke.
- Longva, O., Janbu, N., Blikra, L.H. & Boe, R. 2003: *The 1996 Finneidfjord slide: seafloor failure and slide dynamics*. In: Locat, J. & Mienert, J. (eds.): *Submarine Mass Movements and Their Consequences*, 531-538. Dordrecht, Netherlands: Kluwer academic Publishers.
-

- 
- Lord A. E., Fisk C. L., Koerner R. M., 1982. Utilisation of steel rods as AE waveguides: *J. Geotech. Eng. Div., Proc. ASCE*, 108, 300-305.
- Marchi L., Arattano M., Deganutti A. M., 2002. Ten years of debris-flow monitoring in the Moscardo Torrent (Italian Alps), *Geomorphology*, 46, 1-17.
- Marescot, L., Monnet, R., Chapellier, D., 2008. Resistivity and induced polarization surveys for slope instability studies in the Swiss Alps. *Engineering Geology* 98, pp 18–28.
- Maurer, H., Spillmann, T., Heincke, B., Hauck, C., Loew, S., Spingman, M., Green, A., 2010. Geophysical characterization of slope instabilities, *First Break*, 28, August, 53-61.
- Mauritsch, H.J., Seiberl, W., Arndt, R., Romer, A., Schneiderbauer, K., Sendlhofer, G.P. 2000. Geophysical investigations of large landslides in the Carnic region of southern Austria. *Eng. Geol.*, 56, 373–388.
- McCann, D.M. and Forster, A., 1990. Reconnaissance Geophysical Methods in Landslide Investigations. *Engineering Geology* 29 (1), 59-78.
- Menke, W., 1989. *Geophysical Data Analysis: Discrete Inverse Theory. International Geophysics Series*, Ed. R. Dmowska and J. R. Holton, Academic Press, Inc., Harcourt Brace Jovanovich, Publishers. Volume 45.
- Méric O., Garambois S., Malet J.P., Cadet H., Guéguen P., Jongsmans D., 2007. Seismic noise-based methods for soft-rock landslide characterisation. *Soc. géol. Fr.*, 178 (2), 137-148.
- Méric, O., Garambois, S., Malet, J.-P., Cadet, H., Guéguen, P., Jongmans, D., 2007. Seismic noise-based methods for soft-rock landslide characterization. *Bull. Soc. Geol. France*, 178, 2, 137-148.
- Méric, O., Garambois, S., Orengo Y., 2006. Large gravitational movement monitoring using a spontaneous potential network. In: *Proc. 19th Annual meeting of SAGEEP, Seattle, USA, EEGS Ed., Denver, USA*, 6 p.
- Méric, O., Garambois, S., Jongmans, D., Wathélet, M., Chatelain, J.-L., Vengeon, J.-M., 2005. Application of geophysical methods for the investigation of the large gravitational mass movement of Séchilienne, France. *Can. Geotech. J.*, 42, 1105-1115.
- Milsom, J., 2003. *Field Geophysics, Third Edition. The Geological Field Guide Series*, Wiley, ISBN 0-470-84347-0.
- Mourot P., 2008. *Méthodes et outils pour l'auscultation et la surveillance des instabilités gravitaires. Thèse de Doctorat, Laboratoire de Géophysique Interne et de Tectonophysique, Université de Savoie, Chambéry.*
- Mucciarelli M., Gallipoli M. R., 2001. 10 years of Nakamura's technique: a review of theory, experiments and applications. *Bollettino di Geofisica Teorica ed Applicata*, 42, 3-4, 255-266.
- Nakamura Y., 1989. A method for dynamic characteristics estimation of subsurface using microtremor on ground surface. *Quar. Report. Railway. Tech. Res. Institute*, 30, 25-33.
- Nakamura Y., 1989. A method for Dynamic Characteristics estimation of subsurface using microtremor on the ground surface. *Quarterly Report of railway Technical Research Institute (RTRI)*, 30, No. 1.
- Nakazato H., Kuroda S., Okuyama T., Sasaki Y., 2006. The aim at a rich rural village utilizing water and soil. Improvement of production basis for improving productivity and exhibiting many-sided functions, and development of management techniques. Improvement of airborne electromagnetic method and three-dimensional resistivity distribution exploration in landslide areas. *Mizu to Tsuchi o Ikashi Yutakana Noson o Mezashite Saishin Nogyo Kogaku Kenkyu Seikashu Heisei 18nen*, pp 216-217.
- Nanoseismic monitoring - <http://nanoseismic.net>
- Nguyen, F., Garambois, S., Jongmans, D., Pirard, E., Locke, M., 2005. Image processing of 2D resistivity data to locate precisely faults. *J. App. Geophys.*, 57, 260-277.
- Nicholson, C., 1992. Recent developments in rockburst and mine seismicity research. In: T.A. Wawersik (Ed.), *Rock Mechanics*, Balkema, Rotterdam, 1079-1086.
- Novosad S., Blaha P., Kneizlik J., 1977. Geoacoustic methods in the slope stability investigation. *Bull. of the Int. Ass. of Engineering Geology*, 16, 228-231.
- Obert, L., 1977. The microseismic method: discovery and early history. *First conf. on acoustic emission / microseismic activity in geologic structures and materials*, Trans Tech Publications, 11-12.
- Obert L., 1941. Use of subaudible rock noises for prediction of rock bursts. *United States Bureau of Mines RI* 3555.
- Obert L., Duvall W., 1942. Use of subaudible rock noises for prediction of rock bursts. Part II, *United States Bureau of Mines RI* 3654.
-

- 
- Obert L., Duwall W., 1945a. *Microseismic method of predicting rock failure in underground mining. Part I, General Methods*, United States Bureau of Mines RI 37m97.
- Obert L., Duwall W., 1945b. *Microseismic method of predicting rock failure in underground mining. Part II, Laboratory Experiments*, United States Bureau of Mines RI 3903.
- Obert L., Duwall W., 1957. *Microseismic method of determining the stability in underground workings*. United States Bureau of Mines Bulletin 573.
- Observatoire des Instabilités de Versants - [http://eost.u-strasbg.fr/omiv/Super\\_Sauze\\_intro.html](http://eost.u-strasbg.fr/omiv/Super_Sauze_intro.html)
- Palacky, G.J., 1987. Resistivity characteristics of geologic targets. *Geosciences Journal*, 3, 138-144.
- Park, C.B., Miller, R.D., Xia, J., 1999. Multichannel analysis of surface waves. *Geophysics* 64, 800–808.
- Park, C.B., Miller, R.D., Xia, J., 2001. Offset and resolution of dispersion curve in multichannel analysis of surface waves (MASW): *Proceedings of the SAGEEP 2001*, Denver, Colorado, SSM4.
- Patella, D., 1997. Introduction to ground surface self-potential tomography. *Geophys. Prospect.*, 45, 653–681.
- Pettinelli, E., Beaubien, S., Tommasi, P., 1996. GPR investigations to evaluate the geometry of rock slides and bulking in a limestone formation in northern Italy. *European J. Env. Eng. Geophys.*, 1, 271-286.
- Pfaffhuber A.A., Grimstad E., Domaas U., Auken E., Halkjær M., 2010. The hunt for sliding planes in a phyllitic rock slide in Western Norway using airborne electromagnetic mapping, *EGU General Assembly 2010*, *Geophysical Research Abstracts*, 12, EGU2010-4492.
- Pinson, L., Henstock, T.J., Dix, J., Bull, J.M. 2008: Estimating quality factor and mean grain size of sediments from high-resolution marine seismic data. *Geophysics*, VOL. 73, NO. 4
- Polom, U., Hansen, L., Sauvin, G., L'Heureux, J.-S., Lecomte, I., Krawczyk, C. M., Vanneste, M., Longva, O., 2010. High-resolution SH-wave Seismic Reflection for Characterization of Onshore Ground Conditions in the Trondheim Harbor, Central Norway, *Geophysical References*, Society of Exploration Geophysicists, in press.
- Pugin, A.J.M., Larson, T.H., Sargent, S.L., McBride, J.H., Bexfield, C.E., 2004. Near –surface mapping using SH-wave and P-wave seismic land-streamer data acquisition in Illinois, U.S.: *The Leading Edge*, 23, 677-682.
- Rankka, K., Andersson-Sköld, Y., Hultén, C., Larsson, R., Leroux, V., and Dahlin, T., 2004, *Quick clay in Sweden*, Swedish Geotechnical Institute, report 65.
- Renalier F., Bièvre, G., Jongmans, D., Campillo, M., Bard, P.-Y., 2010. Characterization and monitoring of unstable clay slopes using active and passive shear wave velocity measurements, *SEG reference publications*, in press.
- Renalier F., Jongmans, D., Campillo, M., Bard, P.-Y., 2010. Shear wave velocity imaging of the Avignonet landslide (France) using ambient noise cross correlation, *Journal of Geophysical Research*, 115, F03032, 14p.
- "Reynolds, J.M. 1992. ""The identification and mitigation of glacier-related hazards: examples from the Cordillera Blanca, Peru."" In: McCall, G.J.H., Laming, D.C.J. and Scott, S. (Eds), *Geohazards*, London, Chapman & Hall, 143-157."
- Reynolds, J.M., 1997. *An introduction to applied and environmental geophysics*, John Wiley & Sons, Chichester, 806 pp., ISBN 0-471-95555-8.
- Reynolds, J.M., 2006. Role of geophysics in glacial hazard assessment, *First Break*, 24, no. 8, August, 61-66.
- Roch, K.H., Schwatal, B., Bruckl, E., 2006. Potentials of monitoring rock fall hazards by GPR: considering as example the results of Salzburg. *Landslides*, 3, 87-
- Rømoen, M., Pfaffhuber, A.A., Karlsrud, K., Helle, T. E., 2010. The use of a CPTU-probe with resistivity module on marine sediments. *CPT'10: 2nd international symposium on Cone Penetration Testing*, Huntington Beach, California.
- Rønning, J.S., Dalsegg, E., Elvebakk, H., Ganerød, G., Tønnesen, J.F., 2006. *Geofysiske målinger Åknes og Tafford, Stranda og Nordal kommuner, Møre og Romsdal*. Geological Survey of Norway, report 2006.02, in Norwegian.
- Rønning, J.S., Dalsegg, E., Heincke, B., Tønnesen, J.F., 2007. *Geofysiske målinger på bakken ved Åknes og ved Hegguraksla, Stranda og Nordal kommuner, Møre og Romsdal*. Geological Survey of Norway, report 2007.26, in Norwegian.
-

- Roth M., Dietrich M., Blikra L. H., Lecomte I., 2005. *Seismic monitoring of the unstable rock slope site at Åknes, Norway. NORSAR Report.*
- Rouse C., Styles P. and Wilson S. A., 1991a. *Acoustic Emissions from two Landslip Areas in South Wales. Z. Geomorph. N. F., Suppl.-Bd. 83, 135-154.*
- Rouse C., Styles P., Wilson S.A., 1991b. *Microseismic emissions from flowslide-type movements in South Wales. Engineering Geology, 31, 91-110.*
- Rubin, Y., and Hubbard, S.,(2005. Eds: Springer, The Netherlands, 530 pp.
- Sailhac, P., and Marquis, G., 2001. *Analytic potentials for the forward and inverse modeling of SP anomalies caused by subsurface fluid flow. Geophys. Res. Lett., 28, 1851-1854.*
- Sasaki Y., Nakazato H., 2004. *Inversion of airborne EM data accounting for terrain and inaccurate flight height, SEG Expanded Abstracts 23, 648.*
- Schmutz, M., Albouy, Y., Guérin, R., Maquaire, O., Vassal, J., Schott, J.-J., Descloîtres, M., 2000. *Joint electrical and time domain electromagnetism (TDEM) data inversion applied to the Super Sauze earthflow (France). Surveys in Geophys., 21, 371-390.*
- Seigel, H.O., 1995 *A guide to high precision land gravimeter surveys. Scintrex Limited, Concord, Ontario, Canada, p122*
- Seabeam 1999: *Multibeam Sonar - Theory of Operation. 2101-8289*
- Senfaute G., Duperret A., Lawrence J. A., 2009. *Micro-seismic precursory cracks prior to rock-fall on coastal chalk cliffs: a case study at Mesnil-Val, Normandie, NW France. Nat. Hazards Earth Syst. Sci., 9, 1625-1641.*
- SESAME European research project, 2004. *Guidelines for the implementation of the H/V spectral ratio technique on ambient vibrations - Measurements, processing and interpretation. WP12 – Deliverable D23.12, European Commission – Research General Directorate, Project No. EVG1-CT-2000-00026, p62.*
- "Sherif, R.E., 2002. *Encyclopedic Dictionary of Applied Geophysics, fourth edition, Society of Exploration Geophysicists, ISBN 9781560801184 (13); 1560801182 (10), 429 p.*"
- Shiotani T., 2006. *Evaluation of long-term stability for rock slope by means of acoustic emission technique. NDT&E International, 39, 217-228.*
- Socco, V. and Jongmans, D., 2004. *Special issue on Seismic Surface Waves. Near Surf. Geophys., 2, 163-258.*
- Solberg, I.L., Rønning, J.S., Dalsegg, E., Hansen, L., Rokoengen, K., Sandven, R., 2008. *Resistivity measurements as a tool for outlining quick-clay extent and valley-fill stratigraphy: a feasibility study from Buvika, central Norway. Canadian Geotechnical Journal, 45: 210-225, doi:10.1139/T07-089.*
- Spillmann T., Maurer H., Green G. A., Heincke B., Willenberg H., Husen S., 2007. *Microseismic investigation of an unstable mountain slope in the Swiss Alps. J. Geophys. Res., 112.*
- Steffens G.S., Shipp R.C., Prather B.E., Nott J.A., Gibson J.L., and Winker C.D. 2004: *The use of near seafloor 3D seismic data in deepwater exploration and production. In Davies R.J., Cartwright J.A., Stewart S.A., Lappin M., and Underhill J.R. (eds.), 3D Seismic Technology: Application to the Exploration of Sedimentary Basins. Geol Soc Spec Publ 29:35–43.*
- Stuart G., Murray T., Brisbourne A., Styles P. And Toon S., 2005. *seismic emissions from a surging glacier: Bakaninbreen, Svalbard. Annals of Glaciology, 42, 151-157.*
- Supper, R., Ahl, A., Römer, A., Jochum, B., Bieber, G., 2008. *A complex geo-scientific strategy for landslide hazard mitigation - from airborne mapping to ground monitoring, Advances in Geosciences, 14, 1-6.*
- Supper, R., and Römer, A., 2003. *New achievements in developing a high speed geoelectrical monitoring system for landslide monitoring. In: Proc. 9th Meeting Env. Eng. Geophys., Prague, Czech Republic, EAGE Publications, Houten, The Netherlands EEGS Ed., O-004.*
- Suriñach E., Sabot F., Furdada G., Vilaplana J. M., 2000. *Study of seismic signals of artificially released snow avalanches for monitoring purposes. Phys. Chem. Earth (B), 25, 721-727.*
- Suriñach E., Vilajosana I., Khazaradze G., Biescas B., Furdada G., Vilaplana J. M., 2005. *Seismic detection and characterization of landslides and other mass movements, Natural Hazards and Earth System Sciences, 5, 791-798.*
- Suwa H., Mizuno T., Suzuki S., Yamamoto Y., Ito K., 2008. *Sequential processes in a landslide hazard at a slate quarry in Okayama, Japan. Nat. Hazards, 45, 321-331.*



- 
- Suwa H., Yamakoshi T., Sato K., 2000. Relationship between debris-flow discharge and ground vibration, *Debris-Flow Hazards Mitigation: Mechanics, Prediction, and Assessment, Proceedings of the Second International Conference on Debris-Flow Hazards Mitigation, Taipei/Taiwan 16-18 August 2000*, 311-318.
- Swiss Geophysical Commission, *Quality guidelines for geophysical methods*. <http://www.sgpk.ethz.ch/>
- Tonnellier A., Malet J.-P., Joswig M., Walter M., Corsini A. 2010. Landslides under microscope: understanding slow-moving landslides through passive micro-seismic monitoring. *International Conference TRAMM 'Triggering of Rapid Mass Movements in Steep Terrains - Mechanisms and Risk'*, 21-25th April 2010, Monté Verità, Switzerland. Abstract-based poster.
- US Army Corps of Engineers, 1995. *Geophysical Exploration for Engineering and Environmental Investigations*. Manual No. 1110-1-1802. 207 p.
- US Army Corps of Engineers, 2001. *Geotechnical Investigations. Engineering and Design*. Manual No. 1110-1-1804. 449 p.
- Van Westen, C.J., 2004. Geo-Information tools for landslide risk assessment: an overview of recent developments. In: *Proc. 9th International. Symp. Landslides, Rio de Janeiro, Brazil, Balkema, Rotterdam*, 39-56.
- Walter M., Joswig M., 2008. Seismic monitoring of fracture processes generated by a creeping landslide in the Vorarlberg Alps. *First Break*, 26, 131-135.
- Walter M., Joswig M., 2009b. Seismic characterisation of slope dynamics caused by softrock-landslides: The Super-Sauze case study, In: Malet, J.-P., Remaitre, A., Boogard, T.A. (Eds.): *Proceedings of the International Conference on Landslide Processes: from geomorphologic mapping to dynamic modelling*, Strasbourg, CERG Editions, 215-220.
- Walter M., Niethammer U., Rothmund S., Joswig M., 2009a. Joint analysis of the Super-Sauze (French Alps) mudslide by nanoseismic monitoring and UAV-based remote sensing. *First Break*, 27, 53-60.
- Wang H., Ge M., 2007. Acoustic emission/microseismic source location analysis for a limestone mine exhibiting high horizontal stresses. *Int. J. of Rock Mechanics & Mining Sciences*, 45, 720-728.
- Wiechert D., Horner R. B., Evans S. G., 1994. Seismic Signatures of Landslides: the 1990 Brenda Mine Collapse and the 1965 Hope Rockslides. *Bull. of the Seism. Soc. of America*, 84-5, 1523-1532.
- Wilkinson, P.B., Chambers, J.E., Meldrum, P.I., Gunn, D.A., Kuras, O., Ogilvy, R.D., 2010. Tracking the movements of electrodes on an active landslide over time using only timelapse resistivity data. Extended abstract, *Near Surface Conference, Zurich*.
- Wilkinson, P.B., Chambers, J.E., Meldrum, P.I., Gunn, D.A., Kuras, O., Ogilvy, R.D., 2010. Tracking the movements of electrodes on an active landslide over time using only timelapse resistivity data. Extended abstract, *Near Surface Conference, Zurich*.
- Willenberg H., Evans K.F., Eberhardt E., Loew S., Spillmann T., Maurer H., 2004. Geological, geophysical and geotechnical investigations into the internal structure and kinematics of an unstable sliding mass in crystalline rock. *9th Internat. Symp. on Landslides, Rio de Janeiro*, 489-494.
- Willenberg, H., Evans, K.F., Eberhardt, E., Loew, S., Spillmann, T., Maurer, H.R., 2004. Geological, geophysical and geotechnical investigations into the internal structure and kinematics of an unstable, complex sliding mass in crystalline rock. In: *Proc. 9th International. Symp. Landslides, Rio de Janeiro, Brazil, Balkema, Rotterdam*, 489-494.
- Wisén, R., Auken, E., Dahlin, T., 2005. Combination of 1D laterally constrained inversion and 2D smooth inversion of resistivity data with a priori data from boreholes. *Near Surf. Geophys.*, 3, 71-79.
- Wisén, R., Christiansen, A.V., Auken, E., Dahlin, T., 2003. Application of 2D laterally constrained inversion and 2D smooth inversion of CVES resistivity data in a slope stability investigation. In: *Proc. 9th Meeting Env. Eng. Geophys., Prague, Czech Republic, EAGE Publications, Houten, The Netherlands*, O-002.
- "Wüst-Bloch G. H., Joswig M., 2006. Pre-collapse identification of sinkholes in unconsolidated media at Dead Sea area by "nanoseismic monitoring" (graphical jackknife location of weak sources by few, low-SNR records). *Geophys. J. Int.*"
- Xia, J., Miller, R.D., Park, C.B., 1999. Configuration of near surface shear wave velocity by inverting surface wave. *Proceedings of Symposium on the Application of Geophysics to Engineering and Environmental Problems '99*, pp. 95-104.
-

- Yang C., Luo Z., Hu G., Liu X., 2007. *Application of a microseismic monitoring system in deep mining. J. of Uni. of Science and Technology of Beijing*, 14-1, 6-8.
- Zhang, S., Hong Y., Yu B. 2004. *Detecting infrasound emission of debris flows for warning purposes. In: Proc. 10th Congress INTERPRAEVENT 2004*, pp. Z/359–Z/364, Riva del Garda, Trento, Italy, 24-27 May 2004.
- Zhdanov, M.S., 2002. *Geophysical inverse theory and regularization problems. Elsevier, Amsterdam New-York*, 628 pp.
- Zimmer V. L., Stock G. M., Sitar N., 2008. *Seismic Monitoring of Rock Falls in Yosemite National Park. AGU, San Francisco, USA, Fall Meeting 2008, Abstract-based Poster.*
- Zobin V. M., Placencia I., Reyes G. and Navarro C., 2009. *The characteristics of seismic signal produced by lahars and pyroclastic flows: Volcán de Colima, Mexico. Journal of Volcanology and Geothermal Research*, 179, 157-167.
- Zyatev G. G., Merkulov V. P., Nikolsky A. A., 1998. *The reflection of landslip processes in geophysical fields, 60th EAGE Conf. and techn. Exhib., Leipzig, 8-12 June 1998, Oral and Poster Present., Geophys. Div., Extend. Abstr. Book, Leipzig, 121.*

## 6.6. SPECIFIC REFERENCES FOR THE CHAPTER 2E

- Burland, J.B, More, J.F.A., Smith, P.D.K. *A simple and precise borehole extensometer. Geotechnique*, Vol. 22, No1, pag 174-177. 1972.
- Corominas, J., Moya, J., Lloret, A., Gili, J.A., Angeli, M.G., Pasuto, A. Silvano, S. *Measurement of landslide displacements using a wire extensometer. Engineering Geology*, vol. 55, issue 3, pp. 149-166. 2000.
- Dunnicliff, J., assisted by Green, G.E. *Geotechnical instrumentation for monitoring field performance. Wiley-Interscience Publication*, 577 p. 1988-1993.
- Dunnicliff, J., La Fonta, J.G. *In place inclinometers. A significant test program. Geotechnical News*, vol. 19, n°1, March, pp. 33-34. 2001.
- Dunnicliff J. et al. *Geotechnical instrumentation for field measurements. Training course, March 13-15, 2005. The University of Florida. 2005.*
- Kovari, K. *Detection and monitoring of structural deficiencies in the rock foundation of large dams. 5<sup>th</sup> Int. Conf. Large Dams. Lausanne*, pp. 695-719. 1985.
- Kovari, K. *Methods of monitoring Landslides. Proc. 5<sup>th</sup> Int. Symp. On Landslides. Lausanne*, vol. 3, 14 p. 1988.
- La Fonta, J.G., Beth, M.B. *In place inclinometers, a significant test program. SolData-France. 2002.*
- Lollino, G. *Automated Inclinometric System. Proceedings of the Sixth International Symposium on Landslides. 10-14 February 1992, Christchurch, New Zealand. 1992.*
- Lovisolo, M., Della Giusta, A. *Precision of D.M.S. columns from real time in-place measurements and improvement in micro-movements analysis with early warning function. In: Computational Methods and Experimental Measurements XII (Brebbia, C.A. and Carlomagno, G.M.). WITpress, Southampton, Boston*, pp.177-186. 2005.
- Machan, G., Bennett, V.G. *Transportation research circular n° E-C129. Use of Inclinometers for Geotechnical Instrumentation on Transportation Projects - State of the Practice. Transportation Research Board, Washington. 2008.*
- Mikkelsen E. *Piezometers in fully grouted boreholes. In: Field Measurements in Geomechanics. OSLO (Myrvoll F., ed.). Balkema Publishers*, pp. 545-554. 2003a.
- Mikkelsen E. *Advances in inclinometer data analysis. In: Field Measurements in Geomechanics. OSLO (Myrvoll F., ed.). Balkema Publishers*, pp. 555-567. 2003b.

## 6.7. SPECIFIC REFERENCES FOR THE CHAPTER 2F

- Bell, F.G. *Engineering Geology. Second edition. Butterworth-Heinemann. 584 p. 2007.*
- Bonnard, Ch., Noverraz, F., Dupraz, H. *“Long-term movements of substabilized versants and climatic changes in the Swiss Alps”. Proceed. 7th Int. Symp. On Landslides, Troidheim, Vol. 3, 1525-1530. 1996.*

- 
- Brunner, F.K., Woschitz, H., Macheiner, K. Monitoring of deep-seated mass movements. In: *Proc. of. The 3rd International Conference on Structural Health Monitoring of Intelligent Infrastructure, Vancouver, Canada. CD-ROM*, 10 p. 2007.
- Chen, Y., He, X., , Ding, X., Sang, W. Steep-Slope Monitoring: GPS Multiple-Antenna System at Xiaowan Dam. *GPS World Magazine*, November 2005, 4p. 2005.
- ClimChalp. Slope Monitoring Methods, A State of the Art Report. ClimChalp is an European Regional Development Project, within the framework of the INTERREG IIIB Alpine Space Programme. The Report of the Work Package 6, was released in Munich, 28.2.2008. 179 p. 2008.
- Gili, J.A., Corominas, J., Rius, J. Using Global Positioning System techniques in landslide monitoring. *Engineering Geology*, 55, pp. 167-192. 2000.
- Malet, J.P., O. Maquaire and E. Calais. The use of Global Positioning System techniques for the continuous monitoring of landslides: application to the Super-Sauze earthflow (Alpes-de-Haute-Provence, France). *Geomorphology*, Volume 43, Issues 1-2, 1 February 2002, pp 33-54. 2002.
- McGuffey, V.C., Modeer, V.A. Jr, Turner, A.K. Subsurface exploration. In: *Landslides, investigation and mitigation*. Tuner, A.K., Schuster, L., editors. Special report 247, Transportation Research Board, National Research Council. 678 p. 1996.
- Schäfer, T. "GPS observations at Mt. Hochstaufen. Practice Example A11 in ClimChalp (2008), pp. 137-142. 2008.
- US Army Corps of Engineers. Geotechnical Investigations. Engineering and Design. Manual No. 1110-1-1804. 449 p. 2001.



# **GLOSSARY**





## 7. GLOSSARY

<b>Accuracy (applied for TLS)</b>	This parameter measures the degree of closeness of a measurement to the real value. The accuracy of a laser measurement is a main function of the range, the reflectivity of the material, the complexity of the scanned surface and the angle of incidence. For monitoring purposes, the accuracy of a given TLS dataset can be estimated through the estimation of the precision of the measurement, i.e., through the comparison of two different point clouds acquired consecutively
<b>Affine Polynomial Model</b>	Set of equations describing the relation of an image to the local reference system in terms of translation, rotation, scaling and distortion
<b>Airborne Electromagnetics</b>	Airborne geophysical method to determine the distribution of the specific electrical resistivity within the subsurface
<b>Airborne geophysics</b>	Geophysical approach which uses sensors that are either mounted on an aircraft or dragged on a cable several tens of meters below the aircraft (an airplane or a helicopter)
<b>Ascending / Descending orbit</b>	South-North / North-South trajectory of the platform.
<b>Azimuth (SAR context)</b>	Distance along the spaceborne flight direction. The azimuthal resolution can be performed by Synthetic Aperture Radar techniques.
<b>Change Detection (Lidar)</b>	The study of the changes or differences that occur during a given portion of time. The sign of the differences depend on the computation technique. But it is common to attribute negative signs to areas that are behind or below the reference surface (i.e. detachment of material) and positive values to areas that are in front or above the reference surface (i.e. scree deposits, advance of a landslide etc.).
<b>Change Detection (Passive Optical Data)</b>	Detection and characterization of episodic or sudden changes by comparison of at least two different images of the same earth surface area. Main criteria for changes are variations in the surface reflectance in several multispectral bands.
<b>Comparison of TLS datasets</b>	The process of point cloud alignment plus change detection. As an output of the process, changes in the slope during the time span (i.e. displacements, rockfall occurrence, deposition, etc), are recorded
<b>Complex signal</b>	Each pixel is registered by a complex number, keeping the information on the amplitude and the phase of the return signal. This is the raw data for an InSAR study.
<b>Data Fusion</b>	Methods for the combination of the data to optimize the utilization of large volumes of data from multiple sources.
<b>Digital Image Correlation</b>	Comparison of grey value co-occurrence within a search window in two images. Points of maximum correlation are used for the co-registration of the two images or two evaluate the displacement of pixels or group of pixels.

---

<b>DInSAR</b>	Differential InSAR. Technique aiming at separating topographic and deformation components of the InSAR phase information. It is based on subtraction of the topographic component (derived from short time span interferograms or simulation using DEM) in order to retrieve the deformation component and map the ground surface deformation. SBAS and PSI are advanced evolutions of the DINSAR technique.
<b>Ephemerides</b>	Satellite position and velocity vectors at any time $t$
<b>Fringe</b>	Line of an interferogram corresponding of one color cycle.
<b>G.C.P</b>	For Ground Control Point: an easily identifiable object with known coordinates used for the geometrical correction of maps and remote sensing imagery.
<b>Gamma-Ray spectroscopy</b>	Measurement of natural gamma radiation at different energy values
<b>Geometric correction</b>	Modeling of systematic and non-systematic geometric errors to derive a relationship between the image and a global coordinate system
<b>GNSS</b>	Global Navigation Satellite System, a radionavigation, timing and positioning system that can provide the user 3D position. This acronym is the common one to enclose the GPS (USA), the GLONASS (former soviet union), the GALILEO (EU), the Beidou (China), and other future satellite navigation systems.
<b>GPS</b>	See GNSS
<b>Ground range</b>	Distance along the perpendicular of the flight direction on the ground's surface. The range resolution can be performed emitting chirped pulses.
<b>Ground Sampling Distance</b>	Measure of the distance between two adjacent samples in an image
<b>Ground-based geophysics</b>	Geophysical approach using sensors located either on the ground (non-intrusive methods) or in boreholes. Also called near-surface geophysics.
<b>Homogenous half space model</b>	Numerical model which describes the ground subsurface with a uniform electrical resistivity $\rho_1$ derived from a multilayer AEM dataset
<b>Image Mining</b>	Automation of the extraction of implicit knowledge, image data relationship, or other patterns not explicitly stored in the imagery in large archives.
<b>InSAR</b>	SAR interferometry. Technique based on the difference of the phase values between two SAR acquisition. The phase difference (interferometric phase) contains geometric information that could be related to ground surface altitude (in order to produce DEM) or deformation.
<b>Intensity</b>	The intensity is defined as the amount of reflected signal with respect to the emitted one. Its value is usually normalized on a 0-255 scale. the intensity parameter mainly depends on the range, angle of incidence, soil moisture, and object material

---

---

<b>Joint interpretation</b>	Used in ground-based geophysics to describe an interpretation process (manual or automated) where results obtained by different methods (e.g., after inversion for each method) are somehow merged to reach a more complete conclusion about the ground under investigation.
<b>Joint inversion</b>	Used in ground-based geophysics to describe an inversion approach where parameters obtained from different methods (e.g., elastic and electrical) are obtained together during the same inversion process, these parameters constraining each others.
<b>LIDAR</b>	Acronym for Light Detection and Ranging. Optical remote sensing technology measures the properties of scattered light to find range and/or other information about a distant target. This can be an Aerial (ALS) or Terrestrial (TLS) Laser Scanning instrument
<b>Look angle <math>\theta</math></b>	Angle between the vertical and the LOS.
<b>LOS</b>	For Line of Sight: an imaginary line from the sensor (optical, radar, laser, etc) to the surveyed point. Direct visibility along this line is mandatory when distance calculation.
<b>Master / Slave images</b>	Reference / comparative images in interferometry.
<b>Model inversion</b>	Find the most suitable parameter model fitting to a set of measurements
<b>Nadir</b>	Projection on the Earth's surface of the platform's trajectory
<b>Near / Far range</b>	Part of the image closest to / furthest from the Nadir.
<b>Object-Oriented Image Analysis</b>	Grouping of image pixels into homogenous and meaningful objects and consequent image analysis incorporating additional object features such as texture, shape and neighborhood relationships.
<b>Penetration depth</b>	Ground-based geophysics: characterize the depth which can be reached and investigated depending of the type of method (seismic, ERT, GPR, etc), the geometry of the survey (e.g., distance between emitters and receivers), the used frequencies, etc. Note that there is often a natural trade-off between penetration depth and resolution: the higher the depth, the lower the resolution because high frequencies - good for high resolution - cannot propagate far due to attenuation, etc.
<b>Point Cloud</b>	A large quantity of 3D points acquired by the ALS/TLS through a rangefinder method, also referred to as ALS/TLS scans or datasets. A point cloud can be considered a "data point cloud" or "reference point cloud"
<b>Pseudo depth sections</b>	Representation of geoelectric measurement results; apparent resistivities are displayed according to the separation of current electrodes, not real depths
<b>Radiometric correction</b>	Pre-processing steps that involve correction of sensor, atmospheric or topographic effects on the recorded radiance in one image (absolute correction), or target the equalization of two or more images that have been recorded under distinct conditions.

---

<b>Range</b>	The distance between the sensor (i.e. TLS, GB-SAR) and the portion of the terrain for which the coordinates are acquired
<b>Rational Function Model</b>	Ratio of two polynomial functions relating 3-D surface coordinates to 2-D image coordinates.
<b>Resolution (airborn imaging)</b>	This parameter determines the level of detail that can be observed from a scanned point cloud. It can be divided into range and angular (or spatial) resolution. The estimation of the TLS resolution is usually misunderstood and commonly interpreted as equal to the point spacing or sampling interval, obviating the influence of the laser beam width.
<b>Resolution (ground-based geophysics)</b>	Resolution - in the strict mathematical sense of an inversion problem - characterizes whether searched parameters can be independently determined or resolved from a certain data set and assuming a model between data and the searched parameters. In a simpler manner, and considering imaging (e.g., seismic, ERT, etc), the level of resolution tells how detailed an image can be. In seismic imaging, a rule of thumb is to state that resolution is a quarter of the minimum wavelength (velocity divided by frequency).
<b>SAR</b>	Synthetic Aperture Radar. System designed for providing higher resolution than conventional radar systems (synthetic aperture compared to real aperture). Processing of the complex value (amplitude related to the backscattered energy and phase related to the distance between the sensor and the targets ) of the backscattered signal acquired with a sampling rate compatible with the expected resolution, allows to relocate the targets contributing to the signal in order to obtain a finer image. Typically, spaceborne SAR resolutions range from the metre to tens of metres.
<b>Scan of Reference</b>	The first TLS dataset acquired for a certain area. Subsequent datasets are aligned towards this dataset.
<b>Shannon sampling theorem</b>	Fundamental work from information theory stating that a signal can be lossless reconstructed from samples taken at intervals two times shorter than the highest frequency of the signal.
<b>Slant range</b>	distance along the perpendicular of the azimuth on the SAR image. The slant range can be different of the ground range due to geometrical distortion.
<b>Spot Dimension</b>	The projection of the laser beam on the ground or target area. Although the laser signal is highly collimated, the spot dimension increases its value with the distance (e.g. 2.1 mm at 50 meters and 9.6 mm at 500 m). This parameter is also referred to as laser beamwidth at a given distance.
<b>Stereoprocessing</b>	Techniques involving the identification of corresponding objects in two or more images and the derivation of their 3D coordinates by point triangulation.
<b>Supervised Classification</b>	Areas with a know class memberships in an image are used as samples to train a classification algorithm. The trained algorithm is then used to classify the rest of the image or other scenes.

<b>TLS</b>	Acronym for Terrestrial Laser Scanner. This instrument consists of a transmitter/receiver of infrared laser pulses and a scanning device mounted over a ground-based platform. Range measurements with centimetric accuracy can be undertaken at a high speed rate. As a result, 3D coordinates of million points are obtained.
<b>Tomography</b>	The word "tomography" is derived from the Greek tomos (part) and graphein (to write). Tomography is imaging by sections or sectioning, through the use of any kind of penetrating wave. In ground-based geophysics tomography can be performed in various ways, e.g., using traveltimes of elastic waves (seismic) or electromagnetic waves (Ground Penetrating Radar - GPR), or apparent resistivity measurements (Electrical Resistivity Tomography - ERT), etc.
<b>Track / Frame</b>	Est-West / North-South limit of a SAR image.
<b>Two strata model</b>	Numerical model which describes the ground subsurface with 2 layers of different thickness (h) and resistivity ( $\rho$ ) derived from a multilayer AEM dataset
<b>Unsupervised Classification</b>	Automatic categorization or clustering of a digital image data into a number of predefined or statistical optimal classes.